Crystallography Reports, Vol. 46, No. 2, 2001, pp. 161–166. Translated from Kristallografiya, Vol. 46, No. 2, 2001, pp. 199–204.

CRYSTALLOGRAPHIC SYMMETRY

Diophantine Laws for Nets of the Highest Symmetries

I. A. Sheremet'ev

Chelyabinsk State University, Chelyabinsk, Russia

e-mail: sheri@cgu.chel.su

Received December 14, 1998

Abstract—The theoretical–numerical properties of the square and the hexagonal nets are presented as well as their characteristic triads of integers—the Denis numbers—applicable to the practical X-ray diffraction analysis of single crystals. © *2001 MAIK "Nauka/Interperiodica".*

In deep grief, I dedicate this article to Russian sailor Denis Sheremet'ev and his shipmates, who passed away.

INTRODUCTION

Notation. *Pythagorean triangle*: a right triangle with integral sides; *Heron triangle*: a triangle with integral area and integral sides; *triangle cotangents*: the cotangents of the internal angles of a triangle; *an empty triangle* (after Academician Belov): a triangle of the net (two-dimensional lattice) with all the nodes being located at the vertices; *S* and *H triangles*: empty triangles of the square and hexagonal nets, respectively; *a primate*: a primitive lattice vector whose crystallographic indices are mutually simple numbers; *to cure*: to convert a number into an integer.

Up to now, two families of integral or Diophantine triangles are known—Pythagorean and Heron. The law of Pythagorean triangles—or the so-called Pyphagorean numbers ($P_1 = u^2 - v^2$, $P_2 = 2uv$, and $P_3 = u^2 + v^2$)—was discovered by Pythagoreans. In the theory of numbers, the law of Heron numbers has not been established as yet. Pythagoras' creative work dates back to the 6th century B.C.; Heron and Diophant worked in the 1st and the 3rd centuries A.D., respectively. P. Fermat wrote down his famous theory of numbers and the formulation of the Diophantine problem on the margins of Diophant's *Arithmetics* in 1665. In physics and crystallography, Pythagorean and Heron triangles and the Pythagorean numbers have not been used as yet. To close this gap, we consider below the astonishing laws of "square" (*S*) and "hexagonal" (*H*) triangles and triads, which follow from these triangles (called here the Denis numbers), which transform the *S* and *H* triangles into Diophantine ones. Then, we shall demonstrate the heuristic nature of the new triads for structural studies on an example of the Laue method well known in X-ray diffraction analysis.

To obtain the most important results of the present study, we used the logical method of indirect proof.

LAW OF *S*-TRIANGLES

A Triangle is Called an S-Triangle if Its Cotangents Are Cured

Hereafter, we use $i, j, k = 1, 2, 3$ and their cyclic permutation. Now, construct a triangle using $\{\mathbf{A}_i\}$ at $\sum \mathbf{A}_i = 0$. For a net in the basis $-\mathbf{A}_i$, $\mathbf{A}_j$ (an empty triangle of the area *S*), the cotangents $\{g_i\}$ of this triangle are set by the obvious equation $g_k = -(\mathbf{A}_i, \mathbf{A}_j)/2S$. For a square (Cartesian) net with $S = 1/2$ [the basis of the unit vectors $\mathbf{a}_{1,2}$, $(\mathbf{a}_1, \mathbf{a}_2) = 0$], this equation directly yields the integrity of $\{g_i\}$; thus, the given condition is a necessary condition for the *S*-triangle. It is also a sufficient condition, which is seen from the analysis of the triangle rotation by $\pi/2$ about the vertex, i.e., the node of the net generated by this triangle.

CONDITION OF *H*-TRIANGLES, DENIS NUMBERS AND DENIS HYPERSECTOR

A Triangle is Called an H-Triangle if Its Cotangents Are Cured by Multiplication by $\sqrt{3}$

The above condition directly follows from the consideration of an empty triangle of the hexagonal net with $S = \sqrt{3}/4$, where $(\mathbf{a}_1, \mathbf{a}_2) = 1/2$ by analogy with the derivation of the law for *S*-triangles.

The sum of the internal angles of the triangle $\{\alpha_i\}$ equals the number π and, therefore, its cotangents obey the equation

$$g_1g_2 + g_2g_3 + g_3g_1 = \sum g_ig_j = 1, \qquad (1)$$

which is another form of the equation $\cot(\alpha_i + \alpha_j) = \cot(\pi - \alpha_k)$. With due regard for the rules established for the *S*- and *H*-triangles, we can transform the rela-

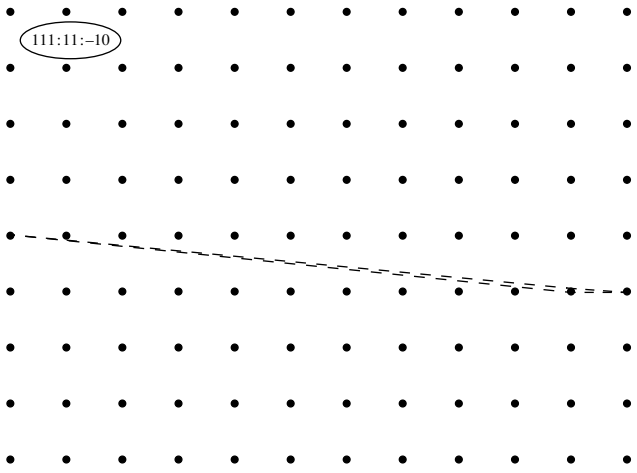

Fig. 1. A triangle and a square net generated by an *S*-triad.

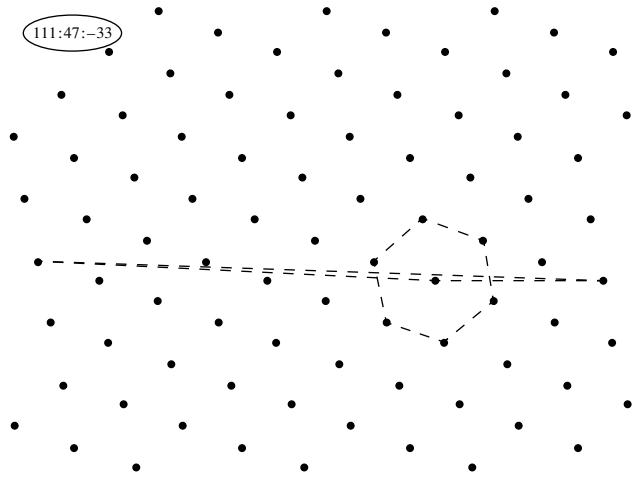

Fig. 2. A triangle and a hexagonal net generated by a true *H*-triad.

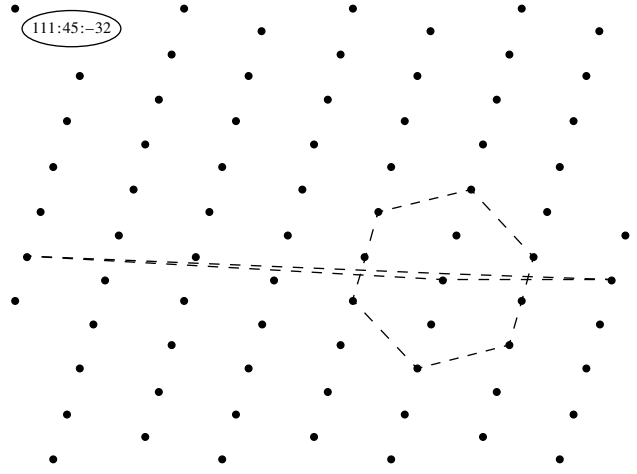

Fig. 3. A triangle and a pseudohexagonal net generated by a false *H*-triad.

tionships for their cotangents $\{g_i^{(S)}\}$ and $\{g_i^{(H)}\}$ into the corresponding Diophantine equations:

$$\sum D_i^{(S)} D_j^{(S)} = 1, \quad (2)$$

$$\sum D_i^{(H)} D_j^{(H)} = 3. \quad (3)$$

We shall call the numbers $\{D_i^{(S,H)}\}$ the Denis number-triads.[1]

The latter equations yield the basic property of the Denis numbers—their mutual simplicity. In the case of *S*-triads, this property is enhanced: any combination of two numbers $\{D_i^{(S)}\}$ yields a mutually simple pair. Since the Denis numbers $\{D_i^{(S,H)}\}$ are proportional to triangle cotangent, it becomes clear that these triads cannot have more than one negative term. All the "positive" variants of the triads are exhausted by the combinations of the numbers {1, 1, 0} for the *S*-triangles and the *H*-triad {1, 1, 1} (the combinations of the [3, 1, 0} numbers are excluded since no empty right triangles can be inscribed into the hexagonal net). Figures 1–3 illustrate the types of nets generated by the Denis numbers (they are indicated in the singled-out regions of the nets).

The initial "law of cotangents" (1) has a deep geometrical meaning. This equation represented in the conventional Cartesian coordinates (the cubic lattice) generates a hyperbolic surface with the [1 1 1] axis and the vertex at the point $[1/\sqrt{3}\ \ 1/\sqrt{3}\ \ 1/\sqrt{3}]$. The cone–asymptote of the given surface ($\sum g_i g_j = 0$) is originated from the 0-node and has the [1 0 0]- and $[2\ 2\ \bar{1}]$-type axes as the Cartesian generatrices. With due regard of the position symmetry of this hyperboloid ([1 1 1] is a threefold symmetry axis) and the fact that only one term of the $\{g_i\}$ triad can be negative, to the infinite set of triangles there corresponds the sector of the hyperboloid separated by the planes lying on the pairs of vectors [1 1 1], [1 0 0] and [1 1 1], [0 1 0], where in all cases $g_{1,2} > 0$.

Since the plane determined by the vectors [1 1 1] and [1 1 0] is a mirror-reflection plane, the symmetry of triangles with cotangents of the form $\{g_1, g_2, g_3\}$ and $\{g_2, g_1, g_3\}$ should also have the mirror-reflection symmetry. Establishing the hierarchy $g_1 \geq g_2 \geq g_3$, we define the triads $\{g_i\}$ of all the imaginary triangles by the points of the sector of the hyperbolic surface cut out by the planes formed by the vector pairs [1 1 2], [1 0 0] and $[1\ 1\ 1]$, $[2\ 2\ \bar{1}]$. The latter image–object is quite new and we shall call it the Denis hypersector. Figure 4 shows the stereographic image of the hyperboloid of cotangents and its hypersector filled with $\{D_i^{(S,H)}\}$ triads

[1] This term is suggested in memory of my son, a sailor, who tragically passed away at the age of 25 and who was the first to appreciate this theory; he also suggested some of the terms–images used in it.

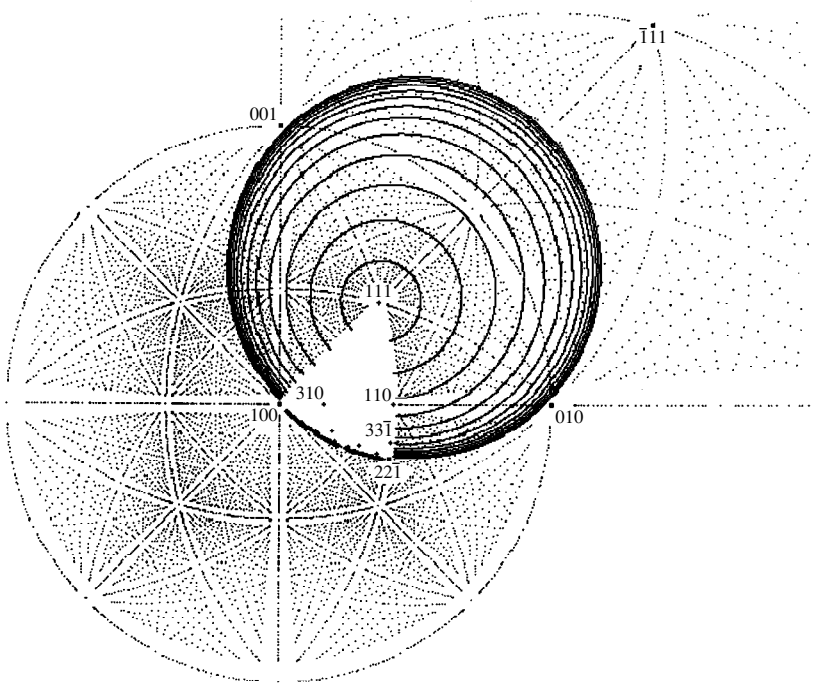

Fig. 4. Hypersector with the Denis triads in an "ocean of Cartesian primates."

(Eqs. (2) and (3) can also be interpreted in terms of the analogous hyperboloid, with the vectors $\mathbf{D}^{(S,H)} = \lfloor D_i^{(S,H)} \rfloor$ having the same cone–asymptote as the vectors $[g_i]$).

"STARLIKE" GENERATION OF PRIMITIVE PATTERNS AND FORMS OF THE DENIS NUMBERS

Let us visualize the Denis numbers on a square net generated by the standard orthogonal basis $\mathbf{a}_{1,2}$ ($S = 1/2$). The independent domain of this net lies between the central primates $\mathbf{a}_1 = [1\ 0]$ and $\mathbf{a} = \mathbf{a}_1 + \mathbf{a}_2 = [1\ 1]$ initiated from the 0-node and representing the new basis of the same net. Obviously, the independent $\pi/4$ sector ($\angle \mathbf{a}_1\mathbf{a}$) of this net includes the infinite set of *S*-triangles with the vertices at the 0-node, whose cotangents are, in fact, the Denis *S*-triads. Our goal is to visualize these triangles.

Let the central vectors $\mathbf{A}_1 = u_1\mathbf{a}_1 + v_1\mathbf{a}_2 = [u_1 v_1]$ and $\mathbf{A}_2 = u_2\mathbf{a}_1 + v_2\mathbf{a}_2 = [u_2 v_2]$ form a certain triangle belonging to the basis $\pi/4$-sector of the net. According to the well-known condition of "an empty loop of the net" (Belov's term),

$$u_1 v_2 - u_2 v_1 = \pm 1, \tag{4}$$

the "vectors–parents" $\mathbf{A}_{1,2}$ for the case of an empty triangle should inevitably be primitive. (By analogy with the well-known Fibonacci problem on rabbit reproduction, we shall also use the adequate semantics.) Then, the baby born as a result of the addition of these two primates, vectors $\mathbf{A} = \mathbf{A}_1 + \mathbf{A}_2 = [u_1 + u_2,\ v_1 + v_2]$, should also be primitive. Applying the emptiness conditions (4), we see that new pairs of primates $\mathbf{A}_1$, $\mathbf{A}$ and $\mathbf{A}$, $\mathbf{A}_2$ are also the basis ones for the net under consideration (i.e., form its new empty triangles). The above process of generation of new primates is continued infinitely with the number of the basis pairs increasing in the geometric progression.

Starting the generation of primates on a square net with the "parents" $\mathbf{a}_1$, $\mathbf{a}$, we arrive at all infinite sets of *S*-triangles and the forms of the corresponding Denis numbers

$$\begin{aligned} D_3^{(S)} &= (\mathbf{A}_1, \mathbf{A}_2) = u_1u_2 + v_1v_2, \\ D_1^{(S)} &= (\mathbf{A}_2, \mathbf{A}_3) = u_2u_3 + v_2v_3, \\ D_2^{(S)} &= -(\mathbf{A}_3, \mathbf{A}_1) = -u_3u_1 - v_3v_1, \end{aligned} \tag{5}$$

where

$$\mathbf{A}_3 = \mathbf{A}_2 - \mathbf{A}_1 = [u_3, v_3] = [u_2 - u_1, v_2 - v_1].$$

Assuming that the act of a "child birth" by newly formed basis pairs occurs only once, we shall call the whole set of the "newly born primates" *a generation*. Figure 5 shows the primitive pattern (which has only the primitive nodes) of the square net with the impressive "sea stars"—successively and rectilinearly con-

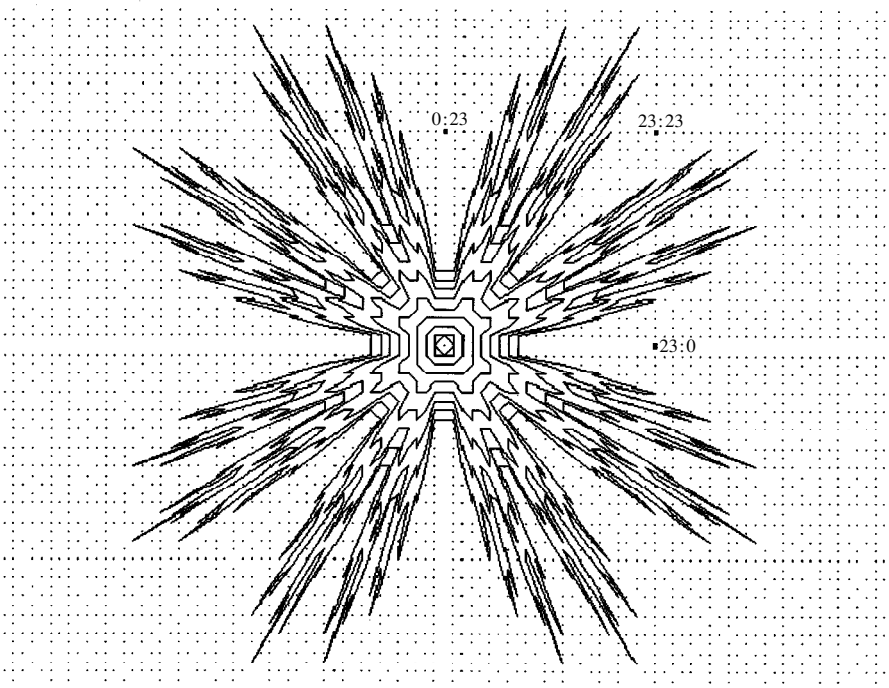

Fig. 5. Starlike primitive pattern of a square net.

toured generation of primates (the spread of the structure of the $\pi/4$-sector over the whole plane by symmetry reflections).

Obviously, the "starlike algorithm" is of a general character and provides the sectorial generation of the central primates by any basis of any net. Figure 6 shows similarly constructed primitive pattern of the hexagonal net with the generating stars–generations [here $(\mathbf{a}_1, \mathbf{a}_2) = 1/2$, the structure of the $\pi/6$ sector $\angle\mathbf{a}_1\mathbf{a}$ is symmetrically reflected].

The "star" way provides the formulation of a simple rule for visualization of the central empty triangles in any of the four initial angular basis sectors of the primitive pattern of any set: *all the sectorial empty triangles (except for the initial basis one) are open by the pair of the azimuthally neighboring vertices of any pair of stars–generations.*

The initial basis stars are reflected by central minimum parallelograms on the prim-pattern of an arbitrary net (in Fig. 5, the basis star is the least square). Only the hexagonal set can have two more "faces"—the initial basis star can be a trigon if $(\mathbf{a}_1, \mathbf{a}_2) = -1/2$ or a hexagon (as in Fig. 6).

The form of the Denis numbers for the hexagonal net are established on the basis of the *condition of H triangles* and by analogy with the procedure for obtaining form (5):

$$D_3^{(H)} = 2(\mathbf{A}_1, \mathbf{A}_2) = 2(u_1u_2 + v_1v_2) + (u_1v_2 + u_2v_1),$$

$$\begin{aligned} D_1^{(H)} &= 2(\mathbf{A}_2, \mathbf{A}_3) \\ &= 2(u_2u_3 + v_2v_3) + (u_2v_3 + u_3v_2), \end{aligned} \tag{6}$$

$$D_2^{(H)} = -2(\mathbf{A}_3, \mathbf{A}_1) = -2(u_3u_1 + v_3v_1) - (u_3v_1 + u_1v_3).$$

On the condition of emptiness (4), the integral numbers-products u_iv_j and u_jv_i in forms (6) are neighbors on the numerical axis and, therefore, their sum [the second brackets in Eq. (6)] is always odd.

THE LAW OF *H*-TRIANGLES, THE TRUE AND FALSE *H*-TRIADS

A Triangle Is an H-Triangle if Its Cotangents Are Oddly Cured by Multiplication by $\sqrt{3}$

The necessity of this law follows from form (6) and condition (4). The cumbersome proof of its sufficiency obtained by the author from the analysis of the $\pi/3$ rotations of an empty triangle with cotangents in the form $\{g_i = D_i^{(H)}/\sqrt{3} = (2D_i - 1)/\sqrt{3}\}$ (where $\{D_i\}$ are the integers) is omitted here.

Upon the detailed study of Eq. (3), we arrive at the important conclusion that the *H*-triads cannot have more than one even number. Omitting the detailed analysis of false *H*-triads, we only formulate here the final

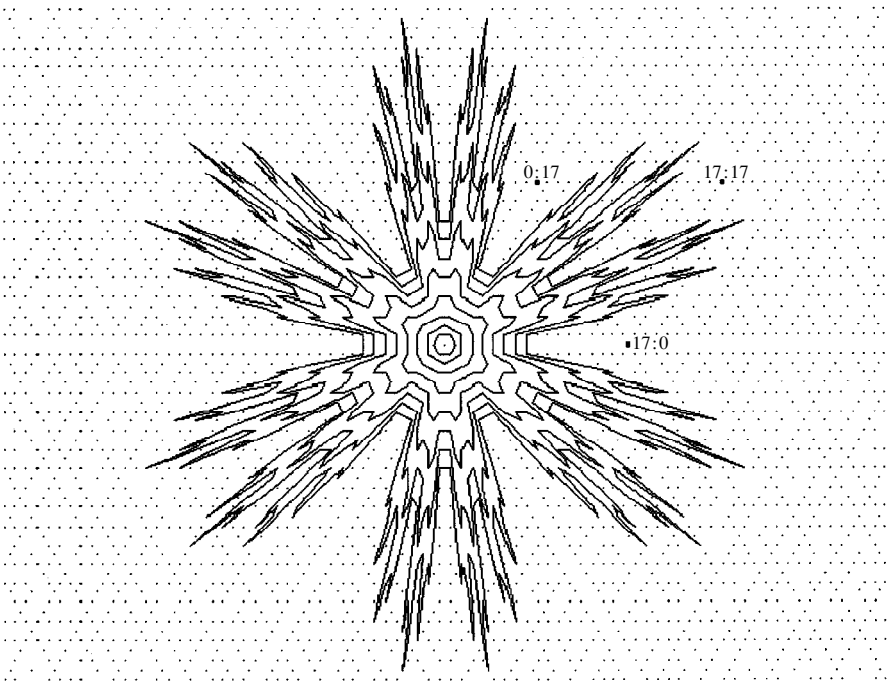

Fig. 6. Starlike primitive pattern of a hexagonal net.

result as the following statement–law:

H-triads with an even term always generate a pseudohexagonal net

(the *H*-triads of the {3, 1, 0} type "visually ejected" earlier determine the reduced right triangles with the angles $\pi/6$ and $\pi/3$ on this net, see Fig. 3).

Substituting the form $\{D_i^{(H)} = 2D_i - 1\}$ into Eq. (3), we arrive at a new highly symmetric Diophantine equation $\sum D_i(D_j - 1) = 0$ characterizing the true hexagonal net. Unlike the *S*- and *H*-triads, the numbers entering the $\{D_i\}$ triad are not necessarily mutually simple.

Comparing forms (6) and (5), we obtain the relationships between all the Denis triads.

DENIS NUMBERS AND THE LAUE METHOD

We believe that a hypersector with the Denis numbers (Fig. 4) and the Diophantine equations of the type $\sum D_i^{(N)} D_j^{(N)} = N$, which are called here the Denis equations in order to single them out from the class of Diophantine equations, are worthy of further theoretical–numerical and crystallographic consideration. We discuss in brief two more results obtained on this path: (1) triads $\{D_i^{(2)}\}$ generate an "important orthogonal net"—the crystallographic zone of the cubic lattice with the [1 1 0] axis coinciding with a twofold symmetry axis; (2) of great importance are also the rational and the irrational *S* and *H* forms of the number $\pi - \pi^{(S)} = 4\sum_{i=1}^{n} \frac{n}{n^2 + i^2 - i}$ and $\pi^{(H)} = 6\sqrt{3}\sum_{i=1}^{n} \frac{n}{4n^2 + n - 2ni + i^2 - i}$, which transcendentally refine the value of π with an increase of *n* (the author revealed no analogues).

Now, proceeding to the Laue method, we should like to indicate that the Laue pattern from a crystal reveals the angles formed by the vectors of the nets–crystallographic zones. For highly symmetric crystals, the direct processing of the zonal curves of an arbitrary Laue pattern allows one to use the Denis numbers in order to determine the corresponding square and other orthogonals as well as hexagonal nets of the crystal lattice. Thus, new vistas are open for designing completely new mathematical methods for X-ray diffraction analysis of a wide class of single-crystal materials using the white (and, first of all, synchrotron) radiation. The corresponding algorithms have already been developed at the Laue laboratory of Chelyabinsk State University. We invite all the interested organizations to take part in this work.[2]

The main results of this study were obtained by the author in 1995 and were reported at the 27th International Winter School–Symposium of Physicists–Theo-

[2] LAUELA, Chelyabinsk State University, ul. Brat'ev Kashirinykh 129, Chelyabinsk, 454021 Russia.

reticians (Yekaterinburg–Chelyabinsk, March 2–7, 1998), where they brought about considerable interest and received a benevolent reaction from the participants.

ACKNOWLEDGMENTS

The author is grateful to the Corresponding Member of the Russian Academy of Sciences Professor S.V. Matveev (Chelyabinsk University) and his student M.A. Ovchinnikov, Doctor in Physics and Mathematics Professor S.I. Pinchuk (Blumington University, Indiana, USA), Corresponding Member of the Russian Academy of Sciences Professor V.S. Urusov (Moscow State University), Corresponding Member of the Russian Academy of Sciences Professor A.M. Askhabov (Institute of Geology of the Ural Division of the Russian Academy of Sciences), and Doctor in Physics and Mathematics Professor R.V. Galiulin (Institute of Crystallography of the Russian Academy of Sciences) for their attention to my work, fruitful discussions, and valuable advice.

Translated by L. Man

Crystallography Reports, Vol. 46, No. 2, 2001, pp. 167–170. Translated from Kristallografiya, Vol. 46, No. 2, 2001, pp. 205–208.

DIFFRACTION AND SCATTERING OF X-RAY AND SYNCHROTRON RADIATION

Diamond Monochromator–Splitter with Enhanced Reflectivity for Synchrotron Radiation

V. V. Lider*, M. V. Kovalchuk*, L. V. Samoĭlova*, S. I. Zheludeva*, Yu. N. Pal'yanov, and Yu. M. Borzdov***

** Shubnikov Institute of Crystallography, Russian Academy of Sciences, Leninskiĭ pr. 59, Moscow, 117333 Russia*

*** Institute of Mineralogy and Petrography, Siberian Division, Russian Academy of Sciences, ul. Akademika Koptyuga 3, Novosibirsk, 630090 Russia*

Received September 13, 1999

Abstract—It has been shown that a damaged surface layer can enhance the reflectivity of a diamond monochromator–splitter for synchrotron radiation. The X-ray diffraction analysis with the use of asymmetric Bragg reflections allowed the determination of the layer thickness and its mosaicity dispersion equal to 3 μm and 19″, respectively. In this case, the observed integrated intensity of a quasisymmetric 422 Laue reflection (Mo_{K_α} radiation) exceeds its calculated value by a factor of 2.5 at a sufficiently high energy resolution ($\delta E/E = 1.1 \times 10^{-5}$). The perspectives of the practical use of a diamond monochromator–splitter with enhanced reflectivity are also discussed. © *2001 MAIK "Nauka/Interperiodica".*

INTRODUCTION

Attempts to obtain a monochromatic X-ray beam using synchrotron-radiation (SR) sources of the third generation encounter a serious problem—cooling the optical element irradiated with the primary SR beam. If the role of such an optical element is played by a single-crystal monochromator, then, in order to compensate the thermal effect, one has to provide the minimum possible distance between the working surface of the crystal–monochromator and the cooling liquid. This condition requires the preparation of a monochromator of a complicated shape [1, 2]. However, in many instances, only a partial compensation of the monochromator deformation can be attained, which has a negative effect on the beam parameters. Usually, monochromators are prepared from silicon with a high degree of structural perfection and are tolerant to high thermal loads. However, recently, those using synchrotron radiation have paid more attention to monochromators prepared from synthetic diamond. Today, the surfaces of such monochromators do not exceed 1 cm^2 and are characterized by high structural perfection [3, 4]. The main advantage of such monochromators is their high thermal conductivity (23 W/cm/K) and low coefficient of linear thermal expansion (1.18×10^{-6} K^{-1}) [5]. The ratio of these two parameters determines the thermoelastic tolerance of the material and, for diamond, is 30–50 times higher than that for silicon [3, 4]. Thus, the use of diamond monochromators can considerably simplify the compensation of thermal loading. For example, thermal loading can be well compensated by cooling a monochromator holder fixing the monochromator along its perimeter [3, 6].

Another characteristic feature of diamond is its transparency for X-ray radiation. Along with the fact that the diamond reflectivity is only slightly worse than the reflectivity of silicon [4], its transparency to X-rays makes diamond an indispensable material for splitters of SR beams [6].

However, both silicon and diamond are characterized by low electron density and a reflectivity insufficient for optical materials. It is well known [7, 8] that the use of mosaic crystals for X-ray optics provides a multiple increase in the integrated intensity of the scattered radiation. This phenomenon can be accompanied by a considerable broadening of the intrinsic dynamical-reflection (rocking) curve of an element—up to several hundreds of angular seconds. The energy resolution of an element is usually determined by the half-width of the intrinsic rocking curve; therefore, it is obvious that the use of mosaic crystals in precision measurements is hardly expedient.

It was demonstrated [9] on silicon single crystals that it is possible to multiply increase the integrated intensity of a diffracted X-ray beam by mechanical grinding and polishing of the working surface and creating a 2-μm-thick disturbed layer. In this case, the half-width of the intrinsic rocking curve does not exceed 16″–20″. Such broadening of the rocking curve can result in a decrease of the relative energy resolution to 10^{-4}–10^{-5}, which, however, is quite sufficient for many precision X-ray diffraction experiments.

The present study was undertaken to characterize of a diamond monochromator with a damaged surface layer by the X-ray diffraction method.

1063-7745/01/4602-0167$21.00 © 2001 MAIK "Nauka/Interperiodica"

SPECIMEN PREPARATION

An initial diamond single crystal with a weight of 3.35 carats was grown on a (111)-oriented seed in the Na–Fe–C system in a multipunch high-pressure apparatus (the cut-sphere type) of the BARS company under a pressure of P = 5.5 GPa and a temperature of T = 1450°C [10]. The plate for the study was cut out from the crystal (a laser cutting technology) and subjected to mechanical grinding and polishing. The final specimen had the shape of a 0.88-mm-thick plane-parallel plate misoriented by 4° with respect to the (111) plane of the crystal and had a 2- to 3-μm-thick damaged surface layer. Physically, this diamond was related to the *Ib* + *IaA* type. The main characteristics of the diamond corresponded to those indicated earlier for a several-carat high-quality synthetic diamond single crystal [11].

EXPERIMENTAL METHODS

The half-width of the rocking curve obtained on a double-crystal diffractometer can be represented as a sum [12]

$$\omega^2 = \omega_m^2 + \omega_\lambda^2 + \omega_i^2, \quad (1)$$

where ω_m is the angular divergence of an X-ray beam formed by the monochromator; ω_λ is the divergence which describes the degree of dispersion in the double-crystal diffraction geometry, $\omega_\lambda = (\delta\lambda/\lambda)(\tan\theta_{sp} - \tan\theta_m)$, $\delta\lambda/\lambda$ is the relative half-width of the spectral line used, θ_{sp} and θ_m are the Bragg angles of the specimen and monochromator, respectively; and ω_i is the half-width of the intrinsic rocking curve.

A crystal with a damaged layer can be considered as a bicrystal consisting of the matrix, dynamically scattering the radiation and a mosaic layer of thickness t [13]. In this case, the half-width of the intrinsic rocking curve of the bicrystal should depend on the half-width of the rocking curves of the layer and the matrix. The first half-width value is determined by the layer mosaicity dispersion Ω, whereas the second, by the following formula:

$$\omega_s = \omega_s b^{-1/2}, \quad (2)$$

where ω_s is the half-width of the symmetric reflection rocking curve $\omega_s = 2\chi_h C/\sin 2\theta$ (χ_h is the real part of the Fourier-component of the crystal polarizability, C = 1 for the π-polarization of the X-ray radiation, $C = \cos 2\theta$ for the σ-polarization) and $b = \gamma_s/\gamma_h$, where γ_s and γ_h are the directional cosines of the incident and the diffracted beams.

Considering the curves obtained in [9], we drew a conclusion that the experimentally measured half-width of the rocking curve and the integrated intensity of the diffracted beam are proportional to the damaged-layer thickness. Then, the half-width of the intrinsic rocking curve of the bicrystal can be represented as

$$\omega_i = (\Omega t + \omega_s \Lambda b^{-1/2})(t + \Lambda)^{-1}, \quad (3)$$

where Λ is the extinction length ($\Lambda = \lambda(\chi_h C)^{-1}(\gamma_o\gamma_h)^{1/2}$).

For the structural characterization of a bicrystal, one has to determine its parameters t, Ω, and ω_s. In order to obtain the sufficient number of equations of type (1), we used four asymmetric Bragg reflections—220, 202, 311, and 113. Since the surface normal does not rigorously coincide with the (111)-axis of the diamond monochromator, the reflections having the equal sums of squared Miller indices have different values of the parameters γ_o and γ_h and, thus, also different symmetry factors b and the extinction length Λ. Moreover, we measured the rocking curves for each reflection two times—prior to and upon the specimen rotation by 180° about the diffraction vector [which corresponds to the change of b by b^{-1} in formula (3)].

Conditions and results of the experimental characterization of a diamond monochromator with the damaged surface layer

Reflection	(220)	(202)	(311)	(113)
θ_s, deg	37.73		45.85	
Monochromator	(331) Si(111)		(333) Si(111)	
θ_m, deg	38.18		47.46	
ω_m, arcsec	1.3		2.0	
ω_λ, arcsec	0.8		3.5	
b	9.1 0.11	18.2 0.055	4.46 0.224	2.6 0.384
ω, arcsec	7.6 13.4	9.6 20.4	6.9 7.7	5.4 6.4
ω_i, arcsec	7.4 13.3	9.5 20.4	5.6 6.6	3.6 5.0
Λ, μm	5.1	3.7	14.9	18.7
ω_s, arcsec	4.1 ± 0.9		1.8 ± 0.1	
ω_s^{calcd}, arcsec	3.1		1.9	
T, μm	3			
Ω, arcsec	19			

RESULTS AND DISCUSSION

Eight rocking curves were measured by the method considered above (the Cu_{K_α} radiation). Using formulas (1) and (3) and the least squares procedure, we evaluated the thickness and mosaicity dispersion in the damaged layer and also the half-width of the intrinsic rocking curve for two types of reflections 220 and 311. The experimental conditions and the results obtained are indicated in the table.

It should be emphasized that the half-width of the experimental rocking curve for the symmetric reflections of the bicrystal matrix (ω_s in table) only slightly differ from the corresponding theoretical values of ω_s^{calcd}, which indicates a high structural perfection of the diamond monochromator.

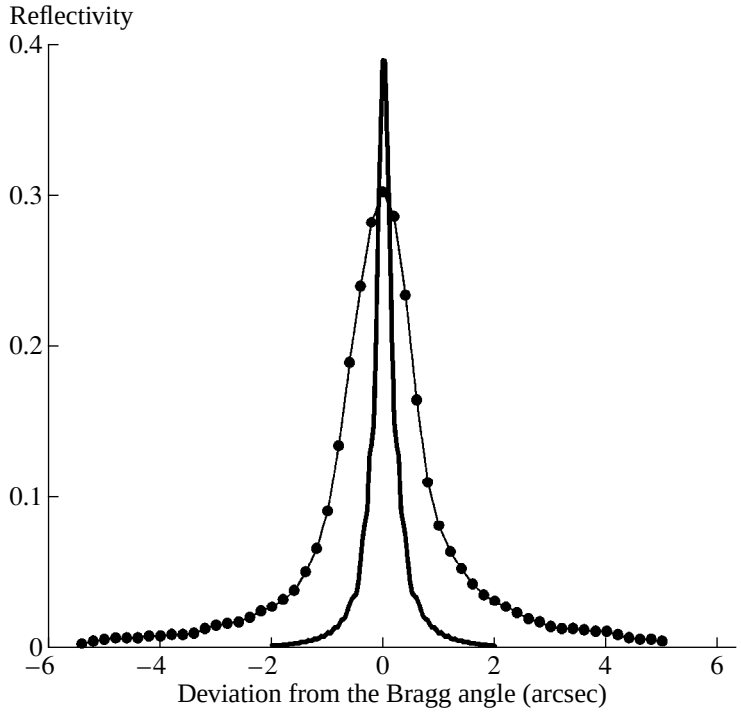

Rocking curves for a single crystal diamond wafer with a damaged surface layer (symmetric 422 Laue reflection, Mo_{K_α} radiation). Solid line indicates the theoretically calculated values ($I_{int} = 0.94 \times 10^{-6}$); dots indicate the experimental values ($I_{int} = 2.48 \times 10^{-6}$).

Special attention in [9] was given to the dependence of the reflectivity of a single crystal with a damaged layer on the method used for working-surface processing. It is obvious that, to attain the optimum bicrystal parameters (the maximum value of the integrated intensity of the diffracted beam at a low value of the half-width of the intrinsic rocking curve), one has to create a damaged layer having the optimum thickness and mosaicity. Moreover, for the Bragg diffraction, the intensity of the radiation scattered by a bicrystal is strongly affected by both primary and secondary extinction [13, 14]. With an increase of the integrated intensity caused by the layer mosaicity, both factors become competitive. Thus, we failed to attain the maximum integrated intensity of the diffracted beam in our experiments because of the nonoptimum values of surface-layer parameters.

The effect of extinction should be less obvious in the transition to the Laue geometry, where the transmitted and the diffraction beams leave the crystal from the same surface.

Indeed, the integrated intensity of the quasisymmetric $22\bar{4}$ Laue reflection (Mo_{K_α} radiation, 642 reflection of the Si(111) monochromator) was higher than the theoretically calculated value by a factor of 2.5 (figure). In this case, the half-width of the intrinsic rocking curve of the bicrystal was 1.3″, which provided a rather high energy resolution ($\delta E/E = 1.1 \times 10^{-5}$).

We hope to increase the reflectivity of a diamond monochromator by optimizing the thickness and mosaicity dispersion of the damaged layer.

In some precision experiments with the use of a focused X-ray beam (e.g., in the studies of biological and medical objects, excitation of X-ray fluorescence, and the related interference phenomena [15, 16]), the energy resolution is not a key parameter; therefore, an increase of the reflectivity is not limited by the width of the intrinsic rocking curve of a diamond monochromator. This is especially important in connection with the attempts to use the Laue diffraction from diamond crystals for polychromatic focusing of the X-ray radiation [5] and determining the structures of molecular crystals [17].

CONCLUSIONS

A diamond monochromator–splitter with a damaged surface layer for the synchrotron radiation has been designed.

It has been shown that the use of such a monochromator for the Laue diffraction provides an increase of the integrated intensity because of the kinematical X-ray scattering from a damaged layer.

It has been demonstrated that the nondestructive X-ray characterization of the damaged layer is possible. This, in turn, provides the further development of

the technology of preparing highly reflective elements of X-ray optics with the necessary properties.

REFERENCES

1. R. K. Smither, Nucl. Instrum. Methods Phys. Res. A **291**, 286 (1990).
2. V. V. Lider, M. V. Kovalchuk, N. V. Zhavoronkov, and S. I. Mazurenko, in *Proceedings of the National Conference on Application of X-ray and Synchroton Radiations, Neutrons, and Electrons for Studying Materials, Moscow, 1997*, Vol. 2, p. 289.
3. L. E. Berman, J. B. Hastings, D. P. Siddons, *et al.*, Nucl. Instrum. Methods Phys. Res. A **329**, 555 (1993).
4. A. M. Khounsary, R. K. Smither, S. Davey, and A. Purohit, Argonne Naional Laboratory, APS Light Source Notes (1997), LS-215, INTERNET: www.aps.anl.gov/techpub/1s notes/1s 215/1s 215.html.
5. M. Sanches del Río, G. Grubel, J. Als-Nielsen, and M. Nielsen, Rev. Sci. Instrum. **66** (11), 5148 (1995).
6. A. K. Freund, J. Susin, and E. Ziegler, Synchrotron Radiation News **8** (4), 28 (1995).
7. A. K. Freund, Nucl. Instrum. Methods Phys. Res. A **266**, 461 (1988).
8. T. Matsushita and H.-O. Hashizume, in *Handbook on Synchrotron Radiation*, Ed. by E. E. Koch (North-Holland, Amsterdam, 1983), Vol. 1, p. 261.
9. S. M. A. Gani, B. T. Tanner, G. McKenny, *et al.*, J. Appl. Crystallogr. **17**, 111 (1984).
10. Yu. N. Pal'yanov, A. F. Khokhryakov, Yu. M. Borzdov, *et al.*, Geol. Geofiz. **38** (5), 882 (1997).
11. Yu. N. Pal'yanov, A. G. Sokol, Yu. M. Borzdov, *et al.*, Dokl. Akad. Nauk **355** (6), 798 (1997).
12. *X-ray Apparatus*, Ed. by V. V. Klyuev (Mashinostroenie, Moscow, 1980), Vol. 2, p. 121.
13. J. Chandhuri and S. Shah, J. Appl. Phys. **66** (11), 5373 (1989).
14. W. H. Zachariasen, Acta Crystallogr. **23**, 558 (1967).
15. T. Gog, R.-H. Menk, F. Arfelli, *et al.*, Synchrotron Radiat. News **9** (3), 30 (1996).
16. T. Gog, D. Bahr, and G. Materlik, Phys. Rev. B **51** (10), 6761 (1995).
17. M. Yamamoto, T. Kumazaka, T. Fujisawa, and T. Veki, J. Synchrotron Radiat. **5**, 222 (1998).

Translated by L. Man

Crystallography Reports, Vol. 46, No. 2, 2001, pp. 171–175. Translated from Kristallografiya, Vol. 46, No. 2, 2001, pp. 209–214.

DIFFRACTION AND SCATTERING OF X-RAY AND SYNCHROTRON RADIATION

X-ray Phase Contrast of Laser-Heated Air Space

V. A. Bushuev* and A. P. Petrakov

Moscow State University, Vorob'evy gory, Moscow, 119899 Russia

** e-mail: vab@surfsite.phys.msu.su*

Received December 2, 1999

Abstract—The image of a thin cylindrical air space heated by the beam of a continuous CO_2 laser has been obtained by the method of X-ray phase contrast in the scheme with a slit (cut) crystal–analyzer. It is shown that the method is extremely sensitive to superlow density values and relative X-ray refractive index of an object. The air temperature in the laser beam is evaluated for several values of the laser power. © *2001 MAIK "Nauka/Interperiodica".*

INTRODUCTION

X-ray phase contrast (PC) provides the visualization of the internal structure of weakly absorbing objects with low density gradients of the material and a high spatial resolution [1–3]. It is based on the use of the phenomenon of X-ray refraction in an objects distorting the phase front of the transmitted wave. As a result of such phase distortion, the X-ray beam deviates from the initial direction of its propagation for certain small angles dependent on the spatial distribution of the material density in an object. The radiation transmitted by the object is recorded with the aid of a perfect crystal–analyzer located in the direct vicinity of the region of Bragg reflection. As a result, even small variations in the angle of X-ray incidence onto the crystal–analyzer give rise to considerable changes in the diffraction–reflection intensities recorded by a coordinate detector or by a photographic method onto a film. The typical refraction angles of the radiation with a wavelength of $\lambda \sim 0.1$ nm are equal to fractions of an angular second and, thus, are comparable with the angular range of the pronounced variation of the rocking curve of the crystal–analyzer. Therefore, the method of the phase contrast allows one to increase the image contrast by one to two orders of magnitude [4–6] in comparison with the contrast attained by the traditional absorption methods based on the phenomenon of absorption, which is of great importance, especially, for studying medical and biological objects [7, 8].

Another important factor is the limiting sensitivity of the method of phase contrast to the variation in the refraction index, $n = 1 - \delta$, in various parts of the object. It follows from [4] that it is possible to record the values on the order of $\Delta\delta \sim 10^{-9}$, which is by three orders of magnitude less than the value of the refraction decrement $\delta \sim 10^{-6}$ for soft tissues of most of the medical and biological objects.

Usually, the objects chosen for studies are real polymer-based model samples or various medical and biological objects [1–9]. In the present study, we managed to obtain for the first time the phase-contrast images of a narrow air beam warmed by the radiation of an infrared CO_2 laser (10.6 μm).

The goal of our study was to demonstrate the unique sensitivity of the phase-contrast method to extremely small variations in the object density. We also consider some problems of design and performance of such experiments. Analyzing the images with the phase contrast, we estimated the refraction angles and the air temperature for beams produce by a laser with a varying power.

EXPERIMENTAL METHOD

The studies were performed on a triple-crystal X-ray diffractometer (Fig. 1). The radiation source was an X-ray tube with a copper anode ($\lambda = 0.154$ nm). The X-rays from source *1* passed through a vertical 0.05-mm-wide slit and then were incident at slit (cut) silicon monochromator *2* with triple symmetric (111) reflection. A vertical slit of width 0.1 mm and a horizontal slit of height 4 mm were placed at a distance of 5 cm from the monochromator (not seen in Fig. 1). Then the radiation was transmitted by object *3* and was incident onto a crystal–monochromator *4* and was recorded by detector *5*. The monochromator–object and the object–analyzer distances in the horizontal plane were 19 and 20 cm, respectively. The analyzer was a slit (cut) silicon single crystal with a triple symmetric (111) reflection.

The object to be studied was a cylindrical air space, which transmitted a beam of a CO_2 laser operating in the continuous mode. The diameter of a laser beam was 4.6 mm, the laser power varied discretely and was equal to 22, 28, and 34 W. The laser beam intersected the horizontal plane from directly above. Such a geometry of the laser beam provided a warm cylindrical air space of a constant (nondeformed) shape formed due to vertical heat flows. Since the laser-beam diameter considerably

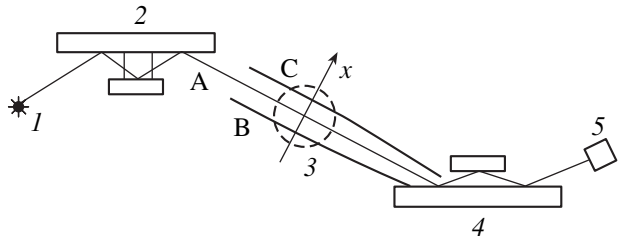

Fig. 1. Schematic of the experiment: (*1*) X-ray source, (*2*) monochromator, (*3*) object (laser beam), (*4*) crystal–analyzer, (*5*) detector, *x* direction of the object motion, and A, B, and C are X-ray paths.

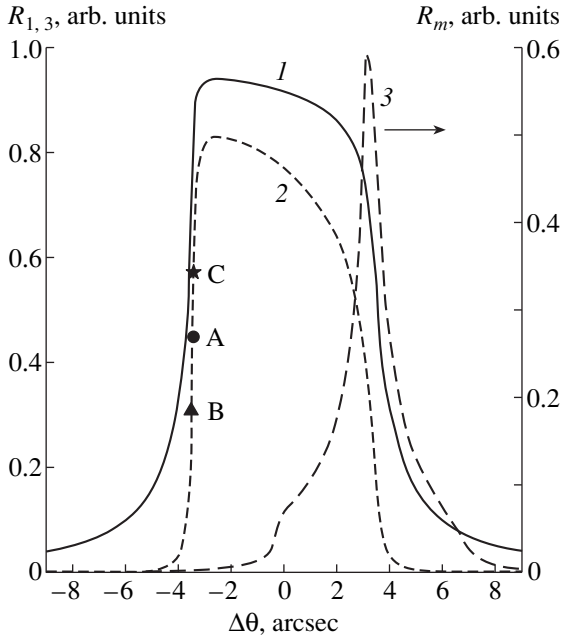

Fig. 2. Rocking curves from Si(111) of the σ-polarized Cu$K_{\alpha 1}$-radiation: (*1*) single reflection, (*2*) triple reflection, (*3*) angular distribution of the radiation at the exit of a slit monochromator with triple reflection for the case of rotation of the shoulder with single reflection through an angle of $\varphi = 3.2''$. The points A, B, and C at the rocking curve (*2*) correspond to beams A, B, and C in Fig. 1.

exceeded the cross section of the X-ray beam, the object (warm air space) moved across the X-ray beam and the image formed was recorded by a scintillation detector calculating X-ray quanta (usually, it is recorded onto a photographic film [1–9]). The laser beam moved normally to the X-ray radiation at a step of 0.3 mm and passed the radiation region within 2 min. The translation motion of a laser beam was provided by a mechanical translational motion of the laser with the aid of a special driving mechanism.

The laser radiation heated the air in the laser-beam cross section; as a result, the air density decreased, which, in turn, changed the refraction index. Figure 1 shows the path of three X-ray beams A, B, and C. Beam A passes through the center of the cylindrical object without refraction. Rays B and C are refracted and are incident onto the crystal–analyzer plane at different angles. It is clear that in order to increase the image contrast, one has to take the analyzer away from the exact Bragg position $\Delta\vartheta = 0$ in the direction toward negative angles, because the small-angle slope of the rocking curve $R_1(\Delta\vartheta)$ is characterized by a higher gradient of the reflection-intensity variation than the positive slope (Fig. 2).

To increase the method sensitivity, we used the analyzer deflected by an angle of $\Delta\vartheta = -3.6''$ from the exact Bragg position towards smaller angles, which is approximately equal to the half-width of the rocking curve at its half-height. However, the preliminary experiments showed that the use of the crystal–analyzer with single reflection is insufficient for recording "supersmall" refraction angles. Therefore, in order to increase the rocking curve steepness, we used a slit analyzer with triple reflection. In this case, the rocking curve of the analyzer has the form $R_3(\Delta\vartheta) = R_1^3$, whereas the maximum of the derivative $dR_3/d\Delta\vartheta$ in the angular range $\Delta\vartheta \approx -3.6''$ is almost twice the steepness of the slope $dR_1/d\Delta\vartheta$ for single reflection (Fig. 2).

An important requirement for the successive use of phase-contrast method is the small angular divergence of the incident X-ray radiation (the requirement of a quasiplane wave). This requirement is usually met by using high-order reflections [1, 3, 8] or strongly asymmetric low-order reflections with the asymmetry coefficient of reflection $b \ll 1$ [2, 4–9]. The angular divergence of the beam can also be reduced by rotating one of the crystals in the monochromator block by a small angle within the width of the rocking curve [10]. Following [10], we used a slit monochromator with the slightly rotated side shoulder, where single reflection by a certain angle φ is attained under the effect of the mechanical load applied to this shoulder. The angular distribution of the radiation from the monochromator is determined by the product $R_m(\Delta\vartheta) = R_1(\Delta\vartheta)R_1(\Delta\vartheta - \varphi)R_1(\Delta\vartheta - 2\varphi)$ (curve *3* in Fig. 2). We empirically found such a rotation angle for which the radiation divergence was minimal (with the half-width of ~0.6″). In this case, the integrated intensity of the beam decreased by about four times.

The intensities of nonrefracted X-rays recorded by the detector correspond to the point A of the rocking curve of the analyzer (Fig. 2). Refraction in the object resulting in a decrease of the angle of incidence onto the crystal–analyzer is accompanied by a decrease of the intensity (beam B in Fig. 1 and point B on the rocking curve of the analyzer in Fig. 2). The change of the angle of incidence in the "opposite direction" gives rise to an increase of the intensity (point C). The geometric width of the X-ray beam in Fig. 1 is considerably

increased (Fig. 1). Experimentally, we recorded each of the narrow refracted beams (0.1 mm in width) separately.

EXPERIMENTAL RESULTS AND DISCUSSION

Figure 3 shows the dependence of the X-ray intensity $I(x)$ measured by a detector during the translational motion of a laser beam. The center of the laser beam is taken to be the zero value on the x-axis. With the penetration of the laser radiation into the X-ray beam, a certain increase of the intensity recorded by the detector (in comparison with the background intensity I_0 outside the laser beam) is observed. Upon the attainment of the intensity maximum, it starts decreasing down to its initial value of I_0 at $x \approx 0$. At the boundary of the laser-beam exit from the X-ray beam, the intensity first decreases and then increases again up to its initial value.

A decrease of the intensity in the region $x < 0$ indicates that, because of refraction, the angle of incidence of the X-ray radiation onto the analyzer became less than the rotation angle of the crystal–analyzer $\Delta\vartheta$. An increase of the intensity in the region $x > 0$ indicates the approach to the Bragg angle. It is seen from Fig. 3 that the amplitude of the intensity change $I(x)$ increases with an increase in the laser power. The contrast values at the maximum, $\eta(x) = (I - I_0)/I_0$, are 0.6, 0.9, and 1.1% at laser powers P = 22, 28, and 34 W, respectively. The statistical measurement errors amount to 0.3%.

Now, proceed to the interpretation of the experimental data obtained. The intensity distribution in the X-ray beam reflected from the crystal–analyzer is determined by the following simple equation [6, 11]:

$$I(x) = I_a(x)R(\Delta\vartheta - \beta(x)), \quad (1)$$

where $I_a(x) = I_0\exp[-\sigma(x)]$ is the intensity of the absorption image, $R(\alpha)$ is the rocking curve from the crystal–analyzer, $\Delta\vartheta$ is the fixed angle of the crystal–analyzer rotation, $\beta(x)$ are the angles of refraction determined by the transverse gradient of the phase change $\Phi(x)$ of a plane wave $\exp(ikn_0z)$ transmitted by the object with the refractive index $n(x, z) = 1 - \delta(x, z)$ and absorption $\mu(x, z)$:

$$\beta(x) = (1/k)d\Phi(x)/dx, \quad (2)$$

where

$$\Phi(x) = -k\int_{-\infty}^{\infty}[\delta(x, z) - \delta_0]dz,$$
$$\sigma(x) = \int_{-\infty}^{\infty}[\mu(x, z) - \mu_0]dz. \quad (3)$$

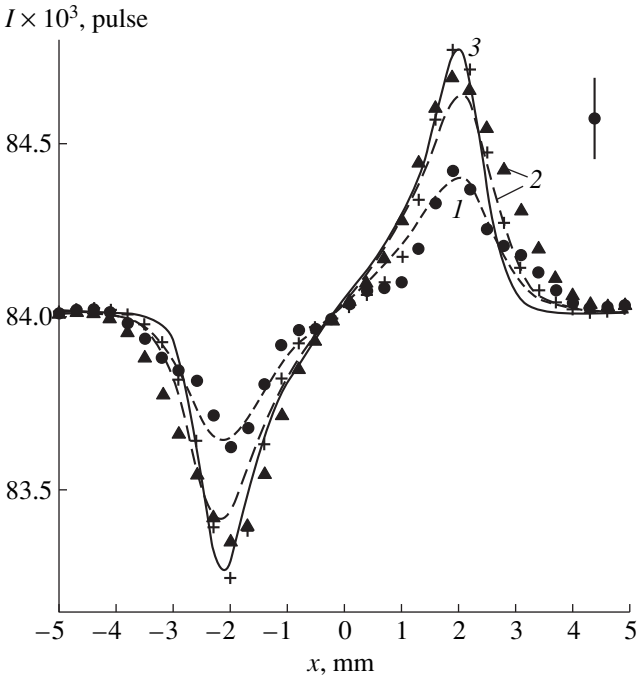

Fig. 3. Intensity of the X-ray radiation recorded by a detector as a function of the laser-beam displacement. The values of the laser power: (*1*) 22, (*2*) 28, and (*3*) 34 W. The points indicate the experiment, the solid and the dashed lines indicate the theoretically calculated data.

Here, $k = 2\pi/\lambda$, $\delta_0 = 1 - n_0$, and μ_0 is the decrement of refraction and the coefficient of air absorption outside the laser beam, respectively. Integration in Eq. (3) is performed along the direction of the X-ray propagation.

Equation (1) was obtained in the geometric-optics approximation and is valid if the following three conditions are met: (1) $r \gg R_F$, where r is the characteristic transverse dimension of the object, $R_F = (\lambda L)^{1/2}$ is the radius of the first Fresnel zone, and L is the distance between the object and the crystal–analyzer; (2) $\Delta r \gg \Lambda_x$, where $\Lambda_x = \Lambda\cot\vartheta_B$, Λ is the extinction depth in the crystal–analyzer, and ϑ_B is the Bragg angle; and (3) $d\beta(x)/dx \ll \Delta\vartheta_B/\Lambda_x$, where $\Delta\vartheta_B$ is the width of the rocking curve of the crystal–analyzer. The first condition signifies that the image is recorded in the geometric shadow of the object; therefore, the effect of the Fresnel X-ray diffraction from the object can be ignored. In our case, $R_F \approx 6$ μm; i.e., it is by two orders of magnitude less than the radius r of the laser beam and the region of beam spreading Δr at its boundary. The second condition signifies that the wave effects taking place at the Bragg reflection from the analyzer (resulting in the image diffusion along the surface of the crystal–analyzer by a value of $\approx 2\Lambda_x$ and equal, in our case, to ~15 μm) can be ignored. Finally, the third condition indicates that the change in the refraction angle (2) at a distance of Δx, which is of the order of the

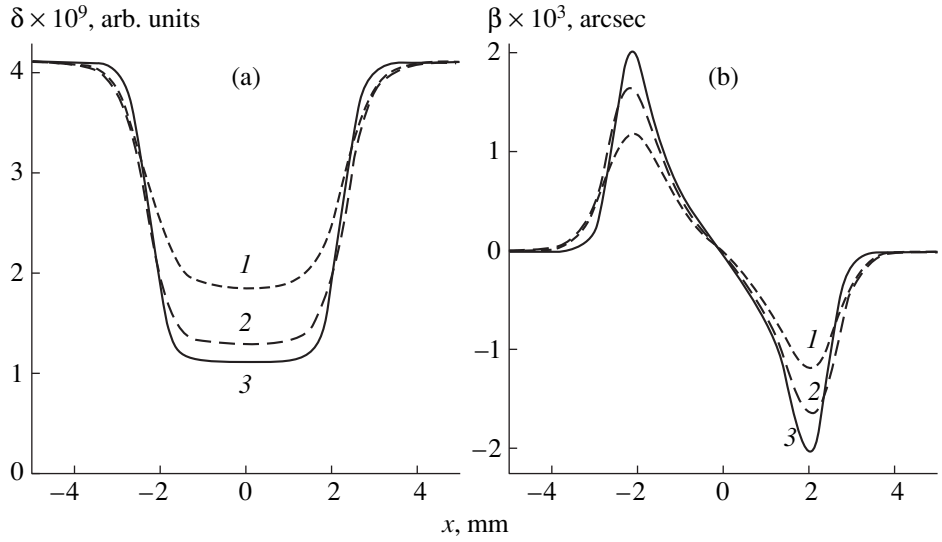

Fig. 4. (a) Decrement of air refraction $\delta(x, 0)$ and (b) angles of refraction $\beta(x)$ as functions of the transverse coordinate in the laser-beam axial section. The values of the laser power: (*1*) 22, (*2*) 28, and (*3*) 34 W.

extinction depth, should not exceed the width of the rocking curve of the analyzer.

Thus, in the geometric-optics approximation, image (1) is determined by the intensity of the local (at the same point x) reflection of a narrow X-ray beam incident onto the crystal–analyzer and characterized by the angular deviation $\Delta\vartheta - \beta(x)$. Since in terms of geometric optics, the record of the phase-contrast image of large objects in the near zone leads to refraction, then, in the scheme with a crystal–analyzer, one has to use for the phase-contrast method such terms as "refraction contrast" [1], "phase-dispersion introscopy" (radiography) [2, 4–7, 9], and "refraction introscopy" [8].

Now, assume that the spatial distribution of temperature in a cylindrical laser beam is described by the function

$$F(\rho) = [1 + \exp\{(\rho - r)/\Delta r\}]^{-1}, \qquad (4)$$

where $\rho = (x^2 + z^2)^{1/2}$, r is the beam radius, and Δr is the spreading of the beam boundary. Since the values of δ and μ are proportional to the air density and to its temperature, then the spatial distributions of the refraction decrement and the absorption coefficient can be represented as

$$\delta(\rho) = \delta_0 - \delta_1 F(\rho), \quad \mu(\rho) = \mu_0 - \mu_1 F(\rho),$$

respectively, where the values of δ_1 and $\mu_1 = \mu_0(\delta_1/\delta_0)$ depend on the temperature in the beam center.

The results of the theoretical calculations by Eq. (1) were compared with the experimental data shown in Fig. 3 by varying the values of δ_1, r, and Δr with the use of the least squares procedure. The calculations were performed with due regard for the convolution of function (1) with the rocking curve of the monochromator, R_m, and the subsequent summation over two states of X-ray polarization. Integrals (3) and the phase derivative in the calculation of the angles of refraction, $\beta(x)$ Eq. (2), were computed numerically.

The air density under normal atmospheric pressure and room temperature is 1.293×10^{-3} g/cm^3. With due regard for the atomic scattering factors and the mass attenuation coefficients [12, 13] for nitrogen in air (78.1%) and oxygen (21%), it was obtained that the refraction decrement of air is $\delta_0 = 4.11 \times 10^{-9}$ and the absorption coefficient is $\mu_0 = 0.011$ cm^{-1}. The best agreement between the calculated and the experimental data was attained at $r = 2.3 \pm 0.05$ and $\Delta r = 0.3 \pm 0.05$ mm with the ratios δ_1/δ_0 equal to 0.55, 0.69, and 0.73 at P = 22, 28, and 34 W, respectively. The calculated spatial distribution of X-ray intensity (1) are shown by the solid and dashed lines in Fig. 3.

The analysis of the decrements in air refraction δ_1 for various values of the laser power provided the estimation of the air temperature in the laser-beam cross section. According to the kinetic theory of gases, the gas pressure can be described as $p = \rho_g V^2/3$, where ρ_g is the gas density, $V = (3kT/m)^{1/2}$ is the root-mean-square velocity of molecules, and T is the absolute temperature. The equality condition of air pressure in the laser-beam region and outside this region can be used to estimate the air temperature T_1 in the laser beam. Since the decrement of refraction is proportional to the air density, then $T_1 = T_0\delta_0/(\delta_0 - \delta_1)$, where T_0 is the temperature of air in the laboratory. The calculated curves satisfactorily agree with the experimental curves if the maximum air temperature in the center of the laser beam is taken to be $T_1 = 380 \pm 30$, 660 ± 50, and 800 ± 50°C at the laser power 22, 28, and 34 W, respectively.

Figure 4 shows the dependences of the refraction decrement and angles on the coordinates at different values of the laser power. It is seen that the refraction angles do not exceed 0.002″, whereas the refraction decrement in the center of the beam and the air density are less than the corresponding values outside the laser-beam region by 50–70%.

CONCLUSION

Thus, we obtained for the first time the X-ray phase-contrast images of the laser beam in air. Our experiments show an extremely high sensitivity of the phase-contrast method in the scheme with a slit crystal–analyzer to extremely small changes in the density and refraction angles in the objects. The sensitivity of the method can be increased several times with the use of multiple asymmetric reflections (including higher-order reflections) in the monochromator and analyzer units.

The optimum choice of the working-point position on the rocking curve of the analyzer, $R(\Delta\vartheta)$, necessary for increasing the contrast is determined by the condition $\Delta\vartheta \approx \Delta\vartheta_0 - \Delta_m$, where $\Delta\vartheta_0$ is the angular position of the derivative maximum, $dR/d\Delta\vartheta > 0$, and Δ_m is the halfwidth of the angular divergence of the primary beam. Despite a certain decrease of the rocking-curve steepness and that of an overall image intensity in comparison with those for $\Delta\vartheta = \Delta\vartheta_0$, the contrast increases by a factor of about 1.5 because of a lesser smoothening of the image caused by divergence of the incident radiation.

The phase-contrast method is especially convenient for studying internal structure of weakly absorbing medical, biological, noncrystalline, and polymer objects. It is well known that the changes in the density of soft tissues of living organisms (blood vessels, lymphatic nodes, malignant neoplasms at the early stages of their development, etc.) do not exceed 3–5%. The calculations made for various organic compound-based (water, polyethylene, fats, etc.) model objects show that even small changes in the object density ($\Delta\rho$ = 0.01 g/cm^3) at the interface of width $\Delta r \sim (0.01–0.1)r$ at the beam divergence $\Delta_m \sim 0.2\Delta\vartheta_B$ result in the formation of a considerable image contrast [5–25% in the vicinity of the object boundaries (AgK_α-radiation, triple symmetric (220) silicon reflections)]. At the same time, without the use of special contrasting substances, the conventional absorption contrast in the central part of the images of the object with the dimension $r \le 5$ mm does not exceed 1%.

We believe that, along with the X-ray diffraction topography, the phase-contrast method can successfully be used for studying large-scale inhomogeneities and defects in crystals at a resolution of the order of 10 μm. Thus, the second-phase inclusions characteristic of highly doped single crystals attain the dimensions of 100–150 μm. The effective radius of defects (clusters) in the X-ray topography is determined by the far fields of the deformational and orientational lattice distortions and, as a rule, exceeds the true defect radii, whereas the phase-contrast method can also be used in the analysis of defect dimensions, shapes, and the density distribution in the bulk. Moreover, it can also be used in the cases where X-ray topographic methods are inapplicable (crystals with low degree of the structural perfection) or the optical methods are invalid (nontransparent objects).

Since the refraction phenomenon is most clearly seen at the well-pronounced interfaces, the phase-contrast method can also be successfully used in flaw detection for visualizing cracks, bubbles, caverns, etc., in various metals, alloys, and composites.

Since the rocking-curve width for the π-polarized radiation is less than for the σ-polarized radiation, the main contribution to the image formation at small angles of refraction in the vicinity of the working point on the steep slope of the rocking curve is provided only by the σ-polarized radiation. We believe that this fact can also be used for the analysis of weak polarization phenomena in noncrystalline objects possessing a natural or an artificially induced anisotropy.

REFERENCES

1. V. A. Somenkov, A. K. Tkalich, and S. Sh. Shil'shteĭn, Zh. Tekh. Fiz. **61** (11), 197 (1991) [Sov. Phys. Tech. Phys. **36**, 1309 (1991)].
2. V. N. Ingal and E. A. Beliaevskaya, J. Phys. D **28** (10), 2314 (1995).
3. T. G. Davis, T. E. Gureyev, D. Gao, *et al.*, Phys. Rev. Lett. **74** (16), 3173 (1995).
4. V. A. Bushuev, V. N. Ingal, and E. A. Belyaevskaya, Kristallografiya **41** (5), 808 (1996) [Crystallogr. Rep. **41**, 766 (1996)].
5. V. A. Bushuev, E. A. Beliaevskaya, and V. N. Ingal, Nuovo Cimento D **19** (2–4), 513 (1997).
6. V. A. Bushuev, V. N. Ingal, and E. A. Belyaevskaya, Kristallografiya **43** (4), 586 (1998) [Crystallogr. Rep. **43**, 538 (1998)].
7. V. N. Ingal and E. A. Beliaevskaya, Phys. Medica **12** (2), 75 (1996).
8. S. Sh. Shil'shteĭn, K. M. Podurets, V. A. Somenkov, and A. A. Manushkin, Poverkhnost', Nos. 3–4, 231 (1996).
9. V. N. Ingal and E. A. Belyaevskaya, Zh. Tekh. Fiz. **67** (1), 68 (1997) [Tech. Phys. **42**, 59 (1997)].
10. K. Kohra, in *Proceedings of the International Summer School on X-ray Dynamical Theory and Topography, Limoges, 1975*, p. K-1.
11. T. E. Gureyev and S. W. Wilkins, Nuovo Cimento D **19** (2–4), 545 (1997).
12. D. T. Gromer and D. Liberman, J. Chem. Phys. **53** (10), 1891 (1970).
13. M. A. Blokhin and I. G. Shveĭtser, *X-ray Spectrum Reference Book* (Nauka, Moscow, 1982).

Translated by L. Man

Crystallography Reports, Vol. 46, No. 2, 2001, pp. 176–181. Translated from Kristallografiya, Vol. 46, No. 2, 2001, pp. 215–220.

STRUCTURE OF INORGANIC COMPOUNDS

Crystal Structure of $K_{2.47}Nb_{2.85}Ti_{1.15}P_{2.5}O_{17}$

O. A. Alekseeva*, N. I. Sorokina*, M. K. Blomberg, I. A. Verin*, T. Yu. Losevskaya***, V. I. Voronkova***, V. K. Yanovskiĭ***, and V. I. Simonov***

**Shubnikov Institute of Crystallography, Russian Academy of Sciences, Leninskiĭ pr. 59, Moscow, 117333 Russia*

***Department of Physics, University of Helsinki, Helsinki, Finland*

****Moscow State University, Moscow, 119899 Russia*

Received June 2, 2000

Abstract—The structure of a crystal grown by crystallization from flux in the K_2O–TiO_2–Nb_2O_5–P_2O_5 system was studied by the methods X-ray diffraction analysis at room temperature. The crystals of the composition $K_{2.47}Nb_{2.85}Ti_{1.15}P_{2.5}O_{17}$ are monoclinic, a = 13.7864(7) Å, b = 6.4078(3) Å, c = 16.9384(7) Å, β = 83.15(1)°, sp. gr. $P2/n$. The structure was solved by the direct method using the SHELXS86 program package and refined by the JANA96 program. The crystal structure consists of a three-dimensional framework of sharing-vertices (Nb,Ti)O_6-octahedra and the PO_4-tetrahedra and two types of channels along the diagonal [101] direction, which are statistically occupied by potassium cations providing ionic transport in the compound. © *2001 MAIK "Nauka/Interperiodica".*

The present investigation continues a series of studies of atomic structures and physical properties of crystals of niobium-doped potassium titanyl phosphate $KTiOPO_4$ (KTP). Earlier, it was found [1] that single crystals with the Nb concentration up to 11% belong to the orthorhombic system (the KTP structural type), whereas crystals with the Nb concentration 75.5 and 66.6% are monoclinic (the unit cell parameters are a = 13.7864(7) Å, b = 6.4078(3) Å, c = 16.9384(7) Å, β = 83.15(1)° and a = 13.804(7) Å, b = 6.413(1) Å, c = 16.918(9) Å, β = 83.17(1)°, respectively). The chemical composition of the latter crystals is approximately described by the formula $K_2TiNb_2P_2O_{13}$. We found no data on this compound in the literature and, therefore, undertook its structural study.

EXPERIMENTAL

A single crystal was prepared by crystallization from flux in the K_2O–TiO_2–Nb_2O_5–P_2O_5 system containing 40 mol % of K_2O, 16.5 mol % of TiO_2, 16.5 mol % of Nb_2O_5, and 27 mol % of P_2O_5.

The X-ray diffraction data were collected from a homogeneous single crystal ground to a sphere 0.245 mm in diameter. The parameters of the monoclinic unit cell are a = 13.7864(7) Å, b = 6.4078(3) Å, c = 16.9384(7) Å, β = 83.15(1)°. A total of 15 026 reflections with $I \geq 3\sigma(I)$ were measured on an automated CAD-4F Enraf-Nonius diffractometer (MoK_α-radiation, $\sin\theta/\lambda \leq 1.0$). Upon averaging symmetrically equivalent reflections (R_{int} = 1.55%), the total set contained 7621 independent reflections. The observed systematic absences indicated two possible space groups—$P2/n$ and Pn. An attempt to generate the second harmonic failed, which makes the centrosymmetric space group $P2/n$ more probable. The structure was established within this space group by direct methods using the SHELXS86 program package [2] (all 22 basis atoms were established) and refined by the JANA96 program [3]. The isotropic and anisotropic refinement by the least squares method yielded the R factor of 7.26 and 4.39%, respectively. In the course of the structure refinement, all three methods of taking into account extinction realized in the programs were tested. The best results were obtained with the use of Becker–Coppens's model of type **I**, which takes into consideration the disorder of mosaic blocks in the crystal. This model was used in all the subsequent calculations.

Initially, it was assumed that in all four crystallographically independent positions, some niobium atoms are replaced by titanium atoms. Their occupancies were refined simultaneously with the structural parameters of these atoms on the condition that the positional and thermal parameters of the isomorphous mixtures of the Nb(1) and Ti(1), Nb(2) and Ti(2), Nb(3) and Ti(3), and Nb(4) and Ti(4) atoms are identical. The total occupancy of each position was taken to be unity. The refinement gave the following occupancies of these positions: $(Nb_{0.86}Ti_{0.14})(1)$, $(Nb_{0.80}Ti_{0.20})(2)$, $(Nb_{0.53}Ti_{0.47})(3)$, and $(Nb_{0.67}Ti_{0.33})(4)$. In other words, the Ti atoms in this structure are incorporated into all four Nb positions but with different occupancies.

The difference electron density syntheses revealed peaks of residual density in the vicinity of all four positions (Fig. 1). The electron density maps can be interpreted with the use of two physically different models. First, they can indicate the split of the Ti and Nb positions or whether these atoms can statistically occupy close positions. Second, the electron density can be

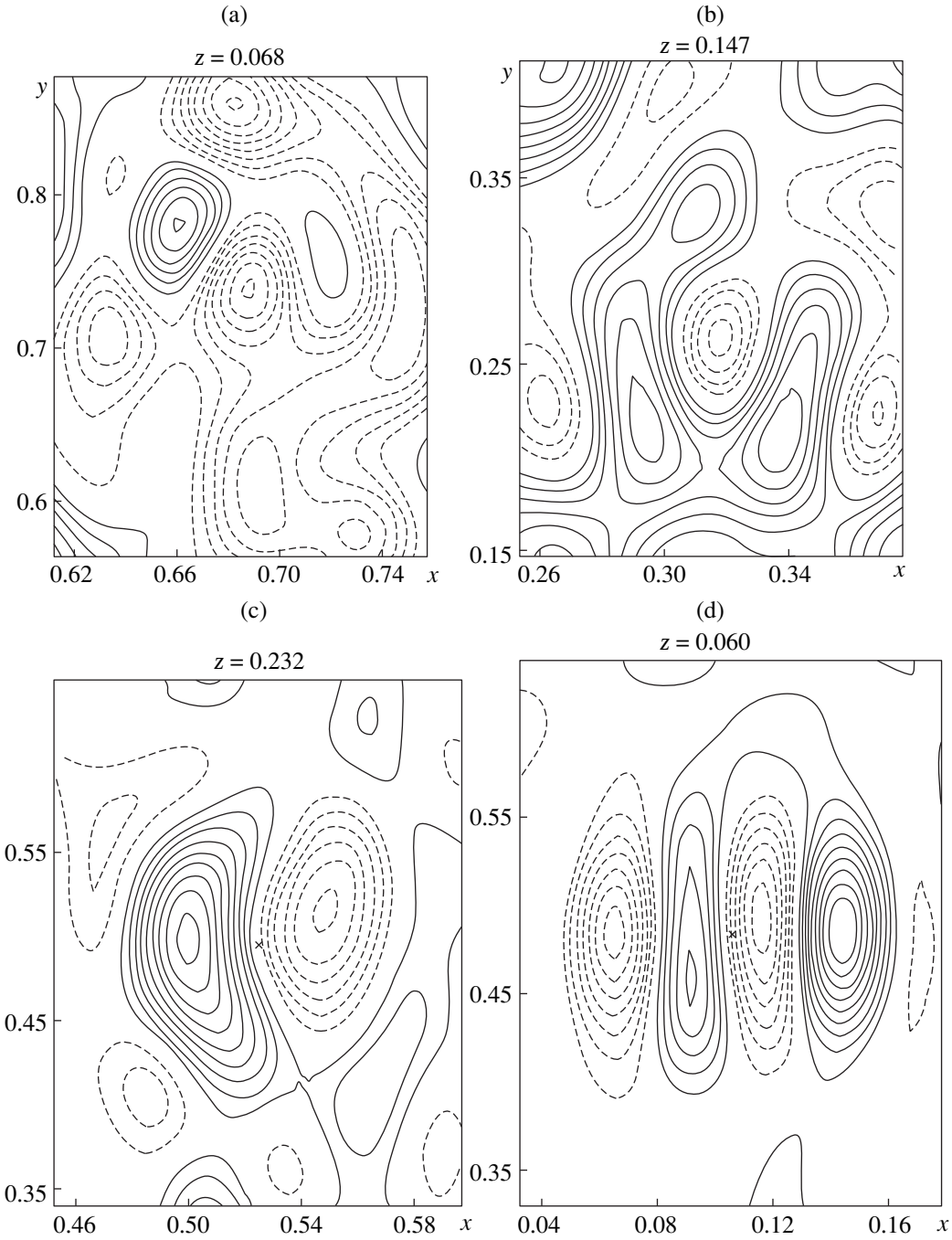

Fig. 1. Difference electron-density syntheses for the structural model refined with anisotropic thermal parameters for all the atoms: (a) the section at $z = 0.068$ passing through the (Nb,Ti) (1) atom; (b) the section at $z = 0.147$ passing through the (Nb,Ti) (2) atom; (c) the section at $z = 0.232$ passing through the (Nb,Ti) (3) atom; and (d) the section at $z = 0.060$ passing through the (Nb,Ti) (4) atom.

interpreted by taking into account possible anharmonicity of thermal vibrations of Ti and Nb atoms occupying one position. The strong correlation between all structural parameters of the Nb and Ti atoms, especially, in the case of position splitting, did not allow the refinement of the first model. The second model was tested by taking into account the anharmonicity of thermal vibrations by expanding the probability density function of atomic displacements from the equilibrium positions into the Gram–Charlier series. The terms up to the fourth order appeared to be significant for the (Nb,Ti) (1) and (Nb,Ti) (2) atoms, and the terms up to the fifth order were significant for the (Nb,Ti) (3) and (Nb,Ti) (4) atoms. The allowance for the anharmonicity of thermal vibrations reduced the reliability factor from 4.39 to 3.81%.

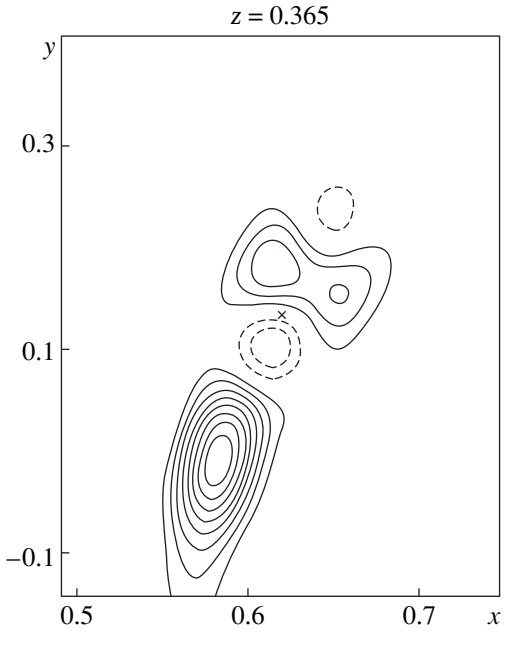

Fig. 2. Difference electron-density synthesis for the structural model with due regard for the anharmonicity of thermal vibrations of the (Nb,Ti) (1), (Nb,Ti) (2), (Nb,Ti) (3), and (Nb,Ti) (4) atoms with the anisotropic thermal parameters of the K, P, and O atoms. The section at $z = 0.365$ passing through the K(3) atom.

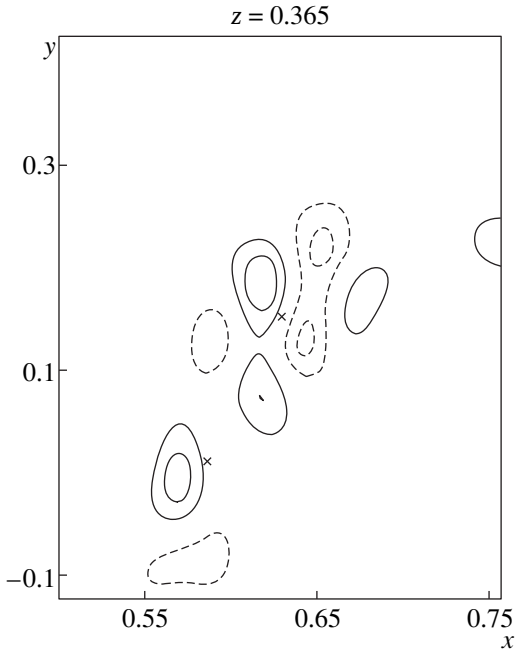

Fig. 3. Difference electron-density synthesis for the structural model with the statistical distribution of potassium atoms over two independent K(3) and K(4) positions. The section at $z = 0.365$ passing through the K(3) and K(4) atoms.

The situation with the localization of the K(3) atom was quite different. A section of the electron density synthesis at $z = 0.365$, showing this potassium atom (Fig. 2), also clearly indicates the presence of an additional position of a potassium atom. In other words, the K(3) position is split into two positions spaced by 1.07 Å. In addition to the different coordinates of the K(3) and K(4) atoms, the distribution of the positive and negative residual electron-density extrema indicated the noticeable anharmonicity of thermal vibrations of the monovalent K cations which, being in the superionic state, provide the ionic transport in the compound. At the subsequent stage, we refined the structural parameters taking into account splitting of the K(3) positions. The solution of this problem was hindered by the strong correlation between the atomic coordinates; the occupancies of the closely located positions; and atomic thermal vibrations in these positions, especially, in the presence of pronounced anharmonicity. To overcome these difficulties, we refined the strongly correlated parameters in the step-scan mode [4]. The occupancy of the position by the K(3) atom

Table 1. Refined coordinates and thermal parameters of the K(3) and K(4) atoms (obtained with the use of a stepwise change of the occupancies of their positions)

Occupancy of K(3) position	Occupancy of K(4) position	R, %	R_w, %	B_{eq} K(3), Å^2	B_{eq} K(4), Å^2	K(3)–K(4) distance
0.50	0.470(3)	2.26	2.88	3.94(5)	14.00(23)	1.015(6)
0.51	0.461(3)	2.25	2.87	3.99(5)	13.69(23)	1.029(6)
0.52	0.451(3)	2.25	2.87	4.03(5)	13.38(23)	1.043(6)
0.53	0.442(3)	2.25	2.87	4.08(5)	13.06(23)	1.057(6)
0.54	0.433(3)	2.25	2.87	4.13(5)	12.73(23)	1.071(6)
0.55	0.423(3)	2.25	2.87	4.18(5)	12.40(22)	1.085(6)
0.56	0.414(3)	2.25	2.87	4.24(5)	12.07(22)	1.099(6)
0.57	0.405(3)	2.25	2.87	4.29(5)	11.73(22)	1.112(6)
0.58	0.396(3)	2.26	2.88	4.35(5)	11.39(22)	1.125(6)
0.59	0.387(3)	2.26	2.88	4.41(5)	11.03(22)	1.138(6)

Table 2. Coordinates, position occupancies q, and thermal parameters B_{eq} (Å^2) of the basis atoms in the $K_{2.47}Nb_{2.85}Ti_{1.15}P_{2.5}O_{17}$ structure

Atom	x/a	y/b	z/c	q	B_{eq}
Nb(1)	0.68435(2)	0.71924(4)	0.06828(1)	0.856(2)	0.55(1)
Ti(1)	0.68435(2)	0.71924(4)	0.06828(1)	0.144(2)	0.55(1)
Nb(2)	0.31510(2)	0.27889(4)	0.14694(1)	0.797(2)	0.59(1)
Ti(2)	0.31510(2)	0.27889(4)	0.14694(1)	0.203(2)	0.59(1)
Nb(3)	0.52479(4)	0.49493(9)	0.23182(3)	0.527(2)	0.65(1)
Ti(3)	0.52479(4)	0.49493(9)	0.23182(3)	0.473(2)	0.65(1)
Nb(4)	0.10608(4)	0.48423(9)	0.06014(3)	0.664(2)	1.17(1)
Ti(4)	0.10608(4)	0.48423(9)	0.06014(3)	0.336(2)	1.17(1)
K(1)	0.25	0.7746(1)	0.25	1	2.17(1)
K(2)	0.40459(7)	0.75572(1)	0.02115(5)	1	2.46(2)
K(3)	0.6500(1)	0.165(1)	0.3573(3)	0.54	7.51(17)
K(4)	0.5840(5)	0.009(1)	0.3734(3)	0.433(3)	7.59(25)
P(1)	0.51460(2)	0.99614(5)	0.18033(2)	1	0.51(1)
P(2)	0.16823(2)	0.99736(5)	0.05196(2)	1	0.49(1)
P(3)	0.75	0.65132(8)	0.25	1	0.54(1)
O(1)	0.51509(7)	0.8055(1)	0.23553(6)	1	0.75(2)
O(2)	0	0.5	0	1	0.89(3)
O(3)	0.02716(7)	0.4826(1)	0.16366(5)	1	0.88(2)
O(4)	0.79920(7)	0.5496(1)	0.03157(5)	1	0.78(2)
O(5)	0.36779(7)	0.2822(1)	0.02968(5)	1	0.77(2)
O(6)	0.54722(7)	0.1863(1)	0.22566(6)	1	0.82(2)
O(7)	0.58326(8)	0.9619(1)	0.10367(6)	1	0.95(2)
O(8)	0.22302(7)	0.4700(1)	0.12277(6)	1	0.75(2)
O(9)	0.40883(7)	0.4646(1)	0.18081(6)	1	0.79(2)
O(10)	0.60049(7)	0.5285(1)	0.12026(6)	1	0.81(2)
O(11)	0.11342(7)	0.7903(1)	0.05790(6)	1	0.84(2)
O(12)	0.09128(7)	0.1714(1)	0.06251(6)	1	0.86(2)
O(13)	0.84033(7)	0.5101(1)	0.23335(6)	1	0.89(2)
O(14)	0.23624(7)	1.0106(1)	0.11651(6)	1	0.82(2)
O(15)	0.74114(7)	0.7892(1)	0.17698(5)	1	0.80(2)
O(16)	0.77158(7)	−0.0140(1)	0.02991(5)	1	0.77(2)
O(17)	0.25	0.2220(2)	0.25	1	0.96(3)
O(18)	0.41129(7)	0.0270(1)	0.15869(6)	1	0.93(2)

was successively fixed at a step of 0.01, and the coordinates and thermal parameters of all the atoms, including the occupancy of the position of the K(4) atom, were refined (Table 1). Such a procedure gave performed for the K(3) and K(4) atoms yielded $q_{K(3)} = 0.54$ and $q_{K(4)} = 0.43$, respectively. The final electron density synthesis was constructed using these parameters. The section of this synthesis at $z = 0.365$ (the coordinate of K(3) and K(4) atoms) is shown in Fig. 3.

The refinement with allowance for the anharmonicity of thermal vibrations and the expansion terms up to the fourth order was taken into account for the K(1) and K(2) atoms, whereas the expansion terms up to the sixth order were taken into account for the K(3) and K(4) atoms. The final reliability factors were $R = 1.67\%$ and $R_w = 2.18\%$.

The coordinates of the basis atoms of the structure, the occupancies of the crystallographic positions q, and the equivalent isotropic thermal parameters B_{eq} are given in Table 2. With due regard for the determined occupancies q, the refined chemical formula of the compound can be written as $K_{2.47}Nb_{2.85}Ti_{1.15}P_{2.5}O_{17}$.

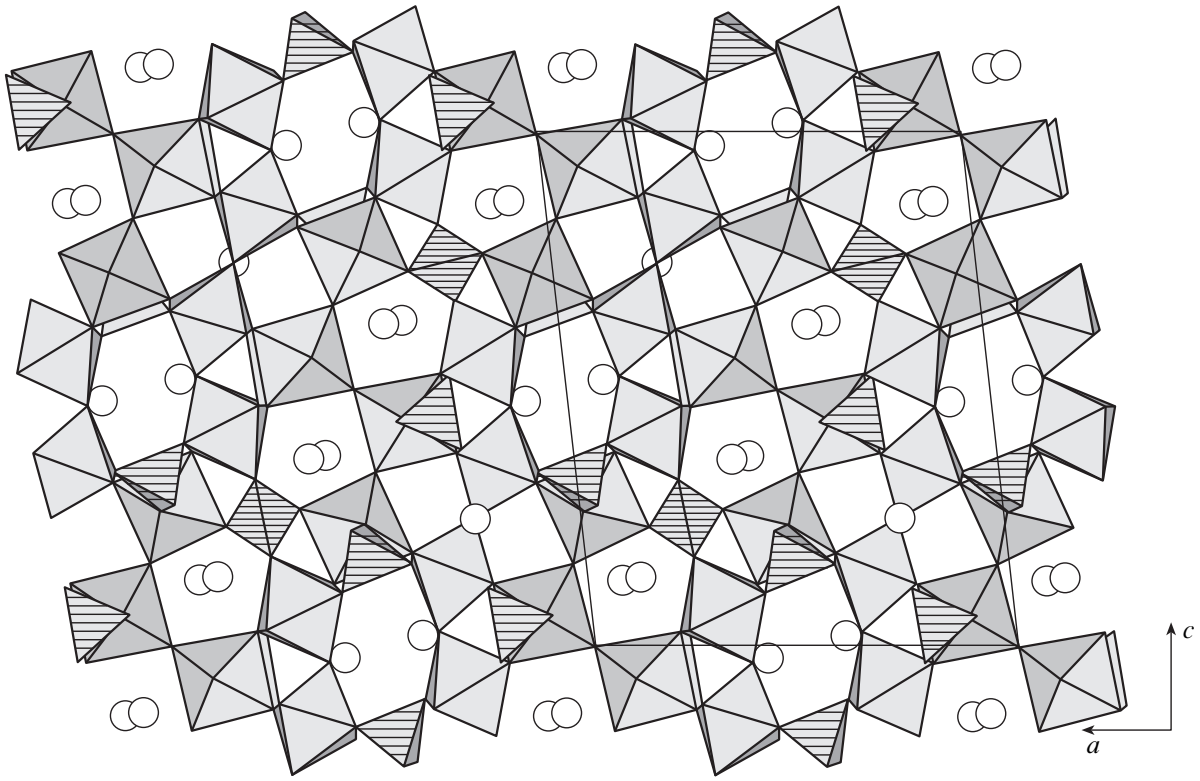

Fig. 4. The $K_{2.47}Nb_{2.85}Ti_{1.15}P_{2.5}O_{17}$ structure projected onto the *xy* plane. The (Nb,Ti) atoms are located in octahedra and the P atoms are located in tetrahedra. The K atoms are represented by circles.

RESULTS AND DISCUSSION

The crystal structure of $K_{2.47}Nb_{2.85}Ti_{1.15}P_{2.5}O_{17}$ consists of shared-vertices $(Nb,Ti)O_6$-octahedra and PO_4-tetrahedra forming a three-dimensional framework. The framework has two types of channels along the diagonal [101] direction (Fig. 4). The channels are filled with potassium cations K(3) and K(4) statistically occupying their positions. The potassium atoms in wider channels (the average K(1)–O and K(2)–O distances are 2.94 and 3.08 Å, respectively) fill their positions with the occupancies of 100%. The remaining potassium atoms are located in narrower channel (the K(3)–O and K(4)–O distances are 2.89 and 2.87 Å, respectively) with the occupancies of 54 and 43% for the K(3) and K(4) atoms, respectively.

It is also possible that some Nb and Ti ions in the structure are distributed over the pairs of closely located positions. This follows from different nature of these atoms. Thus, a niobium atom tends to be displaced from the center of the coordination polyhedron formed by oxygen atoms and form the distances of the types 3 + 3 (three short distances in the *trans* positions with respect to the long distances), 2 + 2 + 2, or 1 + 4 + 1 [5]. In the TiO_6-octahedra, the distances to four equatorial oxygen atoms are almost identical, whereas the Ti–O distances to the axial oxygen atoms are essentially different [6]. In the (Nb,Ti) (1) (q_{Ti} = 0.14) and (Nb,Ti) (2) (q_{Ti} = 0.20) octahedra, three short (Nb,Ti)–O distances (1.834, 1.886, and 1.886 Å, and 1.845, 1.895, and 1.901 Å in two octahedra, respectively) and three long distances (2.126, 2.133, and 2.146 Å, and 2.032, 2.113, and 2.130 Å, respectively) can be distinguished. The (Nb,Ti) (4) (q_{Ti} = 0.33) and (Nb,Ti) (3) (q_{Ti} = 0.47) octahedra characterized by the higher titanium concentration have one short (Nb,Ti)–O distance (1.882 and 1.831 Å, respectively) and one long distance (2.034 and 2.058 Å, respectively). The remaining four (Nb,Ti)–O distances range from 1.950 to 2.014 Å and from 1.916 to 2.019 Å, respectively.

Since the ionic radius of Ti^{4+} (0.68 Å) is somewhat shorter than that of Nb^{5+} (0.69 Å), the replacement of the Nb^{5+} ions by the Ti^{4+} ions leads to a decrease in the average (Nb,Ti)–O distance in the octahedra correlating with the titanium concentration. The average (Nb,Ti)–O distances in the (Nb,Ti) (1), (Nb,Ti) (2), (Nb,Ti) (4), and (Nb,Ti) (3) octahedra are 2.002, 1.986, 1.971, and 1.970 Å, respectively.

We intend to use the data on the crystal structure of $K_{2.47}Nb_{2.85}Ti_{1.15}P_{2.5}O_{17}$ and the results of the investigation of their physical properties (which are close to completion) to establish relationships between the structure and the properties of the crystalline materials of this new structural type.

ACKNOWLEDGMENTS

This work was supported by the Russian Foundation for Basic Research, projects nos. 00-02-16059, 00-02-17802, and 00-15-96633.

REFERENCES

1. T. Yu. Losevskaya, O. A. Alekseeva, V. K. Yanovskiĭ, *et al.*, Kristallografiya **45** (5), 809 (2000) [Crystallogr. Rep. **45**, 739 (2000)].
2. G. M. Sheldrick, *SHELXS 86: Program for the Solution of Crystal Structures* (Univ. of Göttingen, Germany, 1986).
3. V. Petricek and M. Dusek, *JANA96: Crystallographic Computing System* (Inst. of Physics, Praha, 1996).
4. L. A. Muradyan, S. F. Radaev, and V. I. Simonov, *Methods of Structural Analysis* (Nauka, Moscow, 1989), p. 5.
5. T. S. Chernaya, B. A. Maksimov, I. A. Verin, *et al.*, Kristallografiya **42** (3), 421 (1997) [Crystallogr. Rep. **42**, 375 (1997)].
6. J. Tordjman, R. Masse, and J. Y. Guitel, Z. Kristallogr. **139**, 103 (1974).

Translated by T. Safonova

Crystallography Reports, Vol. 46, No. 2, 2001, pp. 182–189. Translated from Kristallografiya, Vol. 46, No. 2, 2001, pp. 221–229.

STRUCTURE OF INORGANIC COMPOUNDS

Crystal Structure and Resistivity Characteristics of New Tantalum Bronze $K_6Ta_{6.5}O_{15+x}F_{6+y}$

A. V. Arakcheeva*, V. V. Grinevich*, A. V. Mitin, G. U. Lubman*, and V. F. Shamraĭ***

** Baĭkov Institute of Metallurgy and Materials Science, Russian Academy of Sciences, Leninskiĭ pr. 49, Moscow, 117334 Russia*

*** Kapitsa Institute for Physical Problems, Russian Academy of Sciences, ul. Kosygina 2, Moscow, 117334 Russia*

e-mail: arakchee@ultra.imet.ac.ru

Received November 18, 1999

Abstract—The structure of $K_6Ta_{6.5}O_{15+x}F_{6+y}$ (**I**) with partly reduced tantalum has been determined by the methods of X-ray diffraction analysis (SYNTEX P1 diffractometer, λMoK_α radiation, 808 independent reflections): sp. gr. $P\,6/m$, $a = 13.118(4)$, $c = 3.862(1)$ Å, $R_F = 0.0292$. The resistivity of metal-like crystals **I** is almost independent of temperature in the temperature range $T = 4$–300 K. The physical properties studied allow one to relate the crystals to the group of tantalum bronzes. The structure of compound **I** is compared with that of the well-known crystals of the transparent dielectric $K_6Ta_{6.5}O_{14.5}F_{9.5}$ (**Ia**) containing only pentavalent tantalum not belonging to the group of bronzes. The **I** and **Ia** structures have the same basic frameworks but different distributions of additional Ta atoms located along the channel axes and different degrees of delocalization as well as the numbers and degrees of delocalization of the surrounding anions. The relation between these structural features and the resistivity characteristics of the two compounds is also discussed. © *2001 MAIK "Nauka/Interperiodica".*

INTRODUCTION

The structures and properties of the solid oxide and oxyfluoride phases containing transition metal atoms from the group of bronzes have been studied and discussed in numerous monographs and articles (e.g., [1, 2]) in connection with their unusual physical and chemical properties—the dark grey or black color with metal luster, metal or semiconductor type of conductivity, the existence of the homogeneity region, and a high chemical resistance to acids (producing no oxidizing effect). Usually, the bronze structures are built by $M(O, F)_6$-octahedra sharing the edges and vertices and forming various frameworks, with alkali metal atoms being located inside these frameworks. The *M* atoms with reduced oxidation degrees [1] in such compounds include W, V, Ti, Nb, Ta, Mo, Re, and Ru and form the tungsten, vanadium, etc., bronzes, respectively. However, not all of the compounds possessing the structures and the compositions characteristic of bronzes are real bronzes; i.e., they can demonstrate the physical and the chemical properties indicated above. Thus, $K_{0.5}WO_3$ is a bronze, whereas the isostructural compound $K_{0.5}(W_{0.5}Ta_{0.5})O_3$ is not [1]. Usually, the transition to the fully oxidized state of the transition metals without the change of the initial structure type results in the loss of the metal properties characteristic of bronzes. In this connection, the oxide and oxyfluoride compounds with the properties characteristic of bronzes are usually synthesized under the reduction conditions. The most widespread efficient method of their synthesis is electrolysis of salt melts [2].

Studying the electrolysis of the melted K_2TaOF_5–$(KF + NaF + LiF)_{eut}$ salt system, we observed the formation on the cathode of dark grey $K_6Ta_{6.5}O_{15+x}F_{6+y}$ (**I**) crystals with metal luster and the hexagonal–prismatic habit. The characteristic metal-like appearance of the crystals and the resistivity measured at room temperature ($\rho \approx 4 \times 10^{-3}$ Ω cm) showed that the crystals belong to the group of bronzes. The powder X-ray diffraction pattern indicated that crystals **I** are isostructural to the well-known transparent colorless hexagonal crystals of the composition $K_6Ta_{6.5}O_{14.5}F_{9.5}$ (**Ia**) with the structure although close to that of the hexagonal tungsten bronze, but not really related to bronzes [3]. The conditions for synthesis of compound **Ia** (solid-phase sintering of the pentavalent-tantalum-containing compounds such as K_2TaF_7, $KTaO_3$, and Ta_2O_5 [3]) exclude the presence of tantalum with the reduced oxidation degree, whereas the reduction conditions of electrocrystallization on the cathode provide the presence of tantalum with a reduced oxidation degree in compound **I**.

Thus, our goal was to determine the structure of new tantalum bronze **I** with partly reduced tantalum and compare it with the structure of compound **Ia** having a

similar composition but containing only pentavalent tantalum.

The traditional interest in the structural studies of bronzes was additionally stimulated by the indication that $Na_{0.05}WO_3$ may possess high-temperature superconductivity (T_c = 91 K) [4]. Thus, we have also to check the temperature dependence of conductivity of this new tantalum bronze (which was later proved to be unique).

SYNTHESIS AND PHASE IDENTIFICATION

Compound **I** was crystallized on a cathode (a molybdenum rod 5 mm in diameter) during transmission of a current with the density 0.15 A/cm^2 through a melted electrolyte containing monoxyfluoride $[TaOF_6]^{3-}$ and dioxyfluoride $[TaO_2F_4]^{3-}$ tantalum complexes (the total Ta concentration was 0.6 mol/kg of the electrolyte). The three-hour electrolysis was performed with the use of a TaO anode at 750°C. The current was switched off, and the cathode was removed from the electrolysis vessel and cooled to room temperature in the argon atmosphere. Then the product formed on the cathode was washed for three hours with an HCl solution heated up to 60°C to remove the salts captured during electrolysis.

However, even upon such a treatment, the radial intergrowth of small metal-like crystals of the precipitate on the cathode were still covered with a considerable amount of transparent colorless crystalline mass. Moreover, the washed precipitate contained transparent crystals of a similar shape and crystals with suddenly or gradually changing transparency along the elongation axes along with well-faceted metal-like crystals in the shape of elongated hexagonal prisms.

The product precipitated on the cathode was identified by the methods of X-ray phase analysis prior to and upon its washing in the hydrochloric acid (DRON-3M diffractometer, λCuK_α radiation, Ni-monochromator). The specimens not washed in the hydrochloric acid showed the presence of alkali metal (Na, Li, and K) fluorides, with the amount of KF being minimal, which disappeared upon washing in HCl. The washed specimens appeared to be two-phase, but their X-ray patterns were identical with the spectrum calculated by the data for **Ia** [3]. The mechanical separation of the metal-like elongated hexagonal prismatic crystals from the transparent colorless ones and the subsequent study of the corresponding X-ray diffraction patterns proved their isostructurality with **Ia** (sp. gr. $P\bar{6}$, a = 13.109 Å, c = 3.880 Å). Proceeding from these data, we made the conclusion that the transparent phase was identical to the phase **Ia** and that this phase belongs to the same structure type of metal-like crystals studied in detail by the single-crystal X-ray diffraction method.

It should be emphasized that the colorless crystalline mass of compound **Ia** is not the product of electrocrystallization on the cathode. This compound is formed due to chemical reactions in the electrolyte. The mechanisms of these reactions will be considered in another article.

X-RAY STUDY

The X-ray study of compound **I** was performed on a well-faceted dark grey single crystal with metal luster having the shape of an almost isometric hexagonal prism. The X-ray diffraction data were collected within a hemisphere of the reciprocal space on a SYNTEX P1 diffractometer (λMoK_α radiation; $\sin\theta/\lambda < 1.08$; 2063 reflections). The parameters of the hexagonal unit cell of compound **I** and the unit-cell parameters of compound **Ia** are given in Table 1. Upon the introduction of the absorption correction (by numerical integration with due regard for the real shape of the crystal) and averaging the equivalent reflections within the diffraction class 6/m (R_{eq} + 0.043), the further computations were made using 808 independent reflections with $I > 2\sigma(I)$.

The structure model of **I** obtained by the direct method within the sp. gr. $P6/m$ (AREN program complex [5]) confirmed the isostructurality of the main frameworks of compounds **I** and **Ia** with the composition $[K_6Ta_6(O, F)_{21}]$ in both cases. This framework can be described within three space groups of the diffraction class considered, namely, $P6$, $P\bar{6}$, and $P6/m$. The further refinement of the structure was made within all these tree groups in parallel by the program complex JANA98 [6]. The parameters of the basis atoms of the framework were refined in the following sequence: coordinates of Ta and K cations in the isotropic approximation of thermal vibrations up to $R(F) \approx 0.14$; coordinates of anions with the use of the f-curves for O atoms in the isotropic approximation up to $R(F) \approx 0.135$; coordinates of cations in the anisotropic approximation up to $R \approx 0.11$; coordinates of cations and anions in the anisotropic approximation up to $R \approx 0.10$. The values of the positional and thermal atomic parameters for the framework obtained within the three space groups at the close values of R-factors slightly differed at all the stages of the refinement. In the sp. gr. $P6/m$, the main framework of the structure is described by one Ta(1) position, one K position, and five anionic (O, F) positions (Table 2). The kinds of the anions of the main framework were established upon calculation of the valence-strength balance by the method suggested in [7] (Table 3), which showed that all the shared vertices of Ta(1)-octahedra are occupied by oxygen atoms, whereas the "isolated vertices" looking inside the channels are occupied by F atoms (Fig. 1). Thus, the main framework of compound **I** has the composition $[K_6Ta_6O_{15}F_6]$.

As is seen from Fig. 1, the framework has wide channels (with a diameter exceeding 6.5 Å) elongated in the [001] directions with the axes coinciding with the

Table 1. Crystallographic characteristics of the $K_6Ta_{6.5}O_{15+x}F_{6+y}$ bronze (**I**) and transparent $K_6Ta_{6.5}O_{14.5}F_{9.5}$ crystals (**Ia**)

Characteristic	$K_6Ta_{6.5}O_{15+x}F_{6+y}$ (**I**) (Ta^{n+}, $n < 5$)	$K_6Ta_{6.5}O_{14.5}F_{9.5}$ (**Ia**) [3] (Ta^{5+})
Sp. gr.	$P6/m$	$P\bar{6}$
Unit-cell parameters, Å	a = 13.118(4) c = 3.862(1)	a = 13.109(7) c = 3.880(7)
c/a ratio	0.2944	0.2960
Framework:		
composition and charge	$[K_6Ta_6O_{15}F_6]^{(30-6n)-}$	$[K_6Ta_6O_{15}F_6]^0$ (*)
Ta–X distances, Å	⟨Ta–O⟩ 1.93; ⟨Ta–F⟩ 2.06	⟨Ta–O⟩ 1.93; ⟨Ta–F⟩ 2.01
K–X distances, Å	⟨K–F⟩ 2.86; ⟨K–O⟩ 2.96	⟨K–F⟩ 2.87; ⟨K–O⟩ 3.04
Channel:		
composition and charge	$[Ta_{0.5}(O, F)_m]^{(30-6n)+}$	$[Ta_{0.5}F_{2.5}]^0$ (*)
Ta_{chan}	“Centered” dumbbell: 0.025Ta(3)–0.45Ta(2)–0.025Ta(3); $z_{Ta(2)} = 0.5$; $z_{Ta(3)} = \pm 0.28$	“Dumbbell”: 0.25Ta–0.25Ta; $z_{Ta} = \pm 0.371$
X_{chan}	~1.5(O, F); $z \sim \pm 0.17$; (are delocalized)	2.5F (*); z = 0;
Ta_{chan}–Ta_{chan} distances along the sixfold axis, Å	– 0.85 – 0.85 – 2.16 –	–1.0 – 2.88 –
K–Ta_{chan} distance, Å	4.50 × 2	4.41, 4.48
Conductivity, Ω cm	$\rho = 4 \times 10^{-3}$	Dielectric

* Data corrected in the present study. According to [3], the framework and the channel are characterized by $[K_6Ta_6O_{12.688}F_{8.312}]^{2.312+}$ and $[Ta_{0.5}O_{1.812}F_{1.188}]^{2.312-}$, respectively.

Table 2. Coordinates, thermal factors, and parameters of anharmonic atomic thermal vibrations in $K_6Ta_{6.5}O_{15+x}F_{6+y}$ ($x + yz \approx 1.5$)

Atoms of the main framework $[K_6Ta_6O_{15}F_6]$

Atom	x/a	y/b	z/c	β11	β22	β33	β12	B_{iso}
Ta(1)	0.36955(7)	0.84397(7)	0.5	0.002090	0.001854	0.020153	0.000771	1.13(2)
K	0.6564(2)	0.9134(1)	0	0.008221	0.003666	0.030588	0.001799	2.92(9)
O(1)	0.4673(4)	0.7786(4)	0.5	0.002138	0.002264	0.055757	0.000877	1.9(5)
O(2)	0.5	0	0.5	0.003742	0.000855	0.054650	–0.000524	2.2(6)
O(3)	0.6441(5)	0.1497(5)	0	0.007851	0.007807	0.019811	0.004238	3.0(7)
F(1)	0.6540(3)	0.7425(3)	0.5	0.002536	0.004161	0.042360	0.001509	2.0(5)

Atoms of the main framework $[Ta_{0.5}(O, F)_m]$ (m = 1.5)

Atom	q	x/a	y/b	z/c	β11	β22	β33	β12	B_{iso}
Ta(2)	0.45(1)	0	0	0.5	0.004208	0.004208	0.00645	0.002104	1.57(6)
Ta(3)	0.025	0	0	0.7197(1)	0.00442	0.00442	0.022633	0.00221	1.97(9)
F(2)	0.13(4)	0.038(2)	0.131(2)	0.171(4)	–	–	–	–	2.0

Independent and nonzero components of the tensors of anharmonic vibrations

Ta(2): $D1111 = 0.0022(2)$; $D1112 = 0.0011(1)$; $D1113 = -0.044(2)$; $D1233 = -0.0221(8)$; $D3333 = 14.27(3)$; $F111133 = 0.0034(3)$; $F112233 = 0.0017(1)$; $F113333 = -0.082(2)$; $F123333 = -0.0041(1)$; $F222233 = (3)$; $F333333 = 56.9(1)$.

Note: Only independent values of thermal factors and the values of $C \times 10^3$, $D \times 10^4$, $E \times 10^5$, and $F \times 10^6$ are given.

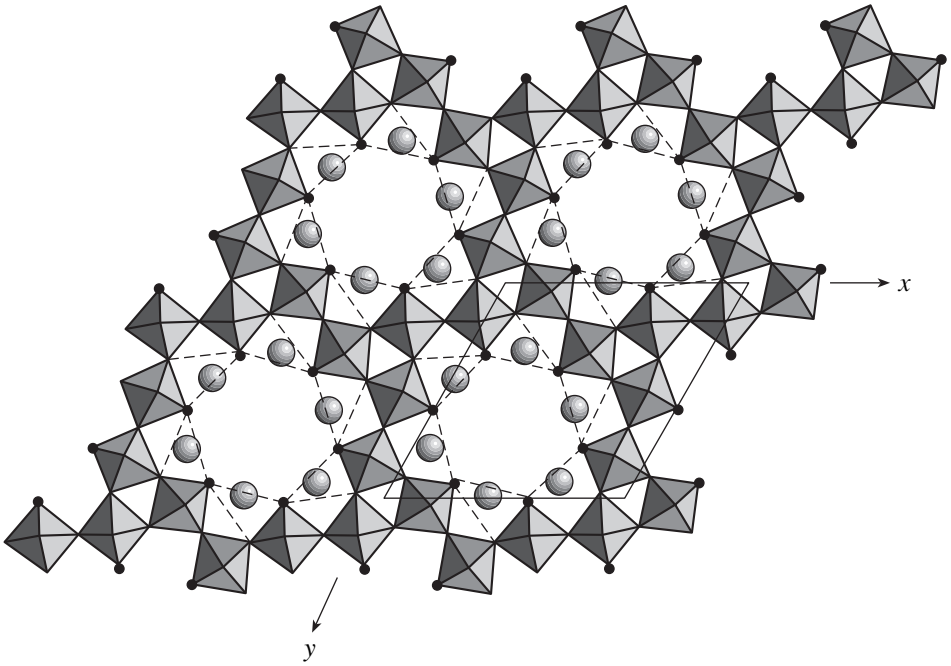

Fig. 1. The main $[K_6Ta_6O_{15}F_6]$ framework of structures **I** and **Ia** projected onto the (001) plane; small black circles at the vertices of the $[TaO_5F]$ octahedra denote F atoms; large circles denote K atoms; dashed lines indicate the K prisms projected onto the (001) plane.

sixfold axis. The difference electron-density maps calculated for all the three space groups were almost equivalent. The peak coordinate $z = 0.5$ along the channel axis (Fig. 2a) indicated the presence of an additional atom identified as Ta(2) with the occupancy 0.45 (the use of the *f*-curve of K resulted in the negative values of the isotropic thermal factor). The introduction of this atom reduced the *R*-factor down to ~0.07.

The difference electron-density maps calculated at this stage of the refinement showed an extended region of the positive electron density along the channel axis (Fig. 2b), which indicated the considerable delocalization of the Ta(2) atoms probably with the anharmonic thermal vibrations. Since the difference maps constructed at various stages of the structure refinement within the above three space groups showed no considerable deviations from the maps constructed within the sp. gr. *P*6/*m*, further refinement was performed in the latter space group.

The refinement of the structure parameters in the anharmonic approximation of thermal vibrations of both Ta atoms (we used the Gram–Charlier expansion with the terms up to the sixth order) reduced the reliability factor to 0.05 and indicated the considerable anharmonicity of thermal vibrations only for Ta(2) atoms located inside the channels. As was expected, this effect was the most pronounced along the [001] direction and the sixfold axis (Table 2). The difference electron-density map constructed with due regard for anharmonicity of thermal vibrations of Ta(2) atoms showed new well-pronounced maxima on the sixfold axis with $\rho = 3.5$ e/Å^3 (Fig. 2c), which later were identified with Ta(3) atoms with the occupancy 0.025 of the position of multiplicity two. Thus, we revealed "centered" dumbbells on the channel axis, Ta(3)–Ta(2)–Ta(3) (Table 1), whose centers were most probably occupied by Ta atoms. The reliability factors at this stage of the refinement were $R(F) = 0.0305$ and $R(w) = 0.0415$ ($w = 1/\sigma^2$). The positional and thermal parameters of atoms corresponding to this model are indicated in Table 2. The framework Ta(1) atoms are characterized by the octahedral environment, whereas a coordination polyhedron of K atom is a trigonal prism. The K-prisms that form the channel walls and share their bases located along the channel axis (Fig. 1). Some dimensional characteristics of the cationic polyhedra of the framework of structure **I** are listed in Table 1. For comparison, Table 1 also gives similar data for structure **Ia** [3]. The framework anions closest to the Ta(2)

Table 3. Balance of valence strengths in the main $[K_6Ta_6O_{15}F_6]$ framework of the $K_6Ta_{6.5}O_{15+x}F_{6+y}$ structure ($x + y \approx 1.5$) according to Brown

Anions	Ta(1)	K	Total charge at anions
O(1)	1.16 + 0.82	0.11 × 2	2.2
O(2)	1.05 × 2	0.03 × 4	2.22
O(3)	0.93 × 2	0.08 × 0.06	2.0
F(1)	0.51	0.12 × 2 + 0.08 × 2	0.91

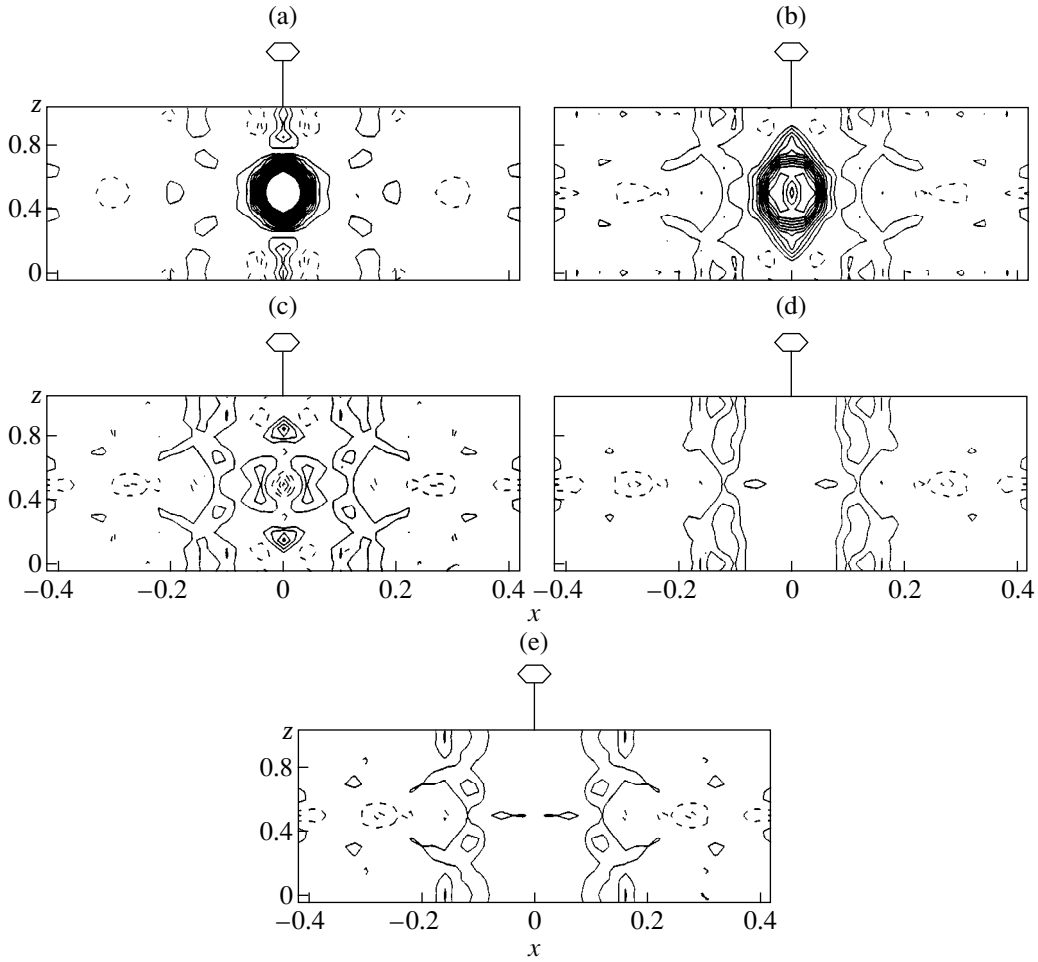

Fig. 2. Ta atoms located on the sixfold axis in the channel. The sections of difference electron-density maps are obtained at various stages of the refinement of structure **I**: (a) anisotropic refinement of the atoms of the main framework (the isolines are spaced by 10 e/Å^3); Ta(2) positions are well distinguishable; (b) anisotropic refinement of the atoms of the framework and Ta(2) atoms (the isolines are spaced by 1 e/Å^3); one can see delocalized Ta(2) atoms; (c) refinement in the anharmonic approximation of the Ta(2) vibrations (the isolines are spaced by 0.5 e/Å^3); the Ta(3) position is seen; (d) the refinement in the anharmonic approximation of Ta(2) vibrations with due regard for the Ta(3) position (the isolines are spaced by 0.3 e/Å^3), one can distinguish the regions of the anionic environment; and (e) the final stage of the refinement upon localization of the anions in the channels (the isolines are spaced by 0.3 e/Å^3; one can still see the regions of the residual electron density).

and Ta(3) atoms in **I** are spaced by the distances exceeding 3.5 Å. The absence of any anionic environment for the atoms lying in the channels required a more detailed study of their neighborhoods.

The difference map constructed for the model with three Ta positions had the maximum and the minimum electron-density values equal to 1.8 and –1.7 e/Å^3, respectively. The positive electron-density regions are located in six symmetry-related "rods" (0.13, 0.038, *z*) along the channel axis with the *z*-coordinate ranging from $z = -0.33$ to $z = 0.33$. These rods can be considered as the regions of delocalized anions around the Ta atoms located in the channel, because the distance from any point of these rods to the Ta(2) atom ranges within 1.9–2.2 Å. All attempts to localize anions lying in the channels within the low-symmetric *P*6, $P\bar{6}$ (and also *P*3 and $P\bar{3}$) space groups yielded no more reliable results. Therefore, we considered the *P*6/*m* group to be the true one for compound **I**. In structure **Ia**, the anions in the channels were localized within the sp. gr. $P\bar{6}$ [3].

The local electron-density maximum with the coordinates (0.13 0.038 0.171) from the region singled out in Fig. 3a was conditionally identified as an anion localized in the channel. The following refinement of the position occupancy at the fixed value of the isotropic thermal parameter based on the *f*-curves for F [see F(2) in Table 2] reduced the reliability factors to $R(F) = 0.0292$ and $R(w) = 0.0398$. The distances from this position to the nearest cationic ones are F(2)–Ta(2) 1.99 Å, F(2)–Ta(3) 1.59 and 2.32 Å, and F(2)–K 2.92 Å. The electron-density sections corresponding to the last cycle of the refinement (Figs. 2e, 3b) showed again the residual electron density, which confirms delocalized

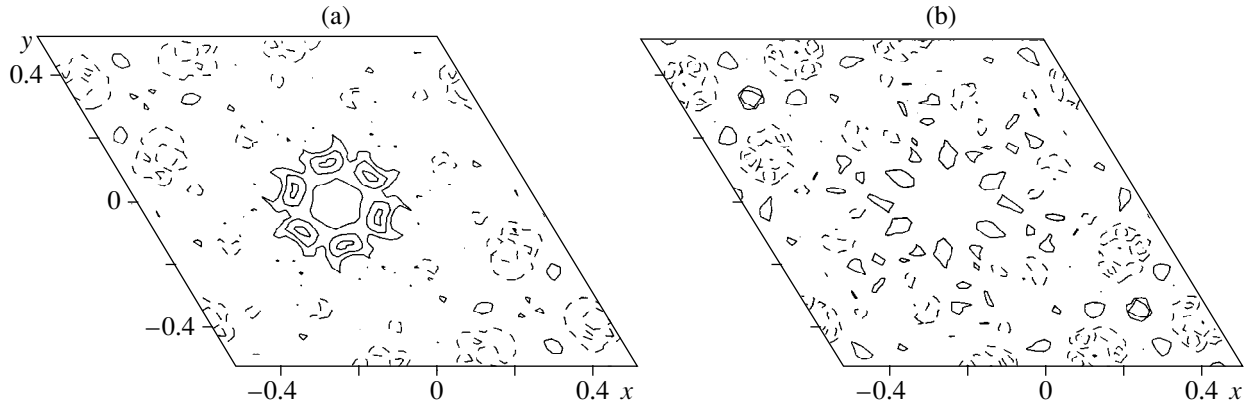

Fig. 3. Sections of difference electron-density maps by the (001) plane at a height of $z = 0.2$: (a) prior to and (b) upon the localization of anions in the channels (the isolines are spaced by 0.3 e/Å^3).

arrangement of the anions in the channels. We failed to determine the exact number and ratios of the O and F atoms.

The assumption on the incommensurability of the sublattices of the main framework and the atoms in the channels has not been confirmed by our study of the reciprocal space by the oscillation and the local scanning methods on a SYNTEX P1 diffractometer. However, it cannot be excluded that the X-ray tube used in our experiments was insufficiently powerful and, therefore, did not allow us to record reflections from the intrachannel sublattice.

According to our estimates, the formula of the new Ta-bronze (**I**) can be written as $[K_6Ta_6O_{15}F_6]$ $[Ta_{0.5}(O, F)_m] = K_6Ta_{6.5}O_{15+x}F_{6+y}$. The compositions of the main framework of the channel are given in the first and the second square brackets, respectively. The value of $m = x + y \approx 1.5$ following from the refinement of the occupancy of the conditional position F(2) should be considered only as an approximate value.

TEMPERATURE DEPENDENCE OF CONDUCTIVITY

Electric conductivity of metal-like single crystals of compound **I** was measured on two ~0.3 × 0.3 × 0.5-mm-large specimens by the four-contact method with the current $j \parallel c$ in the temperature range 4.2–293.0 K. The potential contacts were spaced by ~0.2 mm. The change of the measuring-current density by two orders of magnitude (from 0.5 to 50 A/cm^2) did not change the linear character of the current–voltage characteristics of the specimens within the experimental accuracy. Irrespectively of measuring currents, the conductivities were almost temperature-independent (Fig. 4). The calculated resistivity was equal to $\rho \approx 4 \times 10^{-3}$ Ω cm (the conductivity $\sigma \approx 250$ Ω^{-1} cm^{-1}). The transparent crystals identified with the phase **Ia** showed dielectric properties.

DISCUSSION OF RESULTS

Now, compare the structural characteristics of **I** and **Ia** (Table 1) in order to establish the relation between the crystal structure and its properties. The differences between these two compounds can be attributed to a lower degree of reduction of tantalum in **I** in comparison with its reduction degree in **Ia** (where Ta has the maximum oxidized state, Ta^{5+}).

In both compounds, the symmetry of the main framework is described by the sp. gr. *P*6/*m*; therefore, the structures of the frameworks in both compounds are almost identical. The balance of valence strengths at anions calculated for the framework of **I** (Table 3) uniquely indicated that the O and F atoms are separated

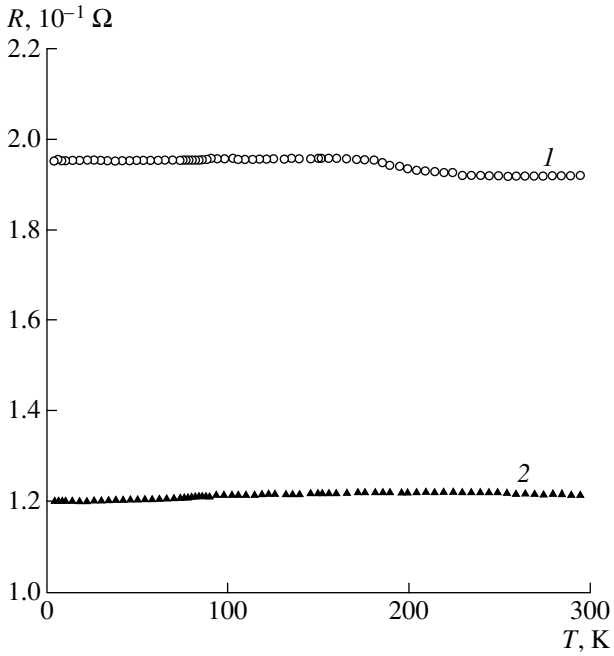

Fig. 4. Temperature dependence of conductivity measured for crystals **I**.

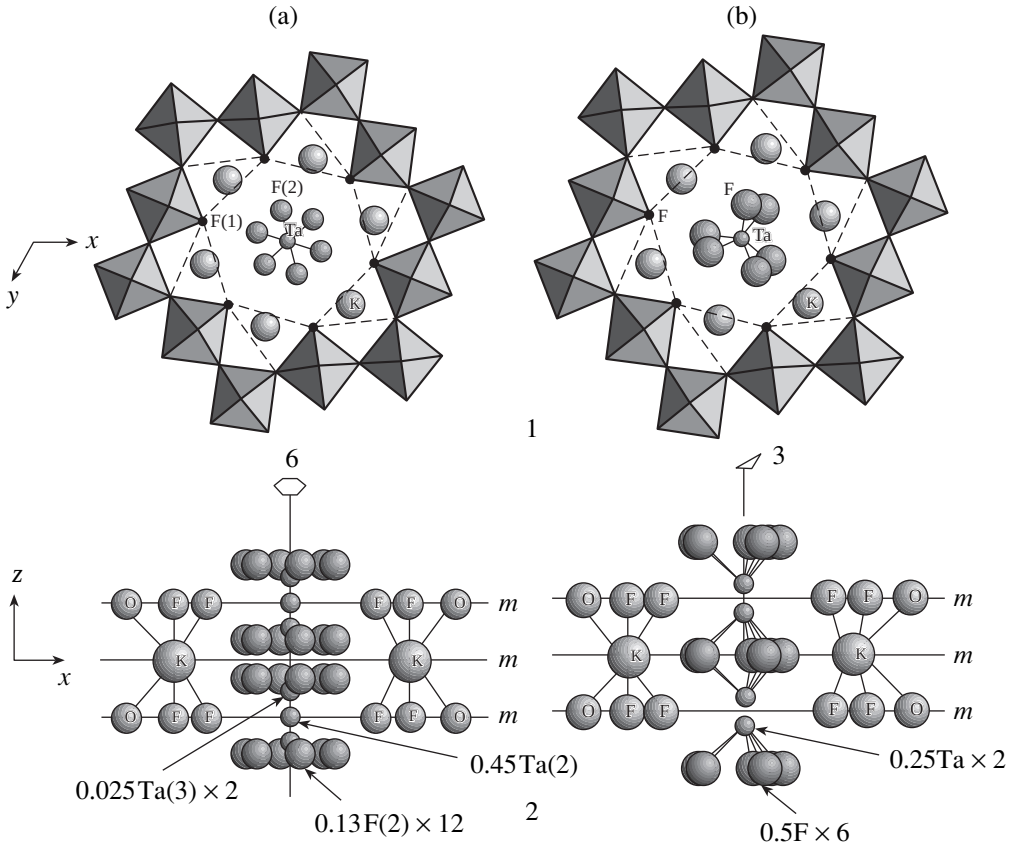

Fig. 5. Comparison of the atomic positions in the channels for the structures (a) **I** (sp. gr. *P*6/*m*) and (b) **Ia** (sp. gr. $P\bar{6}$) projected along the (1) [001] and (2) [100] directions.

and led to the framework formula $[K_6Ta_6O_{15}F_6]$. Similar computations based on data [3] yielded the same formula for the framework of **Ia**. Taking into account different oxidation state of tantalum in these two compounds, we can draw a conclusion that the framework in **Ia** is electrically neutral (pentavalent tantalum), whereas the framework of **I** is negatively charged (the degree of Ta oxidation is less than +5). An increase of the Ta–F distances and shortening of the K–O distances in **I** in comparison with the analogous distances in **Ia** (Table 1) is consistent with this statement.

Different charges of the frameworks in **I** and **Ia** result in different structures and different charges of the channel space (Fig. 5). In both cases, the content of this space is described as $[0.5Ta_{chan}mX_{chan}]$ (Table 1): the Ta_{chan} cations occupy the positions on the axis with different occupancies, whereas the X_{chan} = (O, F) anions provide the electric neutrality of each compound. A lower content of X_{chan} in **I** in comparison with that in **Ia** at the same amount of Ta_{chan} provides the positive charge of the intrachannel space in **I** and its neutrality in **Ia**. The formula of the channel complex $[Ta_{0.5}X_3]$ [3] in **Ia** even at X = F provides the negative charge of this complex, which is inconsistent with the electric neutrality of its framework. This inconsistency can be caused by an insufficient accuracy in the determination of the occupancy of the positions of the intrachannel anions in [3] (q = 0.5 corresponding to X_3, instead of a more probable value q = 0.417 corresponding to $X_{2.5} = F_{2.5}$), which is quite admissible at the reliability factor R = 6.1%.

The intrachannel complex in **Ia** is a column composed by trigonal prisms sharing the bases formed by anions located at the levels z = 0 and 1 (Fig. 5b, part 2). Each set of prisms contains a Ta atom statistically occupying two positions related by the plane *m*. The anionic environment of Ta_{chan}^{5+} in the prisms sufficient for neutralization corresponds to the ionic–covalent Ta–X bonding and provides the mutual screening of Ta atoms. Crystals **Ia** are transparent and colorless; they possess dielectric properties characteristic of most inorganic compounds with prevalent ionic bonding.

Unlike **Ia**, structure **I** is characterized by a low anion concentration in the positively charged intrachannel complex and the location of Ta_{chan} cations at the maximum distance from the nearest framework K cation (Fig. 5a, part 2, Table 1). In this case, the maximum screening of Ta_{chan} from K is attained if the regions of the prevalent location of the channel anions are dis-

placed from the plane *m* (Fig. 5a, part 2). The deficiency of anions in the first coordination sphere of Ta_{chan} results in the Ta–Ta interaction of the metal nature between these partly reduced cations located along the channel axis. The existence of such interactions is confirmed by short distances between the positions with an elevated probability of Ta_{chan} (Table 1). As has already been indicated, Ta_{chan} atoms, as well as the surrounding anions, are considerably delocalized. The formation of Ta–Ta bonds in **I** (absent in **Ia**) manifests itself in the changed resistivity characteristics and the dark grey color and metal luster, which allows us to relate compound **I** to bronzes.

Thus, the crystal lattices of both compounds can be considered as two mutually penetrating sublattices—those of the framework and the channel. The differences in the physical properties of two compounds are associated with differences in the structures of the channel sublattices. Proceeding from this representation, the evolution of the temperature dependence of conductivity during tantalum reduction can be associated with the changes in the distribution of Ta_{chan} atoms along the central axis of the channel. In **I**, the distances between the neighboring positions of these atoms are $d_{Ta–Ta} \le 2.16$ Å and provide a rather high probability of tunneling due to overlap of the wave functions of Ta. Since the integral of this overlap exponentially decreases with the distance, the probability of such tunneling in **Ia** drastically decreases because the maximum distance between the neighboring Ta positions increases up to 2.88 Å.

According to the data obtained, the channel sublattice in **I** can be considered as a system of periodically located regions extended along the channels usually occupied by Ta_{chan} atoms. Each region includes a "centered" dumbbell of Ta_{chan} positions (Fig. 5, Table 1).

The potential of the crystal field in such a system can be represented by a set of potential wells with the random distribution of their extreme values along the [001] direction. The main parameter determining the conductivity of such system is the V_0/B ratio, where V_0 determines the region of potential spreading and B determines the overlap of the wave functions [8]. The characteristic feature of such systems is the existence of the critical energy E_C in their spectrum separating the regions of the localized and nonlocalized states of atoms. In this case, the temperature dependence of conductivity is described by the equation

$$\sigma = \sigma_{min}\exp[-(E_C - E_F)/kT],$$

where E_F is the Fermi energy and σ_{min} is the temperature-independent minimum metal conductivity.

If E_F lies within the region corresponding to the localized states of the atoms ($E_F < E_C$), the conductivity mechanisms can be provided by thermally activated hoppings of atoms from one localized state to another or excitation of electrons to the mobility edge. In both cases, the derivative $d\rho/dT$ has a negative value. At $E_C = E_F$, we have $\sigma = \sigma_{min}$; i.e., σ attains the value of the minimum conductivity independent of temperature. In this case, the estimation of the order of σ_{min} made in [8] by formula $0.026e^2/\hbar a$ (Ω^{-1} cm^{-1}), where a is the interatomic distance, yields ~200 Ω^{-1} cm^{-1}.

The values of σ of specimens **I** are close to the estimate of σ_{min}, which, with due regard for the independence of resistivity of the temperature, allows one to invoke the concepts of the minimum metal conductivity. It seems that the value of V_0/B in the compounds of type **I** can vary within certain limits. Indeed, delocalization of Ta_{chan} and the nonuniform occupancy of the positions should stimulate a certain disorder, whereas the different degrees of the reduction of Ta cations can lead to a displacement of E_F. Thus, there are serious prerequisites for the application of the concept of minimum metal conductivity to the compounds of the bronze type. It is expedient to discuss this problem in more detail upon studying the crystals with degrees of Ta reduction different from that in **I**.

ACKNOWLEDGMENTS

This study was supported by the Russian Foundation for Basic Research, project no. 98-03-32804.

REFERENCES

1. A. Wells, *Structural Inorganic Chemistry* (Clarendon Press, Oxford, 1984; Mir, Moscow, 1987), Vol. 2, p. 334.
2. *Oxide Bronzes*, Ed. by V. I. Spitsyn (Nauka, Moscow, 1982).
3. M. Vlasse, A. Boukhari, J. P. Chaminade, and M. Pouchard, Mater. Res. Bull. **14**, 101 (1979).
4. Inf. Byull. *Perst* **6** (9), 5 (1999); High Tc Update **13**, 9 (1999).
5. V. I. Andrianov, Kristallografiya **34** (6), 592 (1989) [Sov. Phys. Crystallogr. **34**, 352 (1989)].
6. V. Petříček, *Computing System JANA98* (Institute of Physics, Academy of Sciences of the Czech Republic, Prague, 1998).
7. I. D. Brown and R. D. Shannon, Acta Crystallogr., Sect. A: Cryst. Phys., Diffr., Theor. Gen. Crystallogr. **A29** (3), 266 (1973).
8. N. F. Mott and E. A. Davis, *Electronic Processes in Non-Crystalline Materials* (Clarendon Press, Oxford, 1979; Mir, Moscow, 1982), Vol. 1.

Translated by L. Man

Crystallography Reports, Vol. 46, No. 2, 2001, pp. 190–193. Translated from Kristallografiya, Vol. 46, No. 2, 2001, pp. 230–233.

STRUCTURE OF INORGANIC COMPOUNDS

Crystal Structure of Litvinskite: A New Natural Representative of the Lovozerite Group

N. A. Yamnova, Yu. K. Egorov-Tismenko, I. V. Pekov, and I. A. Ekimenkova

Faculty of Geology, Moscow State University,
Vorob'evy gory, Moscow, 119899 Russia
e-mail: elbel@geol.msu.ru

Received December 20, 1999

Abstract—A new representative of the lovozerite group—Na, Zr, Mn-silicate litvinskite (Na, H_2O, □)$_3$(□, Na, Mn^{2+})$Zr[Si_6O_{12}(OH)_3(OH, O)_3]$—was discovered in ultraagpaitic pegmatites from the Lovozero massif. The crystal structure of the mineral was solved on an automated Syntex $P\bar{1}$ diffractometer (MoK_α radiation, 1398 reflections, 2θ/θ scanning technique, anisotropic refinement to R_{hkl} = 0.065). The unit-cell parameters are a = 10.589(7) Å, b = 10.217(8) Å, c = 7.355(5) Å, β = 92.91(5)°, V = 794.6(9) Å^3, sp. gr. Cm, Z = 2, d_{calcd} = 2.63 g/cm^3. The structure of the mineral consist of a three-dimensional framework of discrete six-membered rings of Si-tetrahedra linked to isolated Zr-octahedra. The framework cavities are occupied by Na cations. The litvinskite composition and the structure differ from all known natural and synthetic compounds of the lovozerite group, which supports the assumption about diversity of mineral types in this group. © *2001 MAIK "Nauka/Interperiodica".*

INTRODUCTION

Litvinskite was discovered in the aegirine zone of a large ultraagpaitic pegmatitic body from the Alluaĭv mountain in the northwestern region of the Lovozero massif (the Kola Peninsula). The mineral was named after G.P. Litvinskaya (1920–1994), a leading teacher at the Department of Crystallography and Crystal Chemistry of the Faculty of Geology of the Moscow State University. Litvinskite (IMA no. 99-017) was recognized as a new mineral type by the Commission on New Minerals and Mineral Names of the International Mineralogical Association on August 3, 1999. The mineralogical description of the litvinskite can be found elsewhere [1]. Its chemical composition is described by the empirical formula $Na_{2.51}K_{0.01} \cdot Mn_{0.14}Ca_{0.01}Fe_{0.01}Ze_{0.96}Ti_{0.01}Hf_{0.01}Si_6O_{12.76}(OH)_{5.24} \cdot 0.47H_2O$. Litvinskite belongs to a large group of natural and synthetic compounds derived from lovozerite, a Na, Zr-silicate of the formula $Na_2ZrSi_6O_{15} \cdot 3H_2O \cdot 0.5NaOH$. (This formula gives rise to serious doubt because of the absence of divalent cations, which, as was demonstrated in more recent studies, should be present in the formula.) The lovozerite structure type is based on the framework of six-membered silicon–oxygen rings linked through isolated octahedra with the cavities being occupied by bulky Na cations and H_2O molecules. As was shown in [2, 3], the structures of all the lovozerite-like compounds may be composed of identical pseudocubic (with the a parameter approximately equal to 7.5 Å) blocks of the general formula $A_3B_3C_2M[Si_6O_{18}]$. This block containing one lovozerite-like ring has four types of (*ABCM*) positions, which can be occupied by nine cations. The block vertices are occupied by octahedrally coordinated M cations (M = Zr, Ti, Mn, Fe, Ca, Sn, Cd, etc.). The centers of two free (not occupied by Si cations) octants located on one of the threefold axes of the protocell are also occupied by octahedrally coordinated C cations (C = Ca, Mn, Na, etc.). The positions at the middle of the edges (A) and in the centers of the faces (B) are filled mainly with Na cations (sometimes, with Fe, Ti, Mn, Nd, Ca, Cd, or H). Different structures of lovozerite-like compounds and, thus, the diversity of the mineral types of this group are explained by different filling of the above positions in the block and at the junctions of the adjacent blocks. The fact that the litvinskite composition and its X-ray diffraction characteristics differ from those of all known natural and synthetic compounds of the lovozerite family has stimulated the determination of its structure.

EXPERIMENT, STRUCTURE DETERMINATION, AND ITS REFINEMENT

X-ray diffraction data were collected from a 0.15 × 0.20 × 0.25-mm-large single crystal. The unit-cell parameters and the monoclinic symmetry of the crystal (the Laue class is 2/m) were determined by the photographic method and refined on an automated single-crystal Syntex $P\bar{1}$ diffractometer (a = 10.589(7) Å, b = 10.217(8) Å, c = 7.355(5) Å, β = 92.91(5)°, V = 794.6(9) Å^3). The X-ray data were collected on the same diffractometer. The details of X-ray diffraction

study are presented in Table 1. The systematic absences of the *hkl* reflections not satisfying the condition $h + k = 2n$ indicate the face-centered Bravais lattice and three possible space groups—*C*2/*m*, *Cm*, or *C*2. The intensities were converted into $|F_{hkl}|$ without regard for absorption ($\mu_{max} = 0.25$). All subsequent calculations were performed with the use of the AREN program package [4]. Taking into account the similarity of the compositions, symmetry, and unit-cell parameters of lovozerite and litvinskite, the coordinates of the basis Zr and Si atoms of the lovozerite structure, $Na_2ZrSi_6O_{15} \cdot 3H_2O \cdot 0.5NaOH$ (a = 10.48 Å, b = 10.20 Å, c = 7.33 Å, $\beta = 92°33'$, the sp. gr. *C*2) [5] were used as the starting model in the structure determination of litvinskite. The positions of the absent light Na and O atoms were localized by successive approximations. The resulting structural model was refined by the least squares method within three possible space groups. An additional maximum with the coordinates $x \approx 0.75$, $y \approx 0$, $z \approx 0.25$ was revealed on the difference electron-density maps constructed within all three possible groups. This maximum was attributed to the *C* position of the lovozerite structure type (the position statistically occupied by Na, Mn, Ca, and Fe), which is the only position in the structure having neither an inversion center nor a twofold axis. This fact uniquely determines the space group of litvinskite as *Cm* and accounts for different structures of litvinskite and lovozerite. The statistical distribution of Zr, Ti, Hf, Na, K, Mn, Ca, and Fe over independent crystallographic positions was established by the refinement of the occupancies for the positions with fixed B_{iso} with the use of mixed atomic scattering curves and taking into account the data of the chemical analysis, the effective ionic radii of cations, the thermal parameters of atoms, and average cation–oxygen distances. The minimum final reliability factors after the least squares refinement of the model with isotropic ($R_{hkl} = 0.101$) and anisotropic ($R_{hkl} = 0.065$) thermal parameters corresponded to the distribution of the cations indicated in Table 2 and the detailed crystallochemical formula

$$(Na_{1.54}K_{0.01}(H_2O)_{0.45})Na_{0.78}(Na_{0.19}Mn^{2+}_{0.14}Ca_{0.01}Fe^{2+}_{0.01})$$

$$\cdot (Zr_{0.96}Ti_{0.01}Hf_{0.01})[Si_6O_{12}(OH_3)\{(OH)_{2.24}O_{0.76}\}]$$

($z = 2$, $d_{calcd} = 2.63$ g/cm^3). The idealized structural formula of litvinskite can be written as $(Na, H_2O, \square)_3 \cdot (\square, Na, Mn^{2+})Zr[Si_6O_{12}(OH)_3(OH, O)_3]$; the general formula, as $A_3CM[Si_6O_{18}]$. The final coordinates of the basis atoms and the equivalent thermal parameters are given in Table 2. The high thermal parameters can be explained by predominance of light atoms in the mineral structure. Proceeding from the calculations of the local balance of valence strengths with due regard for the cation–anion distances [6], the anionic portion of the structure was "separated" into O^{2-} ions and $(OH)^-$ groups.

Table 1. Some details of X-ray diffraction study of litvinskite

Characteristic	Parameter
Crystal dimensions, mm	$0.15 \times 0.20 \times 0.25$
Diffractometer	$P\bar{1}$ Syntex
Radiation	MoK_α
Monochromator	Graphite
Sp. gr.	*Cm*
Unit-cell parameters, Å, deg	a = 10.589(7)
	b = 10.217(8)
	c = 7.355(5)
	β = 92.91(5)
	V = 794.6(9)
Number of formula units Z	2
Scanning technique	$2\theta : \theta$
Maximum $\sin\theta/\lambda$	1.063
Scan rate	4–24 deg/min
Number of measured reflections with $I > 1.96\sigma(I)$ within the Ewald hemisphere	2554
Number of independent reflection	1398
Program package	AREN
Reliability factors $R_{(hkl)}$:	
isotropic refinement	0.101
anisotropic refinement	0.065
Weighting scheme used in the least-squares procedure	$w = 1/(A + F + BF^2)$
	$A = 2F_{min}$
	$B = 2F_{max}$

DESCRIPTION OF THE STRUCTURE

The litvinskite structure (Fig. 1a) consists of the framework of six-membered lovozerite-type rings of tetrahedra $[Si_6O_{12}(OH)_3 \cdot (OH, O)_3]$, with the average Si–O distances in the Si-tetrahedra ranging from 1.58 to 1.62 Å, sharing oxygen vertices with isolated *M*-octahedra (the *M*–O distances range within 2.02–2.10 Å). The *M*-octahedra are located at the vertices and in the centers of the basal faces of the unit cell (Fig. 1a) and are occupied predominantly by Zr^{4+} cations. Free vertices of the Si-tetrahedra are occupied by

Table 2. Coordinates of basis atoms and individual thermal parameters in the litvinskite structure

Atom	Multiplicity of the position	Occupancy of the position	*x*/*a*	*y*/*b*	*z*/*c*	B_{eq}, Å^2
A(1)	2	0.78Na	0.003(2)	0	0.497(3)	4.4(2)
A(2)	4	0.77Na + 0.225H_2O + 0.005K	0.754(1)	0.252(1)	−0.004(2)	4.1(1)
M	2	0.96Zr + 0.01Ti + 0.01Hf	0	0	0	2.70(8)
C	2	0.19Na + 0.14Mn + 0.01Ca + 0.01Fe	0.747(1)	0	0.254(2)	4.2(3)
Si(1)	4	Si	0.4905(3)	0.2203(3)	0.2866(3)	3.15(8)
Si(2)	2	Si	0.2900(3)	0	0.2614(7)	3.3(1)
Si(3)	4	Si	0.5117(2)	0.2271(2)	0.7124(3)	2.8(1)
Si(4)	2	Si	0.7160(3)	0	0.7298(5)	2.7(1)
O(1)	2	O	0.179(1)	0	0.109(2)	5.1(3)
O(2)	4	O	0.372(1)	0.1311(9)	0.238(2)	5.8(2)
O(3)	4	O	−0.005(2)	0.245(1)	0.504(2)	5.5(2)
O(4)	4	O	0.044(1)	0.142(1)	0.809(2)	6.2(2)
O(5)	4	(OH)	0.381(1)	0.151(2)	0.765(2)	8.5(3)
O(6)	2	(OH)	0.235(2)	0	0.471(3)	7.0(3)
O(7)	2	O	0.810(1)	0	0.904(2)	5.2(4)
O(8)	4	O	0.623(1)	0.121(1)	0.750(2)	6.0(3)
O(9)	4	O	0.961(1)	0.1435(9)	0.178(1)	5.1(3)
O(10)	4	(OH, O)	0.618(1)	0.157(1)	0.220(2)	5.7(2)
O(11)	2	(OH, O)	0.780(2)	0	0.543(2)	5.3(3)

the $(OH)^-$ groups, whereas *C*-octahedra (the C–O distances are in the range of 2.11–2.77 Å) statistically filled (by 35%) with Na^+, Mn^{2+}, Ca^{2+}, and Fe^{2+} cations share the oxygen faces with *M*-octahedra and are also involved in the framework. The remaining three vertices of each *C*-octahedron are occupied by the O^{2-} ions and $(OH)^-$ groups. The number of the O^{2-} ions replaced by the $(OH)^-$ groups correlates with the degree of filling of the *C* position. The Na cations occupy the cavities of the framework and two crystallographically nonequivalent positions, namely, the position *A*(1) at the midpoints of the *c* axis of the unit cell between the *M*-octahedra related by a translation and the position *A*(2) in the channels of hexagonal section along the [001] direction (the cation–anion distances in the eight-vertex polyhedra *A*(1) and *A*(2) range within 2.39–2.78 and 2.43–2.79 Å, respectively). The water molecules and a small fraction of K and Na cations can be located in the channel cavities (because of their somewhat larger volume). The litvinskite structure differs from the lovozerite structure (Fig. 1b): the former has an additional cationic position (*C*); thus, the sp. gr. *C*2 (of lovozerite) is "transformed" into the sp. gr. *Cm* (of litvinskite). Theoretically, this position can also be filled in the structure of another lovozerite variety [7] with a high content of divalent Ca^{2+} and Mn^{2+} cations:

$$(Na_{2.47}K_{0.01}Ca_{0.45}Mn_{0.20}TR_{0.02})_{\Sigma 3.16}$$

$$\cdot (Zr_{0.75}Fe^{3+}_{0.19}Ti_{0.08})_{\Sigma 1.02}(Si_{5.81}Al_{0.19})_{\Sigma 6.0}$$

$$\cdot O_{13.86}(Cl_{0.06}(OH)_{4.76})_{\Sigma 4.82}:$$

(a = 10.18 Å, c = 13.10 Å or a_{rh} = 7.32 Å, α_{rh} = 88°04′, the possible sp. gr. $R\bar{3}m$) [7]. It was assumed [7] that the latter mineral is structurally similar to monoclinic lovozerite, and the matrix of the transformation from the rhombohedral to monoclinic unit cell was given in the form |–1/3 –2/3 –2/3|1 0 0|–1/3 –2/3 –1/3|. Proceeding from the similarity of the chemical compositions of trigonal lovozerite and litvinskite, we examined the possibility of a higher (trigonal) symmetry for litvinskite. However, the transformation of the litvinskite structure to the rhombohedral one (with the transformation matrix |1/2 –1/2 1|0 1 0|–1 0 1|) and the refinement of the structure obtained showed that the arrangement of most of the light atoms is inconsistent with the trigonal symmetry. The wide range of the Si–O distances in the Si-tetrahedra also indicates that the symmetry should be lowered. The low symmetry of

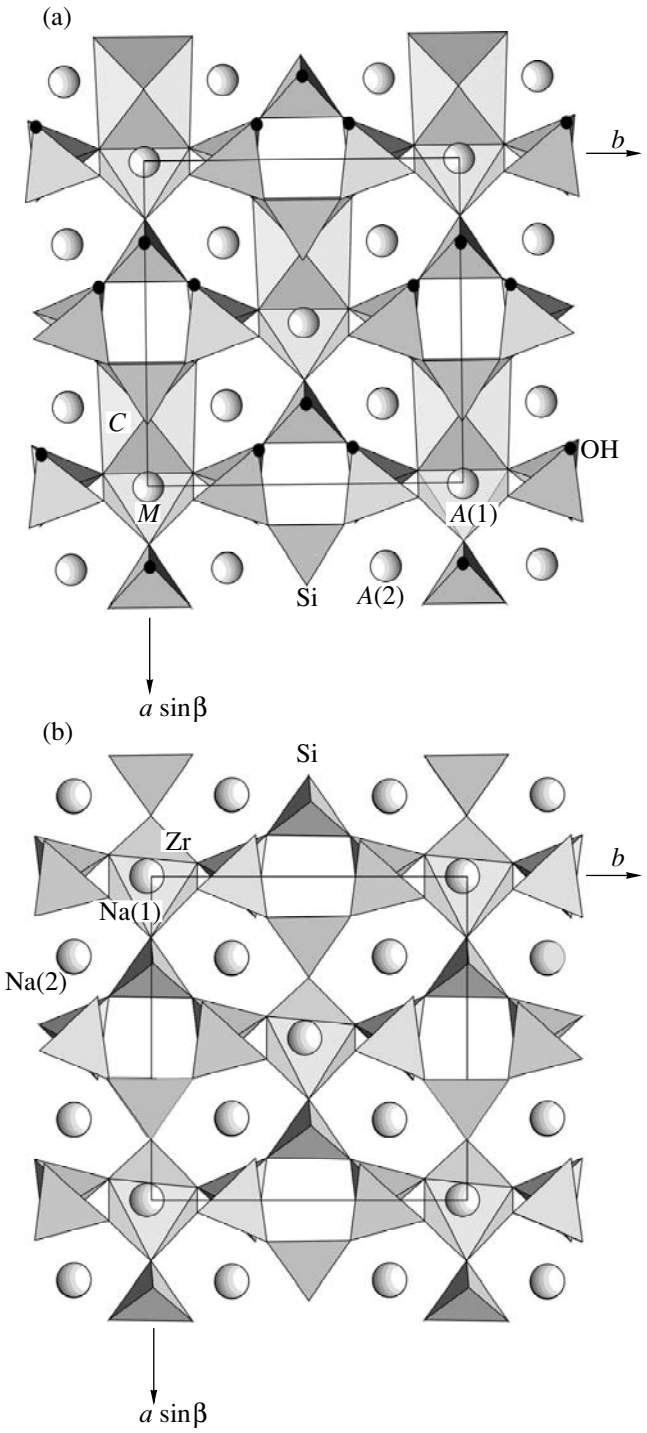

Fig. 1. Crystal structures of (a) litvinskite and (b) lovozerite projected onto the *xy* plane: *A*(1) = Na; *A*(2) = Na, H_2O, or K; *M* = Zr, Ti, or Hf; and *C* = Na, Mn, Ca, or Fe.

litvinskite was also confirmed by the crystal optics data [1].

The *C* position in the litvinskite structure filled with Na, Mn^{2+}, Ca, and Fe^{2+} cations is also typical other representatives of this family, for example, kazakovite $Na_6MnTi[Si_6O_{18}]$ [8] and zirsinalite $Na_6CaZr[Si_6O_{18}]$ [9]. However, a high Na content in these minerals results in symmetry and structure considerably different from those of litvinskite. The structure determination of litvinskite confirms the conclusion drawn in [2, 3] that the lovozerite group includes a wide variety of mineral types.

ACKNOWLEDGMENTS

We are grateful to E.L. Belokoneva for her help in X-ray data collection.

This study was supported by the Russian Foundation for Basic Research (project no. 97-05-65167) and the National Science Foundation of China (NSFC) (joint project with the Russian Foundation for Basic Research no. 99-05-39019).

REFERENCES

1. I. V. Pekov, I. A. Ekimenkova, N. V. Chukanov, *et al.*, Zap. Vseross. Mineral. O–va **129** (1), 45 (2000).
2. N. M. Chernitsova, Z. V. Pudovkina, A. A. Voronkov, *et al.*, Zap. Vses. Mineral. O–va **104** (1), 18 (1975).
3. R. A. Tamazyan and Yu. A. Malinovskiĭ, Kristallografiya **35** (2), 398 (1990) [Sov. Phys. Crystallogr. **35**, 227 (1990)].
4. V. I. Andrianov, Kristallografiya **32** (1), 228 (1987) [Sov. Phys. Crystallogr. **32**, 130 (1987)].
5. V. V. Ilyukhin and N. V. Belov, Dokl. Akad. Nauk SSSR **131** (1), 176 (1960).
6. Yu. A. Pyatenko, Kristallografiya **17** (4), 773 (1972) [Sov. Phys. Crystallogr. **17**, 677 (1972)].
7. Yu. L. Kapustin, A. V. Bykova, and Z. V. Pudovkina, Izv. Akad. Nauk SSSR, Ser. Geol., No. 8, 106 (1973).
8. A. A. Voronkov, Z. V. Pudovkina, V. A. Blinov, *et al.*, Dokl. Akad. Nauk SSSR **245** (1), 106 (1979) [Sov. Phys. Dokl. **24**, 132 (1979)].
9. Z. V. Pudovkina, N. M. Chernitsova, A. A. Voronkov, and Yu. A. Pyatenko, Dokl. Akad. Nauk SSSR **250** (4), 865 (1980) [Sov. Phys. Dokl. **25**, 69 (1980)].

Translated by T. Safonova

Crystallography Reports, Vol. 46, No. 2, 2001, pp. 194–195. Translated from Kristallografiya, Vol. 46, No. 2, 2001, pp. 234–235.

STRUCTURE OF INORGANIC COMPOUNDS

Refined Crystal Structure of *TR*-Fersmite (*TR* = Ce)

O. A. Gurbanova*, R. K. Rastsvetaeva*, A. A. Kashaev, and A. S. Smolin****

**Shubnikov Institute of Crystallography, Russian Academy of Sciences, Leninskiĭ pr. 59, Moscow, 117333 Russia*

***Irkutsk Pedagogical Institute, Irkutsk, Russia*

e-mail: rast@rsa.crystal.msk.su

Received May 31, 2000

Abstract—The structure of *TR*-fersmite $(Ca_{0.89}Ce_{0.11})(Nb_{1.3}Ti_{0.7})O_5(O, OH)$ was refined to $R = 0.032$. The parameters of the orthorhombic unit cell are $a = 5.762(2)$ Å, $b = 14.988(8)$ Å, $c = 5.246(1)$ Å, sp. gr. *Pcan*, $Z = 4$. The mixed *A* position is occupied by Ca and Ce atoms, and the mixed *B* position is occupied by Nb and Ti atoms. © *2001 MAIK "Nauka/Interperiodica"*.

Fersmite $CaNb_2O_6$ belongs to the family of the minerals described by the general formula AB_2O_6, where *A* = Ca, U, Th, or *TR* and *B* = Nb, Ti, or Ta. The structure of La-containing *TR*-fersmite has been established by V.B. Aleksandrov [1] based on X-ray powder diffraction data up to $R = 15\%$. Recently, an analogous mineral was found in rocks of the Ust'-Biran rare-metal–rare-earth deposit [2] (where it is distributed in rich complex mineral association) in the form of individual grains with up to 65% of the Ca atoms being replaced by Ce atoms. Below, we describe the new structural study of this mineral.

An isometric black single crystal of *TR*-fersmite was studied. The parameters of the orthorhombic unit cell were determined and refined on a Syntex *P*1 diffractometer based on 15 high-angle reflections in the range $2\theta = 22°–28°$. The main characteristics of the crystal and the details of X-ray study are indicated in Table 1. The atomic coordinates and the interatomic distances are listed in Tables 2 and 3, respectively.

Since we failed to refine the structure of *TR*-fersmite using the atomic coordinates from [1], we decided to solve the structure by direct methods, although the exact chemical formula of the compound was unknown. First, the cationic fragment consisting of Nb and Ca atoms was determined and refined isotropically to $R = 14\%$. This fragment was used to localize oxygen atoms from the *F* synthesis. The refinement of the structure model to $R = 8\%$ demonstrated that the thermal parameters of cations are inconsistent with the set kinds of atoms. We managed to obtain a rather low *R* factor (0.032) and reasonable atomic thermal parameters by varying the Nb : Ti and Ca : Ce ratios in the

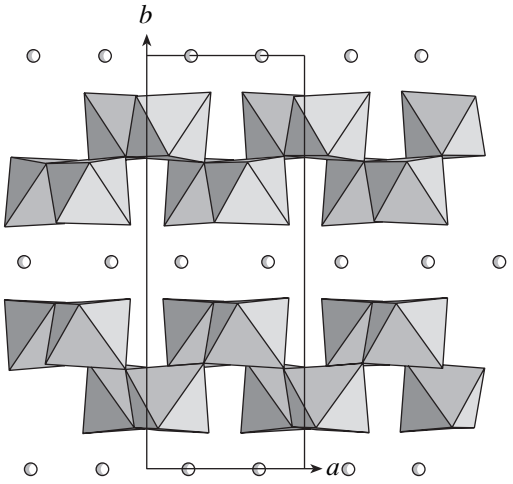

Fig. 1. Structure of *TR*-fersmite (*TR* = Ce) projected onto the (001) plane. Two-layer octahedral sheets are linked via *A* cations (represented by circles).

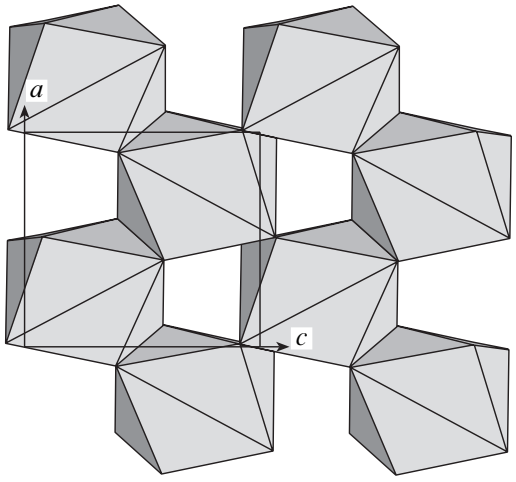

Fig. 2. Layer of (Ca,Ce)-eight-vertex polyhedra projected onto the (010) plane.

1063-7745/01/4602-0194$21.00 © 2001 MAIK "Nauka/Interperiodica"

Table 1. Structural data and details of X-ray diffraction study

Characteristic	Data and conditions
Unit-cell parameters, Å	$a = 5.762(2)$, $b = 14.988(8)$, $c = 5.246(1)$
Unit-cell volume, Å^3	$V = 453.05$
Sp. gr., Z	*Pcan*, 4
Radiation λ, Å	MoK_α, 0.71073
Crystal dimensions, mm	$0.2 \times 0.2 \times 0.3$
Diffractometer	Syntex *P*1
Scanning mode	ω/2θ
$(\sin\theta/\lambda)_{max}$, Å^{-1}	1.078
Ranges of the indices of measured reflections	$0 < h < 11$, $0 < k < 30$, $-11 < l < 11$
R_{int} for equivalent reflections	0.014
Total number of reflections	1792 $I > 2\sigma(I)$
Number of independent reflections	1017 $F > 4\sigma(F)$
Density ρ_{calcd}, g/cm^3	4.65
Program	AREN [3]
Absorption correction	DIFABS [4]
Extinction parameter E	0.0000020
R factor upon anisotropic refinement	0.032

Table 2. Atomic coordinates and equivalent thermal parameters

Atom	*x*/*a*	*y*/*b*	*z*/*c*	B_{eq}, Å^2
A	0.2260(1)	0.5	0.25	0.96(1)
B	0.1827(1)	0.1662(1)	0.2999(1)	0.82(1)
O(1)	0.3995(5)	0.0886(2)	0.4040(6)	1.46(4)
O(2)	0.4298(5)	0.4013(2)	0.5110(6)	1.49(4)
O(3)	0.3650(5)	0.2576(2)	0.1285(6)	1.30(4)

Table 3. Interatomic distances (Å)

B-octahedron		*A*-polyhedron	
B–O(1)	1.792(3)	*A*–O(2)	2.333(3) × 2
O(2)	1.933(3)	O(1)	2.362(3) × 2
O(3)	1.946(3)	O(1)	2.440(3) × 2
O(3)	2.086(3)	O(2)	2.774(3) × 2
O(2)	2.091(3)		⟨2.452⟩
O(3)	2.337(3)		
	⟨2.034⟩		

anisotropic refinement and taking into account extinction.

The analysis of the local valence balance demonstrated that one of the O positions is partly occupied by a hydroxyl group. The final formula of the mineral determined upon the X-ray diffraction analysis can be written as $(Ca_{0.89}Ce_{0.11})(Nb_{1.3}Ti_{0.7})O_5(O,OH)$.

The structure of *TR*-fersmite under consideration is identical to the structures of the mineral studied earlier in [1] and of its La-containing synthetic analogue [5]. The *B*-polyhedra are distorted octahedra sharing edges to form chains along the *c*-axis. These chains are very rigid structural elements. The chains of octahedra are located in a staggered fashion and linked by shared vertices, thus forming two-layer octahedral sheets (Fig. 1). The sheets are linked along the *b*-axis by edge-sharing eight-vertex Ca polyhedra, which form planar layers (Fig. 2). As a result, the structure of *TR*-fersmite contains six cationic layers normal to the *b* axis. These cations occupy the voids of the hexagonal packing of the oxygen atoms.

To summarize, we established, with a high degree of accuracy that Ce occupies the *A* position together with a Ca atom and that Ti occupies the *B* position together with Nb. These facts confirm the existence of a continuous isomorphous series $CaNb_2O_6$–$(Y,TR)(Nb,Ti)_2O_6$ of columbite-type structures, whose intermediate member is *TR*-fersmite.

ACKNOWLEDGMENTS

This work was supported by the Russian Foundation for Basic Research, (project no. 99-05-65035) and by the Council on Leading Scientific Schools (project no. 00-15-96633).

REFERENCES

1. V. B. Aleksandrov, Dokl. Akad. Nauk SSSR **132**, 669 (1960).
2. V. I. Chernikov, A. A. Konev, E. I. Vorob'ev, *et al.*, Geol. Geofiz., No. 6, 50 (1994).
3. V. I. Andrianov, Kristallografiya **32** (1), 228 (1987) [Sov. Phys. Crystallogr. **32**, 130 (1987)].
4. N. Walker and D. Stuart, Acta Crystallogr., Sect. A: Found. Crystallogr. **39**, 158 (1983).
5. N. A. Yamnova, É. S. Tsomirova, and N. I. Leonyuk, Kristallografiya **38** (1), 232 (1993) [Crystallogr. Rep. **38**, 124 (1993)].

Translated by T. Safonova

Crystallography Reports, Vol. 46, No. 2, 2001, pp. 196–206. Translated from Kristallografiya, Vol. 46, No. 2, 2001, pp. 236–246.

STRUCTURE OF COORDINATION COMPOUNDS

Structural Features of 3*d* Metal Compounds with 1-Hydroxyethylidenediphosphonic Acid

V. S. Sergienko

Kurnakov Institute of General and Inorganic Chemistry, Russian Academy of Sciences, Leninskiĭ pr. 31, Moscow, 117907 Russia

Received August 10, 1999

Abstract—Structural features of 3*d* metal complexes with anions of 1-hydroxyethylidenediphosphonic acid (HEDP, H_4L), in which the *M* : HEDP ratios are equal to 1 : 2, 1 : 1, 3 : 2, and 5 : 2, are discussed. The Cu(II) : HEDP = 1 : 2 complexes are characterized by five types of structures: monomeric structures *trans*-$[Cu(H_{4-n}L)_2(H_2O)_2]^{2-2n}$, *cis*-$[Cu(H_{4-n}L)_2(H_2O)_2]^{2-2n}$, and $[Cu(L)_2]^{6-}$; the dimeric structure $\{[Cu(H_2L)(H_2O)]_2(\mu_2\text{-}H_2L)_2\}^{4-}$; and the polymeric chain structure $\{[Cu(\mu_2\text{-}H_2L)_2]^{2-}\}_\infty$. Six coordination modes exhibited by HEDP in the Cu(II) compounds are described. © *2001 MAIK "Nauka/Interperiodica".*

1. INTRODUCTION

Structures of 3*d* metal complexes with 1-hydroxyethylidenediphosphonic acid (HEDP, H_4L) have been the object of much attention. The crystal structures of about twenty compounds of this class have been determined up to now. A broad spectrum of structures which differ in the degree of aggregation of complexes (monomers, dimers, polymeric chains, ribbons, or three-dimensional frameworks), the type of geometric isomer (*trans* or *cis*), the degree of distortion of the six-vertex metal polyhedron, the coordination mode of the $H_{4-n}L^{n-}$ ligand, etc., can be realized depending on the individuality of the central *M* atom, the *M* : HEDP ratio, the nature of the counterion, the composition of the hydrate sphere, and the presence (or absence) of the accompanying ligands.

Complexes of bivalent copper with the ratio *M* : HEDP = 1 : 2 have been studied most completely. The 1 : 2 compounds of other 3*d* metals [Zn(II), Co(II), Ni(II), and Mn(II)] and Cu(II) complexes with the Cu : HEDP ratio equal to 1 : 1 and 3 : 2 were characterized to a lesser degree. Structures of the mixed-valent Cu(I, II) complex (Cu : HEDP = 5 : 2) and the Ni(II) complex compound in which HEDP plays an unusual part of the "free" anion uninvolved in metal coordination are also known.

In this paper, we consider specific structural features of 3*d* metal compounds with HEDP.

2. COMPLEXES OF COPPER(II) WITH THE RATIO Cu : HEDP = 1 : 2

Structural features of copper(II) compounds with the ratio Cu : HEDP = 1 : 2 are determined primarily by the ligand composition of the complexes. In all the compounds, the coordination sphere of the six-vertex polyhedron of the Cu atom includes two $H_{4-n}L^{n-}$ ligands, whereas the number of coordination water molecules (*m*') varies between zero and two. As a rule, *m*' determines the function and the coordination capacity of the $H_{4-n}L^{n-}$ ligands in the complexes.

Complexes with two water molecules in the coordination sphere of the metal have an island structure. In compounds $[Cu(H_3L)_2(H_2O)_2] \cdot 3H_2O$ (**I**) [1, 2] and $(Et_2NH_2)_2[Cu(H_2L)_2(H_2O)_2]$ (**II**) [3], the copper(II) coordination polyhedra are centrosymmetric elongated tetragonal bipyramids (4 + 2) with a *trans* structure and the $O(H_2O)$ atoms at the axial positions (Fig. 1a), whereas in the triethanolammonium complex salt $[(HOCH_2CH_2)_3NH][Cu(H_{2.5}L)_2(H_2O)_2] \cdot 5H_2O$ (**III**) [4] (Fig. 1b), the *cis* isomer is formed [with the O(*L*) and $O(H_2O)$ atoms at the axial vertices]. In both *trans* and *cis* isomers of the $[Cu(H_{4-n}L)_2(H_2O)_2]^{2-2n}$ complexes, $H_{4-n}L^{n-}$ are bidentate chelate ligands.

In the structures of two complex alkali-metal salts $Cat_2Cu(H_2L)_2 \cdot 3H_2O$ [5], where Cat = K (**IV**) or Cs (**V**), and the $(CH_3NH_3)_2Cu(H_2L)_2 \cdot 2H_2O$ (**VI**) methylammonium salt [6], only one H_2O molecule is involved in the coordination sphere of the Cu atom. The centrosymmetric $[Cu(\mu_2\text{-}H_2L)(H_2L)(H_2O)]_2^{4-}$ anionic complex (Fig. 2) has a dimeric structure. Two independent H_2L^{2-} ligands are *cis* to each other and perform different functions, namely, the bidentate chelate function and the tridentate chelate μ_2-bridging function. Thus, in the anionic complexes of structures **IV**–**VI**, the metal atoms are linked by two H_2L^{2-} ligands into pairs and each Cu atom is coordinated by three H_2L^{2-} ligands (two of them act in the bidentate mode; the third, in the monodentate mode).

The fourth structural type occurs in two dihydrates of the general formula $Cat_2Cu(H_2L)_2 \cdot 2H_2O$, where

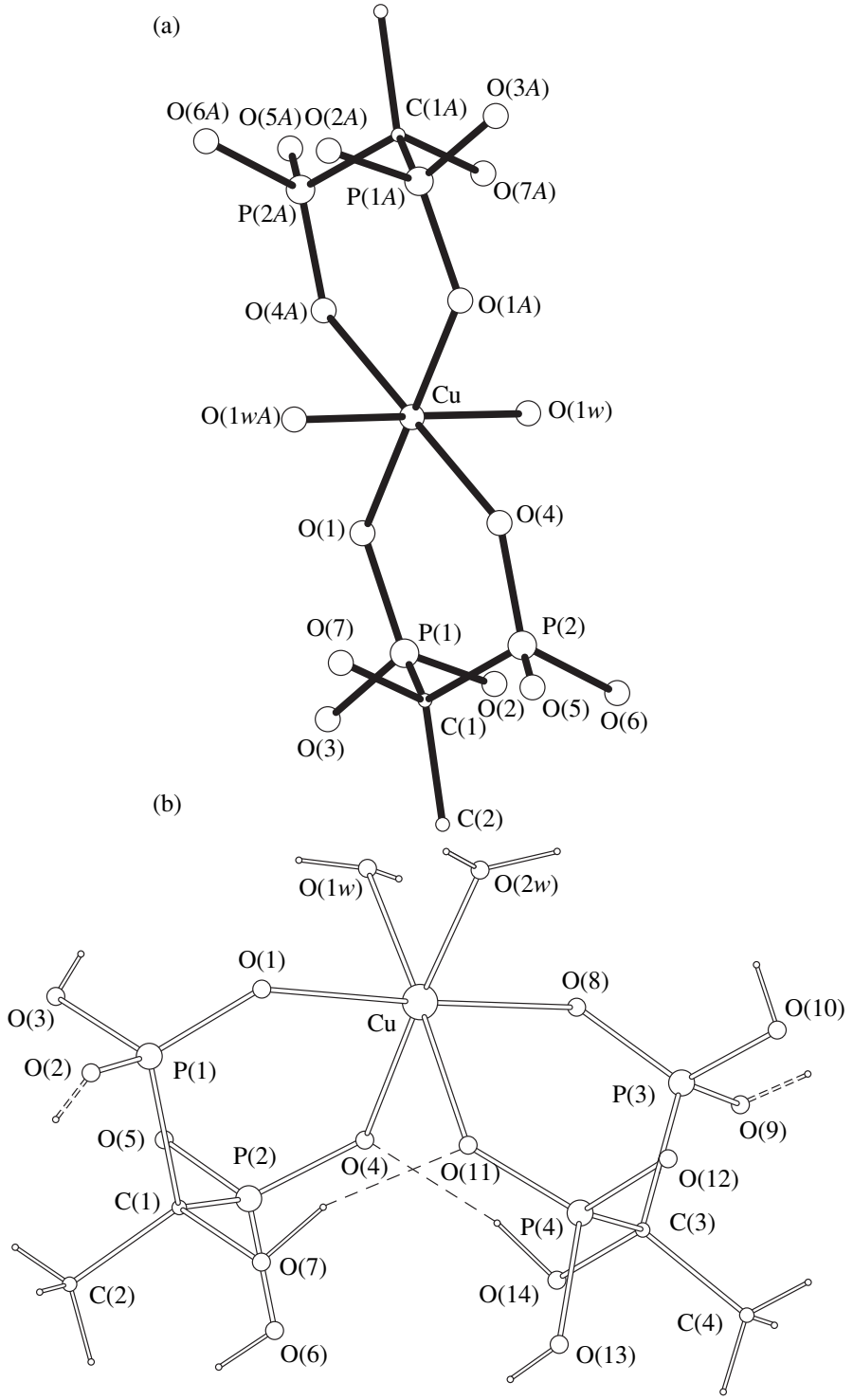

Fig. 1. Structures of (a) *trans*-$[Cu(H_2L)_2(H_2O)_2]^{2-}$ and (b) *cis*-$[Cu(H_{2.5}L)_2(H_2O)_2]^{-}$ complexes.

$Cat_2 = (NH_4)_2$ (**VII**) [7] or $Rb(H_5O_2)$ (**VIII**) [8]. In these compounds, water molecules are not included in the coordination sphere of the metal, and the $\{[Cu(\mu_2\text{-}H_2L)_2]^{2-}\}_\infty$ anionic complex (Fig. 3) has a polymeric chain structure. Both H_2L^{2-} ligands are in the *trans* positions to each other (the Cu atoms occupy the inversion centers) and perform the tridentate chelate μ_2-bridging function.

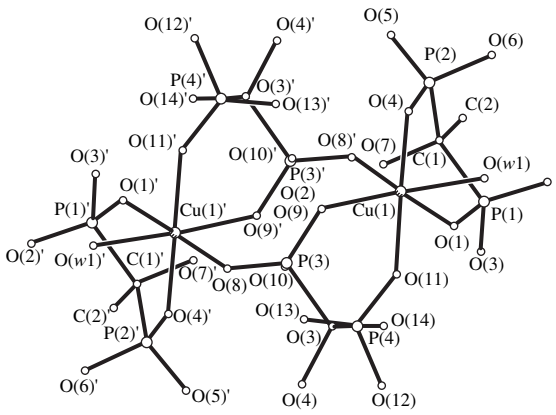

Fig. 2. Structure of the $\{[Cu(\mu_2\text{-}H_2L)(H_2L)(H_2O)]_2\}^{4-}$ binuclear complex.

Similar to structures **VII** and **VIII**, in the polyhydrate mixed potassium–sodium $K_4Na_2Cu(L)_2 \cdot 12H_2O$ (**IX**) complex salt [9], water molecules are not included in the coordination sphere of the Cu atom. However, unlike **VII** and **VIII**, which have polymeric chain structures, the centrosymmetric $[Cu(L)_2]^{6-}$ anionic complex in structure **IX** is monomeric (Fig. 4) and the completely deprotonated L^{4-} ligands perform the uncommon tridentate chelate function. Except for **IX**, there is only one example of the tridentate chelate coordination mode of the HEDP ligand in a transition metal complex, namely, in the structure of $[C(NH_2)_3]_5[WO_3(L^*)] \cdot 4.5H_2O$ [10].[1] However, in this complex, two deprotonated O(P) atoms of two phosphonate groups and, additionally, the deprotonated O(C) atom of the α-hydroxy group take part in metal coordination, whereas in **IX**, the protonated α-(C)OH atom is involved in metal coordination. The latter coordination mode is rather unusual. There is only one more example of coordination of a transition metal by a protonated α-hydroxy group, namely, the polymeric ribbon structure of the Cu : HEDP = 3 : 2 complex $[Cu_3(HL)_2(H_2O)_4] \cdot 2H_2O$ [11].

In all the compounds with the general formula $Cat_{2n-2}Cu(H_{4-n}L)_2 \cdot mH_2O$ (**I**–**IX**), the six-vertex Cu(II) coordination polyhedron has the shape of an elongated tetragonal bipyramid (4 + 2). The Cu–O bond lengths are given in Table 1. The mean lengths of the $Cu–O(L)_{eq}$ equatorial bonds lie within the narrow range 1.959–1.990 Å. The $Cu–O(H_2O)_{eq}$ distance in structure **III** (1.985 Å) falls in the same range. The Cu–O_{ax} axial bonds are significantly longer than the equatorial bonds due to the Jahn–Teller effect in six-coordinate Cu(II) complexes. The ranges of the mean $Cu–O(H_2O)_{ax}$ and $Cu–O(L)_{ax}$ bond lengths in structures **III**–**VIII** overlap (2.311–2.469 and 2.353–2.445 Å, respectively). The mean difference between the axial and equatorial bond lengths Δ in structures **I**–**VIII** lies between 0.326 and 0.504 Å. Structure **IX** stands out, since the axial Cu–OH(*L*) bond with the protonated oxygen atom of the α-hydroxy group (2.667 Å) is significantly (by 0.198–0.356 Å) longer than the axial Cu–$O(H_2O)$ and Cu–O(*L*) bonds (with the phosphonate oxygen atoms). Therefore, the Δ parameter in **IX** (0.710 Å) is 0.206–0.384 Å greater than that in **I**–**VIII**.

[1] Unlike the usual tetrabasic L^{4-} form, the $(L^*)^{5-}$ ligand is the completely deprotonated (not only at the four phosphonate oxygen atoms, but also at the α-hydroxy group) HEDP ion.

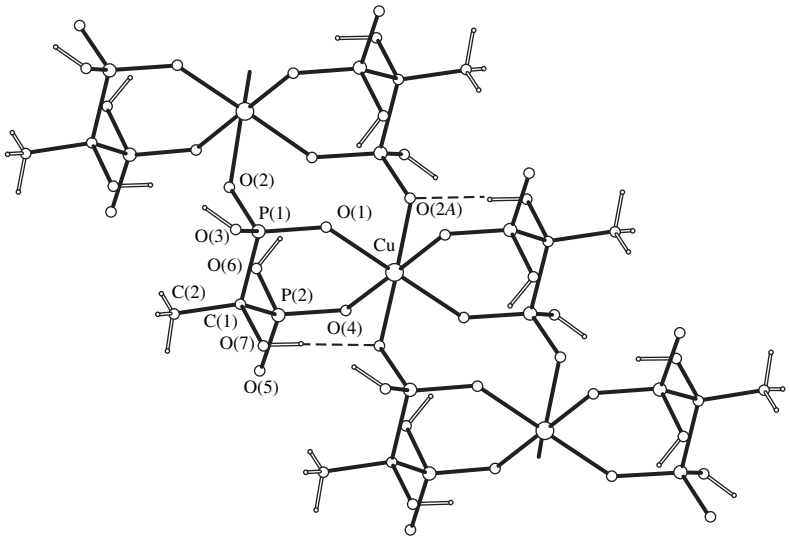

Fig. 3. A fragment of the polymeric chain structure of the $\{[Cu(\mu_2\text{-}H_2L)_2]^{2-}\}_\infty$ complex.

3. COMPLEXES OF Zn(II), Co(II), AND Ni(II) WITH THE RATIO *M* : HEDP = 1 : 2

In addition to the copper(II) compounds, four complexes of other 3*d* metals (Zn, Co, and Ni) with the *M* : HEDP = 1 : 2 ratio have been characterized structurally.

The $(Et_2NH_2)_2[M(H_2L)_2(H_2O)_2]$ complexes, where *M* = Co (**X** [3]) and Zn (**XI** [12]), are isostructural to the Cu analogue **II** [3]. According to crystallographic data [12], this isostructural series, except for the complexes of M^{2+} = Cu, Co, and Zn, includes the compounds of nickel(II), manganese(II), and even magnesium(II). The six-vertex coordination polyhedron of the metal in **X** and **XI**, as in **II**, has the *trans* structure.

The complex triethanolammonium salts $\{(HOCH_2CH_2)_3NH\}[M(H_{2.5}L)_2(H_2O)_2] \cdot 5H_2O$ form the second isostructural series. The structures of the copper (**III** [4]) and zinc (**XII** [13]) complexes were determined by the single-crystal X-ray diffraction technique. The isostructurality of the Ni, Co, Mn, and Mg compounds to **III** and **XII** is supported by the coincidence of the lattice parameters [4, 13]. In this series of structures, the complexes are mononuclear and the six-vertex polyhedra of the metal atoms are the *cis* isomers.

The anionic complex in the $(NH_4)_2[Ni(H_2L)_2(H_2O)_2] \cdot 7H_2O$ ammonium salt (**XIII** [14]) also has the *cis* structure.

The mean *M*–O bond lengths in four monomeric 3*d* metal (Zn, Co, and Ni) complexes $Cat_2[M(H_{4-n}L)_2(H_2O)_2] \cdot mH_2O$ are listed in Table 2.

A comparison of the geometric parameters of the Zn(II), Co(II), and Ni(II) complexes with those of the Cu(II) complexes reveals essential differences. In the former compounds, the equatorial *M*–O(*L*) and *M*–$O(H_2O)$ bonds are significantly longer than those in the latter complexes; the mean values are as follows: 2.076 Å for **XI** and **XII** (*M* = Zn), 2.073 Å for **X** (*M* = Co), 2.057 Å for **XIII** (*M* = Ni), and 1.957–1.988 Å for **I**–**IX** (*M* = Cu). At the same time, the axial *M*–O bonds in **I**–**IX** ($Cu–O_{ax}$, 2.311–2.667 Å) are significantly elongated relative to the *M*–O_{ax} bonds in **X**–**XIII** (2.177, 2.179, and 2.077 Å for *M* = Zn, Co, and Ni, respectively) due to the Jahn–Teller effect. The six-vertex coordination polyhedron of the metal atom in **X**–**XIII** can be described as a distorted octahedron in which the conventionally denoted axial bonds *M*–O_{ax} are slightly

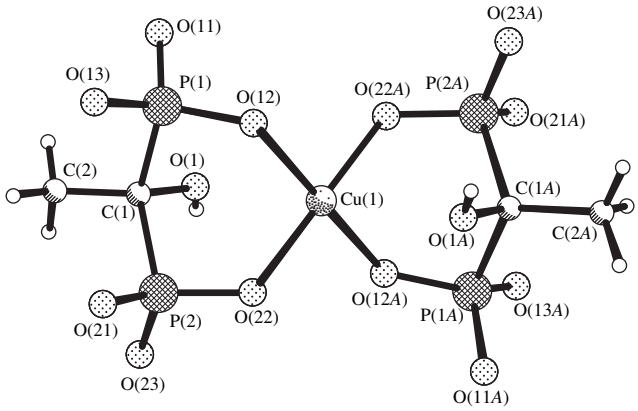

Fig. 4. Structure of the $[Cu(L)_2]^{6-}$ complex.

Table 1. Mean Cu–O bond lengths and the Δ(Δ)* parameters in the $Cat_{2n-2}Cu(H_{4-n}L)_2 \cdot mH_2O$ structures

No.	Formula	Cu–O bond lengths, Å		Δ(Δ), Å	Reference
		equatorial	axial		
Ia	$[Cu(H_3L)_2(H_2O)_2] \cdot 3H_2O$	1.959 O(*L*)	2.456 $O(H_2O)$	(0.497)	[1]
Ib	$[Cu(H_3L)_2(H_2O)_2] \cdot 3H_2O$**	1.965 O(*L*)	2.469 $O(H_2O)$	(0.504)	[2]
II	$(Et_2NH_2)_2[Cu(H_2L)_2(H_2O)_2]$	1.978 O(*L*)	2.443 $O(H_2O)$	(0.465)	[3]
III	$\{(HOCH_2CH_2)_3NH\}[Cu(H_{2.5}L)_2(H_2O)_2] \cdot 5H_2O$	1.990 O(*L*)	2.428 O(*L*)	0.438	[4]
		1.985 $O(H_2O)$	2.311 $O(H_2O)$	0.326	
IV	$K_2[Cu(\mu_2\text{-}H_2L)(H_2L)(H_2O)] \cdot 2H_2O$	1.990 O(*L*)	2.359 O(*L*)	0.369	[5]
			2.326 $O(H_2O)$	(0.353)	
V	$Cs_2[Cu(\mu_2\text{-}H_2L)(H_2L)(H_2O)] \cdot 2H_2O$	1.982 O(*L*)	2.415 O(*L*)	0.433	[5]
			2.425 $O(H_2O)$	(0.438)	
VI	$(MeNH_3)_2[Cu(\mu_2\text{-}H_2L)(H_2L)(H_2O)] \cdot H_2O$	1.979 O(*L*)	2.353 O(*L*)	0.374	[6]
			2.331 $O(H_2O)$	(0.363)	
VII	$(NH_4)_2[Cu(\mu_2\text{-}H_2L)_2] \cdot 2H_2O$	1.968 O(*L*)	2.445 O(*L*)	0.477	[7]
VIII	$Rb(H_5O_2)[Cu(\mu_2\text{-}H_2L)_2] \cdot 2H_2O$	1.978 O(*L*)	2.365 O(*L*)	0.387	[8]
IX	$K_4Na_2[Cu(L)_2] \cdot 12H_2O$	1.957 O(*L*)	2.667 OH(*L*)	(0.710)	[9]

* Δ(Δ) is the mean difference between lengths of the axial and equatorial Cu–O bonds (Δ for identical bonds and (Δ) for all bonds).
** In [2], the formula of this compound is represented by mistake as $[Cu(H_3L)_2(H_2O)_2] \cdot 2H_2O$.

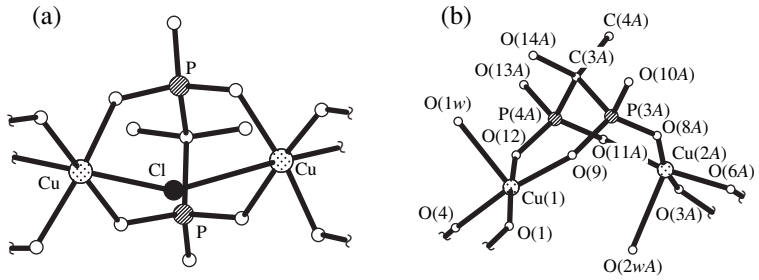

Fig. 5. Structural fragments of (a) $\{[Cu(\mu_2\text{-}H_2L)(\mu_2\text{-}Cl)]^-\}_\infty$ and (b) $[Cu(\mu_2\text{-}H_2L)(H_2O)]_\infty$ complexes.

longer in comparison with the equatorial bonds (on average, by 0.020–0.134 Å).

4. POSSIBLE REASONS FOR THE DIVERSITY OF STRUCTURES IN THE *M* : HEDP = 1 : 2 COMPLEXES

As already noted, we distinguish five types of structures among the copper(II) complexes with HEDP (Cu : HEDP = 1 : 2). These types differ in the mutual arrangement of the ligands (*trans* and *cis* isomers), the degree of aggregation of complexes (mononuclear, binuclear, and polymeric chain structures), and the function of the $H_{4-n}L^{n-}$ ligands (bidentate chelate, tridentate chelate, and tridentate chelate μ_2-bridging ligands).[2] The Cu : HEDP = 1 : 2 complexes are close in composition, and the reasons for the diversity of their structures are not entirely clear.

It is obvious that the charge of the $H_{4-n}L^{n-}$ ligand (the degree of its deprotonation) and, hence, the charge of the complex have no effect on the type of structure. The individuality of the complexing agent determines only the degree of distortion of the six-vertex coordination polyhedron under the Jahn–Teller effect [for Cu(II)] but not a particular type of structure.

Most likely, the roles played by the outer-sphere cation and crystallization water molecules are more important. In particular, they affect the "decision" between the geometric isomers (*cis* or *trans*) in the monomeric $[M^{2+}(H_{4-n}L)_2(H_2O)_2]^{2-2n}$ complexes (*M* = Cu, Zn, Co, Ni, or Mn). Possible reasons for the diversity of the types of structures in the *M* : HEDP = 1 : 2 complexes are discussed in more detail in [16].

[2] It is notable that replacement of the metal substituent *R* in HEDP *R*C(OH)$(PO_3H)_2$ by aminopropyl [H_4L', *R* = $(CH_2)_3NH_3^+$) or aminopentyl [H_4L'', *R* = $(CH_2)_5NH_3^+$] results in the formation of the dimeric $\{[Cu(H_2L')(H_2O)]_2(\mu_2\text{-}H_2L')_2\}$ structure in $Cu(H_2L')_2 \cdot 2H_2O$ [15] and the monomeric *trans*-$[Cu(H_2L'')_2(H_2O)_2]$ structure in $Cu(H_2L'')_2 \cdot 4H_2O$ [15] (structures of the T^{001} and B^{01} types, see Section 9).

5. COPPER(II) COMPLEXES WITH THE RATIO *M* : HEDP = 1 : 1

Three Cu(II) compounds with the ratio Cu : HEDP = 1 : 1 have been characterized structurally, namely, $Na[Cu(H_2L)Cl] \cdot 3H_2O$ (**XIV** [17]), $[Cu(H_2L)(H_2O)] \cdot 3.5H_2O$ (**XV** [18]), and $[Cu(H_2L)(Bipy)(H_2O)] \cdot 2H_2O$ (**XVI** [19]).

In **XIV** (Fig. 5a) and **XV** (Fig. 5b), copper atoms are linked through the tetradentate bischelate μ_2-bridging H_2L^{2-} ligands into polymeric chains (anionic and neutral, respectively). The coordination polyhedra and coordination numbers of the metal atoms in structures **XIV** and **XV** depend on the nature of the accompanying ligand *X* (Cl or H_2O). In **XIV**, in addition to the H_2L^{2-} ligands, the complexes are joined through the bridging chlorine atoms, which occupy the axial sites in the six-vertex polyhedron [elongated tetragonal bipyramid (4 + 2)] of the copper atom. In **XV**, the oxygen atom of the terminal water molecule occupies the axial site in the five-vertex polyhedron [tetragonal pyramid (4 + 1)]. Equatorial planes in the coordination polyhedra of the Cu atoms in structures **XIV** and **XV** are occupied by four O atoms of four phosphonate groups of two H_2L^{2-} ligands. The above two compounds differ not only in the coordination number of the metal atom but also in the general structural motif: in **XIV**, the chains are approximately linear, whereas the structure of **XV** consists of zigzag chains.

In the mononuclear neutral $[Cu(H_2L)(Bipy)(H_2O)]$ complex in structure **XVI** (Fig. 6), the presence of three different ligands, two of which fulfill the bidentate chelate function, determines the tetragonal–pyramidal coordination of the metal atom (4 + 1). The equatorial plane of the tetragonal pyramid is formed by two O(*L*) atoms of two phosphonate groups of the H_2L^{2-} ligand and two N atoms of bipyridyl, and the axial site is occupied by the O(*w*) atom of the water molecule. The Cu atom deviates from the basal plane of the pyramid toward the axial O(*w*) atom by 0.214 Å.

Table 3 presents the mean geometric parameters of complexes **XIV**–**XVI** with the ratio Cu : HEDP = 1 : 1 and two complexes with the ratios Cu : HEDP = 3 : 2 and 5 : 2 (see below). As usual, the axial Cu–O (Cu–Cl) bonds in the Cu(II) coordination polyhedra are substan-

Table 2. Mean *M*–O bond lengths in monomeric octahedral *trans* (*t*) and *cis* (*c*) $Cat_{2n-2}[M(H_{4-n}L)_2(H_2O)_2] \cdot mH_2O$ complexes of 3*d* metals (Zn, Co, and Ni)

No.	Formula	*M*–O bond lengths, Å		Δ(Δ)*, Å	Reference
		equatorial	axial		
X	$(Et_2NH_2)_2[Co(H_2L)_2(H_2O)_2](t)$	2.073 O(*L*)	2.179 O(H_2O)	(0.106)	[3]
XI	$(Et_2NH_2)_2[Zn(H_2L)_2(H_2O)_2](t)$	2.066 O(*L*)	2.200 O(H_2O)	(0.134)	[12]
XII	$\{(HOCH_2CH_2)_3NH\}$-$[Zn(H_{2.5}L)_2(H_2O)_2] \cdot 5H_2O(c)$	2.067 O(*L*)	2.175 O(*L*)	0.108	[13]
		2.105 O(H_2O)	2.133 O(H_2O)	0.028	
XIII	$(NH_4)_2[Ni(H_2L)_2(H_2O)_2] \cdot 7H_2O(c)$	2.056 O(*L*)	2.085 O(*L*)	0.029	[14]
		2.058 O(H_2O)	2.069 O(H_2O)	0.011	

* Δ(Δ) is the mean difference between lengths of the axial and equatorial *M*–O bonds (Δ for identical bonds and (Δ) for all bonds).

Table 3. Mean Cu–*Lig* bond lengths and the Δ(Δ) parameters* in the Cu : HEDP = 1 : 1, 3 : 2, and 5 : 2 complexes

No.	Formula	Cu–O bond lengths, Å		Δ(Δ), Å*	Reference
		Cu-*Lig* (eq)	Cu-*Lig* (ax)		
XIV	$Na[Cu(H_2L)Cl] \cdot 3H_2O$	1.984 O(*L*)	2.794 Cl		[17]
XV	$[Cu(H_2L)(H_2O)] \cdot 3.5H_2O$	1.90 O(*L*)	2.39 O(H_2O)	(0.42)	[18]
XVI	$[Cu(H_2L)(Bipy)(H_2O)] \cdot 2H_2O$	1.940 O(*L*)	2.258 O(H_2O)	(0.318)	[19]
		2.003 *N*(*Bipy*)			
XVII	$[Cu_3(HL)_2(H_2O)_4] \cdot 2H_2O$**	1.969 O(*L*)	2.458 OH(*L*)	(0.489)	[11]
		1.942 O(*L*) and			
		1.966 O(H_2O)	2.347 O(H_2O)	0.381	
XVIII	$Na_2[Cu_6^{1+}Cu_9^{2+}(L)_6(OH)_2] \cdot H_2O$***	1.980 O(*L*)	2.630 O(*L*)	0.650	[20]
		1.927 OH			

* Δ(Δ) is the mean difference between lengths of the axial and equatorial Cu–O bonds [Δ for identical bonds and (Δ) for all bonds].
** For structure **XVII**, the bond lengths are given for Cu coordination polyhedra of two types: tetragonal bipyramid (4 + 2) (upper line) and tetragonal pyramid (4 + 1).
*** For structure **XVIII**, the bond lengths are given for the six-vertex Cu(II) polyhedra (4 + 2).

tially elongated. In compounds **XV** and **XVI**, the lengths of the axial and equatorial Cu–O bonds differ by Δ = 0.32–0.49 Å.

6. COMPLEX WITH THE RATIO Cu : HEDP = 3 : 2, $Cu_3(HL)_2 \cdot 6H_2O$

In $Cu_3(HL)_2 \cdot 6H_2O$ (**XVII**) [11], which is the only structurally characterized compound with the ratio Cu : HEDP = 3 : 2, the neutral $[Cu(\mu_3\text{-}HL)_2(H_2O)_4]_\infty$ complex has a polymeric structure (ribbons consisting of double chains, see Fig. 7). The HL^{3-} ligand fulfills the hexadentate trischelate μ_3-bridging function. It coordinates one of the two independent copper atoms [Cu(1)] in the tridentate chelate mode, the Cu(2) atom in the bidentate chelate mode, and the Cu(2)' atom [symmetrically related to Cu(2)] in the monodentate mode. The (H)O(C) oxygen atom of the protonated α-hydroxy group, together with two O(P) atoms of the phosphonate groups, participates in the coordination of Cu(1). Two independent copper atoms have different coordination environments. The coordination polyhedron of the Cu(1) atom is a centrosymmetric elongated tetragonal bipyramid (4 + 2), and the polyhedron of the Cu(2) atom is a tetragonal pyramid (4 + 1). In the latter pyramid, one of two oxygen atoms of the coordinated water molecules occupies an equatorial site, and the other water oxygen occupies the axial site.

The Cu(2) atom is displaced from the equatorial plane defined by four O atoms toward the O(2*w*) atom by 0.196 Å. The sixth vertex in the Cu(2) coordination polyhedron is blocked by the methyl group of the HL^{3-} ligand of the adjacent molecule, which is related to the reference molecule by the inversion center (the

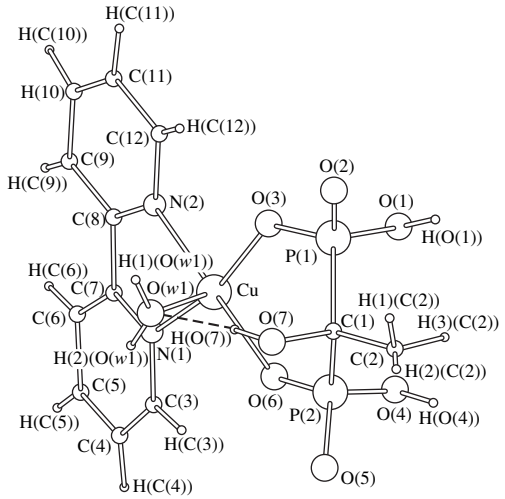

Fig. 6. Structure of the $[Cu(H_2L)(Bipy)(H_2O)]$ complex.

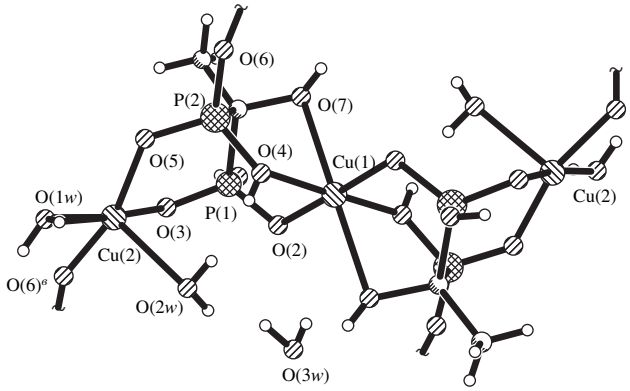

Fig. 7. Structural fragment of the $[Cu_3(\mu_3\text{-}HL)_2(H_2O_4)]_\infty$ complex.

Cu(2)...C distance is 3.283 Å, and the O(2*w*)Cu(2)C angle is 175.4°).

In the coordination polyhedra of both metal atoms, the axial bonds are significantly longer than the equatorial bonds [by 0.49 and 0.38 Å for Cu(1) and Cu(2), respectively].

The coordination of a metal atom by the oxygen atom of the protonated α-hydroxy group, which is observed in **XVII**, is uncommon to the HEDP complexes of transition metals. This coordination mode was revealed in one more compound, namely, the $[Cu(L)_2]^{6-}$ complex of the earlier described structure **IX**.

7. MIXED-VALENT Cu(I, II) COMPLEX WITH THE RATIO Cu : HEDP = 5 : 2, $Na_2Cu_{15}(L)_6(OH)_2 \cdot H_2O$

The crystal structure of $Na_2[Cu_6^{1+}Cu_9^{2+}(L)_6(OH)_2] \cdot H_2O$ (**XVIII**) [20], the first mixed-valent copper(I, II) complex with the ratio Cu : HEDP = 5 : 2 [Cu(I) : Cu(II) : HEDP = 2 : 3 : 2], was determined recently [20]. The framework structure is built of "honeycomb" layers of two types: (i) the $[Cu_3^{2+}(OH))O_3$ structural units share edges to form the *A* layer and (ii) the NaO_6 octahedra and the planar $Cu^{2+}O_4$ fragments share edges to form the *B* layer. The *A* and *B* layers are linked through 18-membered rings $Cu_3P_6O_6C_3$, which are sandwiched between the layers. The ring includes three L^{4-} ligands and three $Cu^{1+}O_2$ structural units (Fig. 8). The channels formed in the three-dimensional structure accommodate crystallization water molecules. In structure **XVIII**, there are two crystallographically nonequivalent copper(II) atoms [Cu(1) and Cu(2) (at the inversion center)] and copper(I) atom [Cu(3)]. The environments of the Cu(1) and Cu(2) atoms are described as four-vertex polyhedra. The polyhedron of the Cu(2) atom is a nearly regular square (the Cu–O distances are 1.952 and 1.967 Å, and the OCuO angles are 86.8° and 93.2°), and the polyhedron of the Cu(1) atom shows pronounced distortions [the Cu–O distances are 1.927–2.040 Å, the OCuO angles are 75.5°–101.5°, and the Cu(1) atom deviates from the plane of four O atoms by 0.128 Å). The monovalent Cu(3) atom is two-coordinate (Cu–O, 1.822 and 1.825 Å and OCuO, 177.8°). The coordination sphere of the Cu(1) atom includes three O(*L*) oxygen atoms of two HEDP ligands and the μ_3-hydroxo OH ligand, which connects three Cu(1) atoms. The coordination octahedron of the Na atom (av. Na–O, 2.442 Å) shares an edge with the Cu(2) polyhedron.

The L^{4-} ligand fulfills the hexadentate bischelate μ_5-bridging function (with respect to the copper atoms): it coordinates a Cu(2) atom, two Cu(1) atoms, and two Cu(3) atoms with all the six phosphonate O(*L*) atoms and forms two joint six-membered metallocycles $\overline{\text{Cu(1)–O–P–C–P–O}}$ and $\overline{\text{Cu(2)–O–P–C–P–O}}$.

As noted above, the coordination polyhedra of the Cu(1) and Cu(2) atoms are characterized in [20] based on the coordination number equal to four. In reality, the coordination polyhedra of the Cu(1) and Cu(2) atoms in structure **XVIII**, as in the structures of other copper(II) complexes, are completed to six-vertex polyhedra, namely, elongated tetragonal bipyramids (4 + 2). The bipyramid of Cu(1) is asymmetric [Cu(1)–O(5), 2.506 Å and Cu(1)–O(1), 2.779 Å], and the bipyramid of Cu(2) is symmetric [Cu(2)–O(6), 2.617 Å × 2] (Table 3).

8. UNUSUAL FUNCTIONS OF THE ANION OF 1-HYDROXYETHYLIDENEDIPHOSPHONIC ACID IN THE STRUCTURE OF $Ni(Phen)_3(H_3L)_2 \cdot 2H_2O$

Formally, the $Ni(Phen)_3(H_3L)_2 \cdot 2H_2O$ (**XIX**) compound belongs to the *M* : HEDP = 1 : 2 complexes considered above. However, it is doubtful that the HEDP

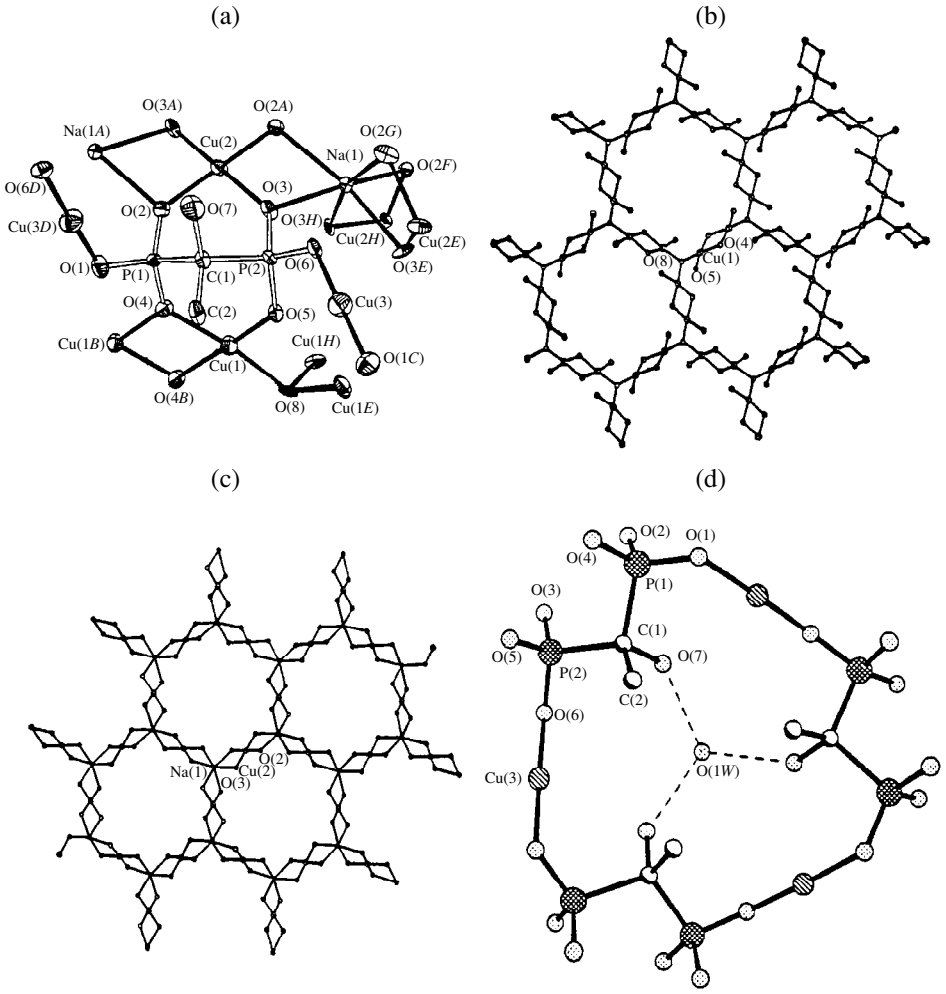

Fig. 8. Structural fragments of the mixed-valent $\{[Cu_6^{1+}Cu_9^{2+}(L)_6(OH)_2]^{2-}\}_\infty$ anionic complex: (a) coordination of the L^{4-} ligand and atomic numbering, (b) structure of the $(Cu_3^{2+}(OH))O_3$ layer (*A*), (c) structure of the $NaO_6 + Cu^{2+}O_4$ layer (*B*), and (d) 18-membered $Cu_3P_6O_6C_3$ ring involving three L^{4-} ligands and three $Cu^{1+}O_2$ fragments.

ligand is involved in the coordination sphere of the metal in the presence of the accompanying ligands (1,10-phenanthroline molecules). Actually, addition of *Phen* · H_2O to an aqueous solution of $Ni(H_3L)_2$ results in the formation of the thermodynamically stable $[Ni(Phen)_3]^{2+}$ cationic complex ($\log K_{st}$ = 23.9 vs. 4.03 for $[Ni(H_2L)_2]^{2-}$ [21]), and the H_3L^- anion is forced out of the coordination sphere. It follows from the X-ray diffraction data that the structural formula of **XIX** is $[Ni(Phen)_3](H_7L_2)_{0.5}(H_5L_2)_{0.5} \cdot 2H_2O$ [22].

In the octahedral $[Ni(Phen)_3]^{2+}$ cationic complex, the Ni–N distances fall in the range from 2.074 to 2.107 Å. The most remarkable (and unusual) feature of **XIX** is the structure of the outer-sphere HEDP anions. There are two independent anions with different charges in the structure: $H_{3.5}L^{0.5-}$ and $H_{2.5}L^{1.5-}$. Each anion is linked by a strong linear hydrogen bond with a neighboring anion of the same kind to form a centrosymmetric dimer (Fig. 9). The interionic O··H··O contacts in both $H_7L_2^-$ and $H_5L_2^{3-}$ dimers are the strongest in the structure (the O··O distances are 2.436 and 2.466 Å, and the H··O distances are 1.22 and 1.23 Å, respectively). Note that the exactly symmetric hydrogen bonds in the $H_7L_2^-$ and $H_5L_2^{3-}$ anions,[3] most probably, result from the superposition of two equiprobable orientations of statistically disordered H_4L and H_3L^- fragments for $(H_7L_2^-)$ and the H_3L^- and H_2L^{2-} fragments for $(H_5L_2^{3-})$. In this case, the structural formula

[3] A similar dimeric $H_5L_2^{3-}$ anion, in which two $H_{2.5}L^{1.5-}$ "halves" are related by the crystallographic twofold axis, was also found in the structure of $(NH_4)_3(H_5L_2) \cdot 2H_2O$ [23] (O··O, 2.508 Å; H··O, 1.28 Å; and OHO, 160°).

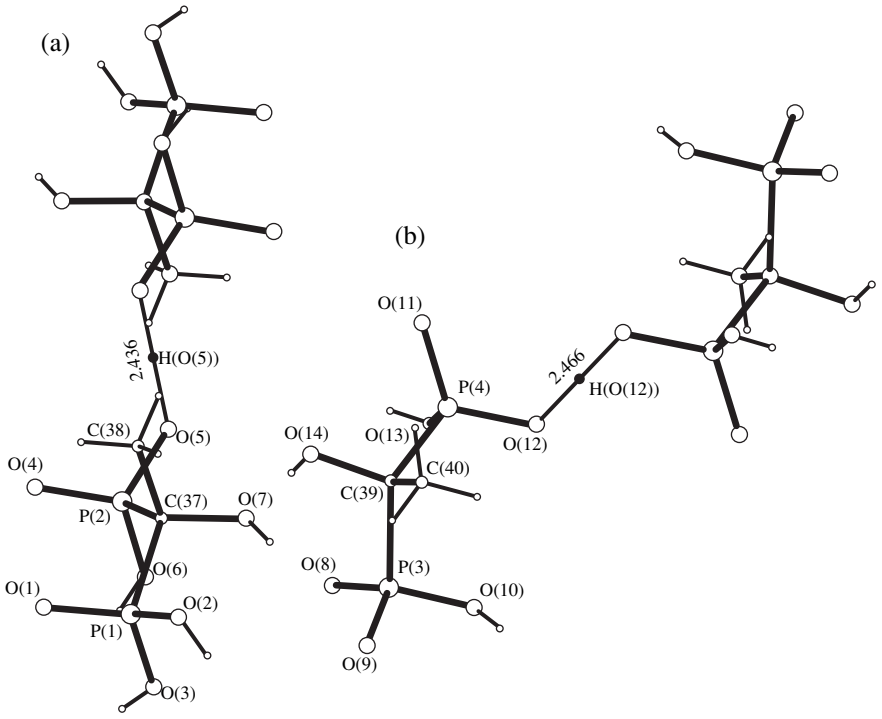

Fig. 9. Structures of (a) $H_7L_2^-$ and (b) $H_5L_2^{3-}$ dimers in the Ni(*Phen*)$_3$(H$_3L$)$_2 \cdot 2H_2O$ complex.

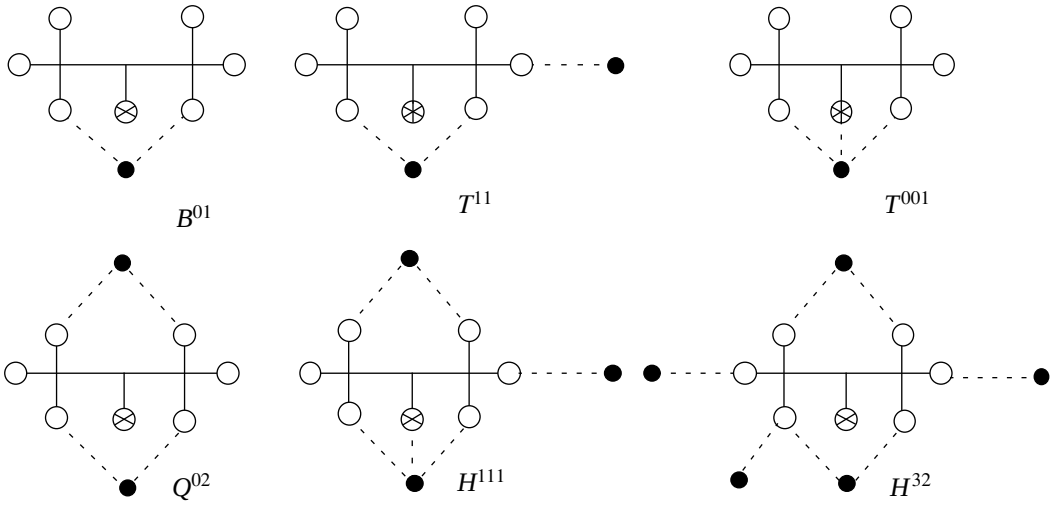

Fig. 10. Six modes of coordination of metal atoms by HEDP ligands in the *M* : HEDP = 1 : 2 complexes.

of compound **XIX** is represented as [Ni(*Phen*)$_3$](H$_3L$)(H$_2L$)$_{0.5} \cdot 0.5H_4L \cdot 2H_2O$.

In addition to the contacts in the dimers, structure **XIX** is characterized by a number of short O(*L*)–H··O(*L*) contacts between the neighboring ionic pairs (the O··O distances are 2.482–2.578 Å and the H··O distances are 1.84–1.90 Å), O(*L*)–H··O hydrogen bonds involving water molecules (O··O, 2.468–2.912; and H··O, 1.69–2.22 Å), and weaker C–H··O interactions between the cationic and anionic complexes (C··O, 3.019–3.469 and H··O, 2.36–2.74 Å).

9. COORDINATION MODES OF THE HEDP LIGAND IN 3*d* METAL COMPLEXES

Figure 10 schematically represents six coordination modes of the HEDP ligands that occur in the 3*d* metal complexes—bidentate chelate, tridentate chelate μ_2-bridging, tridentate chelate, tetradentate bischelate μ_2-

Table 4. Characterization of the coordination modes of the HEDP anions in Cu(II) complexes [24]

Coordination mode of HEDP	Ligand (HEDP = H_4L)	$Z = m + b + t$*	$N_b = m + 2b + 3t$**	$C^n = b + 2t$***	Type of the rings		Number of compounds
					C^5	C^6	
B^{01}	H_3L^-, $H_{2.5}L^{1.5-}$, H_2L^{2-}	1	2	1	0	1	8
T^{001}	L^{4-}	1	3	2	2	0	1
T^{11}	H_2L^{2-}	2	3	1	0	1	5
Q^{02}	H_2L^{2-}	2	4	2	0	2	2
H^{111}	HL^{3-}	3	6	3	2	1	1
H^{32}	L^{4-}	5	7	2	0	2	1

* Z is the total number of the M atoms bonded to a ligand.
** N_b is the total number of coordination bonds of a ligand with the M atoms.
*** $C^n = C^5 + C^6$ is the total number of five- and six-membered metallocycles formed by a HEDP ligand.

bridging, hexadentate trischelate μ_3-bridging, and hexadentate bischelate μ_5-bridging[4] (according to the notations proposed in [24],[5] B^{01}, T^{11}, T^{001}, Q^{02}, H^{111}, and H^{32}, respectively). These six modes of metal coordination by HEDP are characterized in Table 4. It is seen that the B^{01} coordination mode occurs most frequently (in eight of the eighteen compounds). The compounds with this coordination mode contain monomeric complexes in which the $H_{4-n}L^{n-}$ ligands use one O(P) oxygen atom of each of the two phosphonate (phosphonic) groups. The T^{11} coordination mode (the H_2L^{2-} ligand coordinates two M atoms by three O(P) atoms of two PO_3H^- groups) occurs more rarely (in five compounds). The Q^{02} coordination mode, according to which the H_2L^{2-} ligand coordinates two metal atoms by four O(P) oxygen atoms (by two oxygens of two phosphonate groups), occurs in two structures. The remaining three coordination modes of HEDP were found in one compound each. In the monomeric $[Cu(L)_2]^{6-}$ complex, there is the T^{001} coordination mode: the L^{5-} ligand coordinates the metal by two O(P) atoms of two phosphonate groups and the oxygen atom of the protonated α-hydroxy group. In the neutral $[Cu_3(HL)_2(H_2O)_4]$ complex, the H^{111} coordination mode occurs: the HL^{3-} ligands are bound to the Cu(1), Cu(2), and Cu(2)' atoms in the tridentate cyclic, bidentate cyclic, and monodentate modes, respectively. The O(C) atom of the protonated α-hydroxy group is involved in coordination [of the Cu(1) atom] along with five O(P) atoms. Finally, in the structure of the $\{[Cu_6^1\ Cu_9^{2+}(L)_6(OH)_2]^{2-}\}_\infty$ anionic framework, the H^{32} coordination mode occurs: the L^{4-} ligand coordinates two Cu(I) atoms and one Cu(II) atom in the monodentate mode and two Cu(II) atoms in the bidentate cyclic mode. All six phosphonate O(P) atoms are involved in coordination.

Note that the HEDP ligand, independent of its protonation degree, can coordinate the same metal atom with no more than three of the seven potential donor oxygen atoms. This specific feature of all metal (not only 3*d* element) complexes with HEDP is determined by at least two reasons. The first reason has to do with the steric strain that would arise under the deformation of the three-dimensional structure of the HEDP ions (i.e., the rigid *W*-shaped conformation of the O–P–C–P–O fragment, which results from the sp^3-hybrid state of the C and P atoms.[6] The second (possibly more important) reason for the limitation of the number of donor atoms of the HEDP ligand coordinating a metal atom is that the coordination of the M atom by the fourth (fifth, etc.) oxygen atom of the same HEDP ligand would necessarily result in the formation of the four-membered $\overline{M}$–O–P–$\overline{O}$ metallocycles that include two O atoms of the same phosphonic (phosphonate) group. It is known that, for energy reasons, the four-membered rings are less favorable than the five- and six-membered chelate rings.

10. CONCLUSION

Based on the data for a large number of structurally characterized 3*d* metal complexes with HEDP, we can outline some factors responsible for the specific structural features in this class of compounds.

[4] The description of the last coordination mode is conventional, because it is based on the coordination number equal to four for the bivalent copper atoms, as it is accepted in [20], without regard for the longer axial contacts in the elongated tetragonal bipyramid (4 + 2).

[5] The coordination capacity of the ligand is specified by the capital letter of the D^{mbt} symbol (*B*, bidentate; *T*, tridentate; *Q*, tetradentate (quadridentate); and *H*, hexadentate), and the *m*, *b*, and *t* positions indicate the number of metal atoms coordinated by the HEDP ligand in the monodentate, bidentate cyclic, and tridentate cyclic modes, respectively.

[6] The deviation of five atoms of the above fragment from their plane, averaged over 34 crystallographically independent ligands in the structures of the HEDP compounds with different metals, is 0.07(3) Å [24].

The M : HEDP ratio, to a large extent, determines the type of the structure and the coordination capacity of the $H_{4-n}L^{n-}$ ligand: an increase in this ratio (from 1 : 2 to 5 : 2) results, as a rule, in an increase in the degree of aggregation of the complexes (from the monomeric structure to the framework structure) and the coordination capacity of the diphosphonic ligand (from the bidentate function to the hexadentate function).

The nature of the M^{2+} complexing agent determines the degree of distortion of the six-vertex coordination polyhedron [octahedron for M = Zn, Ni, and Co and elongated tetragonal bipyramid (4 + 2) for Cu].

The presence of the accompanying X ligands (H_2O, *Bipy*, or Cl) and their amount determine to a large extent the type of the structure and the coordination number of the metal atom in the Cu : HEDP = 1 : 2 and 1 : 1 complexes.

The M : HEDP : X ratio and the competing donor atoms involved [N (*Phen*) and O (H_3L)] determine the unusual function of HEDP as outer-sphere dimeric anions in the $[Ni(Phen)_3](H_7L_2)_{0.5}(H_5L_2)_{0.5} \cdot 2H_2O$ structure.

ACKNOWLEDGMENTS

The author is grateful to G.G. Aleksandrov, who performed the X-ray diffraction analysis of the majority of the compounds discussed in this paper.

REFERENCES

1. E. G. Afonin, G. G. Aleksandrov, and V. S. Sergienko, Koord. Khim. **23** (11), 846 (1997).
2. K. A. Lysenko, V. M. Akimov, M. Yu. Antipin, *et al.*, Zh. Neorg. Khim. **42** (8), 1283 (1997).
3. V. S. Sergienko, G. G. Aleksandrov, and E. G. Afonin, Zh. Neorg. Khim. **42** (8), 1291 (1997).
4. V. S. Sergienko, E. G. Afonin, and G. G. Aleksandrov, Koord. Khim. **25** (2), 133 (1999).
5. V. S. Sergienko, G. G. Aleksandrov, and E. G. Afonin, Koord. Khim. **25** (6), 451 (1999).
6. E. G. Afonin, G. G. Aleksandrov, and V. S. Sergienko, Koord. Khim. **25** (12), 923 (1999).
7. V. S. Sergienko, G. G. Aleksandrov, and E. G. Afonin, Koord. Khim. **24** (6), 455 (1998).
8. G. G. Aleksandrov, V. S. Sergienko, and E. G. Afonin, Zh. Neorg. Khim. **43** (11), 1811 (1998).
9. Z. Pan, X. Jin, M. Shao, *et al.*, Chem. J. Chin. Univ., **6** (1), 69 (1985).
10. V. S. Sergienko, E. O. Tolkacheva, and A. B. Ilyukhin, Koord. Khim. **20** (3), 195 (1994).
11. A. Neuman, A. Safsaf, H. Gillier, *et al.*, Phosphorus, Sulfur Silicon Relat. Elem. **70** (2), 273 (1992).
12. V. S. Sergienko, E. G. Afonin, and G. G. Aleksandrov, Zh. Neorg. Khim. **43** (6), 1006 (1998).
13. V. S. Sergienko, G. G. Aleksandrov, and E. G. Afonin, Kristallografiya **45** (2), 262 (2000) [Crystallogr. Rep. **45**, 230 (2000)].
14. V. S. Sergienko, E. G. Afonin, and G. G. Aleksandrov, Koord. Khim. **24** (4), 293 (1998).
15. Y. Leroux, A. Neuman, H. Gillier, *et al.*, Supramolec. Chem. **5** (2), 267 (1995).
16. V. S. Sergienko, Zh. Neorg. Khim. **45** (11), 1815 (2000).
17. G. G. Aleksandrov, V. S. Sergienko, and E. G. Afonin, Zh. Neorg. Khim. **42** (8), 1287 (1997).
18. G. G. Aleksandrov and V. S. Sergienko, Kristallografiya **44** (5), 939 (1999) [Crystallogr. Rep. **44**, 877 (1999)].
19. L. M. Shkol'nikova, A. A. Masyuk, G. V. Polyanchuk, *et al.*, Koord. Khim. **15** (10), 1424 (1989).
20. L.-M. Zheng, C.-Y. Duan, X.-R. Ye, *et al.*, J. Chem. Soc., Dalton Trans., No. 6, 905 (1998).
21. Z. R. Amirov and Z. A. Saprykova, Zh. Obshch. Khim. **57** (7), 1526 (1987).
22. V. S. Sergienko, G. G. Aleksandrov, and E. G. Afonin, Kristallografiya **45** (3), 475 (2000) [Crystallogr. Rep. **45**, 432 (2000)].
23. V. S. Sergienko, E. O. Tolkacheva, and A. B. Ilyukhin, Zh. Neorg. Khim. **38** (7), 1129 (1993).
24. V. N. Serezhkin, L. B. Serezhkina, and V. S. Sergienko, Zh. Neorg. Khim. **45** (4), 592 (2000).

Translated by I. Polyakova

Crystallography Reports, Vol. 46, No. 2, 2001, pp. 207–209. Translated from Kristallografiya, Vol. 46, No. 2, 2001, pp. 247–249.

STRUCTURE OF COORDINATION COMPOUNDS

Crystal Structure of Chloro[1-Hydroxyethane-1,1-Diphosphonato(3–)]ditin(II) Monohydrate $Sn_2(HL)Cl \cdot H_2O$

V. S. Sergienko*, G. G. Aleksandrov*, and E. G. Afonin**

** Kurnakov Institute of General and Inorganic Chemistry, Russian Academy of Sciences, Leninskiĭ pr. 31, Moscow, 117907 Russia*

*** State Enterprise "Chemical Engineering Laboratory," Kaluga, Russia*

Received February 22, 1999

Abstract—The synthesis and X-ray structure analysis of $Sn_2(HL)Cl \cdot H_2O$, where HL^{3-} is the anion of 1-hydroxyethane-1,1-diphosphonic acid, are reported. The coordination polyhedra of two independent tin(II) atoms are the $Sn(1)O_2Cl$ and $Sn(2)O_3$ trigonal pyramids, in which one of the vertices is occupied by a lone electron pair (Sn–O, 2.144–2.218 Å and Sn–Cl, 2.573 Å). The pyramids are complemented by weaker Sn···O and Sn···Cl contacts to form severely distorted (3 + 3) octahedra. The SnO_2Cl and SnO_3 pyramids are linked by the HL^{3-} bridging ligands into the $[Sn_2(HL)Cl]_6$ cyclic molecules, which, in turn, are joined by additional Sn···O, Sn···Cl, $O(H_2O)\cdots O(L)$, and $O(H_2O)\cdots Cl$ contacts with each other and with crystallization water molecules into a three-dimensional framework. © *2001 MAIK "Nauka/Interperiodica".*

INTRODUCTION

Only two tin(II) complexes with methanediphosphonic acids $R_1R_2C(PO_3H_2)_2$ are known, namely, Sn_2L and $Sn(H_2L') \cdot H_2O$, where H_4L is 1-hydroxyethane-1,1-diphosphonic acid ($R_1 = CH_3$, $R_2 = OH$) and H_4L' is methanediphosphonic acid ($R_1 = R_2 = H$). Their structures were determined by X-ray diffraction analysis [1]. Ditin(II) 1-hydroxyethane-1,1-diphosphonate was prepared in the form of colorless rhomboid plates by hydrothermal synthesis from an aqueous solution of $SnCl_2 + 3.87H_4L$ (a buffer solution with pH 3.5, $t \sim 150$°C). Needle-shaped crystals of tin(II) methanediphosphonate were isolated from an aqueous solution of $SnCl_2 + 2.9H_4L'$ ($t \approx 4$°C).

In this paper, we report the preparation and crystal structure of a new compound, namely, chloro[1-hydroxyethane-1,1-diphosphonato(3–)]ditin(II) $Sn_2(HL)Cl \cdot H_2O$ (**I**).

EXPERIMENTAL

Synthesis. A solution of $SnCl_2 \cdot 2H_2O$ (2.25 g, 0.01 mol) in water (3 ml) was added to a solution of $H_4L \cdot H_2O$ (2.24 g, 0.01 mol) in water (12 ml). The mixture was allowed to stand for a day. Then, the solution was drawn off and the crystals were rapidly washed with water and dried on a paper filter in air at room temperature.

IR spectrum (a suspension in Vaseline oil; ν, cm^{-1}): 1657 and 1641 (δ_{H_2O}); 1140, 1069, 1037, 1000, 955, and 919 (the stretching vibrations of the PO_3^{2-} and PO_3H^- groups); and 819, 659, 555, 480, and 445.

X-ray structure analysis. Crystals **I** ($C_2H_7ClO_8P_2Sn_2$) are cubic, $a = 24.800(6)$ Å, $V = 15253(6)$ Å^3, $\rho_{calcd} = 2.581$ g/cm^3, $\mu_{Mo} = 44.07$ cm^{-1}, $F(000) = 11040$, $M = 493.85$ amu, $Z = 48$, and space group $Pn3n$.

A set of experimental data was collected on a Syntex $P2_1$ four-circle automated diffractometer (λMoK_α, graphite monochromator, $\theta/2\theta$ scan mode, $2\theta_{max} = 70°$). An empirical correction based on ψ scans was made for anisotropic absorption. A total of 3110 reflections were measured, of which 2749 unique reflections with $I > 2\sigma(I)$ were used in the structure determination ($R_{int} = 0.0465$; $0 \le h \le 19$, $0 \le k \le 36$, $0 \le l \le 40$).

The structure was solved by the direct method and refined on F^2 by the least-squares procedure in the anisotropic approximation (SHELXL93 [2]). The hydrogen atoms were not located. The positions of the H(*Me*) atoms of the HL^{3-} ligand were calculated geometrically (C–H = 0.96 Å). These H atoms at the fixed positions ($U_H = 0.08$ Å^2) were taken into account in the refinement. The O(2*w*) oxygen atom of a water molecule is disordered; its occupancy factor is 0.75.

The final refinement parameters are $R = 0.054$, $wR = 0.140$, and $GOOF = 1.264$. The extinction coefficient is 0.00024(4), and the residual electron density lies between $\Delta\rho_{min} = -2.086$ and $\Delta\rho_{max} = 1.938$ e/Å^3.

The atomic coordinates and thermal parameters are listed in the table.

RESULTS AND DISCUSSION

Compound **I** is obtained in the form of colorless transparent crystals, which become white after a long

Atomic coordinates and thermal parameters U_{eq}

Atom	*x*	*y*	*z*	U_{eq}, Å^2
Sn(1)	0.08782(4)	0.81075(3)	0.55803(3)	0.0295(2)
Sn(2)	0.18531(3)	0.64458(3)	0.59231(3)	0.0271(2)
P(1)	0.0950(1)	0.6861(1)	0.4946(1)	0.0193(5)
P(2)	0.0550(1)	0.6860(1)	0.6092(1)	0.0274(6)
Cl(1)	0.1797(2)	0.7827(2)	0.5976(2)	0.070(1)
O(1)	0.1001(3)	0.7475(3)	0.4959(3)	0.025(1)
O(2)	0.0817(3)	0.6641(3)	0.4384(3)	0.024(2)
O(3)	0.1449(3)	0.6577(3)	0.5169(3)	0.027(2)
O(4)	0.0611(5)	0.7467(4)	0.6099(4)	0.049(3)
O(5)	0.1048(3)	0.6554(4)	0.6259(3)	0.032(2)
O(6)	0.0072(4)	0.6682(6)	0.6446(4)	0.056(3)
O(7)	–0.0090(3)	0.6952(4)	0.5231(3)	0.035(2)
C(1)	0.0391(4)	0.6665(5)	0.5394(5)	0.026(2)
C(2)	0.0292(6)	0.6057(5)	0.5370(6)	0.039(3)
O(1*w*)	0.25	0.75	0.50	0.088(9)
O(2*w*)*	–0.1004(8)	0.668(1)	0.574(1)	0.15(1)

* The occupancy factor of the O(2*w*) atom is 0.75.

period of time. The substance is poorly soluble in water, aqueous solutions of Na_2CO_3 and KCl, nitric and acetic acids, ethanol, ethyl acetate, acetone, carbon tetrachloride, and benzene. It is soluble in hydrochloric acid, alkali, EDTA, and (slowly) ammonium solutions. It is also soluble in hot concentrated sulfuric acid but poorly soluble in diluted sulfuric acid.

In structure **I**, the coordination polyhedra of two independent tin atoms are the distorted trigonal pyramids $Sn(1)O_2Cl$ and $Sn(2)O_3$ (figure). The Sn(1) atom is bonded to the O(1) and O(4) oxygen atoms of two phosphonate groups of the same HL^{3-} ligand and also to the Cl(1) atom. The Sn(2) atom forms bonds with the O(2), O(3), and O(5) oxygen atoms of three phosphonate groups belonging to two HL^{3-} ligands. Hence, HL^{3-} acts as a pentadentate bischelate μ_3-bridging ligand.

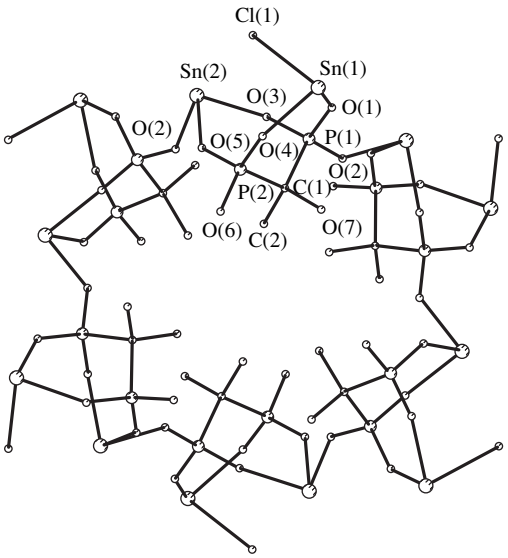

Molecular structure of $[Sn_2(HL)Cl]_6$.

The Sn–O distances in structure **I** (2.144–2.218 Å, av. 2.168 Å) are comparable with similar distances in structures Sn_2L [1] and $Sn(H_2L') \cdot H_2O$ [1] (Sn–O, 2.10–2.16 and 2.12–2.17 Å, respectively). The Sn(1)–Cl(1) bond length in **I** (2.573 Å) is close to the Sn–Cl distances in the compounds of tin(II) with the coordination number equal to three (Sn–Cl, 2.42–2.63 Å) [3].

The $Sn(2)O_3$ pyramids are linked by the HL^{3-} bridging ligands into the $[Sn(HL)]_6$ hexanuclear macrocycles about the crystallographic threefold axes. The $Sn(1)O_2Cl$ pyramids are attached to the outside of the macrocycle, thus forming the $[Sn_2(HL)Cl]_6$ molecule.

Forming bonds with the Sn(1) and Sn(2) atoms, the HL^{3-} ligand closes two six-membered chelate rings. The Sn(1)–O(1)–P(1)–C(1)–P(2)–O(4) chelate ring has a sofa conformation: the C(1) atom deviates from the plane of the remaining five atoms (*A*), which are coplanar within $\Delta = \pm 0.02$ Å, by 0.90 Å. The Sn(2)–O(3)–P(1)–C(1)–P(2)–O(5) ring adopts a chair conformation in which the Sn(2) and C(1) atoms deviate from the plane of the remaining four atoms (*B*, $\Delta = \pm 0.02$ Å) by –0.51 and 0.88 Å, respectively. The *A*/*B* dihedral angle is equal to 66.5°.

As noted above, HL^{3-} is a pentadentate ligand. Only the O(7) atom of the alcohol group and one of the oxygen atoms of the phosphonate group do not form bonds with tin atoms. We can say with confidence that the O(6) terminal atom is the protonated atom. This conclusion is supported by the analysis of the P–O distances. The P(2)–O(6) terminal bond is the longest bond in the structure (1.545 Å). Two other bonds [P(2)–O(4) and P(2)–O(5)] in the $P(2)O_3H^-$ monoprotonated phosphonate group are, on the average, 0.020 Å shorter than three bonds P(1)–O(1), P(1)–O(2), and P(1)–O(3) in the $P(1)O_3^{2-}$ group (1.509 and 1.529 Å, respectively). This difference is apparently due to the increased negative charge at the oxygen atoms in the PO_3^{2-} group as compared to the PO_3H^- group.

In addition to three short bonds, each tin atom has three contacts at much longer distances. All these contacts lie on the side opposite to the base of the pyramid. The Sn(1) atom approaches three oxygen atoms (the Sn··O contacts are 2.768, 2.911, and 3.008 Å),[1] and the Sn(2) atom approaches an oxygen atom (Sn··O,

[1] In addition, the Sn(1) atom has three even weaker Sn··O contacts (3.273, 3.560, and 3.580 Å).

2.967 Å) and two chlorine atoms (Sn··Cl, 3.315 and 3.431 Å). This "one-sided" (3 + 3) coordination is typical of bivalent tin [3, 4]. It is determined by the stereochemically active lone electron pair, which occupies the vacant (axial) position of the SnO_3 (SnO_2Cl) pyramid as viewed from the distant Sn··O (Sn··Cl) contacts. The coordination polyhedra of the Sn(1) and Sn(2) atoms in structure **I** can be described as either distorted tetrahedra with a lone electron pair in one of the vertices or (with allowance made for the additional contacts) severely distorted octahedra (3 + 3) in which the O(Cl)–Sn··O(Cl) angles between the atoms in the *trans* positions fall in the range 147.4°–162.7°.

The stronger additional Sn··O (Sn··Cl) contacts link the $[Sn_2(HL)Cl]_6$ molecules into a three-dimensional framework. The structure is stabilized by short intermolecular contacts involving crystallization water molecules (1*w* and 2*w*). The O(1*w*) atom, which occupies a special position on the fourfold axis, approaches four chlorine atoms [O(1*w*)··Cl, 3.093 Å]. The O(2*w*) atom approaches the phosphonate O(6) and alcohol O(7) atoms of the HL^{3-} ligand and two O(2*w*) atoms related to the reference atom by a threefold axis [O(2*w*)··O(6), 2.69; O(2*w*)··O(7), 2.70; and O(2*w*)··O(2*w*), 2.86 Å]. We believe that each of the O(1*w*) and O(2*w*) atoms is involved in two donor and two acceptor bonds. The crystallographic equivalence of all the four O(1*w*)··Cl bonds and two O(2*w*)··O(2*w*) bonds [and the disorder of the O(2*w*) atom (see above)] suggests a high probability of disordering of the hydrogen atoms of both water molecules.

REFERENCES

1. P. J. Zapf, D. J. Rose, R. C. Haushalter, and J. Zubieta, J. Solid State Chem. **125** (2), 182 (1996).
2. G. M. Sheldrick, *SHELXL93: Program for the Refinement of Crystal Structures* (Univ. of Göttingen, Göttingen, 1993).
3. Yu. N. Kokunov and I. É. Rakov, Zh. Neorg. Khim. **40** (4), 583 (1995).
4. J. Zubieta and J. J. Zucherman, Prog. Inorg. Chem. **24**, 251 (1978).

Translated by I. Polyakova

Crystallography Reports, Vol. 46, No. 2, 2001, pp. 210–213. Translated from Kristallografiya, Vol. 46, No. 2, 2001, pp. 250–253.

STRUCTURE OF ORGANIC COMPOUNDS

Crystal Structure of 2,5-Cyclohexadien-4-one-Spiro-3'-(2'-Methylthio-5',5'-Dimethyl-1'-Pyrroline)

V. I. Sokol*, V. S. Sergienko*, V. A. Glushkov, Yu. V. Shklyaev**, and V. V. Davydov*****

** Kurnakov Institute of General and Inorganic Chemistry, Russian Academy of Sciences, Leninskiĭ pr. 31, Moscow, 117907 Russia*

*** Institute of Technical Chemistry, Ural Division, Russian Academy of Sciences, ul. Lenina 13, Perm, 614600 Russia*

**** Russian University of Peoples' Friendship, ul. Miklukho-Maklaya 6, Moscow, 117198 Russia*

Received March 3, 1999; in final form, April 28, 1999

Abstract—The crystal structure of the pyrrole derivative 2,5-cyclohexadien-4-one-spiro-3'-(2'-methylthio-5',5'-dimethyl-1'-pyrroline) is determined by X-ray diffraction. Two independent molecules have similar structures and close geometric parameters but differ in configuration of the pyrrole ring and orientation of the thiomethyl group with respect to the pyrrole ring. *© 2001 MAIK "Nauka/Interperiodica".*

INTRODUCTION

Earlier [1], the reaction of aromatic compounds activated by two methoxy groups with oxiranes and nitriles, which led to the formation of substituted 6,7- (or 5,8-) dimethoxy-3,4-dihydroisoquinolines, was reported. A similar reaction between oxiranes and anisole unexpectedly resulted in the spirocyclohexadienone derivative of pyrroline 2,5-cyclohexadien-4-one-spiro-3'-(2'-methylthio-5',5'-dimethyl-1'-pyrroline) (**I**, see scheme) [2]

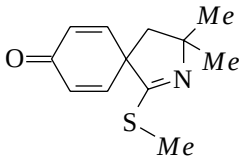

instead of the substituted 3,4-dihydroisoquinoline.

In this paper, we report the results of the X-ray diffraction study of compound **I**.

EXPERIMENTAL

Light brown prismatic crystals **I** ($C_{12}H_{15}NOS$) are monoclinic, a = 13.404(3) Å, b = 11.303(2) Å, c = 17.086(3) Å, β = 105.47(3)°, V = 2494.8(8) Å^3, ρ_{calcd} = 1.326 g cm^{-3}, $\mu(MoK_\alpha)$ = 2.64 cm^{-1}, M = 221.31, $F(000)$ = 1062, Z = 8, and space group $P2_1/a$.

A set of experimental intensities was collected from a faceted crystal 0.45 × 0.60 × 0.20 mm in size on an Enraf–Nonius CAD4 automated four-circle diffractometer (MoK_α radiation, graphite monochromator, $\theta/2\theta$ scan mode, $2\theta_{max}$ = 56°). A total of 7508 reflections were measured, of which 3933 had $I > 2\sigma(I)$.

The structure was solved by the direct method (SHELXS86 [3]) and refined by the least-squares procedure in the full-matrix anisotropic approximation with the SHELXL93 program package [4]. The hydrogen atoms were calculated geometrically (the C–H distances were 0.96 Å). Their coordinates were included in the refinement, and the isotropic thermal parameters were fixed (U_j = 0.08 Å^2). The refinement led to the following final parameters: R_1 = 0.0516, wR_2 = 0.1369, and $GOOF$ = 1.071 for 3933 observed reflections; R_1 = 0.0615 and wR_2 = 0.1531 for all 7508 reflections; the extinction coefficient was 0.0009(9); and the maximum and minimum residual electron densities were equal to 0.306 and –0.318 e Å^{-3}, respectively.

The atomic coordinates and equivalent isotropic thermal parameters U_{eq} are listed in Table 1.

RESULTS AND DISCUSSION

There are two independent molecules A and A' in the unit cell of crystal **I** (Fig. 1). Since the main geometric parameters of these molecules are very close, hereafter, we will give the mean values for the analogous bond lengths and angles.

The geometric parameters of the pyrroline ring in structure **I** are close to the corresponding values in the structure of 3,3,4,4-tetracyano-3,4-dihydro-5-isopropyl-2-(nitrophenyl)-1-pyrrole (**II**) [5]. In structure **I**, two endocyclic N–C bonds in the pyrrole ring significantly differ in length: N(1)–C(1) [1.264(3) Å] is considerably shorter (by Δ = 0.229 Å) than N(1)–C(9) [1.493(3) Å]. In structure **II**, one of the N–C bonds (1.265 Å) almost coincides in length with the N(1)–C(1) bond in **I**, whereas the other N–C bond (1.447 Å)

Table 1. Coordinates ($\times 10^4$) and equivalent thermal parameters U_{eq} ($\times 10^3$) of the non-hydrogen atoms in structure **I**

Atom	*x*	*y*	*z*	U_{eq}, Å^2	Atom	*x*	*y*	*z*	U_{eq}, Å^2
S(1)	4855(1)	1170(1)	3253(1)	59(1)	S(1')	7808(1)	1441(1)	1303(1)	75(1)
O(1)	3560(2)	–3228(2)	2916(1)	96(1)	O(1')	9394(3)	3067(3)	–1010(2)	132(1)
N(1)	6757(1)	1028(2)	4273(1)	48(1)	N(1')	6891(2)	3371(2)	1717(1)	57(1)
C(1)	5973(2)	479(2)	3850(1)	42(1)	C(1')	7417(2)	2928(2)	1279(1)	55(1)
C(2)	5994(2)	–899(2)	3873(1)	45(1)	C(2')	7734(2)	3768(2)	667(2)	61(1)
C(3)	5756(2)	–1421(2)	3036(2)	57(1)	C(3')	7248(2)	3390(2)	–184(2)	64(1)
C(4)	4988(2)	–2167(2)	2734(2)	61(1)	C(4')	7775(3)	3193(2)	–725(2)	71(1)
C(5)	4285(2)	–2552(2)	3201(2)	59(1)	C(5')	8901(3)	3283(3)	–514(2)	78(1)
C(6)	4488(2)	–2090(2)	4024(1)	53(1)	C(6')	9410(3)	3622(3)	309(2)	81(1)
C(7)	5256(2)	–1343(2)	4332(1)	47(1)	C(7')	8878(3)	3848(3)	846(2)	79(1)
C(8)	7141(2)	–1078(2)	4341(2)	61(1)	C(8')	7261(4)	4939(3)	886(2)	109(1)
C(9)	7549(2)	150(2)	4699(1)	51(1)	C(9')	6682(2)	4646(2)	1512(1)	57(1)
C(10)	8563(2)	446(3)	4516(2)	82(1)	C(10')	7068(3)	5384(3)	2268(2)	92(1)
C(11)	7652(3)	240(3)	5597(2)	84(1)	C(11')	5537(3)	4801(4)	1190(3)	114(1)
C(12)	5253(2)	2703(3)	3328(2)	79(1)	C(12')	7265(3)	859(3)	2067(2)	83(1)

is noticeably shorter than the N(1)–C(9) bond in **I**. As a consequence, the Δ value for structure **II** (0.182 Å) is substantially smaller than that for **I**. Nonetheless, the π electron density in the pyrrole rings of both **I** and **II** is localized at the N(1)–C(1) bond. Note that, in structures **I** and **II**, this bond is considerably shorter than the bonds observed earlier in other N heterocycles, specifically in 3,3-dimethyldihydroisoquinoline derivatives. Among the latter compounds, 3,3-dimethyl-6,7-dimethoxy-1-(4,4-dimethylcyclohexa-2,6-dion-1-yl)-3,4-dihydroisoquinoline [6] has the shortest N–C bond (1.277 Å). The N(1)–C(1) bonds in **I** and **II** are also shorter than the standard double N(sp^2)=C(sp^2) bond (1.273 Å [7]). The N(1)–C(9) distance in structure **I** agrees with the standard length of the single N(sp^2)–C(sp^3) bond (1.465–1.493 Å [7]). The lengths of all the three C–C bonds in the pyrrole ring in structure **I** are almost equal (1.518–1.559 Å). Their mean value (1.547 Å) slightly exceeds the standard length of the single C(sp^3)–C(sp^3) bond (1.535 Å [7]). In structure **II**, one of the C–C bonds lengthens to 1.622 Å and the mean length of the remaining two bonds is 1.575 Å. The endocyclic angles in the pyrrole ring of structure **I**

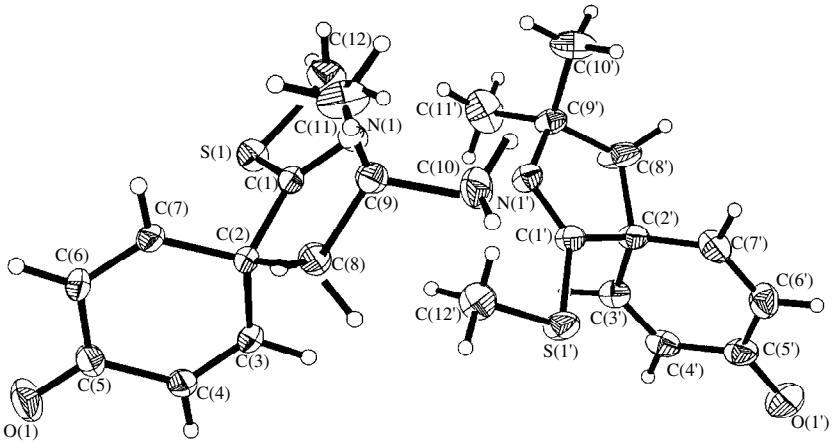

Fig. 1. Structures of two independent molecules in compound **I**.

Table 2. Selected torsion angles (deg) in structure **I**

Angle	Molecule *A*	Molecule *A*'
N(1)C(1)SC(12)	7.4	0.0
C(2)C(1)SC(12)	–179.5	–173.9
C(3)C(2)C(1)S	63.5	53.9
C(7)C(2)C(1)S	–61.4	–70.1

are also inequivalent. The angle at the C(1) atom, which is bonded to the sulfur atom, is markedly increased (up to 117.4°), and the angle at the C(2) spiro atom, on the contrary, is significantly decreased (to 99°) compared to the ideal angle in the five-membered ring (108.3°). The three remaining angles at the N(1), C(8), and C(9) atoms fall in the range 105.8°–110.2°; their mean value (107.5°) is close to the ideal angle. In the pyrrole ring of structure **II**, the angles at the C(1) and N(1) atoms (114° both) are significantly larger than the remaining three angles (the mean value is 102°).

The pyrrole rings in two independent molecules of structure **I** slightly differ in conformation and, hence, in endocyclic torsion angles (Fig. 2).

The pyrrole ring of molecule *A* has an envelope conformation: the C(8) atom deviates from the C(1)C(2)N(1)C(9) plane of four atoms, which are coplanar within 0.003 Å, by –0.231 Å. The pyrrole ring of molecule *A*' is virtually planar: the mean deviation of the five atoms from their plane is 0.020 Å. The largest deviation is observed for the C(8') atom (+0.031 Å). In structure **II**, the maximum deviations from the mean plane of the pyrrole ring are exhibited by the C(3) (–0.12 Å) and C(4) (+0.12 Å) atoms.

The thiomethyl group in molecule **I** is in the *cis* position with respect to the N(1)–C(1) bond, and the N(1)C(1)SC(12) torsion angle is close to 0° (Table 2). However, in molecule *A*, the S(1) and C(12) atoms deviate from the mean plane of the pyrrole ring by 0.132 and 0.431 Å, respectively. In molecule *A*', the S*Me* group lies in the plane of the pyrrole ring. Two S–C bonds differ in length. The S–C(1) bond with the pyrrole ring is 0.038 Å shorter than the S–C(12) bond with the methyl group [1.757(2) and 1.795(3) Å, respectively]. The angles at the sulfur atoms of the thiomethyl groups of two molecules are almost equal and are significantly smaller than 120° (the mean value is 101.2°).

The benzophenone ring has a quinoid structure: the C–C bonds in this ring are distinctly divided into three groups. The lengths of two short bonds are almost equal [C(3)–C(4), 1.324(3) Å and C(6)–C(7), 1.328(3) Å]. The two longest C–C bonds adjoin the C(2) spiro atom [C(2)–C(3), 1.495(4) Å and C(2)–C(7), 1.494(3) Å]. The C(4)–C(5) and C(5)–C(6) bonds at the carbonyl group are slightly shorter than the C(2)–C(3) and C(2)–C(7) bonds; their mean value is 1.453(4) Å. The endocyclic angles at the C(2) spiro atom (111.7°) and the C(5) atom of the carbonyl group (116.5°) are significantly smaller than the remaining four CCC angles (121.6°–124.6°, the mean value is 123.0°).

The oxygen atom of the carbonyl group lies in the plane of the quinone ring. The O(1)–C(5) distance [1.230(2) Å] agrees with the standard length of the O=C(sp^2) bond in benzoquinone (1.222–1.230 Å [7]).

The pyrrole and benzoquinone rings in both molecules are mutually almost perpendicular: the dihedral angle between their planes is 85°. The angle between the planes of the pyrrole rings in the neighboring molecules is 81°.

All the intermolecular distances in the structure agree with the normal van der Waals contacts. The shortest contact (2.60 Å) occurs between the O(1) (*x*, *y*, *z*) and H(8') (–0.5 – *x*, –0.5 – *y*, +*z*) atoms.

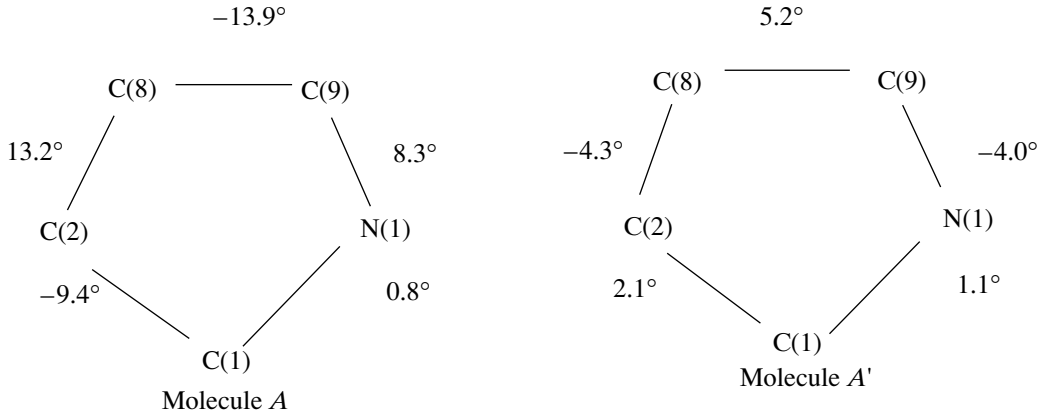

Fig. 2. Endocyclic torsion angles in the pyrrole rings of structure **I**.

ACKNOWLEDGMENTS

This work was supported by the Russian Foundation for Basic Research (project no. 98-03-32689a) and by the Ministry of Education of Russia and the Russian Academy of Sciences within the "Integration" Federal Special Purpose Program (project no. K0512).

REFERENCES

1. V. A. Glushkov and Yu. V. Shklyaev, Mendeleev Commun., No. 1, 17 (1998).
2. V. A. Glushkov, Yu. V. Shklyaev, V. I. Sokol, *et al.*, Mendeleev Commun., No. 6, 227 (1998).
3. G. M. Sheldrick, Acta Crystallogr., Sect. A: Found. Crystallogr. **46**, 467 (1990).
4. G. M. Sheldrick, *SHELXL93: Program for Refinement of Crystal Structures* (Univ. of Göttingen, Göttingen, 1993).
5. T. Ibata, Y. Isogami, H. Nakawa, *et al.*, Bull. Chem. Soc. Jpn. **65**, 1771 (1992).
6. V. V. Davydov, V. I. Sokol, E. V. Balebanova, *et al.*, Khim. Geterotsikl. Soedin., No. 7, 922 (1995).
7. F. H. Allen, O. Kennard, D. Watson, *et al.*, J. Chem. Soc., Perkin Trans. 2, Suppl. **11**, S1 (1987).

Translated by I. Polyakova

Crystallography Reports, Vol. 46, No. 2, 2001, pp. 214–218. Translated from Kristallografiya, Vol. 46, No. 2, 2001, pp. 254–258.

STRUCTURE OF ORGANIC COMPOUNDS

Molecular and Crystal Structures of 1*R*,4*R*-*cis*-2-(4-Phenylbenzylidene)-*n*-Menthan-3-one

A. S. Tolochko*, V. I. Kulishov*, L. A. Kutulya, V. P. Kuznetsov**, and V. V. Vashchenko****

** Institute of Physics, National Academy of Sciences of Ukraine, pr. Nauki 144, Kiev, 258650 Ukraine*

*** Institute of Single Crystals, National Academy of Sciences of Ukraine, pr. Lenina 60, Kharkov, 310141 Ukraine*

e-mail: tolochko@iop.kiev.ua

Received June 23, 1999; in final form, March 15, 2000

Abstract—The molecular and crystal structures of chiral 1*R*,4*R*-*cis*-2-(4-phenylbenzylidene)-*n*-menthan-3-one (**I**) have been determined by X-ray diffraction analysis. Crystals **I** are monoclinic, $a = 6.755(3)$ Å, $b = 9.860(3)$ Å, $c = 14.103(6)$ Å, $\beta = 98.95(1)°$, space group $P2_1$, $Z = 2$, and $R = 0.035$ for 1031 reflections. A chair conformation of the cyclohexanone ring in the molecule is substantially distorted toward a "half-chair" conformation. The enone and benzylidene groupings are virtually planar (the torsion angles are equal to 13.0° and 4.9°, respectively). The benzene rings of the biphenyl fragment are rotated with respect to each other through an angle of 40°–43°. Among the compounds under consideration, the distortion of bond angles at the sp^2 carbon atoms of the benzylidene grouping as a criterion for the steric stress of molecules is maximum in structure **I**. © *2001 MAIK "Nauka/Interperiodica"*.

INTRODUCTION

As a continuation of systematic investigations into the structure of chiral α,β-unsaturated ketones—derivatives of diastereomeric *n*-menthan-3-ones [1–6], in the present work, we applied X-ray structure analysis to determine the molecular and crystal structures of 1*R*,4*R*-*cis*-2-(4-phenylbenzylidene)-*n*-menthan-3-one (**I**)

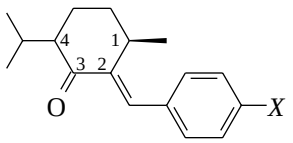

1*R*,4*R*-*cis* diastereomers: $X = C_6H_5$ (**I**), $N(CH_3)_2$ (**II**) [5], NO_2 (**III**) [5];
1*R*,4*S*-*trans* diastereomer: $X = C_6H_5$ (**IV**) [3],

which is an efficient chiral dopant for liquid-crystal materials with an induced helical supramolecular structure [7, 8].

The main purposes of our investigation were as follows:

(i) to perform a comparative analysis of specific features in the conformation of the cyclohexanone ring and the geometry of the enone and arylidene fragments in compound **I** and the earlier studied structures **II** (with a strong electron-donor substituent *X* in the arylidene grouping) and **III** (with a strong electron-acceptor substituent *X*) of the same 1*R*,4*R*-*cis* diastereomeric series [5];

(ii) to elucidate how different stereochemical configurations of molecules **I** (1*R*,4*R*-*cis* diastereomer) and **IV** (1*R*,4*S*-*trans* diastereomer) [3] affect their molecular structures.

In the general case, the X-ray diffraction data on certain structural features of molecules containing π-conjugated fragments reflect the effect of intramolecular (electronic and steric) factors and intermolecular interactions in crystals. In this respect, we carried out a comparative analysis of the X-ray diffraction data obtained and the results of molecular mechanics (MM) calculations [9]. The cyclohexanone ring in its different conformations in the studied compounds was characterized by the Zefirov–Palyulin method of puckering parameters [10, 11].

RESULTS AND DISCUSSION

The figure displays the molecular structure of compound **I** (with atomic numbering), which was determined from the X-ray diffraction data.

Similar to the earlier studied structures **II** and **III**, compound **I** is characterized by the *cis* orientation of the alkyl groups at the C(1) and C(4) chiral centers with respect to the cyclohexanone ring: the deviations of the C(7) and C(8) atoms from the calculated root-mean-square (rms) planes passing through pairs of the C(1)–C(2) and C(4)–C(5) (P_1) [C(1)–C(6) and C(3)–C(4) (P_2)] opposite bonds in the cyclohexanone ring are equal to 1.323 and 0.707 Å (1.487 and 0.804 Å),

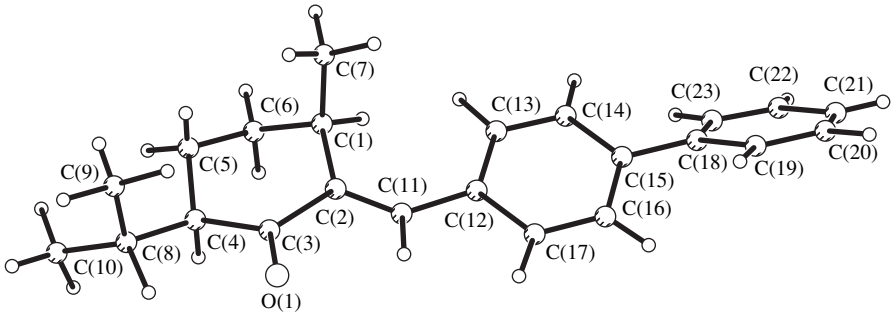

Molecular structure of compound **I** and the atomic numbering.

respectively. These deviations indicate that the methyl group has an axial orientation and the isopropyl group exhibits an equatorial orientation (see also the φ_1–φ_4 torsion angles in Table 1). Note that compounds **I**–**III** were prepared according to the same procedure from enantiomerically pure chiral synthon [(–)-menthone] [5, 12] with the known *R* configuration of the C(1) chiral center distant from the carbonyl group (see, for example, [13]), which underwent no changes in the course of the chemical reactions involved.[1] Therefore, compound **I**, like compounds **II**, **III**, and some related α,β-unsaturated ketones [1], should be assigned to the 1*R*,4*R*-*cis* diastereomers.

A chair conformation of the cyclohexanone ring (see the φ_5–φ_{10} torsion angles in Table 1) in crystal **I** is considerably distorted compared to that in structure **III**. In the cyclohexanone ring of **I**, pairs of the opposite bonds C(1)–C(2) and C(4)–C(5), C(1)–C(6) and C(3)–C(4), and C(2)–C(3) and C(5)–C(6) deviate from a planar geometry by 0.04, 0.08, and 0.13 Å, respectively (cf. 0.004, 0.04, and 0.05 Å in **III** [5]). A substantial decrease in the φ_5, φ_6, and φ_{10} torsion angles in comparison with those in structure **III** and a tendency toward flattening of the C(1)C(2)C(3)C(4) fragment (these atoms are coplanar to within 0.07 Å) allow one to judge qualitatively the distortion of a chair conformation of the cyclohexanone ring in molecule **I** toward a "half-chair" conformation. This is also supported by the puckering parameters calculated from the endocyclic torsion angles φ_5–φ_{10} (the X-ray diffraction data). Specifically, the polar angle θ is close to the phase angle ψ, and the puckering amplitude *S* is decreased (Table 1). The distortion of a chair conformation of the cyclohexanone ring in compound **I** is similar to that observed in structures of 2-benzylidenecyclohexanone and its derivatives with a strong electron-donor dimethylamino substituent in the arylidene grouping [14].

An unexpected feature of the molecular structure in crystal **I** is the substantial flattening of the enone (φ_{11} = 13.0°) and arylidene (φ_{12} = 4.9°) fragments as compared to **III** and some compounds of the 1*R*,4*R*-*cis* series [1, 2, 4]. A considerable flattening of the cinnamoyl fragment in structures of α,β-unsaturated ketones is usually observed upon the introduction of strong electron-donor substituents (for example, the $N(CH_3)_2$ group) into the benzene ring [5, 14]. However, a substantial enhancement of the conjugation in the cinnamoyl fragment of molecule **I** in comparison with **II** is excluded, especially as two benzene rings in the biphenylyl grouping of structure **I** are acoplanar (see the torsion angles φ_{13} and φ_{14}). It is of interest that, although the biphenylyl fragment in crystals of the diastereomeric compound **IV** is considerably flattened, the torsion angles in the enone and arylidene groupings are equal to 30.6° and –32.6°, respectively (Table 1). Therefore, the substantial flattening observed in the cinnamoyl fragment of structure **I**, which is even more considerable than that in compound **II** with a strong electron-donor dimethylamino group (see Table 1), cannot be associated with intramolecular electronic factors. It is also important that the molecular mechanics calculations for compound **I** demonstrate neither such a strong distortion of the conformation of the cyclohexanone ring, as occurs in the crystal according to the X-ray diffraction data, nor a considerable flattening of the enone and arylidene groupings (Table 1). The fact that the results of these calculations quite reliably reflect the geometry of isolated molecules of the compounds under consideration follows, for example, from the conformation investigation of 2-benzyl substituted isomeric *n*-menthen-3-ones by the molecular mechanics method in a combination with the ^{1}H NMR study in solutions [15]. It is evident that the aforementioned structural features revealed from the X-ray diffraction data for molecule **I** reflect the effect of intermolecular interactions in the crystal. Apparently, the same is also true for different degrees of planarity of the biphenylyl fragment in the diastereomeric structures **I** and **IV**.

It is worth noting that the difference in the configurations of the C(4) chiral center in the diastereomeric structures **I** and **IV** is responsible not only for different orientations of the alkyl substitutions with respect to the cyclohexanone ring but also for the substantial difference in its conformations in the crystal (Table 1).

[1] This fact served as a basis for the choice of the absolute molecular configuration in analysis of the experimental data.

Table 1. Selected torsion angles (φ_i, deg) and puckering parameters in compounds **I**–**IV** according to the data of X-ray structure analysis and molecular mechanics calculations

Parameter	Compound				
	I		**II**	**III**	**IV**
	X-ray structural data	MM calculations	X-ray structural data [5]	X-ray structural data [5]	X-ray structural data [3]
Torsion angles, φ_i					
φ_1, C(7)C(1)C(2)C(3)	92.5(3)	71.6	87.9(5)	75.6(4)	118.4(2)
φ_2, C(7)C(1)C(6)C(5)	–70.0(3)	–68.0	–68.2(5)	–67.1(4)	–167.2(2)
φ_3, C(8)C(4)C(3)C(2)	–159.4(3)	–176.9	–156.8(4)	–173.7(3)	119.8(2)
φ_4, C(8)C(4)C(5)C(6)	177.1(2)	177.7	174.0(4)	179.8(2)	–166.5(2)
φ_5, C(1)C(2)C(3)C(4)	20.8(4)	52.3	21.6(6)	43.2(4)	33.2(3)
φ_6, C(3)C(3)C(4)C(5)	–27.2(4)	–48.7	–23.1(6)	–42.2(4)	–9.2(3)
φ_7, C(3)C(4)C(5)C(6)	46.2(3)	49.5	42.1(6)	49.0(3)	–39.8(2)
φ_8, C(4)C(5)C(6)C(1)	–61.1(3)	–56.2	–60.5(6)	–58.2(4)	69.6(2)
φ_9, C(5)C(6)C(1)C(2)	53.4(3)	54.3	56.7(5)	55.6(4)	–44.9(2)
φ_{10}, C(6)C(1)C(2)C(3)	–32.7(4)	–51.5	–37.5(5)	–47.2(3)	–4.7(3)
φ_{11}, C(1)C(3)C(2)C(11)	13.0(4)	55.8	20.2(7)	42.0(5)	30.6(3)
φ_{12}, C(2)C(11)C(12)C(13)	4.9(5)	51.2	23.2(8)	42.4(5)	–32.6(4)
φ_{13}, C(14)C(15)C(18)C(19)	–40.2(4)	–40.2	–	–	2.9(4)
φ_{14}, C(16)C(15)C(18)C(23)	–43.0(4)	–39.7	–	–	4.8(4)
Puckering parameters					
θ, deg	19.00	2.1	19.59	6.32	63.92
ψ, deg	19.66	19.4	6.53	5.95	26.87
S	0.88	1.08	0.89	1.03	0.82

A common feature of all the earlier studied structures of 2-arylidene derivatives of cyclohexanone [14] and chiral *n*-menthan-3-one with different configurations of the C(4) atom [1–5] is the considerable distortion of the bond angles at the sp^2 carbon atoms in the C(1)H*R*C(2)=C(11)HC$_6$H$_4$*X* fragment: the bond angles C(1)C(2)C(11) [ω_α = 126.1(2)°], C(2)C(11)C(12) [ω_β = 134.1(3)°], and C(11)C(12)C(*ortho*) [ω_γ = 127.3(2)°] are appreciably more than 120°. In the earlier studied compounds, the strongest distortion of these angles was observed in structure **IV**: the ω_α, ω_β, and ω_γ angles are equal to 126.2(2)°, 132.3(2)°, and 125.1(2)°, respectively [3]. It is seen that this effect in structure **I** is even more pronounced. This is consistent with the tendency noted in [5] that a decrease in the torsion angle in the arylidene grouping, i.e., its flattening, is accompanied by an increase in the bond angles ω_β and ω_γ in the structures of α,β-unsaturated ketones—the derivatives of cyclohexanone and *n*-menthan-3-one. Among the compounds under consideration, the minimum torsion angle φ_{12} and the maximum bond angle ω_β were found in structure **I**. These values confirm the conclusion made in [5, 14] that the distortion observed for the above bond angles is caused by the steric effects between the *ortho* hydrogen and carbon atoms of the aryl group and the atoms of the >C(1)H*R* (*R* = H or CH$_3$) cyclic fragment (see the shortened intramolecular contacts in Table 2). Undoubtedly, these effects in the

Table 2. Shortened intramolecular contacts (*d*, Å)* in structures **I**–**IV**

Contact	Structure			
	I	**II**	**III**	**IV**
H(1)···H(13)	1.93	2.13	2.28	2.16
H(1)···C(13)	2.65	2.64	2.68	2.84
H(13)···C(1)	2.66	2.68	2.83	2.84
C(1)···C(13)	3.28	3.35	3.32	3.32
H(1)···C(11)	2.68	2.62	2.66	2.76
H(13)···C(7)	2.90	2.78	2.97	–
C(11)···C(7)	3.26	3.41	3.51	3.14
H(11)···O(1)	2.33	2.38	2.52	–
H(11)···H(17)	2.10	2.23	2.54	–
H(17)···C(11)	2.46	2.55	2.66	2.83

* The sums of the van der Waals radii are as follows [16]: H···H 2.32, H···C 2.87, H···O 2.45, and C···C 3.42 Å.

studied structures are enhanced with a flattening of the cinnamoyl fragment, specifically of the arylidene grouping.

The strongly shortened contact H(1)··H(13) (1.93 Å) is close to a similar contact (1.90 Å) in 2-benzylidene-6-benzylcyclohexanone [14], whose benzylidene grouping in the crystal is also substantially flattened (the torsion angle is 10.4°).

A comparison of the data presented in Table 2 shows that the steric stress of molecule **I** is considerably more than those of the diastereomeric molecule **IV** and molecules of ketones **II** and **III** in the same 1*R*,4*R*-*cis* series. It is evident that, in structures **II**–**IV**, the unfavorable nonbonded interactions in the aforementioned molecular fragment are at least partly eliminated at the expense of an increase in the φ_{11} and φ_{12} torsion angles.

It should be noted that a substantial flattening of the arylidene grouping in molecule **I** (as in **II**) is responsible for considerably shortened contacts between the *ortho* hydrogen atom H(17) and atoms [C(11) and H(11)] of the =CH– group (Table 2). A substantially flattened conformation of the O=C–CH= enone grouping in molecules **I** and **II** is likely stabilized, to a certain degree, by attractive interactions between the O(1) oxygen and H(11) hydrogen atoms of the ethylene group [see the shortened contacts H(11)··O(1)]. Similar shortened contacts are absent in the diastereomeric structure **IV** and nitro-substituted compound **III** with the aplanar enone fragment.

As in **II** [5] and certain derivatives of 2-benzylidenecyclohexanone [14] with the flattened arylidene grouping, the C(12)··C(17) benzene ring in structure **I** is arranged in such a way that the *ortho* hydrogen atom H(13) is located between the H(1) atom and atoms of the axial methyl group. The deviations of the H(1), C(7), H(7*A*), H(7*B*), and H(7*C*) atoms from the rms plane of the benzene ring are equal to –0.49, 1.42, 2.04, 1.91, and 1.49 Å, respectively.

The conformation of the isopropyl fragment in crystal **I** is virtually identical to that in structures **II** and **III** [5]: the H(4)–C(4) and H(8)–C(8) bonds exhibit a *gauche* orientation [the torsion angle is equal to 66.3(4)°], one methyl group is in the *trans* position to the C(4)–H(4) bond [the torsion angle is 178.7(3)°], and the other methyl group is in the *gauche* position to this bond [the torsion angle is –54.9(4)°].

A substantial flattening of the conjugated cinnamoyl grouping O=C–C=C–C_6H_4– is inconsistent with the concept of intramolecular electronic effects and can be explained by the intermolecular interaction between these highly polarizable π electron fragments in the crystal. The molecular packing contains stacks formed by the cinnamoyl groupings.

EXPERIMENTAL

Compound **I** was synthesized according to the procedure described in [17]. Single crystals suitable for X-ray diffraction analysis were grown from acetonitrile. Crystals **I** were obtained in the form of colorless plates. A single crystal $0.01 \times 0.4 \times 0.4$ mm in size was chosen for X-ray structure analysis. The crystals are monoclinic, a = 6.755(3) Å, b = 9.860(3) Å, c = 14.103(6) Å, β = 98.95(1)°, V = 927(6) Å^3, M = 318.4 ($C_{23}H_{26}O$), space group $P2_1$, Z = 2, d_{calcd} = 1.140 g/cm^3, and μ(MoK_α) = 0.068 mm^{-1}.

X-ray diffraction analysis was carried out on a Siemens P3/PC automated diffractometer (MoK_α radiation, graphite monochromator, θ/2θ scan mode, $2\theta_{max}$ = 45°). The intensities of 1031 independent reflections with $I > 3\sigma$ were measured. The structure was solved by the direct method. The hydrogen atoms were located from successive electron-density difference syntheses and refined in a rider model with the fixed thermal parameters u_{iso} = 0.08 Å^2. The structure was refined by the full-matrix least-squares procedure in the anisotropic approximation up to R = 0.035, R_w = 0.034, and S = 1.57. The calculations were performed using the SHELXTL PLUS/PC software package [18]. The coordinates of non-hydrogen atoms are listed in Table 3.

Table 3. Coordinates of non-hydrogen atoms (×10^4) and equivalent isotropic thermal parameters B_{eq} (Å^2) for structure **I**

Atom	x	y	z	B_{eq}
O(1)	13494(3)	4863(2)	13511(2)	8.4(1)
C(1)	13603(3)	1743	12088(2)	6.1(1)
C(2)	12959(3)	3156(3)	12324(2)	5.2(1)
C(3)	14190(3)	3884(3)	13155(2)	5.9(1)
C(4)	16333(3)	3444(3)	13502(2)	6.1(1)
C(5)	16722(3)	1956(3)	13309(2)	7.5(1)
C(6)	15852(4)	1564(3)	12299(3)	7.6(1)
C(7)	12510(4)	722(3)	12613(3)	8.7(1)
C(8)	17086(4)	3915(3)	14539(2)	7.4(1)
C(9)	16041(4)	3156(3)	15261(3)	10.2(1)
C(10)	19336(4)	3835(4)	14791(3)	11.2(1)
C(11)	11318(3)	3799(3)	11904(2)	5.7(1)
C(12)	9715(3)	3468(3)	11106(2)	5.1(1)
C(13)	9449(3)	2253(3)	10595(2)	5.6(1)
C(14)	7850(3)	2057(3)	9875(2)	5.1(1)
C(15)	6407(3)	3045(3)	9636(2)	4.8(1)
C(16)	6650(3)	4250(3)	10150(2)	5.9(1)
C(17)	8252(3)	4462(3)	10852(2)	5.8(1)
C(18)	4653(3)	2840(3)	8876(2)	5.0(1)
C(19)	2756(3)	3292(3)	9000(2)	6.0(1)
C(20)	1141(4)	3118(3)	8293(3)	7.3(1)
C(21)	1369(4)	2548(3)	7435(3)	7.8(1)
C(22)	3231(4)	2085(3)	7292(2)	7.6(1)
C(23)	4850(3)	2238(3)	8010(2)	6.0(1)

ACKNOWLEDGMENTS

This work was supported by the International Association of Assistance for the promotion of cooperation with scientists from the New Independent States of the former Soviet Union, project no. INTAS-1997-1730.

REFERENCES

1. V. I. Kulishov, L. A. Kutulya, V. E. Kuz'min, *et al.*, Zh. Obshch. Khim. **61** (1), 155 (1991).
2. L. A. Kutulya, V. P. Kuznetsov, E. E. Lakin, *et al.*, Kristallografiya **38** (5), 86 (1993) [Crystallogr. Rep. **38**, 630 (1993)].
3. L. A. Kutulya, V. P. Kuznetsov, L. D. Patsenker, *et al.*, Kristallografiya **39** (5), 860 (1994) [Crystallogr. Rep. **39**, 782 (1994)].
4. L. A. Kutulya, V. V. Vashchenko, V. P. Kuznetsov, *et al.*, Kristallografiya **40** (6), 1015 (1995) [Crystallogr. Rep. **40**, 941 (1995)].
5. L. A. Kutulya, V. P. Kuznetsov, V. I. Kulishov, *et al.*, Kristallografiya **44** (3), 475 (1999) [Crystallogr. Rep. **44**, 435 (1999)].
6. L. A. Kutulya, V. V. Vashchenko, V. P. Kuznetsov, and E. E. Lakin, Zh. Strukt. Khim. **35** (5), 133 (1994).
7. L. A. Kutulya, I. B. Nemchenok, and T. V. Khandrimaĭlova, Kristallografiya **35** (5), 1234 (1990) [Sov. Phys. Crystallogr. **35**, 724 (1990)].
8. L. A. Kutulya, I. B. Nemchenok, and S. S. Oleĭnik, Kristallografiya **35** (5), 1242 (1990) [Sov. Phys. Crystallogr. **35**, 729 (1990)].
9. U. Burkert and N. Allinger, *Molecular Mechanics* (American Chemical Society, Washington, 1982; Mir, Moscow, 1986).
10. N. S. Zefirov and V. A. Palyulin, Dokl. Akad. Nauk SSSR **252** (1), 111 (1980).
11. N. S. Zefirov, V. A. Palyulin, and E. E. Dashevskaya, J. Phys. Org. Chem. **3**, 147 (1990).
12. L. A. Kutulya, Doctoral Dissertation in Chemistry (Kharkov, 1992).
13. J. D. Morrison, A. Tomash, and R. A. Rigdway, Tetrahedron Lett., No. 7, 565 (1969).
14. V. P. Kuznetsov, V. I. Kulishov, L. A. Kutulya, *et al.*, Kristallografiya **44** (2), 229 (1999) [Crystallogr. Rep. **44**, 196 (1999)].
15. V. V. Vashchenko, N. S. Pivnenko, L. A. Kutulya, *et al.*, Izv. Akad. Nauk, Ser. Khim., No. 7, 1221 (2000).
16. Yu. V. Zefirov and P. M. Zorky, Usp. Khim. **58**, 713 (1989).
17. L. A. Kutulya, N. F. Krivosheeva, V. V. Vashchenko, *et al.*, USSR Inventor's Certificate No. 1 617 881, Byull. Izobret., No. 4 (1993).
18. G. M. Sheldrick, *SHELXTL PLUS, PC Version: A System of Computer Programs for the Determination of Crystal Structure from X-ray Diffraction Data. Rev. 4.2*, 1992.

Translated by O. Borovik-Romanova

Crystallography Reports, Vol. 46, No. 2, 2001, pp. 219–224. Translated from Kristallografiya, Vol. 46, No. 2, 2001, pp. 259–264.

STRUCTURE OF ORGANIC COMPOUNDS

Crystal Structure of Radical Cation Salt $(BEDT\text{-}TTF)_4(GaCl_4)_2 \cdot C_6H_5CH_3$

L. V. Zorina*, S. S. Khasanov*, B. Zh. Narymbetov*, R. P. Shibaeva*, A. I. Kotov, and É. B. Yagubskiĭ****

** Institute of Solid-State Physics, Russian Academy of Sciences, Chernogolovka, Noginskiĭ raĭon, Moscow oblast, 142432 Russia*

*** Institute for Problems of Chemical Physics, Russian Academy of Sciences, Noginskiĭ raĭon, Chernogolovka, Moscow oblast, 142432 Russia*

e-mail: zorina@issp.ac.ru

Received March 23, 1999

Abstract—A new radical cation salt based on bis(ethylenedithio)tetrathiafulvalene (*BEDT-TTF*) with the tetrahedral anion $GaCl_4^-$, namely, $(BEDT\text{-}TTF)_4(GaCl_4)_2 \cdot C_6H_5CH_3$, has been synthesized. The crystal structure of this salt is determined by X-ray diffraction analysis [a = 31.757(2) Å, b = 6.8063(3) Å, c = 34.879(2) Å, β = 90.453(4)°, V = 7538.8(7) Å^3, space group $I2/c$, and Z = 4]. In the structure, the radical cation layers alternate with the anion layers along the c-axis. The anion layers consist of the $GaCl_4^-$ tetrahedra and solvent molecules. The packing of *BEDT-TTF* molecules in the radical cation layer differs from that in the structure of the known salt $(BEDT\text{-}TTF)_2GaCl_4$, even though both compounds exhibit semiconductor properties. © *2001 MAIK "Nauka/Interperiodica".*

INTRODUCTION

Radical cation salts based on bis(ethylenedithio)tetrathiafulvalene (*BEDT-TTF*) and its analogues have been extensively studied in recent years. These compounds are of considerable interest owing to their electrical and magnetic properties. The majority of these salts exhibit the properties of quasi-two-dimensional organic metals down to the lowest temperatures, and certain of these compounds transform into a superconducting state at temperatures ranging from 1.15 to 12.8 K [1, 2].

The anionic components in the *BEDT-TTF* salts can vary over a wide composition range. This provides a way of preparing crystals with different packings of the radical cation layer whose nature determines the crystal properties. Furthermore, it is possible to change the structure of a conducting layer in compounds with the same anion by varying the conditions of crystal preparation, which can result in the formation of different polymorphic modifications and (or) incorporation of any third neutral component, for example, solvent molecules.

In the present work, we investigated the crystal structure of the *BEDT-TTF* radical cation salt with the $GaCl_4^-$ tetrahedral anion by X-ray diffraction. In 1991, Kurmoo *et al.* [3] obtained the first radical cation salt based on *BEDT-TTF* and the $GaCl_4^-$ anion with the semiconductor properties. However, more recently, Montgomery *et al.* [4] and Kobayashi *et al.* [5] synthesized the radical cation salt based on bis(ethylenedithio)tetraselenafulvalene (*BEDT-TSF*) with the same anion, which has a different structure and can exist in two crystalline modifications: κ-$(BETS)_2GaCl_4$ (organic metal stable at temperatures below 2 K) and λ-$(BETS)_2GaCl_4$ (superconductor with T_c = 8 K) [4, 5]. In this respect, we once again synthesized the *BEDT-TTF* radical cation salt with the same anion in order to obtain its other crystalline modification with different properties. The preliminary X-ray structure investigation demonstrated that crystals of the newly synthesized salt differ in parameters from the crystals prepared earlier in [3]. Moreover, a detailed X-ray diffraction analysis revealed that the crystals contain molecules of the $C_6H_5CH_3$ toluene solvent.

EXPERIMENTAL

Crystals of $(BEDT\text{-}TTF)_4(GaCl_4)_2 \cdot C_6H_5CH_3$ were obtained by the electrochemical oxidation on a Pt electrode. A solution of *BEDT-TTF* (Aldrich, 1.5×10^{-3} mol/l) and an $(Et)_4NGaCl_4$ electrolyte (9×10^{-3} mol/l) in a benzonitrile–toluene (1 : 1) mixture was placed in a *U*-shaped electrochemical cell and was left to stand for two weeks under a direct current ($i \sim 1$ μA/cm^2). The $(Et)_4NGaCl_4$ electrolyte was synthesized in the following way. Metallic Ga was dissolved in a concentrated HCl acid upon heating. After the complete dissolution of Ga, the solution was evaporated with water bath with the aim of removing an excess acid. The calculated

Table 1. Atomic coordinates and isotropic equivalent thermal parameters U_{eq} (Å^2)

Atom	*x*/*a*	*y*/*b*	*z*/*c*	U_{eq}	Atom	*x*/*a*	*y*/*b*	*z*/*c*	U_{eq}
S(1)	0.17545(4)	0.7663(2)	0.77932(3)	0.0647(3)	S(12)	0.42106(4)	0.6582(2)	0.27636(3)	0.0754(3)
S(2)	0.18946(4)	1.1805(2)	0.76116(3)	0.0668(3)	S(13)	0.48345(6)	–0.0373(2)	0.14313(4)	0.1082(6)
S(3)	0.21051(4)	0.6448(2)	0.69589(3)	0.0661(3)	S(14)	0.49887(5)	0.4573(2)	0.11959(4)	0.0918(4)
S(4)	0.22959(4)	1.0570(2)	0.68012(3)	0.0632(3)	S(15)	0.37421(4)	0.3147(2)	0.37178(3)	0.0728(3)
S(5)	0.13722(4)	0.8377(2)	0.85465(3)	0.0729(3)	S(16)	0.38075(5)	0.8081(2)	0.34539(4)	0.0963(5)
S(6)	0.15175(5)	1.3333(2)	0.83143(4)	0.0954(5)	C(11)	0.4463(1)	0.3613(7)	0.2291(1)	0.065(1)
S(7)	0.23819(5)	0.4963(2)	0.62143(4)	0.0808(4)	C(12)	0.4282(1)	0.4147(7)	0.2629(1)	0.064(1)
S(8)	0.25968(4)	0.9887(2)	0.60142(3)	0.0760(3)	C(13)	0.4732(1)	0.1699(7)	0.1708(1)	0.071(1)
C(1)	0.1935(1)	0.9376(6)	0.7465(1)	0.056(1)	C(14)	0.4789(1)	0.3581(7)	0.1618(1)	0.069(1)
C(2)	0.2097(1)	0.8860(2)	0.7118(1)	0.054(1)	C(15)	0.3929(1)	0.4116(9)	0.3292(1)	0.061(1)
C(3)	0.1587(1)	0.9378(2)	0.8132(1)	0.058(1)	C(16)	0.3966(1)	0.6032(7)	0.3196(1)	0.064(1)
C(4)	0.1647(1)	1.1282(7)	0.8044(1)	0.062(1)	C(17)	0.5184(2)	0.0643(10)	0.1090(2)	0.089(2)
C(5)	0.2331(1)	0.6978(2)	0.6515(1)	0.059(1)	C(18)	0.5016(2)	0.2429(10)	0.0896(2)	0.092(2)
C(6)	0.2412(1)	0.8857(7)	0.6440(1)	0.059(1)	C(19)	0.3811(2)	0.5267(9)	0.4024(2)	0.090(2)
C(7*a*)*	0.1191(4)	1.053(4)	0.8810(6)	0.074(4)	C(20)	0.3599(2)	0.7050(9)	0.3882(2)	0.097(2)
C(8*a*)*	0.1491(4)	1.226(2)	0.8782(3)	0.070(3)	Ga	0.35175(2)	0.97312(8)	0.50537(1)	0.0687(1)
C(7*b*)*	0.1409(6)	1.044(4)	0.8853(6)	0.088(6)	Cl(1)	0.39303(5)	1.0724(2)	0.46005(4)	0.1008(5)
C(8*b*)*	0.1238(5)	1.236(3)	0.8691(4)	0.094(4)	Cl(2)	0.31108(5)	1.2107(2)	0.52247(4)	0.1069(5)
C(9*a*)*	0.2565(3)	0.607(2)	0.5768(3)	0.076(3)	Cl(3)	0.38796(5)	0.8792(3)	0.55493(4)	0.1070(5)
C(10*a*)*	0.2399(3)	0.812(2)	0.5680(3)	0.075(3)	Cl(4)	0.31466(5)	0.7314(2)	0.48343(5)	0.1119(5)
C(9*b*)*	0.2321(7)	0.606(4)	0.5766(7)	0.071(7)	C(21)	0.4736(4)	0.361(2)	–0.0113(3)	0.222(8)
C(10*b*)*	0.2640(9)	0.769(5)	0.5722(8)	0.094(8)	C(22)	0.4547(4)	0.505(2)	0.0055(3)	0.231(7)
S(9)	0.45190(5)	0.1182(2)	0.21568(3)	0.0846(4)	C(23)	0.4841(6)	0.651(2)	0.0187(2)	0.201(6)
S(10)	0.46592(4)	0.5316(2)	0.19682(3)	0.0740(3)	C(24)*	0.4662(7)	0.762(3)	0.0327(5)	0.207(12)
S(11)	0.41229(4)	0.2417(2)	0.29632(3)	0.0707(3)					

* Site occupancies are equal to 0.52 for the C(7*a*) and C(8*a*) atoms, 0.48 for the C(7*b*) and C(8*b*) atoms, 0.72 for the C(9*a*) and C(10*a*) atoms, 0.28 for the C(9*b*) and C(10*b*) atoms, and 0.50 for the C(24) atom.

amount of $(Et)_4NCl$ was added to the cooled solution. The $(Et)_4NGaCl_4$ white crystalline powder precipitated was filtered off, washed with small portions of cooled water and alcohol, and then was recrystallized from absolute alcohol.

The main crystal data are as follows: $a = 31.757(2)$ Å, $b = 6.8063(3)$ Å, $c = 34.879(2)$ Å, $\beta = 90.453(4)°$, $V = 7538.8(7)$ Å^3, space group $I2/c$, $Z = 4$, formula $C_{47}H_{40}Cl_8Ga_2S_{32}$, $F(000) = 4128$, $M = 2053.8$, $d_{calcd} = 1.81$ g/cm^3, and $\mu(MoK_\alpha) = 19.21$ cm^{-1}. The intensities of 5255 reflections from a single crystal $0.18 \times 0.07 \times 0.36$ mm^3 in size were measured on an Enraf–Nonius CAD4 automated diffractometer [MoK_α radiation, graphite monochromator, ω scan mode, $(\sin\theta/\lambda)_{max} = 0.595$ Å^{-1}]. After the averaging of equivalent reflections, the final data set included 3656 independent reflections with $I > 2\sigma(I)$ ($R_{av} = 0.010$). The structure was solved by the direct method according to the AREN software package [6] and then was refined by the least-squares procedure in the anisotropic (for the non-hydrogen atoms) approximation using the SHELXL93 software package [7] up to $R = 0.031$. The set of reflections corrected for absorption according to the DIFABS program of the AREN software package was used in the refinement. The hydrogen atoms in the *BEDT-TTF* **II** molecule were located from the difference Fourier synthesis and refined in the isotropic approximation. The coordinates of the hydrogen atoms in the *BEDT-TTF* **I** and toluene molecules were determined geometrically and used in further calculations without refinement. The final coordinates of the non-hydrogen atoms and their thermal parameters are presented Table 1.

RESULTS AND DISCUSSION

Figure 1 shows the projection of the $(BEDT\text{-}TTF)_4(GaCl_4)_2 \cdot C_6H_5CH_3$ structure onto the *ac* plane. The structure consists of the *BEDT-TTF* radical cation

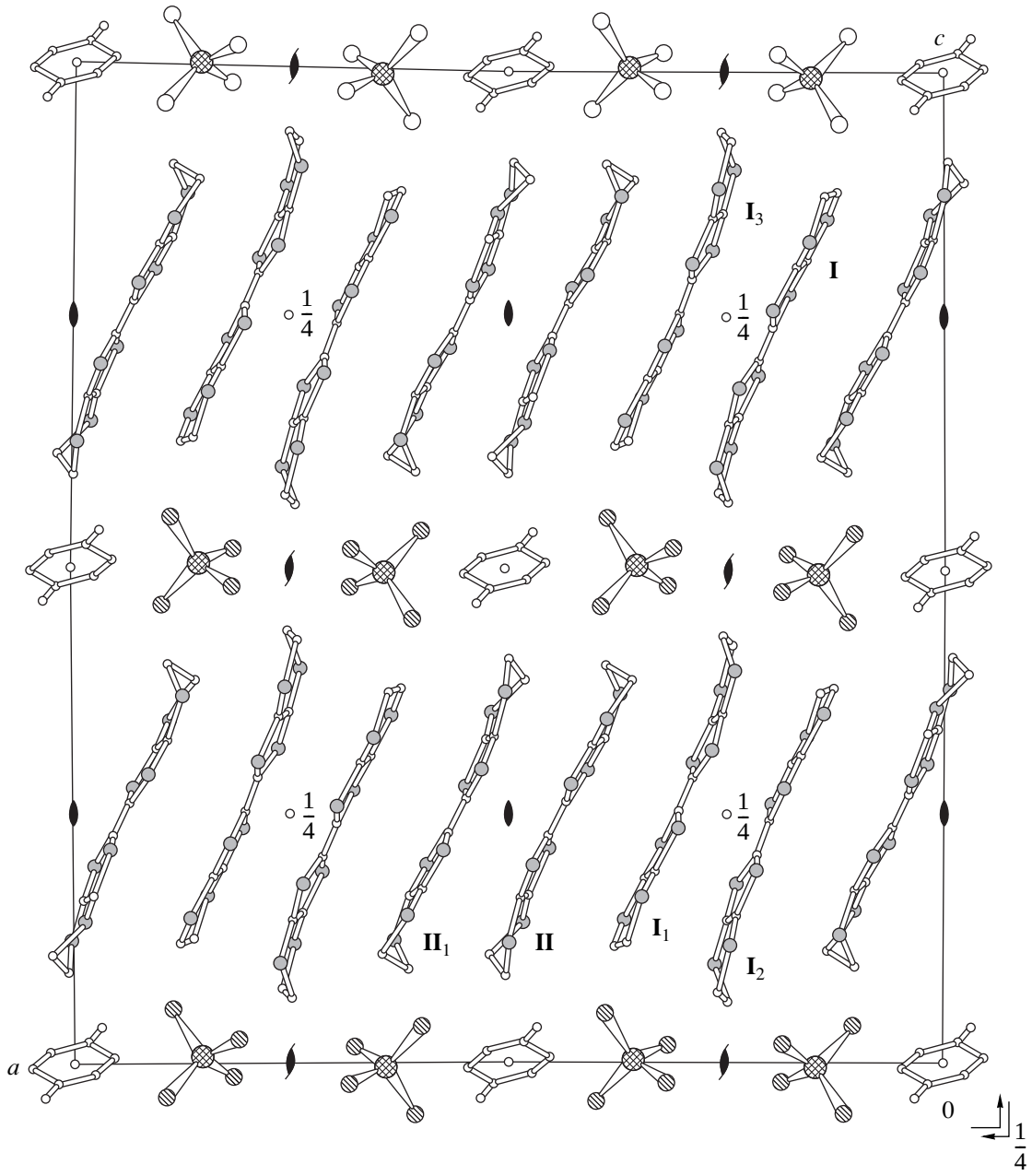

Fig. 1. Projection of the $(BEDT\text{-}TTF)_4(GaCl_4)_2 \cdot C_6H_5CH_3$ structure onto the *ac* plane. Symmetry operations for the radical cations *BEDT-TTF* **I** and **II** are as follows: $1/2 - x, y - 1/2, 1 - z$ ($\mathbf{I}_1$); $x, 1 - y, z - 1/2$ ($\mathbf{I}_2$); $1/2 - x, 3/2 - y, 3/2 - z$ ($\mathbf{I}_3$); and $1 - x, y, 1/2 - z$ ($\mathbf{II}_1$).

layers, which alternate along the *c*-axis with the anion layers containing solvent (toluene) molecules.

In the structure, there are two crystallographically independent *BEDT-TTF* radical cations **I** and **II** (Fig. 2), which occupy the general positions. The terminal ethylene groups in the *BEDT-TTF* **I** cation are disordered. The ethylene groups in the *BEDT-TTF* **II** cation adopt an eclipsed conformation without orientational disordering. The lengths of the central C=C bond in both radical cations are identical (to within the accuracy of determination) and equal to 1.369(5) Å in *BEDT-TTF* **I** and 1.363(6) Å in *BEDT-TTF* **II**. These lengths and the S–C bond lengths in the tetrathiafulvalene skeleton are close to the lengths of the corresponding bonds in the $BEDT\text{-}TTF^{1/2+}$ radical cation [8]. The projection of the radical cation layer along the *c*-axis is depicted in Fig. 3. The radical cation layer is formed by the *BEDT-TTF* stacks, which are aligned parallel to the *a*-axis. There exist three types of the *BEDT-TTF* cations that overlap in the stack: $\mathbf{I}_1$–$\mathbf{I}_2$, $\mathbf{I}_1$–**II**, and **II**–$\mathbf{II}_1$ (Fig. 4). The $\mathbf{I}_1$–$\mathbf{I}_2$ radical cations are parallel, and the interplanar distance is equal to 3.63 Å. The midplanes of the $\mathbf{I}_1$–**II** and **II**–$\mathbf{II}_1$ radical cations are not parallel and form dihedral angles of 5.34(6)°

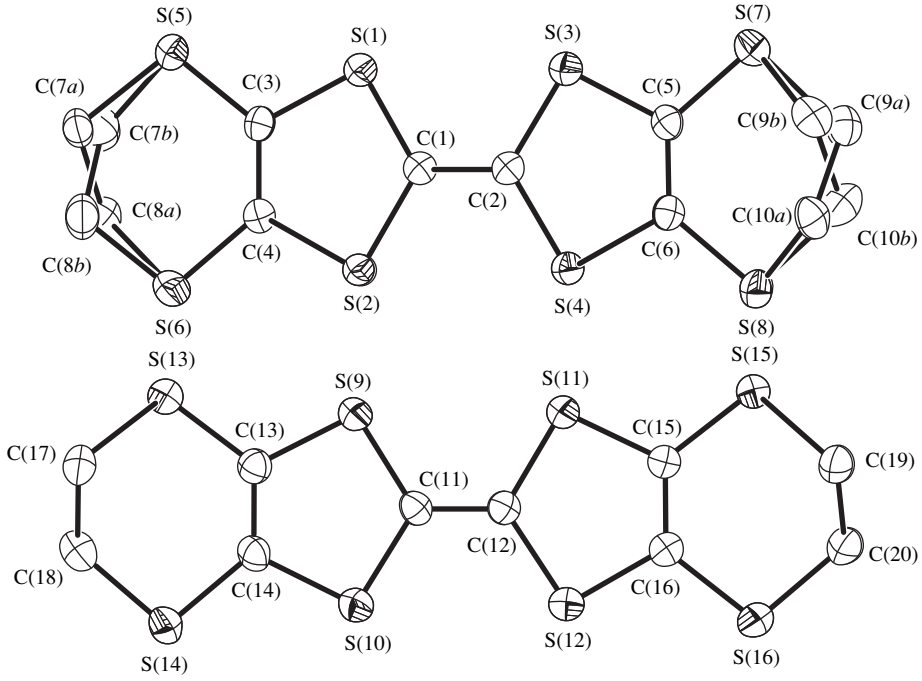

Fig. 2. Molecules *BEDT-TTF* **I** (top) and **II** (bottom) with atomic numbering.

and 1.18(6)°, respectively. Furthermore, the radical cation **II** is rotated with respect to the neighboring cations $\mathbf{I}_1$ and $\mathbf{II}_1$ about the normal to the *BEDT-TTF* plane in such a way that the angle between the C=C central bonds is equal to approximately 30°. Intercation shortened S···Scontacts ≤3.70 Å are absent within the stack. At the same time, a number of shortened S···Scontacts are observed between the stacks along the *b*-axis. These contacts are listed in Table 2.

Table 2. Shortened S···S contacts ($r \le 3.70$ Å) between the *BEDT-TTF* radical cations

Contact	*r*, Å	*BEDT-TTF**
S(1)···S(6), S(6)···S(1)	3.547(2)	**I**–$\mathbf{I}_b$, **I**–$\mathbf{I}_{\bar{b}}$
S(4)···S(7), S(7)···S(4)	3.635(2)	**I**–$\mathbf{I}_{\bar{b}}$, **I**–$\mathbf{I}_b$
S(5)···S(6), S(6)···S(5)	3.559(2)	**I**–$\mathbf{I}_b$, **I**–$\mathbf{I}_{\bar{b}}$
S(7)···S(8), S(8)···S(7)	3.591(2)	**I**–$\mathbf{I}_b$, **I**–$\mathbf{I}_{\bar{b}}$
S(10)···S(13), S(13)···S(10)	3.528(2)	**I**–$\mathbf{II}_{\bar{b}}$, **I**–$\mathbf{II}_b$
S(11)···S(16), S(16)···S(11)	3.559(2)	**I**–$\mathbf{II}_b$, **I**–$\mathbf{II}_{\bar{b}}$
S(13)···S(14), S(14)···S(13)	3.571(2)	**I**–$\mathbf{II}_b$, **I**–$\mathbf{II}_{\bar{b}}$
S(15)···S(16), S(16)···S(15)	3.575(2)	**I**–$\mathbf{II}_b$, **I**–$\mathbf{II}_{\bar{b}}$

* Symmetry operations for the radical cations are as follows: $x, y + 1, z$ ($\mathbf{II}_b$) and $x, y - 1, z$ ($\mathbf{I}_{\bar{b}}$ and $\mathbf{II}_{\bar{b}}$). Symmetry operations for the radical cations *BEDT-TTF* **I** and $\mathbf{II}_b$ are given in the captions to Figs. 1 and 2.

The projection of the anion layer in the $(BEDT\text{-}TTF)_4(GaCl_4)_2 \cdot C_6H_5CH_3$ crystals along the *c*-axis is displayed in Fig. 5. The interatomic distances in the $GaCl_4^-$ tetrahedral anion are equal to 2.156(2), 2.160(2), 2.165(2), and 2.169(1) Å. The noncentrosymmetric molecules of toluene occupy two equiprobable positions at the centers of symmetry. They are freely arranged between the $GaCl_4^-$ tetrahedra and form shortened contacts neither with anions nor with *BEDT-TTF* radical cations.

In the structure, there are three shortened Cl··S contacts between the anion and radical cation layers: Cl(1)··S(15), 3.539(1) Å ($\mathbf{II}_b$); Cl(2) ··S(8), 3.550(2) Å (**I**); and Cl(3)··S(5), 3.578(1) Å ($\mathbf{I}_3$). Here, $\mathbf{II}_b$ has the coordinates $(x, y + 1, z)$.

It is of interest to compare the structure of the radical cation salt under consideration and the structure of the $(BEDT\text{-}TTF)_2GaCl_4$ compound [3]. The latter crystallizes in the triclinic crystal system $P\bar{1}$ (a = 31.911 Å, b = 16.580 Å, c = 6.645 Å, α = 98.15°, β = 85.60°, γ = 90.55°, V = 3470 Å^3, and Z = 4) and has quite a different packing of *BEDT-TTF* in the radical cation layers. These layers are formed by the *BEDT-TTF* stacks, which are aligned parallel to the *b*-axis and contain four crystallographically independent radical cations. This indicates that the incorporation of solvent molecules into the radical cation salt leads to a considerable

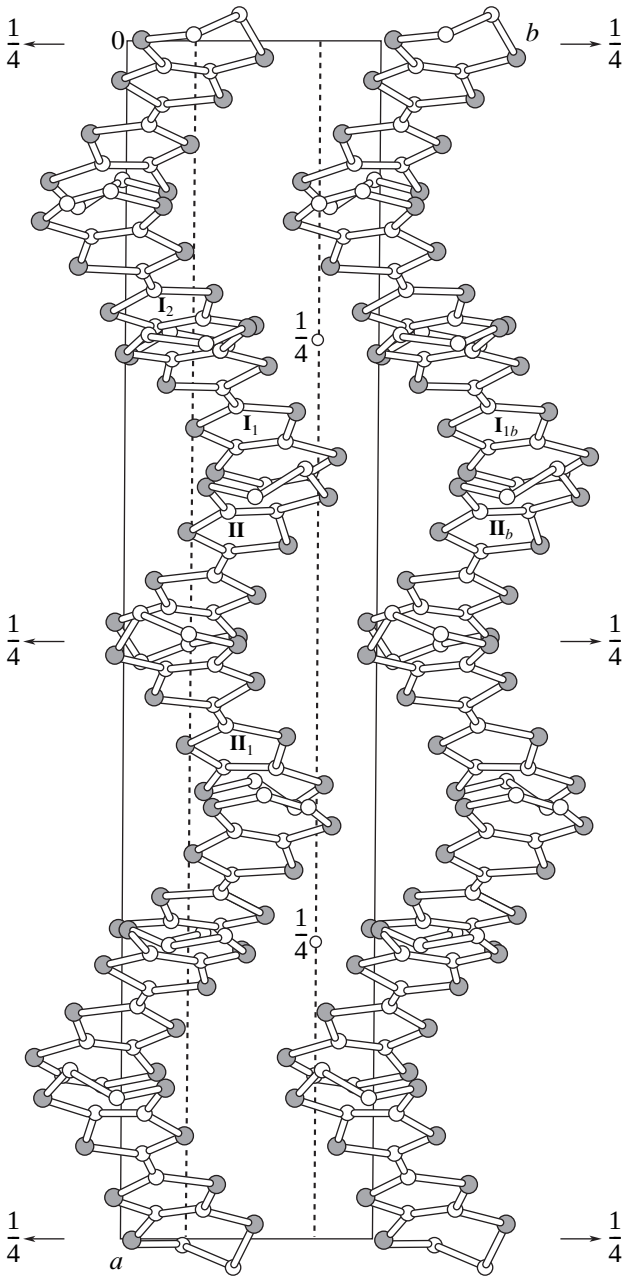

Fig. 3. Projection of the radical cation layer along the *c*-axis. Symmetry operations for the radical cations *BEDT-TTF* $\mathbf{I}_1$, $\mathbf{I}_2$, **II**, and $\mathbf{II}_1$ are given in the caption to Fig. 1. Symmetry operation for the radical cations $\mathbf{I}_{1b}$ and $\mathbf{II}_b$: $x, y + 1, z$.

change in the crystal structure, which, in turn, can bring about a change in the physical properties. In this case, both salts possess the semiconductor properties. However, there are numerous examples when the properties change radically. In particular, the (*BEDT-TTF*)$_2$Ag(CN)$_2$ radical cation salt has two crystalline modifications α" and θ with semiconducting and metallic properties, respectively [9, 10]. The κ-(*BEDT-TTF*)$_2$Ag(CN)$_2$ · H_2O radical cation salt, which involves water molecule as a guest component, represents the organic superconductor with $T_c = 5$ K [10, 11]. In the last case, the incorporation of the third guest component into the crystal composition changes the structure of the conducting layer; modifies the Fermi surface topology; and, as a consequence, leads to a radical change in the transport properties [12].

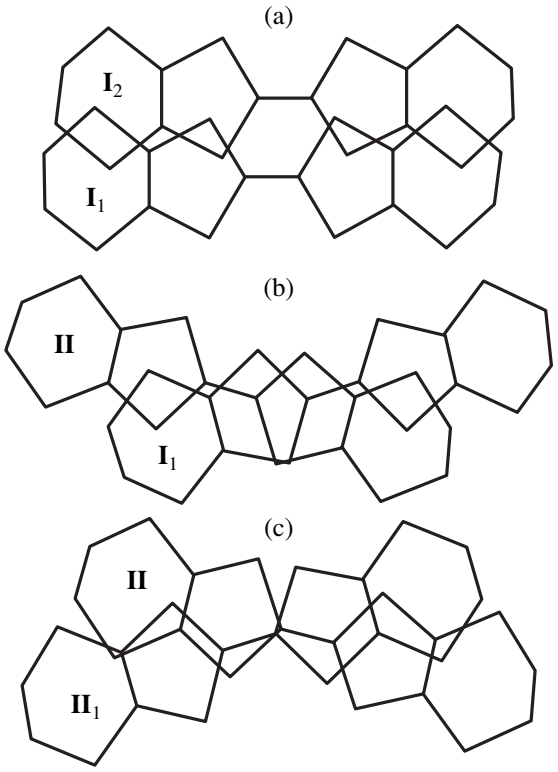

Fig. 4. (a–c) Overlapping of the *BEDT-TTF* radical cations in a stack.

It should be noted that the structure of the radical cation layer in the (*BEDT-TTF*)$_4$(GaCl$_4$)$_2$ · $C_6H_5CH_3$ crystals closely resembles that of the (*BEDT-TTF*)$_4$(Hg$_2$Br$_6$) · $C_2H_3Cl_3$ crystals [13]. The internal structure of radical cation stacks, which form the donor layers, is approximately the same in these crystals. Apparently, the crystals also possess the semiconductor properties. The characteristic rotation of radical cations in the stacks with respect to the normal to the plane (Fig. 4) was observed earlier in many salts, for example, in (*BEDT-TTF*)$_4$Cl$_2$ · 4H_2O [14], (*BEDT-TTF*)$_4$Cl$_2$ · 6H_2O [15], (*BEDT-TTF*)$_2$Br · $C_2H_4(OH)_2$ [16], β- and γ-(*BEDT-TTF*)$_2$PF$_6$ [17, 18], (*BEDT-TTF*)$_2$TlHg(Se$_{1-x}$S$_x$CN)$_4$ [19], (*BEDT-TTF*)$_2$Br(H_2O)$_3$ [20], etc. Among these crystals, there are semiconductors [18, 19], metals with the metal–dielectric transition [15–17], and metals stable down to liquid helium temperature [14, 20]. It seems likely that the complex structure of the radical cation layer in (*BEDT-TTF*)$_4$(GaCl$_4$)$_2$ · $C_6H_5CH_3$ with a weak intrastack and interstack intermolecular interactions does not provide necessary conditions for manifestation of metallic

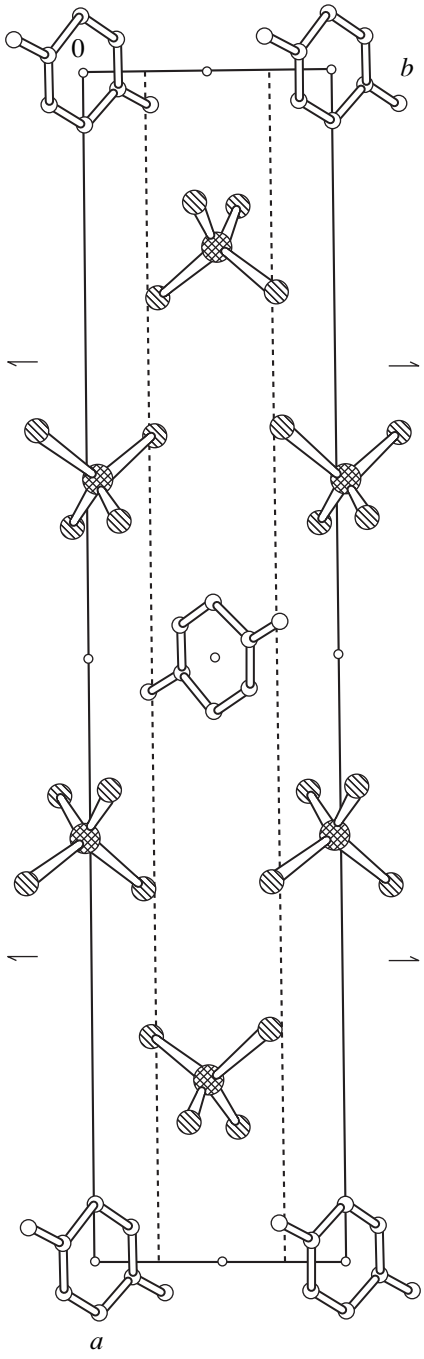

Fig. 5. Projection of the anion layer along the *c*-axis.

properties, and the crystals of this salt are semiconductors.

ACKNOWLEDGMENTS

We would like to thank L.P. Rozenberg for the preliminary testing of crystals by the photo method and G.M. Mikhaĭlova for preparing the illustrations to the manuscript.

This work was supported by the NWO grant and the Russian Foundation for Basic Research (project no. 97-03-33581).

REFERENCES

1. J. M. Williams, J. R. Ferraro, R. J. Thorn, K. D. Carlson, U. Geiser, H. H. Wang, A. M. Kini, and M.-H. Whangbo, *Organic Superconductors (Including Fullerenes)* (Prentice Hall, Englewood Cliffs, 1992).
2. T. Ishiguro, K. Yamaji, and G. Saito, *Organic Superconductors* (Springer-Verlag, Berlin, 1998).
3. M. Kurmoo, M. Allan, R. H. Friend, *et al.*, Synth. Met. **41–43**, 2127 (1991).
4. L. K. Montgomery, T. Burgin, C. Husting, *et al.*, Mol. Cryst. Liq. Cryst. **211**, 283 (1992).
5. H. Kobayashi, T. Udagawa, H. Tomita, *et al.*, Chem. Lett. 1559 (1993).
6. V. I. Andrianov, Kristallografiya **32** (1), 228 (1987) [Sov. Phys. Crystallogr. **32**, 130 (1987)].
7. G. M. Sheldrick, *SHELXL93: Program for the Refinement of Crystal Structures* (Univ. of Göttingen, Göttingen, 1993).
8. J. M. Williams, H. H. Wang, T. J. Emge, *et al.*, Prog. Inorg. Chem. **35**, 51 (1987).
9. C. Bellitto, M. Bonamico, V. Fares, *et al.*, Chem. Mater. **7**, 1475 (1995).
10. M. Kurmoo, D. R. Talham, K. L. Pritchard, *et al.*, Synth. Met. **27**, A177 (1988).
11. H. Mori, I. Hirabayashi, S. Tanaka, and T. Mori, Solid State Commun. **76**, 35 (1990).
12. E. Canadell, in *Supramolecular Engineering of Synthetic Metallic Materials: Conductors and Magnets*, Ed. by J. Veciana, C. Rovira, and D. B. Amabilino (Kluwer Academic, Dordrecht, 1998), NATO ASI Ser., p. 337.
13. U. Geiser, H. H. Wang, S. Kleinjan, and J. M. Williams, Mol. Cryst. Liq. Cryst. **181**, 125 (1990).
14. R. P. Shibaeva, L. P. Rozenberg, A. F. Shestakov, and T. A. Khannanova, Zh. Strukt. Khim. **32**, 98 (1991).
15. G. Bravic, D. Chasseau, J. Gaultier, *et al.*, Synth. Met. **42**, 2035 (1991).
16. N. P. Karpova, S. V. Konovalikhin, O. A. Dyachenko, *et al.*, Acta Crystallogr., Sect. C: Cryst. Struct. Commun. **48**, 62 (1992).
17. H. Kobayashi, R. Kato, T. Mori, *et al.*, Mol. Cryst. Liq. Cryst. **107**, 33 (1984).
18. X. Bu, I. Cisarova, P. Coppens, *et al.*, Acta Crystallogr., Sect. C: Cryst. Struct. Commun. **48**, 516 (1992).
19. R. P. Shibaeva, S. S. Khasanov, L. P. Rozenberg, *et al.*, Kristallografiya **42** (5), 846 (1997) [Crystallogr. Rep. **42**, 778 (1997)].
20. M. Luo, T. Ishida, A. Kobayashi, and T. Nogami, Synth. Met. **96**, 97 (1998).

Translated by O. Borovik-Romanova

Crystallography Reports, Vol. 46, No. 2, 2001, pp. 225–229. Translated from Kristallografiya, Vol. 46, No. 2, 2001, pp. 265–270.

STRUCTURE OF ORGANIC COMPOUNDS

Low-Temperature Study of the Molecular and Crystal Structures of 2-(2'-Tosylamino-5'-Nitrophenyl)-4*H*-3,1-Benzoxazin-4-one, an Organic Luminophore

A. N. Utenyshev*, O. S. Filipenko*, B. M. Bolotin, and V. I. Ponomarev*****

** Institute for Problems of Chemical Physics, Russian Academy of Sciences, Chernogolovka, Moscow oblast, 142432 Russia*

*** IREA State Research Institute of Chemical Reagents and Special-Purity Substances, Bogorodskiĭ val 3, Moscow, 107076 Russia*

**** Institute of Structural Macrokinetics and Problems of Materials Technology, Russian Academy of Sciences, Chernogolovka, Moscow oblast, 142432 Russia*

e-mail: atom@icp.ac.ru

Received November 11, 1998; in final form, June 4, 1999

Abstract—The crystal structure of 2-(2'-tosylamino-5'-nitrophenyl)-4*H*-3,1-benzoxazin-4-one (**I**) is studied by X-ray diffraction at 100 K ($C_{21}H_{15}N_3O_6S$, a = 20.899(2) Å, b = 10.948(1) Å, c = 8.260(1) Å, V = 1889.3(1) Å^3, Z = 4, and space group $Pbn2_1$). The compound exhibits an anomalous Stokes shift. Upon cooling, the oxazineaminophenyl fragment of compound **I** acquires a quinoid structure and the linear parameters of the intramolecular N–H···N hydrogen bond increase (the distance between the heterocyclic nitrogen atom and the hydrogen atom of the tosylamino group becomes 1.92 Å). The complete optimization of the geometry of molecules in compound **I** and unsubstituted 2-(2'-tosylaminophenyl)-4*H*-3,1-benzoxazin-4-one in the ground singlet electronic state is performed by the semiempirical method with the MOPAC program. It is shown that the oxygen atoms in the sulfo group of molecule **I** are nonequivalent, because one of them is involved in the intermolecular C–H···O hydrogen bond.

INTRODUCTION

Earlier [1–4], we reported the crystal structures of some representatives of the new class of organic luminophores, which are active in the crystal state and show anomalous Stokes shifts (ASS). These compounds are 2-(2'-tosylaminophenyl)-4*H*-3,1-benzoxazin-4-one (**II**) and its derivatives: 2-(2'-tosylamino-5'-nitrophenyl)-4*H*-3,1-benzoxazin-4-one at 300 K (**Ia**) [2], 2-(2'-tosylamino-4'-nitrophenyl)-4*H*-3,1-benzoxazin-4-one (**III**) [3], 2-(2'-tosylaminophenyl)-6-bromo-4*H*-3,1-benzoxazin-4-one (**IV**) [4], and 2-(2'-tosylamino-4'-methoxyphenyl)-4*H*-3,1-benzoxazin-4-one (**V**) at 100 and 300 K [4]. To exhibit the luminophore properties, an organic molecule should contain a sufficiently extended and rigid planar conjugated π system. This requirement is fulfilled in all molecules **Ia**–**V** due to the formation of the intramolecular N(1)–H···N(2) hydrogen bond, which links planar benzoxazine (*A* and *B*) and aminophenyl (*C* and *E*) fragments into a common conjugated system. In these molecules, the dihedral angles between the phenyl ring (*D*) of the tosyl group and the conjugated system vary from 96.7° in **II** to 64.2° in **IV**. The molecular structure of 2-(2'-tosylaminophenyl)-4*H*-3,1-benzoxazin-4-one is represented by the following scheme:

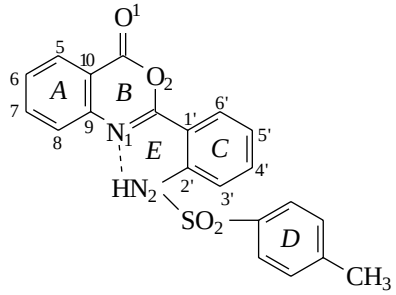

For the first time, the immediate relation between the anomalous Stokes shift and the strength and topology of the intramolecular hydrogen bond between the heterocyclic nitrogen atom and the hydrogen atom of the tosylamino group was shown in [5] based on the data of fluorescence and IR spectroscopic studies of compounds **Ia**–**V**. The strength of the hydrogen bond depends on the electron nature and the position of the substituent in the molecule. The anomalous Stokes shift changes symbately with the strength of the intramolecular hydrogen bond: the strong electron-seeking NO_2 group at the *p*-position to the tosylamino group strengthens the intramolecular N–H···N hydrogen bond

1063-7745/01/4602-0225$21.00 © 2001 MAIK "Nauka/Interperiodica"

Table 1. Fluorescence maxima and anomalous Stokes shifts (ASS) for compounds **I**–**V**

Compound	Fluorescence λ_{max}, nm	ASS, nm	ν_{NH}, cm^{-1}	N(1)···H, Å
I	520	185	2965	1.85
II	535	198	3021	1.93
III	564	200	3105	1.80
IV	542	197	3061	2.08
V		150	2985	1.84

and shifts the frequency of the NH stretching vibrations toward smaller wave numbers from 3021 (**II**) to 2965 cm^{-1} (**Ia**) (Table 1). The anomalous Stokes shifts, which are characteristic of compound **II** and its derivatives, are due to proton-transfer energy losses upon transition to the excited state. The anomalous component of the Stokes shift depends on the strength of the intramolecular hydrogen bond. This strength is affected by the substituents, which enhance the proton-releasing or proton-seeking properties of the groups involved in the intramolecular hydrogen bond. For example, the weakening of the intramolecular hydrogen bond under the action of 4'-NO_2 (**III**) and 6-Br (**IV**) substituents correlates with an increase in the anomalous stokes shift (Table 1). The opposite changes are observed for compounds **I** and **V**: the strengthening of the intramolecular hydrogen bond is accompanied by a decrease in the anomalous Stokes shift (Table 1).

The N(2)–H bond observed in the crystal structure of **Ia** at 300 K is the longest among the corresponding bonds in the compounds studied. This agrees with the fact that the NO_2 group conjugated only with the N(2) nitrogen atom (see the above scheme) reduces the basicity of the amino nitrogen; promotes the mobility of the hydrogen atom; and, thus, strengthens the intramolecular hydrogen bond. The NO_2 group introduced into the 4'-position (**III**) produces only the inductive effect on the mobility of the hydrogen atom of the tosylamino group. At the same time, the NO_2 group is conjugated with the N(1) atom, reduces its basicity, and weakens the intramolecular hydrogen bond. In this case, the N(2)–H bond is shorter.

The X-ray diffraction studies of the above compounds at room temperature revealed the inequality of the S–O bond lengths. In all the structures, the sulfo

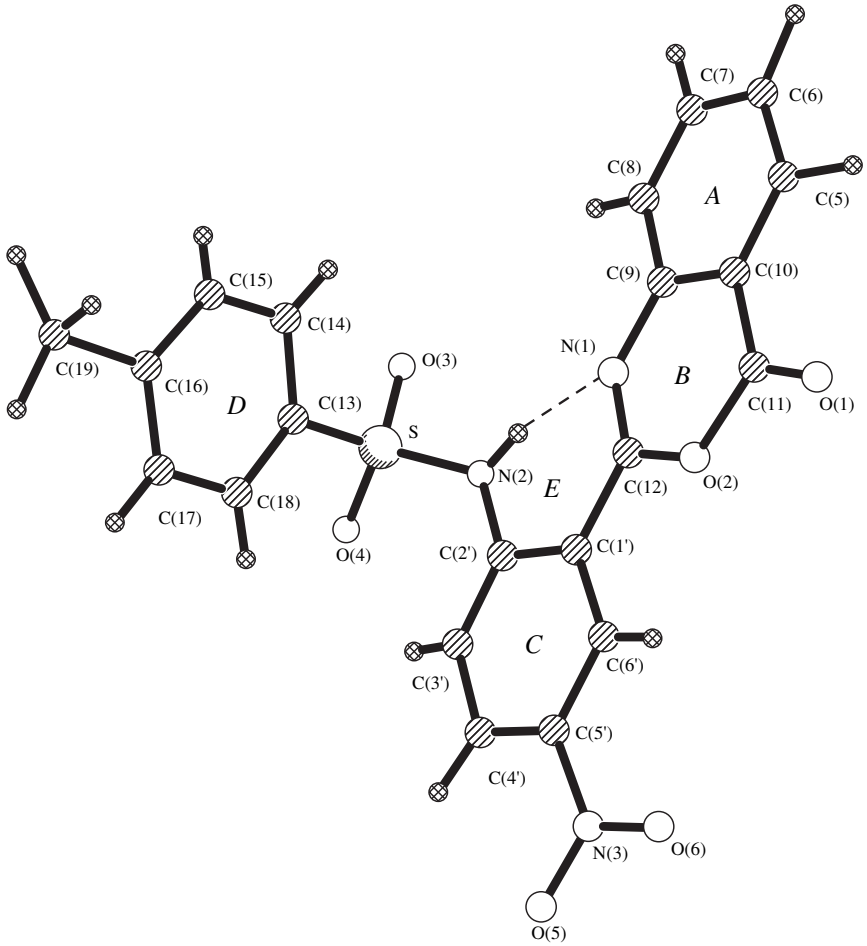

Fig. 1. A general view of molecule **I**.

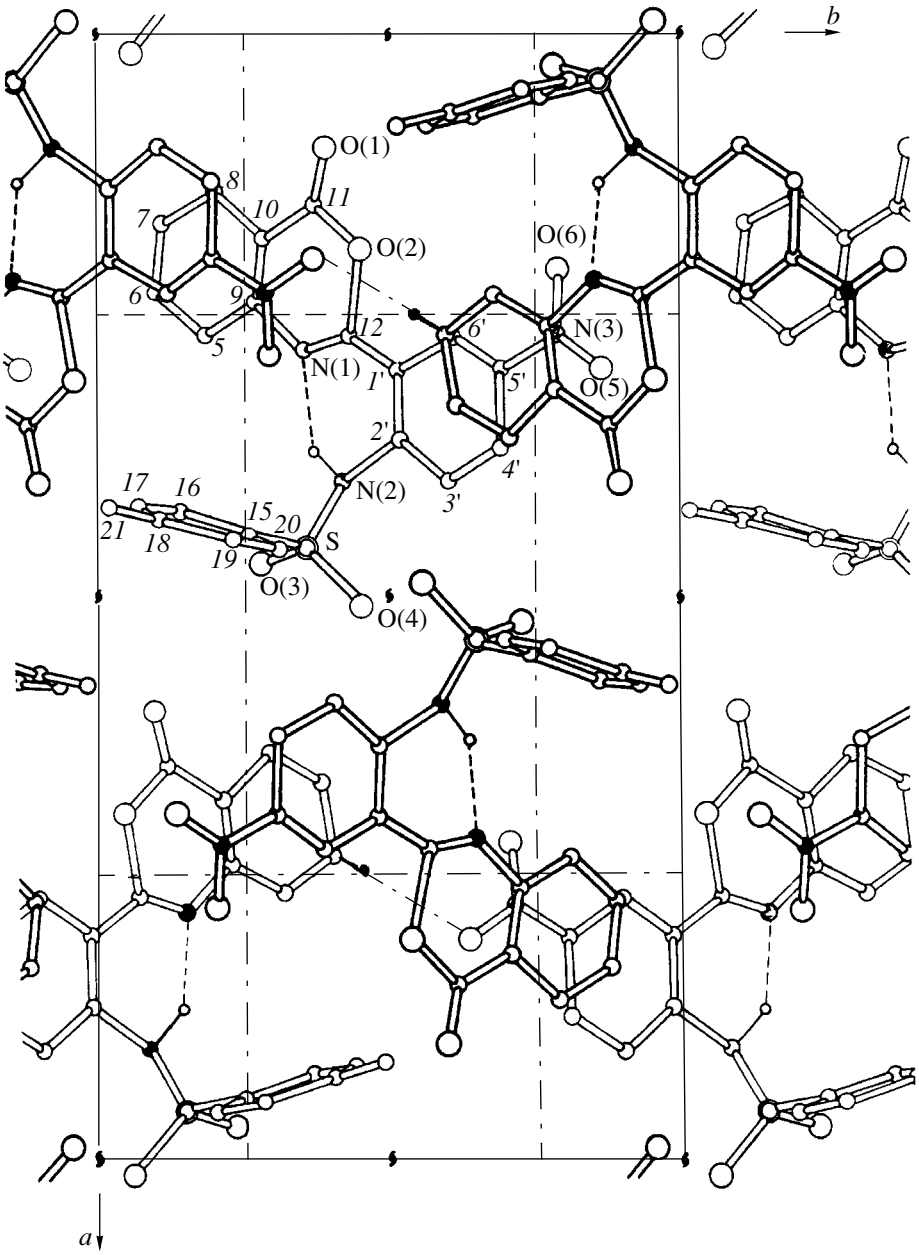

Fig. 2. Projection of structure **I** onto the *a*0*b* plane. The O(5)··H(7)–C(7) hydrogen bond is shown by the dot-dashed line.

group is asymmetric relative to the S–C(*Ph*) bond because of the sterical hindrances produced by the aminophenyl ring. In structures **I** and **III**, the S–O bonds are additionally affected by the intramolecular C–H··O interactions between the oxygen atom of the sulfo group and the hydrogen atom in the *ortho*-position of the phenyl ring (the O··H distances are 2.1–2.5 Å). The mobility of its proton increases under the effect of the nitro group. It is of interest to study the crystal structure of **I** at low temperature in order to gain more details of the molecular structure, intramolecular hydrogen bond, and the specific intermolecular S–O··H–C(*Ph*) interactions.

Table 2. Crystal data for compound **I**

T, K	*a*, Å	*b*, Å	*c*, Å	*V*, Å^3	*Z*	*d*, g/cm^3	|*Fhkl*|	*R*
300	21.099(9)	10.960(5)	8.358(5)	1932.7	4	1.51	1055	0.05
100	20.898(2)	10.948(1)	8.260(2)	1889.8	4	1.54	1141	0.04

Table 3. Coordinates of non-hydrogen ($\times 10^4$) and hydrogen ($\times 10^3$) atoms and equivalent isotropic thermal parameters B_{eq} in structure **I** at 100 K

Atom	*x*	*y*	*z*	B_{eq}, Å^2
S	4644(2)	3562(2)	7903(2)	0.58
O(1)	940(2)	3906(2)	7214(1)	1.08
O(2)	1946(2)	4470(2)	7690(2)	1.22
O(3)	4758(2)	2825(2)	6545(1)	1.39
O(4)	5111(2)	4465(2)	8399(2)	1.08
O(5)	2998(2)	8649(2)	11776(2)	1.76
O(6)	2086(1)	7976(2)	10894(2)	1.35
N(1)	2829(1)	3510(2)	6494(2)	0.80
N(2)	3963(1)	4255(2)	7498(2)	1.09
N(3)	2666(1)	7924(2)	10964(2)	1.19
C(1')	2972(2)	5201(1)	8366(2)	1.15
C(2')	3644(2)	5141(1)	8432(2)	0.99
C(3')	3986(2)	5988(2)	9347(2)	1.08
C(4')	3666(1)	6885(2)	10250(2)	0.80
C(5')	3014(2)	6958(1)	10147(2)	1.05
C(6')	2661(2)	6116(1)	9228(2)	0.88
C(5)	1345(2)	1927(2)	5134(2)	1.19
C(6)	1622(2)	1020(1)	4153(2)	1.27
C(7)	2275(2)	0972(2)	4000(2)	1.35
C(8)	2683(2)	1796(2)	4725(2)	1.14
C(9)	2413(2)	2692(2)	5716(2)	0.89
C(10)	1759(1)	2766(2)	5869(2)	0.93
C(11)	1482(1)	3707(2)	6942(2)	0.78
C(12)	2579(1)	4328(2)	7445(2)	0.80
C(15)	4493(1)	2630(1)	9632(1)	0.74
C(16)	4296(1)	1408(1)	9319(2)	1.22
C(17)	4193(1)	0687(1)	10704(2)	1.07
C(18)	4276(2)	1120(2)	12239(2)	0.99
C(19)	4448(2)	2330(1)	12521(2)	1.29
C(20)	4563(2)	3091(2)	11147(2)	0.66
C(21)	4200(2)	0276(2)	13670(2)	1.52
H(1)	369(2)	393(3)	699(2)	
H(3')	445(2)	601(3)	935(2)	
H(4')	393(2)	738(3)	1100(2)	
H(6')	222(2)	618(3)	927(2)	
H(5)	86(2)	202(2)	500(2)	
H(6)	133(2)	32(2)	362(3)	
H(7)	246(2)	33(2)	335(2)	
H(8)	318(2)	175(1)	462(2)	
H(16)	424(2)	110(3)	824(2)	
H(17)	417(2)	2(2)	1040(2)	
H(19)	449(2)	264(2)	136(2)	
H(20)	469(3)	393(3)	1129(2)	
H(21*A*)	415(3)	83(3)	1487(3)	
H(21*B*)	372(3)	8(3)	1362(2)	
H(21*C*)	442(3)	−71(3)	1331(2)	

EXPERIMENTAL

The main crystal data for colorless crystals **I** ($C_{21}H_{15}N_3O_5S$, space group $Pbn2_1$) at two temperatures are summarized in Table 2. A set of intensities was obtained on a DAR-UM three-circle diffractometer (equi-inclined scheme of data collection, ω–ω/2ω scan mode, CuK_α radiation, graphite monochromator, no correction for absorption). The crystal was cooled to the temperature required with a nitrogen stream in a low-temperature open-type attachment to the DAR-UM diffractometer. The temperature variations were within ±2°. The unit cell parameters were refined using high-angle reflections. The atomic coordinates of structure **Ia** at room temperature [2] were used as a starting set for the least-squares refinement of structure **I** in the anisotropic approximation with the ROENTGEN-75 program [6]. The difference synthesis ρ(*x*, *y*, *z*) calculated after the anisotropic least-squares refinement to $R = 0.06$ revealed the positions of all the hydrogen atoms. The simultaneous refinement of the non-hydrogen atoms in the anisotropic approximation and the coordinates of the hydrogen atoms led to $R = 0.040$. The final atomic coordinates are listed in Table 3. The quantum-chemical calculation of the geometry of molecule **I** in the ground state was performed by the PM3 parametrization method using the MOPAC-7 program [7]. The energies of the crystal lattice and intermolecular interactions in the crystal were calculated within the atom–atomic potential approach with the 6-exp parameters [8].

RESULTS AND DISCUSSION

Upon cooling, crystal **I** retained the orthorhombic symmetry. The *b* parameter remained almost unchanged, the *a* and *c* parameters decreased markedly, and the volume decreased by 42.9 Å^3 (Table 2).

A general view of molecule **I** is shown in Fig. 1. The conformation of the molecule at 100 K remained almost unchanged compared to that at 300 K. Molecule **I** is characterized by the planar conjugated system formed by the benzoxazineaminophenyl fragment (Fig. 1; rings *A*, *B*, *C*, and *E*). Table 4 shows that, at both temperatures, molecule **I** inherits the main conformational features of the unsubstituted molecule **II**. Introduction of the nitro group into the *p*-position of the tosylamino group resulted in a decreased angle of rotation of the *p*-methylphenyl fragment relative to the central fragment of the molecule.

Similar to other organic structures [9–11], the bonds that were effectively shortened at 300 K because of an improper consideration for thermal vibrations lengthened at low temperatures. This lengthening is most pronounced in the benzoxazine rings *A* and *B*: C(10)–C(11), 1.471 Å (vs. 1.460 Å)*[1] and O(2)–C(11), 1.429 (1.383 Å). Apparently, the same effect is responsible for the lengthening of the other peripheral bonds upon cooling and, as a consequence, for the changes in the bond angles by approximately 1°.

[1] The bond lengths in parentheses refer to room temperature.

Table 4. Dihedral angles (deg) between the planar fragments in molecules **I** (at 100 and 300 K) and **II**

Molecule	*A*/*B*	*B*/*C*	*B*/*D*	*B*/*E*	$-NO_2$/C	O(3)SO(4)/CSN(1)
I	2.0	6.6	78.3	4.6	1.9	93.2
Ia	2.0	6.2	79.0	4.5	2.7	92.4
II	1.2	7.1	95.4	6.2	–	92.5

Table 5. Geometric parameters (Å, deg) for intramolecular hydrogen bonds and sulfo groups in molecules **I** (at 100 and 300 K) and **II**

Molecule	N(1)···N(2)	N(1)–H	H···N(2)	N(1)HN(2)	S–O(3)	S–O(4)	S–N(1)	S–C(15)	O(3)SO(4)
I	2.653(3)	0.79(2)	1.92(3)	132.8(2)	1.399(2)	1.453(2)	1.652(2)	1.779(2)	120.8(2)
Ia	2.632(5)	1.09(11)	1.85(3)	125.0(2)	1.405(4)	1.439(3)	1.645(3)	1.769(3)	119.6(2)
II	2.673(3)	0.89(4)	1.93(3)	140.0(0)	1.426(3)	1.433(3)	1.640(3)	1.759(3)	120.1(2)

Upon cooling, the bond lengths in the *p*-nitrophenyl fragment change so that N(2)–C(2') becomes the shortest bond, 1.401(2) Å [1.427(3) in **Ia** and 1.416(3) Å in **II**] and the C(1')–C(12) bond length becomes 1.408(2) Å [1.464(4) and 1.483(3) Å in **Ia** and **II**, respectively]. The N(3)–C(5') bond shortens to 1.444(2) Å vs. 1.468(4) Å at 300 K.

The effect of cooling is most pronounced in the parameters of the intramolecular hydrogen bond (Table 5). The intramolecular hydrogen bond links the planar rings *A*, *B*, and *C* into a common conjugated system. Upon cooling from 300 to 100 K, the N(1)–N(2) distance increases by 0.02 Å and remains shorter than that in **II** by the same value. As expected, the intramolecular hydrogen bond in the nitro-substituted luminophore is stronger than that in the unsubstituted compound.

The low-temperature investigation of compound **I** confirmed the nonequivalence of the oxygen atoms in the sulfo and nitro groups (Table 5). The S–O(3) and N(3)–O(5) bonds [1.453(2) and 1.256(2) Å, respectively] are significantly longer than the S–O(4) and N(3)–O(6) bonds [1.399(2) and 1.216(2) Å, respectively]. This indicates that, in the crystal packing, the O(3) and O(5) atoms are possibly involved in nonbonded interactions. Actually, the crystal structure of compound **I** is characterized by an anisotropic energy distribution of intermolecular interactions. The total energy of the crystal structure is –41.2 kcal/mol. The planar nitrophenyl and benzoxazine fragments of molecules **I** that are related by the glide plane *b* (*–x* + 05, *y* + 0.5, *z*) overlap. The energy of this intermolecular interaction is the largest among the pairs of molecules, 15.2 kcal/mol (Fig. 2). There is also a short intermolecular contact between the molecules related by the translation along the *b*-axis: the O(5)··H(7) distance between the nitro group and the hydrogen atom of the phenyl ring is 2.50 Å, and the O(5)··C(7) distance is 3.468 Å (Fig. 2). On the other hand, the *p*-methylphenyl fragments *D* are nearly perpendicular to the conjugated *ABCE* system of the molecule. This orientation favors the intermolecular O(3)··H(19)–C(19) interaction between the molecules related by the twofold screw axis (1/2 1/2 *z*): O(3)··H(19), 1.84 Å and O(3)··C(19), 2.70 Å. The quantum-chemical calculation revealed that, in the absence of the crystal environment, the lengths of the S–O bonds in the sulfo group and the N–O bonds in the nitro group of molecule **I** are identical and equal to 1.407 and 1.203 Å, respectively.

REFERENCES

1. O. S. Filipenko, V. I. Ponomarev, B. M. Bolotin, and L. O. Atovmyan, Kristallografiya **24** (5), 957 (1979) [Sov. Phys. Crystallogr. **24**, 547 (1979)].
2. O. S. Filipenko, B. M. Bolotin, L. O. Atovmyan, and V. I. Ponomarev, Dokl. Akad. Nauk SSSR **254**, 365 (1980) [Sov. Phys. Dokl. **25**, 679 (1980)].
3. O. S. Filipenko, L. O. Atovmyan, B. M. Bolotin, and V. I. Ponomarev, Kristallografiya **26** (4), 711 (1981) [Sov. Phys. Crystallogr. **26**, 404 (1981)].
4. O. S. Filipenko, V. I. Ponomarev, L. O. Atovmyan, and B. M. Bolotin, Kristallografiya **32** (1), 102 (1987) [Sov. Phys. Crystallogr. **32**, 56 (1987)].
5. M. V. Loseva and B. M. Bolotin, Zh. Fiz. Khim. **46**, 2195 (1972).
6. V. I. Andrianov and Z. Sh. Safina, in *ROENTGEN-75: Automated Software System for the Solution of Crystal Structures* (Inst. Chem. Phys., USSR Acad. Sci., Chernogolovka, 1975).
7. J. J. P. Stewart, QCPE, No. 455.
8. T. V. Timofeeva, N. Yu. Chernikova, and P. M. Zorky, Usp. Khim. **49**, 966 (1980).
9. V. I. Ponomarev, O. S. Filipenko, and L. O. Atovmyan, Kristallografiya **21** (6), 392 (1976) [Sov. Phys. Crystallogr. **21**, 215 (1976)].
10. V. I. Ponomarev, O. S. Filipenko, and L. O. Atovmyan, Kristallografiya **25** (5), 956 (1980) [Sov. Phys. Crystallogr. **25**, 549 (1980)].
11. V. I. Ponomarev and G. V. Shilov, Kristallografiya **28** (4), 674 (1983) [Sov. Phys. Crystallogr. **28**, 397 (1983)].

Translated by I. Polyakova

Crystallography Reports, Vol. 46, No. 2, 2001, pp. 230–234. From Kristallografiya, Vol. 46, No. 2, 2001, pp. 271–275.

Crystallographic Analysis of Royline Monohydrate [$C_{25}H_{41}NO_7 \cdot H_2O$]*

Rajnikant, V. K. Gupta, and M. Lal**

X-ray Crystallography Laboratory, Postgraduate Department of Physics, University of Jammu, Jammu Tawi, 180 006 India

Received September 8, 1999; in final form, April 17, 2000

Abstract—The crystal and molecular structures of the alkaloid Royline {(1α,6β,14α,16β)-20-ethyl-4-hydroxymethyl)-1,6,14,16-tetramethoxyaconitane-7,8-diol} with a water molecule has been determined by X-ray diffraction analysis. The compound crystallizes in the space group $P2_1$ with the unit cell parameters a = 10.985(1) Å, b = 7.898(1) Å, c = 14.956(1) Å, β = 102.96(1)°, V = 1264.52 Å^3, Z = 2, λMoK_α = 0.71073 Å, and R = 0.033 for 2067 observed reflections. Rings *A*, *B*, and *C* adopt a chair conformation, ring *D* is a half-boat, ring *E* is a half-chair, and ring *F* is in an envelope conformation with C(14) at the flap. Molecules are linked together in the crystal by hydrogen bonds. © *2001 MAIK "Nauka/Interperiodica"*.

INTRODUCTION

The title compound is a diterpenoid alkaloid isolated from *Inula royleana*, a shrub growing on the western temperate Himalayas at an altitude of 7000–12000 ft above the sea level. The plant is considered to be poisonous and is used as a disinfectant and as an insectiside. It is known to be commonly used against the head louse [1]. The chemical structure as assigned to this compound on the basis of its IR, UV, NMR, and mass spectral data is shown in Fig. 1 [2].

EXPERIMENTAL

Transparent single crystals of Royline in the form of plates were grown from methanol by the slow evaporation technique at room temperature. Three-dimensional intensity data were collected on an Enraf–Nonius CAD4 diffractometer (MoK_α radiation). The unit cell parameters were refined by the least-squares procedure. Data were corrected for Lorentz and polarization factors, but no absorption or extinction corrections were made.

The structure was solved by direct methods using the SHELXS86 software package [3] and refined by using the SHELXL93 software package [4]. A total of 43 hydrogen atoms were used in the structure determination, of which 25 hydrogen atoms were located from the difference Fourier map, and their positions and isotropic temperature factors were refined. The remaining 18 hydrogen atoms were placed in geometrically calculated positions, and their coordinates were refined in the structure factor calculations. The final refinement cycle converged to R = 0.033, $wR(F^2)$ = 0.087, and S = 1.176. Atomic scattering factors were taken from the *International Tables* for X-ray Crystallography (1992, Vol. C, Tables 4.2.6.8 and 6.1.1.4). The crystallographic data are summarized in Table 1.

RESULTS AND DISCUSSION

The fractional coordinates and equivalent isotropic temperature factors for non-hydrogen atoms are presented in Table 2. Endocyclic torsion angles for different rings of the molecule are listed in Table 3. A general view of the molecule with atomic labeling is shown in Fig. 2 [5].

The geometric parameters of the molecule, that is, bond lengths and bond angles, are quite close to those of some analogous structures [6–8]. The central ring system of Royline is formed by the fusion of four six-membered and two five-membered rings. The mean value of three C(sp^3)–N bonds [1.465(11) Å] is comparable with the corresponding values obtained in the case of Delvestine [6] and Delsoline [7].

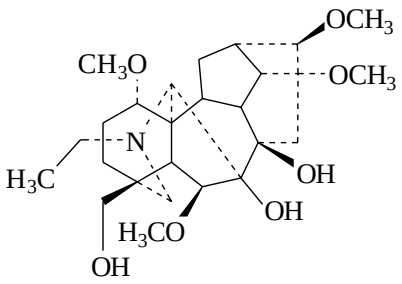

Fig. 1. Chemical structure of Royline.

* This article was submitted by the authors in English.
** Author for correspondence.

1063-7745/01/4602-0230$21.00 © 2001 MAIK "Nauka/Interperiodica"

Table 1. Crystal data and other experimental details

Crystal habit	White transparent plate
Chemical formula	$C_{25}H_{41}NO_7 \cdot H_2O$
Molecular weight	485.65
Unit cell parameters	a = 10.985(1) Å, b = 7.898(1) Å c = 14.956(1) Å, β = 102.96(1)°
Unit cell volume	1264.52 Å^3
Crystal system	Monoclinic
Space group	$P2_1$
Density d_{calcd}	1.275 g/cm^3
No. of molecules per unit cell (Z)	2
Radiation	MoK_α
Wavelength (λ)	0.71073 Å
Absorption coefficient (μ)	0.09 mm^{-1}
F(000)	528
Crystal size	0.30 × 0.22 × 0.12 mm
Refinement of unit cell	25 reflections, (8.1° < θ < 13.9°)
θ range for the entire data collection	2° < θ < 25°
No. of measured reflections	2399
No. of unique reflections	2264
No. of observed reflections	2067
No. of parameters refined	462
Final R-factor	0.033
wR	0.087
Weighting scheme	$1/[\sigma^2(F_0^2) + (0.0472P)^2 + 0.16P]$, where $P = [F_0^2 + 2F_0^2]/3$
Final residual electron density	–0.12 < Δρ < 0.20 eÅ^{-3}
$(\Delta/\sigma)_{max}$ in the final cycle	0.809, where z H(241)
Flack parameter X	0.65

Ring *A* [C(1)C(2)C(3)C(4)C(5)C(11)] exists in a distorted chair conformation with the C(2) and C(5) atoms lying above and below the plane of the remaining four atoms [the deviation is 0.583(3) Å for C(2) and –0.675(3) Å for C(5)]. Ring *B* [C(4)C(5)C(11) C(17) NC(19)] adopts a distorted chair conformation with C(5) [–0.815(3) Å] and N [0.540(2) Å] atoms lying below and above the plane. Ring *C* [C(7)C(8) C(9)C(10) C(11)C(17)] also takes the shape of a distorted chair with the C(11) atom lying below [–0.718(2) Å] and the C(8) atom lying above [0.652(2) Å] the plane. Ring *D* [C(8)C(9)C(14)C(13)C(16)C(15)] adopts a half-boat conformation with the C(14) and C(15) atoms deviating below the plane by –0.853(3) and –0.213(3) Å, respectively. The five-membered ring *E* [C(5)C(6)C(7) C(17)C(11)] acquires a half-chair conformation with the asymmetry parameter ΔC_2[C(11)–C(17)] = 3.9 and the pseudorotation parameters Δ = 5.5° and ϕ = 53.4° [9].

Table 2. Atomic coordinates and equivalent isotropic thermal parameters (Å^2)

Atom	*x*	*y*	*z*	U^*_{eq}
O_w	1.1562(3)	0.2405(4)	1.1106(2)	0.0762(10)
O(1)	1.0877(2)	0.5436(3)	0.5842(1)	0.0607(7)
O(6)	1.3822(2)	0.3215(3)	0.9440(1)	0.0473(6)
O(7)	1.3359(2)	0.0201(2)	0.7870(1)	0.0429(6)
O(8)	1.2220(2)	0.0689(3)	0.9293(1)	0.0438(6)
O(14)	0.9719(2)	0.2065(3)	0.9405(1)	0.0465(6)
O(16)	0.8525(2)	–0.0040(3)	0.7576(2)	0.0618(8)
O(18)	1.5962(2)	0.6612(3)	0.8463(2)	0.0732(9)
N	1.3283(2)	0.2598(3)	0.6407(1)	0.0395(7)
C(1)	1.1966(3)	0.5876(3)	0.6525(2)	0.0392(9)
C(2)	1.3012(3)	0.6285(4)	0.6049(2)	0.0459(9)
C(3)	1.4242(3)	0.6500(4)	0.6731(2)	0.0491(11)
C(4)	1.4544(2)	0.4943(4)	0.7348(2)	0.0430(9)
C(5)	1.3554(2)	0.4749(3)	0.7937(2)	0.0363(7)
C(6)	1.3812(2)	0.3085(4)	0.8482(2)	0.0376(8)
C(7)	1.2823(2)	0.1815(3)	0.7961(2)	0.0336(7)
C(8)	1.1724(2)	0.1596(3)	0.8448(2)	0.0344(8)
C(9)	1.1239(2)	0.3349(3)	0.8641(2)	0.0369(8)
C(10)	1.1158(2)	0.4580(3)	0.7824(2)	0.0369(8)
C(11)	1.2229(2)	0.4503(3)	0.7293(2)	0.0327(7)
C(12)	0.9799(3)	0.4271(4)	0.7237(2)	0.0481(9)
C(13)	0.9205(2)	0.2941(4)	0.7744(2)	0.0445(9)
C(14)	0.9880(2)	0.3276(4)	0.8732(2)	0.0414(8)
C(15)	1.0704(2)	0.0397(3)	0.7931(2)	0.0428(9)
C(16)	0.9449(3)	0.1142(4)	0.7432(2)	0.0441(9)
C(17)	1.2400(2)	0.2671(3)	0.7008(2)	0.0335(7)
C(18)	1.5873(3)	0.5149(5)	0.7925(2)	0.0544(11)
C(19)	1.4531(3)	0.3298(4)	0.6782(2)	0.0455(10)
C(20)	1.3350(3)	0.0969(4)	0.5958(2)	0.0507(11)
C(21)	1.3649(7)	0.1152(6)	0.5026(3)	0.0902(22)
C(22)	1.4944(4)	0.3925(6)	0.9969(3)	0.0704(13)
C(23)	0.8501(3)	0.2127(5)	0.9584(3)	0.0578(12)
C(24)	0.7406(4)	–0.0033(9)	0.6886(4)	0.0989(23)
C(25)	1.0218(5)	0.6870(8)	0.5427(4)	0.1000(20)

* $U_{eq} = (1/3)\Sigma_i\Sigma_j U_{ij} a^*_i a^*_j \mathbf{a_i} \cdot \mathbf{a_j}$.

Table 3. Endocyclic torsion angles (deg)

C(17)–N–C(19)–C(4)	−39.7(3)	C(7)–C(8)–C(9)–C(10)	41.9(3)
C(19)–N–C(17)–C(11)	57.4(3)	C(9)–C(8)–C(15)–C(16)	17.0(3)
C(2)–C(1)–C(11)–C(5)	43.6(3)	C(15)–C(8)–C(9)–C(14)	28.8(3)
C(11)–C(1)–C(2)–C(3)	−45.7(3)	C(8)–C(9)–C(14)–C(13)	−71.0(3)
C(1)–C(2)–C(3)–C(4)	54.8(3)	C(8)–C(9)–C(10)–C(11)	−39.0(3)
C(2)–C(3)–C(4)–C(5)	−64.2(3)	C(10)–C(9)–C(14)–C(13)	49.2(2)
C(5)–C(4)–C(19)–N	40.2(3)	C(14)–C(9)–C(10)–C(12)	−29.9(2)
C(3)–C(4)–C(5)–C(11)	61.0(3)	C(9)–C(10)–C(12)–C(13)	0.6(3)
C(19)–C(4)–C(5)–C(11)	−60.9(3)	C(9)–C(10)–C(11)–C(17)	52.0(3)
C(4)–C(5)–C(11)–C(1)	−49.6(3)	C(5)–C(11)–C(17)–C(7)	53.4(2)
C(4)–C(5)–C(11)–C(17)	74.2(2)	C(5)–C(11)–C(17)–N	−70.1(2)
C(6)–C(5)–C(11)–C(17)	−41.9(2)	C(10)–C(11)–C(17)–C(7)	−63.9(2)
C(11)–C(5)–C(6)–C(7)	14.6(3)	C(10)–C(12)–C(13)–C(14)	29.1(3)
C(5)–C(6)–C(7)–C(17)	18.4(2)	C(12)–C(13)–C(14)–C(9)	−48.1(3)
C(6)–C(7)–C(17)–C(11)	−45.5(2)	C(16)–C(13)–C(14)–C(9)	70.4(3)
C(8)–(7)–C(17)–C(11)	73.9(2)	C(14)–C(13)–C(16)–C(15)	−27.8(3)
C(17)–C(7)–C(8)–C(9)	−63.7(3)	C(8)–C(15)–C(16)–C(13)	–17.7(3)

Ring *F* [C(9)C(10)C(12)C(13)C(14)] exists in a C(14)-envelope conformation with the asymmetry parameter $\Delta C_s = 1.05$, the phase angle of pseudorotation $\Delta = 34.1°$, and the maximum torsion angle $\phi = 51.6°$. The C(14) atom in this ring is disposed below the plane defined by the other four atoms [the deviation is –0.738(3) Å].

The general view of the molecule shows that the molecule is folded within itself (Fig. 2). Molecular folding of this kind is generally observed in multiple

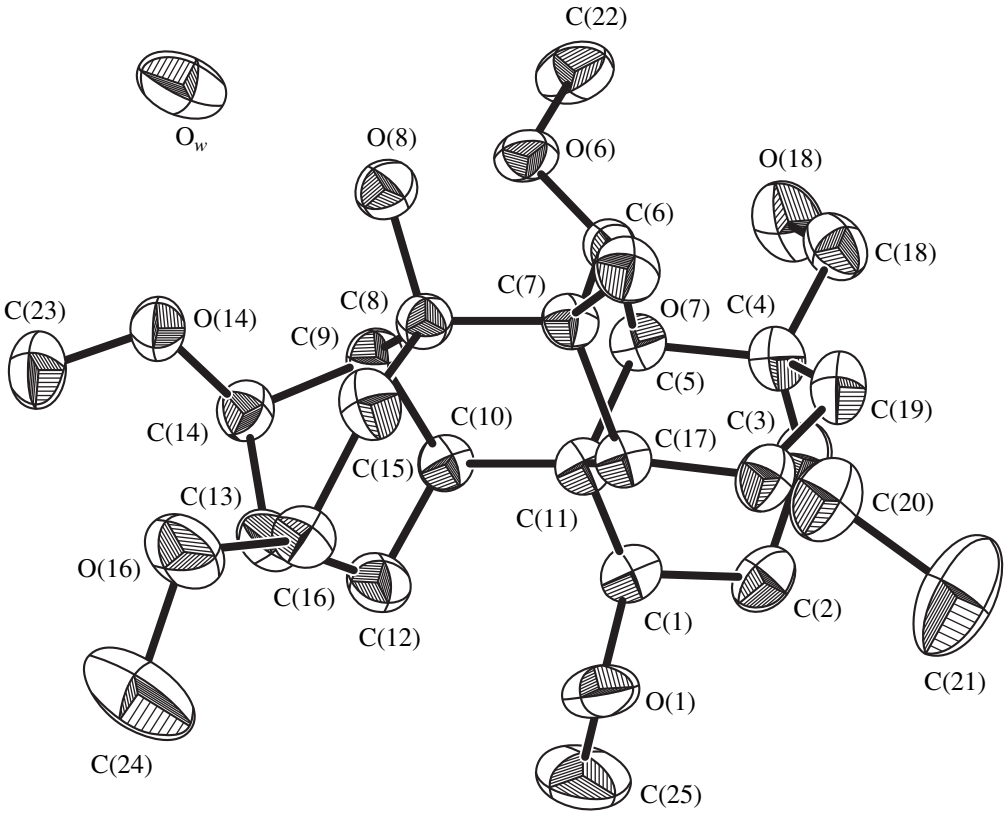

Fig. 2. A general view of the molecule with atomic labeling.

Table 4. Geometry of intra- and intermolecular hydrogen bonds

D	H	*A*	*D*–H(Å)	H…*A*(Å)	*D*…*A*(Å)	*D*–H…*A*(°)	Symmetry code
O(7)	H(7O)	O(8)	0.81	2.23	2.73	120	*x*, *y*, *z*
O(8)	H(8)	O(6)	0.86	1.86	2.64	148	*x*, *y*, *z*
O_w	H(1_w)	O(14)	0.83	2.07	2.89	169	*x*, *y*, *z*
O_w	H(2_w)	O(16)	0.82	2.06	2.84	159	2 – *x*, *y* + 1/2, 2 – *z*
O(18)	H(18O)	O_w	0.95	1.80	2.73	164	3 – *x*, *y* – 1/2, 2 – *z*

ring structures and is attributed mainly to the distortions developed in individual ring systems. The crystal structure of Royline monohydrate is stabilized by the O–H··O type intermolecular contacts involving the molecule of crystal water. The geometries of hydrogen bonds are listed in Table 4.

ACKNOWLEDGMENTS

Rajnikant is grateful to B.D. Gupta, Scientist, Natural Products Chemistry Divisions, Regional Research Laboratory, Jammu Tawi for supplying the samples. He also acknowledges the financial support received from the University Grants Commission, Government of India, New Delhi, under its COSIST Research Program, project no. F.2-3/95(COS-II).

REFERENCES

1. I. C. Chopra, J. D. Kohli, and K. L. Handa, Indian J. Med. Res. **33**, 139 (1945).
2. B. D. Gupta, private communications (Regional Research Laboratory, Jammu Tawi, India, 1996).
3. G. M. Sheldrick, *SHELXS86: Program for the Solution of Crystal Structures* (Univ. of Göttingen, Göttingen, 1986).
4. G. M. Sheldrick, *SHELXL93: Program for the Refinement of Crystal Structures* (Univ. of Göttingen, Göttingen, 1993).
5. C. K. Johnson, *ORTEP-II: A Fortran Thermal Ellipsoid Plot Program for Crystal Structure Illustrations, Report ORNL-5138* (Oak Ridge National Laboratory, Tennessee, USA, 1976).
6. K. K. Bhandary, N. Ramasubbu, B. S. Joshi, *et al.*, Acta Crystallogr., Sect. C: Cryst. Struct. Commun. **46**, 1704 (1990).
7. B. S. Joshi, H. K. Desai, S. W. Pelletier, and M. G. Newton, J. Crystallogr. Spectrosc. Res. **22**, 477 (1992).
8. P. W. Codding, Acta Crystallogr., Sect. B: Struct. Crystallogr. Cryst. Chem. **B38**, 2519 (1982).
9. C. Altona, H. J. Geise, and C. Romers, Tetrahedron **24**, 13 (1968).

Crystallography Reports, Vol. 46, No. 2, 2001, pp. 235–238. Translated from Kristallografiya, Vol. 46, No. 2, 2001, pp. 276–279.

CRYSTAL CHEMISTRY

A Prognostic Complication Scheme and Its Realization

N. L. Smirnova

Moscow State University, Vorob'evy gory, Moscow, 119899 Russia

e-mail: snl194@mail.ru

Received December 30, 1999

Abstract—A scheme of zone development is shown to be universal for systems and prognostic. The quantitative compositions of silicon–oxygen radicals and atomic positional formulas are analyzed. It is demonstrated that the systems obey the generalized law of small numbers, which is at variance with the Goldschmidt assumption that only the first four complication series are realized in the scheme. © *2001 MAIK "Nauka/Interperiodica".*

Crystallography is the science dealing with a system of chemical compounds in a completely or partially crystalline state. Tectology is the science concerned with the organization of systems, specifically with universal phenomena and rules which make it possible to simulate and, thus, to predict objects and events. Crystallography, as all other sciences, overlaps with tectology. The region of their overlap is referred to as system crystallogy.

In order to answer questions as to why a particular phenomenon or object exists and what can exist, it is necessary to construct prognostic schemes. The construction of universal schemes should account for the universal principles of system organization. The science of system organization was developed in the late 19th and early 20th centuries by A.A. Bogdanov (1873–1928) [1]. He showed that the system organization is unified and the development of a particular system occurs through the differentiation–integration. The method of zone development from the initial crystallographic symbols {*hkl*} is one of the differentiation–integration methods. This method was proposed by H. Weiss (1780–1856) and was then applied by V. Goldschmidt (1853–1933) in the form of sequences of series to systems. A scheme for the development of symbols (formulas) of the {*hk*0} zone is shown in Fig. 1. The basis of the allowed values for *h*, *k*, *l* can be extended beyond *h*, *k*, *l* = 0, 1, 2, 3 by a simple step-by-step summation of *h*, *k*, *l*, which is used in the development of a particular zone. The summation is started with the "zeroth" step for *h*, *k*, *l*, i.e., with the 010 and 110 formulas (depicted at the right and left corners of the scheme in Fig. 1). A term-by-term summation of these formulas gives the formula of a new step, viz., 120 (at the center of the scheme). The summation of 120 and 010 results in 130 at the right of the diagram, the summation of 110 and 120 gives 230 at the left of the diagram (where 130 and 230 are the formulas of the second step), etc.

Goldschmidt [2] divided the zone symbols into series (steps) of different ranks: N_0, N_1, N_2, N_3, N_4, …, N_n. The simpler the series and the closer it to the origin of the sequence, the higher the rank. In other words, the smaller the number *n*, the higher the rank. Series of ratios belong to the aforementioned numerical series. These series can consist of terms which are written as formulas composed of the numbers (for example, 1/1 is represented in the form of 11; 1/10, in the form of 1.10; etc.): N_0 (10, 01), N_1 (10, 11, 01), N_2 (10, 21, 11, 12, 01), N_3 (10, 31, 21, 32, 11, 23, 12, 13, 01), and N_4 (10, 41, 31, 52, 21, 53, 32, 43, 11, 34, 23, 35, 12, 25, 13, 14, 10). The number of terms in the series is determined by the relationship $C_n = 2^n + 1$. According to Goldschmidt, these series are referred to as the complication series. He noted that a particular complication series differs from other infinite series in that its new terms are inserted between the available terms rather than being added to them at the end of the series. Similar series were also obtained by mathematician Brokochi (see [2] and references therein).

A system of series was used in our earlier work [3] for the investigation into the distribution of formulas describing faces, reflections, and binary compositions. Unlike the complete series, we analyzed only half series. Hence, the initial series N_0 was written as (11, 01) or (110, 010) for face symbols. In each new series, we considered only new formulas without the division sign (12 rather than 1/2). The complex formulas containing a common divisor were represented in the form of simple formulas with an exponent equal to a divisor (for example, 22 was written as 11^2). Exponents were given only for the realized formulas. Therefore, our table is a modified variant of the Weiss–Goldschmidt table. The number of formulas in the *n*th step is equal to 2^{n-1}. This relationship differs from the Goldschmidt expression, because the initial symbols in our case were 110 and 010 (for half-series) rather than 100 and 010. The step numbers are specified on the left

1063-7745/01/4602-0235$21.00

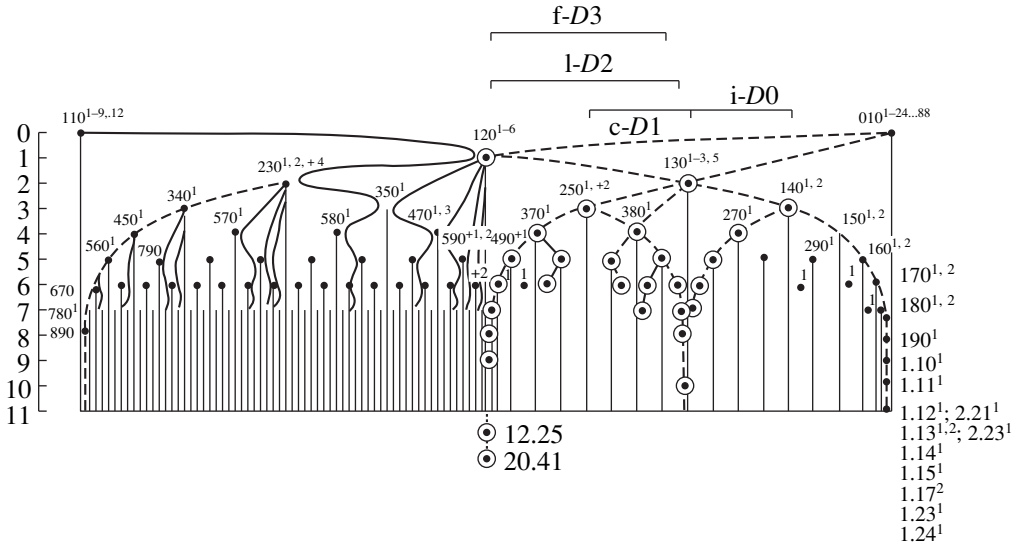

Fig. 1. A scheme for development of the formulas of the *hk*0 zone and their realization (designations are given in the text).

vertical scale in Fig. 1, solid lines correspond to selected Fibonacci sequences, dashed lines represent arithmetic series, and exponents indicate atomic positional formulas.

According to Goldschmidt, the frequency of occurrence of the zeroth series (n = 0) is the largest. The fourth series is so feeble that it occurs extremely rarely [1]. The frequency of occurrence and the importance of the fifth and higher series are so negligible that the fifth series virtually does not exist. The intensity (importance) of terms in a series decreases with an increase in the series number. Goldschmidt believed that results obtained would be also valid for other systems (which is in agreement with Bogdanov's inference that the organization of all systems is unified). The Goldschmidt proposition correlates with the parsimony law: the number of essentially different constituents of a system is small (four series).

However, as was shown earlier in [3], not all the criteria follow this law. Let us confirm our result by new examples.

The atomic positional formulas can be derived from the Shubnikov formulas. Each of these formulas consists of several modules p_k, where the symbol p is the number of atomic positions with the same multiplicity and the index k is the multiplicity. A set of the k multiplicities that correspond to a given atom was earlier termed the alphabetic Shubnikov formula, and a set of the p symbols was referred to as the positional formula [4]. For example, in the Mg_2Zn_{11} structure, the Mg atoms occupy 6(*f*) orbits and the Zn atoms fill the 1(*b*), 6(*g*), 6(*e*), 8(*i*), and 12(*k*) orbits. Correspondingly, the Shubnikov formula for the Mg atom can be written in the form of 1_6, and the formula for the Zn atom, in the form of $1_12_61_81_{12}$; in this case, the positional formulas (composed of the p symbols) take the form of 1 and 1112 (1_32), respectively. Only 158 positional formulas comprised of numbers 1–6 (i.e., their arity is equal to 1–6) are deduced for thousands of atoms in crystal structures presented in [5]. Figure 1 shows 34 single- and 64 double-arity (binary) positional formulas which consist of two numbers (zero in the first and last places is disregarded). The first and second numbers correspond to the smaller and larger p values, respectively. Five formulas that are absent among the binary formulas but have additional symbols in the 3- and 4-arity formulas are marked with the plus sign. It is found that all the formulas of the first four steps are realized without exceptions, even though the fourth step (the fifth series), according to Goldschmidt, is not realized. Moreover, the formula 0.88.0 corresponds to the 88th step (the 89th series).

In addition to the complication series, the formulas form sequences that consist of the simplest terms and series of formulas obtained from the first terms by consecutive addition of the same simplest formula, i.e., the difference. For example, 110(010), 120, 130, 140, 150, …, or 010(010), 010^2, 010^3, … . This is the longest series. When going along this series, all the positional formulas up to the formula 0.24.0 can be realized (the fused part) and the range up to the formula 0.88.0 involves both realized and nonrealized formulas (the "beaded" part according to Bogdanov).

Let us consider the coefficients in binary formulas of silicon–oxygen radicals (the ratio between the numbers of Si and O atoms) [6] in terms of the system of formulas (Fig. 1). The realized formulas are marked with circles. It is easy to see that formulas for the coefficients of silicate radicals in the composition range 120–140 completely fill four steps and form the three most representative series 140(130), 130(120), and 250(130) and also several short series. The oddest

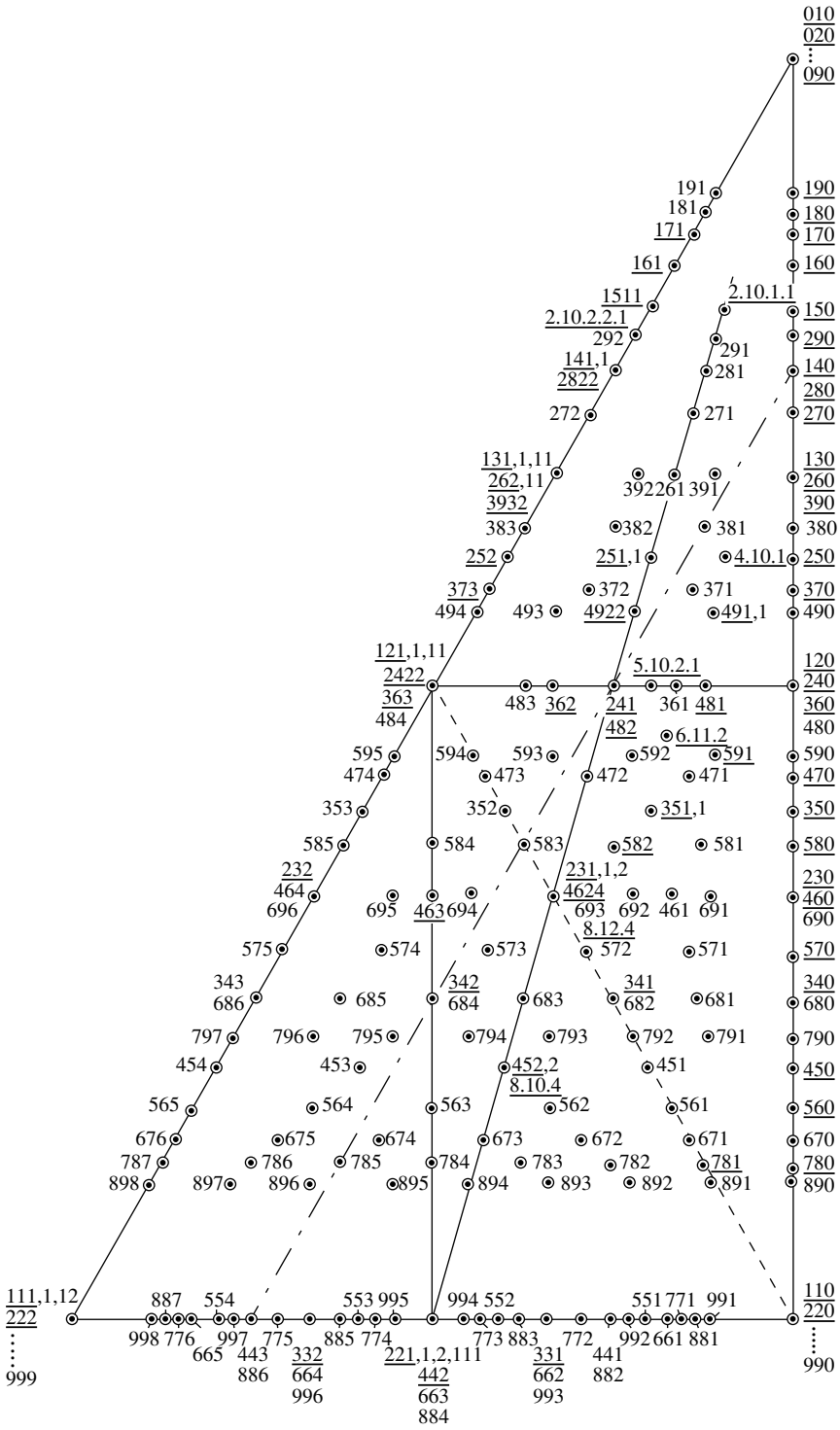

Fig. 2. A scheme of ternary formulas and their realization (designations are given in the text).

ratios regularly fall into sequences in the scheme. Undoubtedly, new ratios will also fit well in this scheme. The formulas that correspond to framework (f), layered (l), chain (c), and island (i) silicates are indicated.

The zone with the one third constant index equal to zero was considered above. Now, we turn our attention to the system of zones in which the third index is equal to 1–9. The prognostic scheme that involves indices 1–9 for independent region of the symmetry group *m*3*m* (a total of 219 formulas) is depicted in Fig. 2. This system was not analyzed by Goldschmidt. The lines indicate the typical zones which contain typical series. Selected binary and 35 ternary (3-arity) positional for-

mulas (out of 158 formulas we revealed) which consists of three numbers are underlined. Among these formulas, four formulas involve symbols .10, .11, and .12. Twenty quaternary (4-arity) formulas are also shown in Fig. 2. Some of them are formed from the ternary formulas by adding a fourth symbol (given after the comma). Certain quaternary formulas are not follows from the ternary formulas. In this case, the comma is absent. Four 5- and one 6-arity formulas are derived. The third, fourth, fifth, and sixth symbols are equal to unity in the majority of cases and two in rare cases and do not exceed four in the other cases.

Thus, the number of realized formulas in all the systems (marked with a particular symbol) sharply decreases with an increase in the indices *h*, *k*, *l*. However, it should be noted that the formulas realized in nature with large constituent numbers are much more frequently occur when going along the series formed according to the following rule. Let the first term of the series be the formula consisting of the simplest numbers, for example, 010. To this formula, we term by term add the difference—the constant gradient $d = (m, n, s)$ which characterizes the given series. By this means, we obtain the second formula $m, 1 + n, s$. The addition of the same difference d to the latter formula gives the third term of the series and so on. The arithmetic series is written as *hkl*(*mns*).

The results obtained in this work confirm the validity of the inference made in [3]: according to the law of small numbers (parsimony), the formulas realized in nature with symbols larger than several unities (1–4) are nonuniformly distributed and form arithmetic series in which the initial formulas and the differences are composed of small numbers.

The proposed scheme is prognostic. All new formulas will regularly fall into this scheme. The scheme can also be used to investigate the relations in other systems.

REFERENCES

1. A. A. Bogdanov, *Essays in Tectology* (Seaside, Calif., Intersystem Publ., 1984; Ékonomika, Moscow, 1989), Vols. 1, 2.
2. V. Goldschmidt, *Über Complikation und Displikation* (Carl Winters Universität, Heidelberg, 1921; Geological Inst., Kola Research Center, Russ. Acad. Sci., Apatity, 1998), p. 6.
3. N. L. Smirnova and N. V. Belov, Dokl. Akad. Nauk SSSR **279** (3), 633 (1984) [Sov. Phys. Dokl. **29**, 866 (1984)].
4. N. L. Smirnova, Acta Crystallorg. Suppl., 441 (1999).
5. P. Villars and L. D. Calvert, *Pearsons Handbook of Crystallographic Data for Intermetallic Phases* (Metals Park, Ohio, 1985).
6. G. B. Bokiĭ, *Systematization of Natural Silicates* (VINITI, Moscow, 1998), p. 47.

Translated by O. Borovik-Romanova

Crystallography Reports, Vol. 46, No. 2, 2001, pp. 239–245. Translated from Kristallografiya, Vol. 46, No. 2, 2001, pp. 280–286.

CRYSTAL CHEMISTRY

Concentration Dependences of the Unit-Cell Parameters of Nonstoichiometric Fluorite-Type $Na_{0.5-x}R_{0.5+x}F_{2+2x}$ Phases (R = Rare-Earth Elements)

P. P. Fedorov*, V. B. Aleksandrov†*, O. S. Bondareva†*, I. I. Buchinskaya*, M. D. Val'kovskiĭ, and B. P. Sobolev***

** Shubnikov Institute of Crystallography, Russian Academy of Sciences, Leninskiĭ pr. 59, Moscow, 117333 Russia*

*** Kurnakov Institute of General and Inorganic Chemistry, Russian Academy of Sciences, Leninskiĭ pr. 31, Moscow, 117907 Russia*

Received October 14, 1999

Abstract—Unit-cell parameter a of the cubic phases with a varying composition $Na_{0.5-x}R_{0.5+x}F_{2+2x}$ (R = Gd–Lu and Y) and with a fluorite-type structure, is described within an accuracy of ±0.003 Å, by the formula $a = 4.454 + 0.874r_3 + x(6.7238r_3 - 7.259)$ where r_3 is the Shannon "crystal ionic radius" R^{3+} at c.n. = 8. © *2001 MAIK "Nauka/Interperiodica".*

INTRODUCTION

The compounds with a varying composition $Na_{0.5-x}R_{0.5+x}F_{2+2x}$ and a fluorite-type structure formed in the NaF–RF_3 systems, where R = Pr–Lu and Y, are high-temperature nonstoichiometric phases thermodynamically unstable at room temperature. In some of these systems, the processes of phase decomposition and ordering are somewhat decelerated and, therefore, these phases can be grown in the form of single crystals, which are rather promising matrices for solid-state lasers [1, 2], fluoride-ion-based electrolytes [3], and luminescent materials [4, 5]. These phases are also very good model objects for studying various manifestations of nonstoichiometry in fluoride systems.

The NaF–RF_3 systems have been studied in a number classical works by Thoma and his coworkers [6–11], who managed to construct a number of complete phase diagrams. Unfortunately, these studies also have some shortcomings. First, the authors failed to avoid partial pyrohydrolysis of the samples enriched with rareearth trifluorides. This is seen, in particular, from erroneous morphotropy scheme in the RF_3 series with polymorphic transitions for TbF_3, DyF_3, and HoF_3 [12, 13]. Moreover, an insufficient number of the studied samples and attempts to fit the data obtained to the chosen model (the authors postulated the existence of the compounds with the composition $5NaF \cdot 9RF_3$ possessing a high-temperature cubic and low-temperature ordered fluorite-like modifications) resulted in a rather schematic phase diagrams and even in a violation of the rule of phases in some occasions (the systems with Pr–Tb trifluorides). We studied the phase equilibria in a number of NaF–RF_3 systems [14–19] and revealed considerable deviations from the Thoma scheme (different compositions and symmetries of the ordered fluorite-like phases, essentially different coordinates of the maxima on the melting curves of the $Na_{0.5-x}R_{0.5+x}F_{2+2x}$ phases with the fluorite structure, etc.). The same can also be said about the lattice parameters of the fluorite phases, the knowledge of which is very important, e.g., for fast determination of the compositions of the synthesized single crystals.

Our present study was aimed at obtaining a consistent system of the a parameters of the cubic lattices for the fluorite-type nonstoichiometric phases formed in the NaF–RF_3 systems and establishing the general analytical expression which can describe the dependence of the lattice parameter on the parameters of the chemical composition.

Table 1. Impurity concentration in yttrium fluoride, wt %

Nd	<0.0005	Cu	<0.00005
Sm	0.0002	O	0.027
Gd	0.0005	Si	<0.001
Tb	0.0001	Mn	<0.00005
Dy	0.0002	Co	<0.00005
Ho	<0.001	Ni	0.00005
Tm	0.0005	Ti	<0.00005
Fe	0.0005	Cr	0.00005

† Deceased.

Table 2. Compositions, lattice parameters, and conditions for obtaining fluorite-type $Na_{0.5-x}R_{0.5+x}F_{2+2x}$ solid solutions (single-phase samples)

R	RF_3, mol %	*x*	*a*, Å	Annealing temperature	Annealing time
Gd	64	0.14	5.601	800	100
Tb	62	0.12	5.564	800	100
	60	0.10	5.5525	800	100
Dy	54	0.04	5.499	800	100
	56	0.06	5.508	800	100
	58	0.08	5.521	800	100
	60	0.10	5.532	800	100
	62	0.12	5.5465	800	100
	64	0.14	5.557	800	100
Ho	58	0.08	5.507	800	100
	60	0.10	5.517	800	100
	62	0.12	5.528	800	100
Er	52	0.02	5.464	800	100
	54	0.04	5.473	800	100
	56	0.06	5.481	800	100
	58	0.08	5.491	800	100
	60	0.10	5.498	800	100
	62	0.12	5.507	800	100
	63	0.13	5.514	800	100
Tm	52	0.02	5.455	800	100
	54	0.04	5.460	800	100
	56	0.06	5.468	800	100
	58	0.08	5.475	800	100
	60	0.10	5.481	800	100
	62	0.12	5.489	800	100
	63	0.13	5.495	800	100
Yb	50*	0	5.437	–	–
	52	0.02	5.441	720	360
	56	0.06	5.456	720	360
	58	0.08	5.458	720	360
	60	0.10	5.464	720	360
	60	0.10	5.466	550	720
	62	0.12	5.471	720	360
	62	0.12	5.476	550	720
Lu	48	–0.02	5.425	570	500
	56	0.06	5.443	700	100
Y	54	0.04	5.475	850	75
	56	0.06	5.486	850	75
	62	0.12	5.515	850	75
	62	0.12	5.515	660	215
	62	0.12	5.517	900	77
	64	0.14	5.524	850	75

* Sample was obtained by precipitation from an aqueous solution at room temperature.

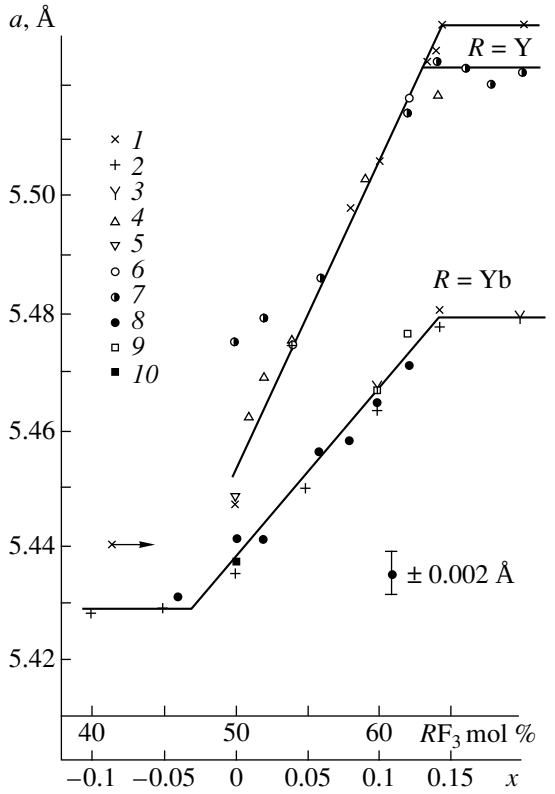

Fig. 1. Lattice parameters a of the fluorite-type $Na_{0.5-x}R_{0.5+x}F_{2+2x}$ solid solutions (R = Y, Yb): (*1*) Thoma data [7, 9]; (*2*) Schmutz data [20], annealing at 700°C; (*3*) Schmutz data [20], annealing at 900°C; (*4*) Pontonnier data [21]; (*5*) Hund data [22]; (*6*) our data, annealing at 900°C; (*7*) our data, annealing at 850°C; (*8*) our data, annealing at 720°C; (*9*) our data, annealing at 550°C; and (*10*) our data, remelting in the fluorinating atmosphere upon precipitation from the aqueous solution.

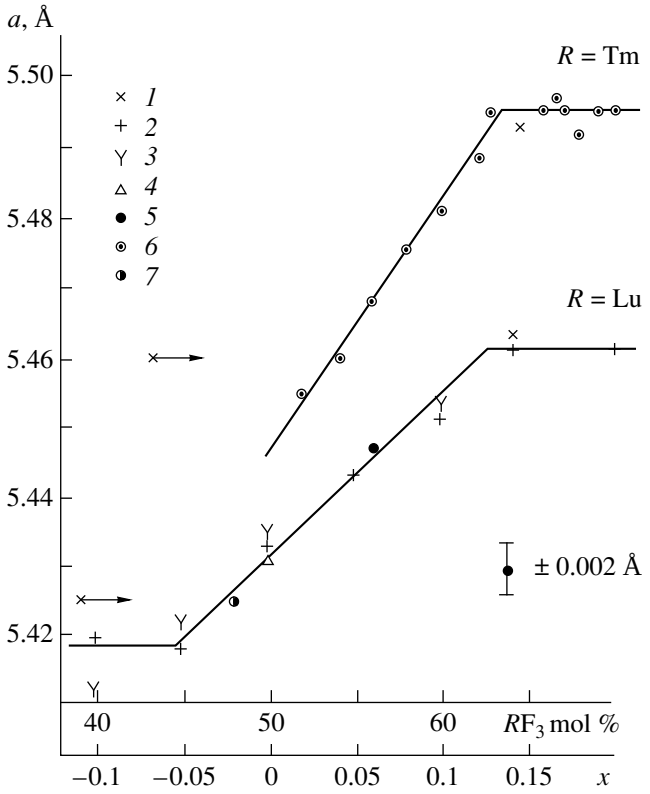

Fig. 2. Lattice parameters a of the fluorite-type $Na_{0.5-x}R_{0.5+x}F_{2+2x}$ (R = Tm, Lu) solid solutions: (*1*) Thoma data [9]; (*2*) Schmutz data [20], annealing at 700°C; (*3*) Schmutz data [20]; annealing at 900°C; (*4*) Schmutz data, annealing at 550°C; (*5*) our data, annealing at 700°C; (*6*) our data, annealing at 800°C; and (*7*) our data, annealing at 550°C.

EXPERIMENTAL

The initial chemicals were extra-pure-grade NaF and rare-earth trifluorides produced by the GIREDMET experimental plant in Pyshminsk with the main-component concentration ~99.9%. The typical concentrations of various impurities are indicated in Table 1. In order to purify the crystals of oxygen and adsorbed moisture, the starting materials were remelted in the fluorinating atmosphere of the products of Teflon pyrolysis in a vacuum setup. The samples of $Na_{0.5-x}R_{0.5+x}F_{2+2x}$ solid solutions were synthesized by the method described in [15–17]. The thoroughly ground mixtures were packed into copper or nickel capillary vessels and were placed into a sealed metal container (arch welding). To create the fluorinating atmosphere in the container, we also added $BaF_2 \cdot HF$ and Teflon shavings. Then the containers were annealed and quenched in water. The annealing modes are indicated in Table 2.

The parameters a of the cubic lattice were determined on AFV-202E (Toshiba) and HZG-4 (Karl Ziess, Jena) diffractometers using the (440), (531), and (660) reflections and a Si inner standard. The typical error in the a parameter calculated from the Student distribution with the confident probability of 95% was ±0.002 Å.

EVALUATION OF EXPERIMENTAL DATA

The lattice parameters of one-phase samples of various compositions are listed in Table 2. The known data and the data obtained for NaF-systems with YF_3, TmF_3, YbF_3, and LuF_3 are given in Figs. 1 and 2. Within the homogeneity ranges of the $Na_{0.5-x}R_{0.5+x}F_{2+2x}$ phases, the parameters of the cubic lattice vary linearly with the change in the composition (in mol %). The constancy of the unit-cell parameters in the regions with high RF_3 concentration corresponds to two-phase regions containing saturated $Na_{0.5-x}R_{0.5+x}F_{2+2x}$ solid solutions. At high NaF concentrations, the deviations from the linear dependence are caused by melting during annealing at the corresponding temperature (the Schmutz data for annealing at 900°C, < 50% LyF_3 [20]), and also by the partial fluorite–gagarinite transformation during

Table 3. Parameters which describe the concentration dependences of the lattice parameters for the fluorite $Na_{0.5-x}R_{0.5+x}F_{2+2x}$ phases

R^{3+}	r_3, Å	r^*_{av}, Å	a_0, Å	k, Å/mol	a_0, calculated by Eq. (3)	ε, Å/mol	ε, calculated by Eq. (6)	k_1, calculated by Eq. (7)	k_2, calculated by Eq. (8)
Pr	1.266	1.293			5.5609		0.697	1.259	1.2533
Nd	1.249	1.2845			5.5461		0.6615	1.1455	1.1390
Sm	1.219	1.2695			5.5198		0.598	0.9435	0.9373
Eu	1.206	1.263			5.5085		0.5705	0.8560	0.8499
Gd	1.193	1.257		(0.742)	5.4971	(0.530)	0.545	0.7725	0.7625
Tb	1.180	1.250		(0.693)	5.4858	(0.521)	0.515	0.680	0.6751
Dy	1.167	1.2435	5.4739	0.5927	5.4744	0.488	0.487	0.5915	0.5876
Ho	1.155	1.2375	5.4640	0.5375	5.4639	0.475	0.461	0.5095	0.5070
Er	1.144	1.232	5.4550	0.4419	5.4543	0.441	0.4365	0.433	0.4330
Tm	1.134	1.227	5.4460	0.3662	5.4455	0.416	0.415	0.365	0.3658
Yb	1.125	1.223	5.4369	0.2984	5.4377	0.393	0.397	0.3065	0.3052
Lu	1.117	1.219	5.4308	0.2318	5.4307	0.370	0.379	0.2505	0.2515
Y	1.159	1.2395	5.4530	0.5357	5.4674	0.469	0.469	0.5355	0.5339

* $r_{av} = 0.5(r_3 + r_{Na}) = 0.5(r_3 + 1.32)$.

quenching from the high-temperature state (our data, 50–52 mol % YF_3, annealing at 850°C).

The Thoma data on the NaF–YF_3 system [7] were confirmed by Pontonnier [21] and by our studies. For the $NaYF_4$ composition, Hund [22] obtained a correct value, a = 5.448 Å. However, for other systems, the boundary values of the lattice parameter a indicated by Thoma [9] are given mainly for two-phase regions; therefore, the linear interpolation of the boundary values given in [9] cannot characterize the parameters of the cubic lattice of the $Na_{0.5-x}R_{0.5+x}F_{2+2x}$ solid solutions. According to our data, the composition $5NaF \cdot 9RF_3$ (64.3 mol % RF_3) is located in the two-phase region (including the composition with the ordered fluorite-like phases) for all the systems studied beginning with NaF–DyF_3. Thus, in the course of the further analysis, the Thoma data were invoked only for the NaF–YF_3 system, whereas in all the other cases, these data were excluded from consideration. The mathematical processing was performed on the data for one-phase fluorite samples in the systems studied, on the Schmutz data obtained for the NaF–YbF_3 and NaF–LuF_3 systems [20], and on the Pontonnier data for the NaF–YF_3 system [21].

SEARCH FOR THE APPROXIMATING EXPRESSION

Using the experimental data and the least squares procedure, we obtained the concentration dependences of the lattice parameters for the $Na_{0.5-x}R_{0.5+x}F_{2+2x}$ phases (R = Dy–Lu and Y) in the form

$$a = a_0 + kx. \quad (1)$$

The calculated a_0 and k values are listed in Table 3. For R = Gd and Tb, we obtained the a values only for a narrow concentration range (Table 2) (under the quenching conditions and lower RF_3 concentrations, the material decomposed with the separation of the low-temperature gagarinite phase). These data were insufficient for establishing of the dependence similar to Eq. (1).

Further analysis was made in the way described in [23]. Using the system of "crystal" ionic radii [24] based on the ionic radius F^- = 1.19 Å for c.n. = 8, we obtained that the compositions with $x = 0$ ($Na_{0.5}R_{0.5}F_2$) correspond to the stoichiometry of fluorite MF_2 and, in accordance with the Hund model [22], it was possible to expect that the Na^+ and R^{3+} cations would statistically occupy the a positions in the sp. gr. $Fm\bar{3}m$ (occupied by M^{2+} cations in the fluorite structure). It was also expected that, similar to the case of the MF_2 compounds, the lattice parameter a_0 of the structures with such compositions would also be dependent on the (average) ionic radius of the cation.

For the MF_2 fluorite structure, the following correlation dependence was suggested in [23]:

$$a = 2.30 + 2.50r_2, \quad (2)$$

where r_2 are the ionic radii of M^{2+} [24]. However, the use of this formula for the compositions $Na_{0.5}R_{0.5}F_2$, where r_2 is substituted by the average value $0.5(r_1 + r_3)$, $r_1 = r_{Na}$ = 1.32 Å, and r_3 are the ionic radii of R^{3+} yields

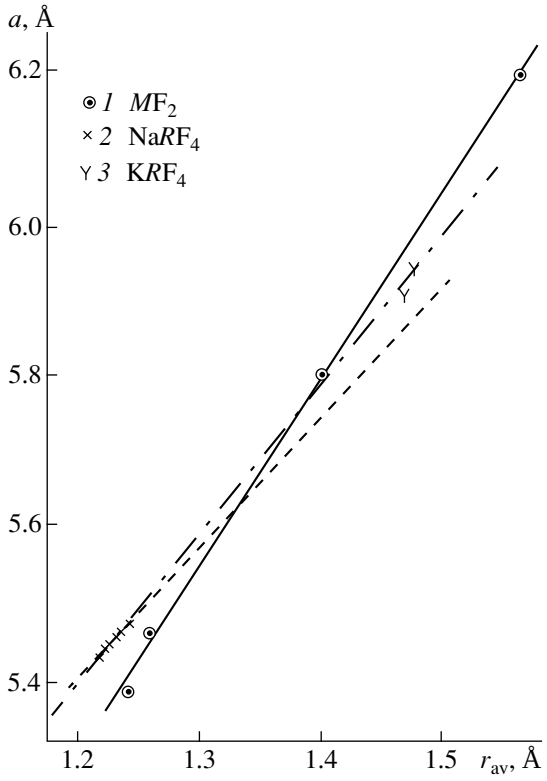

Fig. 3. Lattice parameter a of the fluorite-type phases of the compositions (*1*) MF_2, (*2*) $Na_{0.5}R_{0.5}F_2$, and (*3*) $K_{0.5}R_{0.5}F_2$ versus the average cationic radius, r_{av}. Solid line indicates the data calculated by Eq. (2); dashed line, by Eq. (3); chain–dotted line, by Eq. (4).

quite unrealistic results (Fig. 3). Using the a_0-values obtained from Eq. (1) processed by the least squares method, we arrive at the following dependence with the correlation coefficient 0.999:

$$a_0 = 4.4543 + 0.8741 r_3. \quad (3)$$

In what follows, we shall use just this dependence. The parameter a_0 for other rare-earth elements (Table 3) can be evaluated from Eq. (3). For R = Gd, Tb, we managed to estimate the k-values (Table 3) from $a_{0,\,calcd}$ and our experimental data (Table 2).

One should also pay attention to the formula

$$a_0 = 2.99 + 2.00 r_{av}, \quad (4)$$

which satisfactorily (within an accuracy of ±0.005 Å) describes the lattice parameter not only of the fluorite $N_{0.5}R_{0.5}F_2$ phases but also of KRF_4 (R = La, Ce) with the use of data [25] (Fig. 3).

Analyze the dependence of k on ionic radii of cations. This dependence is shown in the graphical form in Fig. 4 together with the coefficients of the concentration dependences of the lattice parameter for the fluorite-type solid solutions $M_{1-x}R_{1+x}F_{2+x}$ [23] and $Ca_{1-x}X_{1+x}F_{2+2x}$(X = Th, U, Zr, Hf) [26–28].

The change in the lattice parameters of the $Na_{0.5-x}R_{0.5+x}F_{2+2x}$ solid solutions with the variation of the composition is explained, first of all, by the different dimensions of isomorphous cations (in our case, Na^+ and R^{3+}) and the loosening effect of the interstitial fluoride ions, which have to "accompany" the RE cat-

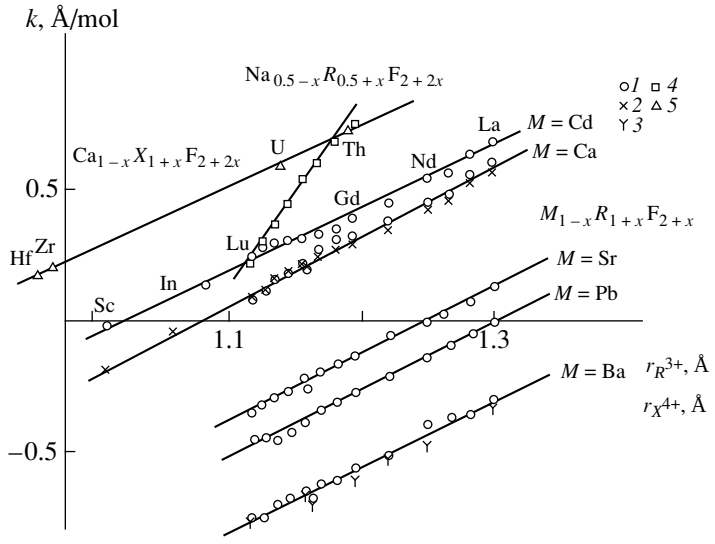

Fig. 4. Coefficient k in the concentration dependences $a = a_0 + kx$ of the lattice parameters of the fluorite-type phases as functions of ionic radius of the R^{3+} cations in the systems: (*4*) $Na_{0.5-x}R_{0.5+x}F_{2+2x}$ and (*1–3*) $M_{1-x}R_{1+x}F_{2+x}$ (M = Ca, Sr, Ba, Pb; data of different authors [23]) and (*5*) $Ca_{1-x}X_{1+x}F_{2+2x}$ (X = Th [26], U [27], Zr [27, 28], and Hf [28]).

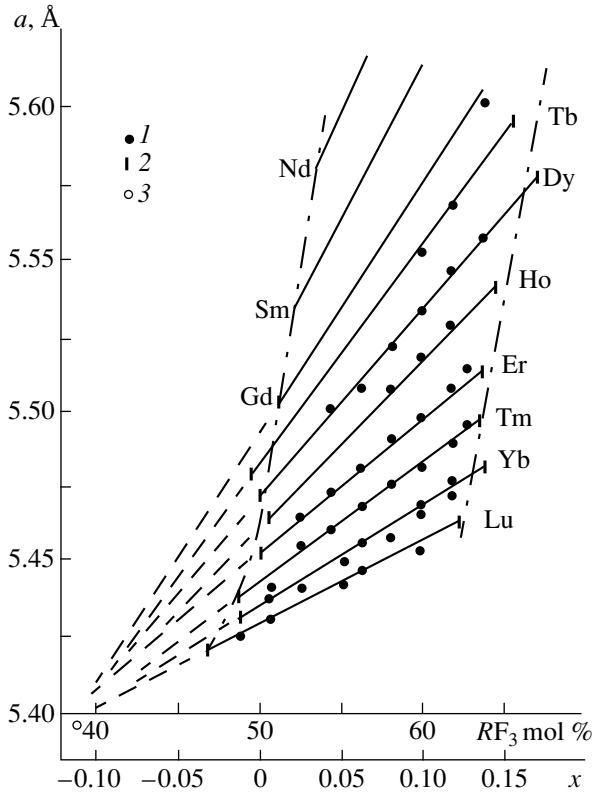

Fig. 5. Lattice parameters a of the fluorite-type phases of the $Na_{0.5-x}R_{0.5+x}F_{2+2x}$ solid solutions: (*1*) experimental data, (*2*) values for the concentration boundaries for the existence range of $Na_{0.5-x}R_{0.5+x}F_{2+2x}$, (*3*) the common point of the functions $a(x)$. The solid lines were calculated by Eq. (7), the dashed lines were extrapolated outside the existence range of the phase, the chain–dotted line represents the boundaries extrapolated outside the existence ranges of the phase.

ions in order to preserve the electrical neutrality of crystals (to each R^{3+} ion there correspond two additional fluoride ions). The fine distortions of the anionic sublattice [29] can be neglected [29]. The efficiency of such a crude approach was demonstrated on the $M_{1-x}R_{1+x}F_{2+x}$ solid solutions [23]. Unlike heterovalent isomorphism in $M_{1-x}R_{1+x}F_{2+x}$, the heterovalent isomorphism in the $Na_{0.5-x}R_{0.5+x}F_{2+2x}$ solid solutions is accompanied by the appearance of two interstitial anions per each cation according to the scheme $Na^+ \longleftrightarrow R^{3+} + 2F^-$. A similar situation is also observed in the $M_{1-x}X_{1+x}F_{2+2x}$solid solutions (the substitution mechanism $M^{2+} \longleftrightarrow X^{4+} + 2F^-$), which justifies the use of these solid solutions in our analysis.

Thus, one can write the following equation for $Na_{0.5-x}R_{0.5+x}F_{2+2x}$:

$$k = \lambda(r_3 - r_1) + 2\varepsilon. \quad (5)$$

For $M_{1-x}R_{1+x}F_{2+x}$, we obtained the following value [23]: $\lambda = 2.502$ Å/mol; parameter ε for an interstitial fluoride ion is described by the equation $\varepsilon = 0.794r_2^{-2.094}$ Å/mol. As is seen from Fig. 4, parameter λ (proportional to the difference between the ionic radii of isomorphous cations) does not change its value upon the substitution of bivalent cations to tetravalent ones (i.e., at the difference in the valences equal to two). Thus, one can assume that $\lambda = 2.50$ also for the $Na_{0.5-x}R_{0.5+x}F_{2+2x}$ solid solutions. The ε values approximated by the equation

$$\varepsilon = -0.688 + 12.411\log(r_{av}) \quad (6)$$

with the correlation coefficient 0.988 are given in Table 3. The values calculated by Eq. (6), ε_{calc}, are also given in Table 3.

Thus, the final equation for the $Na_{0.5-x}R_{0.5+x}F_{2+2x}$ solid solutions has the form

$$a = 4.4543 + 0.874r_3 + x[2.5(r_3 - r_{Na}) + 2(-0.688 + 12.411\log r_{av})] \quad (7)$$

or

$$a = 4.4543 + 0.874r_3 + x[2.5r_3 + 24.822\log(0.5r_3 + 0.62) - 4.476]. \quad (7a)$$

The k_1 values calculated by Eq. (7) are also indicated in Table 3.

It should be noted that, although the ε values thus calculated are rather close to the values obtained in [23] for the $M_{1-x}R_xF_{2+x}$ solid solutions, Eq. (5) for these solid solutions has an anomalous form, because the contribution of the interstitial ions increases with an increase of the lattice parameter. This seems to be associated with the change in the atomic structure of the solid solution depending on the rareearth element used. Therefore, we had to search for a simpler expression for the lattice parameter as an alternative to Eq. (7).

THE SECOND APPROXIMATING EXPRESSION

The graphic analysis of the functions $a(x)$ (Fig. 5) shows that they all almost converge at one point with the coordinates $x = -0.13$, $a = 5.398$ Å; i.e., they form a "beam." Using Eq. (3), we arrive at the equation

$$a = 5.398 + (6.7238r_3 - 7.259)(x + 0.13) \quad (8)$$

or

$$a = 4.454 + 0.874r_3 + x(6.7238r_3 - 7.259). \quad (8a)$$

The values of the angular coefficients k_2 calculated by Eq. (8a) are also given in Table 3.

The accuracy of Eqs. (7) and (8) is not lower than 0.003 Å, which is seen from Fig. 3, where the lines calculated by both equations almost coincide. Thus, both approximating equations can be used in practice (i.e., in chemical analysis, calculation of densities and refractions, etc.). Although the physical sense of Eq. (8) is not

quite clear, it has some advantages because of its simple form. The question about the accuracy of the above equations in the application to the fluorite phases in the NaF–RF_3 systems with other rare-earth elements (R = Pr–Sm), where all our attempts to quench the one-phase samples were unsuccessful, is still open.

REFERENCES

1. Kh. S. Bagdasarov, A. A. Kaminskiĭ, and B. P. Sobolev, Kristallografiya **13** (5), 900 (1968) [Sov. Phys. Crystallogr. **13**, 779 (1968)].
2. M. Yu. Sharonov, A. L. Bratus, B. K. Sevastyanov, *et al.*, Opt. Commun. **111**, 245 (1994).
3. N. I. Sorokin, A. K. Ivanov-Shitz, L. L. Vistin', and B. P. Sobolev, Kristallografiya **37** (2), 421 (1992) [Sov. Phys. Crystallogr. **37**, 217 (1992)].
4. D. M. Roy and R. Roy, J. Electrochem. Soc. **111** (4), 421 (1964).
5. T. Kano, H. Yamamoto, and Y. Omoto, J. Electrochem. Soc. **119** (11), 1561 (1972).
6. R. E. Thoma, G. M. Hebert, H. Insley, and C. F. Weaver, in *Proceedings of the 3rd Conference on Rareearth Research, April 21–24, 1963* (Gordon and Breach, New York, 1963), p. 290.
7. R. E. Thoma, G. M. Hebert, H. Insley, and C. F. Weaver, Inorg. Chem. **2**, 1005 (1963).
8. R. E. Thoma, in *Proceedings of the 4th Rareearth Research Conference, Phoenix, Arizona, 1965*, p. 561.
9. R. E. Thoma, H. Insley, and G. M. Hebert, Inorg. Chem. **5** (7), 1222 (1966).
10. R. E. Thoma, in *Progress in the Science and Technology of the Rareearths*, Ed. by L. Eyring (Pergamon, Oxford, 1966), Vol. 2, p. 90.
11. R. E. Thoma, Rev. Chim. Miner. **10**, 363 (1973).
12. R. E. Thoma and G. D. Brunton, Inorg. Chem. **5** (11), 1937 (1966).
13. P. P. Fedorov and B. P. Sobolev, Kristallografiya **40** (2), 315 (1995) [Crystallogr. Rep. **40**, 284 (1995)].
14. P. P. Fedorov, B. P. Sobolev, and S. F. Belov, Izv. Akad. Nauk SSSR, Neorg. Mater. **15** (5), 816 (1979).
15. P. P. Fedorov, A. V. Rappo, F. M. Spiridonov, and B. P. Sobolev, Zh. Neorg. Khim. **28** (3), 744 (1983).
16. L. N. Pavlova, P. P. Fedorov, L. A. Ol'khovaya, *et al.*, Zh. Neorg. Khim. **34** (8), 2168 (1989).
17. P. P. Fedorov, L. R. Pavlova, L. A. Ol'khovaya, *et al.*, Zh. Neorg. Khim. **35** (11), 2948 (1990).
18. P. P. Fedorov, I. I. Buchinskaya, A. A. Bystrova, *et al.*, Zh. Neorg. Khim. **41** (10), 1715 (1996).
19. P. P. Fedorov, Zh. Neorg. Khim. **44** (11), 1791 (1999).
20. H. Schmutz, Thesis (Institut fur Radiochemie, Karlsruhe, 1966).
21. L. Pontonnier, Thesis (L'Universite Scientifique et l'Institute National Polytechnique, Grenoble, 1985); L. Pontonnier, G. Patrat, S. Aleonard, *et al.*, Solid State Ionics **9/10**, 549 (1983).
22. F. Hund, Z. Anorg. Allg. Chem. **261**, 106 (1950).
23. P. P. Fedorov and B. P. Sobolev, Kristallografiya **37** (5), 1210 (1992) [Sov. Phys. Crystallogr. **37**, 651 (1992)].
24. R. D. Shannon, Acta Crystallogr., Sect. A: Cryst. Phys., Diffr., Theor. Gen. Crystallogr. **A32** (5), 751 (1976).
25. W. H. Zachariasen, Acta Crystallogr. **2**, 388 (1949).
26. J. P. Laval, A. Micou, B. Frit, and J. Pannetier, J. Solid State Chem. **61**, 359 (1986).
27. J. P. Laval, A. Micou, B. Frit, *et al.*, Rev. Chim. Miner. **24**, 165 (1987).
28. I. D. Ratnikova, Candidate's Dissertation in Chemistry (Mosk. Gos. Univ., Moscow, 1977).

Translated by L. Man

Crystallography Reports, Vol. 46, No. 2, 2001, pp. 246–252. Translated from Kristallografiya, Vol. 46, No. 2, 2001, pp. 287–293.

CRYSTAL CHEMISTRY

Layer Perovskite-Like Crystals with CsCl-Type Blocks

B. V. Beznosikov and K. S. Aleksandrov

Institute of Physics, Siberian Division, Russian Academy of Sciences, Krasnoyarsk, Russia

e-mail: aaleks@iph.krasn.ru

Received November 4, 1999; in final form, February 29, 2000

Abstract—The crystal chemistry of layer perovskite-like structures with CsCl-type blocks have been analyzed. Some characteristic features of their formation are described and new praphases are derived. Possible oxyhalides and oxides are indicated. © *2001 MAIK "Nauka/Interperiodica".*

INTRODUCTION

All the numerous praphases of layer perovskite-like structures[1] can be represented as combinations of stacks (formed by layers of octahedra, pyramids, or squares inherited from perovskite-like structures) alternating with several dozens of different types of intermediate blocks [1–3]. According to [4], a *praphase* is a hypothetical phase with a symmetric structure from which the structure of a real crystal can be obtained with the aid of small atomic displacements. The arrangement of the atoms in intermediate blocks is similar to those in the elements of the well-known NaCl, CsCl, CaF_2, BiF_3, etc., structures. Below, we consider the parenthal phases (praphases) which include CsCl-type blocks.

The principle of the geometric construction of praphases of perovskite-like layer structure, which are in fact intergrowth structures, is rather simple. This principle provides the determination of general and coordination formulas, symmetry, undistorted space groups, approximate unit-cell parameters, and sometimes even relative atomic coordinates along the principal axis.

Most of praphases of layer perovskite-like structures belong to the tetragonal system (sp. gr. *I*4/*mmm* or *P*4/*mmm*). However, real the symmetry of crystals may be lower depending on their chemical composition or thermodynamic conditions of their growth. The structural phase transitions in all families of layer perovskite-like crystals are most often associated with the soft lattice modes corresponding to small rotations of bound octahedral groups. By analyzing layer perovskite-like crystals with the sp. gr. *I*4/*mmm* and *P*4/*mmm* [5], one can construct models of distorted phases, in which one can determine the directions not only of all the anionic displacements but, in many cases, also the displacements of bulky cations. These data with due regard for the unit-cell parameters and the systematic absences of rejections can be used in structure determinations.

The method for combining stacks and blocks enables one to derive not only all the known structures of this type but, more importantly, also hundreds of new praphases [6–9]. The close correspondence of the praphases thus obtained to real structures confirms the reliability of this method for prediction of new structures.

POSSIBLE PRAPHASES

Structures of the CsCl type (*Pm*3*m*, *Z* = 1) are formed by monovalent metals with large halide anions (Cl^-, Br^-, or I^-). Two types of blocks with the structure similar to that of CsCl are the well-known layer perovskite-type structures.

Block Cs1. A Cl or Br anion is located in the block center and has the cationic environment close to cubic one.

It was shown [2] that all the known stacks can be divided into four types (*A*, *B*, *C*, and *D*). Type *A* consists of *n* layers of octahedra. If $n \longrightarrow \infty$, this type becomes similar to cubic perovskite. Type *B* has anionic vacancies in the stack. The *C* and *D* types have vacancies in the positions of apical anions of the octahedra. When constructuting praphases, the Cs1 block is matched to the *C* and *D* stacks (Fig. 1) with anionic vacancies in the shared planes. Layer perovskite-like structures involving the *C*1 stack are formed with the participation of two types of blocks. The unit cell of this stack has one anionic vacancy. The Cs1 block can grow from the side of this vacancy. The opposite face of the *C*1 stack containing an anion in the center can grow into the blocks, whose outer planes are formed by anions. A series of blocks used to construct praphases are shown in Fig. 2. The notation of these blocks corresponds to the conventional notation, namely, *R* (from rock salt), *F* (from fluorite), etc. Since the only known

[1] The term *praphase*, which can be translated as *forephase* or *parenthal phase*, is widely used in Russian literature and, in particular, in this paper. Therefore, we decided to retain it here (Translator's note).

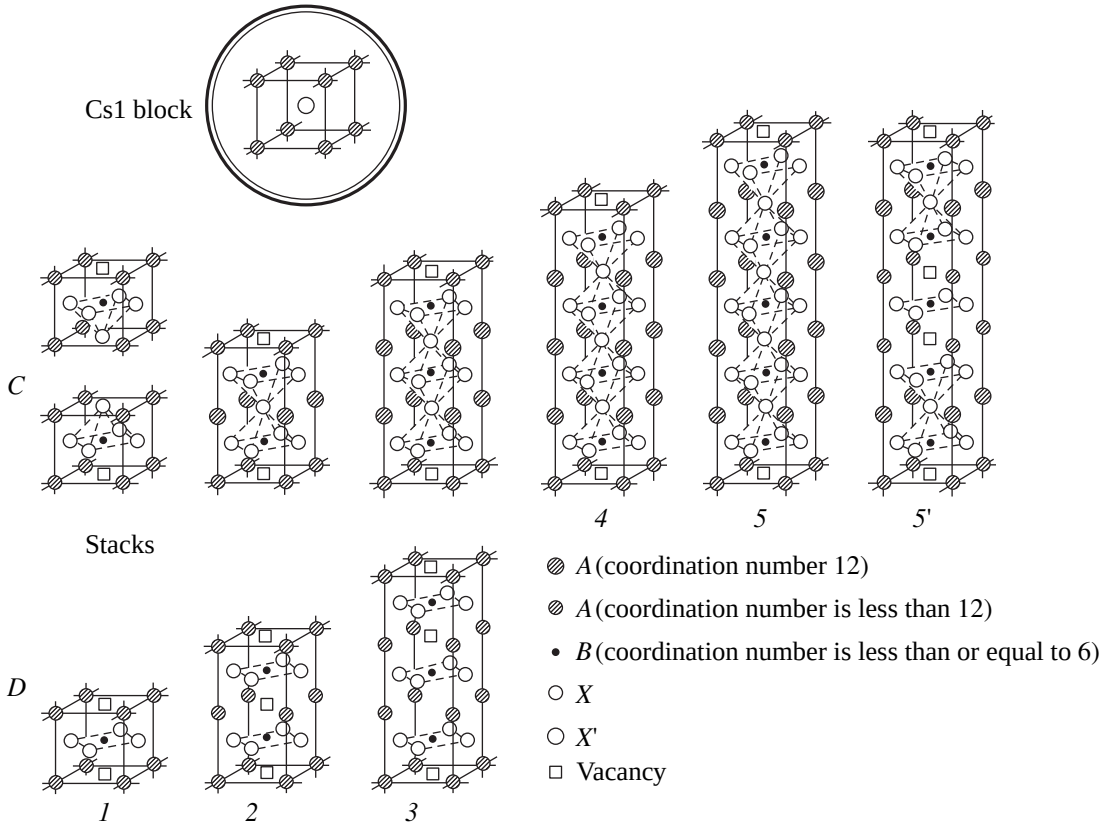

Fig. 1. Block of the Cs1 type and the corresponding stacks.

P-type blocks include lead, we retained the symbol of this element in the labelling atoms in Fig. 2 and in the coordination formulas of the praphases obtained (see below). In praphases with *P*2, *P*4, and *P*6 blocks, the latter can have two orientations without any change of the crystal symmetry. Therefore, we added symbols (1) and (2) to the notation of these blocks in Fig. 2. The praphases obtained by combining the Cs1 block with the *C* and *D* stacks are indicated in Table 1.

Block Cs'1. The block center is occupied by a cation in an pseudocubic (eight vertices) anionic environment. This block is an "antipode" of the Cs1 block and can be formed only in the presence of cationic vacancies in the boundary layer of the stack. Consequently, the stack structure at the site of its junction with the block should be similar to the ReO_3 structure. The junction of these stacks obtained from the *A* and *B* types (denoted *A** and *B**) with the Cs'1 block is shown in Fig. 3. In fact, *A**-type stacks are combined from two structures—perovskite (inner layers) and ReO_3 (layers adjacent to the block). The *B** stacks, similar to the *B* stacks, have anionic vacancies.

Nine possible praphases with Cs'1 blocks are indicated in Table 2; the corresponding figures can be found elsewhere [8, 9].

PREREQUISITES FOR CRYSTALLOCHEMICAL CONSTRUCTION OF PRAPHASES

(1) A necessary condition for the formation of layer perovskite-like structures with Cs1 blocks is the presence of one large monovalent anion (Cl, Br, or I) per formula unit.

(2) Only monovalent *A* cations can be included into structures with a Cs'1 block, because at higher cation valences, the repulsion between the cations in the adjacent unit cells considerably increases.

(3) The *B* cation in these structures should have a valence equal to or higher than three, because a monovalent *A* cation requires a good "assistant." The anionic environment of the *A* cation is close to cubic, but it is also surrounded by eight additional anions from the second coordination sphere which provide the connection of octahedra into layers. This anionic construction (8 + 8) can be held only by the joint effect of the *A* and *B* cations.

The experience gained in the studies of other layer structures [7, 9] allows for the formulation of the following rules:

(4) If the coordination number is equal to 4 or 5 (a square or a square pyramid), the *B* cation in the stack can only have valence 2+ or 3+.

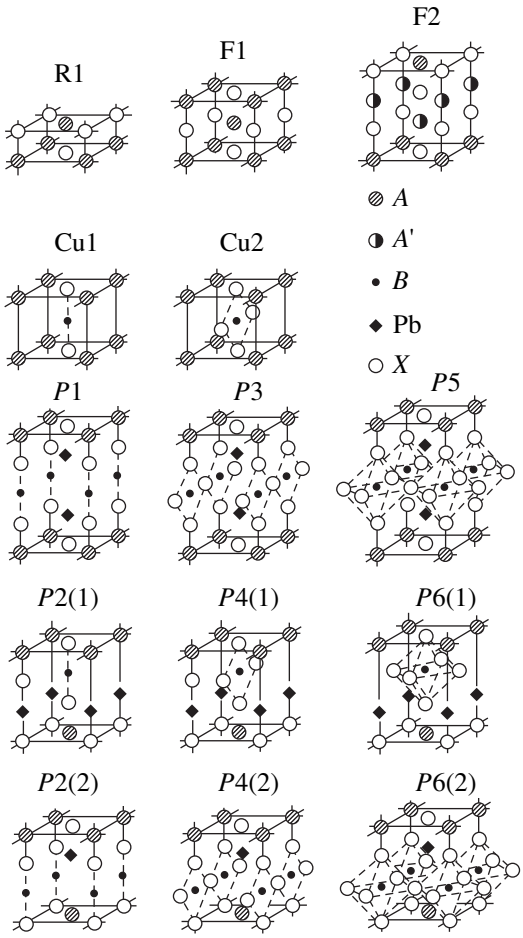

Fig. 2. Blocks matching the *C*1 stack.

(5) If the coordination number is equal to 6 (an octahedron), the *B* cation in a multilayer stack can be multicharged.

KNOWN CRYSTAL STRUCTURES

Altogether, about twenty crystals with the perovskite-like layered structure have been studied. The $Pb_4Fe_3O_8Cl$ [10] and $Sr_2Pb_2Cu_2TaO_8Cl$ [11] structures belong to the sp. gr. *P*4/*mmm*, *Z* = 1 and consist of three-layer stacks and Cs1-type blocks slightly "compressed" along the principal axis. A number of other oxyhalides were considered in [11, 12].

Several compounds with layer structures containing Cs1 and *P*1 blocks and *C*1 stacks were also reported in [13]: $Sr_3Pb_3Cu_3O_8Cl$, $Ba_3Pb_3Cu_3O_8Cl$, and $Ba_2SrPb_3Cu_3O_8Cl$. These structures are distorted (sp. gr. *Cmmm*, *Z* = 2) in comparison with their praphase (*P*4/*mmm*, *Z* = 4).

Until recently, only one-layer structures (mainly fluorides) with Cs'1 blocks have been known. The "fatter" of this family is a $TlAlF_4$ crystal (Fig. 4).

The structures of the $TlAlF_4$ type with the general formula ABX_4 consist of square octahedral networks perpendicular to the *z*-axis. These networks are linked by alkali metal or complex organic cations forming a Cs'1-type block. The structures of the $TlAlF_4$ type are high-temperature phases stable only at high temperatures. About one hundred of the known crystalline phases belong to this family, with most of them being considered as the structures formed upon distortion of the praphase caused by rotation of the BX_6 octahedra.

Recently, two compounds have been synthesized—$RbLaTa_2O_7$ with a Cs'1 block and a double layer of octahedra in the stack [14] and $RbCa_2Ta_3O_{10}$ with the same block and a triple layer of octahedra [15] (Fig. 4). We believe that other multilayer crystals of this family of oxides may also be synthesized.

Thus, the existence of the above structures with Cs1 and Cs'1 blocks gives grounds to expect the synthesis of other praphases indicated in Tables 1 and 2.

PREDICTION OF NEW COMPOUNDS

Compound with Cs1 blocks. Consider probable compounds with blocks involving Pb^{2+} cations. The *B* cations in the stacks were chosen proceeding from the known chemical compounds. In the general formulas, *A* and *B* are cations and *X* and *X*' are anions.

Possible Cs1*C*2 compounds with the general formula $A_3B_2X_6$. To our knowledge, the following combinations of the *B* cations can exist in *C*2 stacks: Fe_2, Co_2, CuFe, CuCo, and $Mn^{2+}Mn^{3+}$. The total valence of two *B* cations in the stack should range from five to six.

The following compounds are probable:

$BaPb_2B_2X'O_{5\pm\delta}$	B_2 = Co_2, Fe_2, Mn_2, CuFe, CuCo
$SrPb_2B_2X'O_{5\pm\delta}$	X' = Cl, Br.
$P6_3B_2X'O_{5\pm\delta}$	

Possible Cs1*C*3 compounds with the general formula $A_4B_3X_9$. The following combinations of *B* cations are known for *C*3 stacks: Fe_3, Cu_2Nb, Cu_2Ta, Cu_2Pb, and Cu_2Fe. The total valence of three *B* cations is 9+. One of *A* cations should provide the formation of the block, whereas the remaining three *A* cations should form the stack. Two *A* cations have the coordination number 12 and two other *A* cations have the coordination number 8. Thus, the following compounds are possible:

$Pb_4B_3X'O_{8\pm\delta}$	B_3 are the combinations of the cations indicated above
$Ba_2Pb_2B_3X'O_{8\pm\delta}$	
$Sr_2Pb_2B_3X'O_{8\pm\delta}$	X' = Cl or Br.

The compositions of the known compounds, show that the following substances may be synthesized: $Sr_4Fe_3O_8Cl$, $Sr_4Fe_3O_8Br$, $Sr_4Cu_2TaO_8Cl$,

Table 1. Possible praphases of layer perovskite-like structures with a Cs1 block

Block\stack	Sp. gr.	Z	General formula	Coordination formula
Cs1*C*2	*P*4/*mmm*	1	$A_3B_2X_6$	$A^{XII}A_2^{VIII}B_2^{V}X_5X'$
Cs1*C*3*	*P*4/*mmm*	1	$A_4B_3X_9$	$A_2^{XII}A_2^{VIII}B^{VI}B^{V}X_8X'$
Cs1*C*4	*P*4/*mmm*	1	$A_5B_4X_{12}$	$A_3^{XII}A_2^{VIII}B_2^{VI}B_2^{V}X_{11}X'$
Cs1*C*5	*P*4/*mmm*	1	$A_6B_5X_{15}$	$A_4^{XII}A_2^{VIII}B_3^{VI}B_2^{V}X_{14}X'$
Cs1*C*5'	*P*4/*mmm*	1	$A_6B_5X_{13}$	$A_2^{XII}A_2^{VIII}A_2^{VIII}B_4^{V}B^{IV}X_{12}X'$
Cs1*D*1	*P*4/*mmm*	1	A_2BX_3	$A_2^{VIII}B^{IV}X_2X'$
Cs1*D*2	*P*4/*mmm*	1	$A_3B_2X_5$	$A_2^{VIII}A^{VIII}B_2^{IV}X_4X'$
Cs1*D*3	*P*4/*mmm*	1	$A_4B_3X_7$	$A_2^{VIII}A_2^{VIII}B_3^{IV}X_6X'$
*R*1*C*1\Cs1	*I*4/*mmm*	2	$A_4B_2X_7$	$A_2^{IX}A_2^{VIII}B_2^{V}X_6X'$
Cu1*C*1\Cs1	*P*4/*mmm*	1	$A_4B_3X_7$	$A_2^{VIII}A_2^{VIII}B_2^{V}B^{II}X_6X'$
Cu2*C*1\Cs1	*Pmmm*	1	$A_4B_3X_8$	$A_2^{VIII}A_2^{VIII+II}B_2^{V}B^{IV}X_7X'$
*F*1*C*1\Cs1	*P*4/*mmm*	1	$A_5B_2X_8$	$A_2^{IX}A_2^{VIII}A^{VI}B_2^{V}X_7X'$
*F*2*C*1\Cs1	*I*4/*mmm*	2	$A_6B_2X_9$	$A_2^{IX}A_2^{VIII}A_2^{VI}B_2^{V}X_8X'$
*P*1*C*1\Cs1*	*P*4/*mmm*	1	$A_6B_3X_9$	$A_2^{IX}A_2^{VIII}Pb_2^{V}B_2^{V}B^{II}X_8X'$
*P*3*C*1\Cs1	*Pmmm*	1	$A_6B_3X_{10}$	$A_2^{IX}A_2^{VIII}Pb_2^{VII}B_2^{V}B^{IV}X_9X'$
*P*5*C*1\Cs1	*P*4/*mmm*	1	$A_6B_3X_{11}$	$A_2^{IX}A_2^{VIII}Pb_2^{IX}B^{VI}B_2^{V}X_{10}X'$
*P*2*C*1\Cs1	*I*4/*mmm*	2	$A_5B_3X_8$	$A^{IX}A_2^{VIII}A^{VIII}Pb^{V}B_2^{V}B^{II}X_7X'$
*P*4*C*1\Cs1	*P*2/*mmm*	2	$A_5B_3X_9$	$A^{IX}A_2^{VIII}A^{VIII+II}Pb^{VII}B_2^{V}B^{II}X_8X'$
*P*6*C*1\Cs1	*P*4/*mmm*	2	$A_5B_3X_{10}$	$A^{XII}A_2^{VIII}A^{IX}Pb^{IX}B^{VI}B_2^{V}X_9X'$

Note: In general formulas, *A* and *B* are cations and *X* and *X*' are anions; *Z* is the number of formula units per unit cell. The superscripts signify the coordination numbers of the cations.

* Praphases corresponding to the already synthesized compounds, are primed; however, real crystals may be more distorted than the praphases.

$Sr_4Cu_2NbO_8Cl$, $Sr_4Cu_2TaO_8Br$, $Sr_4Cu_2NbO_8Br$, $Ba_3Pb_3Cu_3O_8Br$, and $Ba_2SrPb_3Cu_3O_8Br$.

Possible Cs1*C*4 compounds with the general formula $A_5B_4X_{12}$:

$Pb_5B_4X'O_{11-\delta}$	$B_4 = Fe_4, Cu_2Ti_2, Cu_2Sn_2$
$Ba_3Pb_2B_4X'O_{11-\delta}$	X' = Cl, Br.
$Sr_3Pb_2B_4X'O_{11-\delta}$	

Possible Cs1*C*5 compounds with the general formula $A_6B_5X_{15}$:

$Pb_6B_5X'O_{14-\delta}$	$B_5 = Cu_2Ti_3$
$Ba_4Pb_2B_5X'O_{14-\delta}$	X' = Cl, Br.
$Sr_4Pb_2B_5X'O_{14-\delta}$	

Possible Cs1*D*1 compounds with the general formula $A_3B_2X_5$:

$Pb_3B_2X'O_{4+\delta}$	$B_2 = Cu_2, Ni_2$
	X' = Cl, Br.

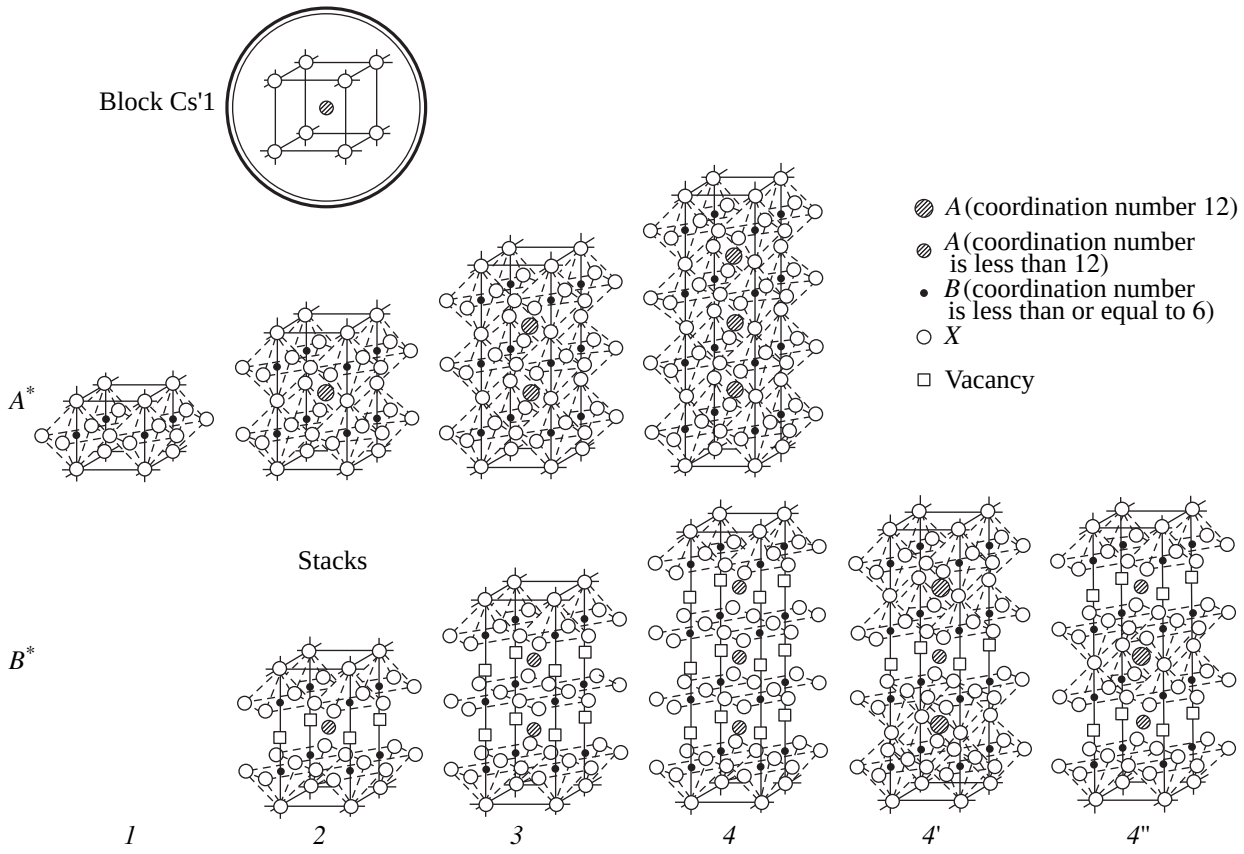

Fig. 3. Cs'1-type block and corresponding stacks.

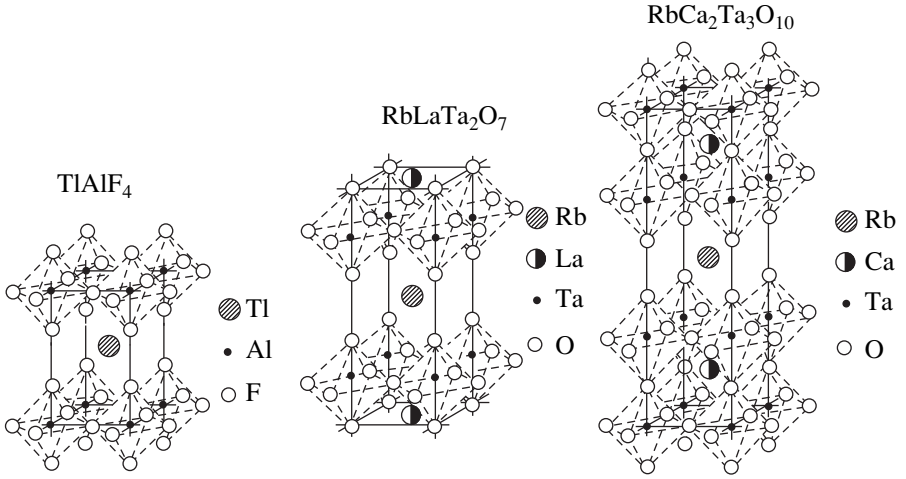

Fig. 4. Well-known structures containing the Cs'1 block.

Possible Cs1*D*3 compounds with the general formula $A_4B_3X_7$:

$Ba_2Pb_2B_3X'O_{6+\delta}$	$B_3 = Cu_3, Ni_3$
$Sr_2Pb_2B_3X'O_{6+\delta}$	$X' = Cl, Br.$

For the Cs1*C*1*P*3 praphases, the following compounds are possible:

$Ba_4Pb_2Cu_3X'O_{9-\delta}$ and $Sr_4Pb_2Cu_3X'O_{9-\delta}$ (X' = Cl, Br).

The synthesis of Cs1*C*1*P*5 praphases is more difficult. To provide their electroneutrality, one has to introduce into the crystal trivalent cations, but unfortunately

Table 2. Possible praphases of layer perovskite-like structures with Cs'1 blocks

Block\stack	Sp. gr.	*Z*	General formula	Coordination formula
Cs'1*A**1**	*P*4/*mmm*	1	ABX_4	$A^{VIII}B^{VI}X_4$
Cs'1*A**2**	*P*4/*mmm*	1	$A_2B_2X_7$	$A^{XII}A^{VIII}B_2^{VI}X_7$
Cs'1*A**3**	*P*4/*mmm*	1	$A_3B_3X_{10}$	$A_2^{XII}A^{VIII}B_3^{VI}X_{10}$
Cs'1*A**4	*P*4/*mmm*	1	$A_4B_4X_{13}$	$A_3^{XII}A^{VIII}B_4^{VI}X_{13}$
Cs'1*B**2	*P*4/*mmm*	1	$A_2B_2X_6$	$A^{VIII}A^{VIII}B_2^{V}X_6$
Cs'1*B**3	*P*4/*mmm*	1	$A_3B_3X_8$	$A^{VIII}A_2^{VIII}B_2^{V}B^{IV}X_8$
Cs'1*B**4	*P*4/*mmm*	1	$A_4B_4X_{10}$	$A^{VIII}A_3^{VIII}B_2^{V}B_2^{IV}X_{10}$
Cs'1*B**4'	*P*4/*mmm*	1	$A_4B_4X_{12}$	$A_2^{XII}A^{VIII}A^{VIII}B_2^{VI}B_2^{V}X_{12}$
Cs'1*B**4''	*P*4/*mmm*	1	$A_4B_4X_{11}$	$A^{XII}A^{VIII}A_2^{VIII}B_4^{V}X_{11}$

Note: For hole and notation see Table 1.

they are too small. Here, the following compounds are probable: $La_4Pb_2Cu_3X'O_{10+\delta}$ (X' = Cl or Br).

Altogether, we obtained 105 possible chemical compounds with Cs1-type blocks that have layer perovskite-like structures.

The blocks in both well known and predicted crystals include divalent lead. The number of such compounds can be increased by using blocks with Sr^{2+}, Eu^{2+}, Sm^{2+}, Nd^{2+}, or Sn^{2+} cations with the size close to that of lead. Thus, the number of the probable compounds amounts 600.

Compounds with Cs'1 blocks. In 1986, new fluoride-containing compounds were predicted [16]. In subsequent years, about 14 new crystalline fluoride compounds were synthesized, in full accord with the prediction made.

In oxide systems, the structures of the $TlAlF_4$ type have not been revealed, and, apparently, they are difficult to synthesize. This brings up the question as to the types of new oxide compounds with possible multilayer structures. Proceeding from the sizes of the *A* and *B* cations in the known compounds with $n = 2$ or 3, the probable compounds should lie in the existence range of structures with $n = 1$. It may be that the ranges of existence of these structures would be the same, as is the case of Ruddlesden–Popper-type layer phases [6]. In order to be able to predict new multilayer phases with Cs'1 blocks, one has to use the geometric conditions of existence of the structures which belong to the $TlAlF_4$ family. The problem of possible formation of structures with $n > 3$ is still open. Therefore, in the present study we restricted ourselves only to compounds with $n = 2$ and 3.

Proceeding from the known compositions $RbLaTa_2O_7$ and $RbCa_2Ta_3O_{10}$, one can obtain some modified compounds by replacing the Ta^{5+} ions by the Nb^{5+} cations. Indeed, such compounds have been reported (for example, $RbLaNb_2O_7$ [17]). A Rb^+ cation can be replaced by a Cs^+ or Tl^+ cation, a Ca^{2+} cation can be replaced by a Sr^{2+}, and a La^{3+} cation can be replaced by another (more appropriate) trivalent cation. These modified compounds have *A**-type stacks.

The question arises about the types of layered perovskite-like structures, formed with the participation of Cs'1 blocks and *B**-type stacks. The structures with *B**4' blocks are most probable because octahedra in these blocks can have highly charged cations, whereas the second *A* cation (in the cuboctahedron) would stabilize the stack.

We considered only some possible new compounds with Cs1 and Cs'1 blocks. The synthesis of other praphases depends on the requirements of physicists, skill of chemists, and the available technical facilities.

CONCLUSIONS

The number of new compounds with CsCl-type blocks can be multiply increased.

In layered perovskite-like crystals, the stacks and blocks produce an effect similar to that of high pressure. Hence, some cations in the layers may exist in an unusual crystallochemical state. This phenomenon may be of great importance when studying physical properties of such crystals.

If some oxygen atoms in a layer perovskite-like structure are replaced by halogen atoms, the latter atoms are usually incorporated by the blocks. There-

fore, halides (or other anions) can be used to obtain new blocks, to change the block composition, and thus increase the anisotropy of various physical properties.

The results obtained give grounds to expect the discovery of new unique properties (other than the high-T_c superconductivity) in layer crystals.

ACKNOWLEDGMENTS

The study was supported by the Russian Foundation for Basic Research, (project nos. 96-15-96790 and 99-02-17375) and the INTAS (grant no. 97-10177).

REFERENCES

1. K. S. Aleksandrov and B. V. Beznosikov, Fiz. Tverd. Tela (St. Petersburg) **39**, 785 (1997) [Phys. Solid State **39**, 695 (1997)].
2. K. S. Aleksandrov and B. V. Beznosikov, *Perovskite-Like Crystals* (Nauka, Novosibirsk, 1997).
3. K. S. Aleksandrov and B. V. Beznosikov, Kristallografiya **42** (4), 1 (1997) [Crystallogr. Rep. **42**, 556 (1997)].
4. *Solid State Physics. Encyclopaedia* (Naukova Dumka, Kiev, 1998), Vol. 2.
5. K. S. Aleksandrov, Kristallografiya **40** (2), 279 (1995) [Crystallogr. Rep. **40**, 251 (1995)].
6. B. V. Beznosikov and K. S. Aleksandrov, Kristallografiya **45** (5), 864 (2000) [Crystallogr. Rep. **45**, 792 (2000)].
7. B. V. Beznosikov and K. S. Aleksandrov, Preprint No. 791 F (Inst. Fiz. Sid. Otd. Ross. Akad. Nauk, Krasnoyarsk, 1998).
8. B. V. Beznosikov and K. S. Aleksandrov, Preprint No. 794 F (Inst. Fiz. Sid. Otd. Ross. Akad. Nauk, Krasnoyarsk, 1999).
9. B. V. Beznosikov and K. S. Aleksandrov, Zh. Strukt. Khim. (in press).
10. J. Pannetier and P. Batail, J. Solid State Chem. **39**, 15 (1981).
11. Rukang Li, J. Solid State Chem. **130**, 154 (1997).
12. R. J. Crooks, C. S. Knee, and M. T. Weller, Chem. Mater. **10**, 4169 (1998).
13. R. J. Cava, P. Bordet, J. J. Capponi, *et al.*, Physica C (Amsterdam) **167**, 67 (1990).
14. T. Honma, K. Toda, Z. G. Ye, and M. Sato, J. Phys. Chem. Solids **59** (8), 1187 (1998).
15. K. Toda and M. Sato, J. Mater. Chem. **6**, 1067 (1996).
16. B. V. Beznosikov, Kristallografiya **33** (3), 658 (1988) [Sov. Phys. Crystallogr. **33**, 388 (1988)].
17. R. Armstrong and P. Anderson, Inorg. Chem. **33**, 4366 (1994).

Translated by T. Safonova

Crystallography Reports, Vol. 46, No. 2, 2001, pp. 253–255. Translated from Kristallografiya, Vol. 46, No. 2, 2001, pp. 294–297.

CRYSTAL CHEMISTRY

Classification of Hydrated Oxygen Compounds of Boron

M. A. Simonov

Faculty of Geology, Moscow State University, Vorob'evy gory, Moscow, 119899 Russia

Received June 17, 1999; in final form, May 17, 2000

Abstract—The known structural classifications of borates are based on the analysis of boron–oxygen radicals consisting of B-triangles and B-tetrahedra sharing O atoms to form more complicated structures. Such classifications ignore the possible presence and the role of hydrogen bonds, which may be the only bonds or additional bonds linking the $[BO_3]$- and $[BO_4]$-groups. A new detailed classification of hydrated boron compounds taking into account hydrogen bonds between the B-polyhedra is proposed. *© 2001 MAIK "Nauka/Interperiodica".*

The structural classification of compounds is one of the most important problems of crystal chemistry. The classification of crystalline borates is based on the type of a boron–oxygen radical, i.e., the consideration of the degree of association of elementary structural units such as B-triangles and B-tetrahedra, through common (shared) oxygen atoms. Similar to silicates [1], borates are classified depending on the types of their radicals as island, chain, layered, and framework borates. This classification is applied to all the borates, including hydrated compounds, i.e., water-containing borates, in which hydrogen bonds often play a significant role. Boron triangles and tetrahedra in these compounds can be linked to each other not only via common oxygen vertices but also via hydrogen bonds. The latter can only be bonds or can be additional bonds to those of boron polyhedra. The detailed classification of hydrated borates also distinguishes the compounds in which the B-polyhedra are linked only through common oxygen atoms, borates in which the $[BO_3]$- and $[BO_4]$-groups are linked only by hydrogen bonds, and borates with mixed bonds.

Consider first the structure of frolovite $Ca[B(OH)_4]_2$ (a = 7.774 Å, b = 5.680 Å, c = 8.136 Å, α = 113.15°, β = 101.67°, γ = 107.87°, the triclinic space group $P\bar{1}$) [2]. The independent region of the unit cell contains one Ca atom, two B atoms, eight H atoms, and eight O atoms. The structure consists of two crystallographically independent individual (according to the classical concepts) $[B(OH)_4]$-tetrahedra and the Ca-polyhedra, which link the tetrahedra through the oxygen vertices. The analysis of the complex system of hydrogen bonds shows that all the B-tetrahedra are linked by hydrogen bonds into a complex framework. The B-tetrahedra and the system of hydrogen bonds projected along the b-axis of the unit cell of frolovite are shown in Fig. 1. For a clearer representation, the Ca atoms and their polyhedra are omitted. The overall view of the structure and the numbering scheme of the basis atoms can be found in [2]. According to this numbering scheme, the B(1) atom is coordinated by the O(1), O(2), O(3), and O(4) atoms, and the B(2) atom is coordinated by the O(5), O(6), O(7), and O(8) atoms. The oxygen atoms forming the tetrahedron about B(1) participate in the following hydrogen bonds: O(1)–H(1)···O(5), O(1)···H(5)–O(5'), O(2)–H(2)···O(6), O(3)–H(3)···O(7),O(4)–H(4)···O(5''), and O(4)···H(8)–O(8), through which the B(1)- and B(2)-tetrahedra are linked to each other. In addition, the B(2)-tetrahedra are linked to each other through the O(6)–H(6)···O(8') and O(7)–H(7)···O(7') hydrogen bonds.

The structure of vimsite $Ca[B_2O_2(OH)_4]$ (a = 10.26 Å, b = 4.440 Å, c = 9.558 Å, γ = 91.31°, the monoclinic space group $B2/b$) [3] is another example showing the role of hydrogen bonds. The crystallographically independent atoms in the structure are one Ca atom, one B atom, three O atoms, and two H atoms. According to the conventional classification, this compound belongs to chain borates and has the chains of B-tetrahedra linked to each other through common oxygen vertices. These chains along the b-axis are

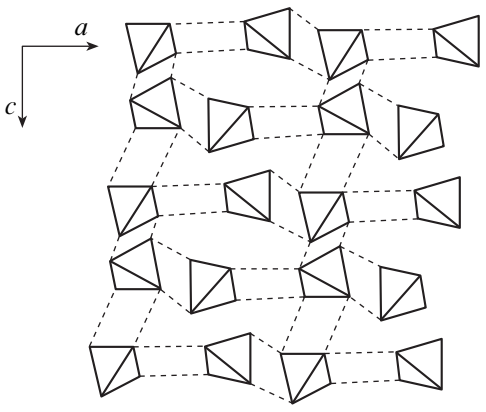

Fig. 1. B-tetrahedra and the system of hydrogen bonds in the frolovite $Ca[B(OH)_4]_2$ structure projected onto the *ac* plane.

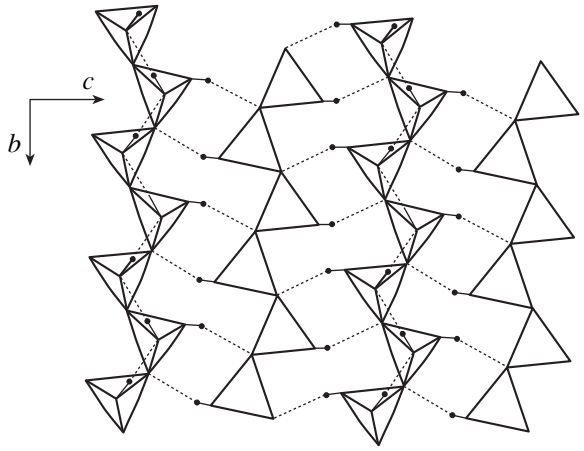

Fig. 2. Chains of the B-tetrahedra, the H atoms, and the system of hydrogen bonds in the structure of vimsite $Ca[B_2O_2(OH)_4]$ projected onto the *bc* plane.

linked to each other by the Ca-polyhedra to form a three-dimensional framework. The chains of the B-tetrahedra, the H atoms, and the hydrogen bonds projected onto the *bc* plane are shown in Fig. 2. For clearer representation, the Ca-polyhedra are omitted. The O(2)–H(1)··O(2') hydrogen bonds determine and fix the geometry of the chains of B-tetrahedra, with all the successive units of each chain being additionally linked through these hydrogen bonds. The adjacent chains are linked to each other through the O(3)–H(2)··O(1) hydrogen bonds and form networks parallel to the *bc* plane of the crystal.

The structure of uralborite $Ca_2[B_4O_4(OH)_8]$ is also of interest. The empirical chemical formula of this compound is identical to that of vismite [4], but the atomic structures of these borates are totally different. According to the conventional classification, uralborite (a = 6.927 Å, b = 9.836 Å, c = 12.331 Å, γ = 97.81°, the monoclinic space group $P2_1/n$) belongs to island borates containing the $[B_4O_4(OH)_8]^{4-}$-groups consisting of four B-tetrahedra each. Three tetrahedra are closed to form a ring to which the fourth B-tetrahedron is linked via the common oxygen vertex. In addition to the above-described island, the basic region of the unit cell also has two Ca atoms. Of total 12 basis O atoms, eight atoms belong to hydroxyl (OH)-groups. Of the remaining four oxygen atoms, two atoms are involved in hydrogen bonding and act as acceptors. All the hydrogen atoms of the hydroxyl groups form hydrogen bonds, among which there are both strong (the donor–acceptor distance is 2.60 Å) and weak (the corresponding distance is 3.17 Å) bonds. There are eight crystallographically independent hydrogen bonds linking the $[B_4O_4(OH)_8]^{4-}$ islands, which form a loose three-dimensional framework with the cavities occupied by Ca atoms.

The above examples demonstrate the role of different-type hydrogen bonds in hydroborates and essentially refine the crystal chemistry of these compounds. Taking into account hydrogen bonds, oxygen compounds of boron can be divided into three families. The first family of boron–oxygen compounds consists of borates, in which elementary boron polyhedra in radicals are not linked via hydrogen bonds. The second family includes compounds in which individual B-tetrahedra and B-triangles are linked to each other only via hydrogen bonds (hereafter, we refer to these borates as borates with H radicals). The frolovite structure is an example of this type of compounds. Borates in which the B-tetrahedra and B-triangles are linked to each other by both common oxygen vertices and hydrogen bonds (vismite, uralborite, and analogous compounds) form the third family and hereafter will be given the name “borates with mixed bonds”.

The classification of hydrogen-containing oxygen compounds of sulfur, boron, phosphorus, and silicon with allowance for hydrogen bonds has been considered elsewhere [5]. In the particular case of hydrated oxygen compounds of boron, the classification scheme is shown in Fig. 3. The characteristic feature of the above-considered scheme is the division of the three structural families into five groups containing radicals of the island, chain, layered, framework, and mixed

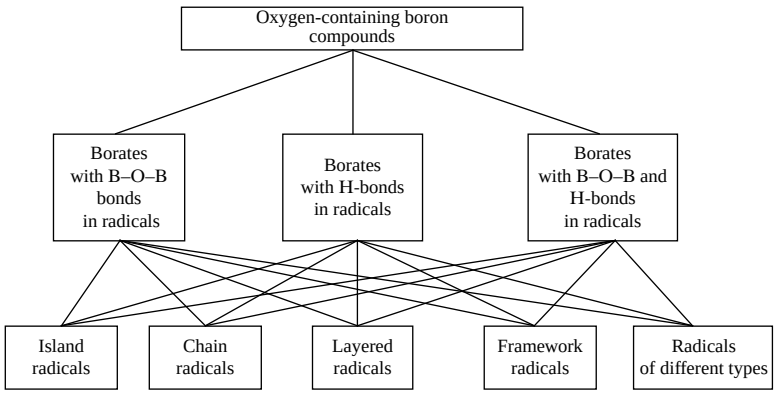

Fig. 3. Classification scheme for hydrated oxygen-containing borates with allowance for hydrogen bonds linking the B-polyhedra.

Some examples of classification of radicals in hydrated borates with and without allowance for hydrogen bonds

Name and chemical formula	Structural formula	Radical without allowance for hydrogen bonds	Radical with allowance for hydrogen bonds	References
Sussexite $Mn_2[B_2O_4(OH)_2]$	$Mn_2^{[6]}[B_2^{[3]}O_4(OH)_2]^{\infty H}$	Island: two vertex-sharing triangles	Chain: $[B_2O_4(OH)_2]^{\infty H}$	[6]
Inderborite $CaMg[B_3O_3(OH)_5]_2 \cdot 6H_2O$	$Ca^{[8]}Mg^{[6]}[B_3^{[4,4,3]}O_3(OH)_5]_2^{\infty 2H} \cdot 6H_2O$	Island: a ring consisting of two tetrahedra and one triangle	Layered: $[B_3O_3(OH)_5]_2^{\infty 2H}$	[7, 8]
Barium hydroborate $Ba[B(OH)_4]_2$	$Ba^{[9]}[B^{[4]}(OH)_4]_2^{\infty 3H}$	Layered: tetrahedra	Framework: $[B(OH)_4]^{\infty 3H}$	[9]
Calcium hydroborate $Ca[B_3O_4(OH)_3]$	$Ca^{[8]}[B_3^{[4,4,3]}O_4(OH)_3]^{\infty 2H}$	Chain: ribbons of tetrahedra and triangles	Layered: $[B_3O_4(OH)_3]^{\infty 2H}$	[10]
Sodium hydroborate $Na_2[B_4O_6(OH)_2]$	$Na_2^{[7,6]}[B_4^{[4,4,3,3]}O_6(OH)_2]^{\infty 3H}$	Chain: ribbons of tetrahedra and triangles	Framework: $[B_4O_6(OH)_2]^{\infty 3H}$	[11]
Tuzlaite $NaCa[B_5O_8(OH)_2] \cdot 3H_2O$	$Na^{[7]}Ca^{[8]}[B_5^{[4,4,4,3,3]}O_8(OH)_2]^{\infty 3H}$	Chain: ribbons of tetrahedra and triangles	Framework: $[B_5O_8(OH)_2]^{\infty 3H}$	[12]

types. In the three structural families, these groups of structures are formally identical. The essential difference between these structures is in the type of bonds providing the linkage of B-polyhedra and formation of complex radicals. In the first case, only the B–O–B-type bonds exist. The structures of the second type include hydrogen bonds. The structures of the third type are characterized by the presence of both types of bonds. Each of the five groups of the structures can be divided into smaller subgroups of structures. Island borates are divided into structures with diortho-, triortho-, ring-, and more complex radicals. Chain structures include compounds with chains and ribbons of different compositions and configurations.

Along with the proposed detailed classification of hydroborates, it is also expedient to use the developed structural formulas of radicals existing in these compounds suggested [5]. In this case, the radicals in brackets have the superscripts ∞H, ∞2H, or ∞3H for chain, layered, and framework radicals, respectively, formed via hydrogen bonds. Several examples of the classification of hydrated borates in accordance with the types of radicals with and without allowance for hydrogen bonds are given in table. The developed form of the structural formulas and radicals proposed in [5] is used. It can be seen that the allowance for hydrogen bonds "transforms" the island radicals into chain, layered, or framework ones and the chain radicals into layered or framework ones.

REFERENCES

1. N. V. Belov, *Crystal Chemistry of Silicates with Large Cations* (Akad. Nauk SSSR, Moscow, 1961).
2. M. A. Simonov, E. V. Kazanskaya, Yu. K. Egorov-Tismenko, *et al.*, Dokl. Akad. Nauk SSSR **230** (1), 91 (1976) [Sov. Phys. Dokl. **21**, 471 (1976)].
3. M. A. Simonov, Yu. K. Egorov-Tismenko, and N. V. Belov, Kristallografiya **21** (3), 592 (1976) [Sov. Phys. Crystallogr. **21**, 332 (1976)].
4. M. A. Simonov, Yu. K. Egorov-Tismenko, and N. V. Belov, Dokl. Akad. Nauk SSSR **234** (4), 822 (1977) [Sov. Phys. Dokl. **22**, 277 (1977)].
5. M. A. Simonov, Zh. Strukt. Khim. **31** (5), 129 (1990).
6. C. Hoffman and T. Armbruster, Schweiz. Mineral. Petrogr. Mitt. **75**, 123 (1995).
7. P. C. Burns and F. C. Hawthorne, Can. Mineral. **32**, 533 (1994).
8. E. N. Kurkutova, I. M. Rumanova, and N. V. Belov, Dokl. Akad. Nauk SSSR **164** (1), 90 (1965) [Sov. Phys. Dokl. **10**, 808 (1966)].
9. K. Watanabe and S. Sato, Bull. Chem. Soc. Jpn. **67**, 379 (1994).
10. N. A. Yamnova, Yu. K. Egorov-Tismenko, S. V. Malinko, *et al.*, Kristallografiya **39** (6), 99 (1994) [Crystallogr. Rep. **39**, 905 (1994)].
11. S. Menchetti and C. Sabelli, Acta Crystallogr., Sect. B: Struct. Crystallogr. Cryst. Chem. **B34** (4), 1080 (1978).
12. V. Bermanec, T. Armbruster, D. Tibljas, *et al.*, Am. Mineral. **79**, 562 (1994).

Translated by T. Safonova

Crystallography Reports, Vol. 46, No. 2, 2001, pp. 256–267. Translated from Kristallografiya, Vol. 46, No. 2, 2001, pp. 298–310.

Phase Transitions Characterized by Polarization Vector and Rotation Pseudovector in Crystals of Arbitrary Point Symmetry

V. A. Adamov, B. M. Darinskiĭ, and V. V. Shalimov

Voronezh State Technical University, Voronezh, Russia

Received June 18, 1997; in final form, January 17, 2000

Abstract—A thermodynamic theory of phase transitions in crystals characterized by the rotational and polarization components has been developed. A list of phase transitions accompanied by the change of the group to a subgroup is compiled for crystals whose thermodynamic potential can be represented by a fourth-order polynomial with respect to the order-parameter components. Spontaneous polarization arising by the mechanism of improper phase transitions provided by the nonlinear relation between the polarization and rotational components is considered. © *2001 MAIK "Nauka/Interperiodica".*

1. INTRODUCTION

In a large number of instances, phase states in crystals are characterized by multicomponent order parameters whose components can have different physical sense and dimensions. As examples, we indicate here the crystals containing atomic groups which change their orientations in the unit cell with the variation of the specimen temperature, and ions interacting with these groups whose displacements result in the appearance of macroscopic polarization. Possible phase transitions associated with rotations of atomic groups in crystals were classified in [1]; a more detailed classification eliminating discrepancies contained in [1] was developed in [2]. In monographs [3, 4], the concept of rotating octahedral atomic complexes was successfully used to classify crystal structures, interpret the cascades of phase transitions, etc.

The present study was undertaken to develop a theory of phase transitions in crystals characterized by order parameters with the rotational and polarization order-parameter components irrespectively of the symmetry classes under the condition that the number of atoms in the unit cell of a crystal does not change in the phase transition. We shall compile a list of phase transitions accompanied by the change of the group to a subgroup for crystals whose nonequilibrium thermodynamic potential can be represented as a fourth-order polynomial of the order-parameter components. A special attention is paid to the nonlinear effects, which can give rise to spontaneous polarization in different symmetry classes occurring by the mechanism of improper phase transitions [5].

2. GENERAL SCHEME OF PHASE TRANSITIONS IN CRYSTALS CHARACTERIZED BY POLARIZATION VECTOR AND ROTATION PSEUDOVECTOR

The general form of a nonequilibrium thermodynamic potential Φ is represented by the following polynomial:

$$\begin{aligned}\Phi = {} & \frac{\alpha_{ij}}{2}P_iP_j + \frac{1}{3}\omega_{ijl}P_iP_jP_l + a_{ijlm}P_iP_jP_lP_m \\ & + \frac{\beta_{ij}}{2}\phi_i\phi_j + \frac{1}{3}\omega_{ijl}\phi_i\phi_j\phi_l + b_{ijlm}\phi_i\phi_j\phi_l\phi_m \\ & + \gamma_{ij}P_i\phi_j + g_{ijl}P_iP_j\phi_l + \frac{1}{2}d_{ijlm}P_iP_j\phi_l\phi_m \\ & + h_{ijl}P_i\phi_j\phi_l + f_{ijlm}P_iP_jP_l\phi_m + f_{ijlm}P_i\phi_j\phi_l\phi_m,\end{aligned} \quad (1)$$

where α_{ij} and β_{ij} are the symmetric second-rank tensors ($[V^2]$), γ_{ij} is the nonsymmetric second-rank tensor ($[V^2]$), ω_{ijl} is a third-rank tensor symmetric with respect to all the three subscripts ($[V^3]$), f_{ijl} is a third-rank pseudotensor symmetric with respect to all the three subscripts ($\varepsilon[V^3]$), g_{ijl} is a third-rank pseudotensor symmetric with respect to the first two subscripts ($\varepsilon[V^2]V$), h_{ijl} is the third-rank tensor symmetric with respect to the two last subscripts ($V[V^2]$), a_{ijlm}, b_{ijlm} is the fourth-rank tensor symmetric with respect to all the subscripts ($[V^4]$), d_{ijlm} is the fourth-rank tensor symmetric with respect to the first and the second pair of the subscripts ($[V^2]^2$), and f_{ijlm} and g_{ijlm} are the fourth-order pseudotensors symmetric with respect to the first three and last three indices, respectively ($\varepsilon[V^3]V$ and $\varepsilon V[V^3]$).

1063-7745/01/4602-0256$21.00 © 2001 MAIK "Nauka/Interperiodica"

All the components except for f_{ijlm} and g_{ijlm} are indicated in [6]. However, here, we use the methods of the group theory more appropriate for computer construction of invariants.

To analyze the possible phase transitions in crystals characterized by various symmetry elements, there is no necessity to know the thermodynamic potential Φ in the explicit form. Later, we shall show that the possible scenario of phase transitions and their characteristics can be determined by using the sets of the second-, third-, and fourth-order order parameters. Therefore, we compile the list of invariants for each symmetry class used to represent the thermodynamic potential in the form of a linear combination with the coefficients smoothly dependent on temperature. In what follows, we assume that only the components of the second-rank tensor are temperature dependent.

The lists of invariants of the first-, second-, and third-order parameters are given for each symmetry class, with each list playing a certain role in the classification of possible phase transitions in the crystals of the given symmetry group.

The list of the first-order invariants contains those components of the order parameter that enter the thermodynamic potential in the second, third, and fourth powers. Therefore, the crystals can undergo first-order phase transitions with the jumpwise change of the order-parameter components from this list. These phase transitions occur without a change of the symmetry class; i.e., they are isomorphous transitions. Thus, the possible occurrence of isomorphous phase transitions is determined by the list of the first-order invariants of the order-parameter components. These transitions are not considered here.

The list of second-order invariants of the order-parameter components allows one to indicate a set of possible phase transitions occurring with the change of the order-parameter components not indicated in the list of the first-order invariants. The list of the order-parameter components taking the nonzero values upon the group–subgroup transition are determined by the set of cross products of various order-parameter components. Thus, the whole set of the order-parameter components can be divided into the groups of the components indicated in the list of the first-order invariants and the groups of nonintersecting components. The latter can be used as the basis for compiling a list of the group–subgroup phase transitions in crystals. The characteristic features of these transitions can be studied by using a reduced thermodynamic potential, i.e., a potential obtained from Eq. (1) by retaining in it only the terms dependent on the components entering the separated group.

The list of third-order invariants allows the establishment of the phase-transition type. The existence of nonzero third-order invariants dependent only on the components of the thermodynamic potential of the phase transition under consideration shows that this transition is the first-order phase transition. If there are no such invariants, the transition is of the second order. Moreover the third-order invariants allow one to indicate possible nonlinear effects resulting in the formation of the order-parameter components not indicated in the list of second-order invariants and providing the occurrence of the phase transition under consideration. These invariants determine the characteristic features of improper ferroelectric phase transitions given a special attention in the present article.

The fourth-order invariants of the order-parameter components determine the temperature dependence of the order parameter in the low-symmetric phases and, in some cases, also the directions of the spontaneous-polarization vectors and rotation angles. Since the number of fourth-order invariants is rather large, they are not written here in the explicit form, and the possible directions of spontaneous vectors of the order parameters are determined from the symmetry consideration, which is sufficient for our goals. We assume that the quartic part of the thermodynamic potential is positively indefinite, which provides the stability of the material with respect to an infinite increase of the order parameter.

Now consider phase transitions taking place in various symmetry classes (point symmetry groups) of the crystals.

3. TRICLINIC SYSTEM (C_1, C_i)

3.1. Since in the general case of triclinic crystals of the C_1 class the components obey the condition $\gamma_{ij} \neq 0$, then in the phase transition from the paraelectric ($P_i = 0$ and $\phi_i = 0$) to the ferroelectric phase, all the components of P_i and ϕ_i acquire nonzero values; the third-order monomial in Eq. (1) takes the zero value, and the phase transition is the first order and phase transition occurring with the jumpwise change of the order parameter at the phase-transition point, whereas the symmetry class remains unchanged.

3.2. For the symmetry class C_i with the only symmetry elements of the point group—a center of inversion—the list of invariants is

$$[\phi_1, \phi_2, \phi_3]$$

$$[P_1^2, P_1P_2, P_1P_3, P_2^2, P_2P_3, P_3^2,$$

$$\phi_1^2, \phi_1\phi_2, \phi_1\phi_3, \phi_2^2, \phi_2\phi_3, \phi_3^2]$$

$$[P_1^2\phi_1, P_1^2\phi_2, P_1^2\phi_3, P_1P_2\phi_1, P_1P_2\phi_2, P_1P_2\phi_3, P_1P_3\phi_1,$$
$$P_1P_3\phi_2, P_1P_3\phi_3, P_2^2\phi_1, P_2^2\phi_2, P_2^2\phi_3, P_2P_3\phi_1, P_2P_3\phi_2, \quad (2)$$

$$P_2P_3\phi_3, P_3^2\phi_1, P_3^2\phi_2, P_3^2\phi_3, \phi_1^3, \phi_1^2\phi_2, \phi_1^2\phi_3, \phi_1\phi_2^2,$$

$$\phi_1\phi_2\phi_3, \phi_1\phi_3^2, \phi_2^3, \phi_2^2\phi_3, \phi_2\phi_3^2, \phi_3^3]$$

3, 12, 28

The first-order invariants of the order parameter are given in the first square brackets, the second-order invariants are given in the second square brackets, etc. The total numbers of the first-, second-, and third-order invariants are indicated in the last line of the list (3, 12, and 28, respectively).

The first-order invariants of the order parameter can be rejected from the thermodynamic potential by translating the origin in the space of the order parameters to the position corresponding to the equilibrium value of the order parameter in the paraelectric phase.

Second-order invariants are divided into two groups: the group with the polarization-vector components and the group with the pseudovectors of rotation angles. Therefore, in the crystals of this class, only one ferroelectric phase transition is possible. To identify the phase transition to the ferroelectric phase, we should remember that the third-order invariants contain no invariants which depend only the components of the polarization vector P_i. Therefore, this transition is a second-order phase transition occurring by the bifurcation mechanism. To determine the conditions for the phase transition by this mechanism, one has to determine the matrix of the second derivatives Φ_{ij} of the thermodynamic potential from the zeroth values of the components P_i

$$\Phi_{ij} = \begin{pmatrix} \alpha_1 & \alpha_{12} & \alpha_{13} \\ \alpha_{12} & \alpha_2 & \alpha_{23} \\ \alpha_{13} & \alpha_{23} & \alpha_3 \end{pmatrix}. \quad (3)$$

Matrix (3) for the paraelectric phase is positively defined; i.e., it has three positive eigenvalues.

The condition for the occurrence of the phase transition requires at least one zeroth eigenvalue for matrix (3), which is associated with the temperature dependence of its elements. This is equivalent to the zeroth value of the matrix determinant (3). The direction of the spontaneous-polarization vector e_i of the ferroelectric phase is determined as the direction of the eigenvector of matrix (3). The magnitude of the latter vector is readily determined if one takes into account the fourth-order monomials in the thermodynamic potential. Since in the narrow temperature range in the vicinity of the phase-transition temperature (T_0), the polarization vector coincides, within high accuracy, with the eigenvector directions corresponding to the zeroth eigenvalue, one can pass from the initial thermodynamic potential to the reduced one ($\bar{\Phi}$) by making the change $P_i = Pe_i$. As a result, we obtain

$$\bar{\Phi} = \frac{\alpha}{2}P^2 + \frac{a}{4}P^4, \quad (4)$$

where

$$\alpha = a_{ij}e_ie_j, \quad a = a_{ijlm}e_ie_je_le_m. \quad (5)$$

Now, determine the temperature dependence $\alpha(T)$ in the vicinity of T_0 under the assumption that the components of $\alpha_{ij}(T)$ depend on temperature linearly, i.e.,

$$\alpha_{ij}(T) = \alpha_{ij}(T_0) - \alpha'_{ij}(T_0 - T), \ \alpha'_{ij} = \frac{d}{dT}\alpha_{ij}(T), \quad (6)$$

whence

$$\alpha(T) = \alpha_{ij}(T_0)e_ie_j + \alpha'(T_0)(T - T_0), \quad \alpha'(T_0) = \alpha'_{ij}(T - T_0)e_ie_j. \quad (7)$$

Taking into account that the first term in Eq. (7) equals zero, we obtain that in the vicinity of the transition temperature, the function $\alpha(T) = \alpha'(T - T_0)$ linearly depends on temperature.

Differentiating Eq. (4) with respect to P, we obtain the magnitude of the vector P in the form

$$P = \pm\sqrt{\frac{-\alpha}{a}} \sim \sqrt{T_0 - T}. \quad (8)$$

Thus, in the crystals of the symmetry class C_i, a second-order phase transition into the ferroelectric phase is possible. As a result, the crystal loses the center of inversion and its symmetry class is changed to C_1.

Consider the effect of the ferroelectric phase transition on the temperature variation of the rotation angles on an example of crystals of the above class. With this aim, take into account the invariants $\frac{\beta_{ij}}{2}\phi_i\phi_j$ and $g_{ij}P_iP_j\phi_l$ in the thermodynamic potential by assuming that ϕ_i are small, (this assumption allows us to ignore higher degrees of ϕ_i).

The reduced thermodynamic potential has the form

$$\bar{\Phi} = \frac{\alpha}{2}P^2 + \frac{a}{4}P^4 + \frac{\beta_{ij}}{2}\phi_i\phi_j + g_l\phi_lP^2, \quad (9)$$

where $g_l = g_{ijl}e_ie_j$. Differentiating Eq. (9) with respect to ϕ_i, we obtain

$$\beta_{ij}\phi_i = -P^2g_i. \quad (10)$$

Equation (10) should be solved together with the equilibrium equation for the polarization vector under the assumption that ϕ_i is a small perturbation. Then ϕ_i can be determined by using the solution (8). As a result, we have

$$\phi_i = +\beta_{ij}^{-1}g_i\frac{\alpha}{a} \sim T_0 - T. \quad (11)$$

Thus, the nonlinear relation between the components of the six-dimensional order parameter of the type $P^2\phi$ in the phase transition with respect to the parameter P gives rise to the kink on the temperature dependence of the heat capacity Φ_i. A similar kink on the temperature dependences of the order-parameter components, which are the invariants of the symmetry group, takes place for all the symmetry classes with the nonzero

first-order invariants. Equation (10) shows that the addition ϕ_i is an even function of the polarization-vector components which does not change its sign upon the change $P \longrightarrow -P$. It will be shown below that for the symmetry classes with four- and sixfold axes, similar changes in the first-invariant components can be written as a quadratic form whose values can vary with the change in the orientation of the spontaneous vector characterizing the low-symmetric phase.

Substituting Eqs. (8) and (11) into Eq. (9), we obtain

$$\bar{\Phi} = \frac{\Delta C}{2}(T - T_0)^2, \tag{12}$$

where ΔC is expressed in terms of all the coefficients α, a, β_{ij}, and g_1. Thus, the allowance for the nonlinear effect results in the change of the jump in the thermal capacity, ΔC, during the phase transition.

4. MONOCLINIC SYSTEM (C_s, C_2, C_{2h})

4.1. The list of invariants for the symmetry class C_s has the form

$$[P_1, P_2, \phi_3]$$

$$[P_1^2, P_1P_2, P_1\phi_3, P_2^2, P_2\phi_3, P_3^2,$$

$$P_3\phi_1, P_3\phi_2, \phi_1^2, \phi_1\phi_2, \phi_2^2, \phi_3^2]$$

$$[P_1^3, P_1^2P_2, P_1^2\phi_3, P_1P_2^2, P_1P_2\phi_3, P_1P_3^2, P_1P_3\phi_1,$$
$$P_1P_3\phi_2, P_1\phi_1^2, P_1\phi_1\phi_2, P_1\phi_2^2, P_1\phi_3^2, P_2^3, P_2^2\phi_3, P_2P_3^2, \tag{13}$$

$$P_2P_3\phi_1, P_2P_3\phi_2, P_2\phi_1^2, P_2\phi_1\phi_2, P_2\phi_2^2, P_2\phi_3^2, P_3^2\phi_3,$$

$$P_3\phi_1\phi_3, P_3\phi_2\phi_3, \phi_1^2\phi_3, \phi_1\phi_2\phi_3, \phi_2^2\phi_3, \phi_3^3]$$

$$3, 12, 28.$$

The high-temperature paraelectric phase is a pyroelectric with the spontaneous-polarization vector lying in the symmetry plane. The second-order invariants can be divided into two groups (P_1, P_2, ϕ_3) and (P_3, ϕ_1, ϕ_2), which signifies that, in addition to the isostructural phase transition, one more phase transition is possible for which the order parameter is "mixed," i.e., consists of the components having different physical meanings.

In this additional phase transition, the nonzero order-parameter components appear, P_3, ϕ_1, and ϕ_2. As a result, the class C_s is changed for the class C_1. Since the list of the third-order invariant contains no invariants dependent only on the components P_3, ϕ_1, and ϕ_2, the transition is of the second-order and leads to two phases in which the corresponding order-parameter components have opposite signs. The existence of the $P_1\phi_1^2$, $P_1P_3^2$, and other invariants of the same type containing the first-order components P_1, P_2, and ϕ_3 and the second-order components P_3, ϕ_1, and ϕ_2 provides their interaction during the phase transition and, as a result, the appearance of the components P_1, P_2, and ϕ_3. The sign reversal for the order parameter (P_3, ϕ_1, and ϕ_2) does not lead to the sign reversal for the additional P_1, P_2, and ϕ_3 arising as a result of the nonlinear relation between the two groups of the order parameter.

4.2. In the symmetry class C_2, the list of invariants is

$$[P_3, \phi_3]$$

$$[P_1^2, P_1P_2, P_1\phi_1, P_1\phi_2, P_2^2, P_2\phi_1, P_2\phi_2, P_3^2, P_3\phi_3, \phi_1^2,$$

$$\phi_1\phi_2, \phi_2^2, \phi_3^2]$$

$$[P_1^2P_3, P_1^2\phi_3, P_1P_2P_3, P_1P_2\phi_3, P_1P_3\phi_1, P_1P_3\phi_2,$$
$$P_1\phi_1\phi_3, P_1\phi_2\phi_3, P_2^2P_3, P_2^2\phi_3, P_2P_3\phi_1, P_2P_3\phi_2, \tag{14}$$

$$P_2\phi_1\phi_3, P_2\phi_2\phi_3, P_3^3, P_3^2\phi_3, P_3\phi_1^2, P_3\phi_1\phi_2, P_3\phi_2^2,$$

$$P_3\phi_3^2, \phi_1^2\phi_3, \phi_1\phi_2\phi_3, \phi_2^2\phi_3, \phi_3^3]$$

$$2, 13, 24.$$

The existence of the invariant P_3 indicates that the crystals of this class are pyroelectrics with the spontaneous-polarization vector directed along the third axis. The set of the second-order invariants allows one to expect a second-order phase transition with the formation of two phases characterized by the mixed order parameters P_1, P_2, ϕ_1, and ϕ_2. The change of the symmetry class occurs by the scheme $C_2 \longrightarrow C_1$. In this transition, a nonlinear effect takes place; as a result, a singular point on the temperature dependence $P_3 \sim (T_0 - T)$ is formed, $\phi_3 \sim (T_0 - T)$.

4.3. Crystals of the class C_{2h} have the following list of invariants

$$[\phi_3]$$

$$[P_1^2, P_1P_2, P_2^2, P_3^2, \phi_1^2, \phi_1\phi_2, \phi_2^2, \phi_3^2]$$

$$[P_1^2\phi_3, P_1P_2\phi_3, P_1P_3\phi_1, P_1P_3\phi_2, P_2^2\phi_3, P_2P_3\phi_1, \tag{15}$$

$$P_2P_3\phi_2, P_3^2\phi_3, \phi_1^2\phi_3, \phi_1\phi_2\phi_3, \phi_2^2\phi_3, \phi_3^3]$$

$$1, 8, 12.$$

The set of invariants is divided into four groups—ϕ_3, (P_1, P_2), P_3, and (ϕ_1, ϕ_2)—indicating four possible phase transitions in this class. The first transition (associated with the change of the angle ϕ_3) is a first-order phase transition taking place without the change of the symmetry class. The second transition is a rotational phase transition with the formation of the rotation angle in the plane (1, 2). The absence of the third-order invariants dependent on ϕ_1 and ϕ_2 indicates that this transition is a second-order phase transition occurring with the change of the symmetry class by the scheme

$C_{2h} \longrightarrow C_i$. The two remaining transitions are second-order ferroelectric phase transitions. In one of the transitions, the polarization vector is directed along the twofold axis, and the transition is accompanied by the change of the symmetry class according to the scheme $C_{2h} \longrightarrow C_2$. In the other transition, a spontaneous-polarization vector arises in the plane (1, 2) and the symmetry class changes by the scheme $C_{2h} \longrightarrow C_h$.

Summing the results for the monoclinic system, we see that in each of the crystallographic classes of this system, only one phase transition takes place without the change of the symmetry class. The total number of the ferroelectric phase transitions is four, of which one second-order phase transition is purely rotational. All the second-order phase transitions are accompanied by a nonlinear effect with the formation of a singular point on the temperature dependence of the order-parameter component not entering the list of the components participating in the phase transition. The nonlinear dependence observed is such that the sign reversal for the order parameter arising in the phase transition does not lead to the sign reversal of the nonlinearly dependent component.

5. ORTHORHOMBIC SYSTEM (C_2, D_2, D_{2h})

5.1. The invariants for the class C_{2v} are

$$[P_3]$$
$$[P_1^2, P_1\phi_2, P_2^2, P_2\phi_1, P_3^2, \phi_1^2, \phi_2^2, \phi_3^2]$$
$$[P_1^2P_3, P_1P_2\phi_3, P_1P_3\phi_2, P_1\phi_1\phi_3, P_2^2P_3, P_2P_3\phi_1, \quad (16)$$
$$P_2\phi_2\phi_3, P_3^3, P_3\phi_1^2, P_3\phi_2^2, P_3\phi_3^2, \phi_1\phi_2\phi_3]$$
$$1, 8, 12.$$

It is seen that the crystals from the class C_{2v} are pyroelectrics with the component of the spontaneous-polarization vector being directed along the symmetry axis. The second-order invariants of the order-parameter component are divided into four groups: (P_3), (ϕ_3), (P_1, ϕ_2), and (P_2, ϕ_1). Thus, four phase transitions are possible. Two last groups are similar in the sense that the one group can be obtained from the other group by rotating the system of coordinate by an angle of $\pi/2$ about the symmetry axis.

The first phase transition takes within the symmetry group C_{2v} and is a first-order phase transition with the jumpwise change of P_3 at the transition temperature. The second transition is a second-order rotational transition, as a result of which the symmetry plane is lost and the component ϕ_3 arises. In this case, the symmetry class changes by the scheme $C_{2v} \longrightarrow C_2$.

Two other transitions are second-order phase transition with the formation of the spontaneous-polarization vectors directed along one of the horizontal axes of the crystallographic coordinate system. Because of the nonlinear effect, the component P_3 of the polarization vector arises. In this transition, $C_{2v} \longrightarrow C_1$.

5.2. Symmetry class D_2 has the following list of invariants:

$$[\ ]$$
$$[P_1^2, P_1\phi_1, P_2^2, P_2\phi_2, P_3^2, P_3\phi_3, \phi_1^2, \phi_2^2, \phi_3^2]$$
$$[P_1P_2P_3, P_1P_2\phi_3, P_1P_3\phi_2, P_1\phi_2\phi_3, \quad (17)$$
$$P_2P_3\phi_1, P_2\phi_1\phi_3, P_3\phi_1\phi_2, \phi_1\phi_2\phi_3]$$
$$0, 9, 8.$$

The second-order invariants are divided into three groups—(P_1, ϕ_1), (P_2, ϕ_2), and (P_3, ϕ_3)—each of which, under the fulfillment of the corresponding conditions, can result in a second-order phase transition. The nonlinear effects considered above for the symmetry class D_2 are absent here. The change of the symmetry class occurs by the scheme $D_2 \longrightarrow C_2$.

5.3. In the crystals of the class D_{2h} the list of invariants has the form

$$[\ ]$$
$$[P_1^2, P_2^2, P_3^2, \phi_1^2, \phi_2^2, \phi_3^2]$$
$$[P_1P_2\phi_3, P_1P_3\phi_2, P_2P_3\phi_1, \phi_1\phi_2\phi_3] \quad (18)$$
$$0, 6, 4.$$

Here, three pure ferroelectric and three pure rotational phase transitions are possible without nonlinear effects. In the case of the ferroelectric transitions, we have $D_{2h} \longrightarrow C_{2v}$; in the case of the rotational transitions, we have $D_{2h} \longrightarrow C_{2h}$.

6. TETRAGONAL SYSTEM (C_4, S_4, C_{4h}, C_{4v}, D_4, D_{2d}, D_{4h})

6.1. The list of invariants for C_4 is

$$[P_3, \phi_3]$$
$$[P_1^2 + P_2^2, P_1\phi_1 + P_2\phi_2, P_1\phi_2 - P_2\phi_1,$$
$$P_3^2, P_3\phi_3, \phi_1^2 + \phi_2^2, \phi_3^2]$$
$$[P_1^2P_3 + P_2^2P_3, P_1^2\phi_3 + P_2^2\phi_3, P_1P_3\phi_1 + P_2P_3\phi_2, \quad (19)$$
$$P_1P_3\phi_2 - P_2P_3\phi_1, P_1\phi_1\phi_3 + P_2\phi_2\phi_3, P_1\phi_2\phi_3 - P_2\phi_1\phi_3,$$
$$P_3^3, P_3^2\phi_3, P_3\phi_1^2 + P_3\phi_2^2, P_3\phi_3^2, \phi_1^2\phi_3 + \phi_2^2\phi_3, \phi_3^3]$$
$$2, 7, 12.$$

Crystals of this class are pyroelectrics with the polarization vector being directed along the symmetry axis. The second invariants allow one to divide the order-parameter components into two groups: (P_3, ϕ_3) and $(P_1, P_2, \phi_1, \phi_2)$, respectively. In these crystals, two

phase transitions are possible. The first one is the first-order isostructural phase transition with the jumpwise change of the components P_3 and ϕ_3. The second one is a second-order phase transition occurring with the formation of nonzero components P_1, P_2, ϕ_1, and ϕ_2. We consider this transition in more detail.

The quadratic part of the thermodynamic potential for the crystals of the class C_4 with the use of the second-order invariant can be represented in the form

$$\Phi_2 = \frac{\alpha}{2}(P_1^2 + P_2^2) + \gamma_1(P_1\phi_1 + P_2\phi_2) + \gamma_2(P_1\phi_2 - P_2\phi_1) + \frac{\beta}{2}(\phi_1^2 + \phi_2^2). \quad (20)$$

The condition that should be met in the phase transition can be written in the conventional form by equating the matrix of the second derivatives to zero. However, the P and ϕ are the functions of temperatures and angles ψ and θ. Therefore, at a certain temperature (corresponding to the equilibrium ferroelectric phase), one arrives at four pairs (P_i, ϕ_i) obtained by the rotation of one of these pairs by an angle of $\pi/2$ about the fourfold axis.

Now consider the temperature dependence of the additions P_3 and ϕ_3 arising due to the nonlinear relation between $(P_1, P_2, \phi_1, \phi_2)$ and (P_3, ϕ_3) determined by the third-order invariants. The thermodynamic potential including the third-order polynomials has the form

$$\Phi_3 = \frac{\alpha_3}{2}P_3^2 + \frac{\beta_3}{2}\phi_3^2 + \omega P^2 P_3 + g_2(P_i\phi_j)P_3 + g_3 P\phi\sin\theta P_3 + g_4 P\phi\cos\theta\phi_3 + g_4 P\phi\sin\theta\phi_3 + h\phi^2\phi_3. \quad (21)$$

Differentiating (21) with respect to P_3 and ϕ_3, we obtain

$$\alpha_3 P_3 = \omega P^2 + g_1\phi^2 + g_2 P\phi\cos\theta + g_3 P\phi\sin\theta,$$
$$\beta_3\phi_3 = g_4 P\phi\cos\theta + g_5 P\phi\sin\theta + h\phi^2\phi_3. \quad (22)$$

The characteristic feature of the invariant forms (22) is their independence of the angle ψ, which signifies that all the four solutions $(P_1, P_2, \phi_1, \phi_2)$ characterized by different directions give the same contributions P_3 and ϕ_3.

Thus, the above second-order phase transition transforms the crystal class from C_4 into C_1 and gives rise to the kink on the temperature dependence P_3.

6.2. Consider the symmetry class S_4. The invariants are

$$[\phi_3]$$
$$[P_1^2 + P_2^2, P_1\phi_1 - P_2\phi_2, P_1\phi_2 + P_2\phi_1, P_3^2, \phi_1^2 + \phi_2^2, \phi_3^2]$$
$$[P_1^2 P_3 - P_2^2 P_3, P_1^2\phi_3 + P_2^2\phi_3, P_1 P_3\phi_2 - P_2 P_3\phi_1,$$
$$P_1 P_3\phi_1 + P_2 P_3\phi_2, P_1 P_2 P_3, P_1\phi_2\phi_3 + P_2\phi_1\phi_3, \quad (23)$$
$$P_1\phi_1\phi_3 - P_2\phi_2\phi_3, P_3^2\phi_3, P_3\phi_1^2 - P_3\phi_2^2,$$
$$P_3\phi_1\phi_2, \phi_1^2\phi_3 + \phi_2^2\phi_3, \phi_3^3]$$
$$1, 6, 12.$$

The second-order invariants allow one to distribute the order-parameter components over the following groups: (P_3), (ϕ_3), and $(P_1, P_2, \phi_1, \phi_2)$. In the class S_4, three phase transitions are possible. The first-order phase transition with the jumpwise change in the angle ϕ_3 occurs without the change of the symmetry class. The second-order ferroelectric phase transition results in the formation of the component P_3 of the polarization vector and is accompanied by the change of the class by the scheme $S_4 \longrightarrow C_2$. The transition with the mixed-order parameter $(P_1, P_2, \phi_1, \phi_2)$ proceeds in the same way as in the symmetry class C_4, but the singular point on the temperature dependence P_3 (caused by the nonlinear dependence of P_3 on the component of the transitions parameter) is somewhat different and requires special consideration.

The thermodynamic potential for the class S_4, which takes into account the third-order invariants, is written in the form

$$\Phi_3 = \frac{\alpha_3}{2}P_3^2 + \frac{\beta_3}{2}\phi_3^2 + \omega(P_1^2 - P_2^2)P_3 + \omega_2 P_1 P_2 P_3 + g_1(P_1^2 + P_2^2)\phi_3 + g_2 P\phi\sin\theta P_3 + g_3 P\phi\cos\theta P_3 + h_1 P\phi\cos\theta\phi_3 + h_2 P\phi\sin\theta\phi_3, \quad (24)$$

whence

$$\alpha_3 P_3 = \omega(P_1^2 - P_2^2) + \omega_2 P_1 P_2 + g_2 P\phi\sin\theta + g_3 P\phi\cos\theta, \quad (25)$$
$$\beta_3\phi_3 = g_1 P^2 + h_1 P\phi\cos\theta + h_2 P\phi\sin\theta.$$

The above formulas show that the addition to the rotation angle ϕ_3 does not depend on the direction of the order parameter arising in the phase transition. The expression for P_3 consists of two parts. The two last terms in the formula for P_3 Eq. (25) do not include the dependence on the orientation of the phase-transition parameter; the first two terms change the sign in the rotation of the polarization vector by an angle of $\pi/2$ about the symmetry axis. Therefore, P_3 can have two different values. As a result, the four polarization vectors arising in the phase transition are split into two pairs of vectors differently tilted to the symmetry axis. The change of the symmetry class in this phase transition occurs by the scheme $S_4 \longrightarrow C_1$.

6.3. Symmetry class C_{4h} has the following invariants:

$$[\phi_3]$$
$$[P_1^2 + P_2^2, P_3^2, \phi_1^2 + \phi_2^2, \phi_3^2]$$

$$[P_1^2\phi_3 + P_2^2\phi_3,\ P_1P_3\phi_2 - P_2P_3\phi_1,$$
$$P_1P_3\phi_1 + P_2P_3\phi_2,\ P_3^2\phi_3,\ \phi_1^2\phi_3 + \phi_2^2\phi_3,\ \phi_3^3] \quad (26)$$
$$1, 4, 6.$$

The second-order invariants indicate four possible phase transitions. One of them is a first-order rotational transition with the formation of an addition to ϕ_3 occurring without the change of the symmetry class. The second one is a second-order rotational phase transition with the formation of components (ϕ_1, ϕ_2). The two remaining transitions are second-order ferroelectric phase transitions. The nonlinear effects result in the kink on the temperature dependence $\phi_3(T)$ observed for all second-order phase transitions.

6.4. For the symmetry class C_{4v}, the following invariants are possible:

$$[P_3]$$
$$[P_1^2 + P_2^2,\ P_1\phi_2 - P_2\phi_1,\ P_3^2,\ \phi_1^2 + \phi_2^2,\ \phi_3^2]$$
$$[P_1^2P_3 + P_2^2P_3,\ P_1P_3\phi_2 - P_2P_3\phi_1,$$
$$P_1\phi_1\phi_3 + P_2\phi_2\phi_3,\ P_3^3,\ P_3\phi_1^2 + P_3\phi_2^2,\ P_3\phi_3^2] \quad (27)$$
$$1, 5, 6.$$

The order-parameter components are divided into three groups, (P_3), (ϕ_3), and (P_1, P_2, ϕ_1, ϕ_2); in each, a phase transition is possible. The transition, which associated with the component P_3, is an isostructural first-order phase transition. The transition with the appearance of the spontaneous rotation angle ϕ_3 is a second-order phase transition, in which the presence of the invariant $P_3\phi_3^2$ gives rise to the kink on the temperature dependence $P_3(T)$. As a result of this phase transition, the symmetry planes passing through the symmetry axis are lost, and the symmetry class of the high-temperature phase is changed according to the scheme $C_{4v} \longrightarrow C_4$.

The second-order phase transition resulting in the formation of the parameter (P_1, P_2, ϕ_1, ϕ_2) is characterized by the vector (P_1, P_2) normal to the pseudovector (ϕ_1, ϕ_2) [see Eq. (16)]. The component P_3 arising in this transition has the same value for all the four orientations of the order parameter because of the nonlinear coupling provided by the third invariants. The symmetry classes change according to the scheme $C_{4v} \longrightarrow C_s$.

6.5. Symmetry class D_4 has the following invariants:

$$[\ ]$$
$$[P_1^2 + P_2^2,\ P_1\phi_1 + P_2\phi_2,\ P_3^2,\ P_3\phi_3,\ \phi_1^2 + \phi_2^2,\ \phi_3^2]$$
$$[P_1P_3\phi_2 - P_2P_3\phi_1,\ P_1\phi_2\phi_3 - P_2\phi_1\phi_3] \quad (28)$$
$$0, 6, 2.$$

Second-order invariants allow one to divide the whole set of the order parameters into two groups: (P_3, ϕ_3) and (P_1, P_2, ϕ_1, ϕ_2). In the crystals of this class, a ferroelectric phase transition is possible with the formation of the mixed order parameter (P_3, ϕ_3). This transition is a second-order phase transition and cannot give rise to nonlinear effects mentioned above. The symmetry class is changed by the scheme $D_4 \longrightarrow C_4$.

The second transition is also of the second order. Since there is no invariant $P_1\phi_2 - P_2\phi_1$, the polarization vector is parallel to the pseudovector of the rotation angle. Under this condition, the third-order invariant goes to zero, which excludes any nonlinear effect. The change of the symmetry class occurs according to the scheme $D_4 \longrightarrow C_2$.

6.6. Symmetry class D_{2d} has the following invariants:

$$[\ ]$$
$$[P_1^2 + P_2^2,\ P_1\phi_1 - P_2\phi_2,\ P_3^2,\ \phi_1^2 + \phi_2^2,\ \phi_3^2] \quad (29)$$
$$[P_1P_3\phi_2 - P_2P_3\phi_1,\ P_1P_2P_3,\ P_1\phi_2\phi_3 + P_2\phi_1\phi_3,\ P_3\phi_1\phi_2]$$
$$0, 5, 4.$$

Here, three second-order phase transitions are possible. The rotational transition results in the formation of the spontaneous rotation angle ϕ_3 (in this case $D_{2d} \longrightarrow S_4$), but a nonlinear effect is impossible. The ferroelectric transition is accompanied by the appearance of spontaneous polarization P_3 and a change of the symmetry class, $D_{2d} \longrightarrow C_{2v}$. The nonlinear effects associated with the formation of other order-parameter components were not observed.

The third second-order phase transition results in the appearance of the spontaneous mixed parameter (P_1, P_2, ϕ_1, ϕ_2). Upon the analysis analogous to that made for the class C_4, the existence of the invariant $P_1\phi_1 - P_2\phi_2$ results in the following relations between the characteristics of the directions of the vector (P_1, P_2) and the pseudovector (ϕ_1, ϕ_2):

$$2\psi + \theta = 0, \pi. \quad (30)$$

The analysis of the fourth-order invariant results in the following two types of the solutions—(P_1, 0, ϕ_1, 0) and (P_1, P_1, $+\phi_1$, $-\phi_1$). The complete sets of the solutions are obtained by decomposing the above solutions using the rotation by angles multiple to $\pi/2$ about the fourfold axis. The selection of one of the two types of the solutions is determined by the minimum value of the thermodynamic potential, which depends on the coefficients in the fourth-order invariants. In the first type of the solutions, the symmetry class is changed according to the scheme $D_{2d} \longrightarrow C_2$; in the second type of the solutions, by the scheme $D_{2d} \longrightarrow C_s$.

The latter phase transition is accompanied by the nonlinear effect, resulting in the appearance of the non-

zero order-parameter components P_3 and ϕ_3. If upon the transition, a phase is formed, which belongs to the class C_2, the third-order invariants have the zero values and nonlinear effects are absent. If the phase transition results in the formation of the mutually perpendicular vector (P_1, P_2) and the pseudovector (ϕ_1, ϕ_2) lying on the bisectors of the angles formed by the axes x_1 and x_2 of the crystallographic coordinate system, the component of the vector P_3 can are determined by the equation

$$\alpha_3 P_3 = gP\phi + \omega P_1 P_2 + h\phi_1\phi_2. \quad (31)$$

The first term in Eq. (31) is independent of the direction of the vector (P_1, P_2), whereas the other two terms change their signs upon the rotation of the solution by $\pi/2$ about the fourfold axis.

6.7. For crystals of the class D_{4h}, the list of invariants coincides with (31); therefore, the possible phase transitions in the approximation taken for the thermodynamic potential for crystals of this class are the same as for the class D_{2d}.

7. TRIGONAL SYSTEM (C_3, S_6, C_{3v}, D_3, D_{3d})

7.1. The list of invariants for crystals of the class C_3 is

$$\begin{gathered}
[P_3, \phi_3] \\
[P_1^2 + P_2^2,\ P_1\phi_2 - P_2\phi_1,\ P_1\phi_1 + P_2\phi_2,\ P_3^2, \\
P_3\phi_3,\ \phi_1^2 + \phi_2^2,\ \phi_3^2] \\
[(1/3)P_1^3 - P_1P_2^2,\ P_1^2P_2 - (1/3)P_2^3,\ P_1^2P_3 + P_3P_2^2, \\
(1/2)P_1^2\phi_1 - P_1P_2\phi_2 - (1/2)P_2^2\phi_1, \\
(1/2)P_1^2\phi_2 + P_1P_2\phi_1 - (1/2)P_2^2\phi_2,\ P_1^2\phi_3 + \phi_3P_2^2, \\
P_1P_3\phi_2 - P_3P_2\phi_1,\ P_1P_3\phi_1 + P_3P_2\phi_2, \\
P_1\phi_1\phi_2 + (1/2)P_2\phi_1^2 - (1/2)P_2\phi_2^2, \\
(1/2)P_1\phi_1^2 - (1/2)P_1\phi_2^2 - P_2\phi_1\phi_2, \\
P_1\phi_2\phi_3 - \phi_3P_2\phi_1,\ P_1\phi_1\phi_3 + \phi_3P_2\phi_2,\ P_3^3,\ P_3^2\phi_3, \\
P_3\phi_1^2 + P_3\phi_2^2,\ P_3\phi_3^2,\ (1/3)\phi_1^3 - \phi_1\phi_2^2, \\
\phi_1^2\phi_2 - (1/3)\phi_2^3,\ \phi_1^2\phi_3 + \phi_3\phi_2^2,\ \phi_3^3] \\
2,\ 7,\ 20.
\end{gathered} \quad (32)$$

The list of second-order invariants coincides with the analogous list for the class C_4. Therefore, all the conclusions made earlier about the mutual orientations of the polarization and rotational components are valid in this case as well. The existence of nonzero third-order invariants dependent on the parameters of the phase transition indicate that these transitions are first-order phase transitions. If the parameter of the phase transitions is (P_3, ϕ_3), then this transition should occur without the change of the symmetry class. If the phase-transition parameter is (P_1, P_2, ϕ_1, ϕ_2), the class is changed by the scheme $C_3 \longrightarrow C_1$. A new fact not discussed above is a jumpwise change of P_3 and ϕ_3 in the phase transition (P_1, P_2, ϕ_1, ϕ_2) provided by the mixed third-order invariants. The equation for determining P_3 has the form

$$\alpha_3 P_3 = g_1 P\phi\sin\theta + g_2 P\phi\cos\theta + \omega P^2 + h\phi^2 \quad (33)$$

and shows that the phase transition with respect to the parameter (P_1, P_2, ϕ_1, ϕ_2) gives rise to the jumpwise formation of the addition P_3 having the same value for all the three directions (P_1, P_2, ϕ_1, ϕ_2).

7.2. The invariants of the class S_6 are

$$\begin{gathered}
[\phi_3] \\
[P_1^2 + P_2^2,\ P_3^2,\ \phi_1^2 + \phi_2^2,\ \phi_3^2] \\
[(1/2)P_1^2\phi_2 + P_1P_2\phi_1 - (1/2)P_2^2\phi_2, \\
(1/2)P_1^2\phi_1 - P_1P_2\phi_2 - (1/2)P_2^2\phi_1, \\
P_1^2\phi_3 + \phi_3P_2^2,\ P_1P_3\phi_1 + P_3P_2\phi_2,\ P_1P_3\phi_2 - P_3P_2\phi_1, \\
P_3^2\phi_3,\ (1/3)\phi_1^3 - \phi_1\phi_2^2,\ \phi_1^2\phi_2 - (1/3)\phi_2^3, \\
\phi_1^2\phi_3 + \phi_3\phi_2^2,\ \phi_3^3] \\
1,\ 4,\ 10.
\end{gathered} \quad (34)$$

Second-order invariants show that in the crystals of the symmetry class S_6, two second-order ferroelectric and two first-order rotational phase transitions are possible. The phase transition resulting in the appearance of the parameter ϕ_3 occurs without the change of the symmetry class. In the transition resulting in the appearance of nonzero (ϕ_1, ϕ_2), the class changes by the scheme $S_6 \longrightarrow C_1$. In the second-order transitions resulting in the appearance of a spontaneous-polarization vector P_3, the class changes, $S_6 \longrightarrow C_3$. In the phase transition with the appearance of the spontaneous-polarization vector in the (001) plane, the class changes by the scheme $S_6 \longrightarrow C_1$, whereas the nonlinear interaction between the order-parameter components results in the formation of nonzero ϕ_1, ϕ_2, ϕ_3 by the mechanism of improper rotational phase transitions.

7.3. The list of the invariants for the crystals of the class C_{3v} is

$$\begin{gathered}
[\phi_3] \\
[P_1^2 + P_2^2,\ P_3^2,\ \phi_1^2 + \phi_2^2,\ \phi_3^2]
\end{gathered}$$

$$[(1/2)P_1^2\phi_2 + P_1P_2\phi_1 - (1/2)P_2^2\phi_2,$$
$$(1/2)P_1^2\phi_1 - P_1P_2\phi_2 - (1/2)P_2^2\phi_1,$$
$$P_1^2\phi_3 + \phi_3P_2^2, P_1P_3\phi_1 + P_3P_2\phi_2, P_1P_3\phi_2 - P_3P_2\phi_1, \quad (35)$$
$$P_3^2\phi_3, (1/3)\phi_1^3 - \phi_1\phi_2^2, \phi_1\phi_2 - (1/3)\phi_2^3,$$
$$\phi_1^2\phi_3 + \phi_3\phi_2^2, \phi_3^3]$$
$$1, 4, 10.$$

The second-order invariants coincide with the analogous invariants of the symmetry class C_{4v}. Unlike the phase transitions in the class C_{4v}, the phase transition in the class C_{3v} occurring with the formation of the nonzero order parameter (P_1, P_2, ϕ_1, ϕ_2) is a first-order phase transition. If the polarization vector is directed along [100], then the class changes, $C_{3v} \longrightarrow C_1$. Since the order-parameter components are related nonlinearly, which is determined by the third-order invariants, then the phase transition is accompanied by the jumplike formation of the addition to the vector P_3.

7.4. For the symmetry class D_3, the following invariants are possible:

$$[\ ]$$
$$[P_1^2 + P_2^2, P_1\phi_1 + P_2\phi_2, P_3^2, P_3\phi_3, \phi_1^2 + \phi_2^2, \phi_3^2]$$
$$[P_1^2P_2 - (1/3)P_2^3, (1/2)P_1^2\phi_2 + P_1P_2\phi_1 - (1/2)P_2^2\phi_2,$$
$$P_1P_3\phi_2 - P_3P_2\phi_1, P_1\phi_1\phi_2 + (1/2)P_2\phi_1^2 - (1/2)P_2\phi_2^2, \quad (36)$$
$$P_1\phi_2\phi_3 - \phi_3P_2\phi_1, \phi_1^2\phi_2 - (1/3)\phi_2^3]$$
$$0, 6, 6.$$

The first- and second-order invariants in the classes D_3 and D_4 are the same, whereas the third-order invariants are different, which results in the fact that the transition determined by the order parameter (P_1, P_2, ϕ_1, ϕ_2) is a first-order phase transition. Similar to the class D_4, nonlinear effect of the type under study are absent in the class D_3. The change of symmetry classes occurs according to the schemes $D_3 \longrightarrow C_2$ and $D_3 \longrightarrow C_1$, depending on the direction of the vector (P_1, P_2).

7.5. The list of invariants for the crystals of the class D_{3d} has the form

$$[\ ]$$
$$[P_1^2 + P_2^2, P_3^2, \phi_1^2 + \phi_2^2, \phi_3^2]$$
$$[(1/2)P_1^2\phi_2 + P_1P_2\phi_1 - (1/2)P_2^2\phi_2, \quad (37)$$
$$P_1P_3\phi_2 - P_3P_2\phi_1, \phi_1^2\phi_2 - (1/3)\phi_2^3]$$
$$0, 4, 3.$$

In these crystals, two ferroelectric and two rotational phase transitions are possible. Both ferroelectric transitions are second-order phase transitions. The phase transition with the formation of the spontaneous polarization vector P_3 results in the change of the classes, $D_{3d} \longrightarrow C_{3v}$. If the spontaneous-crystallization vector is represented in the form (P_1, P_2, 0), then either $D_{3d} \longrightarrow C_2$ or $D_{3d} \longrightarrow C_s$. The rotational transition resulting in the formation of the spontaneous rotation angle (0, 0, ϕ_3) results in the change of the symmetry class, $D_{3d} \longrightarrow C_3$. If the spontaneous-rotation angle has the projections (ϕ_1, ϕ_2, 0), then the change occurs by the scheme $D_{3d} \longrightarrow C_{2h}$ or $D_{3d} \longrightarrow C_1$, depending on the direction (ϕ_1, ϕ_2, 0).

8. HEXAGONAL SYSTEM (C_6, C_{3h}, C_{6h}, C_{6v}, D_{3h}, D_6, D_{6h})

8.1. The list of invariants for crystals of class C_6 is

$$[P_3, \phi_3]$$
$$[P_1^2 + P_2^2, P_1\phi_2 - P_2\phi_1, P_1\phi_1 + P_2\phi_2,$$
$$P_3^2, P_3\phi_3, \phi_1^2 + \phi_2^2, \phi_3^2]$$
$$[P_1^2P_3 + P_3P_2^2, P_1\phi_3 + \phi_3P_2^2,$$
$$P_1P_3\phi_1 + P_3P_2\phi_2, P_1P_3\phi_2 - P_3P_2\phi_1, \quad (38)$$
$$P_1\phi_1\phi_3 + \phi_3P_2\phi_2, P_1\phi_2\phi_3 - \phi_3P_2\phi_1, P_3^3, P_3^2\phi_3,$$
$$P_3\phi_1^2 + P_3\phi_2^2, P_3\phi_3^2, \phi_1^2\phi_3 + \phi_3\phi_2^2, \phi_3^3]$$
$$2, 7, 12.$$

The lists of the first- and second-order invariants of the symmetry classes C_6 and C_4 are the same; therefore, in both classes, the same phase transitions and the same nonlinear effects take place. However, the class C_4 has six (not four) orientations of the vector (P_1, P_2, 0) and the pseudovector (ϕ_1, ϕ_2, 0). The symmetry classes are changed by the schemes $C_6 \longrightarrow C_6$ and $C_6 \longrightarrow C_1$.

8.2. The list of invariants for the symmetry class C_{3h} has the form

$$[\phi_3]$$
$$[P_1^2 + P_2^2, P_3^2, \phi_1^2 + \phi_2^2, \phi_3^2]$$
$$[(1/3)P_1^3 - P_1P_2^2, P_1^2P_2 - (1/3)P_2^3, P_1^2\phi_3 + \phi_3P_2^2,$$
$$P_1P_3\phi_2 - P_3P_2\phi_1, P_1P_3\phi_1 + P_3P_2\phi_2,$$
$$(1/2)P_1\phi_1^2 - (1/2)P_1\phi_2^2 - P_2\phi_1\phi_2, \quad (39)$$
$$P_1\phi_1\phi_2 + (1/2)P_2\phi_1^2, (1/2)P_2\phi_2^2, P_3\phi_3,$$
$$\phi_1^2\phi_3 + \phi_3\phi_2^2, \phi_3^3]$$
$$1, 4, 10.$$

The lists of first- and second-order invariants and the lists of the phase transitions in the classes C_{3h} and C_{4h} are the same. The ferroelectric transition, which results in the spontaneous polarization (P_1, P_2, 0), is a first-order phase transition in this symmetry class which is associated with the existence of third-order invariants dependent on P_1 and P_2.

Consider the nonlinear effect of appearance of electric polarization in the rotational phase transition occurring, with the formation of the spontaneous rotation angle $(\phi_1, \phi_2, 0)$. The reduced thermodynamic potential with preservation of the terms necessary for the determination of P_1 and P_2 can be written as

$$\Phi = \frac{\alpha}{2}P^2 - h_1((\phi_1^2 - \phi_2^2)P_1 - 2\phi_1\phi_1 P_2) - h_2(2\phi_1\phi_1 P_1 + (\phi_1^2 - \phi_2^2)P_2). \quad (40)$$

Differentiating Φ with respect to P_1 and P_2, we obtain

$$P_1 = \frac{h_1}{\alpha}(\phi_1^2 - \phi_2^2) + \frac{2h_2}{\alpha}\phi_1\phi_2,$$
$$P_2 = -\frac{2h_1}{\alpha}\phi_1\phi_2 + \frac{h_2}{\alpha}(\phi_1^2 - \phi_2^2). \quad (41)$$

Assuming that

$$\phi_1 = \phi\cos\chi, \quad \phi_2 = \phi\sin\chi \quad (42)$$

and substituting Eqs. (42) into Eqs. (41), we obtain

$$\tan\psi = \frac{P_2}{P_1} = \tan(\chi_0 - 2\chi). \quad (43)$$

It follows from Eq. (43) that the clockwise rotation of the pseudovector (ϕ_1, ϕ_2) by $\pi/3$ about the symmetry axis (which corresponds to the transitions from one phase to the neighboring one), results in the clockwise rotation of the vector (P_1, P_2) by the angle $2\pi/3$. As a result, the phase transition yields three possible orientations of the polarization vector. Different states of the low-temperature phase with due regard for nonlinear effect can be represented in the plane (ϕ_1, ϕ_2) (Fig. 1).

Figure 1 shows six radius-vectors from a set of pseudovectors of the rotation angles arising in the phase transitions. Small vectors "bound" to the ends of the pseudovectors are the spontaneous polarization vectors arising due to nonlinear relationships (41).

The above example can be considered as an improper ferroelectric phase transition [7] caused by the rotational phase transition and the nonlinear relation between the rotational and polarization components of the order parameter.

8.3. The invariants for the crystals of the symmetry class D_6 coincide, up to the third order, with the analogous invariants for the class D_4. Therefore, the phase transitions in both classes are analogous with the only difference—the number of the phase orientations (P_1, P_2, ϕ_1, ϕ_2) in the class D_6 equals six (not four) as is the class D_4.

8.4–8.6. Similar situation also takes place for the classes C_{6h} and C_{4h}, C_{6v} and C_{4v}, and D_{6h} and D_{4h}.

8.7. Consider the remaining symmetry class D_{3h} of the hexagonal system. The list of invariants for this class is

[ ]

$$[P_1^2 + P_2^2, P_3^2, \phi_1^2 + \phi_2^2, \phi_3^2]$$

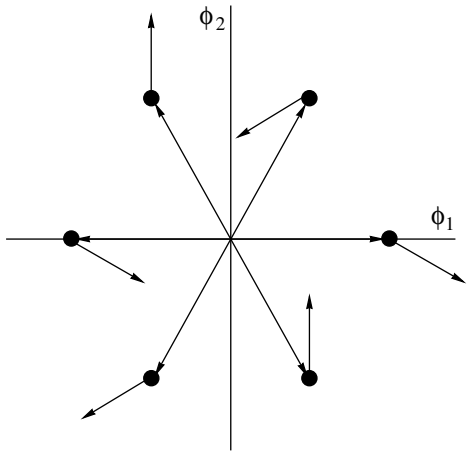

Fig. 1. Directions of the order parameters of possible low-temperature phases in the crystal of the class C_{3h}.

$$[P_1^2P_2 - (1/3)P_2^3, P_1P_3\phi_2 - P_3P_2\phi_1, P_1\phi_1\phi_2 + (1/2)P_2\phi_1^2 - (1/2)p_2\phi_2^2] \quad (44)$$

0, 4, 3.

In the crystals of the class D_{3h}, the following four phase transitions are possible: first-order ferroelectric phase transitions with the formation of the polarization vector $(P_1, P_2, 0)$, second-order ferroelectric phase transition with the polarization vector $(0, 0, P_3)$, and two rotational phase transitions with the pseudovectors of the rotation angles $(0, 0, \phi_3)$ and $(\phi_1, \phi_2, 0)$. The latter phase transition accompanied by the nonlinear effect of the formation of the polarization-vector with the components $(P_1, P_2, 0)$ is absolutely analogous to that considered for the symmetry class D_{3d}.

9. CUBIC SYSTEM (T, T_h, T_d, O, O_h)

9.1. The list of invariants for crystals of the class T is

[ ]

$$[P_1^2 + P_2^2 + P_3^2, P_1\phi_1 + P_2\phi_2 + P_3\phi_3, \phi_1^2 + \phi_2^2 + \phi_3^2]$$
$$[P_1\phi_2\phi_3 + P_2\phi_3\phi_1 + P_3\phi_1\phi_2, P_1P_2\phi_3 + P_2P_3\phi_1 + P_3P_1\phi_2, P_1P_2P_3, \phi_1\phi_2\phi_3] \quad (45)$$

0, 3, 4.

In these crystals, only one first-order phase transition is possible, which is characterized by the spontaneous-polarization vector and the pseudovector of the rotation angle directed along [111]. The symmetry class is changed by the scheme $T \longrightarrow C_3$. The linear dependence between P and ϕ, which determines parallelity or antiparallelity of the polarization and rotational components is determined by minimizing the thermodynamic potential.

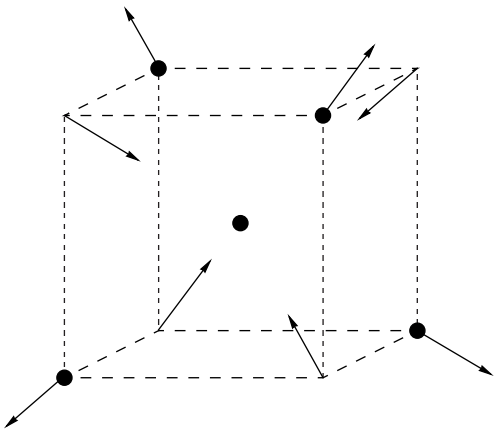

Fig. 2. Directions of the order parameters of possible low-temperature phases in the crystals of the class T_d.

9.2. The list of invariants for the crystals of class T_h is

$$\begin{gathered}[\ ]\\ [P_1^2 + P_2^2 + P_3^2,\ \phi_1^2 + \phi_2^2 + \phi_3^2]\\ [P_1P_2\phi_3 + P_2P_3\phi_1 + P_3P_1\phi_2,\ \phi_1\phi_2\phi_3]\\ 0,\ 2,\ 2.\end{gathered} \tag{46}$$

Two phase transitions are possible in crystals of this class. One of them is a second-order ferroelectric phase transition. Its thermodynamics can readily be obtained by passing to the reduced potential represented in the form:

$$\Phi = \frac{\alpha}{2}P^2 + \frac{a_1}{4}P^4 + \frac{a_2}{4}(P_1^4 + P_2^4 + P_3^4). \tag{47}$$

It is well known that if $a_2 > 0$, the polarization vector is directed along [111], whereas if $a_2 < 0$, it is directed along [100].

The rotational phase transition resulting in the formation of the pseudovector of rotation along [111] can be described in the same way. In the case of the ferroelectric transition with the formation of the polarization vector along [111], the nonlinear effect of the formation of the rotational component along the [111] direction takes place.

9.3. The list of invariants for the crystals of the class T_d has the form

$$\begin{gathered}[\ ]\\ [P_1^2 + P_2^2 + P_3^2,\ \phi_1^2 + \phi_2^2 + \phi_3^2]\\ [P_1\phi_2\phi_3 + P_2\phi_3\phi_1 + P_3\phi_1\phi_2,\ P_1P_2P_3]\\ 0,\ 2,\ 2.\end{gathered} \tag{48}$$

In the crystals of this class, a first-order ferroelectric phase transition with the polarization vector along [111] and a rotational second-order phase transition take place. The direction of the pseudovector of the rotation angle is determined by the sign of the coefficient analogous to a_2 in Eq. (47). If the pseudovector (ϕ_1, ϕ_2, ϕ_3) is directed along [111], a nonlinear effect of the formation of the spontaneous-polarization vector takes place, because the list of invariants includes the expression $P_1\phi_2\phi_3 + P_2\phi_1\phi_3 + P_3\phi_1\phi_2$.

The analytical expression for the polarization vector has the form

$$P_1 = \frac{g}{\alpha}\phi_2\phi_3, \quad P_2 = \frac{g}{\alpha}\phi_1\phi_3, \quad P_3 = \frac{g}{\alpha}\phi_1\phi_2. \tag{49}$$

The vectors at various values of the equilibrium rotational parameter are shown in Fig. 2. It is seen that the polarization vectors exit from four of the cube vertices forming a tetrahedron inscribed into this cube, whereas the vectors at the vertices of an additional tetrahedron are directed inside the cube.

Thus, the rotational transition in the crystals of the class T_d results in the appearance of the polarization vector with a rather weak temperature dependence of P.

9.4. The list of invariants for crystals of the class O is

$$\begin{gathered}[\ ]\\ [P_1^2 + P_2^2 + P_3^2,\ P_1\phi_1 + P_2\phi_2 + P_3\phi_3,\ \phi_1^2 + \phi_2^2 + \phi_3^2]\\ [\ ]\\ 0,\ 3,\ 0.\end{gathered} \tag{50}$$

It is seen that in the crystals of this class, a second-order phase transition with the mixed order parameter is possible. The polarization vector and the pseudovector of the rotation angle have the same direction coinciding either with [111] or [100], depending on the ratio of the coefficients of the quartic part of the thermodynamic potential of the crystal.

9.5. The list of invariants for crystals of the class O_h has the form

$$\begin{gathered}[\ ]\\ [P_1^2 + P_2^2 + P_3^2,\ \phi_1^2 + \phi_2^2 + \phi_3^2]\\ [\ ]\\ 0,\ 2,\ 0.\end{gathered} \tag{51}$$

Thus, in the crystals of this class, two independent second-order phase transitions are possible—ferroelectric and rotational. The phase transitions in the crystals whose state is characterized by the multicomponent order parameter can be divided into two classes. The first one consists of the transitions in which the most pronounced temperature dependence is observed for the set of the order-parameter components having the same physical sense (a polarization vector or a pseudovector of the rotation angles). The second group includes transitions for which the parameter compo-

nents have a different physical sense. The symmetry properties of crystals and adherence to a certain symmetry class allow one to predict possible structural phase transitions and the sets of order-parameter components, which determine the nature of the corresponding phase transitions. The specific temperature behavior is observed in phase transitions not only for the leading components of the order parameter (determined for the given transition by the second-order invariants) but also for a wider spectrum of the order-parameter components because of the nonlinear relation between these components [7].

In the crystals of the classes C_{3h}, D_{3h}, and T_d, improper ferroelectric phase transitions are possible, whose main parameters are the components of the rotation-angle pseudovectors. The rotational component of the order parameter in these crystals provides the appearance of the polarization component.

REFERENCES

1. A. M. Glaser, Acta Crystallogr., Sect. B: Struct. Crystallogr. Cryst. Chem. **B28**, 3384 (1972).
2. K. S. Aleksandrov, Kristallografiya **21** (2), 249 (1976) [Sov. Phys. Crystallogr. **21**, 133 (1976)].
3. K. S. Aleksandrov, A. T. Anistratov, B. V. Beznosikov, and N. V. Fedoseeva, *Phase Transitions in ABX_3 Halide Crystals* (Nauka, Novosibirsk, 1981).
4. K. S. Aleksandrov and B. V. Beznosikov, *Perovskitelike Crystals* (Nauka, Novosibirsk, 1997).
5. V. Dvořak, J. Phys. Soc. Jpn. **28**, 252 (1970).
6. M. P. Shaskol'skaya, *Crystallography* (Vysshaya Shkola, Moscow, 1984).
7. A. P. Levanyuk and D. G. Sannikov, Usp. Fiz. Nauk **112**, 561 (1974) [Sov. Phys. Usp. **17**, 199 (1974)].

Translated by L. Man

Crystallography Reports, Vol. 46, No. 2, 2001, pp. 268–275. From Kristallografiya, Vol. 46, No. 2, 2001, pp. 311–319.

Structural Aspects of Solid-State Amorphization in GaSb Single Crystals[1]

I. M. Shmyt'ko and V. N. Zverev

Institute of Solid State Physics, Russian Academy of Sciences, Chernogolovka, Moscow oblast, 142432 Russia

e-mail: shim@issp.ac.ru

Received May 13, 1997; in the final form, December 16, 1999

Abstract—As is well known, the GaSb I phase that is stable at room temperature is transformed under high pressures and temperatures into the GaSb II phase, which, being frozen in liquid nitrogen, becomes a metastable phase. The X-ray studies of GaSb II under heating showed the formation of two "thermally reversible" phases providing halolike X-ray diffraction patterns. It was also shown that the low-angle scattering spectrum also reversibly changes with the temperature and that macrocrystalline grains appearing during heating at elevated temperatures dissipate in the process of the subsequent specimen cooling. The structural states observed are interpreted as paracrystalline. © *2001 MAIK "Nauka/Interperiodica".*

1. INTRODUCTION

A large number of compounds in binary and ternary systems exhibit solid-state amorphization. In our case, this term signifies the occurrence of broad halos in X-ray reflection spectra in the heating process of initially crystalline metastable high-pressure phases. Among these systems, there are Zn–Sb, Cd–Sb, Al–Ge, Ga–Sb, $Gd_2(MoO_4)_3$, ice, etc. [1]. McDonald *et al.* were the first to observe halos on diffraction patterns from GaSb crystals upon annealing of the frozen high-pressure phases [2]. A thin GaSb disc was compressed between Bridgman anvils up to the pressures that caused the transition of the initial semiconductor phase, GaSb I, into a metal phase, GaSb II; then the sample was cooled in a chamber under a load to the liquid-nitrogen temperature, and chamber was decompressed. The subsequent heating process did not return the sample directly into the initial state; the sample was first transformed into an "amorphous" phase giving rise to formation of halos on the corresponding diffraction pattern. It was assumed that this amorphous phase was a highly disordered GaSb I. Later, the formation of diffraction halos was also obtained during heating of the quenched GaSb II phase [3, 4].

The dilatometric and calorimetric characteristics of GaSb [5] and other compounds [6–8] were measured to show that the solid-state amorphization gives rise to an increase of the sample volume and that this process is exothermic. Since the rate of temperature variations in these experiments ranged from several degrees to several dozens of degrees per minute [5–8], the recorded structural states were nonequilibrium. This fact and the possible formation of halos on diffraction patterns not only due to amorphization but also by the nanocrystalline nature of scattering elements, second-order crystal-lattice defects [9–11], paracrystal [9, 12–15], and some other factors [16, 17] stimulated this study aimed at establishing the structural aspects of the solid-state amorphization.

2. EXPERIMENT

The samples for the study were selected by the following reasons. Usually, the X-ray scattering spectra of pure amorphous and nanocrystalline states can hardly be distinguished. However, in diffraction experiments, these states should have different kinetics of the transition from the crystalline state. In particular, the normalized angular distribution of the diffracted intensities for the amorphous state should be independent of the volume fraction of the crystalline–amorphous state transformation, whereas in the process of nanocrystallization such a dependence should exist.[2] In accordance with the Curie law, the formation of a texture in the subgrain orientation (reflecting the macrosymmetry of the cuts of the initial single crystal) during nanocrystallization is possible at all the stages of the transformation GaSb I ⟶ GaSb II ⟶ solid-state amorphization ⟶ GaSb I. In the case of amorphization of the initially homogeneous sample, no texture formation is expected. Finally, although individual crystallites in a nanocrystalline state are quite small, a certain degree of the long-range order is retained. In X-ray diffraction experiments, this fact should result in the temperature dependence of halo intensities (the Debye–Waller factor [18–20]). For an amorphous sample, the static atomic displacements caused by the topologic disorder usually exceed the amplitudes of atomic thermal vibrations; thus, no temperature dependence of the diffracted

[1] This article was submitted by the authors in English.

[2] The first nanocrystallization stages should be accompanied by broadening of the main reflections of the crystal.

intensities is observed.[3] In view of the above consideration, we decided to study a single crystal. A $1 \times 2 \times 5$ mm-large rectangular sample with the developed face parallel to (100) was cut out from a Czochralski-grown single crystal.

The sample was subjected to the thermobaric treatment in a quasihydrostatic high-pressure cell (P = 70 kbar, the Teflon medium, the loading time 24 h, T = 520 K). Then, the setup under the same pressure was cooled down to 100 K, and the cell was depressurized. The sample was dismounted in liquid nitrogen; the sample holder for X-ray diffraction studies was also kept in liquid nitrogen.

The X-ray studies were performed in an automated DRON-4-07 diffractometer. The sample holder was made in such a way that the electrodes could be brought into contact with a crystal to measure the resistivity simultaneously with the X-ray diffraction experiment. The sample fixation in the holder limited the area of the sample to 2×2-mm-large area.

We used the Bragg–Brentano geometry (CuK_α and AgK_α radiations), the depth of the absorbing layer did not exceed the values of 3 and 63 μm, which corresponds to a strong absorption (ten-times absorption of the layer).

All the experiments on structural rearrangements upon heating of the quenched GaSb II phase were performed by keeping the sample for a long time at each temperature. Such an experimental scenario provided the discovery of a number of new structural states during very slow heating of a frozen amorphous state in an MBBA liquid crystal that were not recorded at rapid heating [21].

3. RESULTS

Figures 1a and 1b show the graphical representation of the diffraction patterns hereafter called, for brevity, diffractograms of the quenched high-pressure GaSb II phase for (Fig. 1b) initially single crystal and (Fig. 1a) initially polycrystalline samples (CuK_α radiation). Comparing reflection indices, we came to a conclusion on the formation of a developed texture in the single crystal sample. In fact, the diffractogram of the polycrystalline sample (Fig. 1a) (similar to the Debye–Scherrer X-ray diffraction patterns obtained in [2]) showed no (00l)-type reflections, whereas the intensity of the (001) on the pattern from a single crystal sample is pronounced. At the same time, the (h00) reflections from the polycrystal pattern are intensive, whereas on the diffraction pattern from the single crystal sample they are absent. Thus, the single crystal GaSb II sample can be regarded as an oriented polycrystal with the texture axis in the [001] direction. The formation of the well-pronounced texture unambiguously indicates

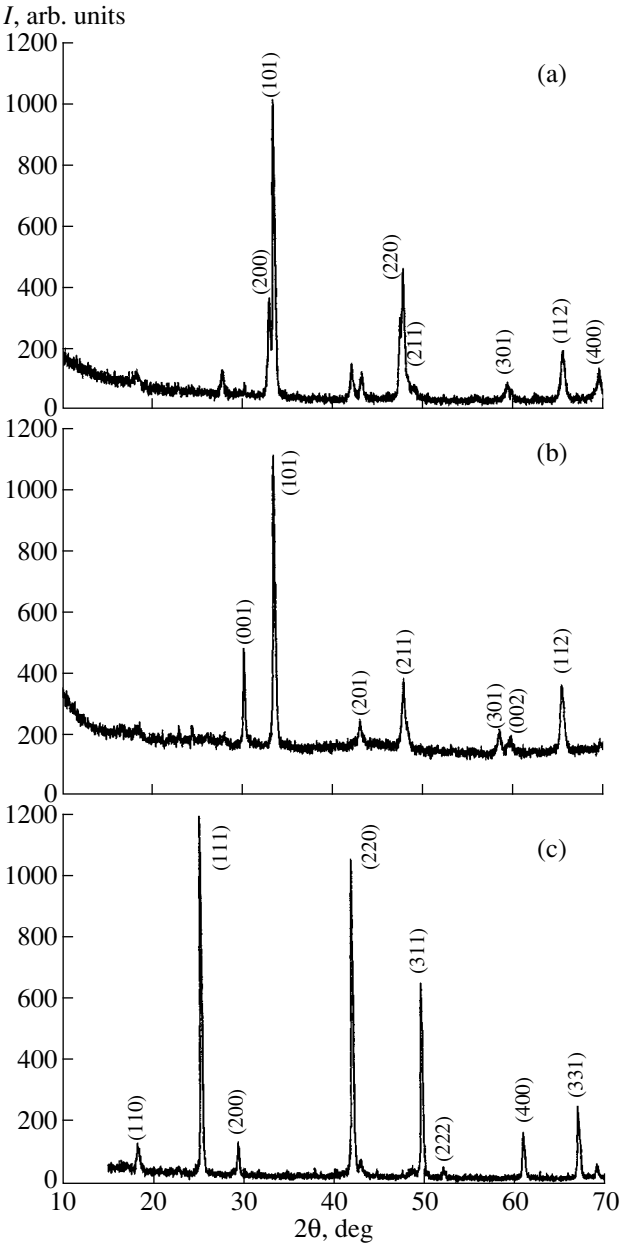

Fig. 1. Diffractograms of the quenched state of the high-pressure GaSb II phase obtained from the initially (a) polycrystalline, (b) single crystal samples; and (c) GaSb I phase of polycrystalline sample.

the existence of the structural memory during the GaSb I ⟶ GaSb II transformation, which should be accompanied by the transition to another symmetry subgroup.

The second run of the experiments consisted in annealing of the GaSb II phase: the sample whose resistance was measured was heated above 77 K and was kept at this temperature until its resistance acquired steady-state value (which indicated the quasiequilibrium state in accordance with resistance measurements). We also recorded the control diffraction patterns. Then the temperature was increased again, and

[3] In principle, a weak change in the scattering intensities for amorphous samples should be observed because of the temperature dependence of the sample density.

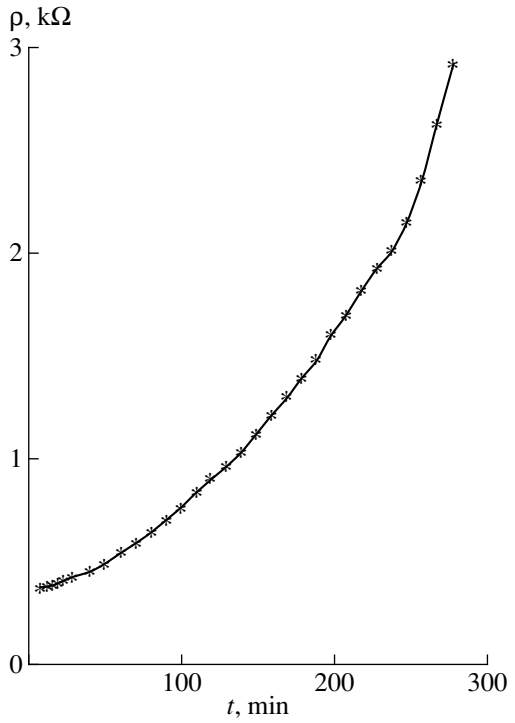

Fig. 2. Resistance of GaSb II vs duration of the intermediate heating stages for an initially single crystal sample.

annealing continued up to the attainment of a new quasiequilibrium state.

The resistance measurements were made simultaneously with the structural studies. Figure 2 shows resistance versus time of annealing at 180 K for the sample which underwent partial transformation during the preliminary heating. This curve confirms the nonequilibrium nature of the structural states during the calorimetric and the dilatometric measurements [1, 3–8]. The rates of the temperature variation were several order of magnitude higher, which indicated the necessity of long keeping of the samples at each temperature.

The diffractograms obtained at the annealing stages, at which the samples underwent the transformation from a metal (resistance measurements) to a semiconductor (an increase of resistance by a factor of 10^8) were similar to those shown in Fig. 1b. In other words, the volume fraction of a dielectric phase forming at this stage is insignificant and that it was nucleated as a planar layer.

Upon the attainment of a steady-state resistance of the sample (the final annealing temperature was 192 K), the sample was cooled to 77 K in liquid nitrogen and was kept at this temperature for quite a long time. Upon keeping the sample at liquid-nitrogen temperature for 1.5 months (resistance measurements), the diffraction pattern of the sample dramatically changed. All the diffraction lines due to GaSb II disappeared and broad halolike reflections formed. Hereafter, we call such patterns "pseudoamorphous" and the corresponding structural states, pseudoamorphous phases. An increase of the layer depth by using the AgK_α radiation changed the diffraction pattern (Fig. 3). In this case, both the reflections due to the GaSb II phase and the halos of the "pseudoamorphous" phase are recorded. Figures 3a–3c illustrate the changes in the diffraction patterns upon the annealing of the sample at high temperatures.[4] A decrease of the reflection intensities from the crystalline phase are not accompanied by the respective changes in the half-width during annealing. The latter fact and a decrease in the temperature of the transformation of the GaSb II-"pseudoamorphous" phase and disappearance of the reflections from the crystalline phase at the use of X-rays with a small penetration depth lead to an assumption about the beginning of a certain stage of transformation of the pseudoamorphous phase on the sample surface in the form of a thin layer. During the subsequent annealing, this phase "spreads" into the crystal depth.

The temperature-induced changes in the diffraction spectra upon a complete disappearance of the "crystal reflections" is shown in Fig. 3. Each diffraction spectrum was recorded from a stable structure, which was confirmed by invariable spectra from a crystal kept at the chosen temperature point for dozens of hours. The sequence of spectra *1–6* corresponds to a gradual increase of the sample temperature. A smooth transformation of the spectrum, recorded at low temperatures (curve *1*) to a new "halolike spectrum" recorded at room temperature (curves *5*, *6*) is clearly seen in Fig. 4. During such transformation, the center of gravity of the first halo smoothly shifts to the small-angle range, whereas its intensity and half-width anomalously increase with the temperature. Sample heating from 89 to 300 K, this increase attains up to 30%.

At the variation of the sample temperature within 77–200 K, the diffraction spectra did not change and were similar to spectrum *1* in Fig. 4. Since the latter spectrum differed from the known spectra of GaSb, we concluded that the spectrum obtained belong to a new low-temperature "pseudoamorphous" phase. Diffraction spectra *5–6* were identified as those of another phase—a high-temperature "pseudoamorphous" phase (or state) because they differed from spectrum *1* and insignificantly changed at room temperatures. The thermal reversibility of these two phase states observed in our experiments was somewhat surprising and manifested itself in changes of the diffraction spectra shown in Fig. 4 in the reverse succession during sample cooling. The thermal reversibility of the structural states signifies that despite the metastable state of the sample, the two pseudoamorphous phases are in equilibrium in the temperature range studied.

Figure 5 shows the diffraction spectrum of the sample heated to 323 K. The narrow crystal peaks appear in the region of the first halo maximum. Some signs of

[4] All the diffraction patterns were obtained at 89 K.

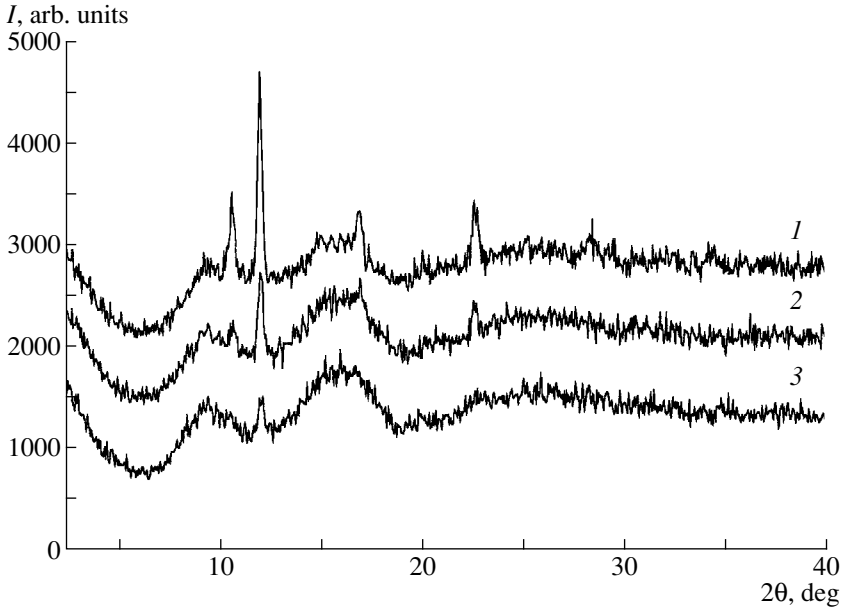

Fig. 3. (*1–3*) Diffractograms of successive structural states of GaSb II during sample annealing at 185–220 K (AgK_α radiation). (For a clearer presentation, spectra *2* and *3* are shifted along the ordinate axis by 500 units with respect to the previous spectrum.)

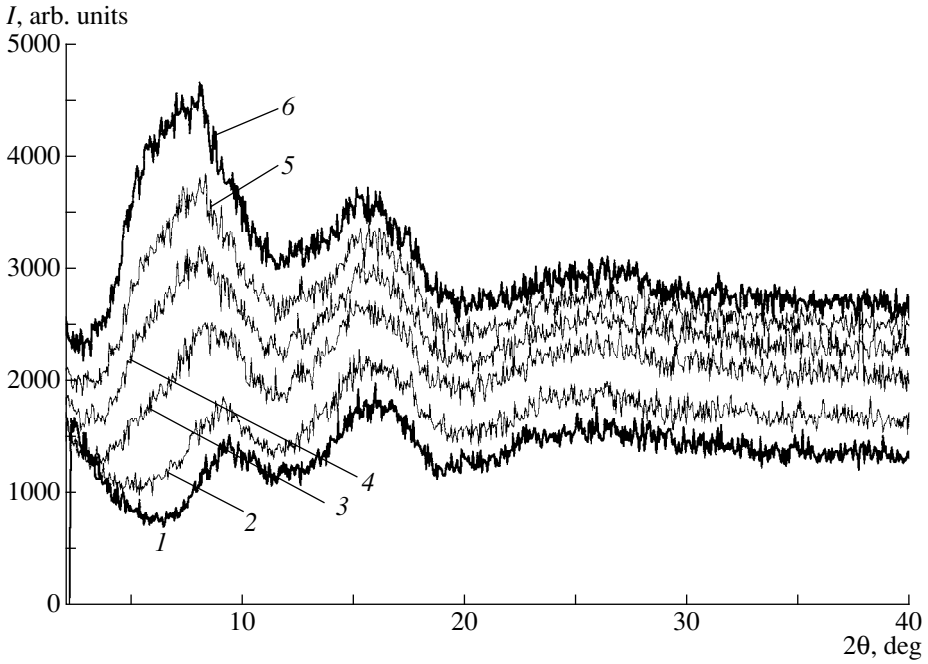

Fig. 4. Diffraction spectra of GaSb in the steady structural states (in the upward direction): (*1*) 89, (*2*) 120, (*3*) 206, (*4*) 231, (*5*) 259, and (*6*) 311 K; diffraction spectra of the low-temperature (*1*) and high-temperature (*2*) "amorphized" phases in the steady state. (For clearer representation spectra *2–6* are shifted along the ordinate axis by 500 units with respect to the previous spectrum.)

formation of these peaks were observed even at 311 K (curve *6* in Fig. 4). Their positions were close to that of the (200) reflection of the GaSb I phase. A reversible transformation of the crystal peaks into an ordinary halolike spectrum with lowering of the temperature is rather unusual. As earlier, the sample restores its low-temperature states (Fig. 3).

Figure 6 shows the diffraction spectra of the partly transformed sample for two temperatures in the low-temperature range of the phase stability.[5] The intensity of the small-angle spectrum range considerably decreases, whereas the shape and the intensity of the

[5] The curves obtained at the intermediate temperatures are located between these two spectra.

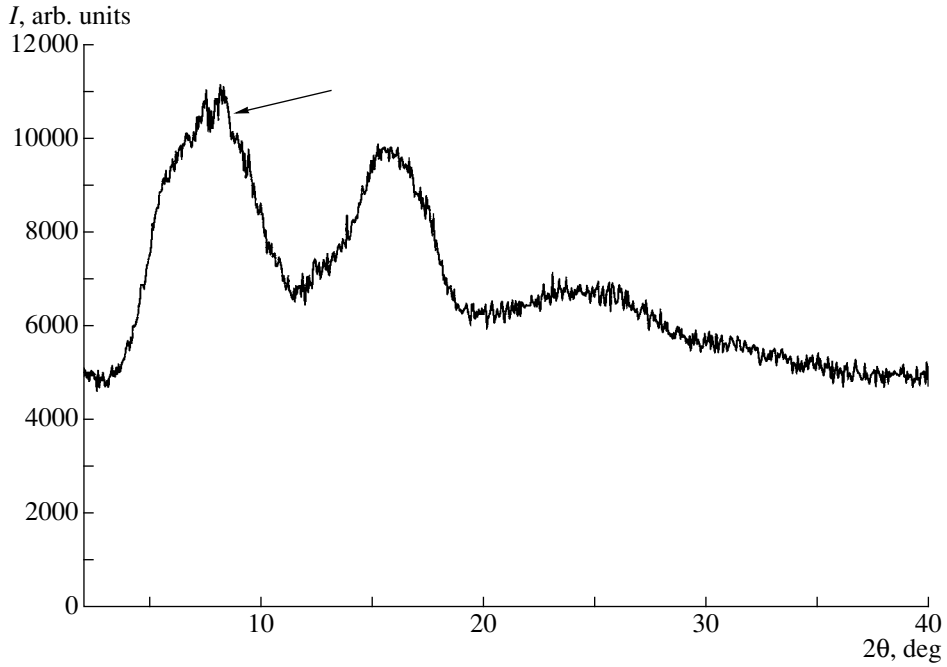

Fig. 5. Diffraction spectrum of the sample in the steady state at 323 K (narrow lines from the crystal are shown by the arrows).

crystal reflection do not change with the temperature rise. The identical behavior of the small-angle spectral range is seen in Fig. 3 for the pure "pseudoamorphous" state. The spectral ranges shown cannot be caused by small-angle scattering proper, however they contain some information about its "fine-disperse tail." High intensities of these tails signify that even during formation of the low-temperature phase it has the precipitates of another phase of different density. The slope of small-angle scattering curve decreases with the temperature rise, thus showing that the fraction of fine-disperse precipitates diminishes at higher temperatures. Possibly, this is explained by coagulation of these precipitates and, finally, their transformation into a high-temperature pseudoamorphous phase. This assumption is confirmed by the thermally reversible behavior of small-angle scattering, which is similar to the reversible behavior of the structural states of the sample upon its "amorphization."

4. DISCUSSION

Figures 7a and 7b shows the atomic positions in GaSb I (diamond-type structure) and GaSb II (β-Sn-type structure) unit cells. At first sight, these phases are quite different. However, the new unit-cell axes chosen along the [110], [$1\bar{1}0$] and [001] directions for the GaSb II unit cell (thin lines in Fig. 7c) show that coordination of atoms in both unit cells is the same; i.e., the symmetry subgroups of the both phases belong to the same group. Such a choice of the unit cell allows one to see that the GaSb I ⟶ GaSb II transition reduces to compression of the original cubic unit-cell by about 50% along the [001] direction and the elongation by about 20% along the [100]- and [010]-directions. The unit-cell volume changes by about 28%. These characteristics of the phase transformation provide the formation of the texture observed for single crystal samples. This texture reflects the quasihydrostatic mode of the load transfer, at which the (100) GaSb I face is usually transformed into the (001) face of GaSb II. This is confirmed by the absence of (*h*00)-type reflections on the diffraction patterns from single crystal GaSb II samples.

Figure 4 shows the typical diffraction patterns from both pseudoamorphous phases. One can clearly see that the maximum intensity of the first reflection of the low-temperature phase (spectrum *1*) is considerably lower than the intensity of the second reflection. Such an intensity ratio is quite unusual for an amorphous phase—usually the intensity ratio is inverse [9–11, 14].[6] For the high-temperature phase (spectrum *6*), the intensity of the first reflection is higher than of the second one, which is characteristic of an amorphous state. However, the half-width of this reflection considerably exceeds the half-width of the second "halo," which is inconsistent with the definition of an amorphous state according to which the half-width of the first peak characterizes the shortest interatomic distance (the first coordination sphere) ranging within smaller limits than for the next coordination spheres. Thus, the features of

[6] In principle, such an intensity ratio is possible also for an amorphous state if the structure consists of atoms having different radii and considerably different scattering powers [22].

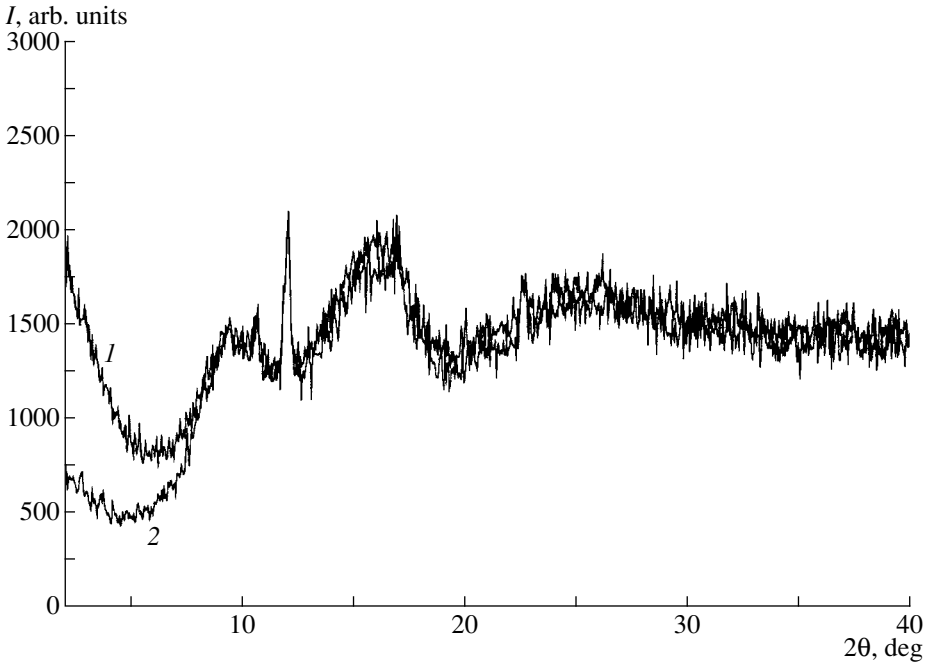

Fig. 6. Small-angle range of the diffraction spectrum of the low-temperature "amorphized" phase at: (*1*) 89 and (*2*) 230 K.

the halolike diffraction spectra and the thermally reversible character of the structural states observed indicate that these states cannot be amorphous phases. This conclusion also agrees with the above analysis of the GaSb I and GaSb II atomic structures, which shows that the coordination of atoms is not changed upon the GaSb I–GaSb II transformation and, hence, there are no structural reasons for the formation of the amorphous state in the reverse transition.

It seems that the nanocrystalline character of the real structure should be responsible for the halolike diffraction spectra upon the GaSb II $\longrightarrow$ GaSb I transformation. In this connection, we analyzed mean sizes of nanoscopic grains that determine the half-widths of reflections. A mean crystallite size calculated from half-width of the first reflection is 25 Å for the low-temperature and 7 Å for the high-temperature phases. The grain size equal to one interatomic distance for the high-temperature phase contradicts the definition of a nanocrystal. Moreover, a reduction of the crystallite size with an increase of the heating temperature can hardly be interpreted because the system usually should attain its equilibrium state. We could not interpret the smooth and continuous transformation of the low-temperature nanostructure (stable within 77–200 K) into the high-temperature nanostructure at room temperature, which is accompanied by an anomalous but smooth increase of the interatomic distance.

The reversibility of narrow crystal reflections formed at 323 K also indicates that the sample cannot be considered as a nanocrystal. Assuming that phase transition into the structure that provide halolike spectra should be accompanied by fractioning of the initial polycrystalline GaSb II grains to nanoscopic sizes, we can conclude that growth of these grains with the temperature rise can occur only due to diffusion processes providing change in the coordination of a neighboring grain. In principle, this is possible at rather high temperatures and in the presence of the thermodynamic driving force of the phase transformation. However, since the crystalline state of GaSb I is energetically more favorable, there is no reason for the reverse grain transformation into nanoscopic ones with an increase of the temperature.

In our opinion, it is more natural to assume that the halolike diffraction spectra reflect pronounced changes of the crystal lattice [9–11, 17] pointed out by McDonald [2]. Here, one has to distinguish between two possible situations—the changes of the type of a disordered solid solution and formation of second-order defects. As was mentioned above, the coordination of atoms in the GaSb I and GaSb II is preserved. This fact allows us to ignore the changes of the type of a disordered solid solution. Thus, we have to analyze only second-order defects for which the displacements $\mathbf{u}$ of lattice atoms located at the distance $\mathbf{r}$ from the defect can be written as $\mathbf{u} \sim \mathbf{r}^{-n}$ ($n < 2$). It is in this case that the situations can take place which are determined by the size and the concentration of defects such that a set of the crystal lines singled out on diffractograms is substituted by halolike spectrum [9–11]. The possible formation of second-order defects and their high concentration in the sample are confirmed by the characteristics of the small-angle range of the diffraction spectra.

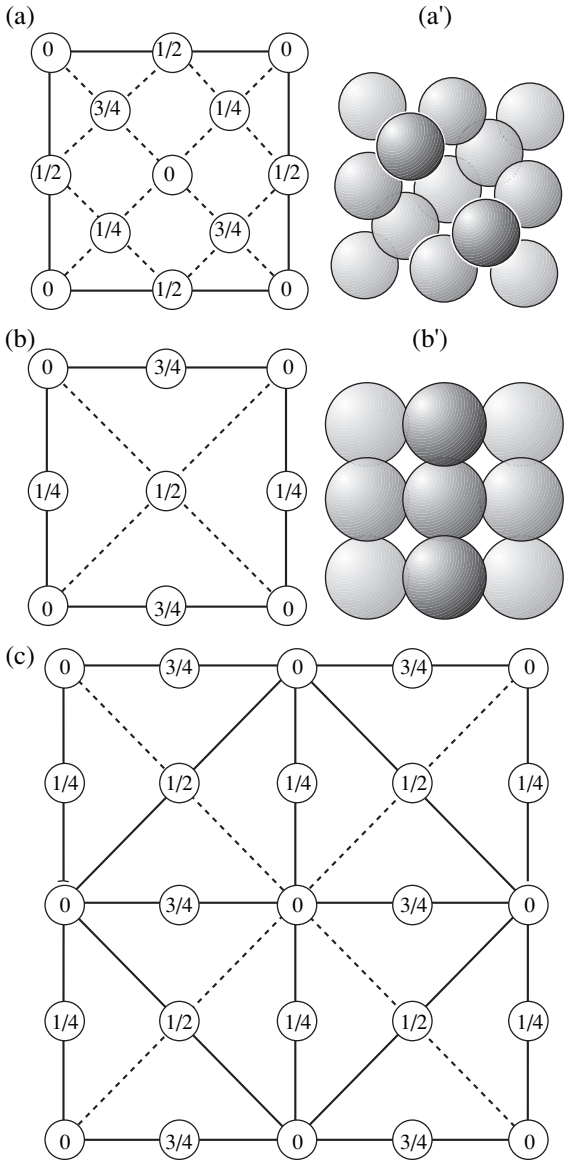

Fig. 7. (a) Atomic positions in the unit cell of the diamond-like atomic arrangement in GaSb I projected onto the face of a cube, (a') packing of atoms in the diamond-like structure, (b) atomic arrangement in the tetragonal unit-cell β-Sn (GaSb II) projected onto the basal *c* plane; (b') packing of atoms in the β-Sn structure; (c) a newly chosen unit cell in the β-Sn structure (thin solid lines).

One may assume that second-order defects in the low-temperature phase are the nuclei with characteristics close to those of the high-temperature phase. This assumption follows from a decrease of the fine-disperse precipitate concentration with the temperature rise, from an anomalously high increase of the intensity of the first halo, and the shift of the center of gravity of this halo toward the small-angle range characteristic of the positions of the strong (111) and (200) reflections of the GaSb I phase. The texture formation with the [001]-axis explains the anomalously pronounced change in the intensity and the shift of the first halo to the small-angle range in the transition from the low- to high-temperature range. The increase of intensity reflects the transformation of the low-intensity (001) reflection of β-Sn to the rather intense (111) and (200) reflections of GaSb I (Fig. 1c). During this transformation, the [001] texture axis of GaSb II becomes the [100]-texture axis of GaSb I, in full accord with the orientation of the faces in initial single crystal sample.

Now, consider the relation between the halolike spectra, the smooth transformation of the low-temperature to high-temperature phase, and the thermal reversibility of gradual disappearance of coarse-grain precipitates formed at room temperatures. Such a relation can be established under the assumption that the nucleating phase (regarded at the first stages as second-order defects) is conjugated with the low-temperature matrix via the transitional zones with a smooth variation of the interatomic distances and bond angles. In such a model, the pseudoamorphous states are characterized by a continuous transition of the lattice from one orientation to another without any changes of the coordination of atoms. Such a state can be classified as a paracrystalline state [9, 12–15].

Paracrystalline systems can yield halolike scattering spectra [12]. They are also characterized by a relatively easy reorientations and phase rearrangements because they are determined mainly by small changes in interatomic distances and bond orientations in the neighboring unit cells, with the coordination of atoms at large distances being retained. This model explains the reversible appearance and disappearance of coarse grains: they appear because some orientations are observed on a "macroscopic scale" and, thus, determine the narrow diffraction lines and the smooth phase rearrangement. As the temperature decreases, the macroscopic regions continuously return to the initial orientational states of the low-temperature phase. The smooth phase reconstruction reflects a continuous change of the interplanar spacing along the initial [001]-axis with the change in the temperature.

5. CONCLUSIONS

Thus, the experimental results obtained and their analysis lead to the conclusion that the structural states providing the formation of halolike diffraction spectra in solid-state amorphization of GaSb are neither amorphous nor nanocrystalline, but seem to be paracrystalline. This state is closer to a perfect crystal because at macrodistances, the coordination of atoms characteristic of the initial structure is preserved. We should like to emphasize once again that the reported results were obtained on initially perfect GaSb single crystals. Moreover, the thermal and temporal "paths" of sample heating in our experiments were essentially different from those for polycrystalline samples described in [1, 3–8]. It is expedient to compare the structural states

observed in our study with those in GaSb II polycrystals upon their keeping at each temperature point.

ACKNOWLEDGMENTS

We express our deep gratitude to V.F. Gantmakher for his help in preparation of the experiments and useful discussions, I.K. Bdikin, S.G. Sal'nikov, and N.S. Afonikova for their assistance in the experiments, and E.G. Ponyatovsky and A.V. Serebryakov for useful discussions.

The study was supported by the Russian Foundation for Basic Research, project nos. 94-02-03277 and 93-02-3271.

REFERENCES

1. E. G. Ponyatovsky and O. I. Barkalov, Mater. Sci. Rep. **8**, 147 (1992).
2. T. R. R. McDonald, R. Sard, and E. Gregory, J. Appl. Phys. **36**, 1498 (1965).
3. E. G. Ponyatovksy, I. T. Belash, and O. I. Barkalov, J. Non-Cryst. Solids **117/118**, 679 (1990).
4. O. I. Barkalov, E. G. Ponyatovsky, and V. E. Antonov, J. Non-Cryst. Solids **156–158**, 544 (1993).
5. V. F. Degtyareva, I. T. Belash, E. G. Ponyatovsky, and V. I. Rashupkin, Fiz. Tverd. Tela (Leningrad) **32**, 1429 (1990) [Sov. Phys. Solid State **32**, 834 (1990)].
6. O. I. Barkalov, I. T. Belash, V. F. Degtyareva, and E. G. Ponyatovsky, Fiz. Tverd. Tela (Leningrad) **29**, 1975 (1987) [Sov. Phys. Solid State **29**, 1138 (1987)].
7. O. I. Barkalov, I. T. Belash, A. I. Bol'shakov, and E. G. Ponyatovsky, Fiz. Tverd. Tela (Leningrad) **30**, 2724 (1988) [Sov. Phys. Solid State **30**, 1570 (1988)].
8. E. G. Ponyatovsky and O. I. Barkalov, Mater. Sci. Eng., A **133**, 726 (1991).
9. A. Guinier, *Théorie et Technique de la Radiocristallographie* (Dunod, Paris, 1956; Fizmatgiz, Moscow, 1961).
10. V. I. Iveronova and G. P. Revkevich, *Theory of X-ray Scattering* (Mosk. Gos. Univ., Moscow, 1978).
11. Ya. S. Umanskiĭ, Yu. A. Skakov, A. N. Ivanov, and L. N. Rastorguev, *Crystallography, X-ray Diffraction Analysis, and Electron Microscopy* (Metallurgiya, Moscow, 1982).
12. R. Hosemann, Z. Phys. **128** (1), 465 (1950); Acta Crystallogr. **4**, 520 (1951).
13. B. K. Vaĭnshteĭn, *Diffraction of X-rays by Chain Molecules* (Akad. Nauk SSSR, Moscow, 1963; Elsevier, Amsterdam, 1966).
14. J. M. Ziman, *Models of Disorder: the Theoretical Physics of Homogeneously Disordered Systems* (Cambridge Univ. Press, Cambridge, 1979; Mir, Moscow, 1982).
15. R. Hosemann, M. P. Hentscel, F. J. Balta-Calleja, and G. Y. Yeh, J. Phys. C: Solid State Phys. **16**, 4959 (1983).
16. V. I. Iveronova and A. A. Katsnel'son, *Short-Range Order in Solid Solutions* (Nauka, Moscow, 1977).
17. M. A. Krivoglaz, *Theory of X-ray and Thermal Neutron Scattering by Real Crystals* (Plenum, New York, 1969; Nauka, Moscow, 1977, 2nd ed.).
18. J. A. Eastman, M. R. Fitzsimmons, and L. J. Thomson, Philos. Mag. B **66** (5), 667 (1992).
19. M. R. Fitzsimmons, J. A. Eastman, M. Muller-Stach, and G. Wallner, Phys. Rev. **B44** (6), 2452 (1991).
20. J. A. Eastman, M. R. Fitzsimmons, A. C. Lawson, *et al.*, Mater. Sci. Forum **126–128**, 813 (1993).
21. V. K. Dolganov, L. A. Novomlinskiĭ, and I. M. Shmyt'ko, Fiz. Tverd. Tela (Leningrad) **23**, 2427 (1981) [Sov. Phys. Solid State **23**, 1418 (1981)]; Fiz. Tverd. Tela (Leningrad) **24**, 2605 (1982) [Sov. Phys. Solid State **24**, 1476 (1982)].
22. V. Yu. Kolosov, in *Abstracts of the International Conference on Aperiodic Crystals, Les Diblerets, Switzerland, September 18–22, 1994*, p. 117.

Crystallography Reports, Vol. 46, No. 2, 2001, pp. 276–283. Translated from Kristallografiya, Vol. 46, No. 2, 2001, pp. 320–327.

REAL CRYSTAL STRUCTURE

An X-ray Topographic Method for Identifying the Active Slip Systems in Cubic Crystals

G. F. Kuznetsov

Institute of Radio Engineering and Electronics, Russian Academy of Sciences, Fryazino, Moscow oblast, 141120 Russia

e-mail: gfk217@ire216.msk.su

Received April 28, 1999

Abstract—An original technique based on the geometric characteristics of dislocations in planar pileups is suggested which allows the estimation of the local thermoelastic stresses and analysis of the influence of a number of growth parameters on the formation of dislocations in $A^{III}B^{V}$ semiconductor crystals. © *2001 MAIK "Nauka/Interperiodica".*

INTRODUCTION

Earlier, we proposed an original X-ray topographic method for determining active slip systems in cubic crystals [1–3]. The method is based on the well-known concepts of the dislocation theory [4, 5], crystallography [6], and the X-ray topography [7] and also uses some new results obtained by the latter technique on $A^{III}B^{V}$ semiconductors with a low dislocation density [8–10].

It is well known that the Burgers vector of a dislocation and the dislocation line always lie in one plane of a certain slip system [4–6]. Either the individual dislocations or their curved segments or, especially, the planar pileups dislocation in single crystals can be regarded as indicators of the related local elastic-stress fields existed in the crystals at the moment of stabilization of their dislocation structure [1–5, 8–13]. The adequate theory of elastic stresses due to individual dislocations and to the one- and the two-sided dislocation pileups was suggested in [4, 5]. An X-ray topograph is a projection of the image dislocation lines distributed in the volume of the single crystal plate studied [1, 2, 8]. The actual sizes of dislocation pileups or the curvilinear segments of dislocations on the topographs are calculated by the formulas of the projective geometry [1, 2, 8]. The topographic studies show that in GaAs, GaSb, and InP semiconductor single crystals with low dislocation densities ($<10^3$ cm^{-2}), dislocations most often form one-sided pileups and, only sometimes, two-sided pileups [1, 2, 8, 9, 11–13].

The method suggested here allowed us to reveal [1, 2, 8, 9, 11–14] 54° dislocations, predicted theoretically in [5], in the $A^{III}B^{V}$ single crystals. In some instances, we also managed to prove the prevalent generation of the dislocations in nonoctahedral slip systems $\langle 10\bar{1}\rangle\{101\}$ and $\langle 110\rangle\{h11\}$ with an insignificant contribution of the octahedral $\langle 110\rangle\{111\}$ system.

EXPERIMENTAL TECHNIQUE

InP, GaAs, and GaSb single crystals with low dislocation densities ($<10^3$ cm^{-2}) were grown by the Czochralski method with the use of liquid hermetization; Si-doped GaAs single crystals were also grown by the method of unidirectional horizontal crystallization. To reduce the dislocation concentration in the ingots, one of the dopants increasing the critical stress of dislocations formation in crystals (Zn for InP, Te or Si for GaAs and GaSb) was added to the melt [15–20].

Topographic studies were made on single-crystal plates cut from the InP, GaAs, and GaSb ingots grown along the [111], [001], and [112] axes. The plate surfaces were coincided with (111), (001), or (112) surfaces normal to the growth axes or were parallel or tilted ({111}, {110}, {112}, or {001}) to the growth axes. Upon chemical and mechanical polishing and chemical dynamical dissolution of the disturbed surface layer, the final plate thickness was 250 μm.

DISLOCATION DISTRIBUTION IN InP, GaAs, AND GaSb SINGLE CRYSTALS WITH LOW DISLOCATION DENSITY

The X-ray topographic study showed that the main characteristic of Zn-doped ($p = 2 \times 10^{18}$ atom/cm^3) InP crystals with low dislocation density ($<10^3$ cm^{-2}) is the presence of the practically dislocation free (0.5–1.5-cm^2) regions [1, 2, 9]. In Te- or Si-doped GaAs [1, 8, 10–13] and GaSb [1, 11, 12] crystals, the dislocation-free regions are 1–12 cm^2 large.

Another important feature of the dislocation distribution in doped InP, GaAs, and GaSb crystals with low

1063-7745/01/4602-0276$21.00

dislocation density is the formation of dislocation pileups on X-ray topographs (Fig. 1a), such planar dislocations pileups have the form of the compact rows of segments of rectilinear dislocations (*1–6*). Such pileups are characterized by increasing interdislocation spacings from the first ("head") to the last ("tail") dislocation. This signifies that such a pileup is pressed to an obstacle located from the side of the first dislocation, while the dislocation source is located to the side of the last dislocation.

X-RAY TOPOGRAPHIC MEASUREMENTS AND CALCULATION OF PARAMETERS OF ONE-SIDED DISLOCATION PILEUPS

Examination of all the planar dislocation pileups on topographs showed that they consist of different numbers of dislocations N_n, have different lengths L_n, and different angles ψ_n (where $n = 1, 2, 3, \ldots$) between the lines of outcrop of the dislocation segments of the pileup at the InP (001) surface and the directions of the lines of the rectilinear dislocations of the pileup on the topograph. The angles φ_n formed by the same lines of the outcrop of the dislocation segments in different pileups and the directions of the diffraction vectors of the $\mathbf{g}\langle 400\rangle$ or $\mathbf{g}\langle 220\rangle$ are also different (see Fig. 1a and schematic in Fig. 2). Moreover, the pileups also have different lengths h_n of the dislocation segments on topographs.

The geometric X-ray topographic analysis considers a topograph taken in symmetric Laue reflection as a planar image of the spatial dislocation distribution in the plate bulk [1, 2, 8, 9, 11–14] onto the surface of the exit of the wave field from the crystal. The plane of the projection parallel to the topograph can be chosen as, e.g., the (001) surface of InP single crystal plates (the radiation exit surface). Such a consideration allows one to use the well-known formulas of the projective geometry [1, 2, 8, 9, 11–13] for calculating the X-ray topographs. As was found from the topographs, for the vast majority of the planar dislocation pileups, the directions of rows of the dislocation outcrop at the (001) surface of the single-crystal InP plate make an angle of $\varphi_n = 45°$ with the $\mathbf{g}\langle 220\rangle$-type diffraction vectors. These directions coincide with one of the crystallographic directions of the $\mathbf{g}\langle 100\rangle$ type in the (001) plane and are parallel to one diffraction vector of the $\mathbf{g}\langle 400\rangle$ type. Such a coincidence of the direction of the rows of the outcrop of the segments of dislocation lines in planar dislocation pileups with the $\langle 100\rangle$ directions in the (001) plane indicates that the dislocations observed in these planar dislocation pileups were generated in the {101} slip planes rather than in the {111} planes of the octahedral slip. In the latter case, the directions of the outcrop lines of the dislocation rows in the planar dislocation pileups on the (001) plane would coincide with one of the $\langle 110\rangle$ directions. A good contrast of the (220) reflection in Fig. 1a and the extinction of the dislocation lines in the planar dislocation pileups with the outcrop lines at the (001) surface coincident with the $\langle 100\rangle$ directions in one of the {400} reflections signifies that the Burgers vectors of dislocations in these planar dislocation pileups to be $\mathbf{b} = a/2\langle 101\rangle$. In other words, the dislocations in these planar dislocation pileups were generated in the $\langle 10\bar{1}\rangle\{101\}$ slip systems (see schematic in Fig. 1b). In fact, a minimum in the contrast of the image of the dislocations in planar dislocation pileups with the Burgers vectors, perpendicular to the diffraction vector of the type $\mathbf{g}\langle 400\rangle$, is observed instead

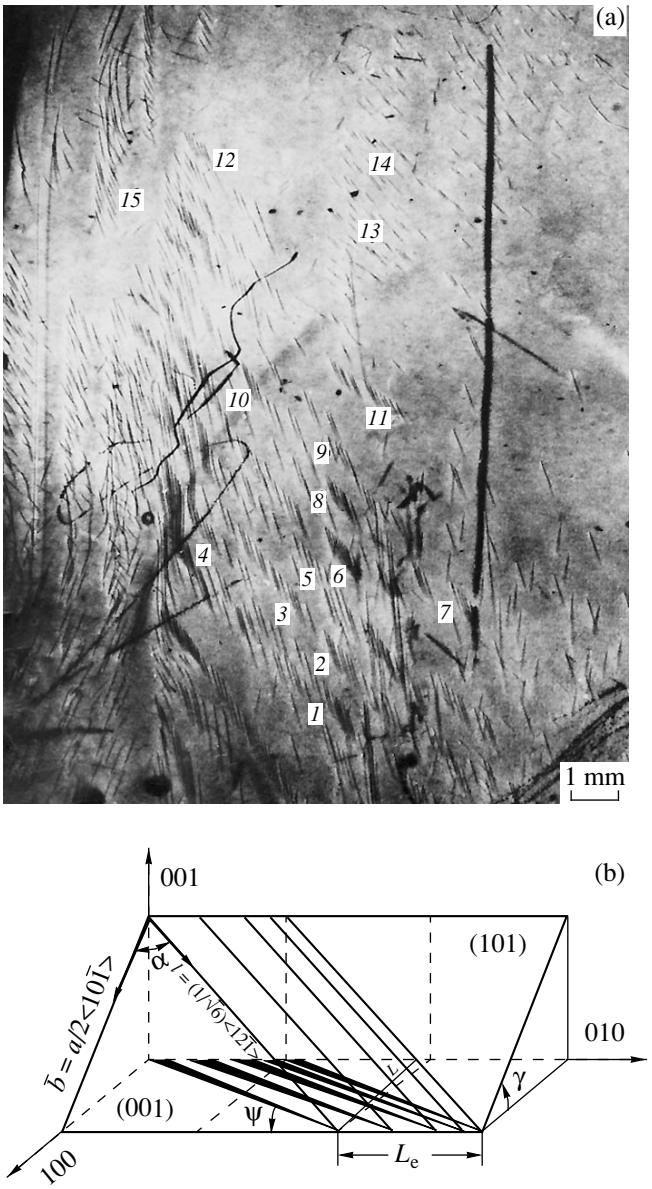

Fig. 1. (a) X-ray topograph obtained in the (220) reflection by the method of anomalous transmission of the $\mathrm{Cu}K_{\alpha_{1,2}}$ radiation and (b) the formation of the image of a planar-dislocation pileup on the topograph.

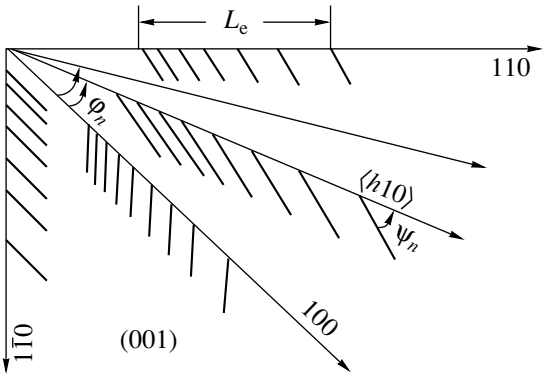

Fig. 2. The schematic of the image of the dislocation rows in the planar dislocation pileup on the topographs.

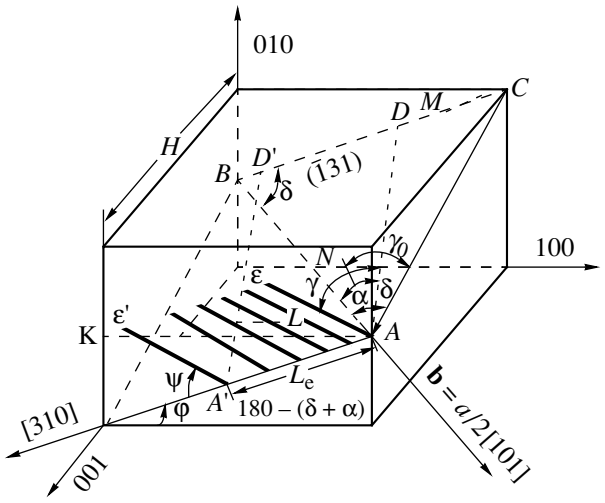

Fig. 3. The schematic of the projection of dislocations in the planar dislocation pileup onto the topograph.

of the complete extinction. The angles between the directions in the image of the dislocation-line segments and the lines of their outcrop at the (001) crystal surface were found from the topographs to be $\psi_n \sim 27°$ for the most of the planar dislocation pileups. Then, knowing the tilt of the {101} slip planes with respect to the (001) surface, $\gamma = 45°$, the formula [1, 2]

$$\tan\alpha_n = \cos\gamma\cot\psi_n \qquad (1)$$

yields the angle formed by the lines of rectilinear dislocations and the direction of their Burgers vectors, $\alpha_n = 54°$, the axis of the dislocation lines in the {101} slip planes being coincident with the crystallographic direction of the type $\mathbf{l} = (1/\sqrt{6})\langle 121\rangle$. Following the Hornstra classification [5] with due regard for the above experimental evidence, one can conclude that the typical 54° dislocations with the axis coincident with the directions of the type $\mathbf{l} = (1/\sqrt{6})\langle 12\bar{1}\rangle$ are generated in the course of the growth in the $\langle 10\bar{1}\rangle\{101\}$ slip system in the vast majority of the planar dislocation pileups in the Zn-doped InP crystals. The 54° dislocations were recognized to be unstable in the crystals of elementary semiconductors (silicon and germanium) [1, 2], where such dislocations were observed very rarely. On the contrary, our data show that the 54° dislocations in the Zn-doped InP crystals play a decisive role in the dislocation generation during crystal growth.

The second frequently encountered type of the planar dislocation pileups, observed on the topographs from the plates of the Zn-doped InP crystals (Fig. 1a), is characterized by that the lines of the dislocation outcrop at the (001) surface are coincident with the $\langle h10\rangle$ directions (where h = 2, 3, 4, 5, 6, 7, 8 …) in the (001) plane (see schematic in Fig. 2) but with no one of the $\mathbf{g}\langle 220\rangle$ or $\mathbf{g}\langle 400\rangle$ diffraction vectors. The images of the segments of dislocations in the planar dislocation pileups of this type have the highest contrast in the topographs in Fig. 1a obtained in the (220) reflection. An almost complete extinction is observed in the $(2\bar{2}0)$ reflection, while in the {400} reflections, the images have a varying contrast. These results signify that the Burgers vector of the segments of the rectilinear dislocations in the planar dislocation pileups of the second type coincides with the diffraction vector $\mathbf{g}[220]$, $\mathbf{b} = a/2[110]$. Therefore, the dislocations obtained in planar dislocation pileups of the second type were generated during the growth of the Zn-doped InP crystals in somewhat unusual systems of the nonoctahedral slip (namely, $\langle 110\rangle\{h11\}$). The generation of dislocations in such systems has already been recorded by the X-ray topographic method in the Si-doped GaAs crystals [13] and the Te-doped GaSb crystals [11, 12]. Hornstra [5] analyzed theoretically one of the slip systems, $\langle 110\rangle\{311\}$, where the formation of the 73° dislocations with the $\langle 211\rangle$ axes is possible. Moreover, the X-ray topographic study and the data from [1, 2, 13] proved that not only the $\langle 110\rangle\{311\}$ slip system, discussed in [5], but the entire zone of the $\{h11\}$ planes with the zone axis coincident with the Burgers vector $\mathbf{b} = a/2[101]$ is active during crystal growth.

The further analysis of the planar dislocation pileups in the $\langle 110\rangle\{h11\}$ slip systems was performed by X-ray topography [1, 2, 9, 11–13]. It follows from the geometry (see Fig. 3) that if the segments of the rectilinear dislocations generated in the $\langle 110\rangle\{h11\}$ slip system had been projected onto the topograph at a small angle γ_0 (γ_0 is an angle between the normals to the $\{h11\}$ slip plane and the (001) surface), then the rows of their segments in the planar dislocation pileups would have an outcrop at the (001) surface along the lines that coincide along direction with the lines of the Burgers vector $\mathbf{b} = a/2\langle 110\rangle$. In such a case, there would have been no planar dislocation pileups on topographs with the dislocation rows outcropped at the (001) surface along the $\langle h10\rangle$ directions. However, if the dislocations generated in the same, $\langle 110\rangle\{h11\}$, slip system are projected within a wider angle ($\gamma = 90 - \gamma_n$) to the (001) crystal surface, then all the $\langle h10\rangle$ disloca-

tion rows in the planar dislocation pileups observed on the topographs, are realized. The formula for the angles α_n, formed by the Burgers vectors with the dislocation axes in individual planar dislocation pileups, is readily obtained from the geometry of the topograph in Fig. 3:

$$\sin\alpha_n = \frac{\sin\delta_n \sin(\psi_n - \varphi_n)}{\sqrt{\sin^2\varphi_n + \sin^2\psi_n}}. \quad (2)$$

Here, the angles φ_n and ψ_n measured for the planar dislocation pileups from the topographs have the values indicated above, while α_n is an angle formed by the Burgers vector of the dislocations in a pileup and the direction of the $\langle h10\rangle$ planar dislocation pileup rows in the topograph. Knowing the Burgers vector $\mathbf{b} = a/2\langle 101\rangle$ and the $(h10)$ direction indices of the planar dislocation pileup rows, one can readily determine the angle δ_n between these directions using the well-known formula for the cosine of the angle between the crystallographic directions.

The calculation by Eq. (2) involving the resulting values of the angles ψ_n and φ_n show that for all the planar dislocation pileups generated in the $\langle 110\rangle\{h11\}$ slip systems, the values of the angles made by the Burgers vectors with the dislocation lines range within $\alpha_n = 7°$–$32°$; thus, as $\alpha_n = 0°$ nothing but a few planar dislocation pileups occur.

Thus, the present paper gives, for the first time, evidence that the dislocations are generated during the InP crystal growth in the $\langle 110\rangle\{h11\}$ slip systems, where the planar dislocation pileups are formed from the dislocations with the well-defined screw component of the Burgers vector (see also [1, 2, 9]). In general, the result obtained contradicts the data by Hornstra [5], who showed that the 73° dislocations with the axes along the $\langle 211\rangle$ crystallographic directions can take place in a slip system, e.g., $\langle 110\rangle\{311\}$. The 73° dislocations have the large edge components of the Burgers vector, which prevail over the screw component. Such a disagreement between the experimental and theoretical data are of fundamental value and is associated with the fact that in the course of the growth of the InP crystals doped with the hardening Zn impurity the screw dislocations with the Burgers vector $\mathbf{b} = a/2\langle 101\rangle$ are generated. Under increasing thermoelastic strains, these dislocations, lacking strong coupling with the primary slip systems, can, upon evolution, pass to other slip systems acquiring a weak edge component of the Burgers vector.

The number of the planar dislocation pileups with the dislocations generated in the basic systems of the octahedral slip $\langle 110\rangle\{111\}$ proved to be rather small. From the topographs, the angles (the segments of the rectilinear dislocations in these planar dislocation pileups formed with the directions of the rows themselves) were found to be $\psi_1 \sim 45°$ or $\psi_2 \sim 30°$, while the directions of the lines of the rows of the dislocation outcrop at the (001) surface coincided with the $\langle 110\rangle$ directions. For the $\langle 110\rangle\{111\}$ system of the octahedral slip, the angle α_n must be calculated by the formula [1, 2]:

$$\sin\alpha_n = \frac{\sqrt{1 + \tan^2\gamma}}{\sqrt{1 + \tan^2\gamma \sin^2\psi_n}} \sin\psi_n, \quad (3)$$

where $\gamma \sim 54.7°$ is the tilt of the $\{111\}$ slip planes at the (001) crystal surface. Measurements and calculations showed that the dislocations in the planar dislocation pileups with $\psi_1 \sim 45°$ correspond to the 60° dislocations ($\alpha_1 \sim 60°$); those with $\psi_2 \sim 30°$, to the dislocations with $\alpha_2 \sim 45°$. Moreover, a small number of the planar dislocation pileups from the pure edge dislocations with $\mathbf{b} = a/2\langle 110\rangle$ and $\mathbf{l} = (1/\sqrt{6})[112]$, for which $\alpha_n = \psi_n = 90°$ were registered in the same octahedral slip system close to the single crystal surface (≤0.4 mm). Thus, the simple geometric measurements in the topographs and the computation by Eqs. (1)–(3) allow one to identify the dislocation types and determine the slip systems for each of the three types of the images on the topographs of the planar dislocation pileup images.

In order to calculate the local elastic strains associated with the planar dislocation pileups, one needs the lengths L_n of the planar dislocation pileups in the active slip systems themselves. These can be computed from the experimentally measured lengths L_e by the following formulas for the corresponding slip systems:

$$L_n = L_e \sin\alpha_n, \quad \text{for} \quad \langle 101\rangle\{111\}, \quad (4)$$

$$L_n = L_e \cos\alpha_n, \quad \text{for} \quad \langle 101\rangle\{10\bar{1}\}, \quad (5)$$

$$L_n = L_e \sin(\alpha_n + \delta_n), \quad \text{for} \quad \langle 101\rangle\{h11\}, \quad (6)$$

where L_e is measured from the topograph as the distance between the first (head) and the last (tail) dislocations in each planar dislocation pileup along the line of the dislocation segments outcrop at the (001) surface of the single-crystal plate (see schematic in Fig. 2).

THE CALCULATION OF THE LOCAL ELASTIC STRAINS

The progress in the theory of planar dislocation pileup [4] allows one to calculate the local elastic strains, responsible for planar dislocation pileups generation in the single crystal during growth under real conditions and the formation of the equilibrium dislocation distribution in the planar dislocation pileups using the parameters (N_n, L_n, ψ_n, φ_n, α_n) measured on topographs [4, 9, 11–13]. Considering topographs in Figs. 1a and 1b and the schematic in Fig. 2, we see that the interdislocation spacing increases from the head to the tail dislocation for each registered pileup. Therefore, in order to calculate the local strains, one should use the theoretical model of the one-sided planar dislocation pileups [4], which are "pressed to" an obstacle by the thermoelastic strains in the growing crystal. The

model of the continuous distribution of the dislocations in the planar dislocation pileups is also attractive because the main parameter necessary for the calculation of the local elastic strains is the planar dislocation pileup length L_n, while the positions of individual dislocations in a pileup are unimportant and, moreover, the inverse elastic strains are assumed to be constant throughout the planar dislocation pileup length. Then, since the vast majority of the planar dislocation pileups studied, independently of the type of the slip systems contain the mixed dislocations with $0° \le \alpha_n \le 90°$, the Eq. (21.32) from [4] should be modified by introducing an orientation factor [1, 2]:

$$\tau_n = \{[\mu/(1-\nu)]\sin\alpha_n + \cos\alpha_n\}\mathbf{b}N_n/\pi L_n, \quad (7)$$

where $\mathbf{b} = 4.14 \times 10^{-10}$ m is the Burgers vector for InP. According to [21], the elastic characteristics for the isotropic case are assumed to be as follows: the shear modulus is $\mu = C_{44} = 4.60 \times 10^{10}$ N/m^2 and the Poisson ratio is $\nu = C_{12}/(C_{11} + C_{12}) \sim 0.36$, where $C_{11} = 10.22 \times 10^{10}$ and $C_{12} = 5.76 \times 10^{10}$ N/m^2 are the elastic constants of the InP crystals.

The present study shows for the InP crystal that the measurements and the X-ray topographic studies of 200 planar dislocation pileups are generated and localized in the slip systems of the three above types. The table presents the results of the topographic measurements and calculations for some planar dislocation pileups, the data include all the τ_n range from the minimum to the maximum value for each of the slip systems.

The local elastic strains associated with the planar dislocation pileups observed in the grown InP crystals calculated by Eq. (7) fall in the ranges $\tau_n = (5–19) \times 10^4$ Pa for the $\langle 110\rangle\{111\}$ slip systems, $(9.5–22) \times 10^4$ Pa for the $\langle 101\rangle\{h11\}$ systems, and $(15–39) \times 10^4$ Pa for the $\langle 10\bar{1}\rangle\{101\}$ systems. If only the planar dislocation pileups with an equal number of dislocations, e.g. $N_n = 4$, are considered, the values of the associated local elastic strains vary within the same ranges as for the planar dislocation pileups with the different dislocation numbers.

It is important that in the model of the one-sided planar dislocation pileup pressed to an obstacle [4], the associated elastic (or inverse) stresses are constant over the length of the planar dislocation pileup L_n and are balanced by the local thermoelastic stresses present at an instant of planar dislocation pileup stabilization in the given section of a growing crystal, i.e., $\tau_n = \tau_{te}$. Hence, it is the local thermoelastic stresses acting in a real growing crystal in the section of the observed planar dislocation pileups and balanced by inverse or thermoplastic stresses that are found from the measured parameters of the individual planar dislocation pileups. The values of τ_c were taken from the experiments on the high-temperature uniaxial static compression [20] performed on the identical low-dislocation Zn-doped InP crystals ($p = 2 \times 10^{18}$ cm^{-3}) and grown under the same conditions as the crystals studied in the present paper [22]. In [20], the dislocations generated during the static loading were revealed by selective chemical etching without an identification of the active slip systems, the Burgers vectors, and their directions with respect to the lines of the generated dislocations. This implies that the curves representing the temperature dependence of τ_c [20] should be considered as averaged over all the active slip systems. Therefore, the data on τ_c for InP, taken from [20], must be compared with the relaxed thermoelastic strains τ_n for the similar InP crystal found from our topographic experiments and averaged over a wide range of their values with no account for the type of the slip system; that is, τ_c must be compared with $\tau_n = (5–39) \times 10^4$ Pa.

THE CALCULATION OF THE PHYSICAL QUANTITIES CHARACTERIZING THE GENERATION OF THE PLANAR DISLOCATION PILEUPS IN A GROWING CRYSTAL

Similar to the yield point [23] and local elastic stresses [1, 2, 9], determined by planar dislocation pileups, the temperature dependence of τ_c for InP [20], is approximated by the exponential function

$$\tau_c = A\exp(U/kT), \quad (8)$$

where k is the Boltzmann constant, A = const, and U is the activation energy of the dislocation source. As is seen from Fig. 4 (line *a*), all the data on critical stresses τ_c necessary for generation of dislocations under deformation of the high-temperature compression taken from [20] fit the logarithmic line well, including the τ_c value extrapolated by the author to the point of the InP crystallization. Since the formation of planar dislocation pileups is associated with the excitation and the operation of the dislocation sources, emitting some number of dislocations under local thermoelastic strains, one can assume that the relaxed local thermoelastic strains τ_n, determined from the topographic data and related to the planar dislocation pileups obey the same exponential temperature dependence as τ_c in Eq. (8). Then, one can arrange all the topographic data $\tau_n \sim (5–39) \times 10^4$ Pa (Fig. 4, line *b*) in an ascending way parallel to the plot of τ_c (Fig. 4, line *a*). The above assumption is identical to that taken in the equality, in the average, of the activation energy in Eq. (8) both in the experiments on the static high-temperature compression [20] and formation of planar dislocation pileups in the InP crystal during growth. Thus, applying (8) to two points on the lines *a* and *b* in Fig. 4, we obtain dose values of the activation energy, $U = 1.32$ eV and $U = 1.28$ eV, for the τ_c from [20] and from topographic data with no distinction made between the slip systems, respectively.

The data of X-ray topographic measurements and the calculations of the parameters of the planar dislocation pileups generated during growth in various slip system of an InP crystal and the calculated local elastic strains τ_l related to planar dislocation pileup

	Slip systems																	
	⟨101⟩ {101}			⟨110⟩ {*h*11}							⟨110⟩					{111}		
	Ψ ≈ 30°; α_n ≈ 54°										mixed dislocations					edge dislocations		
n, the ordinal number of planar dislocation pileup	*N*, the number of dislocations in the planar dislocation pileup	$L_n \times 10^{-4}$ m, the planar dislocation pileup length in the slip plane	$\tau_l \times 10^4$ N/m^2, the local elastic strain	*N*, the number of dislocations in the planar dislocation pileup	Ψ, deg	φ, deg	δ, deg	α, deg	$L_n \times 10^{-4}$ m, the planar dislocation pileup length in the slip plane	$\tau_l \times 10^4$ N/m^2, the local elastic strain	*N*, the number of dislocations in the planar dislocation pileup	Ψ, deg	α, deg	$L_n \times 10^{-4}$ m, the planar dislocation pileup length in the slip plane	$\tau_l \times 10^4$ N/m^2, the local elastic strains	*N*, the number of dislocations in the planar dislocation pileup	L_n, 10^{-4} m, the planar dislocation pileup length in the slip plane	$\tau_l \times 10^4$ N/m^2, the local elastic strain
1	7	5.24	15.0	4	28	8	46	30	3.23	9.7	4	24	37	8.13	5.3	5	10.0	4.7
2	5	3.08	18.3	4	25	8	46	28	3.84	10.3	4	36	52	5.73	6.1	8	15.8	4.8
3	6	3.47	19.5	9	24	8	46	27	6.38	13.9	4	30	45	5.66	7.9	3	3.0	9.5
4	5	2.70	20.8	6	33	14	43	22	3.63	15.3	4	30	45	5.18	8.6	6	4.8	11.8
5	4	1.92	23.5	6	40	25	39	12	3.08	15.6	5	30	45	4.72	11.8	4	3.2	11.8
6	8	3.47	26.0	6	34	5	45	37	3.97	16.2	4	37	53	3.45	13.1	4	3.0	12.6
7	7	2.70	29.2	9	25	8	46	28	5.12	17.4	4	40	56	3.85	13.5	6	4.2	13.5
8	5	1.92	29.3	4	25	12	46	20	1.83	19.8	4	27	42	3.09	14.2	6	3.5	16.2
9	9	2.70	37.5	3	40	23	39	15	1.16	21.6	6	30	45	6.33	14.9	7	4.0	16.6
10	4	1.15	39.2	3	25	12	46	20	1.22	22.3	3	24	38	2.03	15.8	4	2.0	18.9

Note: ψ is the angle formed by the outcrop of the dislocation segments of planar dislocation pileups onto the (001) surface of the crystalline plate and the directions of the lines of the rectilinear dislocation segments in the planar dislocation pileups on the topograph; φ is the angle between the line of the outcrop of the dislocation segments in the planar dislocation pileups at the crystal surface and the direction of the **g**⟨400⟩ or **g** ⟨220⟩ diffraction vectors on the topograph; and α is the angle formed by the direction of the Burgers vector and the dislocation line.

From Fig. 4 (line *b*) approximated by the exponential law (8), it becomes evident that the generation and the formation of an equilibrium dislocation distribution in planar dislocation pileups occurs in the growing InP crystal within the temperature range of $\Delta T \sim 200$ K at cooling from 1343 down to 1130 K. In more detail, the generation of the dislocations and the planar dislocation pileup formation start, first of all, in the ⟨110⟩{111} octahedral slip system and proceeded in the temperature range from the crystallization temperature of 1343 to 1210 K (see circles in Fig. 4, line *b*). Further on, in the ⟨110⟩{*h*11} and the $\langle 10\bar{1}\rangle\{101\}$ systems, the dislocation generation and planar dislocation pileups formation takes place from 1275 to 1190 K (crosses in Fig. 4, line *b*) and from 1235 to 1130 K (triangles in Fig. 4, line *b*), respectively. Although the dislocation generation and the planar dislocation pileups formation in the $\langle 10\bar{1}\rangle\{101\}$ slip systems began later and at a lower temperature than in the octahedral and the ⟨110⟩{*h*11} systems, it is the $\langle 10\bar{1}\rangle\{101\}$ systems that provide the most planar dislocation pileups during the InP crystal growth. This indicates that the conditions of the growth of the particular InP crystal are the most favorable for excitation, generation, and formation of the equilibrium planar dislocation pileups by the dislocation sources localized in the $\langle 10\bar{1}\rangle\{101\}$ slip systems [1, 2, 9] rather than in the octahedral slip systems, as was generally believed for the crystals with the face-centered cubic lattice [1, 5, 6].

The data in Fig. 4 (line *b*) were also used to determine the activation energies by Eq. (8) for τ_n at the

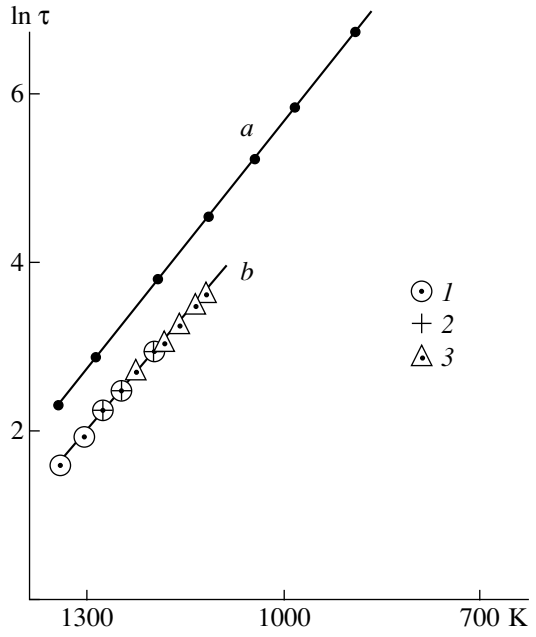

Fig. 4. The temperature dependences of the logarithm of *a* the critical strains of the dislocation generation τ_c in the InP crystal under the high-temperature compressive deformation [20] and *b* the local thermoplastic strains τ_n associated with the planar dislocation pileups in the identical InP crystal representing the XRTG data for the planar dislocation pileups in the (*1*) ⟨110⟩{111}octahedral slip system and in the nonoctahedral: (*2*) ⟨110⟩{*h*11} and (*3*) $\langle 10\bar{1}\rangle\{101\}$ slip systems.

extreme points in the temperature intervals for the planar dislocation pileups formed in the slip systems of different types. These were determined as $U_1 = 1.40$ eV for the planar dislocation pileups in the ⟨110⟩{111} systems of the octahedral slip, $U_2 = 1.28$ eV for the ⟨110⟩{*h*11} systems, and $U_3 = 1.10$ eV for the $\langle 10\bar{1}\rangle\{101\}$ systems [1, 2]. Thus, most of the planar dislocation pileups were formed in the slip systems of the growing InP crystal with a lower (under the given growth conditions) value of the activation energy of the dislocation motion. The latter results qualitatively agree with the data [15] on GaAs and do not contradict the data on reduced the activation energy at higher elastic stresses [15].

Using the intervals of the τ_n value for the planar dislocation pileup groups in each of the ⟨110⟩{111}, $\langle 10\bar{1}\rangle\{h11\}$, and $\langle 10\bar{1}\rangle\{101\}$ slip systems, one can estimate the values of the effective temperature drops and the resulting local thermoelastic and thermoplastic deformations by means of the following approximate formulas [22]:

$$\delta T \sim \tau_n/\beta\mu, \tag{9}$$

$$\varepsilon \sim \tau_n/\mu, \tag{10}$$

respectively, where $\beta = 4.56 \times 10^{-6}$ deg^{-1} is the InP thermal linear expansion coefficient. From Eqs. (9) and (10), one gets $\delta T \sim$ (0.25–0.90), (0.5–1.1), and (0.7–1.9) K and $\varepsilon \sim (1.1–4.6) \times 10^{-6}$, $(2.1–4.8) \times 10^{-6}$, and $(3.3–8.5) \times 10^{-6}$ for the above slip systems, respectively. Such effective temperature differences and the related relaxed thermoelastic deformations, associated with the recorded planar dislocation pileups, existed in the real InP crystal during its growth and provided the low dislocation density. Therefore, even less effective temperature differences and the related levels of the thermoelastic deformation and stresses are necessary for growth of Zn-doped dislocation-free InP crystals [1, 2].

REFERENCES

1. G. F. Kuznetsov, Doctoral Dissertation in Physics and Mathematics (Inst. of Radio Enginnering and Electronics Akad. Nauk SSSR, Moscow, 1990).
2. G. F. Kuznetsov, Preprint, IRÉ Akad. Nauk SSSR (Inst. of Radio Engineering and Electronics, Academy of Science of USSR, Moscow, 1986).
3. L. V. Tikhonov and G. V. Khar'kova, Kristallografiya **13** (3), 479 (1968) [Sov. Phys. Crystallogr. **13**, 386 (1968)].
4. J. P. Hirth and J. Lothe, *Theory of Dislocations* (McGraw-Hill, New York, 1967; Atomizdat, Moscow, 1972).
5. J. Hornstra, J. Phys. Chem. Solids **5** (1/2), 129 (1958).
6. M. P. Shaskol'skaya, *Crystallography* (Vysshaya Shkola, Moscow, 1984).
7. A. R. Lang, Br. J. Appl. Phys. **14**, 904 (1963).
8. G. F. Kuznetsov, in *Proceedings of the 8th Meeting of the Section "Semiconductor Heterostructures" of the Scientific Council "Physics and Chemistry of Semiconductors" of the USSR Academy of Science* (Akad. Nauk Arm. SSR, Yerevan, 1981), p. 73.
9. G. F. Kuznetsov, *Proceedings of the All-Union Conference "Indium Phosphide in Semiconductor Electronics", Kishinev, 1985*, p. 34.
10. G. F. Kuznetsov, Élektron. Tekh., Ser. 8: Upr. Kach., Metrol., Stand. **3** (65), 39 (1978).
11. G. F. Kuznetsov, in *Proceedings of the VI Conference on Processes of Semiconductor Crystals and Films Grow and Synthesis, Novosibirsk, 1982*, Vol. 2, p. 51.
12. G. F. Kuznetsov, A. G. Braginskaya, V. P. Moiseev, and G. P. Kolchina, in *Proceedings of the VI Conference on Growth and Synthesis of Semiconductor Crystals and Films, Novosibirsk, 1982*, Vol. 2, p. 53.
13. G. F. Kuznetsov, Kristallografiya **34** (3), 765 (1989) [Sov. Phys. Crystallogr. **34**, 457 (1989)].
14. G. F. Kuznetsov, Élektron. Tekh., Ser. 8: Upr. Kach., Stand., Metrol., Ispyt. **6** (111), 3 (1984).
15. M. G. Mil'vidskiĭ and V. B. Osvenskiĭ, *Structural Defects in Semiconductor Single Crystals* (Metallurgiya, Moscow, 1984).
16. Y. Seki, H. Watanabe, and J. Matsui, J. Appl. Phys. **49** (2), 822 (1978).

17. S. S. Vakhromeev, V. B. Osvenskiĭ, and S. S. Shifrin, Izv. Akad. Nauk SSSR, Ser. Fiz. **44** (2), 289 (1980).
18. Yu. A. Grigor'ev, S. P. Grishina, G. F. Kuznetsov, *et al.*, Izv. Akad. Nauk SSSR, Ser. Fiz. **44** (2), 300 (1980).
19. A. B. Berkova, A. Ya. Nashel'skiĭ, V. B. Osvenskiĭ, *et al.*, in *Proceedings of the VI Conference on Growth and Synthesis of Semiconductor Crystals and Films, Novosibirsk, 1982*, Vol. 2, p. 59.
20. M. V. Mezhennyĭ, S. S. Shifrin, and V. B. Osvenskiĭ, in *Proceedings of the VI Conference on Growth and Synthesis of Semiconductor Crystals and Films, Novosibirsk, 1982*, Vol. 2, p. 57.
21. V. L. Indenbom, V. I. Al'shits, and V. M. Chernov, in *Defects in Crystals and Their Computer Simulation* (Nauka, Leningrad, 1980), p. 23.
22. V. L. Indenbom and V. B. Osvenskiĭ, *Crystal Growth* (Nauka, Moscow, 1980), Vol. 13, p. 240.
23. J. Gilman and W. Johnston, in *Dislocations and Mechanical Properties of Crystals: An International Conference, Lake Placid, 1956* (Wiley, New York, 1957; Inostrannaya Literatura, Moscow, 1960), p. 82.

Translated by A. Zolot'ko

Crystallography Reports, Vol. 46, No. 2, 2001, pp. 284–287. Translated from Kristallografiya, Vol. 46, No. 2, 2001, pp. 328–331.

PHYSICAL PROPERTIES OF CRYSTALS

Differential Method for Observing Defects with the Use of a Combined Polarized Radiation

V. S. Chudakov

Shubnikov Institute of Crystallography, Russian Academy of Sciences, Leninskiĭ pr. 59, Moscow, 117333 Russia

Received May 18, 1999; in final form, January 14, 2000

Abstract—The conditions for observing crystal defects by a new differential method based on the use of combined radiation with two equally intense orthogonally polarized components have been considered. The conditions for recording three groups of defects possessing different optical properties (absorption, scattering, polarizability, and refraction) are indicated. The new method is implemented on the basis of a scanning image converter widely used in optical flaw detection of crystals. © *2001 MAIK "Nauka/Interperiodica".*

Various kinds of optical radiation are used to detect flaws in crystals. Optical radiations are distinguished by the spectral composition, the degree of monochromatization, and the type of polarization. Below, we describe the method of a combined polarized-light radiation consisting of two components—a linearly and an orthogonally polarized beam. In the process of focusing at the object, these beams are separated by a thin boundary. In the differential visualization of defects with the use of the incident with such a structure, radiation, these is made of narrow regions of a combined radiation adjacent to the interface between the components. The transmitted radiation is optically modulated by a rotating polarizing analyzer [1]. If the orthogonal components involved in this process have the same intensity, the total radiation is recorded by a photoelectric system of the apparatus used as a natural nonmodulated light. As soon as the balance between the orthogonal components is violated because of an encountered defect, the modulated component becomes excessive and is selectively recorded by the rotating analyzer at the double frequency. Thus, linear scanning of an object provides the gradual recording of all the defects. The final pattern can be presented either in the form of intensity distributions or scanning micrographs.

The above configuration of the combined radiation is formed by the natural light with the aid of a compound polarizer, whose image is projected by a lens onto the crystal. The ability of a flaw detector to provide the rigorous orthogonal polarization of the components determines the sensibility of a flaw detector. A precise compound polarizer ensures almost complete "depolarization" of the combined-radiation component used. The residual modulated polarized component does not exceed 0.1%, and the corresponding level of a spurious modulated signal is comparable with the noise level of the electronics of the apparatus used.

Below, we suggest three modifications of a compound polarizer (CP-1, CP-2, and CP-3) (Fig. 1). The simplest one is CP-1, consisting of two polaroid films [2] brought in contact in such a way that their directions of maximum transmission are orthogonal. The CP-2 polarizer is more complicated. It consists of a single polarizing element (not necessarily made of a thin film). For example, it is possible to use crystalline prisms. The orthogonally polarized beams in the CP-2 are formed by two half-wave phase plates brought into contact and located between the polarizer and the object. Each plate cuts off a half of the light field of a polarizer. The optical axes of the half-wave plates must be rigorously directed so that their optical axes would form an angle of 45°. If necessary, a block consisting of two half-wave plates can be located at a considerable distance from the polarizer. The boundary between the orthogonal components is more distinct the thinner the half-wave plates. It is especially important for compound half-wave plates and plates with inclined optical axes.

The CP-3 polarizer also consists of one polarizing element but, unlike CP-2, has only one half-wave plate, which cuts a half of the light field and is tilted at 45° to the direction of maximum transmission. To equate the

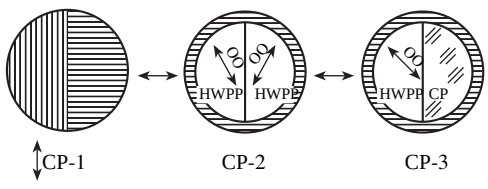

Fig. 1. Three types of compound polarizers for obtaining a combined radiation: HWPP is a half-wave phase plate, OA is the optical axes of the phase plate, CP is a compensating plate. The arrows indicate the directions of the maximum transmission of the polarization element.

1063-7745/01/4602-0284$21.00 © 2001 MAIK "Nauka/Interperiodica"

orthogonal beams, another half of the light field is cut off by a compensating plate made of the transparent isotropic material with the refractive index close to that for a half-wave plate. In particular, to compensate the light losses in quartz, mica, and sapphire (most often used for preparing phase plates) one can use plates made of the glass of the trade mark K-15, TK-3, and TF-5, respectively [3]. The compensating plates of the same thickness as the half-wave plates and are brought in the contact with the latter.

Each of the three compound polarizers has its advantages and disadvantages. As a rule, the CP-1 is achromatic over a broad spectral band, which provides the study of the crystals at various wavelengths without changing of polarizers; it also allows the use a broadband radiation, which, in turn, increases the sensitivity of the optical device. However, the preparation of this polarizer presents some difficulties. The CP-2 and CP-3 polarizers are used only at certain wavelengths, which limits their practical use. Their advantage is the use of a compound polarizing element of an arbitrary design. A CP-3 polarizer is somewhat preferable in terms of preparation and adjustment.

The optical scheme used in the method described above is shown in Fig. 2. The most important feature of the scheme is that block of illumination consisting of a light source *1* with a light filter and condenser *2* also includes a compound polarizer *3* with intermediate lens *4* projecting the boundary between the orthogonal components onto the plane of an object *5*. Main lens *6* transmits the superimposed images of an object and the boundary between the beams through rotating analyzer *7* onto the photosensitive area of photodetector *8*. To increase the device resolution, one has to use a photodetector whose sensitive area would be possibly small. For example, the sensitive area of thin-film PbS-based photodetectors can be 0.1×0.1 mm and even less.

Now, consider the process of defect visualization in the process of object scanning. Similar to other differential methods of defect observation [4], our method records only the local changes in the properties of the object, i.e., its optical transmission. During scanning, defects cross the optical axis of the device and are projected onto a photodetector. At such moments, the balance between the orthogonal components attained during adjustment of the device is violated. A rotating analyzer and a photodetector transform the disbalance into a modulated signal, which, being amplified, is recorded by the device. In most instances, the phase of modulated signals corresponds to the azimuth of the orthogonal component which exerted the minimum distortion from a defect. If the device is equipped with a synchronous phase detector, the change in the phase can be used to record the curves in polar coordinates; photographing can be made in two-color coding, which allows the record of the sign of the derivative.

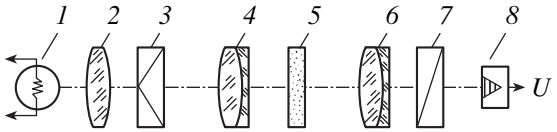

Fig. 2. A version of the basic optical diagram used in experiments.

All the defects that affect the combined radiation can be divided into three groups. The first group is made by defects absorbing and scattering the radiation isotropically. The second group consists of defects polarizing the transmitting radiation. The third group is formed by defects with varying optical density.

It is found that each group defects provides a characteristic signals formed in three stages. At the initial stage, the defect image moves toward the sensitive area of a photodetector. At the second stage, the defect image completely or symmetrically shadows the photodetector. At the third stage, the image leaves the photosensitive area of a detector. The curves obtained from defect of these three groups are shown in Fig. 3. Each group is represented by the two types of signals corresponding to small and large defects. Small defects are such defects for which the condition $D/S < 1$ is fulfilled; for large defects the condition $D/S > 1$ holds (where D is the linear dimension of a defect image along the scanning direction and S is the linear dimension across the sensitive area of a photodetector along the same direction). The curves for isotropic defects are shown in Fig. 3a. If $D/S < 1$, the curve is close to a sinusoid. The zero point between the peaks corresponds to such position of a defect where its image symmetrically shadows the sensitive area of a photodetector. In the case of large defects, the second stage results in the formation not of a point but of a line located between the positive and negative peaks. If a large defect is homogenous, this line coincides with the abscissa.

The radiation-polarizing defects produce an effect on the combined radiation because of the dependence of absorption on the mutual orientation of the polarization plane of the orthogonal component and the direction of maximum defect transmission. For example, if we assume that the azimuths of the components polarization are equal to 0° and 90° and that the direction of the maximum defect transmission is φ, then the intensities of the components transmitted by a defect will change differently,

$$J(0^\circ) \sim \tau_\alpha(1 - P\sin^2\varphi), \quad (1)$$

$$J(90^\circ) \sim \tau_\alpha(1 - P\cos^2\varphi), \quad (2)$$

where τ_α is the defect transmission in the polarized light in the situation where the direction of maximum transmission of light coincides with the polarization plane of the component and P is the defect polarizability. The modulated signal U in the process of light prop-

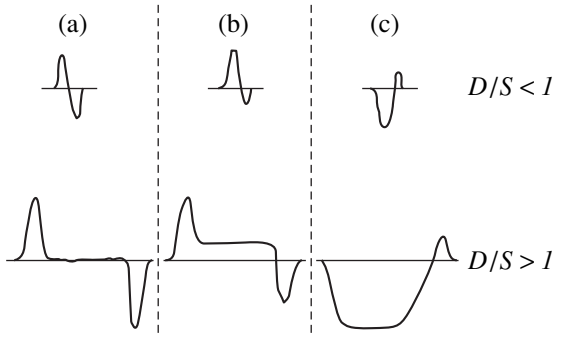

Fig. 3. Fragments of the curves typical of particular groups of defects.

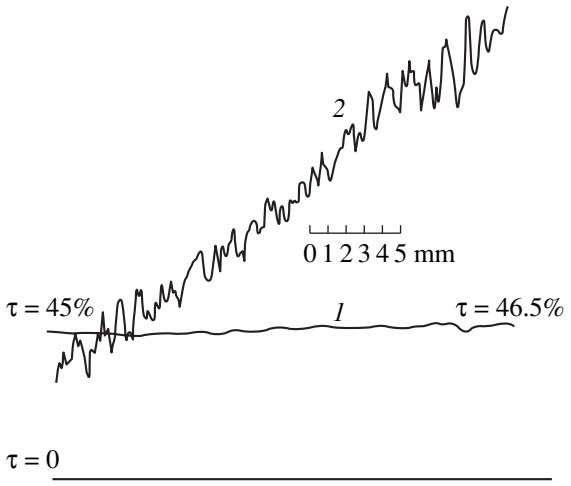

Fig. 4. (*1*) Integrated and (*2*) differential curves of optical transmission obtained by scanning a silicon plate along the growth direction.

agation through a polarizing defect is proportional to the difference between Eqs. (1) and (2) and equals

$$U \sim \tau_d P \cos 2\varphi. \quad (3)$$

It follows from Eq. (3) that at $\varphi = 45°$, the orthogonally polarized components are equally absorbed and, thus, recorded in the same manner as isotropic defects. At other φ values the initial and final peaks always have different heights, and the line connecting these peaks does not coincide with the zero line in Fig. 3b.

The third group of defects (Fig. 3c) essentially differ from the first two groups—they affect the combined radiation quite differently. In the presence of these defects, the disbalance is caused not by inhomogeneous shadowing of the photodetector but by the shift of the image of a boundary between the orthogonal components to the photosensitive area of a detector. A similar shift also takes place under the effect of a wedgelike object or the inclination of a plane-parallel plate. The degree of disbalance caused by the boundary displacement across the photodetector area depends on the steepness of the refraction-index gradient in the place analyzed and its position with respect to the optical axis of the optical device and also on the position of the boundary between the orthogonal components. In particular, the changes in the optical density cannot be recorded if the gradient is parallel to the boundary or to the optical axis of the device.

Various defects can be responsible for the changes in the optical density. The local variations in the refractive indices are observed at the block boundaries [5] are caused by the variations in the composition of solid solutions and also by internal stresses. The most pronounced changes in the optical density in solid solutions and alloys occur in the case where the refractive indices of the mixing components vary within the range 10^{-3}–10^{-1}. The internal stresses are most often the sources of such variations. However, they only slightly affect the measurements made by our method, with the only exception—the crystals with high values of the photoelasticity coefficient—being of the order of 10^{-6} cm^2/kg. Thus, the most promising method for studying a stressed state in crystals is the conventional photoelastic method using a linearly or circularly polarized radiation.

The changes in the optical density can be either local or macroscopic. Most frequently, local variations affects the transmitted radiation similar to a conventional lens, while the macroscopic variations in the optical density manifest themselves in a different way—either as an optical wedge or as an combination of positive and negative cylindrical lenses. As was established, the experimental identification of defects becomes essentially more difficult in the case of a joint action of defects of different nature, in particular, in the case of the varying ratio of the areas occupied by these defects in different parts of the surface. Therefore, to illustrate the method efficiency, we used a simple object with the known defect structure—a Czochralski-grown quartz single crystal. We studied the electrical inhomogeneity caused by the distribution of phosphorus along the growth direction. There are two mechanisms for the formation of the defect distribution along the pulling direction. The first one is the formation of periodical linear aggregates of impurities forming the strata whose shape is similar to that of the crystallization front. The distance between the strata is determined by the rotation and pulling velocities. The second mechanism determines a gradual increase of integrated impurity concentration during crystal growth.

It is well known that the absorption of light by free charge carriers increases as a squared wavelength, which provides achieve a higher contrast in the recorded electrical inhomogeneity in semiconductors and to exclude some of the factors that can affect the optical transmission.

A 1-mm-thick silicon wafer was studied on an FPD-1 photoelectric flaw detector-polariscope at the wavelength 2.1 μm manufactured at the Institute of Crystallography of the Russian Academy of Sciences.

To perform the necessary experiments, the instrument was equipped with a CP-2 compound polarizer. The long wavelength excluded the use of all the spectral characteristics of infrared polarizers. The results of the study of the optical inhomogeneity of a crystal along the growth direction are presented in Fig. 4. Curve *1* shows that the integrated transmission of a plate at a distance of $l = 26$ mm has changed by 1.5%. According to our calculations, this change in τ corresponds to an increase in absorption by 27%. In particular, the absorption coefficient along the growth direction increased from $k = 1.07$ to $k = 1.36$ cm^{-1}. The mean value of the absorption coefficient $K = kd$ is found to be 0.1215. Most probably, the average impurity concentration exponentially increases during crystal growth. At small K, one can approximate the exponent by an inclined straight line. This makes it possible to assume that the impurity concentration in this crystal increased linearly during growth and therefore $d\tau/dl \sim l$. Excluding the effect of impurity strata, we see that differential curve *2* agrees well with the above assumptions. This was also confirmed analytically with the use of the well-known expression $\tau = F(k)$ [6], which, in our case, can be reduced to the form

$$\tau = \frac{(1-R)^2 e^{-kd}}{1-R^2 e^{-2kd}}. \quad (4)$$

Thus, it may be concluded that our studies performed on various crystals confirmed the efficiency of the suggested optical method of flaw detection. The possibility of using the proposed method on available scanning photoelectric instruments has been proved. The new method essentially increases the possibilities of existing well-known instruments. In particular, it becomes possible to visualize the changes in the refractive indices without applying complex interferometric devices.

REFERENCES

1. V. S. Chudakov and B. N. Grechushnikov, Prib. Tekh. Éksp., No. 5, 195 (1975).
2. G. I. Distler, E. I. Kortukova, A. V. Kotov, *et al.*, Opt. Spektrosk. **23** (1), 137 (1967).
3. M. Ya. Kruger, V. A. Panov, V. V. Kulagin, *et al.*, *Handbook of Designer of Mechano-Optical Devices* (Mashinostroenie, Leningrad, 1967), p. 706.
4. V. S. Chudakov, Kristallografiya **44** (3), 497 (1999) [Crystallogr. Rep. **44**, 457 (1999)].
5. *Ruby and Sapphire*, Ed. by L. M. Belyaev (Nauka, Moscow, 1974), p. 236.
6. G. B. Dubrovskiĭ, Fiz. Tverd. Tela (Leningrad) **3**, 1305 (1961) [Sov. Phys. Solid State **3**, 943 (1961)].

Translated by A. Zalesskiĭ

Crystallography Reports, Vol. 46, No. 2, 2001, pp. 288–291. Translated from Kristallografiya, Vol. 46, No. 2, 2001, pp. 332–335.

PHYSICAL PROPERTIES OF CRYSTALS

Preparation and NMR Studies of Cesium Hydroselenite

I. S. Vinogradova

Siberian State Technological University, pr. Mira 82, Krasnoyarsk, 660049 Russia

e-mail RSA@post.krascience.rssi.ru

Received August 31, 1999; in final form, August 29, 2000

Abstract—This work is a part of the systematic study of the structure and the physical properties of alkaline hydroselenite crystals with the general formula *Me*$HSeO_3$, where *Me* is an alkali ion. The characteristic feature of this family is a net of hydrogen bonds between SeO_3 groups forming closed $[HSeO_3^-]_2$ dimers. © *2001 MAIK "Nauka/Interperiodica".*

Dimers found in the structures of sodium, potassium, and rubidium hydroselenites [1–3] stabilize the structure so that no phase transitions have been revealed in this family even in the presence of disordered hydrogen bonds ($NaHSeO_3$, [1]). Heating of hydroselenites results in their dehydration and transformation into pyroselenates accompanied by water release [4] according to the reaction

$$2MeHSeO_3 = Me_2Se_2O_5 + H_2O.$$

Cesium hydroselenite has been studied insufficiently. There are still no data on the structure, solubility, and thermal and other properties. As was reported in [5], the IR and Raman spectra for alkali hydroselenites indicate a phase transition in cesium hydroselenite.

In this paper, we present the NMR data on protonated and deuterated cesium hydroselenite single crystals obtained at H^1, D^2, and Cs^{133} nuclei.

The protonated salt was synthesized from cesium carbonate and selenious acid; the deuterated salt was synthesized from the reagents containing no protons: selenium dioxide and cesium carbonate. Single crystals were grown by slow evaporation of the saturated salt solutions in H_2O and D_2O at a temperature of 40°C. Cesium hydroselenite crystallizes in the form of thin prismatic extremely highly hygroscopic plates. Crystals of protonated and deuterated salts have the same habit (Fig. 1).

To obtain information on the symmetry of single crystals, structural parameters, hydrogen bonds, and local environment of cesium ion, we performed NMR studies at D^2 and Cs^{133} nuclei. To study the orientational dependence of splitting of NMR spectra we used the crystallographic coordinate system *x*, *y*, *z*, which, because of the lack of the structural data, were related to the crystal faces as is shown in Fig. 1. Using the orientational dependences and the Volkov method, we calculated the principal components of the electric-field gradient (EFG) tensors at D^2 and Cs^{133} nuclei, their directional cosines, the quadrupole coupling constants (QCC), and the asymmetry parameter η of EFG.

Cs^{133} NMR. The NMR spectra were recorded in a 13-kOe field. In accordance with the nuclear spin of cesium, $I = 7/2$, the NMR spectrum would consist of a central line and six symmetric satellites for each of the nonequivalent nuclei within the unit cell. The angular dependences of spectrum splitting between the first side components corresponding to the $3/2 \longleftrightarrow 1/2$ and $-1/2 \longleftrightarrow -3/2$ transitions are shown in Fig. 2a. They reflect the orthorhombic symmetry of the crystal and the existence of only one independent position for cesium ion in the unit cell. The parameters of the EFG tensors are given in table. The QCC for Cs^{133} nuclei equals 241 kHz and is close to the corresponding value for cesium trihydroselenite (308 kHz, [6]) and $CsLiH_2(SeO_3)_2$ (280 kHz [7]).

Deuteron Magnetic Resonance (DMR). The DMR spectra were recorded in a 13.5-kOe field. The spectrum of an arbitrarily oriented crystal consists of four components. The orientational dependences of the splitting for these components are given in Fig. 2b, the characteristics of the EFG tensor are listed in table. The existence of one QCC indicates the existence of only one independent hydrogen bond in the unit cell. The same situation also takes place in potassium, rubidium,

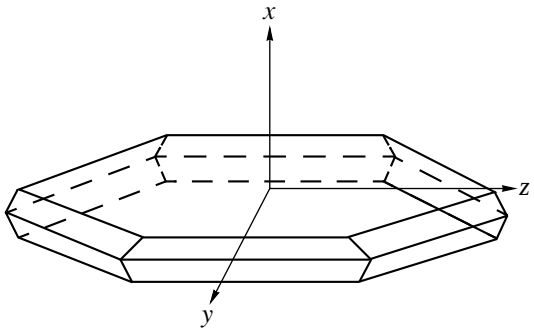

Fig. 1. Habit of a cesium hydroselenite single crystal and the crystallographic coordinate system.

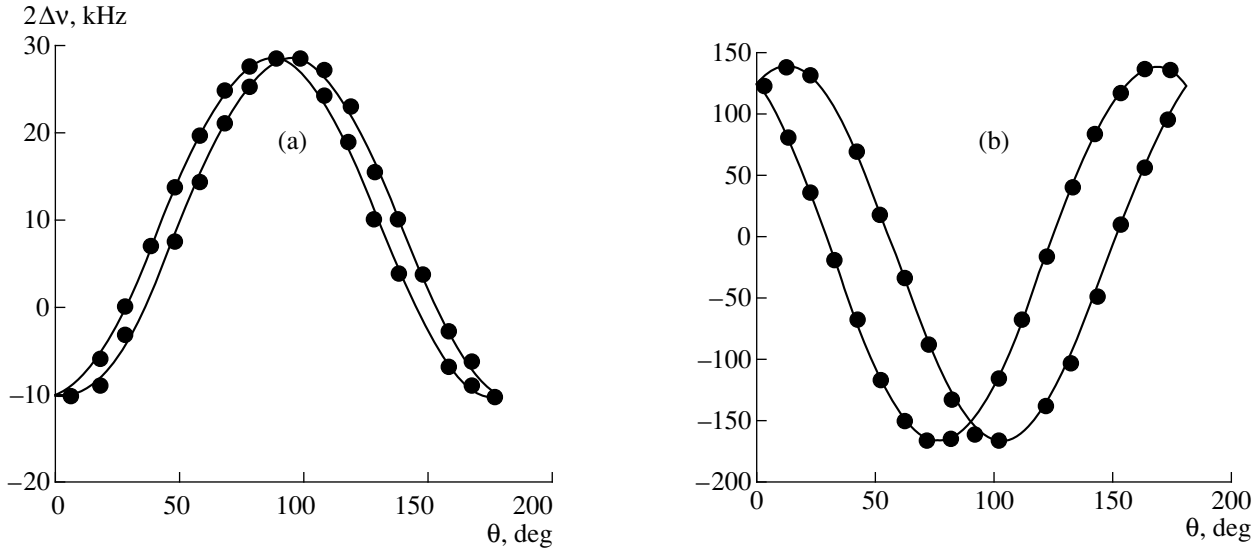

Fig. 2. Orientational dependence of quadrupole splitting of NMR spectra for (a) Cs^{133} and (b) D^2 nuclei in cesium hydroselenite crystals at room temperature. $H_0 \perp y$, $\theta = \angle H_0, z$.

and lithium hydroselenites [2, 3, 8]. The bond length estimated from the QCC equals 2.571 Å and is consistent with the length of hydrogen bonds in trihydroselenites.

To confirm the occurrence of the phase transition found in [5], we measured the dielectric constant along the *x, y, z* axes for three single-crystal specimens in the temperature range from room temperature to –196°C. The measurements revealed no phase transitions. The Cs^{133} NMR spectra also showed no signs of phase transitions: the quadrupole splitting of the spectra was practically constant within the temperature range from room temperature to –140°C both in protonated and deuterated crystals. Such a behavior is typical not only for the cesium salt but for other hydroselenites as well. Contrary to trihydroselenites, the hydroselenites studied so far have rather stable crystal lattices and show no phase transitions. The stabilizing effect seems to be produced by the system of hydrogen bonds (closed dimers). Therefore, it is expedient to study the structure of cesium hydroselenate by diffraction methods. The results obtained in our study show that the behavior of cesium hydroselenite both at low and high temperatures is similar to the behavior of lithium, sodium, potassium, and rubidium hydroselenites.

Thermal decomposition. The effect of heating on hydroselenites have been studied in lithium, sodium, and potassium salts by the thermogravimetric methods [4]. The salts were calcined at various temperatures, and the resulting products were first analyzed chemically and were then subjected to the X-ray diffraction analyses. The experiments show that hydroselenites are transformed into pyroselenites. This transformation takes place in a wide temperature range of about 50°C. Thermogravimetric method does not allow the study of the dynamics of such transformations, but such information can be obtained by the proton NMR. Protons are incorporated into the crystal lattice of hydroselenites in the form of O–H groups. The resulting products of the transformation of hydroselenites into pyroselenites contain no protons. We studied the thermal decomposition of cesium hydroselenites by the proton NMR in polycrystals. At room temperature, the spectrum consists of two lines—a broad and a narrow one. The narrow line is attributed to water molecules not incorporated into the crystal lattice. They are adsorbed at the surfaces of polycrystalline grains. A high hygroscopicity of the salt does not allow one to get rid of this component by drying. A broad spectral line is attributed to O–H groups of the crystal lattice. Heating of a sample above room temperature, does not change the spectrum up to 42°C (Fig. 3). Above this temperature, the intensity of a narrow line drastically increases, while the width of a broad spectral component gradually decreases. These changes in the spectrum cover the temperature range from room to 66°C. At the latter

Principal components of the EFG tensors at D^2 and Cs^{133} nuclei in cesium hydroselenite crystals

Crystal	Nucleus	$\frac{e^2Qq_{ii}}{h}$, kHz	Directional cosines with respect to the axes		
			x	*y*	*z*
$CsHSeO_3$	Cs^{133}	–29	±0.189	±0.442	0.877
		–212	±0.294	±0.827	0.480
		241	±0.937	0.349	±0.027
$CsDSeO_3$	D^2	–68.7	±0.488	0.869	±0.082
		–90.4	±0.145	±0.173	0.974
		159.1	±0.861	±0.463	0.21

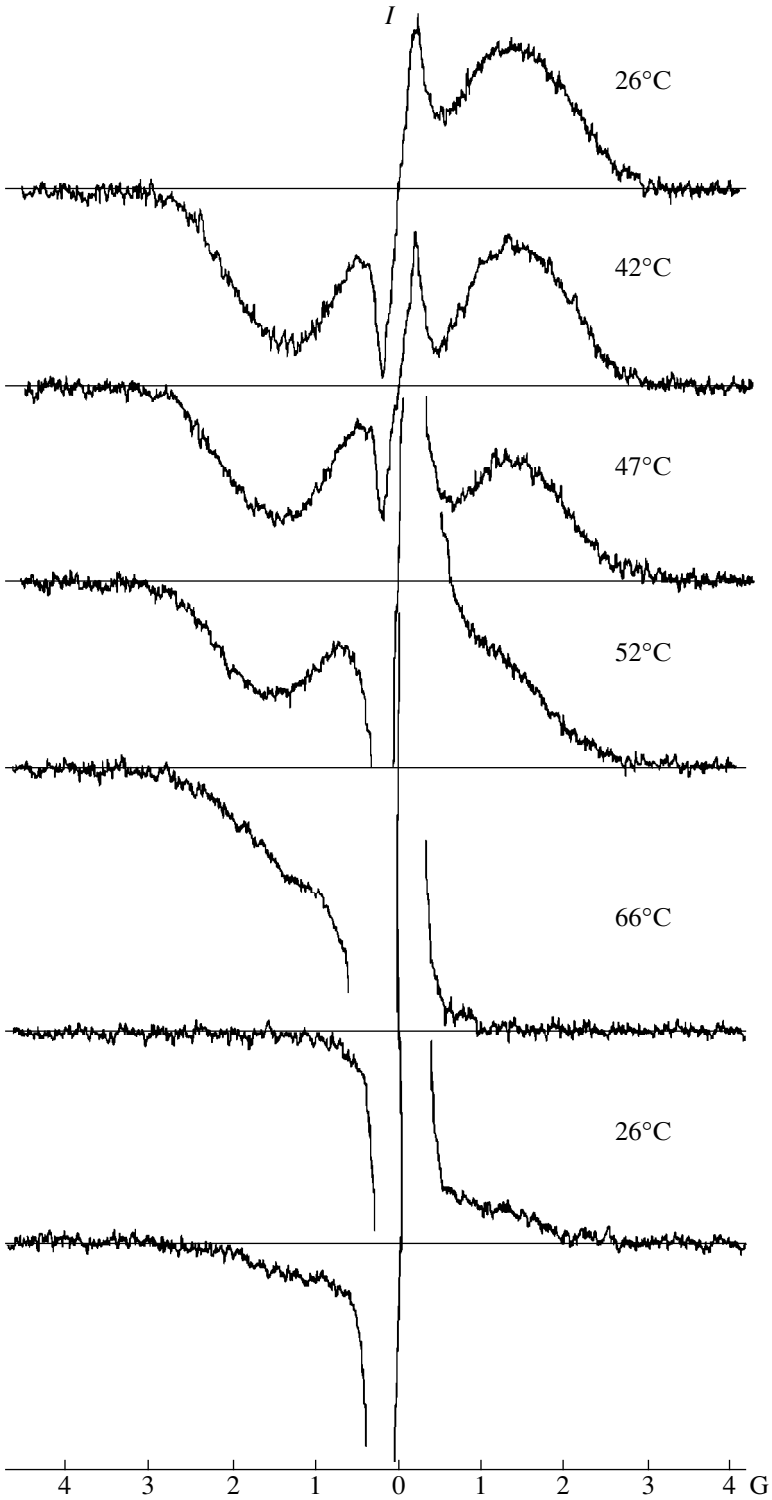

Fig. 3. Proton magnetic resonance spectra of a $CsHSeO_3$ polycrystal.

temperature and above it, the spectrum has only one narrow intense line.

The observed changes in proton NMR spectra show that, in the temperature range 42–66°C, the protons of O–H groups abandon the cesium hydroselenite lattice. By analogy with lithium, sodium, and potassium hydroselenites [4], cesium hydroselenite has to be transformed into cesium pyroselenite $Cs_2Se_2O_5$ containing no protons. Protons leave the lattice in the composition of water molecules. Water drops are con-

densed on the walls of a test tube containing the sample. Condensation proceeds most intensely at temperatures higher than 80–90°C. Water molecules are also condensed at the grain boundaries inside the sample, which is confirmed by the occurrence of an intense narrow line in the spectrum center. If immediately after heating, the sample is cooled to room temperature, its proton spectrum is partly restored and, in addition to the narrow intense line due to water molecules, a broad low-intensity component is observed (the lower spectrum in Fig. 3) after a certain time; the intensity of this line slightly increases. However, the initial spectrum is not fully restored, since some protons included into water molecules "evaporate" in the process of dehydration.

Thus, the structure of the cesium hydroselenite crystals grown is orthorhombic and has the only position occupied by a cesium ion and the only hydrogen bond in the unit cell. This structure is stable in the low-temperature region. Being heated above 66°C, hydroselenite is transformed into pyroselenite.

REFERENCES

1. V. A. Sarin, U. É. Rider, N. N. Bydanov, and I. S. Vinogradova, Kristallografiya **31** (2), 264 (1986) [Sov. Phys. Crystallogr. **31**, 155 (1986)].
2. V. A. Sarin, N. N. Bydanov, U. É. Rider, *et al.*, Kristallografiya **29** (2), 243 (1984) [Sov. Phys. Crystallogr. **29**, 144 (1984)].
3. I. I. Bannova, I. S. Vinogradova, N. M. Kuz'min, *et al.*, Kristallografiya **32** (1), 83 (1987) [Sov. Phys. Crystallogr. **32**, 45 (1987)].
4. Z. V. Roshchina, Author's Abstract of Candidate's Dissertation in Chemistry (Moscow, 1971).
5. C. A. Cody and R. C. Levitt, J. Solid State Chem. **26**, 281 (1978).
6. I. S. Vinogradova, J. Solid State Chem. **40**, 361 (1981).
7. I. S. Vinogradova, V. I. Ponomarev, and S. I. Daryuga, Kristallografiya **34** (3), 364 (1989) [Sov. Phys. Crystallogr. **34**, 216 (1989)].
8. S. Chomnilpan and R. Liminga, Acta Crystallogr., Sect. B: Struct. Crystallogr. Cryst. Chem. **B35**, 3011 (1979).

Translated by A. Zalesskiĭ

Crystallography Reports, Vol. 46, No. 2, 2001, pp. 292–295. Translated from Kristallografiya, Vol. 46, No. 2, 2001, pp. 336–339.

PHYSICAL PROPERTIES OF CRYSTALS

Molecular Dynamics Simulation of the Transport Characteristics of α-$Ag_{1-x}Cu_xI$ ($0 < x < 0.25$)

A. K. Ivanov-Shitz, B. Yu. Mazniker, and E. S. Povolotskaya

Shubnikov Institute of Crystallography, Russian Academy of Sciences, Leninskiĭ pr. 59, Moscow, 117333 Russia

e-mail: ivanov@ns.crys.ras.ru

Received August 16, 1999

Abstract—The transport characteristics of the α-$Ag_{1-x}Cu_xI$ solid solutions have been calculated by the molecular dynamics technique. It was established that the diffusion constant of cations decreases with an increase of the copper concentration, which is consistent with the experimentally observed decrease in conductivity. The concentration curves of the activation energy of diffusion show the maximum at $x \approx 0.15$. The cation-transport numbers obtained in this study are in good agreement with the known experimental data. © *2001 MAIK "Nauka/Interperiodica".*

As is well known, the high-temperature phases of silver and copper iodides possess high ionic conductivities [1] and, having simple crystal structures, can be used as model systems for studying transport properties in solids by various methods, including computer simulation. It was shown [2] that the α-AgI-based solid solutions in the quasibinary AgI–CuI system exist over a wide temperature range. The ionic transport in $Ag_{1-x}Cu_xI$ was studied in [3–5], where a decrease in electric conductivity with an increase of the copper concentration in specimens was observed.

Below, we report the results obtained in the study of the transport characteristics of the $Ag_{1-x}Cu_xI$ system by molecular dynamics (MD) technique.

The MD simulation was performed for a system of 256 ions (128 I^--ions and 128 Ag^+- and Cu^+-ions); in other words, the box was composed by 64 unit cells, in which the anions formed a bcc lattice, whereas cations randomly occupied the centers of the faces of the cubic unit cell. The time step of 5×10^{-15} s provided the stability of the total energy of the system within an accuracy of 0.2%. At the initial moment of time, the particle velocities were assumed to be zeroes. Then, using the thermalization mechanism [6], the system temperature was increased up to the set level. The characteristics of the simulated crystal were averaged over the data collected for 50 ps (10^4 steps).

The interaction potential was chosen in the form

$$V_{i,j} = \frac{z_i z_j e^2}{r} + \frac{H_{ij}}{r^{n_{ij}}} - \frac{P_{ij}}{r^4} - \frac{W_{ij}}{r^6}.$$

The concrete interaction parameters were taken from [7–9] and are listed in Table 1.

Since the interaction parameters (α_{ij}) for the Ag^+–Cu^+ pair were unknown, we considered the following two variants: (a) $\alpha_{Ag-Cu} = \alpha_{Ag-Ag}$ and (b) $\alpha_{Ag-Cu} = \alpha_{Cu-Cu}$. The preliminary results showed that the behavior of the system only weakly depended on the choice of the interaction coefficients; therefore, simulation was performed for variant (a).

The effective charge of cations was taken to be $z(Ag^+) = +0.6e$ and $z(Cu^+) = +0.8e$, whereas the charge of anions was chosen in accordance with the condition for the total electrical neutrality of the crystal [7, 8]. The box dimensions were determined from the experimental data known for AgI and varied from 5.062 Å (at 400 K) to 5.112 Å (at 800 K) [10, 11].

Now, proceed to the transport characteristics. The ion self-diffusion constants are determined from the mean square displacements (MSD) of ions according to the relationship

$$\mathrm{Lim}\{r_\alpha^2(t)\} = 6D_\alpha t + B_\alpha, \quad t \longrightarrow \infty,$$

where D_α is the diffusion constant of an α-type particle and B_α is the Debye–Waller factor.

Table 1. Parameters of ion interactions

Type of the *i*–*j* pair	H_{ij}^*	P_{ij}^*	W_{ij}^*	n_{ij}
I^-–I^-	370.06	2.0706	5.8659	7
I^-–Ag^+	90.971	1.0353	0.0	9
I^-–Cu^+	12.982	1.0353	0.0	9
Ag^+–Ag^+	0.011282	0.0	0.0	11
Cu^+–Cu^+	0.01196	0.0	0.0	11

* In the e^2/Å units (= 14.39 eV).

1063-7745/01/4602-0292$21.00 © 2001 MAIK "Nauka/Interperiodica"

Figure 1 shows the MSD curves $r_\alpha^2(t)$ for the $Ag_{0.9}Cu_{0.1}I$ solid solution at the temperature of 650 K. It is seen that Ag^+- and Cu^+-ions participate in the translational motion, whereas the I^--ions oscillate about their equilibrium positions.

The temperature dependences of D_{Ag^+} for AgI shown in Fig. 2 prove a good agreement between the calculated and observed [12] data (it should be indicated that the diffusion constant of copper ions in α-CuI [13] is close to the D_{Ag^+} values in α-AgI). This proves that the interaction potential was chosen in an appropriate way, which is also confirmed by the good agreement between the Debye–Waller factors for I^--ions in α-AgI (the neutron diffraction data [10, 11] for poly- and single crystals) and $Ag_{0.953}Cu_{0.047}I$ (MD-data) (see Fig. 3).

The decrease in conductivity in the α-$Ag_{1-x}Cu_xI$ solid solutions was first observed in [3, 4] and was then studied in detailed in [5]. Figure 4 shows the "total" diffusion constant D_{Ag+Cu} (determined for all the cations) versus Cu concentration at different temperatures. For comparison, we also indicate the experimental diffusion constants of cations at 700 K calculated by the conductivity data according to the Nernst–Einstein relationship

$$D_\sigma = \frac{\sigma kT}{n(ze)^2},$$

where n is the number of charge carriers (ze). The Haven ratio $H_R = D/D_\sigma$ is about 0.65 for all the compositions at 700 K, which is consistent with the Haven ratio determined experimentally for α-AgI [12, 14] and calculated by the Monte Carlo method [15] (Table 2). Since $H_R < 1$ in the entire temperature range studied, the motion is of the cooperative nature. Considering the "caterpillar mechanism" of the motion, Okazaki [16] obtained the correlation coefficient ranging within 0.50–0.66, which is close to the experimental value, $H_R = 0.6$.

The activation energy of diffusion has the maximum at $x \approx 0.15$ (Fig. 5). The $E_{\sigma T}(x)$ curve has the similar shape [5], but with the maximum lying at $x \approx 0.25$. The MD results provided the determination of the transport numbers and their comparison with the corresponding measured values. As is seen from Fig. 6, the data of the computer and physical experiments are consistent.

As follows from the above-stated, the diffusion constant of cations in the α-$Ag_{1-x}Cu_xI$ solid solutions decreases with an increase of the Cu^+ concentration, although the general consideration allowed one to assume that the smaller lighter Cu^+-ions should move much easier than the large heavy Ag^+-ones. However, it is well known that in crystalline solid electrolytes, the sizes of mobile particles and the dimensions of the "conduction window" obey some optimum relation-

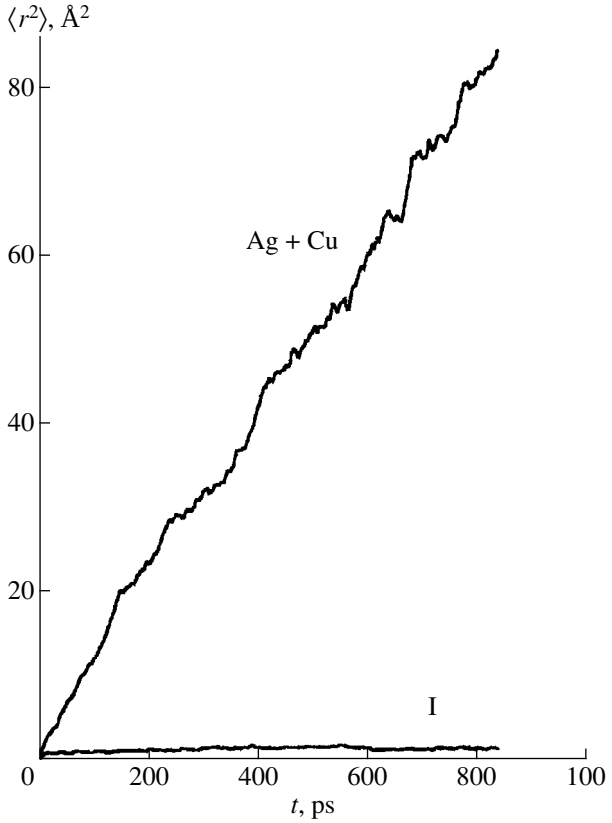

Fig. 1. Mean-square-displacement curves of cations and anions in $Ag_{0.9}Cu_{0.1}I$ at 650 K.

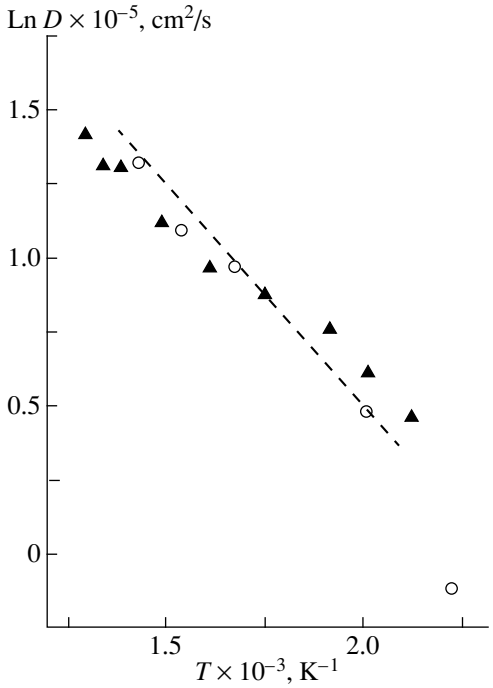

Fig. 2. Diffusion-constant curves of Ag^+ in α-AgI; ▲ experiment [12], ○ MD-data for $Ag_{0.953}Cu_{0.047}I$.

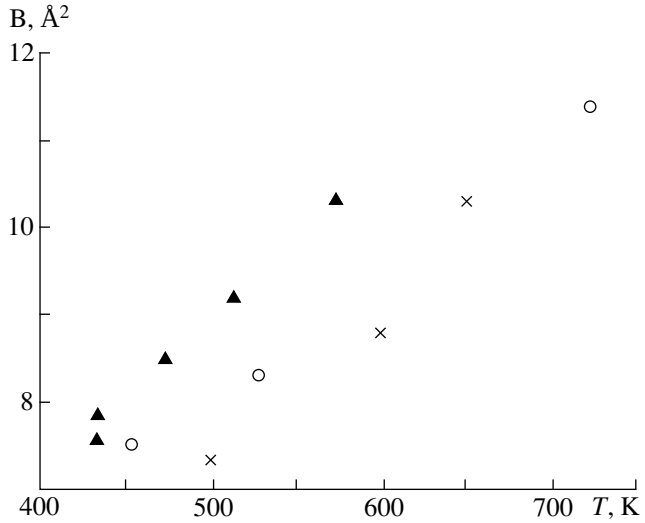

Fig. 3. Temperature curves of the Debye–Waller coefficients for I ions in α-AgI: (○) experiment [10], (▲) experiments [10, 11], (×) MD-data for $Ag_{0.953}Cu_{0.047}I$.

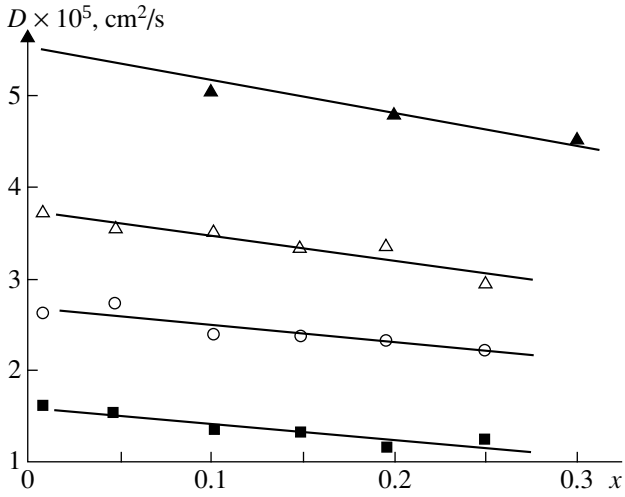

Fig. 4. Concentration curves of the calculated diffusion constants of cations in $Ag_{1-x}Cu_xI$ at the temperatures T of (■) 550, (○) 600, and (△) 700 K. For comparison, the values of D_σ (▲) at 700 K calculated from the conductivity data are also indicated.

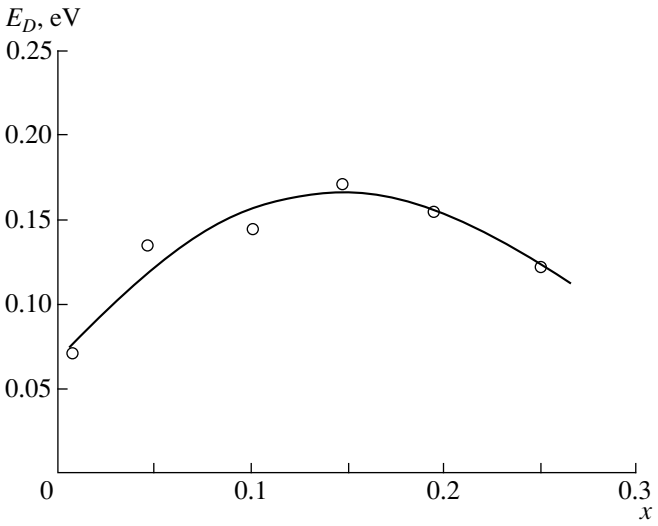

Fig. 5. Concentration curves of the calculated activation energy of diffusion for cations in $Ag_{1-x}Cu_xI$.

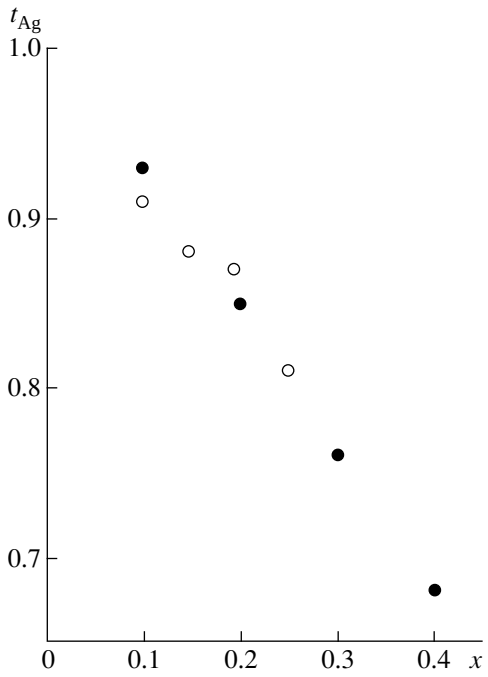

Fig. 6. Concentration curves of the transport numbers for silver cations in $Ag_{1-x}Cu_xI$. (●) Experiment [5], (○) MD-data.

ships [17]. Since with an increase of Cu^+-ion concentration the lattice parameter of the solid solution linearly decreases [5] in accordance with Vegard's law, the free volume available for cation diffusion also decreases. It seems to be a good explanation of the observed decrease in conductivity. However, our additional studies show that the reduction of the lattice parameter produces a negligible effect on the transport characteristics. Moreover, the monotonic variation of the lattice parameter cannot explain the nonmonotonic variation of the activation energy of diffusion. The analysis of the structural characteristics of α-AgI obtained from the EXAFS data [18, 19] provided the establishment of the fact that the preferable path of Ag^+-ions is formed first by jumps of these ions from tetrahedral positions into trigonal ones and then by their

Table 2. Haven ratio H_R for the α-AgI phase

T, K	H_R (experimental data [12, 14])	H_R (calculated data [15])
433	0.69	0.67
623	0.69	0.59
813	0.82	0.56

jumps from the trigonal positions to other tetrahedral positions (the potential barrier equals 0.04–0.07 eV). The barriers for other paths are much higher; thus, the transport via the octahedral positions requires overcoming an ≈0.18-eV-high barrier. As is seen from Fig. 5, the activation energy of diffusion in α-$Ag_{0.99}Cu_{0.01}I$ is 0.07 eV; in α-$Ag_{0.85}Cu_{0.15}I$, it equals 0.17 eV. However, it is almost impossible for copper cations to move via octahedral positions. The theoretical consideration within the stochastic model [20] showed the pronounced dependence of the ion mobility on the shape of the potential relief along which the particles move. In other words, irrespectively of the barrier value, the mobilities (and, therefore, also diffusion) of Cu^+ and Ag^+ ions should be different, because different thermal vibrations of silver and copper atoms result in the particles motion along different paths. Thus, it can be assumed that the cation motion in $Ag_{1-x}Cu_xI$ solid solutions is strongly correlated.

ACKNOWLEDGMENTS

This study was supported by the Program "Universities of Russia."

REFERENCES

1. V. N. Chebotin and M. V. Perfil'ev, *Electrochemistry of Solid Electrolytes* (Khimiya, Moscow, 1978).
2. J. Nölting, Ber. Bunsenges. Phys. Chem. **68** (10), 932 (1964).
3. J. C. Bazán and J. A. Schmidt, J. Appl. Electrochem. **6**, 411 (1976).
4. J. A. Schmidt, R. E. Fornari, and J. C. Bazán, Electrochim. Acta **24**, 1131 (1979).
5. M. Kusakabe, Y. Shirakawa, S. Tamaki, and Y. Ito, J. Phys. Soc. Jpn. **64** (1), 170 (1995).
6. S. Kh. Aĭt'yan and A. K. Ivanov-Shits, Fiz. Tverd. Tela (Leningrad) **32** (5), 1360 (1990) [Sov. Phys. Solid State **32**, 795 (1990)].
7. F. Shimojo and M. Kobayashi, J. Phys. Soc. Jpn. **60** (11), 3725 (1991).
8. A. Fukumoto and A. Ueda, Solid State Ionics **3/4**, 115 (1981).
9. K. Ihata and H. Okazaki, J. Phys.: Condens. Matter **9**, 1477 (1997).
10. R. J. Cava, F. Reidinger, and B. J. Wuensch, Solid State Commun. **24**, 411 (1977).
11. A. F. Wright and B. E. F. Fenders, J. Phys. C: Solid State Phys. **10**, 2261 (1977).
12. A. Kvist and R. Tärneberg, Z. Naturforsch. A **25a**, 257 (1970).
13. J. X. M. Z. Johansson, K. Sköld, and J.-E. Jörgensen, Solid State Ionics **50** (3/4), 247 (1992).
14. A. Kvist and A.-M. Josefson, Z. Naturforsch. A **23a**, 625 (1968).
15. F. Tachibana and H. Okazaki, Solid State Ionics **23**, 219 (1987).
16. H. Okazaki, J. Phys. Soc. Jpn. **23** (2), 355 (1967).
17. *Physics of Superionic Conductors*, Ed. by M. B. Salamon (Springer-Verlag, New York, 1979; Zinatne, Riga, 1982).
18. T. M. Hayes and J. B. Boyce, Phys. Rev. B **21**, 2513 (1980).
19. A. Yoshiasa, F. Kanamuru, and K. Koto, Solid State Ionics **27**, 275 (1988).
20. W. Dieterich, I. Peschel, and W. R. Schneider, Z. Phys. B **27**, 177 (1977).

Translated by L. Man

Crystallography Reports, Vol. 46, No. 2, 2001, pp. 296–298. Translated from Kristallografiya, Vol. 46, No. 2, 2001, pp. 340–342.

PHYSICAL PROPERTIES OF CRYSTALS

Ordinary Electromagnetic Waves in Optically Biaxial Crystals

V. I. Alshits and V. N. Lyubimov

Shubnikov Institute of Crystallography, Russian Academy of Sciences, Leninskiĭ pr. 59, Moscow, 117333 Russia

Received May 13, 1999; in final form, November 18, 1999

Abstract—It is shown that the so-called ordinary electromagnetic waves (the waves whose group velocity is parallel to the wave normal) cannot propagate outside the planes parallel to the principal planes of the permittivity tensor in transparent optically biaxial crystals. For each of the three such planes, the waves of one of the two independent branches are ordinary irrespectively of the direction of their propagation, whereas the waves of the other branch are ordinary only if they propagate along two mutually orthogonal directions of the corresponding eigenvectors of the permittivity tensor. *© 2001 MAIK "Nauka/Interperiodica".*

The present study was undertaken with the aim to establish all the cases where the electromagnetic waves with the group velocity parallel to the wave normal or the so-called ordinary waves [1] can propagate in transparent optically biaxial crystals.

The existence of the branch of ordinary electromagnetic waves in optically uniaxial crystals is a well-known fact [1–6]. At the same time, it should be emphasized that the group velocity of the extraordinary waves can be parallel to the wave normal in two cases—during the propagation of the latter along the optical axis and normally to it. These facts can be understood if one takes into account that the direction of the group velocity is parallel to the geometric normal to the refractive-index surface [2], with the latter being a sphere for the ordinary waves and an ellipsoid of rotation for the extraordinary ones.

In low-symmetric (orthorhombic, monoclinic, and triclinic) crystals, which are optically biaxial, the two-sheet refractive-index surface has a much more complicated shape than for uniaxial crystals. In particular, it always has four points of conic self-intersection corresponding to two optical axes. The existence of the waves with the group velocity parallel to the wave normal in such low-symmetric media requires a special consideration. Below, we consider this problem.

The optical properties of crystals are fully determined by the dielectric-constant or permittivity tensor $\hat{\varepsilon}$ whose structure is dependent on the medium symmetry. In our case, it is more convenient to use the reciprocal tensor $\hat{\varepsilon}^{-1}$, which directly determines the refractive-index surfaces of interest:

$$\hat{\varepsilon}^{-1} = \begin{bmatrix} 1/\varepsilon_1 & 0 & 0 \\ 0 & 1/\varepsilon_2 & 0 \\ 0 & 0 & 1/\varepsilon_3 \end{bmatrix}, \quad (1)$$

where ε_i are the eigenvalues of the tensor $\hat{\varepsilon}$. Without losing the general nature of the consideration, we can assume that $\varepsilon_1 < \varepsilon_2 < \varepsilon_3$ (in the general case of a low-symmetric crystal, all these eigenvalues should be different). As usual, the coordinate system is related to the principal axes of the tensor $\hat{\varepsilon}$ (the principal axes of the tensors $\hat{\varepsilon}$ and $\hat{\varepsilon}^{-1}$ coincide).

Using the Fedorov formalism [2, 4, 5], we can represent the tensor $\hat{\varepsilon}^{-1}$ defined by Eq. (1) in the axial form

$$\hat{\varepsilon}^{-1} = a + b(\mathbf{c}_1 \otimes \mathbf{c}_2 + \mathbf{c}_2 \otimes \mathbf{c}_1), \quad (2)$$

where

$$a = 1/\varepsilon_2, \quad b = (\varepsilon_1 - \varepsilon_3)/2\varepsilon_1\varepsilon_3$$

and $\otimes$ denotes the diadic multiplication of the unit vectors $\mathbf{c}_1$ and $\mathbf{c}_2$ parallel to the optical axes of the crystal,

$$\mathbf{c}_{1,2} = (\pm\sin\alpha, 0, \cos\alpha), \quad (3)$$

where 2α is the angle formed by the optical axes equal to

$$\tan\alpha = \sqrt{\frac{\varepsilon_3(\varepsilon_2 - \varepsilon_1)}{\varepsilon_1(\varepsilon_3 - \varepsilon_2)}}. \quad (4)$$

For an arbitrary direction of propagation $\mathbf{m}$ ($\mathbf{m}^2 = 1$), the refractive indices of the waves of two independent branches $n_\pm$ can be written in the form [2, 4, 5]

$$1/n_\pm^2 = a + b([\mathbf{m}\mathbf{c}_1][\mathbf{m}\mathbf{c}_2] \pm R), \quad (5)$$

where

$$R = \sqrt{[\mathbf{m}\mathbf{c}_1]^2[\mathbf{m}\mathbf{c}_2]^2}.$$

The super- and subscripts in Eq. (5) correspond to the external and internal sheets of the two-sheet refractive-

index surface, respectively [$n_+ \geq n_-$ because, in Eq. (5), $b < 0$].

In addition to the Cartesian coordinate system used above, we also introduce a standard system of spherical coordinates (ϑ, φ) in order to represent the wave normal **m** as a function of the angles ϑ and φ, namely,

$$\mathbf{m} = (\sin\vartheta\cos\varphi, \sin\vartheta\sin\varphi, \cos\vartheta). \quad (6)$$

In this case, Eq. (5) takes the following form for the directions of wave propagation parallel to the coordinate planes:

$$n_+ = \sqrt{\varepsilon_3}, \quad n_- = \sqrt{\frac{\varepsilon_2\varepsilon_1}{\varepsilon_2\sin^2\varphi + \varepsilon_1\cos^2\varphi}} \quad (7)$$

for the *xy* plane,

$$n_+ = \sqrt{\frac{\varepsilon_2\varepsilon_3}{\varepsilon_2\sin^2\vartheta + \varepsilon_3\cos^2\vartheta}}, \quad n_- = \sqrt{\varepsilon_1} \quad (8)$$

for the *yz* plane, and

$$n_+ = \sqrt{\varepsilon_2}, \quad n_- = \sqrt{\frac{\varepsilon_1\varepsilon_3}{\varepsilon_1\sin^2\vartheta + \varepsilon_3\cos^2\vartheta}} \quad (9)$$
$$\vartheta \leq \alpha, \quad \vartheta \geq \pi - \alpha$$

$$n_+ = \sqrt{\frac{\varepsilon_1\varepsilon_3}{\varepsilon_1\sin^2\vartheta + \varepsilon_3\cos^2\vartheta}}, \quad n_- = \sqrt{\varepsilon_2} \quad (10)$$
$$\alpha \leq \vartheta \leq \pi - \alpha$$

for the *xz* plane.

It follows from Eqs. (7)–(10) that in all the sections, we have the coexisting circumference and ellipse (see figure).

Since the geometric normal to the surface, $n_\pm(\mathbf{m})$, yields the direction of the group velocity, it becomes clear that the extreme points of the surface $n_\pm(\mathbf{m})$ correspond to the case, where the wave normal and the group velocity are parallel. Now, the problem reduces to the determination of these extreme points.

The extreme points of the surface $n_\pm(\mathbf{m})$ [Eq. (5)] are defined by the following system of equations:

$$\begin{cases} \partial n_\pm/\partial\varphi = 0 \\ \partial n_\pm/\partial\vartheta = 0. \end{cases} \quad (11)$$

Using Eqs. (3), (5), and (6) and performing rather cumbersome calculations, we arrive at the following expressions convenient for our further consideration:

$$\begin{cases} F^\pm\sin\vartheta\sin 2\varphi = 0 & (12) \\ (F^\pm g + 2\cos^2\alpha)\sin 2\vartheta = 0. & (13) \end{cases}$$

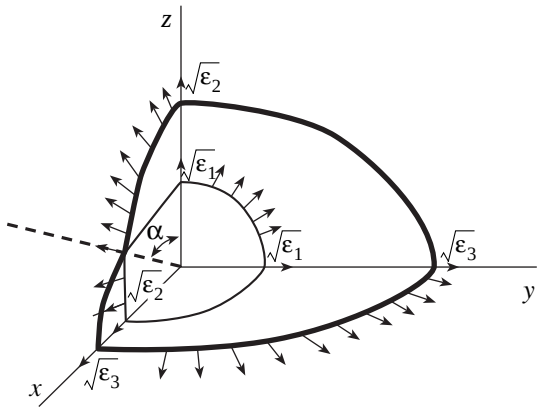

Sections of the refractive-index surface by the principal planes of the permittivity tensor for a transparent optically biaxial crystal. Arrows indicate the circular sections corresponding to the branches of the ordinary waves. The dashed line indicates the direction of the optical axis. The outer sheets are represented by bold lines.

In the above expressions, we used the following notation:

$$F^\pm = \pm R - \cos^2\alpha - \sin^2\alpha\sin^2\varphi - g\cos^2\vartheta,$$
$$g = \cos^2\alpha + \sin^2\alpha\cos^2\varphi, \quad (14)$$
$$R = \sqrt{(\sin^2\alpha - g\sin^2\vartheta)^2 + (\sin 2\alpha\sin\vartheta\sin\varphi)^2}.$$

The function F^+ can be written in the form

$$F^+ = \frac{4\cos^2\alpha}{F^-}\cos^2\vartheta. \quad (15)$$

Taking into account that in a biaxial crystal, $\cos\alpha \neq 0$, we obtain

$$F^- \neq 0. \quad (16)$$

As is seen from Eq. (12), the solutions of the system of equations with due regard for Eq. (15) lie within the coordinate *xy* ($\vartheta = \pi/2$), *yz* ($\varphi = \pm\pi/2$), and *xz* ($\varphi = 0, \pi$) planes.

Thus, irrespectively of a large variety of two-sheet refractive-index surfaces $n_\pm(\mathbf{m})$ for biaxial crystals, in such crystals, the ordinary waves can exist only within the planes indicated above.

Despite the fact that all the other results can be obtained by solving Eq. (13), it is much more convenient to use the rather simple Eqs. (7)–(10) valid for the solutions existing within the coordinate planes. Obviously, all the points on the circumferences described by these equations correspond to the ordinary waves. The extreme directions on the ellipses also correspond to the ordinary waves: in each coordinate plane, two such directions coincide with the corresponding coordinate axes. However, such pairs of directions are not isolated since they belong to the continuous branches of the

solutions for the ordinary waves in the sections orthogonal to the initial ones (see figure).

Finally, we should like to emphasize the analogy between the above circular and the elliptical sections and the corresponding characteristics of the ordinary and extraordinary waves in uniaxial crystals, with the analogy existing not only for the refractive indices but also for the wave polarizations.

Thus, it has been shown that ordinary waves in biaxial crystal can exist only in the sections of the refractive-index surfaces by the coordinate planes that have the circular shape. It it also shown that the situation shown in figure is unique. The fact that the waves corresponding to the sections considered here are ordinary is not surprising, because, in this case, the coordinate planes coincide with the symmetry planes of the tensor $\hat{\varepsilon}$, which, in turn, results in the fact that the normals to the surface $n_{\pm}(\mathbf{m})$ that belong to the circular sections should be aligned along the radial directions. At the same time, the absence of ordinary waves beyond the planes indicated above for the arbitrary biaxial crystals characterized by a complicated surface $n_{\pm}(\mathbf{m})$ with the points of conic self-intersections, which was proven above, seems to be far from obvious.

ACKNOWLEDGMENTS

The present study was supported by the Russian Foundation for Basic Research, project no. 98-02-16069.

REFERENCES

1. Yu. I. Sirotin and M. P. Shaskol'skaya, *Fundamentals of Crystal Physics* (Nauka, Moscow, 1979; Mir, Moscow, 1982).
2. F. I. Fedorov, *Optics of Anisotropic Medium* (Akad. Nauk BSSR, Minsk, 1958).
3. L. D. Landau and E. M. Lifshitz, *Course of Theoretical Physics*, Vol. 8: *Electrodynamics of Continuous Media* (Fizmatgiz, Moscow, 1959; Pergamon, New York, 1984).
4. F. I. Fedorov, *Theory of Gyrotropy* (Nauka i Tekhnika, Minsk, 1976).
5. F. I. Fedorov and V. V. Filippov, *Reflection and Refraction of Light by Transparent Crystals* (Nauka i Tekhnika, Minsk, 1976).
6. A. F. Konstantinova, B. N. Grechushnikov, B. V. Bokut', and E. G. Valyashko, *Optical Properties of Crystals* (Nauka i Tekhnika, Minsk, 1995).

Translated by L. Man

Crystallography Reports, Vol. 46, No. 2, 2001, pp. 299–302. Translated from Kristallografiya, Vol. 46, No. 2, 2001, pp. 343–346.

PHYSICAL PROPERTIES OF CRYSTALS

The Role of Dislocations in the Formation of Mechanical Stresses during Annealing of Gallium Arsenide Single Crystals

M. B. Litvinova and S. V. Shutov

Institute of Physics of Semiconductors, National Academy of Sciences of Ukraine, Kiev, Ukraine

Received June 11, 1999

Abstract—The effect of dislocations on the change of mechanical stresses in undoped semi-insulating gallium arsenide single crystals has been studied during their annealing in vacuum and in the arsenic atmosphere. The phenomena observed are explained by the effect of dislocations playing the role of channels for arsenic diffusion on the concentration of intrinsic point defects in the crystal regions surrounding dislocations. The mechanism of arsenic diffusion over dislocations allows one to consider dislocations as sources and sinks of arsenic without the translational and twinning processes and, thus, makes the well-known data on the reactions of dislocation interaction with point defects and the experimental structural data for single crystals more consistent.

INTRODUCTION

It is believed that the mechanical stresses in gallium arsenide single crystals are determined by the stress field of the dislocations (thermoelastic stresses) and the concentration inhomogeneity of ingots [1, 2]. In the course of annealing and postcrystallization cooling of single crystals, the excessive intrinsic point defects (in comparison with their equilibrium concentration) sink from the bulk to dislocations [3–5], which occurs according the following reactions accompanied by the changes in the concentration of intrinsic point defects: (1) recombination of the vacancies with the corresponding interstitial atoms, (2) absorption of pairs of vacancies (interstitial atoms) belonging to different sublattices, and (3) absorption of the vacancies in one sublattice with the formation of interstitial atoms in the another sublattice.

The latter two reactions should initiate either splitting or climbing of dislocations. However, the experimental data show such splitting in the gallium arsenide single crystals is rather small [6]. No pronounced asymmetry in the arrangement of the regions with modified properties in comparison with the properties of the matrix were observed along the lines of edge dislocations [1]; no pronounced twist of screw dislocations [7] was observed either. All these facts indicate the low efficiency of the above reactions in GaAs crystals.

The recombination of vacancies with the corresponding interstitial atoms can be efficient only if one of the sublattices is disordered and has close concentrations of vacancies and interstitial atoms [3]. Usually, this condition is not fulfilled in growth of the GaAs [1, 3, 8]. Thus, the nature of the interaction between dislocations and intrinsic point defects is still unclear.

Since defect interaction accompanied by the variation of their concentration and their distribution over the ingot bulk strongly affect the mechanical stresses, the measurement of such stresses during annealing of the single crystals is one of the possible methods of studying mechanisms defect interactions.

Below, we consider the effect of annealing of crystals on the mechanical stresses in Czochralski-grown undoped semi-insulating gallium arsenide single crystals with dislocation density ranging within $N_d = 1 \times 10^4$–2×10^6 cm^{-2} and resistivity ranging within $\rho = 6 \times 10^7$–3×10^8 Ω cm.

EXPERIMENTAL METHODS AND RESULTS

We studied plates 40–60 mm in diameter and 3–4 mm in thickness cut out from the ingots normally to the [100] growth axis and also the specimens cleaved from these plates with the sizes not exceeding $15 \times 4 \times 4$ mm^3 both subjected and not subjected to preliminary annealing. The mechanical stresses were measured by the photoelasticity method [9] in the plate plane (σ) or in the three orthogonal planes ($\sigma_\perp$ in the plane normal to the growth axis and the $\sigma_{\parallel 1}$ and $\sigma_{\parallel 2}$ in the planes parallel to this axis). Polarized light with a wavelength of 1.15 μm was generated by an LG-112 laser.

The 20- to 120-min long annealing of the plates and specimens at 950°C was performed either in vacuum or the arsenic atmosphere created with the aid of weighed portions of arsenic placed together with specimens into a sealed graphite cell. The specimens were annealed in atmosphere of hydrogen purified with the aid of a palladium filter. Annealing of the specimens in vacuum and in the As vapors was conducted in the sealed-quartz ampules pumped out to a pressure of $\leq 10^{-5}$ mmHg with

1063-7745/01/4602-0299$21.00

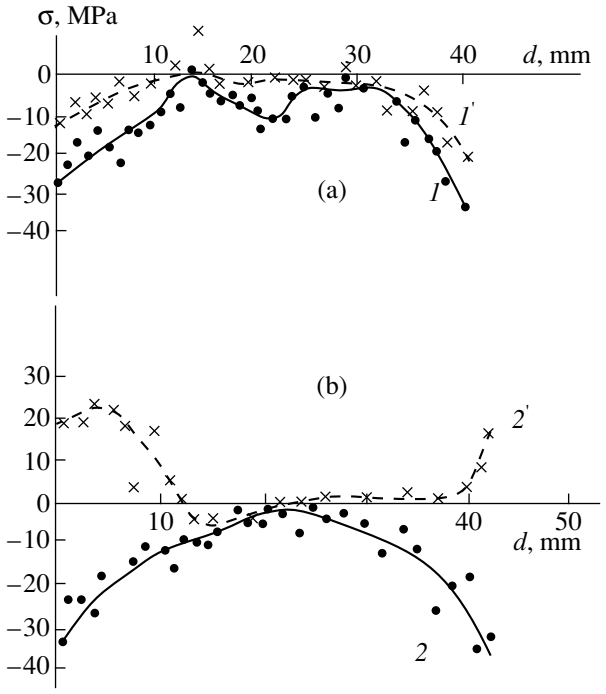

Fig. 1. Mechanical-stress distribution along the diameter of undoped semi-insulating GaAs plates with the average dislocation density (a) $N_d = 4.5 \times 10^4$ cm^{-2} and (b) $N_d = 7.2 \times 10^5$ cm^{-2} obtained before (*1* and *1*') and after (*2* and *2*') 120-min-annealing in the As atmosphere at $T = 950$°C.

the addition of weighed portions of metallic arsenic. Upon annealing, we removed a low-resistivity 10 to 300 μm-thick surface layer by the polishing mixture of the composition $H_2SO_4 : H_2O_2 : H_2O$ (3 : 1 : 1).

The dislocation density was determined from the etching pits in an MIM-7 microscope. The resistivity was determined by the two-probe technique.

The residual mechanical stresses in the initial (unannealed) plates with the typical *W*-shaped dislocation-density distribution along the diameter were negative (compressive [7]) stresses [1, 3]. The maximum σ values were observed at the plate periphery (curves *1*, *2* in Figs. 1a, 1b) and ranged from 10 to 50 MPa in different plates. The $\sigma_\perp$, $\sigma_{\parallel 1}$, and $\sigma_{\parallel 2}$ stresses had close values (see table) and were independent of the specimen dimensions.

Annealing under different conditions did not change the dislocation density and the character of their distribution across the plate cross section. At the average dislocation density in the plates $N_d < 5 \times 10^5$ cm^{-2}, annealing in the arsenic atmosphere decreased σ values (curves *1*, *1*' in Fig. 1a); in the case where $N_d > 5 \times 10^5$ cm^{-2}, the positive (tensile) stresses were observed (curves *2*, *2*' in Fig. 1b).

Upon annealing in the As atmosphere, the $\sigma_\perp$ values for all the samples exceeded the $\sigma_{\parallel 1}$ and $\sigma_{\parallel 2}$ values by three to five times (see table). In this case, all the stresses upon annealing in As vapors were positive. An increase of $\sigma_\perp$ values ($|\Delta\sigma_\perp|$) depended on the dislocation density in the sample (Fig. 2), whereas their relative variation $\sigma_{\perp\,TT}/\sigma_{\perp\,init.}$ (where $\sigma_{\perp\,TT}$ and $\sigma_{\perp\,init.}$ are the stresses in the specimens before and after annealing, respectively) was governed by the annealing duration *t* (Fig. 3). A smooth maximum in the ratio $\sigma_{\perp\,TT}/\sigma_{\perp\,init.}(t)$ at $t = 45$–60 min was observed for all the specimens.

DISCUSSION

The change in vacancy and interstitial concentrations results in the change of the lattice period of gallium arsenide single crystals [5] and, as a result, the formation of stresses in the planes with the concentration gradients of the intrinsic point defects (the stresses are positive if interstitial atoms dominate over vacancies and negative in the opposite case [8, 10]). An increase

Stresses in specimens before and after annealing ($T = 950$°C)

N_d, cm^{-2}	Atmosphere of annealing	Annealing time	σ_{init}, MPa			σ_{ann}, MPa		
			$\sigma_{\parallel 1}$	$\sigma_{\parallel 2}$	$\sigma_\perp$	$\sigma_{\parallel 1}$	$\sigma_{\parallel 2}$	$\sigma_\perp$
4.5×10^4	Vacuum	45 min	–4	–3	–5	–4	–4	–14
2.0×10^4			0*	0	0	–2	–2	–7
5.2×10^5			–5	–5	–9	–5	–6	–22
1.08×10^6			–5	–6	–10	–7	–7	–28
4.9×10^4			–2	–2	–3	–3	–3	–10
5.03×10^5			–3	–2	–5	–5	–4	–12
5.5×10^5			–3	–3	–7	–4	–4	–21
3.2×10^5	As	90 min	–3	–3	–6	+2	0	+7
6.8×10^5			–4	–4	–7	+3	+3	+13

* The stress value is less than the sensitivity threshold (1 MPa) of the set up used.

in the absolute $\sigma_\perp$ values during annealing at constant $|\sigma_{\parallel 1}|$ and $|\sigma_{\parallel 2}|$ bears witness to the change in the crystal composition in the planes normal to the dislocational lines (in accordance with the experimental geometry), i.e., the change in the concentration of intrinsic point defects around the dislocations.

In GaAs, the composition changes during annealing are determined mainly by the volatile component—arsenic [1, 3], whereas dislocations seem to be either sources or sinks of As atoms, depending on the atmosphere in which the specimens are annealed. No essential changes in the N_d values and the dislocation distribution in the specimens prior to and upon the annealing were observed; in other words, no dislocation splitting or climbing was recorded, which indicated that none of the mechanisms of interaction of dislocations and intrinsic point defects was active considered in the Introduction. Therefore, it is possible to assume that arsenic atoms move along the dislocational lines. An indirect confirmation of this mechanism of arsenic diffusion over the dislocations is the fact that the self-diffusion coefficient of arsenic in GaAs is practically temperature independent at the temperatures lower than 1200°C [10], i.e., below the temperature of formation of the dislocation structure.

During annealing in the As atmosphere, arsenic diffusion along dislocations gives rise to an increase of the concentration of interstitial As in the adjacent regions and appearance of tensile stresses. During annealing in vacuum, dislocations "take away" arsenic from the specimens, thus increasing the concentration gradient of arsenic vacancies (V_{As}) and compressive stresses. In terms of the proposed mechanism, the nonmonotonic character of the $(\sigma_{\perp\,ann}/\sigma_{\perp\,init})(t)$ dependence can be explained as follows. A relative increase in the $\sigma_\perp$ values in specimens is observed because of the removal of arsenic from the regions immediately adjacent to dislocations, where the arsenic concentration in semi-insulating undoped GaAs is rather high [3, 5]. An increase in stresses in such a process is more efficient the higher the dislocation density (curves *1*, *2* in Fig. 3). Most likely, a decrease in the $\sigma_\perp$ values with a further increase of the annealing duration is caused by the motion of interstitial arsenic atoms to dislocations, in order to compensate a decrease in the arsenic concentration in the adjacent regions.

The above assumption is based on the following estimate. For time interval *t*, arsenic atoms can move for a distance $l = (D_{As}t)^{1/2}$ at the temperature of $T \sim 1000$°C, where D_{As} is the self-diffusion coefficient of arsenic in gallium arsenide at this temperature. The D_{As} value determined from $D_{As} = 0.7\exp(-3.2/\mathrm{kT})$ [1] is 0.16×10^{-12} cm^2/s. The *l* value obtained for the time $t =$ 60 min specifying the onset of the stress compensation, caused by the removal of arsenic from the regions adjacent to dislocations is ≅0.24 μm. The radius of the activity sphere of an individual dislocation is of radius

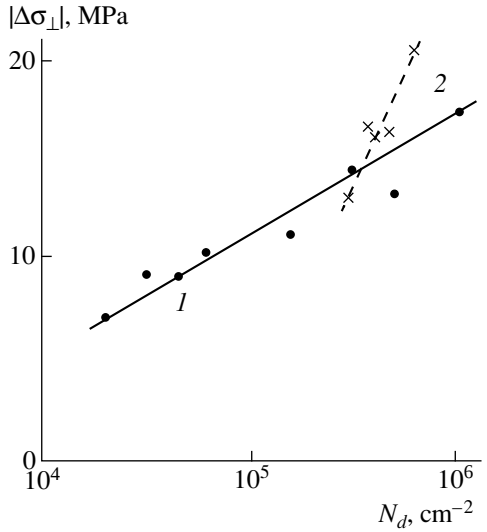

Fig. 2. Change of the stress $\Delta\sigma$ in the plane normal to the growth axis as a function of the average dislocation density N_d during 45-min-annealing in (*1*) vacuum (*2*) the As atmosphere at $T = 950$°C.

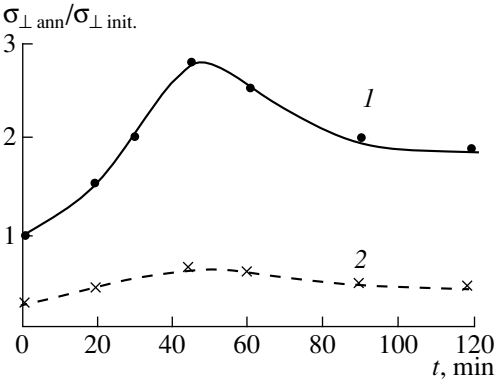

Fig. 3. Relative change of stresses in the specimens with the average dislocation density (*1*) $N_d = 1.08 \times 10^6$ cm^{-2} or (*2*) $N_d = 2 \times 10^4$ cm^{-2} annealed in vacuum at $T = 950$°C.

$r = 0.5N_d^{-1/2}$ for the specimen with $N_d = 10^6$ cm^{-2} equals 5 μm. Thus, within the time interval considered, arsenic atoms from almost half-area of the interdislocational space have enough time to "approach" the dislocations. Despite an increase in the total concentration of interstitial arsenic atoms, the its concentration gradient drops and the stress values decrease.

There should exist the average (over the cross section) critical dislocation density $N_{d\,cr}$, below which the penetration of arsenic atoms into the crystal along dislocations provides merely a decrease of the residual compressive stresses in the plates (curves *1*, *1*' in Fig. 1a). The value of this average critical dislocation density for the crystals annealed in the As atmosphere is $N_{d\,cr} = 5 \times 10^5$ cm^{-2}. If $N_d > N_{d\,cr}$, tensile stresses typ-

ical of undoped crystals (including semi-insulating GaAs(Cr) [11]) are formed (curves *2*, *2*' in Fig. 1b).

The interactions between dislocations and intrinsic point defects during annealing of undoped semi-insulating GaAs crystals are similar to the processes taking place in growth of single crystals where dislocations can be channels of arsenic redistribution between the crystallization front and the bulk of the crystallized ingot [3]. Arsenic diffusion from the regions with higher temperature results in recombination of V_{As} under the conditions of deficit in interstitial arsenic atoms. In a similar way, diffusion of excessive arsenic atoms along dislocations can result in their removal from the crystal bulk. As a consequence, dislocations can play the role either as sources or sinks of arsenic atoms without the processes of displacement twinning. This statement is consistent with the experimental data [3, 5–8].

Thus, we have shown that the change in mechanical stresses during annealing of undoped semi-insulating GaAs specimens is provided by dislocations playing the role channels for arsenic diffusion, which changes the concentrations of vacancies and interstitial arsenic atoms in the regions adjacent to dislocations. The mechanism of arsenic diffusion over dislocations removes the inconsistencies between the well-known reactions of interactions between dislocations and point defects and the experimental data on structural characteristics of single crystals [3, 5–8].

REFERENCES

1. M. G. Mil'vidskiĭ and V. G. Osvenskiĭ, *Structural Defects in Semiconductors Single Crystals* (Metallurgiya, Moscow, 1984).
2. N. S. Zadorozhnyĭ, V. F. Kovalenko, M. G. Mil'vidskiĭ, and A. V. Prokhorovich, Izv. Akad. Nauk SSSR, Neorg. Mater. **27** (6), 1127 (1991).
3. A. V. Markov, M. G. Mil'vidskiĭ, and V. G. Osvenskiĭ, in *Crystal Growth* (Nauka, Moscow, 1990), Vol. 18, pp. 214–233.
4. A. S. Bruk, V. V. Voronkov, and A. V. Govorkov, Izv. Akad. Nauk SSSR, Ser. Fiz. **52** (7), 1368 (1988).
5. V. T. Bublik and K. D. Shcherbachev, Kristallografiya **39** (6), 1105 (1994) [Crystallogr. Rep. **39**, 1016 (1994)].
6. A. M. Gómez and P. B. Hirsch, Philos. Mag. A **59** (6), 733 (1978).
7. S. S. Shifrin and A. V. Markov, Kristallografiya **25** (5), 1089 (1980) [Sov. Phys. Crystallogr. **25**, 625 (1980)].
8. M. G. Mil'vidskiĭ, *Semiconducting Materials in Modern Electronics* (Nauka, Moscow, 1986).
9. A. Ya. Aleksandrov and M. Kh. Fkhmedzyanov, *Polarization Optical Method in Mechanics of Deformable Solids* (Nauka, Moscow, 1973).
10. O. Madelung, *Physics of III–V Compounds* (Wiley, New York, 1964; Mir, Moscow, 1967).
11. V. F. Kovalenko, M. B. Litvinova, and L. G. Shepel', Neorg. Mater. **31** (2), 173 (1995).

Translated by A. Zolot'ko

Crystallography Reports, Vol. 46, No. 2, 2001, pp. 303–305. Translated from Kristallografiya, Vol. 46, No. 2, 2001, pp. 347–349.

SURFACE

Corrosion Resistance of Sapphire Surface as a Function of Its Crystallographic Characteristics

L. A. Litvinov, T. V. Druzenko, V. G. Potapova, and A. B. Blank

Research–Technological Concern Institute for Single Crystals, National Academy of Sciences of the Ukraine, pr. Lenina 60, Kharkov, 310001 Ukraine

e-mail lytvynov@isc.kharkov.com

Received December 8, 1999

Abstract—Corrosion resistance of a sapphire surface has been studied as a function of various technological factors (growth method, presence of impurities, growth medium), the density of structural defects (pores, vacancies, dislocations), and the crystallographic characteristics. It is shown that the main contribution to the corrosion resistance depends on the type of the mechanical treatment and the crystallographic characteristics of the surfaces and that the resistance of different crystallographic planes to aggressive media can differ up to seven times. *© 2001 MAIK "Nauka/Interperiodica".*

INTRODUCTION

The widespread use of sapphire in chemical technology requires the determination of conditions for attaining the maximum corrosion resistance of the surfaces of various sapphire products. The corrosion resistance of sapphire to various aggressive media was studied in numerous works [1, 2], however, all the data obtained relate only to bulk resistance. Although the difference in the dissolution rates of various faces of sapphire crystals was noticed still by G. Lavizzari as far back as 1865, the corrosion resistance of different sapphire surfaces has not been studied as yet.

The resistance of sapphire surface to various aggressive media can depend on the defect state of the subsurface layer and on various structural defects, whose type and density depend, in turn, on the growth method used. Sapphire is anisotropic and, therefore, one has to take into account also the nature of atomic bonding in different crystallographic planes, the electronic structure, and the energy characteristics of various planes.

The present study was undertaken to establish the contributions made by each of the above factors to corrosion resistance of sapphire surfaces.

EXPERIMENTAL

Sapphire crystals were grown by several methods—the Verneuil and Kyropoulos methods, the method of horizontal directional crystallization, and the Stepanov (EFG) technique. We also used waste crystals formed during Verneuil growth. We used different growth media–oxidative (the Verneuil techniques), vacuum (Kyropoulos and horizontal directional crystallization), and argon (the Stepanov technique). The samples were 10 mm in diameter and 2 mm in thickness and had various crystallographic orientations and degrees of surface roughness. For comparison, we also used smooth surfaces of the crystal basis and prisms tapered during growth. The crystals with the maximum anionic nonstoichiometry were obtained upon annealing in the ($CO + CO_2$) atmosphere under the residual pressure 60 Pa and the temperature 1980°C. The crystals with the maximum cationic nonstoichiometry were obtained upon annealing in the oxidative medium containing 12–15 vol % of O_2 in the annealing space at 1750°C. The effect of point defects was studied by thermally varying the densities of cationic and anionic vacancies [3]. The anionic nonstoichiometry was evaluated from absorption (which was maximal at 6.1 eV) and the fluorescence bands of *F*-centers (3.8 eV) excited by the X-ray radiation. We failed to evaluate reliably the cationic nonstoichiometry, because the grown crystals had the wide UV-absorption band.

The corrosion resistance of crystal surfaces was studied on a disklike crystal surface 10 mm in diameter by the method of layer etching in the concentrated phosphoric acid [4] applied to the surface (0.3 ml). Upon 30 min-annealing of the specimen at 300°C, the film formed on the surface was dissolved in bidistilled water. The aluminum concentration in the solution was measured to evaluate the degree of surface destruction. The etching process was repeated six times. The thickness h of the dissolved layer was determined from the formula

$$h = \frac{m}{d}\frac{1.89}{\pi r^2},$$

where $1.89 = Al_2O_3/2Al$ is the ratio of the molecular masses, m is the average value of the aluminum mass transferred to the solution during one etching cycle, d is

1063-7745/01/4602-0303$21.00 © 2001 MAIK "Nauka/Interperiodica"

Table 1. Corrosion resistance of a (0001) surface of a Kyropoulos-grown sapphire crystal treated by different methods

Type of treatment	Depth of the damaged layer, μm	Thickness *h*, μm of the layer removed for one etching cycle
Natural face	0	0.72
Polishing	1–5	0.77
Fine polishing	20–30	0.96
Crude polishing	>40	1.8

Table 2. Corrosion resistance of the supphire surface for different values of the dislocation density

Growth method	ρ, cm^{-2}	Plane	Surface treatment	*h*, μm
Verneuil	$(1–5) \times 10^5$	(0001)	Polishing	0.75
			Natural face	0.82
Kyropoulos	10^3	(0001)	Polishing	0.77
			Natural face	0.72
Horizontal directional crystallization	5×10^3	(0001)	Polishing	0.83
Stepanov	10^5	(0001)	Polishing	0.73
			Natural face	0.72
		$(10\bar{1}0)$	Polishing	0.29
			Natural face	0.23
		$(11\bar{2}0)$	Polishing	0.15
			Natural face	0.12

Table 3. Corrosion resistivity of a doped Verneuil-grown sapphire crystals

Crystal	Dopant concentration, wt %	Plane	*h*, μm
Al_2O_3	–	$(10\bar{1}0)$	0.25
	–	(0001)	0.80
Al_2O_3 : Cr	1×10^{-1}	$(10\bar{1}0)$	0.25
Al_2O_3 : Cr	6×10^{-1}	$(10\bar{1}0)$	0.20
Al_2O_3 : Cr	1.3	$(10\bar{1}0)$	0.12
	1.3	(0001)	0.80
Al_2O_3 : Ti	6×10^{-2}	$(10\bar{1}0)$	0.24
	6×10^{-2}	(0001)	0.80

the density of Al_2O_3 (3.98 g/cm^3), and *r* is the radius of the Al_2O_3 disk.

The relative standard deviation of thickness measurement (*h*) is 0.15.

RESULTS AND DISCUSSION

The rate of the chemical reaction is a function of the surface energy and the bond strength. It also depends on the degree of damage of the subsurface layer. The appropriate mechanical treatment can reduce the surface resistance to corrosion more than two times (Table 1) depending on the degree of the damage in the subsurface layer.

It is well known that dislocations emerging to the surface promote surface dissolution. However, in the range of the dislocation densities $\rho = 10^3–10^5$ cm^{-2} (characteristic of crystals grown by industrial methods), the difference in the dissolution of the same crystallographic plane with and without dislocations can hardly be distinguished (Table 2). Not only dislocations but also pores with diameters not exceeding 0.1 mm, which emerge on the surface, cannot produce noticeable effect on this corrosion resistance of the surface.

It seems that the impurity contribution cannot be the key factor either. A considerable increase of the chromium content only slightly increases the corrosion resistance of the $(10\bar{1}0)$ plane and but does not change at all the resistance of the (0001) plane (Table 3). Point defects in the form of anionic and cationic vacancies produce no noticeable effect on the corrosion resistance of the crystal surface either.

It is seen from the data listed in Tables 2 and 3 that the major contribution to the corrosion resistance of the surface comes from the crystallographic characteristics of this surface. Irrespective of the methods of growth and subsequent thermal treatment, the corrosion resistance of the (0001) plane ranged within 0.72–0.83, of the $(11\bar{2}0)$ plane, within 0.12–0.15, and of the $(10\bar{1}0)$ plane, within 0.12–0.29 μm.

The process of corrosion is caused by a number of surface phenomena. First, the atomic structure in the vicinity of a free surface depends on the surface relaxation (a decrease of the interatomic distances in the subsurface atomic nets) and reconstruction (the symmetry changes in the subsurface layers) characteristic of crystals with covalent bonding. These phenomena increase the surface energy proportionally to the reticular density of the crystallographic planes.

The approximate measure of the surface energy is a number of free bonds per unit surface. According to the estimates made in [5], the maximum number of such bonds is in the (0001) plane (6.6), the number of such bonds in the $(10\bar{1}0)$ plane is 5.2.

Thus, the minimum corrosion resistance shows the (0001) plane. The work function is minimal along the direction of the most densely packed row of atoms in the lattice, therefore, the most intense damage is observed in this plane [6].

The second cause of anomalously low corrosion resistance of the basal plane becomes clear from the consideration of the planar nets formed by the alumi-

num and oxygen atoms. In the (0001) plane, these nets are formed by the O–Al–Al–O–Al–Al–O atoms, whereas in the (1010) plane, by the Al–O–Al–O atoms. The {1010} nets are electrostatically neutral. In the (1120) plane, the alternating Al- and O-nets form slabs. The boundaries of these slabs are located between the planar nets of oxygen atoms.

Thus, the Al–Al nets are located only in the basal planes. The Al–Al bonds are weaker, both chemically and mechanically, than the Al–O bonds. Considering not only the surface bonds in the last layer but also the bonds in several previous layers of a semiinfinite lattice, Guo, Ellis, and Lam [7] established that the cleavage energy of the (0001) plane is minimal for the Al layer. The energy of the Al_2O_3 lattice is rather high (152 eV). The contribution of Al^{3+} ions to the total potential energy of the ions exceeds the contribution of O^{2-} ions, but the contribution of the van der Waals energy of O^{2-} (~1.3 eV) considerably exceeds the contribution from Al^{3+} ions (~0.1 eV) [8], which should enhance interaction of aluminum from the Al–Al nets with the enchant.

Thus, it has been established that the technological and crystallographic factors produce a certain effect on the corrosion resistance of the sapphire surface. The most pronounced of the technological factors is the type of the mechanical treatment of the crystals. Rough polishing reduces the corrosion resistance of the crystal surface by more than 50%.

The major effect on corrosion resistance is produced by crystallographic factors. The corrosion resistance of various crystallographic planes to aggressive media can differ by more than seven times. Such a considerable difference is explained by the specific features of the structure of the planar nets of atoms along different crystallographic directions and by the processes of surface reconstruction and relaxation.

REFERENCES

1. V. A. Timofeeva, *Crystal Growth from Flux* (Nauka, Moscow, 1978), p. 77.
2. A. B. Blank, O. P. Il'chenko, L. A. Litvinov, *et al.*, Zavod. Lab. **58**, 6 (1992).
3. V. S. Konevskiĭ, E. V. Krivonosov, and L. A. Litvinov, Izv. Akad. Nauk SSSR, Neorg. Mater. **25**, 1486 (1989).
4. É. S. Zolotovitskaya, V. G. Potapova, and T. V. Druzenko, Vysokochist. Veshchestva, No. 2, 202 (1990).
5. P. Hartman, Zap. Vses. Mineral. O–va **91**, 672 (1962).
6. G. Tamman and A. A. Botschwar, Z. Anorg. Allg. Chem. **146**, 420 (1925).
7. J. Guo, D. E. Ellis, and D. J. Lam, Phys. Rev. B **45**, 13647 (1992).
8. G. J. Dienes, D. O. Welch, C. R. Fisher, *et al.*, Phys. Rev. B **11**, 3060 (1975).

Translated by L. Man

Crystallography Reports, Vol. 46, No. 2, 2001, pp. 306–309. Translated from Kristallografiya, Vol. 46, No. 2, 2001, pp. 350–353.

CRYSTAL GROWTH

Growth of $R_2Me(SO_4)_2 \cdot 6H_2O$ Single Crystals with Due Regard for Solubility Diagrams of the R_2SO_4–$MeSO_4$–H_2O Systems (R = K, NH_4; Me = Ni, Co)

L. V. Soboleva and L. F. Kirpichnikova

Shubnikov Institute of Crystallography, Russian Academy of Sciences, Leninskiĭ pr. 59, Moscow, 117333 Russia

Received October 27, 1999

Abstract—The optimum conditions for growing $R_2Me(SO_4)_2 \cdot 6H_2O$ crystals are found from the analysis of the $R_2^+SO_4$–$Me^{2+}SO_4$–H_2O systems (R = K, NH_4; Me = Ni, Co) in the temperature range from 55 to 25°C. A new economical technology for growth of single crystals of double sulfate hexahydrates is developed, which allows the use of starting presynthesized solutions of hydrated or anhydrous K, Ni, Co, and (NH_4) sulfates. Transparent $K_2Ni(SO_4)_2 \cdot 6H_2O$, $K_2Co(SO_4)_2 \cdot 6H_2O$, and $(NH_4)_2Ni(SO_4)_2 \cdot 6H_2O$ crystals (35–55) × (25–40) × 10 mm in size are grown on seeds by the method of slow cooling. © *2001 MAIK "Nauka/Interperiodica".*

INTRODUCTION

As shown in [1], it is possible to search for new crystals with valuable physical properties among complex compounds of elements of groups I–III of the Periodic Table with organic, inorganic, and mixed ligands that can be crystallized in ternary aqueous systems.

A method of determining optimum conditions for growth of such crystals from the solubility diagrams of the "parent systems" has been developed.

As a result, a number of well-known and new practically important materials with valuable physical properties (ferroelectrics, ferroelastics, materials for nonlinear optics, acousto- and X-ray optics, etc.) were obtained in the form of large stoichiometric crystals of optical quality [1–4].

This study was undertaken in order to determine the optimum conditions for precipitation of the $R_2Me(SO_4)_2 \cdot 6H_2O$ phases (the so-called Tutton salts) from the analysis of the solubility diagrams for the R_2SO_4–$MeSO_4$–H_2O (R = K, NH_4; Me = Ni, Co) systems and to develop a procedure for growing large optically uniform single crystals. We also plan in the future to study the structure and the properties of the crystals grown.

Prior to the study, we found no information on growth of large crystals of these compounds.

ANALYSIS OF THE SOLUBILITY DIAGRAMS FOR THE R_2SO_4–$MeSO_4$–H_2O (R = K, NH_4; Me = Ni, Co) SYSTEMS

The solubility diagrams for the R_2SO_4–$MeSO_4$–H_2O systems have been studied in the temperature range from 0 to 100°C [5–9].

Figure 1 shows the phase equilibria A–B in the K_2SO_4–$NiSO_4$–H_2O system at 55°C [6], in the K_2SO_4–$Co(SO_4)$–H_2O system at 50°C [8], and in the $(NH_4)_2SO_4NiSO_4$–H_2O system at 46°C [6]. All the systems possess extended fields of crystallization of double sulfate hexahydrates $RMe(SO_4)_2 \cdot 6H_2O$. The A–B lines correspond to the equilibria between the solutions and stable (congruently dissolving) solid phases of the compositions $K_2Ni(SO_4)_2 \cdot 6H_2O$, $K_2Co(SO_4)_2 \cdot 6H_2O$, and $(NH_4)_2Ni(SO_4)_2 \cdot 6H_2O$. The indicated crystallization fields are crossed by singular H_2O–$R_2Me(SO_4)_2 \cdot 6H_2O$ secants.

Table 1 indicates the concentration ranges of the precipitation of the $K_2Me(SO_4)_2 \cdot 6H_2O$ phases at the indicated temperatures [5–9]. The coordinates of the invariant points A and B show that the potassium-containing compounds possess the crystallization fields of similar configurations, whereas the crystallization field of the ammonium-containing compound has different configuration and therefore should be grown from a solution characterized by a different ratio of the components.

Using data [1] and analyzing the solubility diagrams in Fig. 1, we find that the optimum composition of the solution for growth of a Tutton salt should correspond to point M. This point lies at the maximum distance from the invariant (eutonic) points A and B, where the double compounds coprecipitate with the constituent salts. Thus, the composition of the growth solution should correspond to the point lying in the central part of the solubility curve (point M in Fig. 1) of the complex compound at the maximum distance from points A and B (Figs. 1a and 1b). This is explained by the spe-

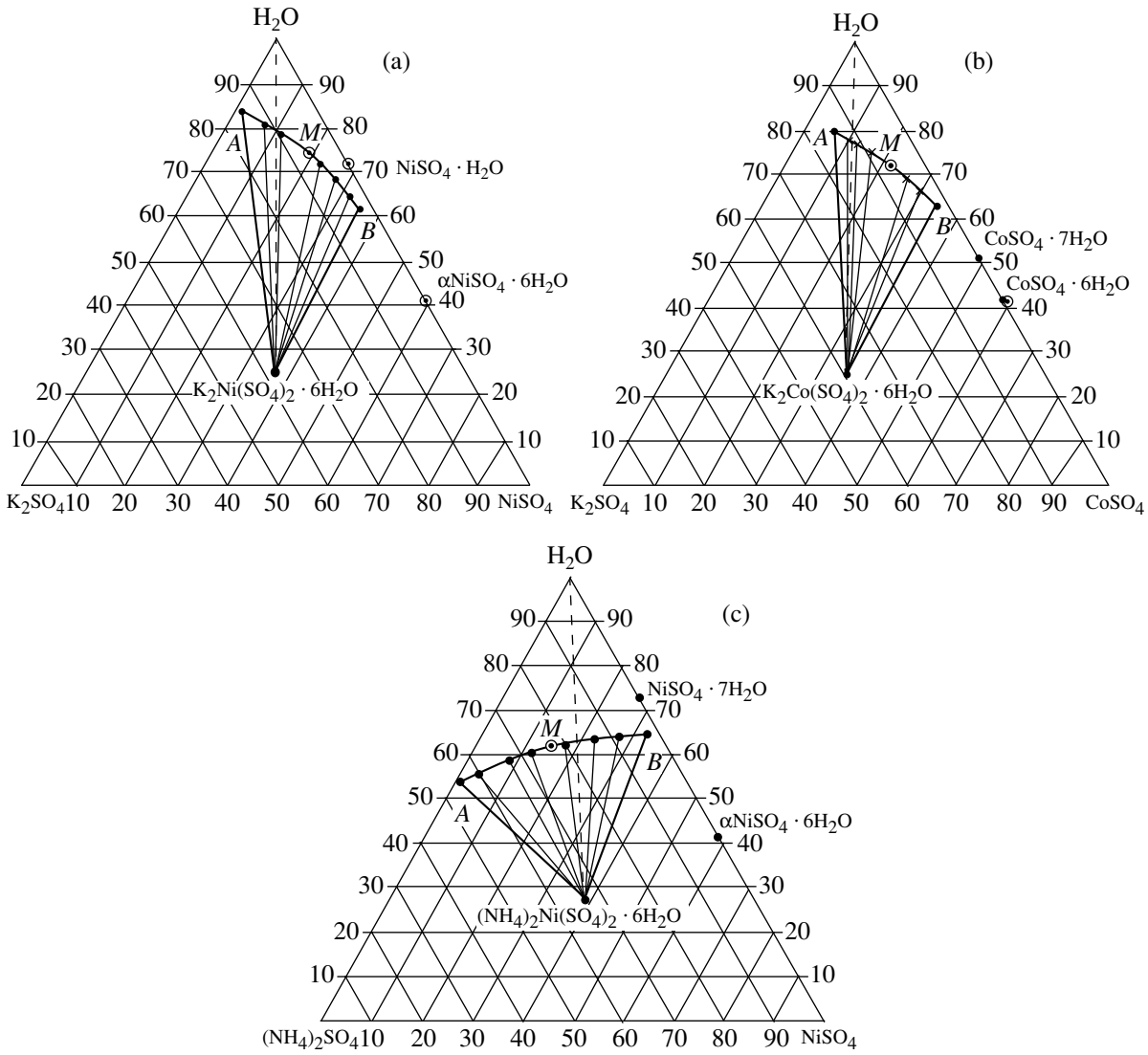

Fig. 1. Solubility diagrams of the (a) K_2SO_4–$NiSO_4$–H_2O system at 55°C, (b) K_2SO_4–$CoSO_4$–H_2O system at 50°C, and (c) $(NH_4)_2SO_4$–$NiSO_4$–H_2O system at 46°C. Concentrations are given in weight percent.

cific characteristics of nonvariant points (eutonics): the solutions with the compositions corresponding to these points provide the simultaneous crystallization of two solid phases—a complex chemical compound and the component of the system on the side either of point *A* or point *B*. The composition of the mother solution at the point *M* is determined from the compositions of noninvariant points *A* and *B* (limiting the solubility curve, within whose concentration limits the given solid phase is crystallized); this composition is the mean arithmetic of the component compositions at these points.

The concentration of the starting solution and the temperatures selected for growth of $K_2Ni(SO_4)_2 \cdot 6H_2O$, $K_2Co(SO_4)_2 \cdot 6H_2O$, and $(NH_4)_2Ni(SO_4)_2 \cdot 6H_2O$ crystals are indicated in Table 2. Since the compounds under study are characterized by extended crystallization fields and thus also extended solubility isotherms, the optimum concentrations of the starting solutions used for crystal growth only approximately correspond to points *M* and range within ~2 wt % on both sides of these points.

EXPERIMENT AND DISCUSSION OF RESULTS

Single crystals of $K_2Ni(SO_4)_2 \cdot 6H_2O$, $K_2Co(SO_4)_2 \cdot 6H_2O$, and $(NH_4)_2Ni(SO_4)_2 \cdot 6H_2O$ were grown from the solutions prepared from recrystallized K_2SO_4, $NiSO_4$, $CoSO_4$, and $(NH_4)_2SO_4$ hydrates and distilled water in the ratios given in Table 2.

The method for growing single crystals was the same for all the Tutton salts studied. We describe it using $K_2Ni(SO_4)_2 \cdot 6H_2O$ as an example. Small portions

Table 1. Coordinates of the invariant points at the boundaries of the crystallization fields of the $R_2^+ Me^{2+}(SO_4)_2 \cdot 6H_2O$ phases in the $R_2^+ SO_4$–$Me^{2+}SO_4$–H_2O (R = K, NH_4; Me = Ni, Co) systems

System	Solid phase	T, °C	Solution composition at the invariant point, wt %				References
			A		*B*		
K_2SO_4–$NiSO_4$–H_2O	$K_2Ni(SO_4)_2 \cdot 6H_2O$		K_2SO_4	$NiSO_4$	K_2SO_4	$NiSO_4$	
		25	8.26	0.33	11.60	27.90	[5]
		40	13.15	0.51	2.08	33.35	[6]
		55	14.76	1.20	2.30	35.00	[6]
K_2SO_4–$CoSO_4$–H_2O	$K_2Co(SO_4)_2 \cdot 6H_2O$		K_2SO_4	$CoSO_4$	K_2SO_4	$CoSO_4$	
		25	11.60	3.15	2.57	27.60	[7]
		38	13.31	4.70	3.80	31.00	[8]
		50	14.36	6.80	3.50	33.30	[8]
$(NH_4)_2SO_4$–$NiSO_4$–H_2O	$(NH_4)_2Ni(SO_4)_2 \cdot 6H_2O$		$(NH_4)_2SO_4$	$NiSO_4$	$(NH_4)_2SO_4$	$NiSO_4$	
		25	43.70	0.10	1.20	29.50	[9]
		46	45.32	0.29	1.94	32.95	[6]

Table 2. Optimum concentrations M of the starting solutions used for growth of $R_2^+ Me^{2+}(SO_4)_2 \cdot 6H_2O$ (R = K, NH_4; Me = Ni, Co) crystals by slow cooling from the initial temperatures T

Crystal	Initial crystallization conditions T, °C	Composition of the mother solution, M, wt %		
$K_2Ni(SO_4)_2 \cdot 6H_2O$		K_2SO_4	$NiSO_4$	H_2O
	25	9.93	15.60	79.59
	40	7.66	16.93	75.41
	55	8.53	18.10	73.37
$K_2Co(SO_4)_2 \cdot 6H_2O$		K_2SO_4	$NiSO_4$	H_2O
	25	7.08	13.75	81.15
	38	8.55	15.75	77.54
	50	8.93	20.05	70.57
$(NH_4)_2Ni(SO_4)_2 \cdot 6H_2O$		$(NH_4)_2SO_4$	$NiSO_4$	H_2O
	25	22.45	14.80	62.75
	46	23.63	16.62	59.75

of the K_2SO_4 and $NiSO_4$ aqueous solutions were mixed under permanent stirring at the temperature of ~60°C to yield the compositions given in Table 2. The reaction between the components proceeded according to the equation

$$K_2SO_4 + NiSO_4 + nH_2O \xrightarrow{60°C} K_2Ni(SO_4)_2 \cdot 6H_2O + (n-6)H_2O.$$

The resulting dark green solution was filtered and poured into a crystallizer with a Teflon platform with a seed crystal grown from solution of the same composition. The crystallizer was placed into a thermostated water bath of the temperature of ~57°C. Crystal growth was performed by slow cooling of the solution from 55 to 25°C within an accuracy of ±0.015°C. After the seed regeneration, a reversive stirring was switched on and the temperature was lowered first at the rate of 0.01°C/day and later, when the seed became faceted, at the rate of 0.02°C/day. A characteristic feature of $K_2Ni(SO_4)_2 \cdot 6H_2O$ growth consists in the change of the initial dark green color of the solution. Similar effects were observed earlier for some other solution-grown crystals. It is well known that structural units of aqua complexes of complicated chemical compounds in the solution have colors different from the color of crystals grown from this solution [4, 10].

Light blue $K_2Ni(SO_4)_2 \cdot 6H_2O$ single crystals 55 × 40 × 10 mm in size, $K_2Co(SO_4)_2 \cdot 6H_2O$ dark red single crystals 45 × 40 × 10 mm in size, and light blue $(NH_4)_2Ni(SO_4)_2 \cdot 6H_2O$ single crystals 35 × 25 × 10 mm

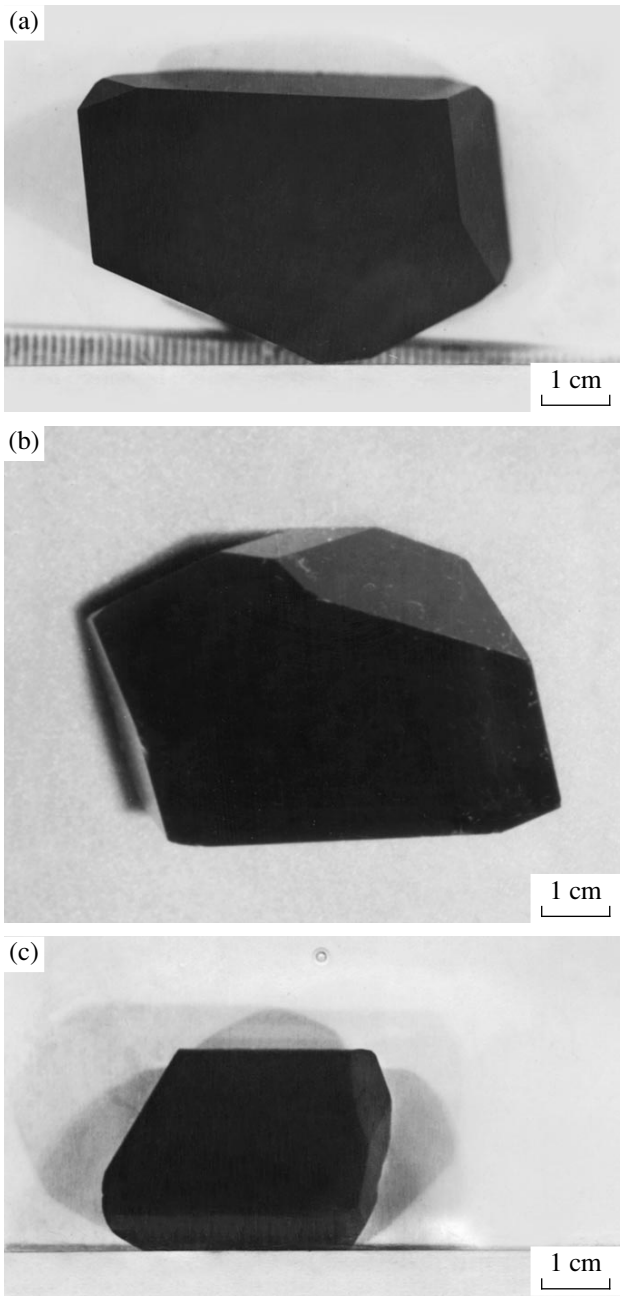

Fig. 2. (a) $K_2Ni(SO_4)_2 \cdot 6H_2O$, (b) $K_2Co(SO_4)_2 \cdot 6H_2O$, and (c) $(NH_4)_2NiSO_4 \cdot 6H_2O$ single crystals.

in size grown by the method described above are shown in Fig. 2. All the crystals were transparent.

The analysis of the solubility diagrams for determining the optimum conditions for growth of $K_2Me(SO_4)_2 \cdot 6H_2O$ crystals allowed us to avoid their synthesis and the experimental search for the concentration and temperature conditions of their crystallization and the use of the appropriate method of crystal growth. This approach allows one to grow crystals of complicated compounds by a simple and economic procedure with the use of their constituents as the solute components.

The solubility diagrams of the ternary K_2SO_4–$NiSO_4$–H_2O, K_2SO_4–$CoSO_4$–H_2O, and $(NH_4)_2SO_4$–$NiSO_4$–H_2O systems in the temperature range between 0 and 100°C were used for determination of the optimum solute concentrations and growth temperatures for $K_2Ni(SO_4)_2 \cdot 6H_2O$, $K_2Co(SO_4)_2 \cdot 6H_2O$, and $(NH_4)_2Ni(SO_4)_2 \cdot 6H_2O$.

A new economic method is suggested for growing sulfate hexahydrate crystals from the mixtures of aqueous solutions prepared from anhydrous K, Ni, Co, and NH_4 sulfates or their hydrates.

Large transparent single crystals of the indicated compounds were grown on seeds under the dynamic conditions.

ACKNOWLEDGMENTS

This study was supported by the Russian Foundation for Basic Research, project no. 97-02-16372a.

REFERENCES

1. L. V. Soboleva, Neorg. Mater. **31** (5), 614 (1995).
2. L. V. Soboleva, Neorg. Mater. **32** (28), 1007 (1996).
3. L. V. Soboleva and I. L. Smol'skiĭ, Kristallografiya **42** (4), 762 (1997) [Crystallogr. Rep. **42**, 700 (1997)].
4. L. V. Soboleva, E. B. Rudneva, and I. L. Smol'skiĭ, Kristallografiya **43** (4), 756 (1998) [Crystallogr. Rep. **43**, 706 (1998)].
5. R. M. Gaven and W. Johnston, J. Chem. Soc. **129** (10), 2628 (1926).
6. A. Benrath, Z. Anorg. Allg. Chem. **208** (2), 169 (1932).
7. R. M. Caven and W. Johnston, J. Chem. Soc. **3** (9), 2506 (1928).
8. A. Benrath and G. Ritter, J. Prakt. Chem. **154** (1), 40 (1939).
9. A. E. Hill and W. J. Taylor, J. Chem. Soc. **60** (4), 1099 (1938).
10. L. M. Belyaev, M. G. Vasil'eva, and L. V. Soboleva, Kristallografiya **25** (4), 871 (1980) [Sov. Phys. Crystallogr. **25**, 499 (1980)].

Translated by A. Mel'nikova

Crystallography Reports, Vol. 46, No. 2, 2001, pp. 310–311. Translated from Kristallografiya, Vol. 46, No. 2, 2001, pp. 354–355.

CRYSTAL GROWTH

Application of the Model of Locally Nonequilibrium Solidification to the Process of Structure Formation in Alloys Rapidly Quenched by Spinning[1]

P. K. Galenko, M. D. Krivilev, B. I. Lad'yanov, and M. V. Osetrov

Udmurt State University, Krasnoarmeĭskaya ul. 71, Izhevsk, 426034 Russia

e-mail: pkg@uni.udm.ru

Received May 19, 2000

Abstract—Solidification of a binary alloy rapidly quenched by spinning [1] has been studied by mathematical simulation. © *2001 MAIK "Nauka/Interperiodica".*

Earlier this problem was studied using the locally nonequilibrium approach [2]. Below, we consider nucleation and growth of cellular and dendritic crystals and establish the dependence of the ribbon structure on the initial supercooling and the spinning rate. The equations defining the model describe the following quantities [3]: mass transport in the bulk of the liquid phase and in the two-phase region; intensity of nucleation and growth rate of the solid phase; temperature distribution over the ribbon thickness; nonequilibrium impurity capture by the growth front advancing with a high velocity; and the slope of the kinetic liquidus line on the phase diagram of the binary alloy. The equation of mass transport is complemented with the term responsible for the diffusion-flow relaxation as was suggested in [2]. This term takes into account the deviations from the local equilibrium both at the solid–liquid interface and in the bulk of the solidifying alloy [4, 5]. The equations were solved by the finite-difference method on a square two-dimensional net.

Solidification of the Ni-based binary alloy with 0.186 wt % B was studied at the ribbon thickness ranging within 90–15 μm and the spinning rate ranging within 60–220 m/c. Two series of calculations were made: (1) calculation of crystallization depending on the initial melt supercooling and (2) determination of the structure parameters depending on the spinning rate of the ribbon and the stationary temperature gradient. It was established that the crystal structure consists of cells, dendrites, and a uniform structure having no cells with the morphologically smooth solidification front of growing structures. These structures are transformed into one another with the variation of the controlled quenching parameters—the spinning rate, the temperature gradient, and the initial supercooling of the melt. The results obtained lead to the following conclusions.

With an increase of the initial supercooling of the melt, ΔT_0, the columnlike continuously growing crystals give way to growth of equiaxial crystals. At $\Delta T_0 < 156$ K, the surface structure on the ribbon-disk side contacting the substrate is columnlike cellular–dendritic one. In the range $156 < \Delta T_0 < 165$ K, growth initiated on the surface and nucleation in the ribbon bulk are competing processes and, therefore, the unidirectional growth is changed to the isotropic growth. In the range of $165 < \Delta T_0 < 174$ K, the unidirectional growth is gradually suppressed, and growth of equiaxial crystals prevails. A further increase of supercooling, $\Delta T_0 \geq 174$ K, initiates explosive crystallization of the melt, avalanche-like nucleation, and superfast advance of the observed solidification front. The interphase boundary advances due to an intense nucleation at a rate that can attain the maximum possible values comparable with the sound velocity in the melt.

With an increase in the spinning rate, i.e., with an increase of the positive temperature gradient, the isotropic growth of equiaxial crystals is changed to unidirectional growth of columnlike crystals. This tendency in formation of zones with different structures in the spinned ribbons was also observed in full-scale experiments [1].

Modeling of the structure formed at the ribbon–disk and ribbon–air interfaces shows that the crystal structures on the ribbon surfaces are different. This is explained by the fact that the melt layer adjacent to the substrate solidifies under the positive temperature gradient, whereas the surface adjacent to the ribbon, under

[1] Available from VINITI, 2000, Izhevsk, no. 827-V00.

1063-7745/01/4602-0310$21.00

the negative temperature gradient. Different structures exist until the heat removal from the ribbon surface and the corresponding temperature drop across the ribbon thickness.

ACKNOWLEDGMENTS

This study was performed in the framework of the "Integration" Special Federal Program, project nos. KO418, KO422 and was supported by the Department of General and Professional Education of Russia, project no. 97-24-7.1-9.

REFERENCES

1. I. S. Miroshnichenko, *Quenching from Liquid State* (Metallurgiya, Moscow, 1982).
2. P. Galenko and S. Sobolev, Phys. Rev. E **55**, 343 (1997).
3. P. K. Galenko, M. D. Krivilev, V. I. Lad'yanov, and M. V. Osetrov, Available from VINITI (1999).
4. P. Galenko and D. A. Danilov, Phys. Lett. A **235**, 271 (1997).
5. P. Galenko and D. A. Danilov, J. Cryst. Growth **197**, 992 (1999).

Translated by A. Mel'nikova

Crystallography Reports, Vol. 46, No. 2, 2001, pp. 312–335. Translated from Kristallografiya, Vol. 46, No. 2, 2001, pp. 356–380.

PHYSICAL PROPERTIES OF CRYSTALS

Optical and Chiro-optical Properties of Crystals with Sillenite Structure

V. I. Burkov*, A. V. Egorysheva, and Yu. F. Kargin****

** Moscow Physicotechnical Institute, Institutskiĭ proezd 9, Dolgoprudnyĭ, Moscow oblast, 141700 Russia*

*** Kurnakov Institute of General and Inorganic Chemistry, Russian Academy of Sciences, Leninskiĭ pr. 31, Moscow, 117907 Russia*

Received June 21, 1999; in final form, January 13, 2000

Abstract—The experimental data on the optical and chiro-optical properties of crystals with the sillenite structure $Bi_{12}M_xO_{20\pm\delta}$ (M = elements of II–VIII groups) have been reviewed. The relations between the changes in the chemical composition, the crystal structure of $Bi_{12}M_xO_{20\pm\delta}$ compounds, absorption, circular dichroism, and optical rotation spectra of sillenites have been established. A model taking into account the contribution of the electronic transitions of optically active tetrahedral $[MO_4]^{n-}$ complexes to the total optical rotation in sillenites is suggested. The data on the state (oxidation degree) and the recharging processes of 3*d*-elements in sillenites are systematized. The models of optical centers responsible for the photochromic effect in sillenites are critically analyzed. *© 2001 MAIK "Nauka/Interperiodica".*

LIST OF CONTENTS

1. INTRODUCTION

Crystals of bismuth oxides with the sillenite structure described by the general formula $Bi_{12}M_xO_{20\pm\delta}$ (where M stands for the elements of II–VIII groups of the Periodic Table or their combinations) are widely used in various optoelectronic devices. The combination of the linear electrooptical effect with high photosensitivity allows one to use sillenites as active media in spatial light modulators. A discovery of high photorefractive sensitivity of $Bi_{12}M_xO_{20\pm\delta}$ crystals gave an impetus to the intense study of the nonlinear interaction of light waves in these materials (two-wave mixing at photorefractive gratings, conjugate wave-front generation, etc.) [1–4]. Sillenites are also promising materials for dynamical real-time interferometry, various devices for optical processing and storage of information, piezoelectric technology, acoustoelectronics and acoustooptics, and for solving other problems [1–6]. The optical and spectroscopic properties of sillenite crystals were intensely studied and the experimental results were summarized in a number of review articles and monographs [7–10]. However, some fundamental problems of electronic structure determining the optical properties of these crystals have been studied insufficiently. The nature of the centers responsible for the additional absorption observed in the vicinity of the fundamental absorption edge, the mechanism of the photochromic effect, and the dependence of these properties on the sillenite-type compounds of the composition $Bi_{12}M_xO_{20\pm\delta}$ and the type of the dopant still found no unambiguous interpretation. The positions of the *p*- and *d*-elements in the crystal lattice of sillenites have not been determined as yet. At the same time, in recent years, some new experimental data on the crystal structure and chiro-optical properties of $Bi_{12}M_xO_{20\pm\delta}$ crystals has been obtained which, in some instances, require the revision of the commonly used models suggested for the description of some physical processes in sillenites.

1063-7745/01/4602-0312$21.00 © 2001 MAIK "Nauka/Interperiodica"

The intense study of the physical properties of crystals with the sillenite structure was triggered still in the mid-1960s by the pioneering works performed on the Bi_2O_3–GeO_2, Bi_2O_3–TiO_2, Bi_2O_3–Fe_2O_3, and Bi_2O_3–SiO_2 systems [11–14]. The first large $Bi_{12}GeO_{20}$ crystals were grown in 1967 [15]. At the same time, $Bi_{12}TiO_{20}$ single crystals were grown at the Kurnakov Institute of General and Inorganic Chemistry of the USSR Academy of Sciences [16]. In the following years, numerous experiments on the growth of sillenite single crystals by the Czochralski (from flux) and the Stepanov methods (hydrothermal synthesis) and single crystal films by the liquid-phase epitaxy, gas-phase deposition (thermal, laser, and HF-sputtering), and chemical transport methods were reported (the list of the related publications can be found in [17]).

Most often, sillenite single crystals are grown either by the Czochralski method or are synthesized under hydrothermal conditions. It is these methods that were used to grow single crystals of the following sillenites: $Bi_{12}GeO_{20}$ (**BGO**), $Bi_{12}SiO_{20}$ (**BSO**), $Bi_{12}TiO_{20}$ (**BTO**), $Bi_{12}MnO_{20}$ (**BMnO**), $Bi_{24}MePO_{40}$ (*Me* = Al, Ga, Fe), $Bi_{12}PO_{20\pm\delta}$ (**BPO**), $Bi_{12}VO_{20\pm\delta}$ (**BVO**), $Bi_{25}FeO_{39}$ (**BFeO**), $Bi_{25}GaO_{39}$ (**BGaO**), $Bi_{25}TlO_{39}$ (**BTlO**), $Bi_{24}B_2O_{39}$ (**BBO**), $Bi_{25}AlO_{39}$ (**BAlO**), $Bi_{38}ZnO_{58}$ (**BZnO**), $Bi_{38}CoO_{58}$ (**BCoO**), $Bi_{12}Cr_xO_{20\pm\delta}$ (**BCrO**), and also BSO-, BGO-, and BTO-based solid solutions.

In this review, we made an attempt to generalize the information on the spectroscopic properties of sillenites obtained for the last ten–fifteen years and to consider these data together with the structural characteristics of various sillenites.

2. CRYSTAL AND ATOMIC STRUCTURE OF $Bi_{12}M_xO_{20\pm\delta}$ COMPOUNDS (*M* ARE THE ELEMENTS OF GROUPS II–VIII)

Sillenites are named after Swedish crystal chemist L.G. Sillen, who studied polymorphism of bismuth (III) oxide and was the first to establish the existence of the metastable cubic body-centered γ-Bi_2O_3 modification [18]. Thus, a rare mineral of this composition and the phases synthesized in the Bi_2O_3–M_xO_y systems (where *M* stands for the elements of groups I–VIII of the Periodic Table) isostructural to γ-Bi_2O_3 were given the name sillenites.

The experimental data on the interaction of the components and the phase equilibria in the Bi_2O_3–M_xO_y systems (where *M* are the elements of groups I–VIII of the Periodic System) indicate the possible formation of various phases with the sillenite-type structures of the composition $Bi_{12}M_xO_{20\pm\delta}$ due to interaction with the Rb, Mg, Zn, Cd, B, Al, Ga, In, Tl, Si, Ge, Ti, Pb, P, V, As, Nb, Cr, Mo, W, Mn, Fe, Co, Ni, Ru, and Ir oxides. Depending on the chemical nature of an *M* atom, these phases can be either stable or metastable compounds or else γ-Bi_2O_3-based solid solutions [17]. No phases with the sillenite structure have ever been observed in systems not containing bismuth oxide.

The first sillenite-type structure was determined by Abrahams *et al*. for bismuth germanate [19]. Later, the X-ray diffraction refinement of the absolute atomic configurations in bismuth germanate and bismuth silicate [20, 21] and, somewhat later, also bismuth titanate [22] showed isostructurality of these compounds. The crystals described by the general formula $Bi_{12}MO_{20}$ (*M* = elements of groups II–VIII) are cubic and have the pentagontritetrahedral symmetry described by the sp. gr. *I*23. The coordinates of the equivalent atomic positions and their point symmetry in the sp. gr. *I*23 are indicated in [23].

The unit cell of $Bi_{12}MO_{20}$ contains two formula units and is a cube, whose center and vertices are occupied by Ge atoms tetrahedrally coordinated with oxygen (Fig. 1a). The coordination of a Bi atom in the 24-fold position (24*f*) includes seven oxygen atoms [19]. Oxygen atoms O(2) and O(3) are located in the eightfold 8*c* positions on the threefold axes, whereas the O(1) atoms are statistically distributed over the 24-fold position The *M* cations are located in the twofold crystallographic position 2*a* with the point symmetry 23. The occupancy of the 2*a* position by Ge and Si atoms is described as q(Ge) = 0.87(2) and q(Si) = 0.87(8) [19–21].

The structural models for Fe-, Zn-, Cd-, Mg-, Ni-, and Co-containing sillenites were suggested under the assumption that the oxygen sublattice of $Bi_{12}M_xO_{20}$ has no defects and that the electrical neutrality of the unit cell is maintained due to oxidation of bismuth atoms in the 2*a* position to the state Bi^{5+} [24–26]. However, the presence of Bi^{5+} in the sillenite compounds contradicts the experimental data on the phase equilibria in the Bi_2O_3–M_xO_y systems and the chemical-analysis data on the $Bi_{12}M_xO_{20\pm\delta}$ crystals [17]. The fact of formation of the sillenite phases with the component ratios 25 : 1 ($Bi_{25}MO_{40}$) and 12 : 1 ($Bi_{24}M_2O_{41}$) in the Bi_2O_3–M_2O_5 systems (*M* = P, V) indicates possible rotation of Bi^{3+} ions in the tetrahedral positions or location of additional oxygen atoms in the unit cell, respectively. It should also be indicated that the structural formula of the metastable γ-Bi_2O_3 ($Bi_{24}Bi^{3+}Bi^{5+}O_{40}$) phase suggested in [24] also allows location of Bi^{3+} ions in the tetrahedral positions in the sillenite-type unit cell.

The neutron diffraction analysis of $Bi_{12}M_xO_{20\pm\delta}$ single crystals with different types of *M* cations in $Bi_{12}Ti_{0.9}O_{19.8}$, $Bi_{12}GeO_{20}$, $Bi_{25}GaO_{39}$, $Bi_{12}(V, Bi)O_{20+x}$, $Bi_{12}(Fe, P)O_{20}$, $Bi_{25}FeO_{39}$, and $Bi_{38}ZnO_{58}$ partly summarized in [27] were then generalized in [28] and later complemented with the neutron diffraction data for $Bi_{25}TlO_{39}$ crystals [29] and X-ray diffraction data for $Bi_{12}MnO_{20}$ [30] and $Bi_{38}CoO_{58}$ [31] single crystals.

Atomic structure of $Bi_{12}MO_{20}$ (*M* = Si, Ge, Ti, and Mn) compounds. The M^{4+} cations (Ge, Si) in the unit

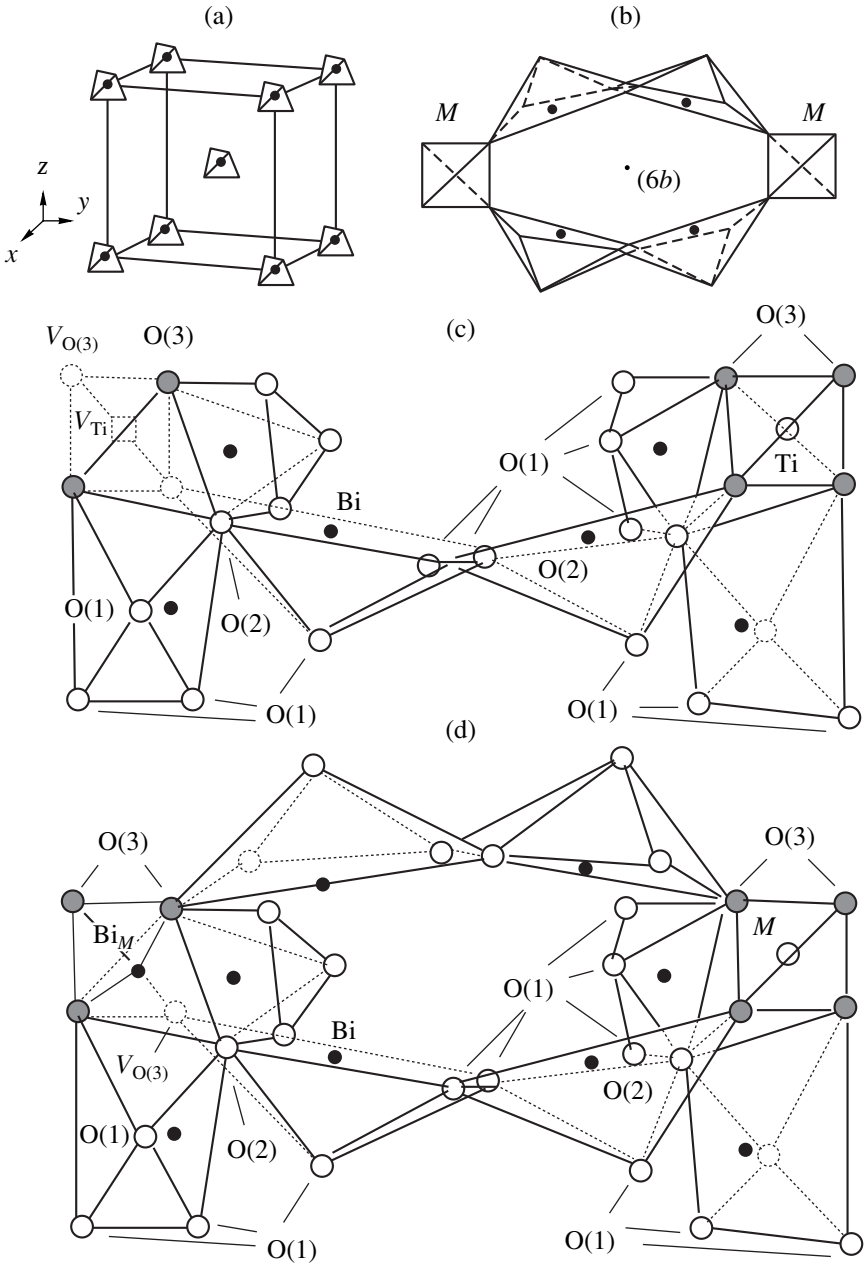

Fig. 1. (a) Unit cell of $Bi_{12}M_xO_{20\pm\delta}$; (b) edge-sharing $[BiO_5]$-polyhedra forming $[Bi_2O_8]$-dimers, which connect by translation the identical $[MO_4]$-tetrahedra; (c) the fragment of the $Bi_{12}Ti_{0.9}O_{19.8}$ structure; and (d) the common fragment of the $Bi_{25}M^{3+}O_{39}$ and $Bi_{38}M^{2+}O_{58}$ structures with an oxygen vacancy $V_{O(3)}$.

cell of ideal compounds with the sillenite structure are located in two tetrahedral voids of the framework consisting of edge-sharing $[BiO_5E]$-polyhedra (where E denotes the lone pair of bismuth electrons) and thus form dimers [27, 28, 30] (Fig. 1). Unlike the data in [19–21], the occupancy of positions 2*a* with Ge atoms according to [27, 28] is q(Ge) = 1.00(3) and q(O(3)) = 1.00(3). For bismuth titanate, the occupancies are q(Ti) = 0.90(8) and q(O(3)) = 0.95(1). Since the radius of Ti^{4+} exceeds by 0.015 nm the optimum radius of Ge^{4+} in an ideal sillenite structure, the local stresses are relaxed because the formation of Ti vacancies (about 10% of the total number of M positions). The formation of each titanium vacancy is accompanied by the formation of two oxygen vacancies in the position O(3). Therefore, the $[BiO_5E]$ polyhedra lose the common vertex O(3) and are rearranged into trigonal $[BiO_4E]$ bipyramids with a lone electron pair of a bismuth atom in the equatorial plane (Fig. 1).

Atomic structure of $Bi_{12}(A^{3+}_{1/2}B^{5+}_{1/2})O_{20}$ compounds (A^{3+} = B, Al, Ga, In, Tl, Fe, Co, Mn and B^{5+} = P, V, As). The unit cells of compounds with different cations located in the tetrahedral positions, e.g., $Bi_{24}FePO_{40}$, are characterized by varying Bi–O(3) distances in the $[BiO_5]$ polyhedra corresponding to the varying *M*–O(3) distance in the $[MO_4]^{n-}$-tetrahedron. The ratio of the A^{3+} and B^{5+} cations does not correspond to the equiprobable filling of the tetrahedral positions, and the compensation of the local stresses (caused by a considerable difference in the Fe^{3+} and P^{5+} sizes) proceeds at the expense of the vacancies in the *M* positions. In other words, the composition of the compound can be written as $Bi_{24}(Fe_{0.35}P_{0.59}\square_{0.06})O_{40}$ (where □ denotes a vacancy).

Atomic structure of the $Bi_{38}M^{2+}O_{58}$, $Bi_{25}M^{3+}O_{39}$ (M^{2+} = Zn, Co and M^{3+} = Al, Ga, Fe, Tl), $Bi_{24}B_2O_{39}$, and γ-Bi_2O_3 compounds. In the unit cells of these compounds containing cations in oxidation degree +3 or +2 ($Bi_{25}M^{3+}O_{39}$, where M^{3+} = Al, Ga, Fe, Tl; $Bi_{38}M^{2+}O_{58}$, where M^{2+} = Zn, Co), one-half or two-thirds of regular $[MO_4]$-tetrahedra are substituted by umbrella-like $[BiO_3E]$-groups (Fig. 1) with the simultaneous formation of O(3) vacancy. The stoichiometric formulas of the compounds are $Bi_{12}(Bi^{3+}_{0.50}M^{3+}_{0.50})O_{19.50}$ and $Bi_{12}(Bi^{3+}_{0.67}M^{2+}_{0.33})O_{20}$. The characteristic feature of $Bi_{24}B_2O_{39}$ is that the Bi : B = 12 : 1 ratio corresponds to complete filling of the position 2*a* with boron atoms. The presence of absorption bands corresponding to the asymmetric valence ν_3 and deformation ν_2 vibrations of triangular $[BO_3]$-groups in the IR spectra of $Bi_{24}B_2O_{39}$, $Bi_{24}BPO_{40}$, and $Bi_{24}BVO_{40}$ indicates the trigonal coordination of boron with oxygen [32].

The structure model of the metastable γ-Bi_2O_3 was suggested on the basis of the neutron diffraction data [28]. The occupancy of the tetrahedral positions with $[BiO_3E]$-groups in this model equals 80%, whereas the remaining 20% of the 2*a* position are vacant.

Atomic structure of Bi_{12}(Bi, V)$O_{20+\delta}$. The excessive charge of the tetrahedral M^{5+} cation in the unit cell of $Bi_{12}M_xO_{20\pm\delta}$ with the cations in the oxidation degrees +5 (P, V) is compensated with an additional O(4) anion located in large voids of the framework in the position 6*b*. The average Bi–O(3) distance in the bismuth–oxygen polyhedron (2.742 Å) considerably exceeds the Bi–O(4) distance (2.5833(5) Å), which results in the redistribution of the valence strengths of four bismuth atoms bonded to O(4). Since the Bi–O(3) distance considerably exceeds the average value, it is assumed that the Bi atoms is not bonded to O(3) and that the O(4) oxygen provides the formation of triangular O(1*b*)–O(1*c*)–O(4) faces shared by pairs of 9% of $[BiO_5E]$ polyhedra.

Thus, the existence of a wide range of isomorphous compounds with the sillenite structure is provided by the possible variations in the bismuth–oxygen sublattice. The changes in the size and the oxidation degree of M^{n+}-cations in the tetrahedral 2*a* positions result in the formation of O(3)-vacancies in the position 8*c* or the location of an additional O(4) oxygen in the position 6*b*, which gives rise to the mutual displacements of Bi and O atoms and the change in the location of the bismuth lone-pair with the formation of new coordination $[BiO_x]$ polyhedra in the distorted anion sublattice. The existence range of the stable phases with the sillenite structure corresponds to the variation in the oxidation degree of M^{n+} cation within $+2 \le n \le +5$ (at $n = +1$ or $n \le +6$, these compounds cannot exist at all) and is provided by the destruction of the framework of $[Bi_2O_8]$-dimers with the change of the oxygen nonstoichiometry in $Bi_{12}M^{n+}_xO_{20\pm\delta}$ because of the change in *n* [17].

It is seen from the description of the $Bi_{12}M_xO_{20\pm\delta}$ structure that with the change of the compound composition (i.e., the type and the oxidation degree of the M^{n+}-cation upon the heterovalent substitution), the number of atoms in the unit cell also changes. These changes should manifest themselves in the fundamental optical and chiro-optical characteristics of the crystals such as the reflection spectra, refractive-index dispersion, and optical rotation. At the same time, sillenites are also characterized by the existence of only one type of defects in the crystal lattice, e.g., the vacancies of *M*-atoms in the centers of $[MO_4]^{n-}$-tetrahedra, vacancies of O(3)-atoms, or the incorporated O(4)-atoms. It is commonly believed that these defects provide the additional absorption in the vicinity of the fundamental absorption edge and the photochromic effect. In light of new information on the sillenite structure, the model description of these phenomena [7] seems to be insufficiently substantiated. In this study, we make an attempt to consider the influence of the specific features of the atomic structure of $Bi_{12}M_xO_{20\pm\delta}$ compound on the optical and spectroscopic characteristics and to describe in detail the influence of various defects on the additional absorption in the vicinity of the absorption edge, the circular dichroism (CD) spectra, and the photochromic effect.

3. ELECTRONIC STRUCTURE OF COMPOUNDS WITH SILLENITE STRUCTURE

3.1. Reflection Spectra

In fact, reflection spectra are the only source of information about the electronic structure of sillenite crystals. The diffuse [33] and specular-reflection [34–39] spectra of BGO, BSO, BTO, and BFeO crystals have been studied in sufficient detail. The use of the Kramers–Kronig relationships allowed the calculation of the real and the imaginary parts of the dielectric con-

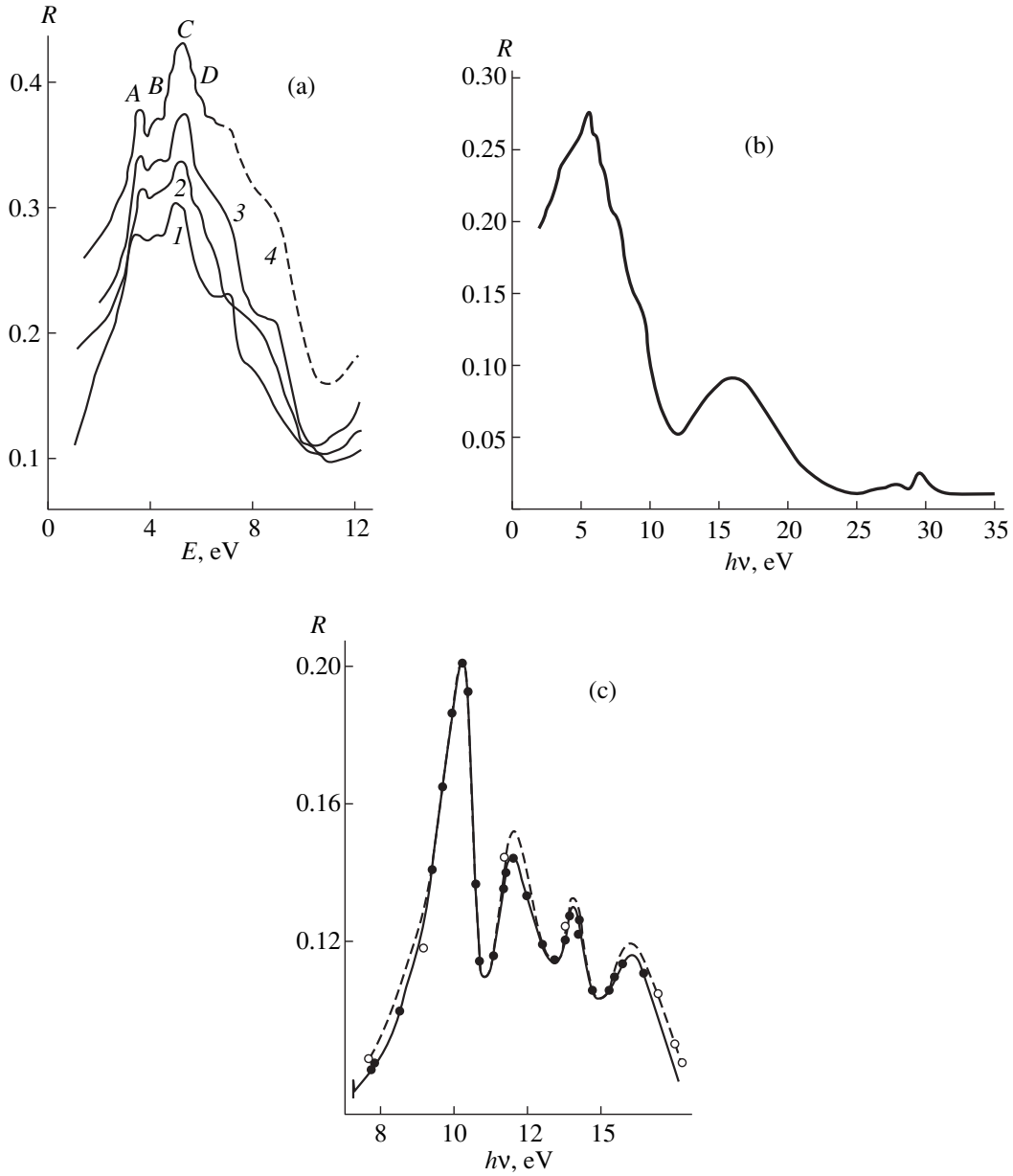

Fig. 2. (a) Reflection spectra of (*1*) BFeO, (*2*) BGO, (*3*) BSO, and (*4*) BTO crystals; (b) reflection spectra of BSO crystals; and (c) reflection spectra of quartz obtained at 300 K [34, 38, 45].

stant of crystals as well as some other characteristic parameters of the electronic structure of sillenites.

The BSO and BGO spectra [34, 35] obtained over a wide spectral range (2–35 eV) clearly show two bands (Fig. 2). The center of gravity of the first band is located in the vicinity of 5 eV, whereas that of the second one, in the vicinity of 15 eV. These bands have fine structure well seen at a low temperature (T = 130 K) [40].

In the energy range 2–10 eV (i.e., in the vicinity of the first band), the reflection spectra of all the sillenites are almost the same. The long-wavelength side of the band contour has a rather sharp maximum (*A*) at $E \approx$ 3.65 eV ($\lambda \approx 0.340$ μm), which is characteristic of the reflection spectra of all the sillenites. At the same time, the reflection spectra also show some distinctive features. Thus, the maximum of the fine structure of the first band in the BFeO spectrum is displaced by 0.1–0.3 eV to the long-wavelength range [38], and the relative intensity of the maximum *A* is much lower. At the short-wavelength of this band, the structure is more pronounced in comparison with the structures of the other sillenite spectra [38]. The reflection spectrum of BFeO different from the spectra of other sillenites indicates the participation of a tetrahedral [FeO_4]-complex in the formation of the spectrum of electronic transitions with a charge transfer, which, according to differ-

ent estimates, occurs in the vicinity of $\lambda < 0.37$ μm ($\nu > 27000$ cm^{-1}, $E > 3.35$ eV) [41].

This fact shows that the orbitals of the tetrahedral [FeO_4]-complex affect, although slightly, the electronic band structure of BFeO. Unfortunately, there are no published data on the reflection spectra of BFeO in vacuum ultraviolet, where these differences are expected to be more pronounced.

An attempt to interpret the reflection spectra of sillenites was made in [40]. Using the obvious correlations between the BGO and the rhombohedral Bi_2S_3 [42] (an $A_2^{V}B_3^{VI}$ semiconductor) structures, Futro [40] managed to interpret the fine structure of the BGO spectrum. Kityk *et al.* [43] used the method of local pseudopotential to calculate the structure of the valence and conduction bands in BGO and BSO crystals. In turn, these calculations provided the determination of the reflection spectrum, which coincides with the experimentally measured spectrum of $Bi_4Ge_3O_{12}$ orthogermanate [57] but does not coincide with the BGO and BSO spectra [34–39, 44].

Thus, the recent results do not provide a reliable interpretation of the reflection spectra and, thus, of the electronic structure (the conduction and valence bands) in the sillenite crystals. In this connection, we should like to consider here the conclusions drawn from the comparison of the reflection spectra of various sillenites (especially, of BGO and BSO) with the well-known reflection spectrum of the crystalline quartz [45, 46] (Fig. 2) and the absorption spectra of Te [47–49], Se [50, 51], and $CdAs_2$ [52]. The long-wavelength edge of the reflection spectrum of quartz and the fundamental absorption of Te, Se, and $CdAs_2$ have sharp maxima, whose formation is associated with the excitation of a Wannier–Mott exciton. We cannot exclude the probability that the first fine-structure maximum (*A*) of the reflection spectra is also associated with an exciton formation. The second band of the BSO reflection spectrum is formed in a shorter wavelength range (11.2–17.2 eV), i.e., in the range of the maximum reflection of quartz [45]. The positions of this band on the energy scale in the BSO and BGO reflection spectra coincide [34, 35]. This coincidence becomes dear from the comparison of almost identical reflection spectra of quartz and GeO_2 [53, 54].

Similar forms of the first band (3–10 eV) in the studied reflection spectra of sillenites and the diffusion-reflection spectrum of bismuth oxide [33] show that this band is caused by the electronic transitions to the excited states, which are usually the *p*-orbitals of Bi^{3+}-ions and, partly, the orbitals of oxygen atoms [55, 56]. Thus, the reflection spectra of sillenites are associated with electronic excitation of two weakly interacting chromophores—the bismuth–oxygen [BiO_x]$^{n-}$-polyhedra and [MO_4]$^{n-}$-tetrahedra. The model of weakly interacting chromophores is often used for calculating electronic structure of multiatomic complexes and complex oxides. In particular, the model of non-interacting structural motifs was used for calculating the electronic structure of bismuth orthogermanate, $Bi_4Ge_3O_{12}$ [55–57].

3.2. Optical Activity of Sillenites

The symmetry of the unit cells of sillenite crystals shows that they are gyrotropic. As is well known, gyrotropy manifests itself via optical rotation (OR) and circular dichroism (CD) [58]. Prior to the consideration and analysis of experimentally measured chiro-optical characteristics of sillenite crystals, consider the role of chromophores in the optical activity by analyzing the crystal structures. Here, we use an approach stated in [59] in application to the cubic crystals [60].

The analysis of the the most perfect bismuth germanate structure shows that it has two chromophores which, in principle, can determine the chiro-optical properties of sillenite-type crystals. One of these chromophores is an asymmetric [BiO_5]-polyhedron of the symmetry C_1, whereas the second one, the [GeO_4]-group of symmetry *T*. As earlier, we assume that these chromophores only weakly interact with one another.

The electronic states of the first chromophore are nondegenerate, and, therefore, the symmetry allows any electronic transition in an electric, magnetic-dipole, and electric-quadrupole approximations, as well as in higher order multipole approximations. Therefore, any transition is active in both absorption and CD spectra (or makes a contribution to the optical rotation). In this case, the tensor of the rotation force of any electronic transition can be described as

$$R = R_M + R_Q, \tag{1}$$

where the tensor R_M takes into account the contribution of the ($\langle p\rangle\langle m\rangle$)-mode, whereas the tensor R_Q, the contribution of the ($\langle p\rangle\langle q\rangle$)-mode; $\langle p\rangle$, $\langle m\rangle$, and $\langle q\rangle$ are the matrix elements of the electric, magnetic, and electric quadrupole moments of the *i*–*j* transition. To obtain the formula for the rotation-force tensor for a crystal of symmetry *T* built by molecular aggregates of symmetry C_1, one has to average *R* with due regard for the symmetry operations of the group *T*. This averaging can be performed by the method of projective operator [61]. As a result, we obtain that the contribution of the $\langle p\rangle\langle q\rangle$ mode is zero, and that the circular dichroism in any electronic transition is determined by a pseudoscalar quantity. In other words, the force of the unit-cell rotation per one molecule equals

$$R = 1/3(\langle p\rangle\langle m\rangle). \tag{2}$$

For the second chromophore (considered as an isolated molecule of symmetry *T*), the situation is somewhat different. The wave functions of the states of such a molecule are transformed either by one-dimensional irreducible representations of *A* (ε and ε*) or the three-dimensional irreducible representation of *T*. In this

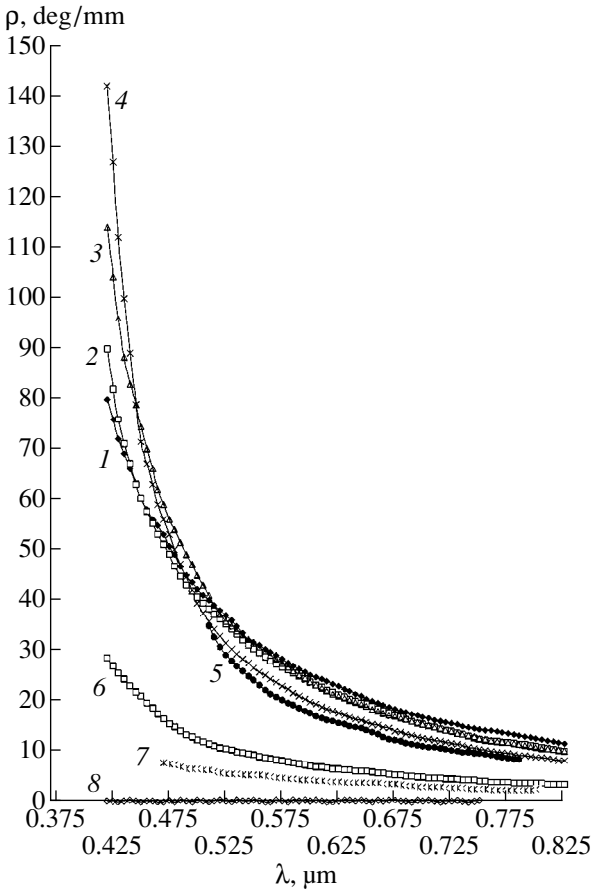

Fig. 3. Optical rotatory dispersion (ORD) spectra of $Bi_{12}M_xO_{20\pm\delta}$ single crystals with the sillenite structure: (*1*) $Bi_{12}SiO_{20}$, (*2*) $Bi_{12}GeO_{20}$, (*3*) $Bi_{25}GaO_{39}$, (*4*) $Bi_{38}ZnO_{58}$, (*5*) $Bi_{25}TlO_{39}$, (*6*) $Bi_{12}TiO_{20}$, (*7*) $Bi_{24}FePO_{40}$, and (*8*) $Bi_{12}VO_{20+\delta}$ [17].

case, only the *A*–*T* transitions are allowed in the electric- and magnetic-dipole approximations and the electric-quadrupole approximation. Thus, the tensor R'_M has a nonzero value and at the same time the tensor R'_Q also has the nonzero value. Averaging $R' = R'_M + R'_Q$ over the operation of the group *T*, we arrive at the result similar to that obtained in the first case, i.e., $R'_Q = 0$, whereas $R' = R'_M = 1/3(\langle p'\rangle\langle m'\rangle)$.

Since we assumed that the two types of chromophores in the unit cell interact weakly with one another, the signs of *R* and *R*' are determined by the concrete electron transitions of the chromophores and can be arbitrary. The corresponding contributions to the total optical rotation can either be summed up or be subtracted from one another.

The presence of the characteristic defects in the crystal lattices of sillenites (e.g., the oxygen vacancy O(3) at the vertex of the $[MO_4]$-tetrahedron lowers the local symmetry of the *M* position. Therefore, the $[MO_3\square]$-groups (where □ is an oxygen vacancy) can be considered as a new set of chromophores. Undoubtedly, these conclusions are also valid for bismuth–oxygen polyhedra, three different types of which are characteristic of the sillenite structures, e.g., of BGaO and BFeO. Of course, all considerations of the rotation-force tensor of a crystal with defects are analogous to the those above.

In connection with the above stated, the conclusions based on the assumption about the T_d symmetry of $[MO_4]$-tetrahedra made in the studies of crystal gyrotropy are erroneous, because they contradict the information about the point symmetry of the position 2*a* occupied by *M*-atoms in the sillenite structure or the well-known statement (see, e.g., [62]) that the symmetry of the unit-cell positions cannot be higher than that of the point group of this unit cell.

3.3. Optical Rotatory Dispersion

The optical rotation and optical rotatory dispersion (ORD) were first measured in [63]. However, the data measured in the range of 0.4–0.55 μm turned out to be erroneous. The correct ORD data for the BSO, BGO, BTO, BGaO, and BZnO crystals were obtained in [16, 33, 58, 64–66]; for BFeO, in [67]. These data uniquely indicate that the electronic transitions localized at $[BiO_x]$ structural fragments provide the contribution to optical rotation. Later [68], it was assumed that electronic transition of $[MO_4]^{n-}$-tetrahedral complexes also make a contribution to the optical rotatory dispersion. This fact was confirmed by the studies of circular dichroism and optical rotary dispersion of doped BSO, BGO, and BTO crystals. Optical rotation and rotary dispersion in BTlO, BFePO, and BVO crystals (Fig. 3) and the corresponding characteristics of the well-known sillenite crystals are cited in this article as reference material.

In some studies, the attempts were made to interpret the experimental ORD data in terms of coupled oscillators [69], which are widely used in the interpretation of the optical activity of crystals [70]. However, all the attempts to apply this model to smooth ORD curves (by approximating the experimental curves by the corresponding "theoretical" formulas) yielded no information on the chromophore type, rotation force, and the position of the electron transitions providing certain contributions to the rotation on the scale of electron transitions [58]. Moreover, it was shown [58, 71] that the approximation of smooth ORD curves by one-term, two-term, etc., polynomials based on various theories and models can be considered only as a convenient empirical dependence. Even the approximation by two-term formulas, which is in fact a multiparameteric problem, has an ambiguous solution within the accuracy of the measurement of the rotation-angle of the polarization plane. As a result, all the conclusions on

the gyrotropy nature, irrespective of the approximation used, have no sense [58].

The experimental data show that the rotation values for the BGO, BSO, BGaO, and BZnO crystals are approximately the same, whereas the rotation values for BFeO and BTO are considerably less within the whole transparency range (Fig. 3). Since the concentrations of $[BiO_x]$-polyhedra are almost the same in all crystals, the lower value of optical rotation indicates that it depends on two chromophores—chains of bismuth polyhedra and tetrahedra. The study of the optical rotation of vanadium- and phosphorus-doped BTO crystals [72–74] provided the direct proof of an essential role of tetrahedral fragments of the structure in the optical rotation in sillenites. Figure 4 schematically illustrates the effect of electronic transitions in $[MO_4]^{n-}$ on optical rotation in sillenites [72]. In particular, in the case of $[VO_4]^{3-}$, the $1t_1-2e$ transition with the charge transfer occurs in the vicinity of the frequency $\nu \approx 36200$ cm^{-1} ($E = 4.5$ eV [75]), which results in considerable reduction of optical rotation in vanadium-doped BTO crystals. Our studies of optical rotation in hydrothermally grown $Bi_{12}VO_{20+\delta}$ single crystals showed the absence of optical rotation in the range 0.50–0.90 μm [73]. In terms of the above schematic, the absence of optical rotation in the whole transparency range seems to be associated with the fact that the energy of the $1t_1-2e$ transition in the $[VO_4]^{3-}$-complex equals the energy of the s^2-sp transition Bi^{3+} in the $[BiO_5]$-polyhedron and that the rotation forces R_{ij} of these transitions are also almost equal. Moreover, it should be taken into account that the oxygen atoms O(4) in $Bi_{12}VO_{20+\delta}$ form triangular faces shared by pairs of $[BiO_5E]$-polyhedra.

Thus, it is possible to conclude that the optical rotary and refractive-index dispersions are determined by the electron excitation of $[BiO_x]$ polyhedral and the $[MO_4]^{n-}$ tetrahedral fragments of the structure. Undoubtedly, weak electron transitions associated with the excitation of the vacancy and dopant states, also give certain contributions to the optical rotation, but these contributions are insignificant. The estimates by the well-known relationships show that at a sufficiently high $\Delta\varepsilon C \approx 1$ value, the anomaly in optical rotation is as low as $\Delta\varphi \approx 0.4°$. Indeed, these anomalies are clearly seen on the ORD curve of a BFeO crystal [76], but they are insignificant in comparison with the total contribution of electronic transitions in $[BiO_x]$-polyhedra and $[MO_4]^{n-}$-tetrahedra to the optical rotation. It is not surprising either that, in most occasions, the ORD curves of doped and nominally undoped crystals are practically the same. The ORD data for cobalt- [77] and nickel-doped [78] BTO and BSO crystals showed that the optical rotation in these crystals is almost the same as the optical rotation in undoped crystals, although, knowing the position of the transition occurring with the charge transfer in CoS_4 and the $[NiO_4]^{6-}$ -complexes ($\nu \sim 28000$ cm^{-1} [41]), one could expect a considerable effect of the optical rotation in the visible spectrum range. However, the low cobalt and nickel concentrations (<0.0025 wt %) in BTO and BSO crystals did not allow one to reveal this effect within the experimental accuracy.

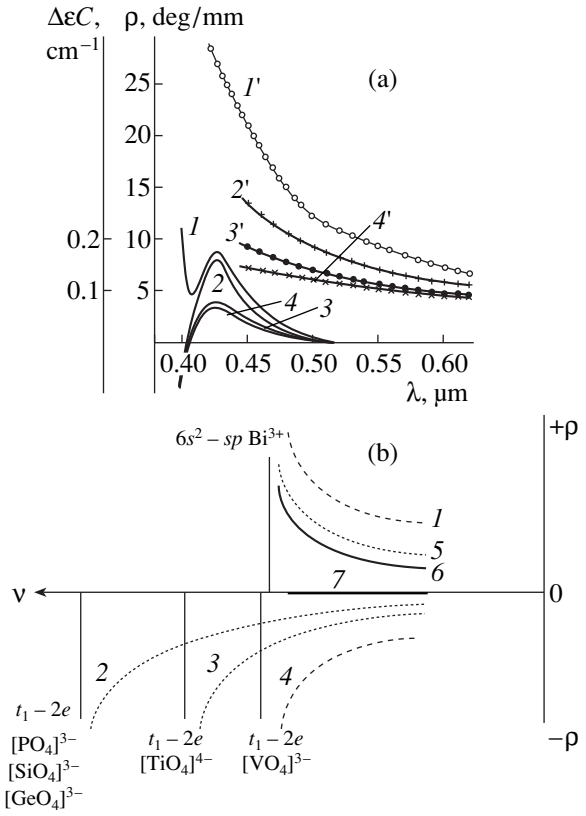

Fig. 4. (a) (*1*–*4*) CD and (*1'*–*4'*) ORD spectra of vanadium-doped $Bi_{12}TiO_{20}$ crystals (*1*) 0.0, (*2*) 0.21, (*3*) 0.40, and (*4*) 0.50 wt % V. (b) Illustrating the role played by transitions of tetrahedral $[MO_4]^{n-}$-complexes accompanied by charge transfer in the optical rotation of sillenite crystals [17]: (*1*) partial contribution of the $6s^2-6sp$ transitions of Bi^{3+} ($\nu = 27800$ cm^{-1}); (*2*) partial contribution of the transitions of tetrahedral $[SiO_4]^{4-}$-, $[GeO_4]^{4-}$-, and $[PO_4]^{3-}$-complexes ($\nu \approx 70000$ cm^{-1}); (*3*) partial contribution of $[TiO_4]^{4-}$-complex ($\nu = 50000$ cm^{-1}); (*4*) partial contribution of $[VO_4]^{3-}$-complex ($\nu = 29411$ cm^{-1}); (*5*) total optical rotation in $Bi_{12}GeO_{20}$, $Bi_{12}SiO_{20}$, $Bi_{24}P_2O_{41}$; (*6*) $Bi_{12}TiO_{20}$; and (*7*) $Bi_{24}V_2O_{41}$.

Concluding this section, we should like to underline some differences in the behavior of the ORD curves of BGaO and BZnO crystals in comparison with the ORD curves of BGO and BSO crystals [79]. In the range 0.40–0.50 μm, the derivative $d\rho/d\lambda$ for the BGaO and BZnO is higher than that for BGO and BSO crystals (Fig. 3), which can be associated with the excitation of OA of chromophores ($[Bi_MO_3]$) and an increase of the

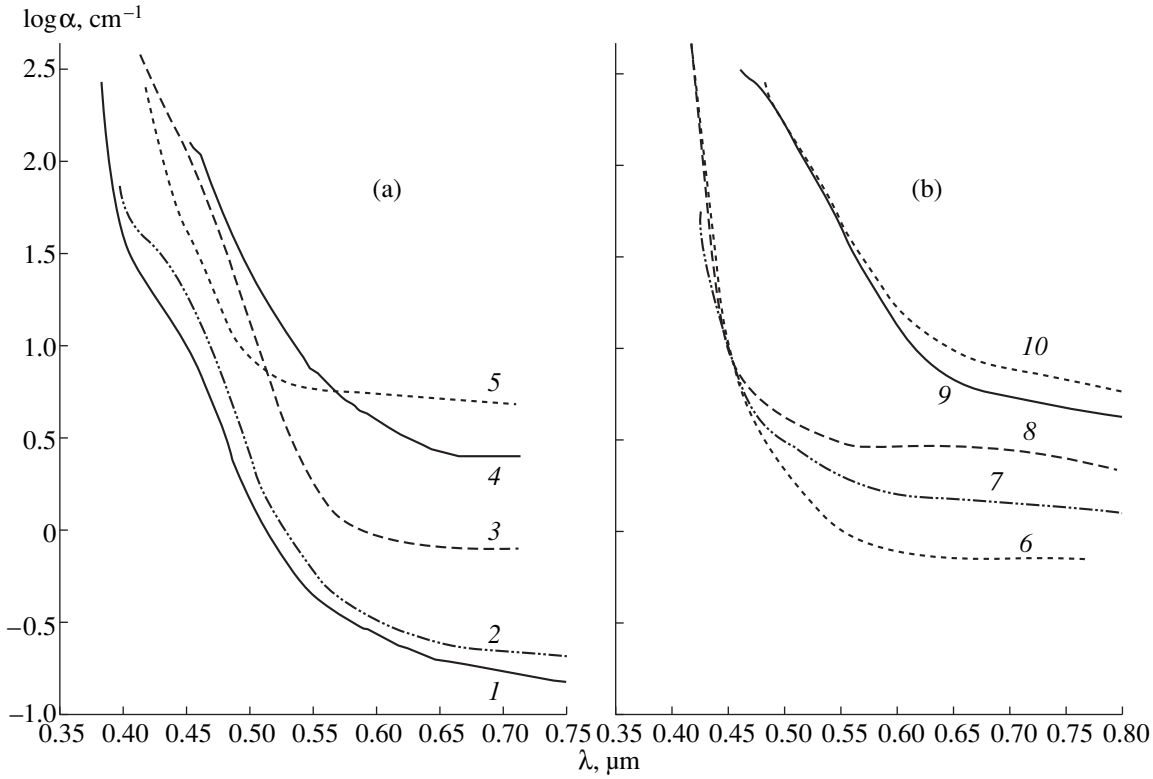

Fig. 5. Absorption spectra of single crystals either grown from melts or synthesized hydrothermally: (a) (*1*) $Bi_{12}GeO_{20}$, (*2*) $Bi_{12}SiO_{20}$, (*3*) $Bi_{12}TiO_{20}$, (*4*) $Bi_{24}P_2O_{41}$ (hydrothermally synthesized), and (*5*) $Bi_{24}V_2O_{41}$ (hydrothermally synthesized) and (b) (*6*) $Bi_{24}B_2O_{39}$, (*7*) $Bi_{25}GaO_{39}$, (*8*) $Bi_{38}ZnO_{58}$, (*9*) $Bi_{25}GaO_{39}$ (hydrothermally synthesized), and (*10*) $Bi_{25}TlO_{39}$ (hydrothermally synthesized).

Bi : *M* ratio from 12 : 1 (for BGO) to 25 : 1 (for the BGaO and BZnO).

4. OPTICAL PROPERTIES OF CRYSTALS WITH SILLENITE STRUCTURE

4.1. Absorption Spectra and Circular Dichroism of Undoped Crystals

In the vicinity of the fundamental absorption edge of the BSO, BGO, and BTO sillenites, their absorption spectra have been repeatedly studied [7, 36, 39, 80, 81]. The results obtained can be summarized in a few words. With a decrease in wavelength, the absorption coefficient increases almost exponentially so that no fine structure is observed in the vicinity of the fundamental absorption edge even at low temperatures.

Absorption in BGaO and BZnO has been studied much less [79, 82, 83] and, similar to the recently studied BBO spectrum (Fig. 5), shows no specific features [84].

The absorption spectra of sillenites show that at $\alpha > 10^2$–10^3 cm^{-1}, the absorption curves are similar for all the sillenites and are located at about ~0.4 μm [67, 80, 81]. The absorption curves of these crystals and the absorption curve of bismuth oxide [85] are similar to the absorption curves of the crystals heavily doped with Al, Ga, etc. [79, 86, 87]. With a decrease in temperature from 300 to 80 K, the fundamental absorption edge of BSO, BGO, and BTO crystals is shifted to the short-wavelength range. The estimates made by the approximate formulas show [80, 81] that the band gap is E_g = 3.25–3.28 eV at T = 300 K and E_g = 3.4 eV at T = 80 K. With a further decrease in temperature, the position of the absorption edge remains practically unchanged.

The absorption spectra of most sillenites in the vicinity of the fundamental absorption edge are characterized by the presence of the well pronounced band the shape of a "shoulder" in the range 0.41–0.50 μm (Fig. 5). The intensity of this band depends on the growth conditions and the thermal treatment of the crystals grown. Of all the Czochralski-grown crystals, the most pronounced shoulder in the absorption spectrum is observed for BTO crystals. The shoulder of the BGaO and BZnO spectra is rather feeble and observed only in a more long-wavelength range at room temperature; the BBO spectrum practically has no shoulder at all. The absorption intensity of the spectra of nominally undoped hydrothermally grown BTlO and BGaO sillenites in the range 0.40–0.60 μm is much higher [83] than that for the corresponding Czochralski-grown crystals. At the same time, the transparency of hydro-

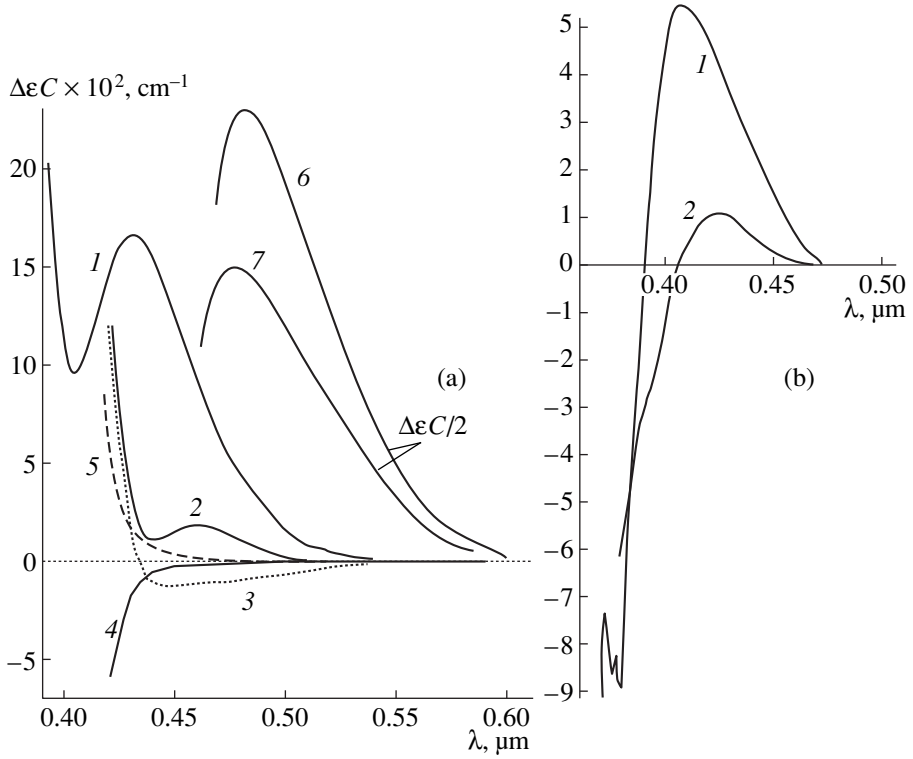

Fig. 6. CD spectra of single crystals (a): (*1*) $Bi_{12}TiO_{20}$, (*2*) $Bi_{25}GaO_{39}$, (*3*) $Bi_{38}ZnO_{58}$, (*4*) $Bi_{24}B_2O_{39}$, (*5*) $Bi_{24}GaPO_{40}$, (*6*) $Bi_{25}GaO_{39}$ (hydrothermally synthesized), and (*7*) $Bi_{25}TlO_{39}$ (hydrothermally synthesized) obtained at 300 K and (b) $Bi_{12}GeO_{20}$ obtained at (*1*) 300 and (*2*) 80 K.

thermally-grown BSO and BGO crystals in the vicinity of the shoulder was higher than for Czochralski-grown one [88]. It seems that higher absorption intensity in hydrothermally grown BTlO and BGaO crystals [83] is associated with the formation of defects of a new types—individual $(OH)^-$-groups. The concentration of hydroxyl groups in the hydrothermally grown crystals attains the values from 10^{18} to 10^{20} cm^{-3} in BVO and BPO crystals, which is much higher than the concentration of OH-groups in Czochralski-grown crystals (10^{16} cm^{-3}) [89]. The low intensity or the complete absence of a shoulder is also characteristic of the absorption spectra of heavily doped BSO, BGO, and BTO crystals with "noncoloring" dopants Al, Ga, Zn, P, etc. [78, 86, 87, 90, 91].

It was shown [68, 92] that the electronic transitions determining the formation of the shoulder in the vicinity of the absorption edge are best seen in the CD spectra of BSO, BGO, and BTO crystals, as positive bands with the maximum at λ = 0.429 μm (T = 300 K, E = 2.9 eV) for the right-handed crystals (Fig. 6). With a decrease in temperature, the band is shifted to the short-wavelength range of the spectrum and, at T = 80 K, its maximum is located at λ = 0.410 μm (E = 3.0 eV) for BSO. At T = 80 K, the CD spectrum of a thin (~30 μm) BSO specimen shows the pronounced bending, whereas the BGO spectrum, two negative bands at λ = 0.3735 μm (3.32 eV) and λ = 0.3777 μm (3.28 eV) and two bendings in the vicinity of 400 μm (Fig. 6b) [79]. The CD spectra of BTO and other sillenites show no such bendings. The bending in the CD spectrum of BSO crystals and the band maxima in the BGO spectrum are located in the range where the photoconductivity spectrum has the broad band and the excitation band of the photochromic effect (E_{max} = 3.4–3.5 eV) [87, 93, 94].

We believe that the atomic structure of BGaO [28] result in the shift of the CD band of the right-handed crystal to the long-wavelength range (Fig. 6a). At the same time, similar to the case of BTO crystals, the CD in the vicinity of the edge is positive [79]. The maximum of the corresponding CD band of right-handed BZnO crystals is located approximately in the same range as for BGaO crystals but has a negative sign at the positive dichroism in the edge range [79].

The band intensity with the maximum at λ = 0.429–0.450 μm in the CD spectra of Czochralski-grown sillenite crystals is maximal for BTO crystals with both Ti and O(3) vacancies.

Of course, an increase of the shoulder intensity and the corresponding CD band cannot be explained only by a higher concentration of Ti or O(3) vacancies. The intensity of these bands can also be dependent on the concentration of vacancy complexes. In this connec-

tion, it is worth mentioning the study of CD spectra of BBO crystals [84]. The CD spectrum of right-handed BBO crystal with the tetrahedra substituted by BO_3-triangles and the simultaneous presence of O(3)-vacancies shows no such bands, whereas the CD in the vicinity of the edge has a negative sign as in the case of BSO and BGO crystals (Fig. 6a).

In the CD spectra of the hydrothermally grown BTlO and BGaO sillenites, the corresponding band is shifted to the long-wavelength range of the spectrum with the maximum at $\lambda = 0.480$ μm. As is seen from Fig. 6a, the intensity of the CD band in the spectra of these crystals is rather high ($\Delta\varepsilon C \approx 45 \times 10^{-2}$ cm^{-1}) and exceeds the intensity of the corresponding band in the CD spectra of BTO crystals ($\Delta\varepsilon C \approx 14 \times 10^{-2}$ cm^{-1}) [83]. The above results show that in this case, the CD spectra provide a more detailed information on the states determining the shoulder at the absorption edge and the band on the CD spectrum. The structural characteristics of the crystals dependent on the type of *M* cations (which almost do not influence the behavior of the absorption edge) give rise to considerable changes in the CD spectra (up to the reversal of the dichroism sign).

Concluding this section, we should like to emphasize that all the absorption studies in the vicinity of the fundamental edge can be divided into two groups. In the first group, the interpretation of absorption in the fundamental-edge range is based on the theory of interband transitions developed for classical semiconductors with strong covalent bonding. This approach is implicitly based on the assumption that sillenites can be treated as classical semiconductors. However, the comparison of the dark conductivity of sillenites ($\rho_T = 10^{11}$–10^{13} Ω cm) [80, 82, 87] and intrinsic semiconductors ($\rho_T = 10^{-2}$–10^{9} Ω cm) [95] shows that such a classification is rather formal.

It was also shown [80] that the absorption curve at $\alpha > 5 \times 10^2$ cm^{-1} is satisfactorily described by the expression

$$\alpha = \alpha_0 \exp[-\sigma_0(h\nu_0 - h\nu)/kT]. \quad (3)$$

For BSO crystals, $\sigma_0 = 0.71$ at $T = 300$ K, which is typical of the situation where the edge of the exciton band is broadened because of strong exciton–phonon interactions [96]. Toyoda *et al.* [97] considered the mechanism of the edge broadening and confirmed the strong exciton–phonon interactions giving rise to exciton-band broadening. Indeed, this conclusion is well justified because the peak *A* in the vicinity of the first maximum of the reflection spectrum of sillenites is seen less distinctly than that in the spectra of quartz and semiconductor crystals mentioned above. It should also be emphasized that the conclusions about strong exciton–phonon interactions [96–98] are based on the absorption-edge measurements made at different temperatures and approximated by formulas of type (3).

We believe that such an approach to the interpretation of the above facts is logically erroneous. If a spectrum with an isolated exciton transition occurring with the broadening of the long-wavelength edge of the corresponding band (caused by strong exciton–phonon interactions) satisfies the conditions

$$d(\ln\alpha)/d(\omega) \sim 1/kT, \quad (4)$$

$$\sigma < 1, \quad (5)$$

then the absorption in the vicinity of the edge is described by Eq. (3), but the reverse statement is invalid. If absorption behavior is described by Eq. (3) under the conditions (4) and (5), this does not necessarily signify that edge broadening is caused by exciton–phonon interactions, especially in the case under consideration. Since the long-wavelength edge of the reflection spectra of sillenites has several maxima, then it is highly probable that the second, third, and fourth maxima would give some contributions to absorption in the range 3.2–3.4 eV; in other words, absorption would be determined by several closely located electron transitions.

However, the data on the reflection spectra show that exciton transitions play the key role in the formation of the absorption edge. It is also possible that the negative bands in the CD spectrum in the range $E \sim 3.3$ eV are associated not with the transition to the vacancy states but rather with a number of Wannier–Mott exciton transitions. However, at present, it is impossible to characterize the nature of these bands more definitely.

We believe that more definite conclusions can be made only upon the detailed study of absorption and circular dichroism in 0.1- to 10.0-μm-thick crystalline films at 4.2 K.

4.2. Circular-Dichroism Spectra of Sillenites Doped with p-Elements

The absorption spectra of a number of heavily-doped sillenites are characterized by much lower absorption intensity in the vicinity of the shoulder and even by it complete disappearance and, sometimes, the characteristic yellow color [79, 87, 91]. The change in adsorption is accompanied by the change in the intensity of the corresponding band in the CD spectrum. At the same time, some experimental facts indicate than doping does not necessarily decrease the absorption intensity in this range [68, 79]. The change of the optical absorption because of a dopant incorporation into the crystal is associated with the crystal chemistry of sillenites and their solid solutions. However, the nature of this phenomenon has not been studied as yet. The first detailed study of the change in the optical characteristics caused by doping of BGO, BSO, and BTO crystals with Al_2O_3, Ga_2O_3, ZnO, and CdO oxides was

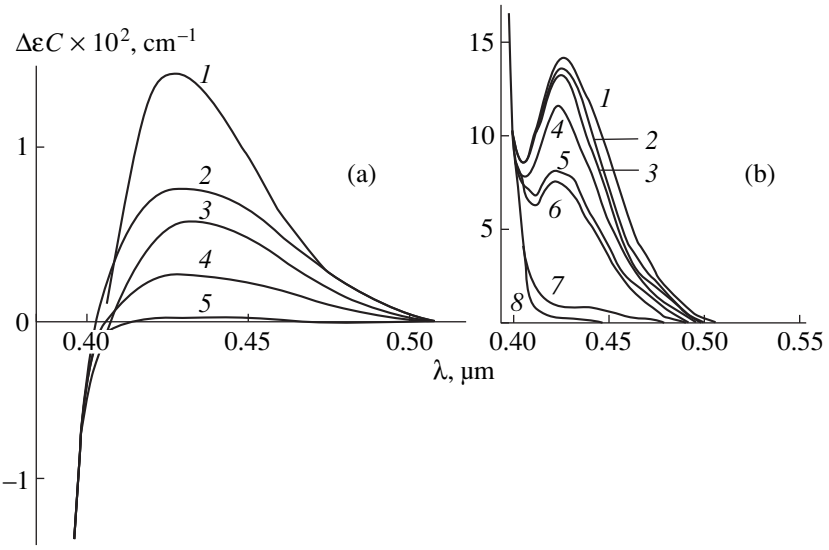

Fig. 7. CD spectra of (a) BSO crystals (*1*) undoped and doped with Al_2O_3 at (*2*) 0.1, (*3*) 0.5, (*4*) 1.0, and (*5*) 1.5 mol % Al_2O_3 and (b) BTO crystals (*1*) undoped and (*2–7*) doped with ZnO at (*2*) 0.035, (*3*) 0.04, (*4*) 0.05, (*5*) 0.06, (*6*) 0.065, (*7*) 0.08, and (*8*) 0.1 wt % ZnO [79].

made on an example of absorption and CD spectra [79]. It was shown that the CD spectra are extremely sensitive to doping. The CD spectra of sillenites doped with Al_2O_3 and Ga_2O_3 oxides showed considerably changed intensity of the CD band with the maximum at $\lambda \approx$ 0.43–0.45 μm (Fig. 7a). The CD spectra of BGO and BSO crystals doped with CdO at a concentration of ~2 mol % showed no band at $\lambda \approx 430$ nm at all. At the same time, the intensity of this band in the corresponding Cd-doped BTO crystals increased by a factor of two at the CdO concentration equal to ≈2 wt %.

The behavior of the CD band at $\lambda = 0.429$ μm (the so-called "defect band") for zinc oxide–doped sillenites is also somewhat unusual. The intensity of the band studied in the spectra of the BGO⟨Zn⟩ and BSO⟨Zn⟩ crystals doped with 1.5 mol % ZnO showed no considerable changes, whereas the corresponding band in the CD spectrum of BTO⟨Zn⟩ completely disappeared at the ZnO concentration 0.1 wt % (Fig. 7b).

Thus, in most cases, the intensities of the CD band and the shoulder at the fundamental absorption edge in the CD spectra of sillenites doped with *p*-elements considerably decrease. The existence of the shoulder in the absorption spectra is associated with the vacancies of metal atoms in the tetrahedrally coordinated positions, whereas, according to the above consideration, the disappearance of the shoulder and the band in the CD spectrum is explained by the incorporation of *p*-elements into the tetrahedrally coordinated positions. In BTO, titanium vacancies are always present in undoped crystals, in other words, there are always some vacant sites ready to incorporate Ga, Zn, and Al atoms.

At the same time, doping can only slightly change the optical rotation [79]. Doping of crystals with *p*-elements results in filling the vacancies in the centers of $[MO_4]$-tetrahedra, and, thus, the formation of new chromophores providing the contributions to the optical rotation. However, the transitions accompanied by charge transfer by these clusters belong to the far ultraviolet range. Taking into account very low concentrations of impurities, this contribution is also very small. The role of the umbrella-like bismuth atoms in the optical rotation of doped crystals and formation of CD spectra has already been discussed.

4.3. Absorption and Circular-Dichroism Spectra of Sillenites Doped with 3d-Elements

Manganese-containing sillenites. The element most interesting for band identification in the spectra is manganese. According to various authors, manganese can occupy different positions: simultaneously tetrahedral and interstitial positions with the orthorhombic symmetry [99], the bismuth position [100, 101], and the tetrahedral positions [102–105] with different oxidation degrees of manganese (Mn^{+1} [99], Mn^{+2} [100–106]. Mn^{+3} [102, 103], Mn^{+4} [30, 102, 103], and Mn^{+5} [105]).

According to the X-ray diffraction data [30], in the crystal lattice of the sillenite $Bi_{12}MnO_{20}$, manganese is tetrahedrally coordinated with oxygen and has the oxidation degree +4 (the d^3-configuration). The study of the Raman and IR spectra of BMnO and BTO⟨Mn⟩ crystals [30, 102, 104] also indicates the existence of $[MnO_4]^{4-}$-complexes. The vibration frequencies indicated for the spectra of manganese-containing sillenites located at 740 cm^{-1} (Raman spectrum) and 725 cm^{-1} (IR spectrum) are lower than those typical of $[MnO_4]^{3-}$, but coincide with the empirically determined frequen-

cies ν_1 and ν_3 of $[MnO_4]^{4-}$ vibrations. The vibrations of a $[MnO_4]^{5-}$-tetrahedron is not reflected in the sillenite spectra because they belong to the vibration range of the Bi–O sublattice. According to [30], the positions of the bands in the MnK XANES spectra of BMnO and MnO_2 coincide. This indicates the presence of manganese in the oxidation degree +4 in BMnO, whereas different intensities of these bands confirm different coordination of manganese in these compounds. The state of Mn^{4+} in BMnO is also confirmed by the gravimetric measurements in the process of solid-phase synthesis of the compounds from the mixture of Bi_2O_3 and Mn_2O_3 (MnO) [17].

The possible presence of Mn^{5+} in sillenites is confirmed by the value of the unit-cell parameter of BMnO, $a = 10.216$ Å, which fits the linear dependence of the lattice parameter on the *M*–O distance in the $[MO_4]$-tetrahedron for sillenites with pentavalent cations, BVO, BCrO, and BPO [17]. The positions of the bands in the IR spectra [30, 102, 104] can also be attributed to the $[MnO_4]^{3-}$ vibrations. Although the frequencies of these vibrations (725 cm^{-1}) are lower than the frequencies characteristic of this group, they correlate with the frequencies of the corresponding $[VO_4]^{3-}$ (760 cm^{-1}) and $[CrO_4]^{3-}$ (745 cm^{-1}) vibrations in BVO and BCrO [107, 108]. The vibration frequencies of these groups in sillenites are also lower than the corresponding frequencies in the compounds with different structures [109].

Earlier [110], we considered two possible interpretations of the spectra of the manganese-containing sillenites—the simultaneous presence in the crystal of Mn^{3+}- and Mn^{4+}-ions and the presence of only Mn^{5+}-ions. The considerable overlap of the bands caused by transitions of various manganese ions in the crystal field of *d*-electrons did not allow us to make any decisive conclusions. The positions and the relative intensities of the bands in the BMnO absorption spectrum in the range 0.35–2.0 μm [103] (Fig. 8, curve *1*) completely coincide with these parameters in the spectra of manganese-doped BGO, BSO, and BTO crystals [99, 101–104, 106]. This indicates that the coordination and the oxidation degree of manganese atoms in these crystals are the same. The study of BSO crystals doped with manganese and phosphorus simultaneously showed that their spectra differ from the spectra of sillenites doped with manganese alone (Fig. 8, curve *2*). This made it possible to separate the overlapping bands formed due to various manganese ions. With due regard for these data, the most probable manganese states in sillenites are +4 and +5. In BSO⟨Mn, P⟩, the Mn^{4+}-ions prevail, whereas in all the other sillenites, the concentrations of Mn^{4+}- and Mn^{5+}-ions are comparable.

Thus, within the symmetry T_d, the band in the range 1.100–1.350 μm, which begins at 1.361 μm (7348 cm^{-1}) can be assigned to the transition $^4T_1(^4F) \longrightarrow {}^4T_2(^4F)$ of Mn^{4+}. A similar band was also observed in the spectrum of 12-tungstomanganic acid [111]. The band formed in the BMnO spectrum with a shoulder at 0.90–1.10 μm (8500–10500 cm^{-1}) (Fig. 8) can be attributed to the $^3A_2 \longrightarrow {}^3T_2(^3F)$ of Mn^{5+} transition allowed in the magnetic dipole approximation and, therefore, is quite intense in the CD spectra (Fig. 9). A narrow band at 1.251 μm (8000 cm^{-1}) should be considered as nonphonon zero–zero band formed due to the spin-forbidden $^3A_2 \longrightarrow {}^1E$ of Mn^{5+} transition, whereas the bands with the maxima at 1.211 and 1.296 μm are vibron 0.0–1.ν_n and 0.ν_n–1.0 bands with the excitation of the deformation vibrations ($\nu_n \approx 270$ cm^{-1}), where $\nu_n - \nu_A$ or $\nu_n - \nu_E$ are the vibration frequencies of the tetrahedral $[MnO_4]^{3-}$-complex or the Bi–O sublattice. The next band in the spectrum of manganese-containing sillenites at 0.68–0.90 μm (13000–11300 cm^{-1}) is attributed to the superposition of the $^3A_2 \longrightarrow {}^3T_1(^3F)$ and $^3A_2 \longrightarrow {}^3T_1(^3P)$ transitions allowed in the electric dipole approximation. The vibron structure at the contour of this band correlates with the frequency $\nu_3 \sim 730$ cm^{-1} of the symmetric vibration of $[MnO_4]^{3-}$. A similar absorption spectrum of the $[MnO_4]^{3-}$-complex was also observed for $Sr_5(PO_4)_3Cl\langle Mn\rangle$ [112]. The remaining bands should be attributed to the transitions in the Mn^{4+}-induced crystal field. The low-intensity bands at 0.57 and 0.62 μm (17700 and 16130 cm^{-1}) correspond to the transition $^4T_1(^4F) \longrightarrow {}^4T_1(^4P)$ which manifests itself as a negative band in the CD spectrum (Fig. 9). The electric-dipole $^4T_1(^4F) \longrightarrow {}^4A_2(^4F)$ transition should be associated with an intense band in the CD spectrum with the maxima at 0.46 and 0.42 μm (21600 and 23700 cm^{-1}). Two bands in the absorption spectrum correspond to the latter maxima (Fig. 8).

The crystal exposed to the blue light ($\lambda \le 500$ nm has a higher absorption in the spectrum ranges corresponding to the bands due to the *d–d* transitions of Mn^{4+} and a lower absorption in the range of the *d–d* transitions of Mn^{5+} [102]. It also provides the formation of a band in the range 0.952–1.251 μm (8000–10500 cm^{-1}) [105] due to reversible recharge of manganese, $Mn^{5+} \longleftrightarrow Mn^{4+}$, in the magnetic circular dichroism (MCD) spectrum [102].

Upon vacuum annealing, the BTO⟨Mn⟩ crystals loose the color so that their absorption spectrum becomes almost identical to that of BTO [102, 103] (if the low-intensity band in the range 0.60–0.73 μm with the maximum at 0.65 μm is ignored). Despite the fact that there is no unique opinion about the nature of this absorption band [99, 103, 105], no detailed study of this spectrum has been undertaken as yet. In this range, the CD spectrum of an annealed crystal shows a weak positive band. There is a pronounced bending at 0.50 μm coinciding with the position of the first band in the excitation spectrum of "green" luminescence [char-

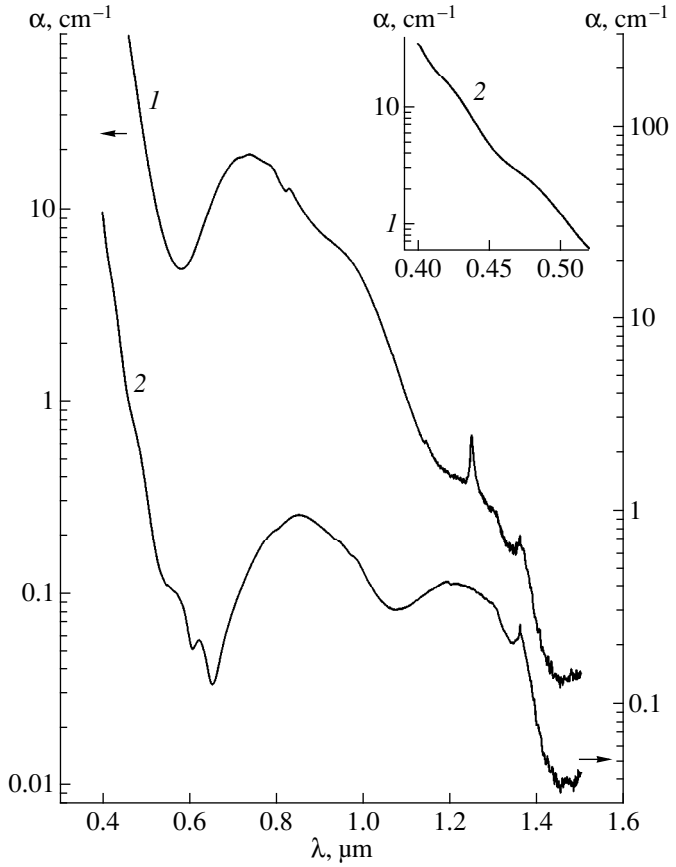

Fig. 8. Absorption spectra of (*1*) BTO⟨Mn⟩ crystals (0.1 wt % Mn) and (*2*) BSO⟨Mn, P⟩ crystals (0.0066 wt % Mn, 0.0037 wt % P) obtained at 300 K.

acteristic of tetrahedral Mn^{2+} (d^5)] (Fig. 10). The structure of the luminescence spectrum of BTO⟨Mn⟩ is similar to the absorption spectrum of tetrahedral Fe^{3+} (d^5) complexes in the range of transitions occurring with the charge transfer ($1t_1 - 2e$, $1t_1 - 4t_2$, …). It is well known that the selection rules forbid all the transitions for d^5, which, therefore, cannot be observed in the absorption spectrum of BTO⟨Mn⟩ at low manganese concentrations. Upon annealing in the oxidative atmosphere, the specimen spectra acquire the initial form [102]. The transformation of the absorption spectra similar to the transformation upon vacuum annealing also takes place upon the exposure of BGO⟨Mn⟩ and BSO⟨Mn⟩ crystals to the blue light at low temperature (1.8 K) [99]. Thus, one can draw the conclusion that vacuum annealing and exposure to the blue light of manganese-containing sillenite crystals reduce the oxidation degree of manganese to +2.

Chromium-containing sillenites. Spectra of all the chromium-containing sillenites are similar. They consist of overlapping bands [101, 104, 107, 113–115] (Fig. 11) and remind the analogous spectra of manganese-doped crystals. A diffuse-reflection spectrum of BCrO [107] is similar to the BMnO spectrum [103].

Today, it is commonly believed that chromium atoms in sillenites have the tetrahedral environment [104, 107, 116–118], but the charge state of chromium has not been determined as yet.

The change of the band-intensity ratio in the absorption and CD spectra of sillenites exposed to the blue light and annealed in vacuum (Figs. 11, 12) leads to a conclusion about the simultaneous existence of chromium with two degrees of oxidation [101, 109, 113, 117, 118]. Thus, the bands observed can be divided into two systems [107, 117]: (I) bands in the ranges 1.000–1.176 μm (8500–10 000 cm^{-1}), 0.714–0.834 μm (12 000–14 000 cm^{-1}), and 0.500–0.541 μm (18500–20000 cm^{-1}) and bendings in the range 0.671–0.685 μm (14600–14900 cm^{-1}), whose intensities increase upon the crystal exposure to the blue light or annealing and (II) bands in the ranges 0.870–1.053 μm (9500–1500 cm^{-1}) and 0.455–0.555 μm (18000–22000 cm^{-1}), which disappear upon such a treatment.

The position of the bands and the ratio of their intensities in system (I) are well consistent with the spectra of tetrahedrally coordinated Cr^{4+} (d^2). For the d^2-configuration in a field of the T_d symmetry, the spin-allowed transitions are those from $^3A_2$ to $^3T_2$, $^3T_1(^3F)$,

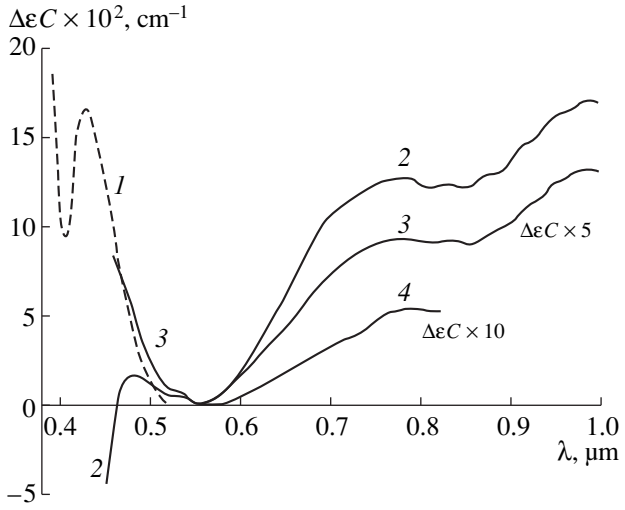

Fig. 9. CD spectra of (*1*) undoped and (*2–4*) Mn-doped BTO crystals at (*2*) 0.57, (*3*) 0.11, and (*4*) 0.03 wt % Mn [103].

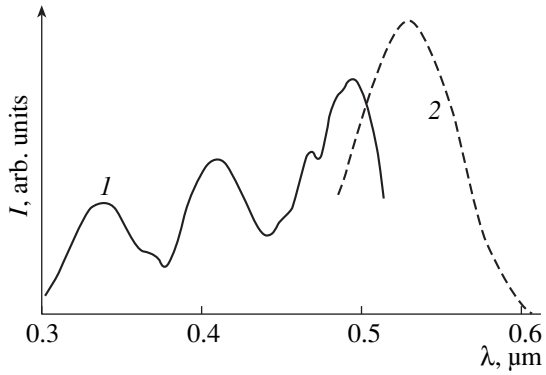

Fig. 10. (*1*) Excitation and (*2*) luminescence spectra of vacuum-annealed BTO⟨Mn⟩ crystals (0.26 wt % Mn) obtained at 300 K [102].

and $^3T_1(^3P)$. According to [107, 117], the bands at λ_1 = 1.000–1.176 μm (8500–10 000 cm^{-1}), λ_2 = 0.823 (12157 cm^{-1}), and λ_3 = 0.537 μm (18600 cm^{-1}) correspond to these transitions. However, by virtue of the restrictions imposed by the selection rules, the intensities of the $^3A_2 \longrightarrow {}^3T_2$ and $^3A_2 \longrightarrow {}^3T_1(^3P)$ transitions in the absorption spectra are low in comparison with the intensities for the transition $^3A_2 \longrightarrow {}^3T_1(^3F)$ (Fig. 11). The $^3A_2 \longrightarrow {}^3T_2$ transition is allowed in the magnetic-dipole approximation, whereas the transitions $^3A_2 \longrightarrow {}^3T_1(^3F, {}^3P)$, in the electric-dipole approximation. This explains the considerable circular dichroism in the vicinity of λ = 1.00 μm (10000 cm^{-1}). The low-intensity band with the nonphonon line at λ = 1.274 μm (7850 cm^{-1}) observed at the long-wavelength edge can be attributed to the $^3A_2 \longrightarrow {}^1E$ transition of a tetrahedral Cr^{4+} ion. It should also be emphasized that all the observed bands have the vibron structure correlating well with the frequency of the symmetric vibrations ν_3 of the $[CrO_4]^{4-}$ complex in the excited state [107].

Band system II corresponds to the electron transitions of a tetrahedrally coordinated Cr^{5+} (d^1) ion [107, 117], The $[CrO_4]^{3-}$ spectrum is characterized by only one transition in a crystal field $^2E \longrightarrow {}^2T_2(t_1^5 e^2)$. The long-wavelength band initiated from a narrow nonphonon line at λ = 1.042 μm (ν = 9598 cm^{-1}) in the BTO⟨Cr⟩ crystals [117] and at λ = 1.036 μm (ν = 9651 cm^{-1}) in the BGO⟨Cr⟩ and BSO⟨Cr⟩ crystals [119]) attributed just to this transition. The shape of this band, the presence of a series of narrow lines at its contour, and its position on the frequency scale correspond to the well-known $[CrO_4]^{3-}$ spectra in the $Ca_2(PO_4, CrO_4)Cl$ and $Ca_2(VO_4, CrO_4)Cl$ crystals [120, 121]. The study of the fine structure at 10 K showed [117] that narrow lines observed in the range of this band form regular "progressions" with the origin at λ = 1.042 (9598 cm^{-1}) and λ = 0.970 μm (10314 cm^{-1}) reflecting interaction of the fine structure with the lattice and nonsymmetric vibrations ν_4 of the $[CrO_4]^{3-}$-complex. The existence of the second origin of the vibrational progression can be a consequence of the vibron interactions with the excited local vibrations of a nonsymmetric type ν_3 of the above complex. This result contradicts the conclusions drawn in [119], where an analogous series of narrow lines in the spectra of Cr-doped BGO and BSO crystals was attributed to the interaction of electronic states of chromium in the interstitial position with the orthorhombic symmetry with lattice vibrations. However, using the tables of line positions given in [119], one can reveal the similar regular progressions with the origins at λ = 1.039 (9621 cm^{-1}) and λ = 1.036 μm (9651 cm^{-1}) in the BGO and BSO absorption spectra and the period of ~300 cm^{-1} corresponding to the nonsymmetric vibrations ν_4 of the $[CrO_4]^{3-}$ complex in the excited state.

Another band with the maximum at λ = 0.4808 μm (20800 cm^{-1}) also belonging to band system of II should be compared with the charge-transfer band corresponding to the transitions $^2E \longrightarrow {}^2T_1(t_1^6 t_2^1)$. The considerable intensity ($f \approx 10^{-1}$) of this band in the absorption and CD spectra (Figs. 11, 12) [107, 118] is characteristic of the transitions occurring with the charge transfer.

The above data and the IR spectra of the chromium-containing sillenite [104, 107] show that in these crystals, chromium is in two oxidation degrees, Cr^{4+} (d^2) and Cr^{5+} (d^1), and is tetrahedrally coordinated with oxygen. Vacuum annealing and exposure of crystals to the blue light results in $Cr^{5+} \longrightarrow Cr^{4+}$ recharge. The reduction of chromium to lower oxidation degrees takes place. A similar degree of chromium oxidation was also observed in MCD spectra of BGO⟨Cr⟩ crystals

[116]. However, a relatively narrow spectral range studied in [116] $\Delta\lambda = 0.357$–0.833 μm (12000–28000 cm^{-1}), considerable width of the bands, and no obvious correlation with the absorption and CD spectra did not allow a reliable interpretation of the results.

There is no unique opinion about the position of chromium in the lattice of doped sillenites. Considering the experimental data on axial compression, Wardzynsky and Szymczak [119] came to a conclusion that chromium occupies the interstitial position with the orthorhombic symmetry. However, there are no typical $[CrO_4]^{2-}$ vibrations in the IR spectra of chromium-containing sillenite [104, 107]. The same reasons make the conclusion drawn in [101] about the octahedral surrounding of chromium in the oxidation degree +3 quite dubious. The EPR studies indicate possible existence of chromium in oxidation degrees +5 and +4 [113, 122, 123].

Iron-containing sillenites. Almost all the phases with the sillenite structure can be doped with iron over a wide concentration range. The spectroscopic characteristics of iron-containing compounds $Bi_{25}FeO_{39}$ and $Bi_{24}FePO_{40}$ were studied in [67, 76, 124].

The absorption spectra of all the iron-containing sillenites are similar [76, 124–127]. The BFeO and Fe-doped BSO spectra [67] in the range 0.4348–1.000 μm (10000–23000 cm^{-1}) have a number of bands characteristic of Fe^{3+} (d^5) in the tetrahedral field of ligands at low temperature. In the IR range 1.0–2.0 μm (5000–10000 cm^{-1}) has a band attributed to ${}^5E \longrightarrow {}^5T_2$ transition of the complex $[FeO_4]^{6-}$ (d^6) of divalent iron [67] also present in the BFeO crystal. A similar band was also observed in the absorption spectrum of BTO⟨Fe⟩ crystals (Fig. 13). The spectrum of vacuum-annealed BTO⟨Fe⟩ crystal did not show such a band [128]. Upon crystal exposure to the light with the wavelength $\lambda \leq$ 500 nm, the band intensity increases [129]. The low intensity of the ${}^5E \longrightarrow {}^5T_2$ (Fe^{2+}) transition with the oscillator strength coinciding (by the order of magnitude) with the oscillator strength of the transition ${}^6A_1 \longrightarrow {}^4T_1$ for Fe^{3+} indicates a very low Fe^{2+} concentration. Thus, the optical properties of iron-containing sillenites are determined by the $[FeO_4]^{5-}$-groups, i.e., Fe^{3+} ions.

The CD spectroscopy turned out to be the most informative method of studying the spectra of the iron-containing sillenite. As is seen from Fig. 14, the CD spectra obtained even at room temperature clearly show the transitions that can hardly be revealed in the absorption spectra. The CD spectra clearly show negative bands with the maxima at $\lambda_1 = 0.725$, $\lambda_2 = 0.615$, $\lambda_3 = 0.525$, and $\lambda_4 = 0.485$ μm. Similar to other iron-containing sillenites [76, 124, 128], one can distinguish three maxima on the broad-band contour at λ_1. In the range 0.85–1.5 μm, i.e., the first absorption band, no CD signal was observed.

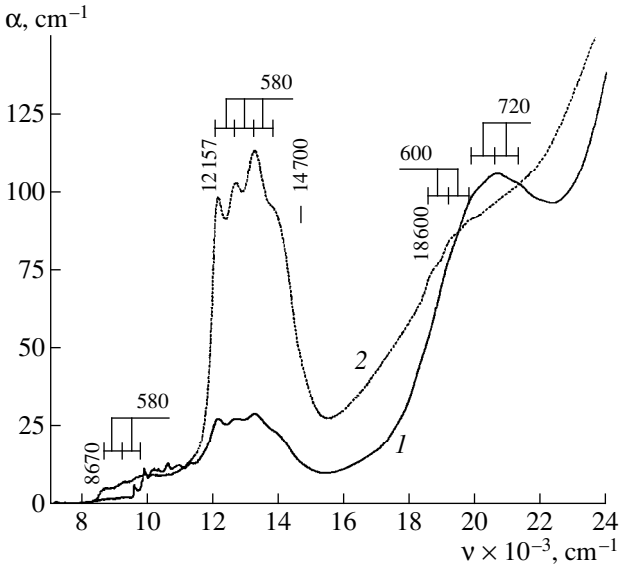

Fig. 11. Absorption spectra of a Cr-doped $Bi_{12}TiO_{20}$ crystals (*1*) prior to and (*2*) upon vacuum annealing obtained at $T = 10$ K [117].

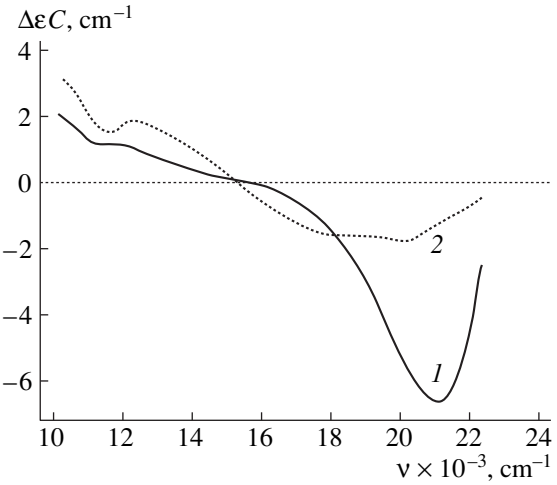

Fig. 12. CD spectra of Cr-doped BTO crystals (*1*) prior to and (*2*) upon vacuum annealing obtained at $T = 300$ K [107].

The CD spectra of unannealed crystals differ from the corresponding spectra of annealed crystals—they indicate a strong additional negative contribution [76, 128] whose intensity linearly increases with the approach to the fundamental absorption edge (Fig. 14). Similar features were also observed for the absorption spectra of annealed (Fig. 13) [76, 128] or light-exposed ($\lambda \leq 0.50$ μm) [129] crystals in comparison with the spectra of unannealed and light-unexposed crystals. However, an additional contribution observed in the CD and absorption spectra cannot be explained only by the presence of iron in the specimens, because this contribution was never observed in the spectra from the crystals doped with iron and phosphorus simulta-

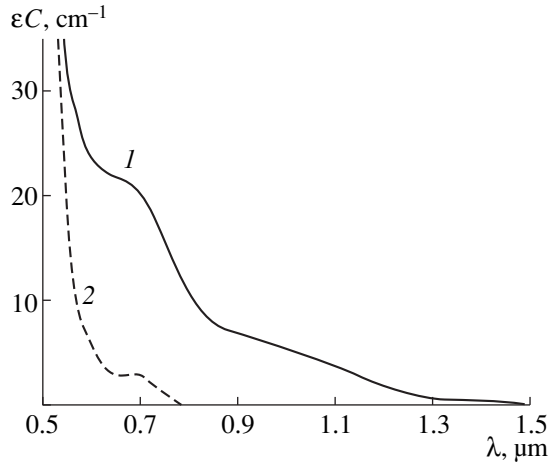

Fig. 13. Absorption spectra of Fe-doped $Bi_{12}TiO_{20}$ crystals (*1*) prior to and (*2*) upon vacuum annealing obtained at T = 300 K [128].

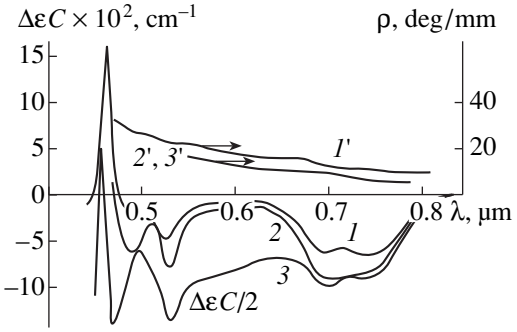

Fig. 14. (*1–3*) CD and (*1'–3'*) OR spectra of (*1*, *1'*) $Bi_{24}FePO_{40}$ and (*2*, *2'*, *3*, *3'*) $Bi_{25}FeO_{39}$ crystals (*3*, *3'*) prior to and (*2*, *2'*) upon vacuum annealing [76].

neously. The positions of the band in the MCD spectra of BFeO crystals [76] correlate with the positions of these bands in the CD spectra. Electron transitions providing the additional linear contribution to the CD spectra are seen in MCD spectra as a broad positive band in the range 0.68–0.78 μm.

The constant intensities of the *d–d* bands in the CD spectra of BFeO crystals prior to and upon vacuum annealing (with due regard for the additional linear contribution) [76, 128] and the constancy of the magnetic susceptibility of BTO⟨Fe⟩ crystals [130] indicate the preservation of the oxidation degree and the coordination of iron atoms. This is also confirmed by the coincidence of the ORD curves of BFeO crystals prior to and upon vacuum annealing (Fig. 14) [76]. The optical rotation of right-handed sillenites depends on the negative contribution from the transition of the tetrahedral $[FeO_4]^{5-}$ complex with the charge transfer which, according to the estimates [128], is located in the range $\nu \approx 28000$ cm^{-1}. Thus, vacuum annealing of iron-containing sillenites is not accompanied by recharging of Fe^{3+}.

However, the EPR studies showed [131–133] that, similar to the case of manganese- and chromium-containing sillenites, Fe^{3+} can also be recharged. Upon exposure of the BSO⟨Fe⟩ and BGO⟨Fe⟩ crystals to the light with $\lambda = 0.350$ μm at 77 K, the signal due to Fe^{3+} disappears. It is believed that this is associated with the $Fe^{3+} \longrightarrow Fe^{2+}$ or $Fe^{3+} \longrightarrow Fe^{4+}$ transitions; however, this opinion was not confirmed experimentally. A considerable photochromic effect was also recorded at the same temperature [134, 135]. The coincidence of the bands due to photochromic-effect excitation [129] in BTO⟨Fe⟩ crystals with the corresponding band in the spectra of sillenites containing other transition elements leads to a conclusion that recharge is accompanied by iron reduction, i.e., the formation of Fe^{2+}. This process is characterized by filling of the shallow traps in the band gap of crystals with the thermal-activation energy equal to 0.3–0.4 eV [129]. In turn, this does not allow the observation of recharge at room temperature. Thus, its effect on the optical spectra is negligible.

In this case, the additional contribution to the CD and absorption spectra at room temperature is provided by optical centers formed due to interaction of $[FeO_4]^{5-}$-tetrahedra and the closest $[BiO_x]$-polyhedra. The changes in the bismuth–oxygen sublattice or the phase composition (the presence of a $[PO_4]$-group) upon vacuum annealing result in the transformation of the state of the $[FeO_4]$-complex caused by the change in the valence strengths of Bi–O bonds along the Fe–O–Bi directions.

Vacuum annealing of iron-containing sillenites results in disappearance of both active centers (giving the contributions to CD and MCD spectra, but not affecting the optical rotation and optical rotatory dispersion) and the centers in the near IR range, which are inactive in the CD spectra.

Thus, the knowledge of the nature of both active and inactive centers would provide new information about crystal chemistry of sillenites and the physical mechanism of ion recharge in photoconductive materials.

Cobalt-, nickel-, and copper-doped sillenites. The absorption spectra of cobalt-doped sillenites in the wavelength range 0.4–2.0 μm (5000–25000 cm^{-1}) [77, 136] have two broad bands at 1.25–2.00 μm (5000–8000 cm^{-1}) and 0.5882–0.7143 μm (14000–17000 cm^{-1}) consisting of several overlapped components (Fig. 15). These bands correspond to the $^4A_2 \longrightarrow {}^4T_1(^4F)$ and $^4A_2 \longrightarrow {}^4T_1(^4P)$ transitions in the crystal field due to a tetrahedrally coordinated Co^{2+} (d^7). This is also confirmed by the information obtained from the CD and MCD spectra [77, 137].

Along with the above bands, the CD spectrum in the 0.500–0.540 μm range also has a negative band which, similar to the "defect" band with the maximum at

430 nm, is not associated with the *d–d* transitions of cobalt and, thus, should be considered as the manifestation of the effect of a certain "defect center" [77]. This band correlates with the band in the photoinduced-absorption spectrum. Taking into account the concentration character of the intensity variation of the band at 0.500–0.540 μm, we assumed [77] that this band is formed due to $[BiO_3E]$ polyhedra in a doped crystal characteristic of sillenites with cations in the oxidation degrees less than <+4. Another possible explanation of this band is the incorporation of a noncontrollable impurity facilitated by cobalt. The possible explanation of the formation of such a defect center suggested in [77] should be complemented with possible formation of a polaron due to excitation of the photochromic effect. The models with participation of polarons are widely used in the description of thermo- and electrochromic effects in disordered media [138].

The presence of nickel in tetrahedral lattice positions of doped sillenites is reliably established in the range of transitions in a crystal field in both absorption and CD spectra [78, 137] (Figs. 16, 17). The absorption spectra show the bands whose energies correspond to the transitions $^3T_1(F) \longrightarrow {}^3T_2(F)$, $^3T_1(F) \longrightarrow {}^3A_2(F)$, $^3T_1(F) \longrightarrow {}^1E(D)$, and $^3T_1(F) \longrightarrow {}^3T_1(P)$ of the tetrahedrally-coordinated Ni^{2+}. The shape of CD band in the region of the $^3T_1(F) \longrightarrow {}^3T_1(P)$ transition repeats the shape of the contour of the absorption band consisting of at least three components. The structure of this band is associated with the spin–orbital interactions [139, 140] both in the ground and the excited states, which is confirmed by the MCD data [78].

The CD spectra in the vicinity of the fundamental absorption edge of BTO⟨Ni⟩ crystals showed a considerable increase of band intensity in the range of the "defect" band in comparison with the intensity of this band for undoped crystals. At the same time, the sign reversal of circular dichroism is observed in the range of $\lambda \le 0.420$ μm as in the the case of BTO⟨V⟩ crystals. Such a behavior of circular dichroism indicates the formation of additional centers in the Ni-doped structure.

Similar to other sillenites, the Co- and Ni-doped BTO and BSO crystals show the photochromic effect [77, 78]. However, an increase in the photoinduced absorption in the region $\lambda \le 0.550$ μm does not influence the intensity of the *d–d* bands. This fact indicates that photoexcitation is not accompanied by recharge of Co^{2+} and Ni^{2+}.

The absorption spectra of Co- and Ni-doped sillenites were also studied in [98, 141, 142]. However, the dopant concentrations were too low, and therefore the spectra obtained did not reveal nickel in the specimens [136, 142]. Although the experimental data [141] gave no rise to any doubt, the obtained spectra were not interpreted. The attempts to explain the results by the substitution of the bismuth in the pseudooctahedral

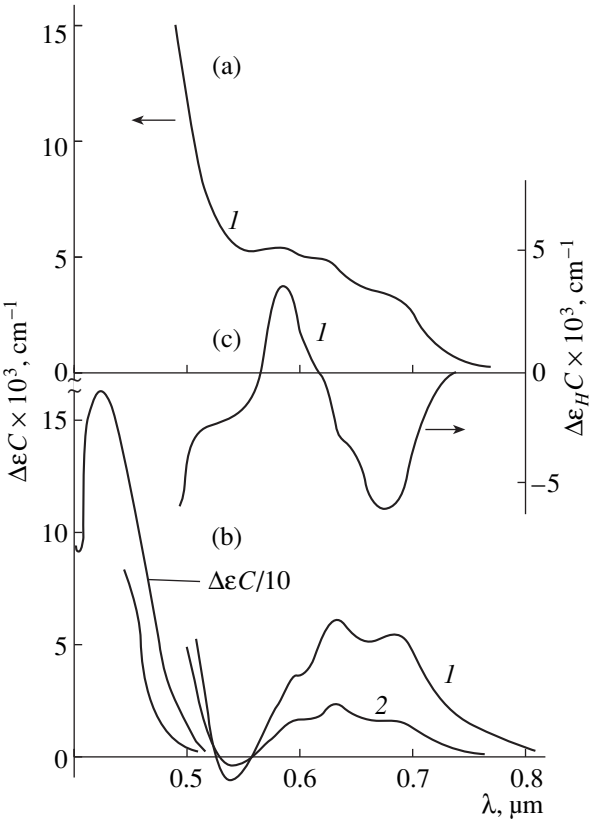

Fig. 15. (a) Absorption, (b) CD, and (c) MCD spectra of BTO⟨Co⟩ crystals doped with (*1*) 0.0025, (*2*) 0.0008 wt % Co [77].

positions in the sillenite lattice by cobalt and nickel are not justified and contradict the known structural data.

It is well known [143] that no compounds with the sillenite structure are formed in the Bi_2O_3–CuO system. However, the study of the absorption spectra of copper-doped sillenites showed [129, 144, 145] that copper is incorporated into the tetrahedral positions in the lattice and has the oxidation degree +2. The fact of Cu^{2+} incorporation into the tetrahedral positions in sillenites is also confirmed by the EPR studies of isostructural BTO powders and copper-doped (up to 2 wt % Cu) $Bi_{12}GeO_{20}$ single crystals [146].

In the range 1.0–2.0 μm (5000–10 000 cm^{-1}), the BTO⟨Cu⟩ and BSO⟨Cu⟩ absorption spectra show a broad band corresponding to the $^2T_2 \longrightarrow E_2$ transition in the crystal field of the $[CuO_4]^{6-}$-complex. In the range of nonphonon line of this transition, the MCD spectrum has the form of the *B*-term [137], which indicates splitting of the $^2T_2$ state, which is induced by the Jahn–Teller effect and the spin–orbital interaction.

The absorption spectra in the vicinity of the fundamental absorption edge of undoped and copper-doped sillenite crystals differ insignificantly, which indicates that the transitions with charge transfer occur in the

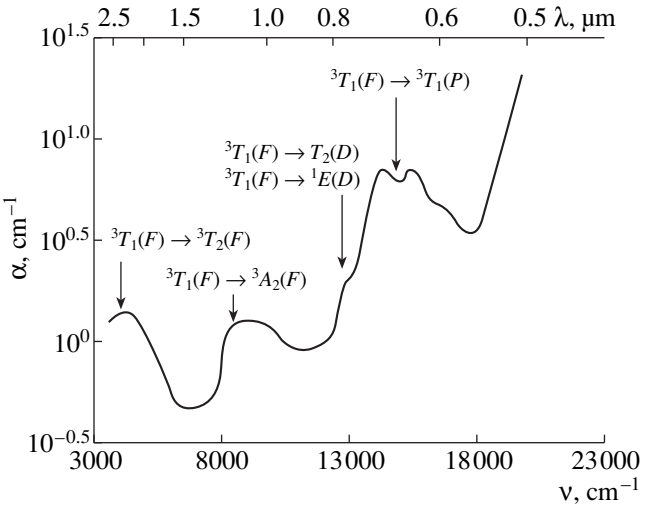

Fig. 16. Absorption spectra of Ni-doped BTO crystal (0.23 wt % of Ni_2O_3 in the charge) [78].

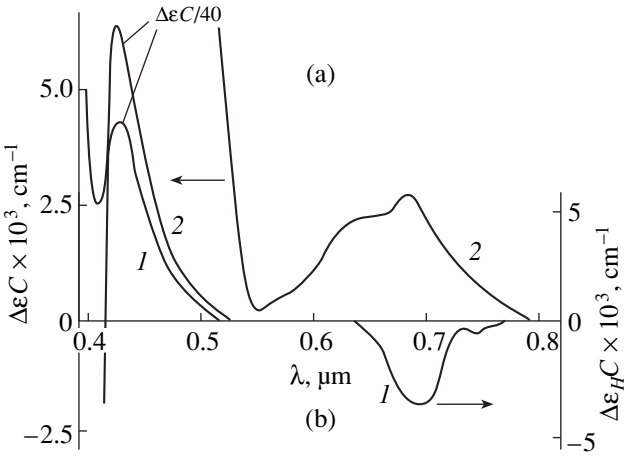

Fig. 17. (a) CD and (b) MCD spectra of (*1*) undoped and (*2*) Ni-doped BTO crystals [78].

range $\lambda < 0.4$ μm ($\nu \geq 25000$ cm^{-1}). Nevertheless, these transitions provide the contribution to ORD and influence the CD spectrum in the vicinity of the defect band with the maximum at $\lambda = 0.430$ μm [145].

The BGO⟨Cu⟩, BSO⟨Cu⟩, and BTO⟨Cu⟩ crystals show considerable photochromic effect at room temperature [129, 144, 145]. The positions of the bands in the spectrum of additional absorption photoexcited in copper-doped crystals and the positions of the excitation bands of photochromic effect correlate with the positions of the corresponding bands for undoped sillenites [145]. Thus, the photochromic effect in undoped and copper-doped crystals is caused by the same centers. The complete analogy between the photoinduced absorption spectra and additional absorption spectra caused by vacuum annealing of copper-doped crystals [129] indicate that the photochromic effect has an electronic mechanism. In photoexcitation, the formation of the additional absorption band in the visible range of the spectra is accompanied by a decrease of the intensity of the band caused by the $^2T_2 \longrightarrow E_2$ transition, which indicates recharging $Cu^{2+} \longrightarrow Cu^{+}$ [129].

This result makes invalid the model of the photochromic effect suggested by Borowiec [144] and based on the interpretation of the photochromic effect by charge transfer between the center Cu^{2+} in the interstitial position 6*b* and the tetrahedrally coordinated Cu^{2+}. The equivalence of the excitation of the photochromic effect in undoped and copper-doped BTO crystals would have indicated the presence of interstitial Cu^{2+} centers also in undoped crystals. The existence of Cu^{2+} in the interstitial 6*b* position also contradicts the EPR data [146].

4.4. Absorption Spectra of Sillenites Doped with 4d- and 5d-Elements

In recent years, a number of publications on spectroscopic properties of sillenites doped with atoms of 4*d*- and 5*d*-elements have appeared [147–151]. However, since most of the authors were interested in the photochromic effect [147, 149, 150], no serious analysis of the oxidation degrees of the dopants and the spectra obtained have been made.

As was shown in [147–151], the absorption and photoinduced absorption spectra of Nb-, Mo-, Cd-, Rh-, and Re-doped sillenite crystals showed no changes from the spectra of the respective undoped sillenites. The lower absorption in BTO⟨Nb⟩ crystals in the spectral range $\lambda < 500$ nm and the concentration quenching of the photochromic effect similar to that observed in sillenite doped with pentavalent vanadium and phosphorus are explained by incorporation of an M^{5+} cation into the tetrahedral positions of the structure [148]. The spectra of the photoinduced absorption of Ru- and Os-doped BSO crystals in the visible and near IR range have the bands attributed to the transitions occurring in a crystal field [149]. These bands indicate the recharge of Ru and Os, also observed in the MCD spectra of BSO⟨Ru⟩ crystals [149]. A narrow band at 9380 cm^{-1} and the bands at 16500, 18000, 20000, and 24000 cm^{-1} are attributed to the substitution of Bi^{3+} in the pseudooctahedral position by Ru^{3+} [149]; however, this assumption is not sufficiently justified.

It should also be indicated that the absence of the data on the dopant concentration in the grown crystal (and not in the starting charge) considerably reduces the value of some of the published data. Since the coefficients of the 4*d*- and 5*d*-dopants incorporation are much less than unity, some of the observed (or unob-

served) effects can be caused merely by a low doping level.

5. MODELS OF OPTICAL CENTERS IN SILLENITES

The results considered and analyzed in this review concern mainly the optical, chiro-optical, and photochromic properties of sillenite crystals containing *d*-elements. Undoubtedly, the photoinduced processes occurring in these crystals also influence the photoelectric characteristics not considered in this review. The most important practical problem is the nature of local centers giving rise to the specific behavior of photochromic effect and photoconductivity in sillenites. We believe that the relation between the composition, structural characteristics, and spectroscopic and chiro-optical properties (ORD and CD) of the compounds with the sillenite structure established in this study would also be useful for better understanding the nature of the photochromic effect in these materials.

At present, the photoinduced phenomena in sillenite crystals are intensely studied by traditional spectroscopic and relatively new methods such as spectroscopy in polarized light and, in particular, the method of optically detectable paramagnetic resonance [152].

There are numerous experimental data on the photoinduced properties of sillenites and, in particular, their photochromic properties. However, most of the experiments were made on the BSO and BGO and, in some instances, on BTO single crystals undoped or doped with *s*-, *p*-, and *d*-elements, whereas the numerous other representatives of this large class of inorganic bismuth oxide-based compounds are still unstudied [17].

Various models were suggested to interpret the nature of the centers responsible for the formation of the shoulder in the absorption spectra, the defect band in CD spectra, and photoinduced absorption in sillenites. In particular, the photochromic properties of BSO, BGO, and BTO crystals were explained in [94, 153] by the presence of oxygen vacancies (the so-called F^+ and F^{++} centers) and a complex "defect center" formed by a vacancy of an *M*-atom ($V_{Si, Ge}$), an oxygen vacancy [V_O], and a Bi^{5+}-ion. It is believed [94] that the formation of this defect center [$V_{Ge}V_OBi^{5+}$] provides the charge compensation in the lattice. However, the model of this complex center is inconsistent with the modern crystallochemical data. Moreover, this "complex bismuth ion" should have had a nonzero effective charge. It is often stated that this defect center is responsible for the formation of the 2.3- to 2.8-eV energy levels. The excitation of charge carriers from these levels to the conduction band and their subsequent capture by the 0.1–1.5-eV levels determine the spectrum of the photoinduced absorption in sillenites. There is still no unique opinion about the nature of the centers responsible for the 0.1- to 1.5-eV levels in the band gap.

Moreover, the models suggested in [94] and [87] (the latter considers a Bi^{5+}-ion located in the tetrahedral position of the structure, [Bi_M^{5+}], as a photosensitive optical center) are based on the Craig and Stephenson hypothesis on the presence of Bi^{5+} ions in the BZnO, BFeO, and γ-Bi_2O_3 compounds [24]. This hypothesis proved to be fruitful for the synthesis of new phases of complicated compositions with the sillenite structure [17] but was not confirmed neither by the methods of the physical and chemical analysis nor by the neutron diffraction data on the atomic structure of sillenites of various compositions [28].

A model of a center consisting of a Bi_M^{3+}-ion and a hole delocalized at the surrounding oxygen ions (the so-called Bi^{4+} center or electrically neutral $[BiO_4]^0$-center) was suggested in [137, 154] on the basis of the data indicating the presence of a certain photosensitive paramagnetic center in BSO single crystals. It was assumed that the "antistructural" Bi_M centers are the main intrinsic defects in sillenites. To ionize Bi_M^{3+} by the photomethod, an energy of 2.4 eV is required. Photoionization of Bi^{3+} or "dressing of Bi^{4+} by a hole delocalized toward the surrounding oxygens," is provided by the capture of one of 6*s*-electrons of bismuth by oxygen vacancies. We believe that such a center including a Bi^{4+} ion is quite formal, because it does not take into account the specific electronic structure of bismuth. Moreover, Briat *et al.* [137] themselves recognized that ionized oxygen vacancies (F^+, F^{++} centers) or ions of a noncontrollable 3*d*-impurity always present in sillenite crystals can play the role of paramagnetic centers in $Bi_{12}M_xO_{20\pm\delta}$. The NMR studies revealed magnetic fields of about 200 G at ^{209}Bi nuclei in some bismuth oxides (α-Bi_2O_3, $Bi_2Al_4O_3$, $Bi_2Ga_4O_3$, Bi_4GaO_{12}, and $Bi_2Ge_3O_9$), whose nature is still unclear [155].

It should be noted that an attractive model of a center responsible for photoinduced absorption based on a Bi_M ion in the tetrahedral position has not been confirmed as yet experimentally. This model cannot explain all the experimental data on the optical properties of $Bi_{12}M_xO_{20\pm\delta}$ and the effect of dopants on these properties. Thus, we showed [79] that doping of BSO and BTO crystals by the same dopants produce different (actually opposite) effect on the absorption coefficient and the sign of circular dichroism in the vicinity of the fundamental absorption edge. We believe that the insufficient justification of the assumption that a [Bi_M] center can be the main structural defect in $Bi_{12}M_xO_{20\pm\delta}$ single crystals is also seen well from the failure of all the attempts to explain in terms of this model the results of the reversible change in the optical and chiro-optical properties during photoexcitation and subsequent annealing of single crystals (both in vacuum and in the oxygen atmosphere) [102].

The hypothesis on the relation of the photochromic effect and the photoionization of *M*-cations was tested on an example of Fe-dopant in sillenite single crystals [131, 132]. It was assumed that photoexcitation is accompanied by the transition $Fe^{3+} \longrightarrow Fe^{4+} + e$. However, the analysis of the excitation spectra of the photochromic effect in nominally undoped and doped single crystals of various sillenites (the constant excitation energy within ≈2.4–2.5 eV) indicates that the role of the main centers is played by ionized oxygen vacancies ($F^{++} \longleftrightarrow V_O + 2e$). In this case, the oxidation degree of doping cations of 3*d*-metals usually decreases (and not increase) because of the trap of electrons ($Mn^{5+}(Mn^{4+}) \longrightarrow Mn^{2+}$, $Cr^{5+} \longrightarrow Cr^{4+}$, etc. [102, 117]).

In order to explain the pronounced photoinduced adsorption in BGO⟨Cu⟩ single crystals, a model of a polaron with a small radius was suggested [144]. A polaron is formed due to capture of a hole by one of the bonds of the tetrahedral $[CuO_4]$ complex and its subsequent trigonal distortion. Absorption of light with the energy ($E_{exp} \approx 22000$ cm^{-1}) equal to the binding energy of "self-captured" hole (the so-called Jahn–Teller pseudoeffect) results in a recapture of the hole from one bond by another bond of a distorted $[CuO_4]$ complex. Taking into account high polarization of both main components (Bi^{3+}, O^{2-}) and the compound as a whole, the photoinduced absorption provided by excitation of polarons should also be observed in other sillenites. This phenomenon requires a more detailed study and a thorough analysis.

The optical properties of sillenites in the range of the fundamental absorption edge can also be associated with the presence of excitons in $Bi_{12}M_xO_{20\pm\delta}$. Their existence is confirmed by the absorption bands revealed in our study of CD spectra of undoped BSO and BGO crystals in the vicinity of ~3.2 eV.

Thus, the interpretation of the optical and chiro-optical properties of sillenite crystals is often ambiguous and requires the allowance for numerous important factors such as the composition, structural characteristics (the type of the prevalent defects), and the nature of absorbing centers. The nature of the optical centers responsible for absorption, including the photoinduced absorption, in the crystals of different compositions can be different (point vacancies V_O, V_M, and V_{Bi} and their associates, impurity states, *d–d* transitions, etc.). Usually, the models of optical centers are based on the structural data for $Bi_{12}M_xO_{20\pm\delta}$ single crystals. The recording and interpretation of different types of defects in the sillenite lattice is hindered by the fact that the formation of a vacancy [e.g., oxygen vacancy in the position of O(3) atoms] is accompanied by the change of the local symmetry of the closest $[BiO_x]$- and $[MO_4]$-polyhedra and, thus, also by their electronic structure.

6. CONCLUSION

It has been established that the optical and chiro-optical properties of $Bi_{12}M_xO_{20\pm\delta}$ crystals with the sillenite structure are determined by the electron transitions of the "building units"—$[BiO_x]$-polyhedra and $[MO_4]^{n-}$-tetrahedra. It has also been established that the contribution of electron transitions accompanied by charge transfer, $t_1 - 2e$, of optically active $[MO_4]^{n-}$-complexes (with the point symmetry 23) to the total optical rotation is opposite to the contribution of the $^1S_0 - {}^3P_1$ and $^1S_0 - {}^1P_1$ ($6s^2 - sp$) transitions of Bi^{3+} in $[BiO_5]$-polyhedra (with the point symmetry C_1). A model is suggested, which relates the change in the optical rotation caused by the compositional variations in the $Bi_{12}M_xO_{20\pm\delta}$ crystal to the position of $[MO_4]^{n-}$-complexes on the energy scale, which is accompanied by the charge transfer and is dependent on the electronegativity of an atom. It is shown that 3*d*-elements different in the oxidation degrees Ti^{4+}, V^{5+}, Cr^{5+}, and Cr^{4+}, Mn^{4+}, Mn^{5+}, and Mn^{2+}, Fe^{3+}, Co^{3+}, and Co^{2+}, Ni^{2+}, Cu^{2+}, Zn^{2+} in crystals with the sillenite structure are tetrahedrally coordinated with oxygen. The change in the oxygen stoichiometry in $Bi_{12}M_xO_{20\pm\delta}$ crystals is accompanied by the reversible change of the oxidation degrees, $Mn^{5+} \longleftrightarrow Mn^{4+} \longleftrightarrow Mn^{2+}$, $Cr^{5+} \longleftrightarrow Cr^{4+}$, and $Cu^{2+} \longleftrightarrow Cu^{+}$.

REFERENCES

1. P. Gunter and J. P. Huignard, in *Topics in Applied Physics*, Vol. 62: *Photorefractive Materials and Their Applications* (Springer-Verlag, Berlin, 1989).
2. M. P. Petrov, S. I. Stepanov, and A. V. Khomenko, *Photorefractive Crystals in Coherent Optics* (Nauka, St. Petersburg, 1992).
3. S. I. Stepanov, Rep. Prog. Phys. **57** (1), 39 (1994).
4. Yu. V. Gulyaev, V. V. Proklov, and G. N. Shkerdin, Usp. Fiz. Nauk **124** (1), 61 (1978) [Sov. Phys. Usp. **21**, 29 (1978)].
5. G. J. Berzins and M. Graser, Appl. Phys. Lett. **34** (8), 500 (1979).
6. I. S. Zakharov, *Spatial Light Modulators* (Tomsk. Univ., Tomsk, 1983).
7. V. K. Malinovskiĭ, O. A. Gudaev, V. A. Gusev, and S. I. Demenko, *Photoinduced Phenomena in Sillenites* (Nauka, Novosibirsk, 1990).
8. G. A. Babonas, *Electrons in Semiconductors*, Vol. 6: *Electronic Structure and Optical Spectra of Semiconductors*, Ed. by Yu. Pozhela (Mokslas, Vilnius, 1987), p. 41.
9. B. I. Sturman and V. M. Fridkin, *The Photovoltaic and Photorefractive Effects in Noncentrosymmetric Materials* (Nauka, Moscow, 1992; Gordon and Breach, 1992).
10. *The Physics and Applications of Photorefractive Materials*, Ed. by L. Solymer, D. J. Webb, A. Grunnet-Jepsen (Oxford Univ. Press, New York, 1996).
11. E. I. Speranskaya and A. A. Arshakuni, Zh. Neorg. Khim. **9** (2), 414 (1964).

12. E. I. Speranskaya, I. S. Rez, L. V. Kozlova, *et al.*, Izv. Akad. Nauk SSSR, Neorg. Mater. **1** (2), 232 (1965).
13. E. I. Speranskaya, V. M. Skorikov, V. A. Terekhova, and E. Ya. Rode, Izv. Akad. Nauk SSSR, Ser. Khim., No. 5, 905 (1965).
14. E. I. Speranskaya, V. M. Skorikov, G. M. Safronov, and G. D. Mitkina, Izv. Akad. Nauk SSSR, Neorg. Mater. **4** (8), 1374 (1968).
15. A. A. Ballman, J. Cryst. Growth **1**, 37 (1967).
16. V. N. Batog, V. I. Burkov, V. A. Kizel', *et al.*, Kristallografiya **14** (5), 928 (1969) [Sov. Phys. Crystallogr. **14**, 803 (1969)].
17. Yu. F. Kargin, Doctoral Dissertation in Chemistry (Inst. Obshch. Neorg. Khim. Ross. Akad. Nauk, Moscow, 1998).
18. L. G. Sillen, Ark. Kemi, Mineral. Geol., Ser. A **12** (18), 1 (1937).
19. S. C. Abrahams, P. B. Jamieson, and J. L. Bernstein, J. Chem. Phys. **47**, 4034 (1967).
20. C. Svensson, S. C. Abrahams, and J. L. Bernstein, Acta Crystallogr., Sect. B: Struct. Crystallogr. Cryst. Chem. **35**, 2687 (1979).
21. S. C. Abrahams, J. L. Bernstein, and C. Svensson, J. Chem. Phys. **71** (2), 788 (1979).
22. Sh. M. Efendiev, T. Z. Kulieva, V. A. Lomonov, *et al.*, Phys. Status Solidi A **74**, K17 (1982).
23. *International Tables for Crystallography*, Vol. A: *Space-Group Symmetry*, Ed. by T. Hahn and D. Reidel (Dordrecht, 1983), p. 589.
24. D. C. Craig and N. C. Stephenson, J. Solid State Chem. **15** (1), 1 (1975).
25. S. D. Kirik, V. A. Kutvitskiĭ, and T. I. Koryagina, Zh. Strukt. Khim. **26** (4), 90 (1985).
26. N. Rangavittal, T. N. Guru Row, and C. N. R. Rao, Eur. J. Solid State Inorg. Chem. **31**, 409 (1994).
27. S. F. Radaev, V. I. Simonov, Yu. F. Kargin, and V. M. Skorikov, Eur. J. Solid State Inorg. Chem. **29**, 383 (1992).
28. S. F. Radaev and V. I. Simonov, Kristallografiya **37** (4), 914 (1992) [Sov. Phys. Crystallogr. **37**, 484 (1992)].
29. S. F. Radaev, M. Tromel, Yu. F. Kargin, *et al.*, Acta Crystallogr., Sect. C: Cryst. Struct. Commun. **50**, 656 (1994).
30. U. Delicat, S. F. Radaev, M. Tromel, *et al.*, J. Solid State Chem. **110**, 66 (1994).
31. T. A. Mary, R. Mackay, P. Nguyen, and A. W. Sleight, Eur. J. Solid State Inorg. Chem. **33** (4), 285 (1996).
32. Yu. F. Kargin and A. V. Egorysheva, Neorg. Mater. **34** (7), 859 (1998).
33. V. A. Kizel', V. I. Burkov, Yu. I. Krasilov, *et al.*, Opt. Spektrosk. **34** (6), 1165 (1973).
34. Sh. M. Éfendiev, A. M. Mamedov, V. É. Bagiev, and G. M. Eĭvazova, Fiz. Tverd. Tela (Leningrad) **22** (12), 3705 (1980) [Sov. Phys. Solid State **22**, 2169 (1980)].
35. Sh. M. Éfendiev, A. M. Mamedov, V. É. Bagiev, and G. M. Eĭvazova, Zh. Tekh. Fiz. **51** (8), 1755 (1981) [Sov. Phys. Tech. Phys. **26**, 1017 (1981)].
36. A. A. Reza, D. B. Senulene, V. A. Belyaev, and E. I. Leonov, Pis'ma Zh. Tekh. Fiz. **5** (8), 46 (1979) [Sov. Tech. Phys. Lett. **5**, 190 (1979)].
37. V. I. Burkov, V. V. Volkov, Yu. F. Kargin, *et al.*, Kristallografiya **32** (5), 1282 (1987) [Sov. Phys. Crystallogr. **32**, 757 (1987)].
38. G. Babonas and D. Senulene, Litov. Fiz. Sb. **26** (1), 48 (1986).
39. Sh. M. Efendiev, V. E. Bagiev, A. Ch. Zeinally, *et al.*, Phys. Status Solidi A **63** (1), K19 (1981).
40. A. T. Futro, J. Phys. Chem. Solids **40** (3), 201 (1979).
41. A. B. P. Lever, *Inorganic Electronic Spectroscopy* (Elsevier, Amsterdam, 1984).
42. D. L. Greenway and G. Harbeke, J. Phys. Chem. Solids **26** (10), 1585 (1965).
43. I. V. Kityk, M. K. Zamorskii, and J. Kasperczyk, Physica B (Amsterdam) **226** (4), 381 (1996).
44. Ya. O. Dovgiĭ, M. K. Zamorskiĭ, and I. V. Kityk, Ukr. Fiz. Zh. **34** (11), 1663 (1989).
45. K. Platzöder and W. Steimann, J. Opt. Soc. Am. **58** (3), 588 (1968).
46. G. Klein and H. U. Chun, Phys. Status Solidi B **49** (1), 167 (1972).
47. K. Winzer, *Exitonen und Magnetoabsorption im Bereich der Electronen-Bandkante des Te* (Springer-Verlag, Berlin, 1962).
48. P. Grosse and K. Winzer, Phys. Status Solidi **26** (1), 139 (1968).
49. H. Stolze, M. Lutz, and P. Grosse, Phys. Status Solidi B **82** (2), 457 (1977).
50. S. Tutihasi and I. Chen, Phys. Rev. **158** (3), 623 (1967).
51. W. Henrion, Phys. Status Solidi B **22** (1), K33 (1967).
52. S. F. Marenkin, A. M. Raukhman, D. I. Pishchikov, and V. B. Lazarev, Neorg. Mater. **28** (9), 1813 (1992).
53. S. H. Wemple, Solid State Commun. **12**, 701 (1973).
54. S. H. Wemple and M. DiDomenico, Phys. Rev. B **3** (4), 1338 (1971).
55. R. Moncorge, B. Jacguer, G. Boulon, *et al.*, J. Lumin. **12/13**, 467 (1976).
56. N. M. Kalinkina, A. V. Kruzhalov, V. A. Lobach, *et al.*, Zh. Prikl. Spektrosk. **48** (5), 783 (1988).
57. B. V. Shul'gin, T. I. Polupanova, A. V. Kruzhalov, and V. M. Skorikov, *Bismuth Orthogermanate* (Ural'skoe Otd. Vneshtorgizdata, Yekaterinburg, 1992).
58. V. A. Kizel' and V. I. Burkov, *Gyrotropy of Crystals* (Nauka, Moscow, 1980).
59. J. Snir and J. Shellman, J. Phys. Chem. **77** (13), 1653 (1973).
60. V. I. Burkov, Neorg. Mater. **32** (12), 1415 (1996).
61. R. Hochstrasser, *Molecular Aspects of Symmetry* (Benjamin, New York, 1966; Mir, Moscow, 1968).
62. J. F. Nye, *Physical Properties of Crystals: Their Representation by Tensors and Matrices* (Clarendon Press, Oxford, 1964; Mir, Moscow, 1967).
63. P. V. Lenzo, E. J. Spencer, and A. A. Ballman, Appl. Opt. **5** (10), 1688 (1966).
64. V. N. Batog, V. I. Burkov, V. A. Kizel', and G. M. Safronov, Kristallografiya **16** (2), 447 (1971) [Sov. Phys. Crystallogr. **16**, 376 (1971)].
65. G. M. Safronov, V. N. Batog, Yu. I. Krasilov, *et al.*, Izv. Akad. Nauk SSSR, Neorg. Mater. **6** (2), 284 (1970).

66. V. I. Burkov, G. S. Semin, and N. M. Sitnikov, Kristallografiya **24** (5), 1060 (1979) [Sov. Phys. Crystallogr. **24**, 607 (1979)].
67. D. B. Senulene, G. A. Babonas, E. I. Leonov, *et al.*, Fiz. Tverd. Tela (Leningrad) **26** (5), 1281 (1984) [Sov. Phys. Solid State **26**, 780 (1984)].
68. V. I. Burkov, V. V. Volkov, Yu. F. Kargin, *et al.*, Kristallografiya **32** (6), 1462 (1987) [Sov. Phys. Crystallogr. **32**, 860 (1987)].
69. S. Chadrasekhar, Proc. R. Soc. London **259**, 531 (1961).
70. J. Jerphagnon and D. S. Chemla, J. Chem. Phys. **65** (4), 1522 (1976).
71. V. I. Burkov, V. V. Ivanov, V. A. Kizel', *et al.*, Opt. Spektrosk. **37** (4), 740 (1974).
72. V. I. Burkov, Yu. F. Kargin, V. V. Volkov, and N. Yu. Zubovich, Neorg. Mater. **30** (8), 1078 (1994).
73. V. I. Burkov, A. V. Egorysheva, Yu. F. Kargin, and A. A. Mar'in, Neorg. Mater. **34** (8), 962 (1998).
74. A. V. Egorysheva, V. I. Burkov, Yu. F. Kargin, *et al.*, in *Proceedings of the XVI Mendeleev Congress on General and Applied Chemistry, St. Petersburg, 1998*, Vol. 2, p. 294.
75. A. Müller, E. Diemann, and A. C. Ranade, Chem. Phys. Lett. **3** (7), 467 (1969).
76. V. I. Burkov, V. V. Volkov, Yu. F. Kargin, and N. Yu. Zubovich, Neorg. Mater. **33** (3), 372 (1997).
77. A. V. Egorysheva, V. I. Burkov, Yu. F. Kargin, and V. V. Volkov, Neorg. Mater. **31** (8), 1087 (1995).
78. V. I. Burkov, A. V. Egorysheva, Yu. F. Kargin, *et al.*, Neorg. Mater. **33** (4), 487 (1997).
79. V. I. Burkov, Yu. F. Kargin, V. V. Volkov, *et al.*, Neorg. Mater. **30** (12), 1552 (1994).
80. S. L. Hou, R. B. Lauer, and R. E. Aldrich, J. Appl. Phys. **44** (6), 2652 (1973).
81. R. E. Aldrich, S. L. Hou, and M. L. Harvill, J. Appl. Phys. **42** (1), 493 (1971).
82. V. V. Volkov, A. V. Egorysheva, and V. M. Skorikov, Neorg. Mater. **29** (5), 652 (1993).
83. A. V. Egorysheva, V. I. Burkov, Yu. F. Kargin, *et al.*, Neorg. Mater. **35** (7), 840 (1999).
84. A. V. Egorysheva, V. V. Burkov, Yu. F. Kargin, and V. M. Skorikov, in *Proceedings of the International Conference on Solid State Crystals, Materials Science, and Applications, ICSSC'98, Poland, 1998.*
85. A. K. Fidrya, *Solid State Physics* (Naukova Dumka, Kiev, 1972), p. 29.
86. K. S. Aleksandrov, A. T. Anistratov, Yu. N. Grekhov, *et al.*, Avtometriya, No. 1, 99 (1980).
87. B. C. Grabmaier and R. Oberschmid, Phys. Status Solidi A **96** (1), 199 (1986).
88. W. B. Leigh, J. J. Larkin, M. T. Harris, and R. N. Brown, J. Appl. Phys. **76** (2), 660 (1994).
89. A. V. Khomich, Author's Abstract of Candidate's Dissertation in Physics and Mathematics (Inst. Radiotekhniki i Élektroniki, Moscow, 1987).
90. C. Coya, C. Zaldo, V. V. Volkov, *et al.*, J. Opt. Soc. Am. B **13** (5), 908 (1996).
91. A. V. Egorysheva, V. V. Volkov, and V. M. Skorikov, Neorg. Mater. **31** (3), 377 (1995).
92. V. I. Burkov, Yu. F. Kargin, V. A. Kizel', *et al.*, Pis'ma Zh. Éksp. Teor. Fiz. **38** (7), 326 (1983) [JETP Lett. **38**, 390 (1983)].
93. A. V. Egorysheva and V. V. Volkov, Neorg. Mater. **30** (9), 1199 (1994).
94. V. A. Gusev, V. A. Detinenko, and A. P. Sokolov, Avtometriya, No. 5, 34 (1983).
95. Ch. Kittel, *Introduction to Solid State Physics* (Wiley, New York, 1976; Nauka, Moscow, 1978).
96. D. L. Dexter and R. S. Knox, *Excitons* (Wiley, New York, 1965).
97. T. Toyoda, H. Nakanishi, S. Endo, and T. Irie, J. Phys. C **19**, L259 (1986).
98. N. I. Anisimov and G. A. Bordovskiĭ, Opt. Spektrosk. **53** (4), 702 (1982) [Opt. Spectrosc. **53**, 417 (1982)].
99. W. Wardzynsky, H. Szymezak, and M. T. Borowiec, J. Phys. Chem. Solids **46** (10), 1117 (1985).
100. Ya. V. Buryak, A. O. Matkovskiĭ, and M. S. Karmanittskiĭ, in *Proceedings of the VII All-Union Symposium on Spectroscopy of Crystals, Leningrad, 1982*, p. 49.
101. T. V. Panchenko and N. A. Truseva, Ukr. Fiz. Zh. **29** (8), 1186 (1984).
102. V. V. Volkov, A. V. Egorysheva, Yu. F. Kargin, and V. M. Skorikov, Neorg. Mater. **29** (11), 1525 (1993).
103. V. I. Burkov, A. V. Egorysheva, Yu. F. Kargin, and V. V. Volkov, Neorg. Mater. **32** (7), 860 (1996).
104. A. B. Dubovskiĭ, A. A. Mar'in, G. A. Sidorenko, and A. A. Fotchenkov, Izv. Akad. Nauk SSSR, Neorg. Mater. **22** (11), 1874 (1986).
105. F. Ramaz, A. Hamri, B. Briat, *et al.*, Radiat. Eff. Defects Solids **136**, 99 (1995).
106. D. Nesheva, Z. Aneva, and Z. Levi, J. Phys. Chem. Solids **56** (2), 241 (1995).
107. A. V. Egorysheva, V. I. Burkov, Yu. F. Kargin, and V. V. Volkov, Neorg. Mater. **33** (5), 574 (1997).
108. V. V. Volkov, Yu. F. Kargin, A. V. Khomich, *et al.*, Izv. Akad. Nauk SSSR, Neorg. Mater. **25** (5), 827 (1989).
109. K. Nakamoto, *Infrared and Raman Spectra of Inorganic and Coordination Compounds* (Wiley, New York, 1986; Mir, Moscow, 1991).
110. A. V. Egorysheva, V. I. Burkov, and Yu. F. Kargin, in *Proceedings of the IV International Conference Crystals: Growth, Properties, Real Structure, and Applications, Aleksandrov, 1999*, Vol. 1, p. 499.
111. D. H. Brown, J. Chem. Soc. **58**, 4408 (1962).
112. R. Borromei, L. Oleari, and P. Day, J. Chem. Soc., Faraday Trans. 2 **77** (9), 1563 (1981).
113. W. Wardzynsky, H. Szymczak, K. Pataj, *et al.*, J. Phys. Chem. Solids **43** (8), 767 (1982).
114. G. Rachyukaitis, V. Gavryushin, V. Kubertavicius, and G. Puzonas, Jpn. J. Appl. Phys., Part 1 **32** (S32-3), 645 (1993).
115. M. V. Shilova, A. V. Chertkova, and V. M. Orlov, Izv. Akad. Nauk SSSR, Neorg. Mater. **20** (3), 541 (1984).
116. B. Briat, V. Topa, C. L. Boudy, and J. C. Launay, J. Lumin. **53**, 524 (1992).
117. A. V. Egorysheva, V. V. Volkov, C. Zaldo, and C. Coya, Phys. Status Solidi B **207**, 283 (1998).
118. C. Coya, J. L. G. Fierro, and C. Zaldo, J. Phys. Chem. Solids **58** (9), 1461 (1997).

119. W. Wardzynsky and H. Szymczak, J. Phys. Chem. Solids **45** (8/9), 887 (1984).
120. J. B. Milestein, J. Ackerman, S. L. Halt, and B. R. McGarvey, Inorg. Chem. **11** (6), 1178 (1972).
121. C. Simo, E. Banks, and S. L. Holt, Inorg. Chem. **9** (1), 183 (1970).
122. Xu Liang-Ying, Liu Jian-Chang, Shu Bi-Yun, and Xiao Bing, in *Proceedings of the Tenth International Conference on Crystal Growth, ICCG-10, San Diego, Calif. 1992*.
123. E. Moya, C. Zaldo, B. Brait, *et al.*, J. Phys. Chem. Solids **54** (7), 809 (1993).
124. V. I. Burkov, V. V. Volkov, Yu. F. Kargin, *et al.*, Fiz. Tverd. Tela (Leningrad) **26** (7), 2216 (1984) [Sov. Phys. Solid State **26**, 1346 (1984)].
125. T. V. Panchenko and Yu. G. Osetskiĭ, Pis'ma Zh. Tekh. Fiz. **15** (20), 20 (1989) [Sov. Tech. Phys. Lett. **15**, 795 (1989)].
126. D. Nesheva, Z. Aneva, and Z. Lewvi, J. Phys. Chem. Solids **55** (9), 889 (1994).
127. F. Mersch, K. Buse, W. Sauf, *et al.*, Phys. Status Solidi A **140** (1), 273 (1993).
128. V. I. Burkov, Yu. F. Kargin, L. T. Burkova, *et al.*, Neorg. Mater. **31** (6), 779 (1995).
129. A. V. Egorysheva, V. V. Volkov, and V. M. Skorikov, Neorg. Mater. **30** (5), 653 (1994).
130. V. I. Burkov, V. V. Volkov, Yu. F. Kargin, *et al.*, *Optics of Anisotropic Media* (Mosk. Fiz.-Tekh. Inst., Moscow, 1988), p. 58.
131. S. I. Goloshchanov, L. B. Kuleva, E. I. Leonov, *et al.*, Izv. Akad. Nauk SSSR, Neorg. Mater. **22** (5), 868 (1986).
132. L. B. Kuleva, E. I. Leonov, and V. M. Orlov, Fiz. Tverd. Tela (Leningrad) **29** (7), 2156 (1987) [Sov. Phys. Solid State **29**, 1240 (1987)].
133. M. G. Jani and L. E. Halliburton, J. Appl. Phys. **64** (4), 2022 (1988).
134. J. J. Martin, I. Foldvari, and C. A. Hunt, J. Appl. Phys. **70** (12), 7554 (1991).
135. D. W. Hart, C. A. Hunt, D. D. Hunt, *et al.*, J. Appl. Phys. **73** (3), 1443 (1993).
136. Y. Nagao and Y. Mimura, Mater. Res. Bull. **24**, 239 (1989).
137. B. Briat, A. Hamri, F. Ramaz, and H. Bou Rjeily, *Solid State Crystals: Growth and Characterization, Zakopane, 1996* (SPIE, Bellingham, 1997), Proc. SPIE **3178**, 160 (1997).
138. O. F. Schirmer and R. Schnadt, Solid State Commun. **18**, 1845 (1976).
139. R. Pappalardo and R. E. Dietz, Phys. Rev. **123** (4), 1188 (1961).
140. H. A. Weakleim, J. Chem. Phys. **36** (8), 2117 (1962).
141. D. Nesheva, Z. Aneva, and Z. Levi, J. Phys. Chem. Solids **56** (2), 241 (1995).
142. V. M. Orlov, M. V. Shilova, and E. E. Kolosov, Izv. Akad. Nauk SSSR, Neorg. Mater. **21** (3), 507 (1986).
143. Yu. F. Kargin and V. M. Skorikov, Zh. Neorg. Khim. **34** (10), 2713 (1989).
144. M. T. Borowiec, Physica B (Amsterdam) **132**, 223 (1985).
145. A. V. Egorysheva, V. I. Burkov, Yu. F. Kargin, and V. V. Volkov, Neorg. Mater. **34** (10), 1199 (1998).
146. V. Chevrier, J. M. Dance, J. C. Launay, and R. Berger, J. Mater. Sci. Lett. **15** (14), 363 (1996).
147. M. T. Borowiec, B. Kozankiewicz, T. Lukasiewicz, and J. Zmija, J. Phys. Chem. Solids **54** (8), 9555 (1993).
148. T. D. Dudkina, A. V. Egorysheva, V. V. Volkov, and V. M. Skorikov, Proc. SPIE **3734**, 408 (1999).
149. H. Bou Rjeily, F. Ramaz, D. Petrova, *et al.*, Proc. SPIE **3178**, 169 (1997).
150. M. T. Borowiec, Proc. SPIE **3178**, 173 (1997).
151. V. I. Chmyrev, V. M. Skorikov, I. V. Tsisar', *et al.*, Vysokochist. Veshchestva, No. 2, 88 (1991).
152. H. J. Reyher, U. Hellwig, and O. Thiemann, Phys. Rev. B **47** (10), 5638 (1993).
153. A. P. Eliseev, V. A. Nadolinnyĭ, and V. A. Gusev, Zh. Strukt. Khim. **23** (3), 181 (1982).
154. B. Briat, H. J. Reyher, A. Hamri, *et al.*, J. Phys.: Condens. Matter **7**, 6951 (1995).
155. E. A. Kravchenko, V. G. Orlov, Suan Hai Fam, and Yu. F. Kargin, Z. Naturforsch. A **53**, 504 (1998).

Translated by L. Man

Crystallography Reports, Vol. 46, No. 2, 2001, pp. 336–337. Translated from Kristallografiya, Vol. 46, No. 2, 2001, pp. 381–382.

JUBILEES

Kirill Sergeevich Aleksandrov (On the Occasion of His 70th Birthday)

Kirill Sergeevich Aleksandrov was born on January 9, 1931, in Leningrad (St. Petersburg). In 1948, he entered the Leningrad Electrotechnical Institute, from which he graduated with distinction. He began his scientific activity as a postgraduate student under the guidance of Academician A.V. Shubnikov at the Institute of Crystallography of the USSR Academy of Sciences. After his postgraduate course, he was invited to the newly opened Institute of Physics of the Siberian Division of the USSR Academy of Sciences in Krasnoyarsk.

The first fundamental results obtained by Aleksandrov are related to the laws of propagation of elastic waves and the elastic properties of anisotropic media. In particular, he was the first to perform the systematic studies of elastic properties of the main rock-forming minerals. He discovered and studied the phenomenon of internal conical refraction and the rotation of polarization planes of elastic waves as well as the laws of reflection and refraction processes of elastic waves in various media. He also developed the methods for measuring elasticity tensors for media of arbitrary symmetries and designed and constructed new ultrasonic devices for studying elastic properties of crystals, textures, and rocks. The results of these studies gave rise to a new field of crystal physics—the so-called acoustic crystallography—and, in particular, were used for designing new acoustoelectronic devices. Some years ago, Aleksandrov returned to the investigation of anisotropy in elastic properties of rocks and minerals and wrote (in cooperation with G.T. Prodaĭvoda, Kiev University, Ukraine) a monograph about this effect, which is now in press.

The pioneering research of the structural phase transitions performed by Aleksandrov has received world recognition. The complex experiments, combined with the theoretical study and creation of the respective theory, allowed Aleksandrov to establish the nature and the mechanisms of structural transformations in numerous ferroelectrics and the related crystals, to discover a number of new ferroelectric structures, and to interpret the sequence of the ordering-type (the model of two and more sublattices, a model with the multiminimum potential) and displacive (condensation of several soft modes of different nature) phase transitions.

All of these studies have made a considerable contribution to understanding the nature of structural instability; possible structural distortions; and the related changes in the dielectric, optical, and other properties of numerous crystals used in modern technology as well as radio-, acousto-, and optoelectronics. They have also provided the development of various methods for synthesis and directional modification of the properties of solid materials for acousto- and magnetooptical applications and designing new devices on the basis of these materials. In 1989, Aleksandrov and his coauthors were awarded the State Prize for the studies of new materials and the design of new devices based on these materials. The purposeful complex study of the structure, crystal chemistry, physical properties, and phase transitions in solids performed under Aleksandrov's supervision and with his direct participation provided the elaboration of the unique approach to the description of large families of crystals, including the materials for modern laser technology and optoelectronics, and high-temperature superconductors. These studies were highly estimated by the scientific community, and in 1999, Aleksandrov was awarded the Fedorov Prize of the Russian Academy of Sciences. In

1063-7745/01/4602-0336$21.00 © 2001 MAIK "Nauka/Interperiodica"

recent years, such studies were actively developed both in Russia in cooperation with the research centers of Moscow and Novosibirsk and with institutions in Spain, France, and some other countries.

Aleksandrov managed to create an efficient, intensely developing scientific school. Four of his students became Doctors of Sciences and several dozen, Candidates of Sciences. For a number of years, Aleksandrov has headed the department of Solid State Physics at the Krasnoyarsk State University; he is also chairman of the Krasnoyarsk Research and Educational Center of High Technologies organized at the Institute of Physics of the Krasnoyarsk State University, the Krasnoyarsk Technical University, and the Aerospace Academy of Siberia within the State Program of Integration of Fundamental Science and Higher Education.

Aleksandrov is an author of more than 350 scientific publications, including eight monographs. He organized and was an active participant of numerous Russian and International scientific conferences, including the National Conferences on Physics of Ferroelectrics and Ferroelastics and Russian–Japanese and Russian–American Symposia on Ferroelectricity.

Aleksandrov is the head of the Scientific Council on Physics of Ferroelectrics and Dielectrics of the Russian Academy of Sciences and a member of some other scientific councils of the Russian Academy of Sciences, a member of the Joint Scientific Council on Physicotechnical Sciences of the Siberian Division of the Russian Academy of Sciences, and a member of a number of editorial boards of several prestigious national and international scientific journals.

Aleksandrov has been awarded the Order of Friendship between Peoples and twice has received the Order of the Red Banner of Labor.

Editorial Board of “Kristallografiya” congratulates Kirill Sergeevich Aleksandrov with his jubilee and wishes him good health and success in his research for many years to come.

Translated by L. Man

Crystallography Reports, Vol. 46, No. 2, 2001, p. 338. Translated from Kristallografiya, Vol. 46, No. 2, 2001, p. 383.

JUBILEES

Leonid Nikolaevich Rashkovich (On the Occasion of His 70th Birthday)

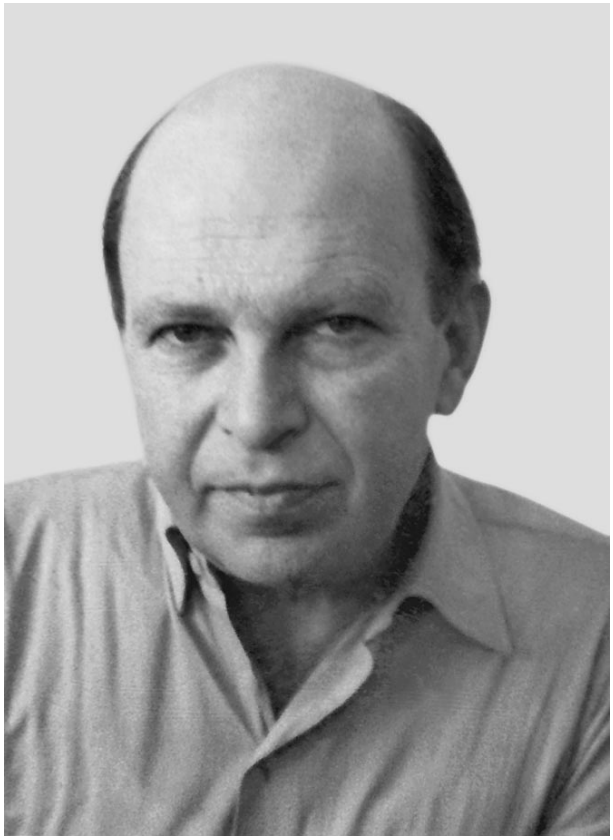

On February 28, 2001, Doctor in Physics and Mathematics Leonid Nikolaevich Rashkovich, one of the most prominent figures in the theory of crystal growth and growth from solutions, an intelligent, gifted, modest, and charming person, celebrated his seventieth birthday.

Irrespective of the place of a new publication on crystal growth from solution, its authors inevitably refer to the fundamental studies performed in this field by Rashkovich.

It is the Rashkovich method that is nowadays used to grow 1-m-long crystals (the largest in the world) necessary for laser pumping in controlled thermonuclear synthesis.

Rashkovich is a hard worker who is not afraid to meet any difficulties; he works systematically and persistently and, most importantly, knows the way to reach his goals. He also manages to inculcate the taste for such work in his numerous colleagues and students. As a teacher, Rashkovich is very sorry to see his students scattered in growth laboratories throughout the whole world, but, being a very understanding person, he always does his best to organize trips.

Rashkovich is completely absorbed by his scientific search. His innate intuition and many years of experience allow him to penetrate into the crux of the matter. Therefore, it is not surprising that, while observing an interference pattern or an atomic-force micrograph of a crystal face already thoroughly examined by his colleagues, Rashkovich comes to quite surprising and original conclusions. He can endlessly discuss the kinks on the steps, stoppers on the faces, one-dimensional nucleation, asymmetry of dislocation hillocks, and the methods for measuring fluctuations on steps. He is devoid of vanity, never dissipates his talents for trifles, and always concentrates his efforts on the main problems. He is always ready to meet his colleagues in Nizhni Novgorod, Kharkov, Obninsk, or in the United States, because he believes scientific communication to be a necessary element for progress in science.

The last three years were especially fruitful for Rashkovich: he wrote a number of original articles, where he finally confirmed (on an example of the protein lysozyme) the experimental model of one-dimensional nucleation suggested by Voronkov as far back as 1970. He also designed new scientific instruments. He supervised the design and the construction of a combined atomic-force and interference microscope necessary for the detailed studies of crystal growth from solutions.

The editorial board of *Kristallografiya* congratulates Rashkovich on his 70th birthday and wishes him good health and every success in his scientific work for many years to come.

Translated by L. Man

1063-7745/01/4602-0338$21.00

Crystallography Reports, Vol. 46, No. 2, 2001, p. 339. Translated from Kristallografiya, Vol. 46, No. 2, 2001, p. 384.

INFORMATION

The Results of the *2000 Struchkov Prize* Competition for Young Scientists and the Announcement of the 2001 Competition

The Struchkov Prize is awarded annually (since 1997) for the best scientific study in crystal chemistry and the application of X-ray structure analysis to the solution of chemical problems. Researchers who are residents of the Commonwealth of Independent States or the Baltic states and who are under 36 years of age at the time of the presentation of their documents are invited to participate in the competition. Each scientific study is presented on behalf of a single author, and each author is allowed to present only one work a year. The results presented to the competition should be stated in at least one published article or be submitted for publication in a journal that participates in the judging process. The winner of the competition is determined by the decision of the special competition jury, which is formed by the leaders of the Center of X-ray Structure Studies and consists of leading Russian scientists in crystal chemistry and X-ray structure analysis. The decision of the jury is announced no later than November 1 of the current year.

The 2000 Struchkov Prize was awarded to É.B. Rusanov, a researcher from the Institute of Organic Chemistry, National Academy of Sciences of Ukraine, Kiev, for his study entitled "$\sigma^3\lambda^5$-Iminophosphoranes: Specific Features of the Spatial Electronic Structure and Chemical Properties." The winner of the competition received a diploma and a monetary award. In addition, four incentive prizes were awarded. The winners are I.S. Neretin (Moscow), A.V. Olenev (Moscow), A.V. Churakov (Moscow), and G.K. Fukin (Nizhni Novgorod).

Since 2000, the competition has been sponsored by the Struchkov Prize Society, which is an International crystallographic association of former students and colleagues of Yu.T. Struchkov. The 2000 prize amounted 20000 rubles and the incentive prizes amounted 2500 rubles each. A winner of the incentive prize is allowed to participate in future competitions.

To take part in the 2001 competition, a competitor should present the following documents to the Center of X-ray Structure Studies no later than June 15, 2001:

1. A completed competitor form including:

(a) his/her full name;

(b) title of the scientific study presented to the competition;

(c) date of birth;

(d) scientific degree and post;

(e) affiliation;

(f) postal address of the institution;

(g) office telephone;

(h) fax;

(i) e-mail.

2. An abstract of the study (not exceeding three standard pages) containing the indication of the competitor's contribution to the study.

3. A list of published (or submitted for publication) papers related to the subject of the study presented to the competition.

4. Reprints or Xerox copies of all or some of these papers (at the author's descretion).

The documents should be sent to the Center of X-ray Structure Studies, Nesmeyanov Institute of Organoelement Compounds, Russian Academy of Sciences (ul. Vavilova 28, Moscow, 117813 Russia).

The data indicated in paragraphs 1–3 should be presented to the jury as MS DOS ASCII files. The files can be sent by post on a diskette or by e-mail to the following address: premiya@xrlab.ineos.ac.ru.

For further information, contact the center by tel. (095) 135-9271 or by e-mail at the following address: star@xrpent.ineos.ac.ru.

Translated by I. Polyakova

1063-7745/01/4602-0339$21.00 © 2001 MAIK "Nauka/Interperiodica"